

INTEGRATED PHOTONICS RESEARCH

Sponsored by

U.S. Air Force Office of Scientific Research

U.S. Army —Harry Diamond Laboratory

National Science Foundation

U.S. Office of Naval Research

Defense Advanced Research Projects Agency

for

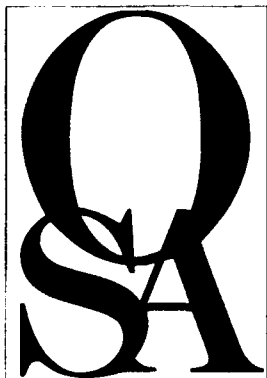
IEEE/Lasers and Electro-Optics Society

Optical Society of America

1992 TECHNICAL DIGEST
SERIES VOLUME 10

APRIL 13–16, 1992
NEW ORLEANS, LOUISIANA





Integrated Photonics Research

*Summaries of papers presented at the
Integrated Photonics Research Topical Meeting*

April 13-16, 1992
New Orleans, Louisiana

1992 Technical Digest Series
Volume 10

CONFERENCE EDITION

Sponsored by
U.S. Air Force Office of Scientific Research
U.S. Army--Harry Diamond Laboratory
National Science Foundation
U.S. Office of Naval Research
Defense Advanced Research Projects Agency

IEEE/Lasers and Electro-Optics Society
Optical Society of America

Optical Society of America
2010 Massachusetts Avenue NW
Washington DC 20036

92-22452



92 8 7 087

392813

415

Approved for public release
distribution is unlimited

AIR FORCE OFFICE OF SCIENTIFIC RESEARCH
NOTATION OF INTEREST
THIS DOCUMENT IS UNCLASSIFIED
DATE 10-12-2001 BY 10101
PER 10101
PROJECT (AF60)
1992-22452-12

Articles in this publication may be cited in other publications. In order to facilitate access to the original publication source, the following form for the citation is suggested:

Name of Author(s), Title of Paper, in Integrated Photonics Research, Vol. 10, OSA
Technical Digest Series, (Optical Society of America, Washington, DC 1992), pp. xx-xx.

ISBN Number

Conference Edition	1-55752-231-6
Postconference Edition	1-55752-232-4
1991 Technical Digest Series	1-55752-261-8

Library of Congress Catalog Card Number

Conference Edition	92-80617
Postconference Edition	92-80618

Copyright © 1992, Optical Society of America

Individual readers of this digest and libraries acting for them are permitted to make fair use of the material in it, such as to copy an article for use in teaching or research, without payment of fee, provided that such copies are not sold. Copying for sale is subject to payment of copying fees. The code 1-55752-261-8/92/\$2.00 gives the per-article copying fee for each copy of the article made beyond the free copying permitted under Sections 107 and 108 of the U.S. Copyright Law. The fee should be paid through the Copyright Clearance Center, Inc., 21 Congress Street, Salem, MA 01970.

Permission is granted to quote excerpts from articles in this digest in scientific works with the customary acknowledgment of the source, including the author's name and the name of the digest, page, year, and name of the Society. Reproduction of figures and tables is likewise permitted in other articles and books provided that the same information is printed with them, permission of one of the original authors is obtained, and notification is given to the Optical Society of America. Republication or systematic or multiple reproduction of any material in this digest is permitted only under license from the Optical Society of America; in addition, the Optical Society may require that permission also be obtained from one of the authors. Address inquiries and notices to the Director of Publications, Optical Society of America, 2010 Massachusetts Avenue, NW, Washington, DC 20036. In the case of articles whose authors are employees of the United States Government or its contractors or grantees, the Optical Society of America recognizes the right of the United States Government to retain a nonexclusive, royalty-free license to use the author's copyrighted article for United States Government purposes.

The views and conclusions contained in this document are those of the author(s) and should not be interpreted as necessarily representing the official policies or endorsements, either expressed or implied, of the Air Force Office of Scientific Research, the Office of Naval Research, the Department of the Army, or the U.S. government.

This material is based upon work supported by the National Science Foundation. Any opinions, findings, and conclusions or recommendations expressed in this publication are those of the author(s) and do not necessarily reflect the views of the National Science Foundation.

AGENDA OF SESSIONS

Sunday, April 12, 1992				
	LE SALON	LA SALLE BALLROOM A		
6:00 pm-8:00 pm	Registration	Informal Reception		

Monday, April 13, 1992				
7:30 am-5:30 pm	THIRD FLOOR FOYER Registration and Speaker Check-in			
8:30 am-11:15 am	LA SALLE BALLROOMS B & C MA, Plenary Session LA SALLE BALLROOM A 10:30 am-11:00 am COFFEE BREAK			
11:15 am-12:30 pm	LA SALLE BALLROOMS B & C MB, Poster Preview Session			
12:30 pm-1:30 pm	Lunch Break			
	LA SALLE BALLROOM B	LA SALLE BALLROOM C	PELICAN ROOM	POYDRAS ROOM
1:30 pm-3:30 pm	MC, Quantum Confinement and Vertical Cavity Devices	MD, Device Simulations	ME, Acousto-optic and Magneto-optic Devices	MF, Spatial Solitons and Planar Waveguide Phenomena
3:30 pm-5:00 pm	LA SALLE BALLROOM A MG, Poster Session			

DTIC QUALITY INSPECTED 5

Accession For	
NTIS CRA&I	<input checked="" type="checkbox"/>
DTIC TAB	<input type="checkbox"/>
Unannounced	<input type="checkbox"/>
Justification	
By	
Distribution /	
Availability Codes	
Dist	Avail and/or Special
A-1	

AGENDA OF SESSIONS—Continued

Tuesday, April 14, 1992			
7:30 am–5:30 pm	THIRD FLOOR FOYER Registration and Speaker Check-in		
	LA SALLE BALLROOM B	LA SALLE BALLROOM C	POYDRAS ROOM
8:30 am–10:00 am	TuA, Optoelectronic Integrated Circuits	TuB, Systems and Components	TuC, Second Harmonic Generation and Waveguides
10:00 am–10:30 am	LA SALLE BALLROOM A COFFEE BREAK		
10:30 am–12:00 m	TuD, Dielectric Waveguides and Devices	TuE, Guided-Wave Structures	TuF, Nonlinear Fiber Phenomena
12:00 m–1:30 pm	Lunch Break		
1:30 pm–3:30 pm	TuG, Electrooptic Devices	TuH, Novel Materials and Processing	TuI, Optical Fiber Solitons
3:30 pm–4:00 pm	LA SALLE BALLROOM A COFFEE BREAK		
4:00 pm–5:30 pm	TuJ, Postdeadline Paper Session		
6:00 pm–7:30 pm	LES CONTINENT ROOM Conference Reception		

Wednesday, April 15, 1992			
8:00 am–3:00 pm	THIRD FLOOR FOYER Registration and Speaker Check-in		
	LA SALLE BALLROOM B	LA SALLE BALLROOM C	POYDRAS ROOM
8:30 am–10:30 am	WA, All-Optical Switching	WB, Waveguide and Device Technology	WC, Lasers: 1
10:30 am–11:00 am	LA SALLE BALLROOM A COFFEE BREAK		
11:00 am–12:30 pm	WD, Special Purpose Glasses and Fiber Amplifiers	WE, Beam Propagation Methods	WF, Lasers: 2
12:30 pm–1:30 pm	Lunch Break		
1:30 pm–3:30 pm	WG, Optical Fiber Devices		WH, Semiconductor Waveguides and Devices

Monday, April 13, 1992

Plenary Session

MA 8:30 am–11:15 am
La Salle Ballrooms B & C

Larry A. Coldren, *Presider*
University of California, Santa Barbara
Raymond J. Hawkins, *Presider*
Lawrence Livermore National Laboratory
William K. Burns, *Presider*
U.S. Naval Research Laboratory

8:30 am—MA1 (Invited)

Erich P. Ippen, *Massachusetts
Institute of Technology*

9:15 am—MA2 (Invited)

D. C. Hanna, *University of
Southampton, U.K.*

10:00 am—10:30 am

COFFEE BREAK

10:30 am—MA3 (Invited)

H. S. Hinton, *AT&T Bell
Laboratories.*

Monday, April 13, 1992

Poster Preview

MB 11:15 am–12:30 pm
La Salle Ballrooms B & C

Larry A. Coldren, *Presider*
University of California, Santa Barbara
Raymond J. Hawkins, *Presider*
Lawrence Livermore National Laboratory

MB1-1

Some optical properties of waveguides made by high energy ion implantation in fused silica

J. Albert, B. Malo, D. C. Johnson, K. O. Hill

Communications Research Centre, P.O.Box 11490, Station H, Ottawa CANADA K2H 8S2
(613-990-7690)

J. L. Brebner, Y. B. Trudeau, G. Kajrys

Groupe des Couches Minces, Université de Montréal, Montréal (Qué) CANADA H3C 3J7

It is known that implantation of dopants in amorphous silica increases the refractive index, and therefore may lead to the formation of an optical waveguide¹. The ion implantation is usually carried out at energies of a few hundred keV, yielding waveguides with losses of the order of 1 dB/cm. In this work, we used much higher energies (3 and 5 MeV) to implant Germanium in pure synthetic fused silica². The objective is to obtain a planar waveguide which would resemble the core of a standard Ge-doped single mode optical fiber, and to study the photosensitive effects which have been observed in these fibers³. We have already shown that these waveguides are very photosensitive to ultraviolet light from a KrF excimer laser². The new results reported here concern annealing experiments, controlled bleaching, and photoluminescence of these samples.

At the energies used, the implanted layer is one μm thick and lies between 2 and 3 μm below the surface. The first result is that implantation increases significantly the absorption in the UV spectral region² (Figure 1). The absorption can be resolved into three main bands centered respectively near 244 nm, 212 nm and beyond 190 nm. Upon exposure of the implanted layer to individual 100 mJ pulses from a KrF excimer laser (operating at 249 nm), the 244 nm band is gradually bleached, and the absorption eventually disappears totally. Figure 2 shows the measured absorbance after each one of a series of individual laser

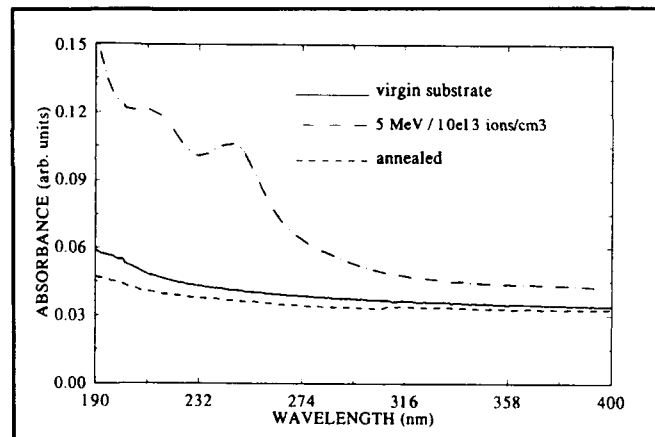


Figure 1 Absorbance spectrum of pure, implanted, and heated implanted silica

pulses (solid lines) and also after a prolonged exposure (two minutes at 50 pps, dashed line). Another method for restoring transparency in the UV spectral region is to heat the samples to 1200°C which is slightly above the annealing temperature of silica (Figure 1).

For implantation doses of 10^{13} ions/cm² and higher, a refractive index increase of the order of 1% is measured. The implantation induced refractive index decreases back to near its original value with both UV bleaching and thermal annealing. It will be of interest to determine if the index change can be correlated with the gradual absorption change observed with shot-by-shot bleaching.

Finally, we measured the fluorescence of the implanted samples under various conditions. The 249 nm KrF excimer laser operating at 2 Hz for 5 pulses was used to pump the samples in the fluorescence measurements. Some of the first results are shown in Figure 3. We see that the bleaching changes the fluorescence spectrum drastically, with the "blue" (470 nm) band

disappearing completely while the "red" (640 nm) band is still strong. The initial spectrum (dotted line) is typical of implanted fused silica. Bleaching eliminates the blue band but the red one remains, in spite of the fact that the absorption at 249 nm has been reduced significantly (continuous line). A possible explanation would be that bleaching changes the state of the glass to one where two-photon absorption becomes significant; two 249 nm photons (at 5 eV each) together bring the energy above the SiO₂ bandgap (9 eV).

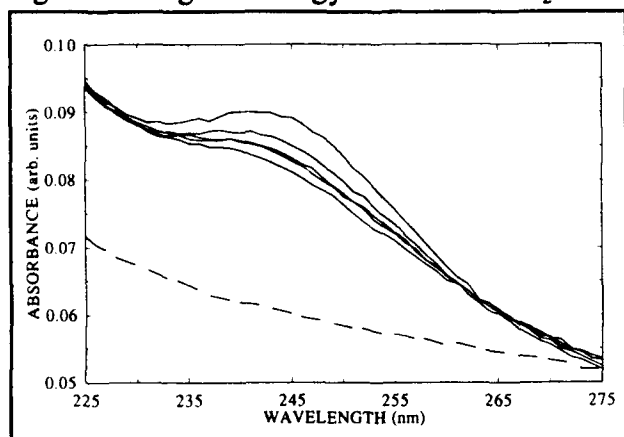


Figure 2 Shot by shot bleaching of 244 nm band and total bleaching after long exposure

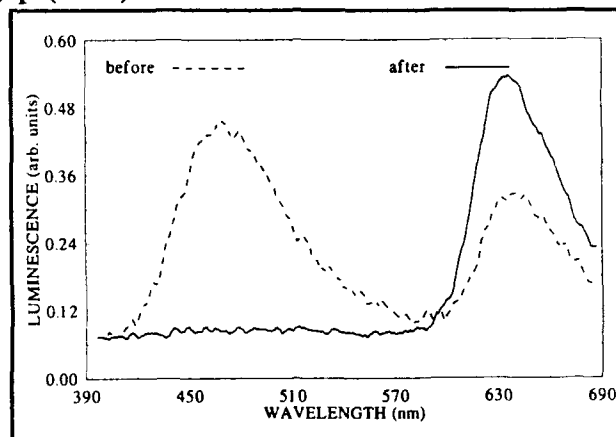


Figure 3 Fluorescence of sample before and after UV bleaching

The strong photosensitivity observed in these samples is believed to be due to the large number of defects created during the relatively high energy implantation. The 212 nm band is associated with the E' defect of silica, generally held responsible for the photosensitivity in Ge-doped fibers. One problem for integrated optics use of this phenomenon is that along with strong photosensitivity, the high ion energy causes some structural damage in the glass, leading to high waveguide losses. But since the photosensitivity is currently much larger than useful values in fibers³, there is room for a trade-off which would reduce the losses to acceptable levels while maintaining a sufficient index change; especially if the implantation is not used to define the waveguide but rather to modify an existing one, to form a grating for instance.

REFERENCES

- [1] R. Th. Kersten and H. Boroffka, "Ion implantation into fused quartz for integrated optical circuits", *Opt. Comm.* **17**, 119-123 (1976)
- [2] Albert, J., K. O. Hill, B. Malo, D. C. Johnson, J. L. Brebner, Y. B. Trudeau, G. Kajrys, "Formation and bleaching of strong ultraviolet absorption bands in germanium implanted synthetic fused silica," accepted for publication in *Applied Physics Letters*
- [3] B. Malo, K. A. Vineberg, F. Bilodeau, J. Albert, D. C. Johnson, K. O. Hill, "Ultraviolet light photosensitivity in Ge-doped silica fibres: Wavelength dependence of the light-induced index change", *Opt. Lett.* **15**, 953-955 (1990)

**STRAIN INDUCED OPTICAL WAVEGUIDING AND
POLARIZATION CONVERSION IN FERROELECTRIC SUBSTRATES**

O. Eknoyan, H.F. Taylor, Z. Tang, V.P. Swenson and J.M. Marx
Department of Electrical Engineering
Texas A&M University
College Station, TX 77843
(409) 845-7441

A localized increase in the refractive index of ferroelectric crystals has been accomplished by the use of static strain induced from a surface film. The technique does not require alteration of substrate composition by diffusion or ion exchange¹⁻³. Optical waveguides have been produced by this method in LiNbO_3 , LiTaO_3 and BaTiO_3 . This represents the first formation of waveguides in BaTiO_3 , which is ideally suited for making compact low-voltage polarization control guided-wave devices and optical filters due to its large r_{51} electrooptic coefficient.

To produce an index increase, a thick film of SiO_2 is deposited on the substrate surface at an elevated temperature then cooled to room temperature and patterned. The static strain resulting from the large thermal expansion mismatch between the substrate and film causes a localized index increase in the crystal beneath regions from which the SiO_2 is removed, as in Fig. 1-a, via the strain optic effect. The resultant change in the index of refraction is related to the strain-optic, piezoelectric, and electrooptic properties of the substrate⁴. Figure 1-a shows calculated strain (or strain-induced index change) contours referenced to the value of strain at the surface of the substrate in the center of the etched channel window. In initial waveguides investigations, films $\sim 3 \mu\text{m}$ thick were deposited by e-beam evaporation on substrates that were maintained at $\sim 300^\circ\text{C}$ during deposition. Using photolithography, straight channel patterns were then delineated by reactive ion etching.

Optical guiding was observed for both TE and TM polarizations using end-fire coupling at $0.633 \mu\text{m}$ wavelength in LiNbO_3 and LiTaO_3 , and at $0.83 \mu\text{m}$ in BaTiO_3 . Near field patterns for TE polarization in a single mode waveguide in LiNbO_3 are shown in Fig 1-b. Propagation losses of 0.8 dB/cm and 0.9 dB/cm for TE and TM polarizations, respectively, were measured by sampling the surface scattered light from the waveguides on LiNbO_3 . Electrooptic polarization modulation was investigated in a strain induced straight channel waveguide formed on LiNbO_3 . By passing the waveguide

output through a linear polarizer, a modulation depth of 92% was obtained, and a value of 0.3 was calculated for the electrical/optical field overlap factor. Polarization conversion has been demonstrated in Zn diffused LiTaO_3 waveguides using a spatially periodic strain-inducing film to obtain TE-TM phase matching. A maximum value of 88% was observed for the conversion efficiency which, as expected, was highly wavelength selective.

In conclusion, optical channel waveguides have been produced in LiNbO_3 , LiTaO_3 and BaTiO_3 crystals utilizing a strain induced index increase, and electrooptic modulation has been demonstrated in strain induced waveguides. Losses of less than 1 dB/cm have been measured in each polarization in LiNbO_3 . The fabrication procedure is quite simple, and the waveguides can be deleted by etching away the SiO_2 film. The method may be applicable to other materials in which waveguide formation is difficult. Furthermore, polarization conversion has been demonstrated in LiTaO_3 using a spatially periodic strain inducing film.

References

1. I.P. Kaminow and J.R. Carruthers, *Appl. Phys. Lett.*, **22**, 326 (1973).
2. R.V. Schmidt and I.P. Kaminow, *Appl. Phys. Lett.*, **25**, 458 (1974).
3. J.L. Jackel, *Appl. Phys. Lett.*, **37**, 379 (1980).
4. D.A. Pinnow, in *Handbook of lasers*, R.J. Pressley ed., (CRC, Cleveland, OH, 1971) p. 478.

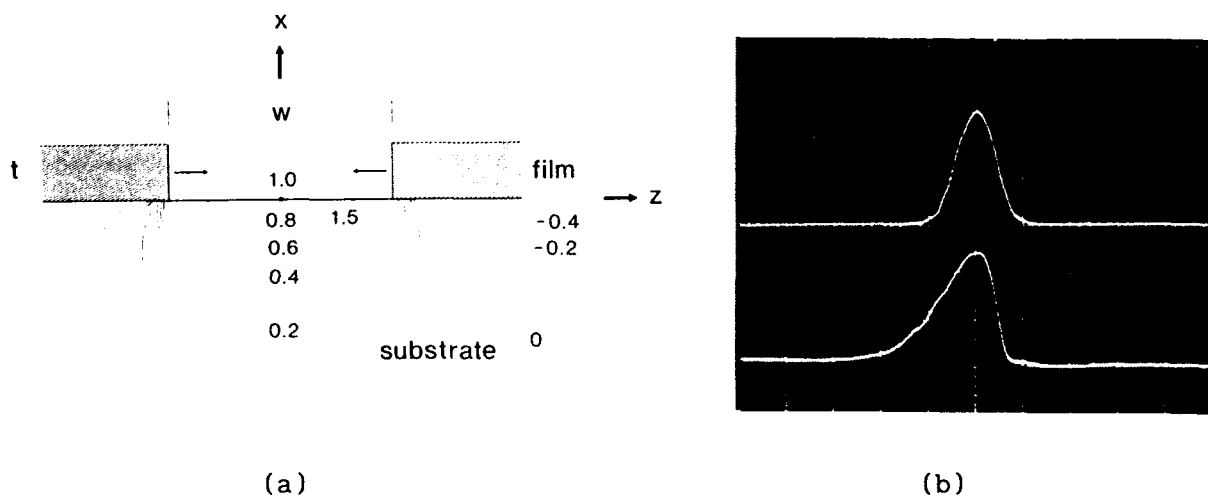


Fig.1. Strain-induced optical waveguides. (a) Calculated constant strain contours drawn normalized relative to the value at the surface of the substrate in the center of the channel. (b) Near-field pattern for TE polarization of a single mode LiNbO_3 waveguide, upper trace is transverse scan with horiz. scale of $10 \mu\text{m}/\text{div}$ and lower trace is depth scan with horiz. scale of $5 \mu\text{m}/\text{div}$.

MB3-1

Ion-exchanged glass waveguides with improved coupling to semiconductor lasers

Janet Lehr Jackel and Shiqing Hu
Bell Communications Research
Red Bank, NJ 07701

Introduction: Ion exchanged glass waveguide components can perform many functions needed in optical communications, but will find a use in communications networks only if insertion losses are low enough. Exchanged guides have been made with low optical propagation loss, and channel guides with excellent coupling to optical fiber have been made.^[1] In some cases, however, we require direct coupling to semiconductor lasers, which have much smaller mode size than fibers. A small mode size also serves to minimize losses in waveguide bends.

We show here that exchanged guides with a large enough Δn and small enough mode size can have low laser-to-guide coupling loss. The usual single-step exchange is of limited use: guides with large Δn can be made, but sideways diffusion creates guides which are considerably wider than they are deep. Using an alternative two-step process^[2] we are able to improve the mode shape and obtain better coupling to lasers.

Waveguide fabrication: Substrates are BK7 glass, an optical quality glass containing sufficient sodium ions to be useful in ion exchange. Low-loss guides can be formed in BK7 using either silver-sodium or potassium-sodium exchange. For our purposes, only silver-sodium exchange is useful, since the maximum index change available with $K^+ - Na^+$ exchange is less than 0.01, too small for laser-compatible guides. In addition, silver exchanged guides are nearly polarization independent, unlike potassium-exchanged guides where stress induced birefringence can be large.^[3]

In order to optimize laser-to-guide coupling it is necessary to match the laser mode as nearly as possible. We have used a buried heterostructure laser,^[4] operating at $\lambda = 1.52 \mu\text{m}$, with a mode approximately $1.5 - 2.0 \mu\text{m}$ wide and deep. The output beam spreads with an angle of $\sim 25^\circ$ in both horizontal and vertical directions. To match this output, we require a similar sized mode, and a guide with the equivalent of a step index increase of $\sim 0.06 - 0.07$. We can achieve index increases of this size using silver-sodium exchange in a mixture of NaNO_3 , KNO_3 , and AgNO_3 in the ratio 1 Mole : 1

Mole : x Moles, with x ranging from 5 to 20. Both maximum index change and diffusion coefficient depend on melt composition. Our initial measurements have been made with exchange in a melt having $x = 5$, although higher silver concentrations may give better results.

Guides were made using either the usual single-step or a two-step exchange. Single-step exchanged guides were made using an aluminum mask with openings $3 - 15 \mu\text{m}$ wide and exchange times of 2, 3, and 4 hours. For the two-step process, a planar exchanged guide is made, and then a mask consisting of $3 - 15 \mu\text{m}$ wide aluminum lines is used as mask against back diffusion of sodium. Because of diffusion under the mask, guides made with the single-step exchange are always *wider* than the mask opening which defines them, while guides made using a two-step exchange are *narrower* than the mask. After exchange, guides were polished and the losses were measured using the semiconductor laser as input.

Loss measurements: For laser to guide coupling, the laser is brought nearly into contact with the end of the guide, and the output face of the guide is imaged onto a detector using a microscope objective with a large enough numerical aperture ($NA = 0.57$) to capture all the light from the laser. Losses for direct laser coupling to a guide made using single step exchange are shown in Fig. 1, for samples exchanged 2, 3, and 4 hours. Guides exchanged for 4 hours are double-moded; coupling into the fundamental mode is shown. All other guides are single moded. Measured loss includes coupling, propagation through $\sim 3 \text{ cm}$ of guide, and Fresnel loss of $\sim 1.8 \text{ dB}$ at both input and output.

Our coupling of 25-50% is considerably better than the 10% typical of butt-coupling to single mode fibers, and compares well with the 70% coupling recently achieved with lensed fiber. However, the most efficient coupling was obtained only in guides having two modes. This is the result of diffusion under the mask which makes the guide wider than it is deep.

Two-step exchange can offer an improvement over single-step exchange for two reasons. First, since the

original exchange which introduces silver ions into the substrate is made without a mask, we avoid the limiting of surface index^[5] and guide depth^[6] which occurs when there is a finite mask opening. Second, the reverse exchange which defines the channel guides creates a guiding region *narrower* than the mask which protects the exchanged surface. Thus, the inevitable side diffusion becomes an asset.

Fig. 2 shows laser-to-guide coupling loss for a two-step exchanged guide with an original exchange time of 2 hours and a back-exchange time of 30 minutes. Comparison with guides made using a 2 hour single-step exchange (also shown in Fig. 2) demonstrates the substantial advantage of the two-step exchange; the best two-step guides have 4 dB less loss than the best single-step guides. Measurements are in progress to evaluate the effect of the two step process in guides with longer initial exchange times.

Discussion: The use of guides with high Δn makes efficient coupling to lasers possible, and the use of a two-step exchange process allows further improvement of the match between laser and guide modes. Low-loss thermal tapering from the laser-compatible to the fiber-compatible mode sizes is feasible; our preliminary results show that thermal annealing of the guides described above can produce guides with less than 1.3 dB fiber-to-guide coupling loss, including reflection and propagation losses. Thus, use of a two-step exchange followed by thermal tapering of the guides should make it possible to couple from laser to device to fiber with no greater loss than direct coupling to an unlensed fiber.

REFERENCES

1. Huo Zhenguang, Ramakant Srivastava, and Ramu V. Ramaswamy, *J. Lightwave Technol.* **7**, 1590-1595 (1989).
2. P. Poyhonen, S. Honkanen, and A. Tervonen, *Opt. Lett.* **15**, 1206-1208 (1990).
3. A. Brandenburg, *J. Lightwave Technol.*, **LT-4**, 1580-1590 (1986).
4. C. E. Zah, R. Bhat, B. Panthak, C. Caneau, F. J. Favire, N. C. Andreadakis, D. M. Hwang, M. A. Koza, C. Y. Chen, and T. P. Lee, *Electron. Lett.* **27**, 1414-1415 (1991).
5. R. A. Betts, F. Lui, and T. W. Whitbread, *Appl. Opt.* **30**, 4384-4389 (1991).
6. A. Miliou, H. Zhenguang, H. C. Cheng, R. Srivastava, and R. V. Ramaswamy, *IEEE J. Quantum Electron.* **25**, 1889-1897 (1989).

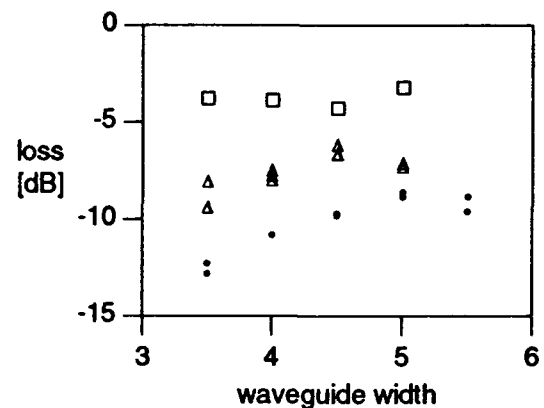


Fig. 1 Laser-to-waveguide coupling losses, for single-step exchanged guides: exchanged \square 4 hours, Δ 3 hours, and \bullet 2 hours.

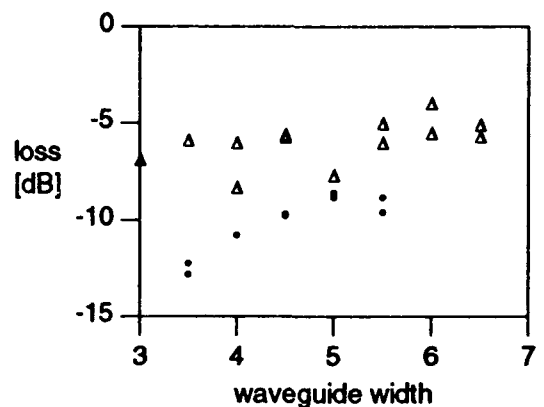


Fig. 2 Laser-to-waveguide coupling losses comparing 2 hour single-step (\bullet) and two-step (Δ) exchange with 2 hour planar exchange and 30 minute back-exchange.

Linear and Nonlinear Optical Properties of Annealed Proton Exchanged Lithium Niobate Waveguides

M. L. Bortz and M. M. Fejer

Edward L. Ginzton Laboratory, Stanford University, Stanford, CA 94305
(415) 725-2160

Annealed proton exchange (APE) is an important technique for the fabrication of waveguides in LiNbO_3 for electrooptic and nonlinear optical applications. Unannealed proton exchanged (PE) waveguides have step-like refractive index profiles and large extraordinary refractive index changes, but suffer from reduced electrooptic and nonlinear coefficients. Post-exchange annealing is necessary to produce single mode waveguides that exhibit electrooptic and nonlinear optical properties comparable to bulk LiNbO_3 and low insertion loss in fiber optic applications.¹ While the PE process is well-characterized, quantitative modeling of APE waveguides is much less well developed. In this paper we present measurements of the effective mode indices and fundamental mode profiles for APE waveguides subjected to a variety of exchange and annealing conditions in both x - and z -cut substrates, along with empirical models for the concentration-dependent diffusion coefficient and dispersion that allow accurate calculation of the refractive index profile for APE waveguides as a function of exchange depth and anneal time for wavelengths between 0.4 and 1.1 μm . The reduction of the nonlinear susceptibility in PE waveguides, measured by a reflected second harmonic generation technique, is also discussed.

Analysis of the APE process is complicated by both concentration-dependent diffusion and a refractive index change that has been reported to be highly nonlinear with proton concentration.^{2,3} To study these properties, planar waveguides were fabricated by exchange in pure benzoic acid to various depths d_e in z -cut substrates, and annealing at 333°C for times t_a . The resulting refractive index profiles were determined at 458 nm using prism coupling and IWKB analysis. The $1/e$ depths d_a and the surface index change Δn_a of the annealed waveguides normalized to d_e and Δn_e , respectively, are plotted vs the normalized anneal time $\tau \equiv t_a/d_e^2$ in Fig. 1. For long τ the depth increased as $\sqrt{\tau}$, as would be expected for linear diffusion with a diffusion coefficient $D_0 = 0.55 \mu\text{m}^2/\text{hr}$. For short times, a description based on linear diffusion is clearly inadequate. We found that the data in Fig. 1 can be accurately predicted with a concentration dependent diffusion coefficient given by $D(C) = D_0[a + (1 - a)\exp(-bC)]$, where C is the concentration normalized to the initial concentration after PE, and the best fit is obtained with $a = 0.1$ and $b = 12$. The results obtained by numerical solution of the diffusion equation with this diffusion coefficient and an initial step profile characteristic of the exchange process are shown as a solid line in Fig. 1. These results are obtained under the assumption that the change in the refractive index is proportional to the proton concentration at least up to 70% of the surface concentration after exchange, i.e. $\Delta n_a = 1.06 \Delta n_e C$ for $C < 0.7$. This assumption is supported by the constant area under the refractive index profile with annealing over this range of concentrations, and by the success of the model in predicting the modal properties over a broad range of processing conditions.⁴ These measurements were repeated in x -cut substrates, with essentially similar results, indicating that the diffusion is isotropic within the resolution of the measurements. Note that the diffusion coefficient is a decreasing function of concentration, a trend opposite that obtained in explaining the step-profile characteristic of PE by an interdiffusion model.³ As it is difficult to assign any microscopic significance to a diffusion coefficient used to describe transport in a two phase mixture, corresponding to $0.12 \leq x < 0.55$ for $\text{H}_x\text{Li}_{1-x}\text{NbO}_3$, it is not clear how to compare these results.

Two further tests were performed to verify the accuracy of the model at $\lambda = 0.458 \mu\text{m}$. The observed effective mode indices for a variety of few-mode APE waveguides were compared with modal dispersion curves calculated using the index profiles determined by the model, and were found to be in good agreement. Also, fundamental mode intensity profiles were imaged and compared with numerical solutions of the scalar wave equation for index profiles derived from the model, and again found to be in good agreement.

Knowledge of the dispersion in the surface refractive index is necessary to design waveguides at wavelengths other than $\lambda = 0.458 \mu\text{m}$. We characterized both a PE and an APE waveguide at wavelengths between 0.4 and 1.1 μm . Dispersion in Δn for the two waveguides along with single pole Sellmeier fits are shown in Fig. 2. The ratio of the index changes for the two waveguides is nearly independent of wavelength, indicating that to a good approximation the dispersion is constant during the annealing process. The dispersion data contained in Fig. 2 may be used to scale the refractive index profiles determined from the diffusion model to wavelengths other than 458 nm.

For efficient nonlinear devices, tightly confined modes are desirable, suggesting the use of PE waveguides. However, we observed extremely low conversion efficiency in PE waveguide frequency doublers, suggesting a severe reduction in the nonlinear coefficient d_{33} . A quantitative measurement of the effect of PE on d_{33} is therefore necessary for the design of optimized nonlinear devices. The difficulty in this measurement is in eliminating the contribution of the LiNbO₃ substrate to the total second harmonic power, as this bulk contribution could be large compared to that of the thin layer of PE material. To address this problem, we focused the 1.06 μm output of a Q-switched Nd:YAG laser on the surface of a PE x-cut substrate, and measured the angle dependence of the power of the backward propagating 532 nm radiation generated at the interface. By fitting the resulting data to the theoretical expression for a nonlinear slab on a nonlinear substrate, it was possible to put an upper bound on d_{33} in the PE film of 1% of the bulk value. This result disagrees with three previously published studies,⁵ which report a reduction of d_{33} in PE waveguides to approximately 50% of the bulk value, but is consistent with the extremely low conversion efficiency we observed in PE waveguide frequency doublers. The source of the discrepancy between this and prior measurements is not clear.

With the results for the concentration dependence for the refractive indices and the two independent components of the diffusivity tensor, it is possible to model the fabrication of APE channel waveguides. Comparison of these calculations with experimental observations will be given. Measurements of the recovery of d_{33} with annealing will be presented, and the implications of the results for the efficiency of APE waveguide nonlinear devices will be discussed.

REFERENCES

1. P. G. Suchoski, T. K. Findakly, and F. J. Leonberger, *Opt. Lett.* **13**, 1050 (1988).
2. C. E. Rice, J. L. Jackel, and W. L. Brown, *J. Appl. Phys.* **57**, 4437 (1985).
3. S. T. Vohra, A. R. Mickelson, and S. E. Asher, *J. Appl. Phys.* **66**, 5161 (1989).
4. M. L. Bortz and M. M. Fejer, *Opt. Lett.* **16**, 1844 (1991).
5. T. Suhara, H. Tazaki, and H. Nishihara, *Electron. Lett.* **25**, 1326 (1989).
R. W. Keys, A. Loni, and R. M. De La Rue, *Electron. Lett.* **26**, 624 (1990).
X. Cao, R. Srivastava, and R. V. Ramaswamy, *IEEE Photon. Tech. Lett.* **3**, 25 (1991).

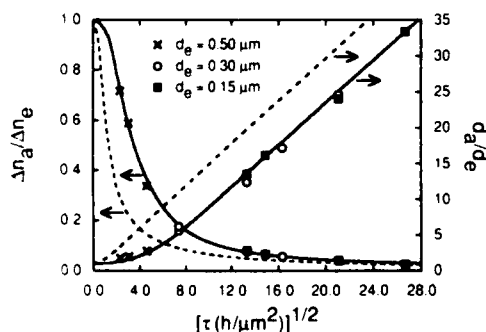


Fig. 1. Normalized index change and waveguide depth versus the square root of the normalized anneal time. The dashed line and curve are the predictions of linear diffusion theory with $D_0 = 0.55 \mu\text{m}^2/\text{h}$. The solid curves are the results of the nonlinear diffusion model described in the text.

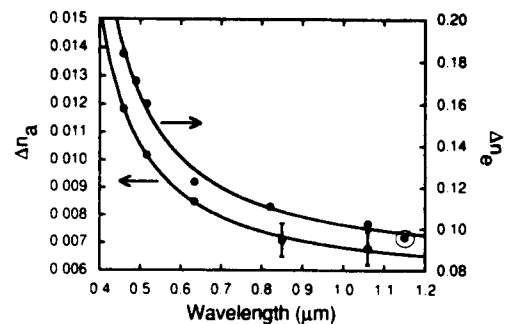


Fig. 2. Dispersion in PE and APE waveguides.

**Optical Switching for a Nonlinear Directional Coupler
Including the Effects of Two Photon Absorption**

M. J. Potasek and J. M. Fang
Department of Applied Physics
Columbia University
New York, New York 10027
(212) 854-4456

All-optical switching is of growing interest. However, complete all-optical switching in materials such as semiconductors has proved difficult. If the nonlinear index of refraction is utilized, there is also strong two photon absorption (TPA).^[1] It has been shown that the typical soliton solutions are not valid in the presence of TPA.^[2] Therefore traditional soliton switching is degraded. However we present a new coupled mode analysis which incorporates TPA and find exact solutions for which complete switching can occur. Using a coupled-mode analysis^[3] in which gain is used to offset the nonlinear loss due to TPA, we derive the set of equations for nonlinear directional couplers.

$$\begin{aligned} i q_{1z} + \frac{1}{2} \beta_2 q_{1u} + \frac{n_2 \omega_0}{c} (|q_1|^2 + |q_2|^2) q_1 + \kappa q_2 \\ = i \gamma_0 q_1 - \frac{i}{2} \gamma_2 q_{1u} - i \frac{\beta}{2} (|q_1|^2 + |q_2|^2) q_1 \end{aligned} \quad (1)$$

$$\begin{aligned} i q_{2z} + \frac{1}{2} \beta_2 q_{2u} + \frac{n_2 \omega_0}{c} (|q_1|^2 + |q_2|^2) q_2 + \kappa q_1 \\ = i \gamma_0 q_2 - \frac{i}{2} \gamma_2 q_{2u} - i \frac{\beta}{2} (|q_1|^2 + |q_2|^2) q_2 \end{aligned} \quad (2)$$

where β_2 is the dispersion parameter of the propagation medium, n_2 is the nonlinear index of refraction, β is the TPA coefficient, γ_0 is the small signal gain, γ_2 is the gain dispersion and κ is the coupling parameter for the directional coupler. The subscripts z and t refer to differentiation with respect to space and time, respectively. We have also assumed equal self- and cross-phase modulation. The effects of the TPA are balanced by a gain medium, for which we have assumed a Lorentzian line shape. We have obtained exact solutions for Eqs. (1) and (2) given by^[3]

$$q_1(z,t) = \frac{1}{\sqrt{2}} (\sin\theta e^{ikz} - \cos\theta e^{-i\phi} e^{-ikz}) q(z,t) \quad (3)$$

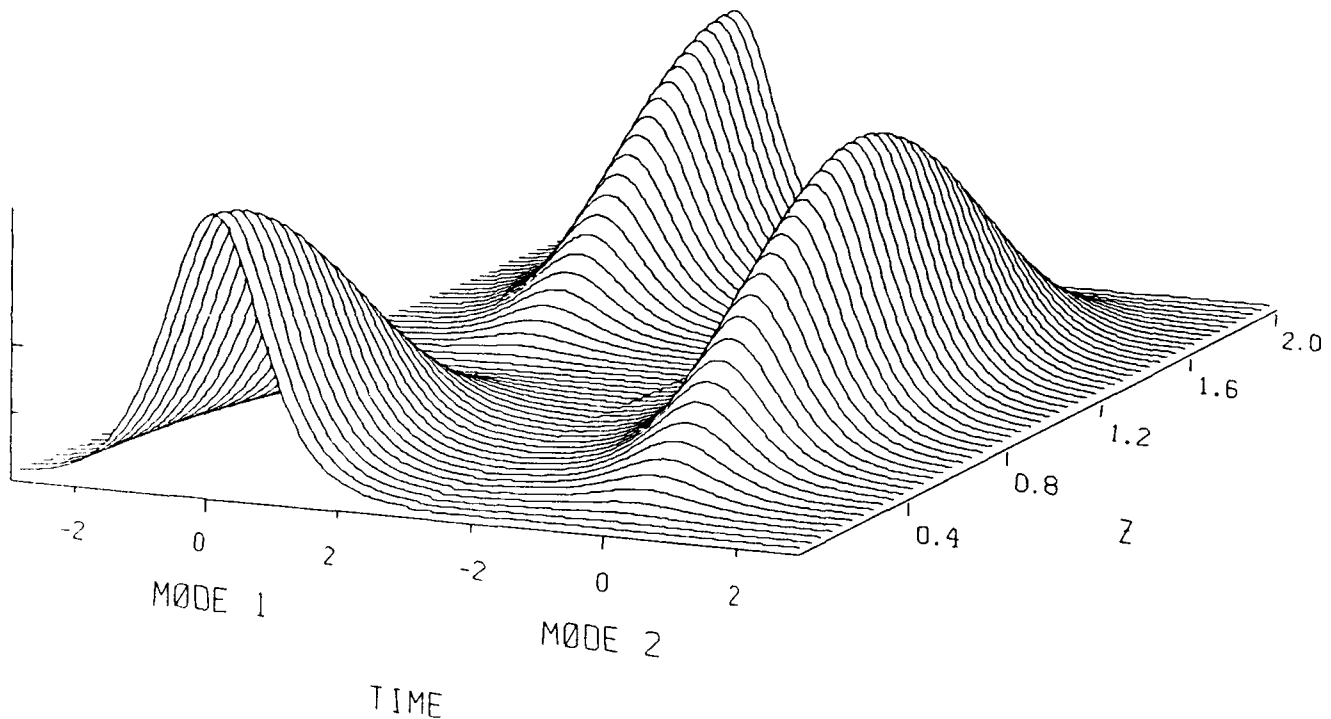
$$q_2(z,t) = \frac{1}{\sqrt{2}} (\sin\theta e^{ikz} + \cos\theta e^{-i\phi} e^{-ikz}) q(z,t) \quad (4)$$

where $q(z,t) = q_0 [\text{sech}(\omega t)]^{1+i\eta} e^{i(Rz+\Omega t)}$ and θ and ϕ are determined by the initial conditions.

When the light is input solely into one waveguide it will transfer to the other waveguide at a distance $L_c = \frac{\pi}{2\kappa}$ as shown in Fig. 1. However for equal input intensities into both waveguides the output depends upon the relative phases between the input pulses.

The expressions for q_0 , ω , R and Ω in terms of physical parameters will be presented and we will evaluate these parameters for various waveguides and present some possible experimental conditions for their realization.

- 1.) V. Mizrahi, K. W. DeLong, G. I. Stegeman, M. A. Saifi and M. J. Andrejco, *Opt. Lett.* **14**, 1140 (1989).
- 2.) K. W. DeLong and G. I. Stegeman, *Appl. Phys. Lett.* **57**, 2063 (1990); K. W. DeLong and K. B. Rochford and G. I. Stegeman, *Appl. Phys. Lett.* **55**, 1823 (1989).
- 3.) J. M. Fang and M. J. Potasek, *Phys. Rev. A*, submitted.



MB6-1

Wavelength Division Multiplexing with Dual-Frequency Laser Sources in Nonlinear Ultra Long Data Transmission

Pavel V. Mamyshev

General Physics Institute, Academy of Sciences of the USSR
38 Vavilov Street, Moscow 117942, USSR. FAX (095)1358139

Dual-frequency laser sources are very promising for nonlinear fiber optics [1,2]. Recently [2] we have suggested an ultra long distance nonlinear fiber optic data transmission using dual-frequency laser sources. Such a transmission has all the advantages of the soliton transmission: dispersive compensation of nonlinear effects; stability against perturbations of the fiber parameters (dispersion, mode area, etc.) along the fiber length; stability of data streams in a chain of lumped amplifiers; potential for multi-channel wavelength division multiplexing (WDM). Here we show that a WDM data transmission system employing dual-frequency laser sources is more stable against interchannel interference in comparison with a conventional soliton system.

We consider the dual-frequency and soliton 10,000 km-long transmission systems both operating at 4 GBits/sec rate in each WDM channel. The maximum pulse duration in a soliton system is limited by the soliton interaction within each channel, and for 4 GBits/s rate the maximum duration (FWHM) is 50 psec. In our dimensionless units the intensity of 50 ps solitons is 19.4. Like in a soliton WDM system [3], adjacent WDM channel pulses in a dual-frequency system interact in a lumped amplifier chain like in a lossless fiber, as long as a collision length is two or more times the amplifier spacing. The main advantage of the dual-frequency systems is that the adjacent pulses have opposite phases [2]. It is this feature that allows to use the pulses (we will call them as beat pulses) with energy about 1.5 less than that of the soliton system. The input intensity of beat pulses is 6.25 and duration of 125 psec. During the propagation through the fiber an isolated beat pulse evolves into a soliton with ~ 70 psec duration and intensity of ~ 9 .

In WDM systems, the main errors can arise due to cross-phase modulation when adjacent WDM channel pulses overlap at the fiber input [3,4]. At the fiber output this results in a temporal shift of the pulses from their initial position. Figure shows this situation for the cases of soliton (A) and dual-frequency (B) systems. The pulse shift is proportional to the pulse intensities at the fiber input, so the pulse shift in the dual-frequency system is about three times less than that in the soliton system. The soliton pulse shifts on more than 125 psec and appears in the adjacent time slot, while the beat pulse remains in its time slot.

Another kind of temporal shift of pulses can arise from collisions among adjacent WDM channel pulses within the fiber [3,4]. Again, this effect is proportional to the pulse intensity, and in a dual-frequency system one can expect the shifts at least two-times less than such shifts in a soliton system.

Note also that because of the lower energy of the beat pulses, the errors caused by Gordon-Haus [5] and electrostrictional [6] effects should be also less in the dual-frequency systems in comparison with the soliton data transmission systems.

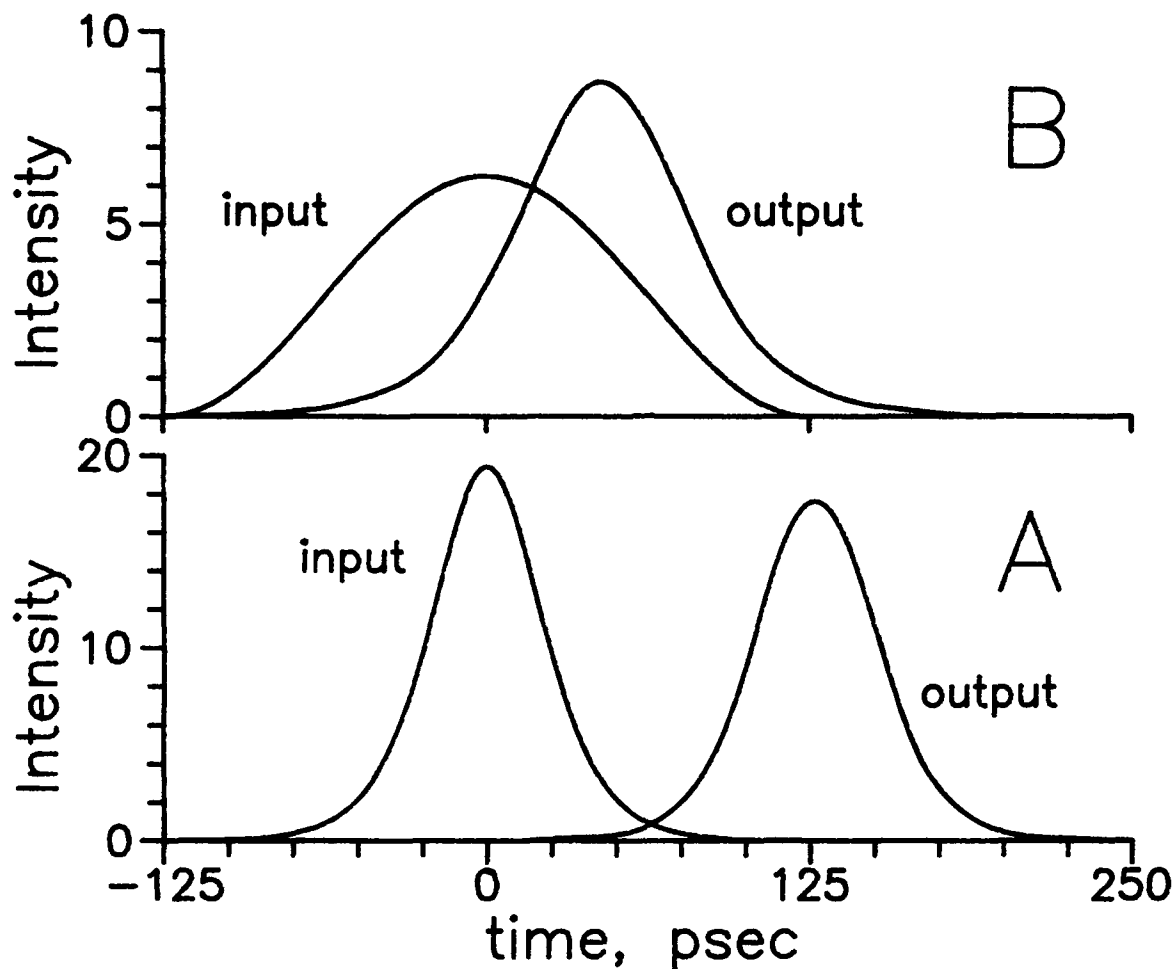


Figure. Numerical simulations of temporal shift of pulses at the fiber output caused by cross-phase modulation effect in WDM system. The pulse overlaps at the fiber input with an adjacent WDM channel pulse (not shown) spectrally separated by 1 cm^{-1} . Fiber length 10,000 km, dispersion $D=1 \text{ ps/nm/km}$. (A)- the soliton system, (B)- the dual-frequency system.

References

1. P.V.Mamyshev, S.V.Chernikov and E.M.Dianov, IEEE J. of Quantum Electron. 27, 2347 (1991); Opt. Lett. 14, 1008 (1991).
2. P.V.Mamyshev, S.V.Chernikov and A.M.Prokhorov. Technical Digest on Nonlinear Guided-Wave Phenomena. 1991, Vol.15, pp.18-21.
3. L.F.Mollenauer, S.E.Evangelides and J.P.Gordon. J. Lightwave Technology, 9, 362 (1991).
4. P.A.Andrekson et al. Electron. Lett., 26, 1499 (1990).
6. J.P.Gordon and H.Haus. Opt. Lett. 11, 665 (1986).
6. E.M.Dianov, A.V.Luchnikov, A.N.Pilipetskii and A.M.Prokhorov. Soviet Lightwave Commun., 1, 235 (1991).

MB7-1

**Soliton Pulse Long-Range Interaction In Optical Fibers:
The Influence of Light Polarization and Fiber Geometry.**

E. M. Dianov, A. V. Luchnikov, A. N. Pilipetskii, A. M. Prokhorov

General Physics Institute of the Academy of Sciences ,

Vavilov Str. 38, 117942 Moscow, Russia.

Tel. 132-83-09, Fax. 135-02-70

Soliton communication lines are promising for high bit rate data transmission on long distances¹. Smith and Mollenauer experimentally discovered the effect of soliton pulse long-range interaction². We have explained the long-range interaction of solitons by electrostrictional excitation of radial acoustic modes of fiber and their subsequent influence on solitons^{3,4}. We have also shown that the excitation of the acoustic waves results in a considerable timing jitter of solitons and can limit the bit rate and distance of data transmission in soliton communication lines⁵.

However this effect requires a more detailed quantitative approach because of its significance for soliton communication lines. Previously⁵ we have taken into account only the electrostrictional excitation of radial acoustic modes R_{0m} for which there is only radial component of displacement vector. That component does not depend on the angular coordinate. We show now that depending on light polarization state another group of acoustic waves can be excited. That are the mixed torsional-radial modes TR_{2m} and their displacement vector is varying sinusoidally as 2φ . Spontaneous scattering of light on this group of modes was experimentally observed in single mode fiber by Shelby et. al.. We

demonstrate that both groups of acoustic modes R_{Om} and TR_{2m} are excited for linear light polarization. Only R_{Om} modes are excited for circular polarization state and the efficiency of their excitation does not depend on light polarization state. Unlike^{3,5} we also discuss the influence of TR_{2m} acoustic modes on soliton long-range interaction.

We analyze the role of such geometrical factors as light mode shape and inhomogeneity of fiber cladding radius. The calculations show a considerable dependence of the acoustic effect on the light mode shape. The variation of cladding diameter along fiber axis result in efficient broadening of the lines of acoustic modes and in the decrease of acoustic vibrations influence on solitons. The effect of sound reflection from the external polymeric cladding is investigated as well.

REFERENCES

1. Mollenauer L. F. et. al., Opt. Lett. 15, 1203 (1990)
2. Smith K. and Mollenauer L. F., Opt. Lett. 14, 1284 (1989)
3. Dianov E. M., Luchnikov A. V., Pilipetskii A. N. and Starodumov A. N., Opt. Lett. 15, 314 (1990)
4. Dianov E. M., Luchnikov A. V., Pilipetskii A. N. and Starodumov A. N., Sov. Lightwave Commun. 1, 37 (1991)
5. Dianov E. M., Luchnikov A. V., Pilipetskii A. N. and Prokhorov A. M., Sov. Lightwave Commun. 1, 235 (1991)
6. Shelby R. M., Levenson M. D. and Bayer P. W., Phys. Rev. B 31, 5244 (1985)

Amplitude squeezed number-phase intelligent state in a directional coupler

P. Adam, M. Bertolotti, J. Janszky, C. Sibia
 Dipartimento di Energetica
 Universita' di Roma I - Via Scarpa 16, 00161 Roma, Italy
 Tel.: 06-49916800
 Fax: 06-4270183

Recently it has been shown how a Gaussian superposition of coherent states along a straight line in alpha plane describes quadrature squeezing [1] while along an arc it is an approximate number phase intelligent state associated with Pegg-Barnet phase operators [2] and shows amplitude squeezing [3]. The amplitude squeezed light is defined by a reduction in the fluctuations of amplitude component of below the coherent state value : for this reason the amplitude squeezing looks very important from the point of view of optical communications. We found that the properties of this state are between coherent and pure number states , it is less vulnerable than the latter while shows some of its advantages .

In the present paper we study the evolution of an amplitude squeezed state in a directional coupler , considering the probability of detection of a suitable photon number at the output of the coupler , to reach a necessary confidence level for switching the signal from one channel to another .

The system of equations describing the space evolution of the field modes in the directional coupler are

$$\begin{aligned}
 a &= U(z)a_0 + V(z)b_0 , & |U|^2 + |V|^2 &= 1, |Z|^2 + |W|^2 = 1 \\
 b &= Z(z)b_0 + W(z)a_0 & U W^* + Z^* V &= 0
 \end{aligned}$$

where a_0 and b_0 are the fields operators at the input of the coupler , specified by a and b channels , and where the functions U, V, Z, W contain all the features of the structure.

Such coupling changes an input state $|in\rangle$ into another output state $|out\rangle$:

$$|in\rangle = \sum_{nm} C_{n,m}^{in} |n\rangle_a |m\rangle_b ; |out\rangle = \sum_{nm} C_{n,m}^{out} |n\rangle_a |m\rangle_b$$

We found the output coefficients C_{nm}^{out} for an arbitrary input state with corresponding coefficients C_{nm}^{in} :

$$C_{nm}^{out} = \sum_{j=0}^{n+m} C_{j,n+m-j}^{in} \left[\frac{(n+m-j)!}{j!n!m!} \right]^{1/2} D^j (Z^m V^n)$$

where $D \equiv [U \frac{\partial}{\partial V} + W \frac{\partial}{\partial Z}]$.

By the help of these formulae we can analyze the output properties of the directional coupler , using the probability distributions $P(n,m) = |C_{nm}|^2$.

In particular we find how the normalized uncertainties

$$\Delta n^2 / \langle n \rangle = \frac{\sum n^2 P(n)}{\sum n P(n)} - \sum n P(n)$$

behave for each channel .

During a switching process the confidence level is an important parameter : usually a confidence level of 10^{-9} needs 21 photons for a coherent state to say that the switching is completed. For an amplitude squeezed state one needs considerably less photons , for example the case of 0.1 amplitude squeezing only 4 photons are needed to achieve the same confidence level of switching .

References

- 1 - J.Janszky , A.V.Vinogradov - Phys.Rev.Lett- 64, (1990), 2771
- 2-D.T.Pegg, S.Barnett,Phys.Rev.A 39 (1989), 483
- 3- P.Adam, J.Janszky - In print in Phys.Lett.

MB9-1

CHALCOGENIDE GLASS PLANAR WAVEGUIDES: Z-SCAN INVESTIGATION OF REFRACTIVE INDEX CHANGES.**M. Bertolotti, F. Michelotti**

Univ. di Roma "La Sapienza" - Dip. di Energetica & GNEQP of CNR

Via Scarpa 16 - 00161 Roma- ITALIA - Tel 39-6-49916542 FAX 39-6-4270183

A. Andriesh, V. Chumash, G. Liakhou

Institute of Applied Physics - Academy of Science of Moldova

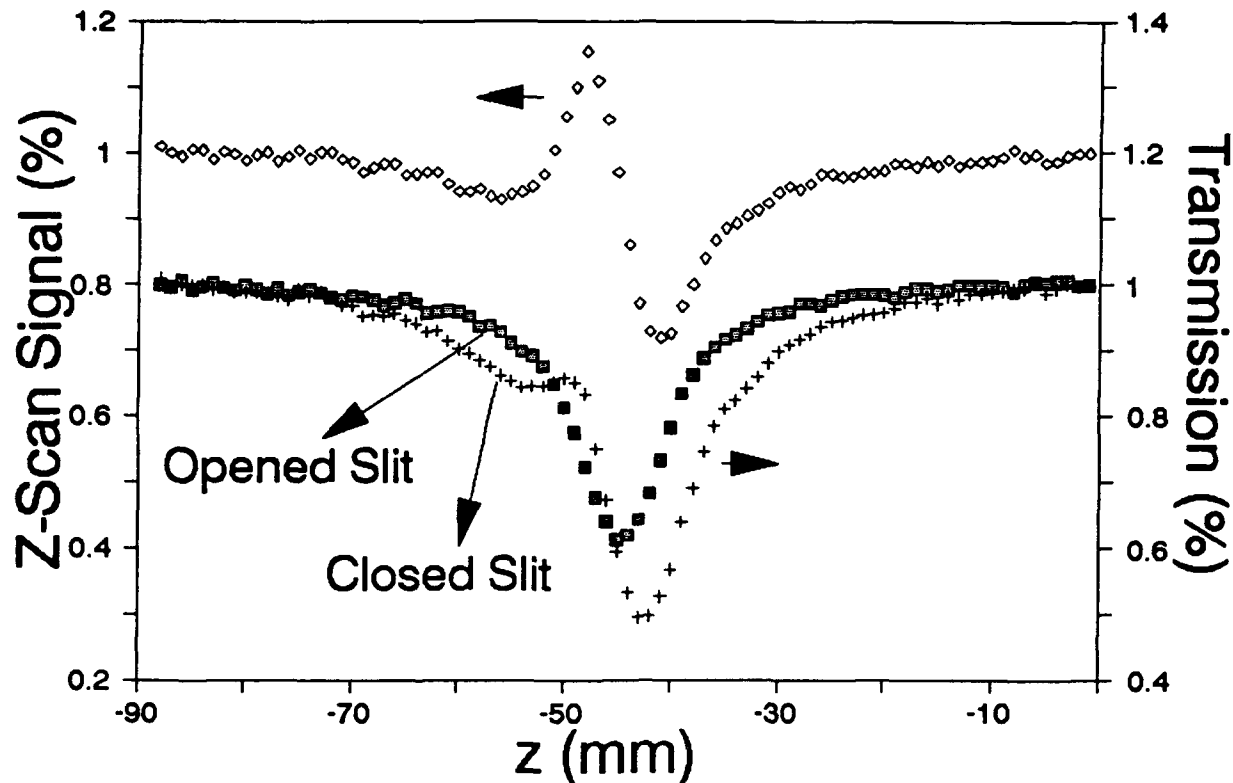
Academica Str. 5 - Kishinev 277028 - USSR

Nonlinear properties of chalcogenide glasses (ChG) are very interesting both from the point of view of potential application in photonic devices (as planar waveguides, fibers, coating films) and new basic mechanisms in the field of short laser pulses. Recently the measurements of optical hysteresis in thin films of ChG were performed, showing the effect at light intensities lower than those reported in the case of crystalline semiconductors [1].

In the present work we have extended the measurements of nonlinear transmission of c.w. ($\lambda=514.5$ nm) and pulsed ($\lambda=532$ nm, $\tau=70$ ps ; 570 nm $< \lambda < 630$ nm, $\tau=4$ ps) laser excitation through thin films of ChG (As_2Se_3 , AsSe, GeSe₂, As_2S_3), which can act as planar waveguides.

The z-scan technique [2] was used to study the basic nonlinear properties of thin films (thickness 0.2-2.0 μm). In this technique the transmission of a focussed laser beam, through a finite aperture in the far field, is measured as a function of the displacement (z) of the film along the propagation direction and about the focal plane. The contributions to the changes of refractive index, due to photostructural effects and nonlinear refractivity and absorption, can be distinguished . The former contribution can be eliminated irradiating large sample areas and then performing measurements in already photostructured films at lower intensities. In figure the nonlinear change of transmission of an As_2Se_3 film (thickness 1.6 μm), under pulsed irradiation ($\lambda=590$ nm, $\tau=4$ ps, $P_{\text{peak}}=10$ W) is shown for closed (+) and opened (■) aperture as a function of film displacement (z). Z-scan curve (\diamond), obtained normalizing (+) to (■), gives the variation of refractive index as a function of the laser pulse intensity.

Measurements were performed using pulses of 70 ps and c.w. radiation too, obtaining the changes of absorption coefficient and refractive index. A Fabry-Perot cavity



effect, due to the high refractive index of chalcogenide glasses ($n=2.0-2.5$), was found to influence the z-scan measurements.

ChG show photostructural changes either when they are exposed to highly absorbed radiation [3] or in the case of induced nonlinear absorption of light [1]. This leads to irreversible changes of refractive index, optical bandgap and film thickness. In fresh prepared samples we performed measurements, which put in evidence the permanent photostructural changes (permanent lenses inside the planar waveguide), giving an additional z-scan signal, used to estimate the refractive index changes. This method can be useful for investigation of film inhomogeneities (channels, lenses) up to few wavelengths spatial resolution.

A possible mechanism of nonlinear light absorption in ChG and its application in guided-wave devices is discussed.

REFERENCES

- [1] A.M.Andriesh, V.N.Chumash, I.A.Cojocaru, Inst. Phys. Conf. Ser. No 115, p. 235, IOP Publisher (1990) and references therein.
- [2] M.Sheik-Bahae, D.C.Hutchings, D.J.Hagan & E.W. Van Stryland, IEEE J. of Quantum Electronics, Vol.27, No.6, p. 1296 (1991).
- [3] K.Tanaka, J.Non-Crystal.Solids, Vol.35-36, p.1023 (1980).

MB10-1

EXACT SOLITON SOLUTIONS IN A PERIODICALLY TWISTED BIREFRINGENT FIBER

R. S. Tasgal and M. J. Potasek
 Department of Applied Physics, Columbia University
 New York, NY 10027
 (212) 854-4456

We have obtained exact soliton solutions for a more general case of birefringent couplers. To our knowledge this represents the most general solution to date of this kind. In addition, we describe aspects of their interesting physical behavior.

The two eigenmodes of a periodically twisted birefringent fiber are described by a set of coupled nonlinear Schroedinger equations (NLS)

$$i q_{1z} + i \delta_- q_{1t} + \frac{1}{2} q_{1tt} + (|q_1|^2 + \gamma |q_2|^2) q_1 + \Delta q_1 + \kappa q_2 = 0 \quad (1a)$$

$$i q_{2z} - i \delta_- q_{2t} + \frac{1}{2} q_{2tt} + (\gamma |q_1|^2 + |q_2|^2) q_2 - \Delta q_2 + \kappa q_1 = 0, \quad (1b)$$

where q_1 and q_2 are nondimensionalized complex amplitudes of the light in the fiber. γ is a function of the ellipticity angle of the fiber. $\gamma=1$ for an angle of approximately 35° . Solitons can exist in the limit $\delta_-=0$ and $\gamma=1$, which we assume henceforth. The former condition may be approached by adjusting the pulse width, birefringence and twist of the fiber. Some previous work has investigated more limited cases, such as $\Delta=\kappa=0$ and $\Delta=0, \kappa \neq 0$. No one has obtained exact solutions for the case with both $\Delta, \kappa \neq 0$.

We have shown that equations (1) have a one soliton solution

$$q_1 = \left[\cos\left(\frac{\theta}{2}\right) \sin(\alpha) e^{i(\Delta'z+\phi)} - \sin\left(\frac{\theta}{2}\right) \cos(\alpha) e^{-i(\Delta'z+\phi)} \right] q \quad (2a)$$

$$q_2 = \left[\sin\left(\frac{\theta}{2}\right) \sin(\alpha) e^{i(\Delta'z+\phi)} + \cos\left(\frac{\theta}{2}\right) \cos(\alpha) e^{-i(\Delta'z+\phi)} \right] q, \quad (2b)$$

where

$$q = q_0 \operatorname{sech}(q_0 t) \exp\left(i \frac{q_0^2}{2} z\right),$$

$$\tan(\theta) = \kappa/\Delta,$$

$$\Delta' = \pm \sqrt{\Delta^2 + \kappa^2}, \quad \operatorname{sign}(\Delta') = \operatorname{sign}(\Delta).$$

The parameters α, ϕ and η are functions of the initial conditions.

The energy intensities of the two modes are

$$I_1 \propto |q_1|^2 = \frac{1}{2} (1 - \cos(\theta) \cos(2\alpha) - \sin(\theta) \sin(2\alpha) \cos(2\Delta'z+2\phi)) |q|^2 \quad (3a)$$

$$I_2 \propto |q_2|^2 = \frac{1}{2} (1 + \cos(\theta) \cos(2\alpha) + \sin(\theta) \sin(2\alpha) \cos(2\Delta'z+2\phi)) |q|^2 \quad (3b)$$

From inspection of the modes' intensities, one sees that energy

oscillates between the two modes with coupling length

$$L_c = \frac{\pi}{2\sqrt{\Delta^2 + \kappa^2}}. \quad (4)$$

Δ is a function of the dispersion in the two modes. Equations (3) show that increasing $|\Delta|$ shortens the coupling length and decreases the completeness of the switching. This trade off may be an impediment to employing a large Δ to reduce the length of a device.

We give three illustrations. In all three figures the energy is input solely into waveguide 1. The spatial dimension is normalized to one coupling length ($\Delta l = \pi$), and each figure is drawn in the comoving reference frames of its pulse. In Fig. 1 $\Delta/\kappa=0$. In Fig. 2 $\Delta/\kappa=0.5$. In Fig. 3 $\Delta/\kappa=1$. The degree of switching clearly diminishes very quickly as Δ becomes large compared to κ .

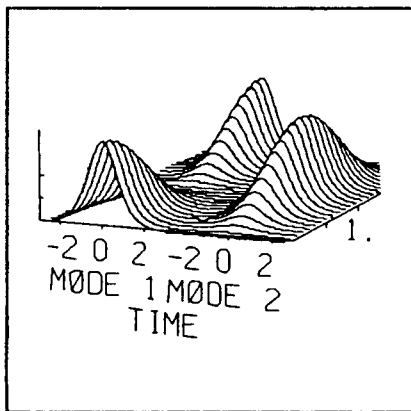


Fig. 1

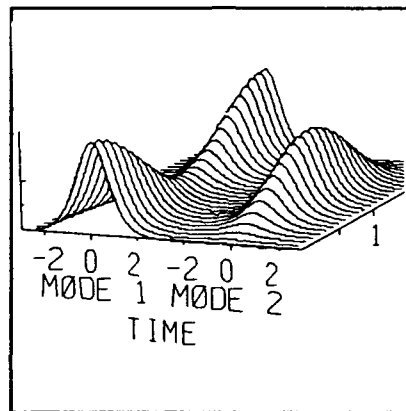


Fig. 2

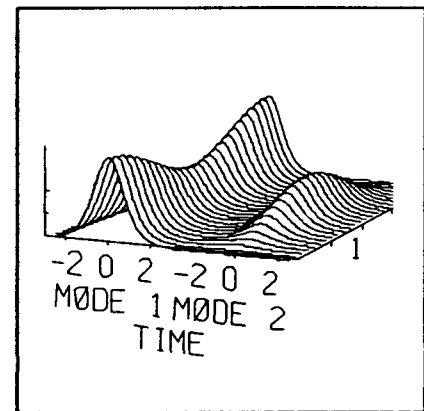


Fig. 3

In summary, we obtained exact soliton solutions for birefringent nonlinear waveguides under certain conditions. The solutions oscillate between the two modes, which makes them useful as part of an all optical switch. The advantages and disadvantages of different combinations of parameters will be discussed in more detail at the conference.

References:

- S. Trillo, S. Wabnitz and G. I. Stegeman, IEEE J. Quantum Electron. QE-25, 1907 (1989).
- S. V. Manakov, Zh. Eksp. Teor. Fiz. 65, 505 (1973) [Sov. Phys JETP 38, 248 (1974)].
- P. A. Bélanger and C. Paré, Phys. Rev. A 41, 5254 (1990).
- R. S. Tasgal and M. J. Potasek, J. Math. Phys., to be published.

MB11-1

Suppression of the soliton self-frequency shift
by dispersion sign reversal in fiber.

A.G.Bulushev, E.M.Dianov, O.G.Okhotnikov, V.N.Serkin
General Physics Institute, Academy of Sciences of the USSR,
38 Vavilov Street, Moscow 117942, USSR

The soliton self-frequency shift (SSFS) suppression first discussed in [1] has been achieved by the bandwidth-limited amplification. Here we propose a novel method of suppression of the SSFS in a fiber based systems. We have found, that efficient inhibition of the SSFS takes place when dispersion of the fiber changes its sign at the wavelength that lies near the spectral profile of the pulse. Namely, SSFS can be suppressed when the pulse propagates in the soliton dispersion region near the dispersion sign reversal (DSR) point, while weak wing of the pulse spectrum falls into the nonsoliton region.

Pulse propagation is modeled using the nonlinear Schroedinger equation:

$$\begin{aligned} \partial E / \partial z - i 0.5 k_2 \partial^2 E / \partial t^2 + i \beta_1 [(1-\beta) |E|^2 + \beta Q |E + \alpha(1+\varepsilon I)^{-1} P|] &= 0, \\ \mu^2 \partial^2 Q / \partial t^2 + 2\mu\delta \partial Q / \partial t + Q = |E|^2, \quad (2\Delta\omega)^{-1} \partial P / \partial t + [1 + i(\omega_0 - \omega_t)(2\Delta\omega)^{-1}] P &= iE. \end{aligned}$$

Here k_2 - second-order group velocity dispersion (GVD), β_1 is the nonlinear coefficient, $E(t)$ - the optical field, Q - real amplitude of molecular oscillations, μ and δ are associated with the resonant frequency of Raman oscillator and relaxation time. Parameter β determines Raman contribution to the nonlinear refractive index. P denotes complex polarization amplitude. $\Delta\omega$, ω_0 are bandwidth and center frequency of gain medium, respectively. ω_t - frequency of laser transition, α - gain. The gain saturation is described by I and parameter ε [2].

Fig.1 shows the evolutions of the central frequency of the fundamental soliton propagating in the fiber with flat dispersion and with DSR (ω_{inv} is frequency of DSR). In fact, soliton reshaping takes place in the fiber with DSR. Nevertheless, modified soliton-like pulse with suppressed SSFS can propagate along the fiber over the distance of few hundreds of the dispersion length z_{disp} even without in-line amplifiers. Our simulations show that DSR in a fiber is delicate method, since SSFS suppression can be provided by slight perturbation of the fundamental soliton.

Similar features were observed in all-fiber soliton laser. We studied a self-starting passive mode locked ring laser (Fig.2) consisting of a nonlinear amplifying loop mirror (NALM) with its output connected to its input and with unidirectional light propagation in the loop outside NALM ([2] and references therein). For flat dispersion $k_2 = -0.5$ and parameters as for Fig.3, after lasing self-started from initial noise, pulse moves down in frequency due to SSFS away from the gain curve and lasing fails periodically.

Our calculations for step-like dispersion with positive GVD in the Stokes band show SSFS suppression (Fig.3). Location of spectrum maximum can be manipulated by changing ω_{inv} in respect to gain profile and can be stabilized at both low- and high-frequency wings of the gain.

We then have verified SSFS suppression in a fiber having parabolic GVD spectral profile with GVD: $k=0.5(\omega/26-1)(\omega/4+1)$. This dispersion profile can be realized in dispersion-flattened fibers. Solitons can exist in such fibers only between zero dispersion points. Moreover, stable solution was also found for the case with $k=0.5(\omega/26+1)(\omega/4-1)$, when GVD is positive in the high-frequency wing of the gain. To confirm that SSFS suppression here is associated with the DSR, and not with the gradient of GVD spectral

dependence, we have modeled fiber laser with step-like dispersion and negative GVD in the Stokes band and have found steady state regime (Fig.3).

For laser with DSR we observe generation of bound soliton-like pulses. We found that frequency components in -GVD and +GVD regions (Fig.2) correspond to the bound pulses with the same group velocity and temporal location.

1. K.J.Blow, N.J.Doran, D.Wood, J.Opt.Soc.Am.B., 5, 1301 (1988).
2. A.G.Bulushev, O.G.Okhotnikov, V.N.Serkin, Sov.J.Lightwave Comm. 1, N4 (1991).

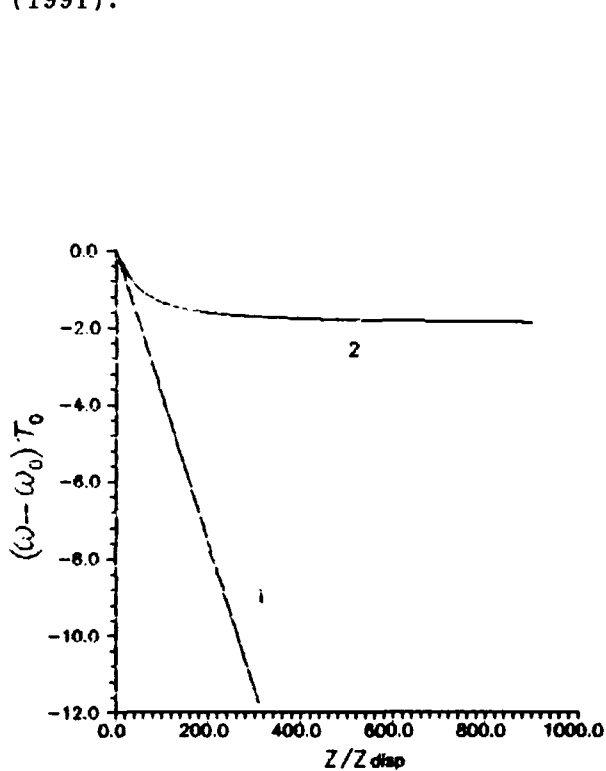


Fig.1. Evolution of soliton central frequency with parameters: $\tau_0 = 50\text{fs}$, $\beta_1 = 1$, $\beta = 0.18$, $\delta = 0.5$ and $\mu = 0.42$. Curve 1 - flat dispersion with $k_2 = -1$; Curve 2 - fiber with DSR with $k_2 = 10$ ($\omega \leq \omega_{inv} = -2$) and $k_2 = -1$ ($\omega > \omega_{inv}$).

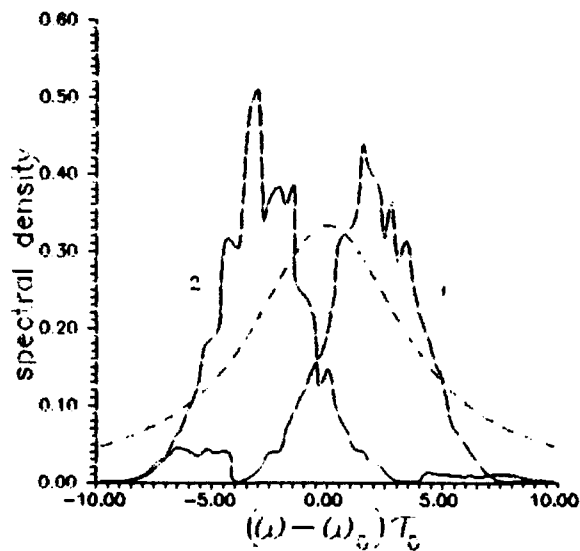


Fig.3 Steady state pulse spectrum for laser with NALM fiber length $L = 0.5$, amplifier length $l_a \ll L$, $\Delta\omega = 4$, $\omega_0 = 0$, $\beta_1 = 1$, NALM coupler coupling ratio $r = 0.39$, $\alpha l_a = 2$, $\varepsilon = 1.2$, $\tau_0 = 100\text{fs}$, $\beta = 0.18$, $\delta = 0.25$, $\mu = 0.21$ and $\omega_{inv} = -4$ (dash line is gain curve). Curve 1 - fiber with DSR with $k_2 = 0.5$ ($\omega \leq \omega_{inv}$) and $k_2 = -0.5$ ($\omega > \omega_{inv}$); Curve 2 - fiber with DSR with $k_2 = -0.5$ ($\omega \leq \omega_{inv}$) and $k_2 = 0.5$ ($\omega > \omega_{inv}$).

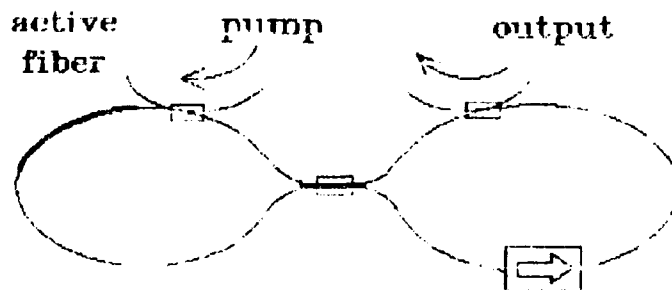


Fig.2 Schematic of fiber laser.

Simulations of Optical Leaky Waveguide Structures by the Vector Beam Propagation Method

C. L. Xu, W. P. Huang, and S. K. Chaudhuri
Department of Electrical and Computer Engineering
University of Waterloo
Waterloo, Ontario, Canada N2L 3G1
(519)-885-1211

Leaky waveguide structures have received great interest lately and several novel devices based on the leaky waveguides have been proposed and demonstrated. For instance, the low-loss ARROW devices have been fabricated on various materials and can be used as a polarizer [1]. ARROW or Bragg-reflection waveguides (BRW) can be used to build strongly coupled directional couplers with large separation [2]. The leaky waveguide structures can also be used in the detector design to achieve efficient absorption [3].

Strictly speaking, no spatial steady modes can be supported by a leaky waveguide. The propagation of electromagnetic wave in the leaky waveguide is a spatial transient state that evolves from the excitation at the input to the radiated modes. The leaky modes can be used to describe this process approximately provided the radiation loss is small. The beam propagation method is an ideal method to simulate the propagation and radiation of the electromagnetic wave of the leaky waveguides. Since most leaky waveguides are polarization sensitive, the conventional scalar BPM is not sufficient. This has been overcome in the newly developed finite-difference vector beam propagation method (FD-VBPM) [4].

In this report, we have applied the FD-VBPM to several typical leaky waveguide structures. As the first example, the quasi-guided modes in an ARROW structure described in Ref. [1] is simulated. Figure 1 shows the field distributions of TE and TM quasi-guided modes. The radiation due to the leakage can be seen very clearly in these field patterns. It is also noted that the TM wave appears more lossy than the TE wave. We also calculated the radiation loss as a function of the thickness of the anti-resonant layer. Figure 2 shows the results for both TE and TM cases. It is obvious that the TM wave has a much larger attenuation than the TE wave so the waveguide can be used as a polarizer. This result is compared with the approximate analysis in Ref. [1] (not shown) and the agreement is excellent for low loss TE wave and a little different for more lossy TM wave since approximate analysis may not valid for very lossy case.

Another example we have simulated is related to the leaky waveguide structure used in a waveguide detector. In this case, the leakage is to be maximized so the approximate leaky mode analysis may become less applicable. We have chosen the configuration in the meeting problem provided by Deri of Bellcore. As requested, we have simulated the propagation behaviors of both TE and TM waves. Figure 3 shows the power absorbed by the detector for the TE and TM cases as a function of propagation distance. It is observed that the absorption is only weakly dependent on the polarization. This may due to the fact that

several leaky modes are involved in the detection process and the overall absorption become less sensitive to the polarization.

Several other examples, such as BRW structures and ARROW based coupler, are also being investigated. The results will be shown at the meeting.

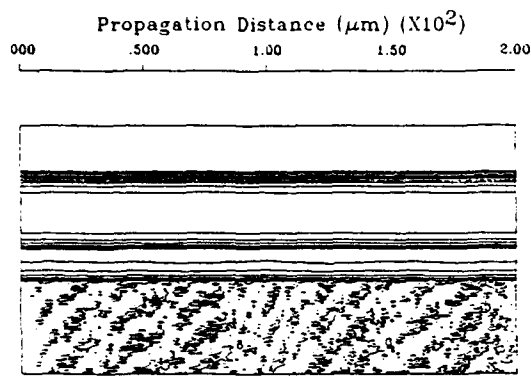


Fig. 1.(a). Field pattern of TE wave

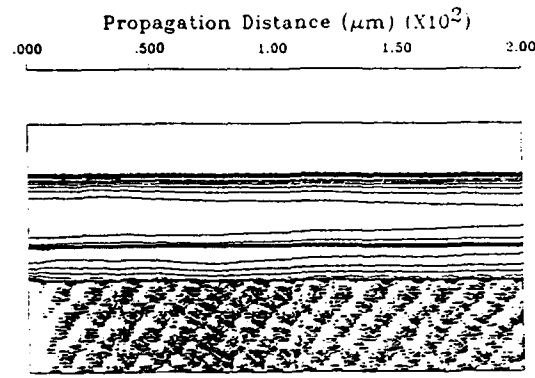


Fig. 1.(b). Field pattern of TM wave

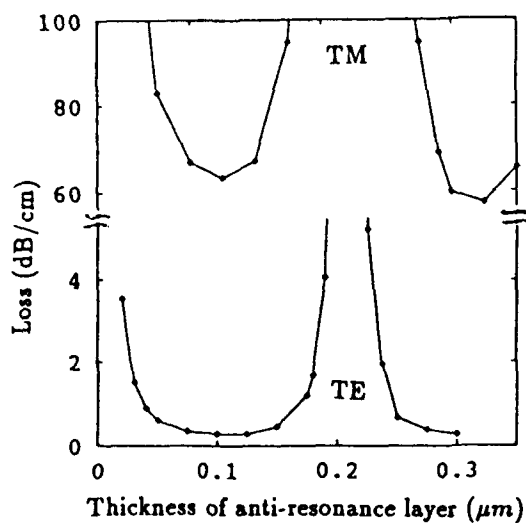


Fig. 2. Loss as a function of the thickness of anti-resonance layer

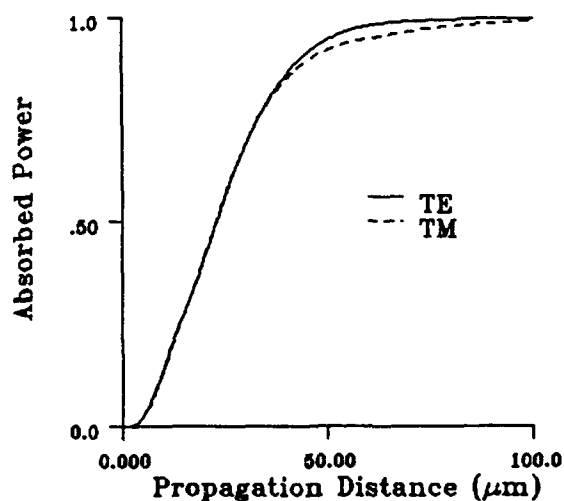


Fig. 3. Absorbed power as a function of propagation distance

References

- [1] M.A. Duguay *et al*, *Appl. Phys. Lett.*, vol.49, pp. 13-15, 1986.
- [2] G. Lenz *et al*, *IEEE J. Quantum Electronics*, vol.26, pp. 519-531, 1990.
- [3] T. Baba *et al*, *Appl. Optics*, vol. 29, pp. 2781-2792, 1990.
- [4] W.P. Huang *et al*, *IEEE Photo. Tech. Lett.*, vol.3, pp. 910-913, 1991.

MB13-1

RESONANT-TUNNELING DIODES:
QUANTUM PHYSICS AT THE COMMON-OR-GARDEN LEVEL

H.J.M.F. Noteborn

Department of Physics, Eindhoven University of Technology

P.O.Box 513, 5600 MB Eindhoven, The Netherlands

Telephone: +31 40 474288

and

D. Lenstra

Department of Physics and Astronomy, Vrije Universiteit Amsterdam

De Boelelaan 1081, 1081 HV Amsterdam, The Netherlands

Telephone: +31 20 5484733

New semiconductor growth techniques have enabled the construction of mesoscopic devices, the operation of which is directly based on quantum phenomena. Both the static and dynamic behaviour of these novel devices, of which the resonant-tunneling diode is an interesting example, have promising applicabilities. In this contribution, we will shortly overview our recent modeling of resonant tunneling and present our latest results.

Our model of resonant tunneling is based on coherent quantummechanical tunneling through the double-barrier structure, calculated within a single-particle envelope wave-function approach. In addition, the electrostatic feedback of the charge build-up in the well is taken into account, yielding selfconsistent current and charge densities. This feedback mechanism leads to a bistability in the I-V characteristic [1]: in a small bias interval on the high-voltage side of the current peak, we find two stable selfconsistent current branches, one with and one without substantial storage of charge in the well.

Applying a magnetic field perpendicular to the barrier structure, will not affect the tunneling process itself. However, the lateral motion is now quantized into Landau levels, changing both charge and current densities. At fixed bias, Shubnikov-de Haas oscillations are found in the current as function of inverse magnetic field strength. A Fourier analysis reveals two periods in these oscillations: one related to the charge accumulation in front of the emitter

barrier, and one related to the charge storage in the well. Our calculations confirm that the B||J configuration provides an excellent method for probing the build-up of charges in emitter and well [2].

A totally different situation arises in the case of a magnetic field parallel to the layers. On the barrier potential is now superposed a magnetic-field dependent potential term, which affects the tunneling directly. Also, the Landau level index is no longer a conserved quantity. If we confine the magnetic field to the central layers of the structure, the whole Landau level idea is to be abandoned. Instead, we have to work with a transmission coefficient that is a function of both the transverse and the lateral momentum of the electron in the emitter reservoir. This is the quantum version of the classical cycloidal motion under the action of the classical Lorentz force. The I-V characteristics exhibit a lower but wider current peak [3]. The width of the peak increases roughly linearly with the magnetic field strength.

Since resonant-tunneling diodes have a voltage region of negative differential resistance (NDR), they can be biased stably only under certain conditions, depending on the diode properties and the biasing circuit. We have obtained stability conditions in terms of a small signal impedance derived from the coupled dynamic equations for the charges in the emitter and well. The equivalent circuit consists of two linked RC-circuits, generalizing the experimental equivalent circuits with or without a 'quantum inductance' [4]. The stabilizing effect of an additional parallel capacitor to the diode can easily be studied within our model. The limiting stability condition is in all cases the demand that the sum of the NDR and the external series resistance be negative, which is the usual one for NDR devices.

References

- [1]. F.W. Sheard and G.A. Toombs, *Appl. Phys. Lett.* 52 (1988) p.1228.
- [2]. L. Eaves, in: *Analogies in Optics and Micro Electronics*, W. van Haeringen and D. Lenstra (eds.), Kluwer Academic Press 1990, pp. 227-242.
- [3]. S. Ben Amor, J.J.L. Rascol, K.P. Martin, and R.J. Higgins, *Phys. Rev. B* 41 (1990) p.7860.
- [4]. J.M. Gering, D.A. Crim, D.G. Morgan, P.D. Coleman, W. Kopp, and H. Morkoç, *J. Appl. Phys.* 61 (1987) p.271; M.G. Boudreau and H.C. Liu, *Superlattices and Microstructures* 8 (1990) p.429.

A New Transfer Matrix Approach to Optical Grating Structures

W. P. Huang and J. Hong

Department of Electrical and Computer Engineering
University of Waterloo
Waterloo, Ontario, Canada N2L 3G1

Optical grating structures are basic elements in filters, DFB/DBR lasers. Coupled-mode theory is often used in the analysis of these devices. The mode patterns in the coupled-mode analysis do not vary along waveguide axis^[1]. The periodic perturbations therefore only change the amplitudes of the ideal modes. This approximation is, however, valid only if the grating perturbation is weak. Otherwise, the ideal mode approximation will become questionable. The problem is more serious for the TM modes because the ideal modes do not satisfy the boundary conditions at the interface. The coupling coefficients evaluated based on the ideal-modes are not correct even for small grating height^[2]. Moreover, as the grating perturbations increases, the possible radiation loss due to the scattering at the surface grating will also become inevitable. The complicated expressions of the radiation modes is required in the coupled-mode analysis to assess the radiation loss^[3].

In this paper, we present a simple transfer matrix method based on the mode-matching of the local normal modes of the structure. The power coupling between the two waveguides and the total insertion loss at one coupling length are derived analytically by this method. The distinct advantages in the present method are: (1) it can be applied to structures with relatively strong index perturbations caused by large grating height and/or large index difference; (2) the TM modes whose transverse electric field is perpendicular to the index interface can be properly treated; (3) the radiation loss due to the scattering at the index discontinuities along the waveguide axis can be estimated without the knowledge of radiation modes. (4) it can be easily used to the analyses of many grating devices such as DFB/DBR lasers and filters.

As an example, the grating coupler made of two dissimilar slab waveguides (Figure 1) was analysed. Figures 2 and 3 show the power coupled from guide 2 to guide 1 for the TE and the TM modes, respectively. The optimum grating period is assumed and the grating heights are chosen to be $2h = 0.1\mu m$. The coupling lengths predicted by this method and the coupled-mode analyses agree well for the TE modes and are quite different for TM modes. In both cases, the decay of the guided power due to the scattering at the junctions of the grating is predicted by the present method. Examples of DFB/DBR structures will be presented and discussed at the meeting.

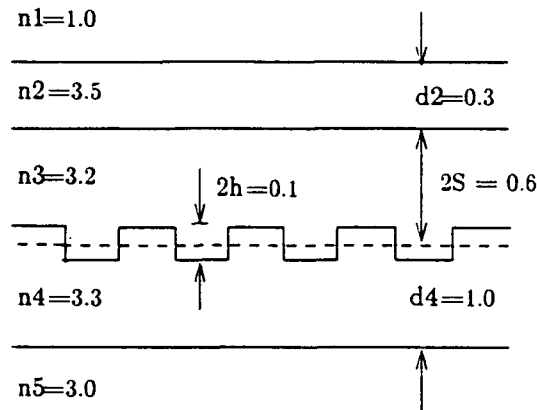


Figure 1: Grating-assisted coupler

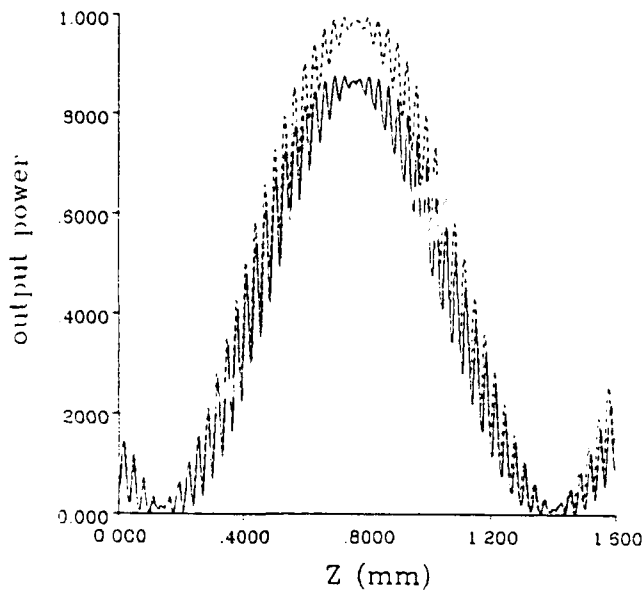


Figure 2: TE mode. solid: this paper; dash: coupled-mode analysis

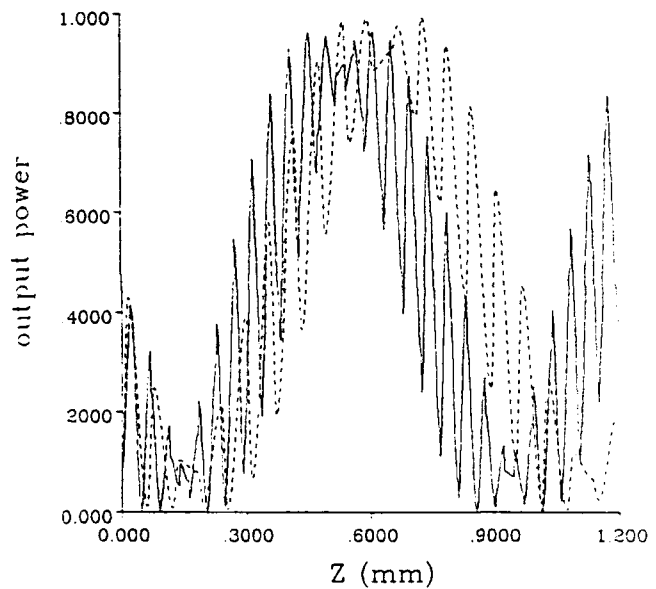


Figure 3: TM mode. solid: this paper; dash: coupled-mode analysis

References

- [1]R. Marz and et al, *Opt. Quantum Electron.*, vol. 19, pp. 273-287, 1987.
- [2]D.G. Hall, *Opt. Lett.*, vol. 15, pp. 619-621, 1990.
- [3]D. Marcuse, *IEEE J. Quantum Electron.*, vol. 26, pp. 675-684, 1990.

MoL-BPM Algorithms for Waveguide Bends and Vectorial Fields

R. Pregla, J. Gerdes, E. Ahlers, S. Helfert

Allgemeine und Theoretische Elektrotechnik

FernUniversität, Hagen, Federal Republic of Germany

Introduction

The hitherto used BPM algorithm based on the MoL [1] was first demonstrated at the Hilton Head Conference [2] and then described in [3]. The MoL-BPM overcomes the disadvantages of the BPM based on the paraxial approximation, e.g. small refractive index steps, artificial absorbers, numerical loss. Special characteristics of the MoL-BPM are the use of Helmholtz (or Sturm-Liouville) Equation, numerical absorbing or radiation conditions, use of eigensolution, implementation of the interface conditions for the fields. In this contribution two new algorithms will be presented. First a special algorithm for waveguide bends is presented. Then an algorithm for the vectorial field is described.

Algorithm for waveguide bends

Figure 1a shows a waveguide bend.

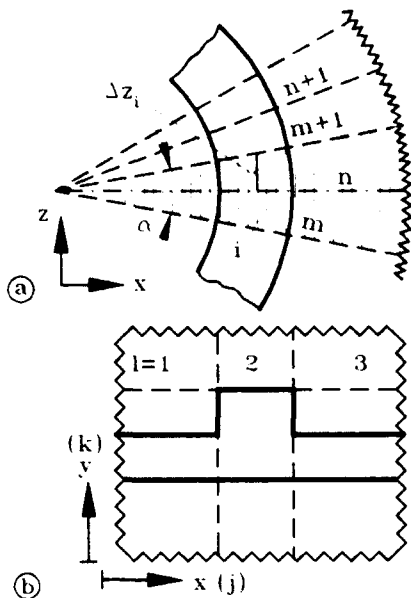


Fig. 1 (a) Waveguide bend

(b) Example for a cross section.

The cross section may be general e.g. like that in Fig.

1b for rib waveguide. The bend is divided in sectors with sector angles α (which may be small). As usual in the MoL-BPM we assume the propagation steps of the field on lines, but in this case the propagation steps are depending on the transverse position. As an example the TM case is analyzed. For the discretized Sturm-Liouville-Equation normalized with k_0^2 we have

$$\frac{d^2}{d\bar{z}^2} \hat{\psi} - \bar{h}_x^{-2} \hat{P}_x \hat{\psi} - \bar{h}_y^{-2} \hat{P}_y \hat{\psi} + \hat{\epsilon}_r \hat{\psi} = 0$$

with

$$\begin{aligned} \hat{P}_x &= P_x \otimes I_y & \hat{P}_y &= \text{Diag}(\hat{P}_y^l) \\ \hat{\epsilon}_r &= \text{Diag}(\hat{\epsilon}_r^l) & \hat{P}_y^l &= I_x^l \otimes P_y^l \\ \hat{\epsilon}_r^l &= I_x^l \otimes \epsilon_r^l & P_y^l &= \epsilon_e^l D_{hy}(\epsilon_h^l)^{-1} D_{cy} \end{aligned}$$

where $l = 1, 2, 3$. The components ψ_i of the potential ψ in the vector $\hat{\psi}$ are obtained as follows: $i = k + N_y(j - 1)$. The same is valid for ϵ_{ri} in ϵ_r . I_x^l, I_y are unity matrices \otimes denotes the Kronecker product. In ϵ_r^l the interface conditions are incorporated as usual in the MoL [1][3]. For D and P see [3]. With the abbreviation Q the transform for diagonalization runs as follows:

$$Q = \bar{h}_x^{-2} \hat{P}_x + \bar{h}_y^{-2} \hat{P}_y - \hat{\epsilon}_r \quad T^{-1}QT = \bar{\lambda}^2$$

$$\frac{d^2}{d\bar{z}^2} \hat{\psi} - Q\hat{\psi} = 0 \quad \frac{d^2}{d\bar{z}^2} \hat{\psi} - \bar{\lambda}^2 \hat{\psi} = 0$$

Now with the propagation steps

$$\Delta z_i = \Delta z_0 + h \text{int}\left(\frac{i-1}{N_y}\right) \tan \frac{\alpha}{2}$$

on the radius line $m+1$ we have

$$\hat{\psi}_{m+1} = \sum_{(S_+),k} \underbrace{T_{ik} e^{-\lambda_k \Delta z_i}}_{(S_+),k} (\hat{\psi}_n)_k$$

or

$$\hat{\psi}_{m+1} = S_+ S_-^{-1} \hat{\psi}_n$$

where S_- is obtained as S_+ but with $-\Delta z_i$ instead of Δz_i . With this solution the field from radius line

to radius line can be calculated. For homogeneous bends in addition Floquets theorem is used

$$\hat{\psi}_m = e^{-m\Gamma} \hat{\psi}_0$$

Therefore the sector angles can be very small and high accuracy is possible. In order to reduce the numerical effort also an algorithm as in [3] can be used with the result

$$\hat{\psi}_{m+1} = e^{-j\hat{\phi}_a} S_+ S_{-1} e^{-j\hat{\phi}_a} \hat{\psi}_m$$

$e^{-j\hat{\phi}_a}$ is the phase correction (or "lensterm") S_{\pm} are the solutions for the basic structure.

In Fig. 2 results for a 2D simulation are shown. They agree very well with analytical results. The loss is 12.53dB/90° in this method and 12.8dB/90° from analytical solution.

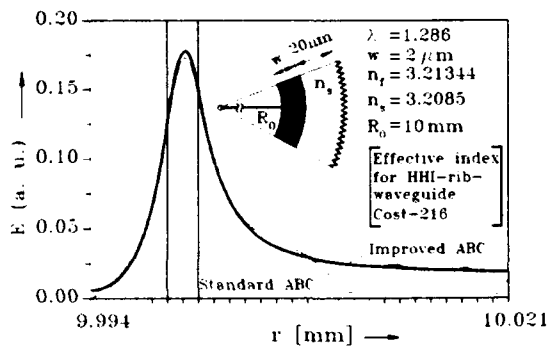


Fig. 2 Fields distribution for a 2D waveguide bend

Algorithm for vectorial field

In this case two coupled Sturm-Liouville Equations must be solved

$$L^{(e)}\psi_e = \epsilon_r^{-1} \frac{\partial \epsilon_r}{\partial \bar{x}} \frac{\partial \psi_h}{\partial \bar{y}}$$

$$L^{(h)}\psi_h = \epsilon_r^{-1} \frac{\partial \epsilon_r}{\partial \bar{y}} \frac{\partial \psi_e}{\partial \bar{x}}$$

This equations are be obtained from [4] with $\epsilon_r = \epsilon_r(x, y)$ and $\mathbf{H} = \psi_e \mathbf{a}_x + \psi_h \mathbf{a}_y$. In Fig. 3 the

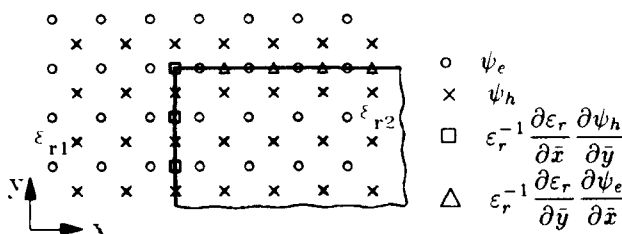


Fig. 3 The positions of discretization points

positions of discretization points are sketched. As can be seen the coupling terms are only nonzero at the interfaces. The coupling term in the first equation results from vertical interfaces (or horizontal changes of ϵ_r) and the coupling term in the second equation results from horizontal interfaces (or vertical changes of ϵ_r). The places of discretization of the coupling terms are different from those of the potentials. Therefore arithmetic mean values must be used for calculation.

$$\hat{\psi}_h^\Delta = \widehat{M}_h \hat{\psi}_h^\times \quad \hat{\psi}_e^\square = \widehat{M}_e \hat{\psi}_e^\circ$$

$$\widehat{M}_h = \mathbf{I}_x \otimes M_h \quad \widehat{M}_e = M_e \otimes \mathbf{I}_y$$

$$M_e = \mathbf{I} + \frac{1}{2} D \quad M_h = \mathbf{I} + \frac{1}{2} D^t$$

The discretized wave equations now run as follows:

$$\frac{d^2}{dz^2} \widehat{M}_e \hat{\psi}_e^\circ - Q_e \widehat{M}_e \hat{\psi}_e^\circ - R_h \hat{\psi}_h^\times = 0$$

$$\frac{d^2}{dz^2} \widehat{M}_h \hat{\psi}_h^\times - Q_h \widehat{M}_h \hat{\psi}_h^\times - R_e \hat{\psi}_e^\circ = 0$$

The transformation is done in two steps. The first one is for the diagonalization of $M_{e,h}$. In principle we obtain

$$\frac{d^2}{dz^2} \begin{bmatrix} \hat{\psi}_e^\circ \\ \hat{\psi}_h^\times \end{bmatrix} - \begin{bmatrix} \bar{Q}_e \bar{R}_h \\ \bar{R}_e \bar{Q}_h \end{bmatrix} \begin{bmatrix} \hat{\psi}_e^\circ \\ \hat{\psi}_h^\times \end{bmatrix} = 0$$

The second transformation is done for the diagonalization of the above bloc-matrix:

$$S_v^{-1} \begin{bmatrix} \bar{Q}_e \bar{R}_h \\ \bar{R}_e \bar{Q}_h \end{bmatrix} S_v = \Gamma^2$$

With the constants Γ the propagation is described and with the eigenvectors S_v the field distribution can be calculated.

References

- [1] R. Pregla, W. Pascher, "The Method of Lines," in T. Itoh, (editor), "Numerical Techniques for Microwave and Millimeter Wave Passive Structures", pp. 381-446, J. Wiley Publ., New York, 1989.
- [2] R. Pregla, J. Gerdes, "New Beam-Propagation Algorithm based on the Method of Lines", *Integrated Photonics Research*, Technical Digest Series, Volume 5, pp. 29-30, 1990
- [3] J. Gerdes, R. Pregla, "Beam-Propagation Algorithm based on the Method of Lines", *J. Opt. Soc. Am. B*, vol. 8, pp. 389-394, Feb. 1991.
- [4] R. E. Collin, "Field Theory of Guided Waves", pp. 232-244, McGraw-Hill, New York, 1960.

Analysis of Electrooptic Device Electrodes: Influence of Metalization Thickness, Substrate Optical Axis Inclination and Buffer Layer.

Marat Davidovitz[†], Zhiqiang Wu[†],
Anand Gopinath[†]

Characterization of the transmission line properties of electrooptic modulators has received considerable attention in recent years. Various analytical and numerical approaches have been applied to solve the boundary value problems involving strip lines on anisotropic substrates [1, 2, 3, 4, 5, 6]. In many cases the effects of the electrode thickness and the general nature of the substrate anisotropy were not considered.

Consider the shielded strip line structure shown in Figure 1. The electrodes of thickness t are assumed to reside on a substrate characterized by an arbitrary permittivity tensor. The presented analysis also allows the inclusion of a buffer layer between the anisotropic substrate and the electrodes.

The approach which was used to analyze this configuration is summarized briefly in the following:

1. The solution domain was partitioned into homogeneous rectangular sub-regions. This is illustrated in Figure (1).
2. Laplace's equation within each sub-region were solved using the Semi-Discrete Finite Element Method. In this method, finite element techniques are used to discretize the sub-domains along one of the Cartesian coordinates, in this case along the direction parallel to the interface supporting the electrodes, while the solution along the remaining dimension is obtained analytically.
3. The boundary conditions at interfaces between the sub-regions, on the metal enclosure and on the strips were enforced.
4. The strip line parameters (capacitance, impedance, charge density, etc.) were calculated.

The accuracy of the numerical solution was verified by applying it to several configurations involving single thick and thin strip lines in homogeneous, isotropic media, for which prior analytical solutions were available. In all cases the relative error in the numerical solution was reducible to less than 0.1%.

[†]Department of Electrical Engineering, University of Minnesota, Minneapolis, MN 55455

In Figures 2,3 the characteristic impedance for electrodes on the LiNbO₃ substrate is plotted. The substrate material is characterized by a tensor permittivity

$$\bar{\epsilon}_1 = \begin{pmatrix} \epsilon_{xx} & \epsilon_{xy} \\ \epsilon_{yx} & \epsilon_{yy} \end{pmatrix}$$

The principal axes of the permittivity matrix, denoted by ξ, η , are inclined at an angle θ with respect to the x, y axis, respectively. Within this framework, the elements of the permittivity tensor can be expressed as follows

$$\begin{aligned} \epsilon_{xx} &= \epsilon_{\xi} \cos^2 \theta + \epsilon_{\eta} \sin^2 \theta \\ \epsilon_{yy} &= \epsilon_{\xi} \sin^2 \theta + \epsilon_{\eta} \cos^2 \theta \\ \epsilon_{xy} &= \epsilon_{yx} = 0.5(\epsilon_{\xi} - \epsilon_{\eta}) \sin 2\theta \end{aligned}$$

where in the case of the LiNbO₃ the values $\epsilon_{\xi} = 28$, $\epsilon_{\eta} = 44$ were used in computation.

In Figure 2 the characteristic impedance for an asymmetrical strip line is plotted as a function of W_1/S and t/S . The second electrode is very wide - $W_2 \approx 15 \times (W_1 + 2S)$ - and is grounded. The results presented in [6] are plotted alongside for comparison. The effect of the substrate principle axis inclination is studied in Figure 3. The difference in characteristic impedance from the cases where the the principle axis are aligned with the electrode surface can be as much as 7% .

Additional results, illustrating influence of the buffer layer, in addition to electrode thickness and substrate anisotropy, will be shown during the presentation.

References

- [1] T. Kitazawa and T. Itoh, "Asymmetrical Coplanar Waveguide with Finite Metallization Thickness Containing Anisotropic Media", *IEEE Trans. Microwave Theory Tech.*, MTT-39, Aug. 1991.
- [2] Manuel Horno, "Quasistatic characteristics of covered coupled microstrips on anisotropic substrates: Spectral and variational analysis", *IEEE Trans. Microwave Theory Tech.*, MTT-30, Nov. 1982.
- [3] Shibata et al. Shielded-strip transmission line with anisotropic medium. *IEEE Trans. Microwave Theory Tech.*, MTT-30:1264-1267, August 1982.
- [4] T. Kitazawa. Metalization thickness effect of striplines with anisotropic media. *IEEE Trans. Microwave Theory Tech.*, MTT-37:769-75, April 1989.

MB16-3

- [5] N. G. Alexopoulos. Integrated-circuit structures on anisotropic substrate. *IEEE Trans. Microwave Theory Tech.*, MTT-33:847-81, October 1985.
- [6] J.P. Donnelly and A. Gopinath, "A comparison of power requirements of traveling-wave LiNbO₃ optical couplers and interferometric modulators", *IEEE J. of Quantum Electronics*, QE-23(1), pp.#30-41, January 1987.

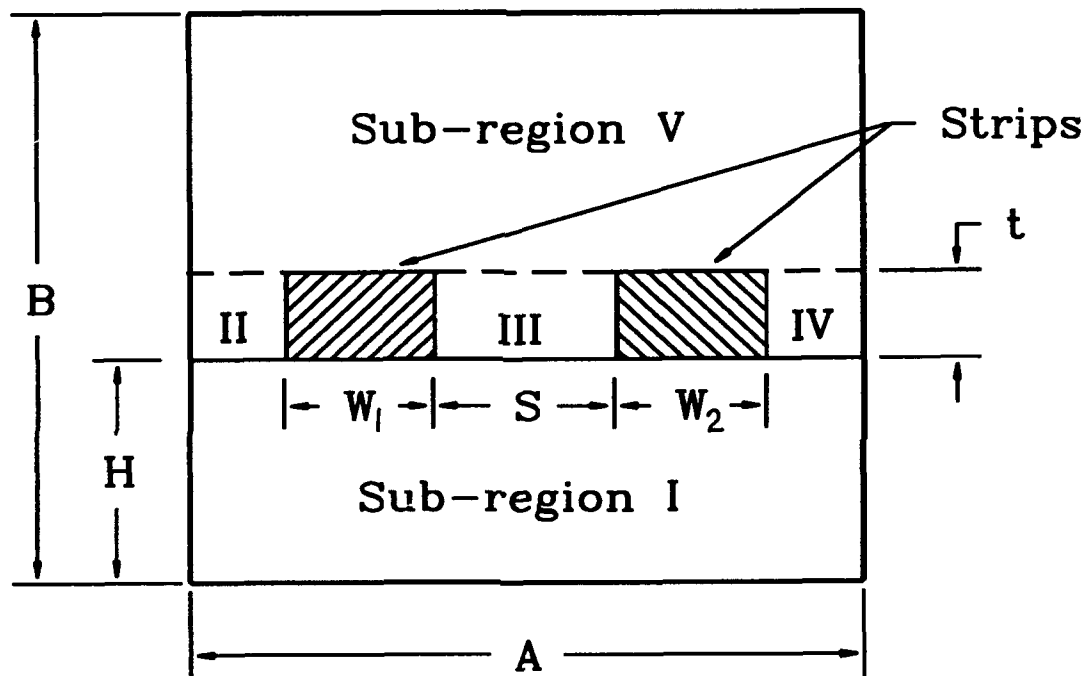


Figure 1: Cross-section of the strip line structure

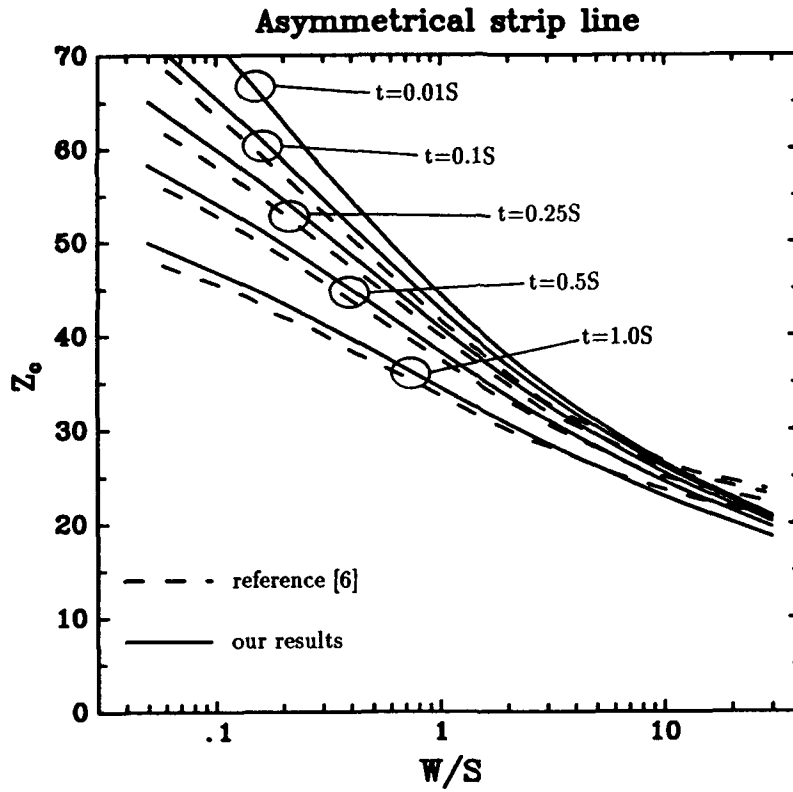


Figure 2: Characteristic impedance for an asymmetrical strip line

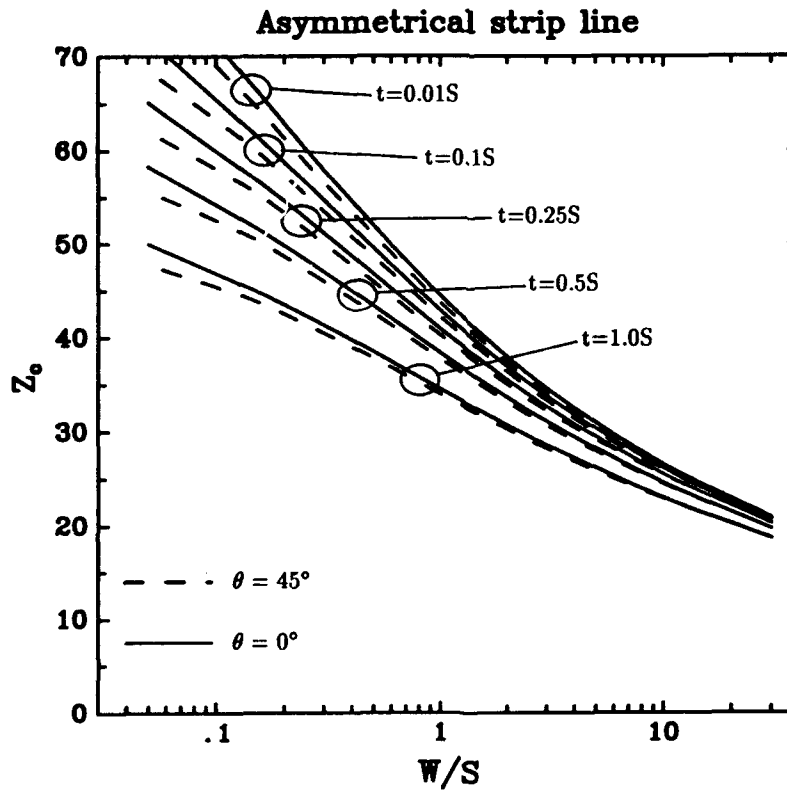


Figure 3: Characteristic impedance for an asymmetrical strip line with different optical axis inclination angles

Using the Finite Difference Time Domain Method as a Design Tool

Robert R. McLeod
University of Colorado, Boulder
(303) 492-0370

and

Raymond J. Hawkins
Lawrence Livermore National Lab
(510) 422-0581

Introduction

The finite-difference time-domain (FDTD) method has been shown in the last several years to be applicable to guided-wave photonics problems. The application of the method to diffraction gratings, intersecting and bending wave-guides [1], and Bragg mirrors has served to demonstrate that method can solve a set of problems not tractable for more traditional techniques such as the beam propagation method. Although these papers have served to demonstrate the applicability of the FDTD technique, few papers have described the use of the FDTD analysis in a design environment.

This paper will describe the use of the FDTD method in two design problems and show how specific engineering questions can be answered with the simulation technique. The first problem, a distributed feedback reflector for a graded index wave-guide laser, will demonstrate the ability of FDTD to model complex structures whose analysis would otherwise be virtually intractable. The second example, a multi-layer Bragg wave guide design, will show how the FDTD technique can be used to complement and extend other analysis methods.

Distributed feedback reflector design problem

A simplified schematic of the problem to be analyzed is shown in figure 1. In this problem, a complex graded-index, single-moded wave-guide is to be terminated in a multi-layer dielectric mirror. The designer of the device needs specific information on the best choice of mirror thicknesses and the number of layers to use. As the number of layers is increased, the reflectance improves, but the losses due to diffraction in the mirror region eventually degrade the response.

The engineer creating this device needs to have design curves detailing the energy reflected back into the fundamental mode of the guide as the geometry and size of the reflecting mirror are varied. He also needs to be able to vary the properties of the graded-index wave-guide to see how they effect the overall reflectance. The use of the FDTD method to produce this data in a simple and automated fashion will be shown.

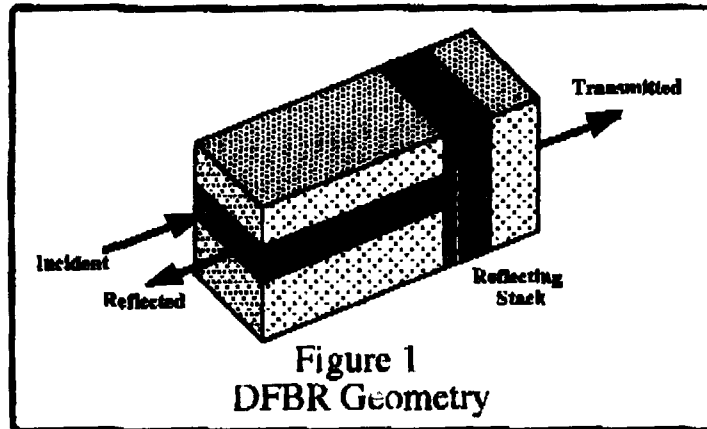


Figure 1
DFBR Geometry

Bragg reflection wave-guide

The second design problem, a Bragg reflection wave-guide, is not so analytically intractable. For an infinite number of layers in the reflecting stack, the solution for guided waves can be found in closed form [2]. However, when the number of layers is made finite, a method such as FDTD must be used for the same reasons as discussed above. In this problem, the design questions involve the loss due to the finite stack size and the dispersive properties of the guide. As will be presented, the FDTD technique can produce engineering design curves that give precise answers about the trade-offs of coupling loss and dispersion versus the size and properties of the stack and the polarization of the light.

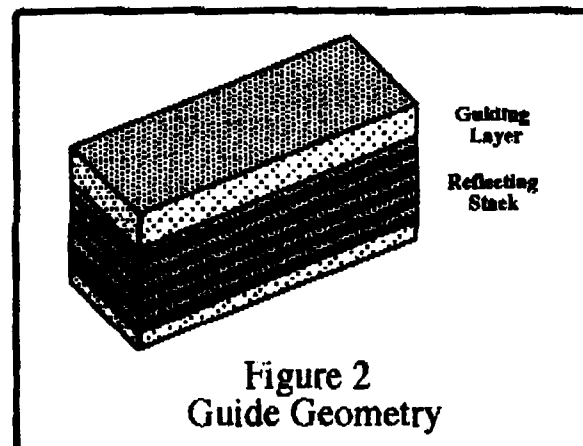


Figure 2
Guide Geometry

In this paper we hope to show that the FDTD method can be brought "out of the lab" and used as a real-world design tool. We believe that the speed, power, and simplicity of the method make it quite suitable as the basis of a computer aided design platform for integrated photonics devices.

References

- [1] Chu, Sai Tak, "Modelling of Guided-Wave Optical Structures by the FDTD Method," PhD. dissertation from University of Waterloo, Canada, 1990.
- [2] Lenz, Gadi, and Salzman, Joseph, "Eigenmodes of Multiwaveguide Structures," *Lightwave Technology*, Vol. 8, No. 12, December 1990, pp. 1803-1809

MB18-1

Programmable electro-optic waveguide filter

H. Okayama and M. Kawahara

R&D Group, Oki Electric Industry Co., Ltd.

550-5 Higashiasakawa, Hachioji, Tokyo 193, Japan

Phone: +81-426-63-1111

Optical switching systems using the wavelength multiplexing technique are considered to be suitable for exchanging large numbers of channels. Electrooptic wavelength tunable filters are one of the key components in this type of system. The electrooptic filters which have been studied have only been capable of selecting single channels. Filters using the acoustooptic effect can overcome this limitation, but the switching speed is slow. A bulk type programmable filter has been proposed [1]. However, to achieve a narrow transmission bandwidth, the number of electrodes and drive circuits increases substantially. Here, we will propose devices that can overcome these limitations using the inherently high speed electrooptic effect.

The structures of the devices which we propose are shown in Fig.1 (a) and (b). The structure of the device shown in Fig. 1(a) is composed of multisection TM/TE mode converters with interdigital electrodes (IDT). The structure of the device shown in Fig. 1(b) is the same as that of Ref. 2. However, each section of the mode converter and phase shifter is controlled independently. To drive the device shown in Fig. 1(a), periodic voltage is applied to mode converters such that the coupling coefficient $C(z)$ between two modes of this device is represented as

$$C(z) = C_0 \cos(Kz) \sum_I \cos(\Delta K_I z)$$

where z is the distance in the direction of propagation, C_0 is the constant, K is the wave number of the IDT and ΔK_I is the wave number of the periodic applied voltage. Since in each mode converter, the electrodes are driven by the same voltage, the term $\cos(\Delta K_I z)$ becomes a quantized function. Efficient mode conversion occurs at wavelengths of

$$\lambda_1^m = 2\pi \Delta n / (K + \Delta K_s m \pm \Delta K_I) \cong \lambda_0^m [1 \pm \Delta K_I / (K + \Delta K_s m)]$$

where $\lambda_0^m = 2\pi \Delta n / (K + \Delta K_s m)$ and Δn is the birefringence. ΔK_s is the sampling wavenumber due to the grouping of IDT electrodes (quantization of $\cos(\Delta K_I z)$) and m is an integer. Wavelength tuning with conventional filters was accomplished by changing the bias voltage, and the tuning range was proportional to the voltage which was applied. Thus, extremely high voltage was needed to tune a device. However, wavelength tuning of this device is accomplished by changing the period ΔK_I of the applied voltages, which is independent of the bias level. The maximum tuning range is $\lambda_0^0 \Delta K_I / K$. An example of the calculated transmission of the device is shown in Fig. 2. The calculation was performed using the transfer matrix of Ref. 2. Figure 2 shows the transmission characteristics when the device is driven to select two wavelengths λ_1 and λ_2 simultaneously. The number of mode converters was 30, $K/\Delta K_s = 30$, $\Delta K_I/\Delta K_s = 0.3$, $\Delta K_2/\Delta K_1 = 1.5$ and $C_0 \times (\text{total length}) = \pi/2$.

The transmission of the device shown in Fig.1(b) is approximated by the next Fourier series when the mode convergence is small.

$$\sum_m B_m \exp[i m (1 - \lambda_0^0 / \lambda) K L_p]$$

where B_m is a complex number which amplitude is controlled by the mode conversion efficiency and which phase is controlled by the phase shifter section with length L_p . By setting

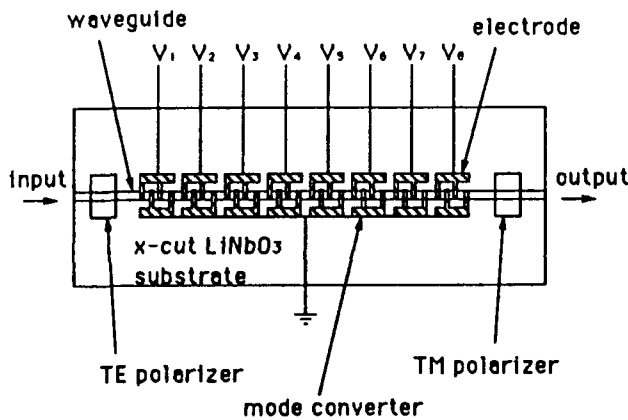
proper values for B_m , the transmission characteristics of the device can be altered such as to select multiple wavelengths simultaneously. A calculated transmission similar to Fig.2 (with shifted center wavelength of the tuning range) was obtained. The equivalent circuit of this filter (like that of the multibranch Mach-Zehnder filter) is the same as the transversal filter.

The transmission 3dB bandwidths of these devices are the same as that of a conventional waveguide device using the mode conversion effect of Ref.2. With N drive circuits $N/2$ channels could be selected. This type of filters and the mode splitters can be cascaded to construct wavelength selective switch matrix.

The results of preliminary experiments are shown in Fig.3. The 16 section mode converters of Fig.1(a) were used to construct the band rejection filter. The length of each mode converter was 1.8 mm. Figure 3 shows the transmission changes from the zero voltage transmission spectrum. The transmission spectrum changes due to changes in the voltage period were observed.

References

- [1] J.F.Lotspeich et al., Opt. Eng., 20, pp. 830 – 836 (1981)
- [2] F. Heismann and R.C. Alferness, J. Quantum Electron., QE-24, pp. 83 – 93 (1988)



(a)

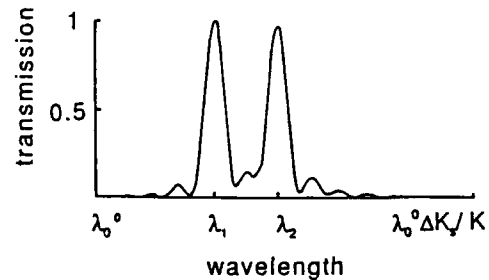
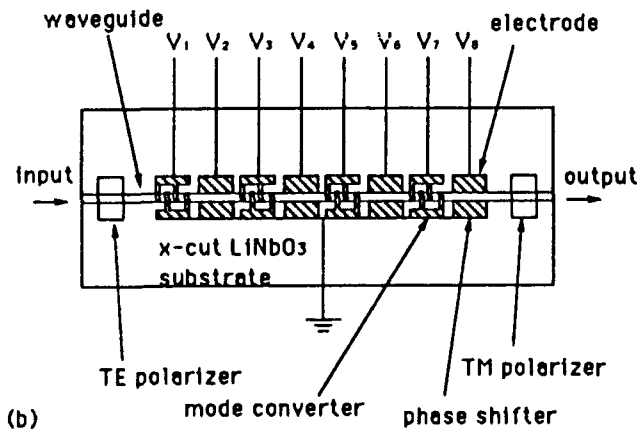


Fig.2 Calculated transmission of the device shown in Fig. 1(a). (Two wavelengths are selected.)



(b)

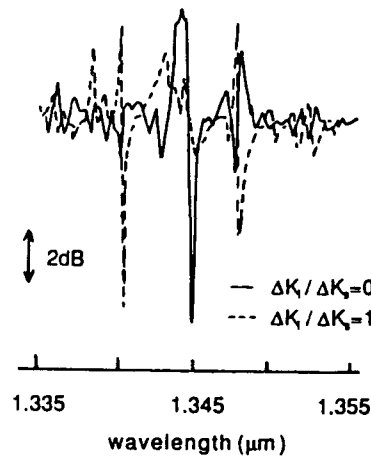


Fig.3 Experimental results for the band rejection filter using electrode structure shown in Fig. 1(a).

Fig. 1 Schematic structure of the device

MB19-1

GUIDED-WAVE ACOUSTOOPTIC MODULATOR IN RB:KTP

**Buritskii K.S., Dianov E.M., Kiselev A.V., Maslov V.A.,
Shcherbakov E.A.**

*General Physics Institute, U.S.S.R. Academy of Sciences
38 Vavilov Str., Moscow, 117942, U.S.S.R.*

telex 411074 LUMEN SU, fax (095)1358139, phone (095)1328231

KTP crystals, characterised by superior properties, are used widely in nonlinear optics, in particular for second harmonic generation. Also, owing to easy fabrication technology of low loss optical waveguides (~ 1 dB/cm), the KTP crystals are used for the fabrication of integrated optical elements [1]. The important advantage of waveguides in KTP (for example, in comparison with that in the more widely used Ti:LiNbO_3) is the high optical damage resistance, up to 0.9W more light power in visible range [2].

These properties of KTP give the possibility of designing some of the integrated optical elements for optical signal processing systems, particularly waveguided acousto-optical modulators and deflectors, using the surface acoustic waves (SAW) and optical waves interaction. Recently, the direct SAW excitation in KTP crystal by means of interdigital transducers (IDT) has been demonstrated [4].

The substrates of $10 \times 15 \times 1$ mm in dimension along X, Y, Z axes respectively were cut from the KTP boule, grown by flux method. The optical waveguide was formed by means of ion exchange in RbNO_3 melt at a temperature of 350 C for 1h [1]. Measurement of KTP substrate conductivity before and after the ion exchange has showed that after ion exchange it decreased by about two orders up to 6 nSm. Then by using photolithography technique the gold interdigital electrodes with the following parameters have been fabricated: structure period $L=8 \mu\text{m}$, electrode length $W=1$ mm, number of pairs $N=30$, interval between transducer systems 5.9mm. The light was launched into the waveguide through the polished endface (Fig.1).

The distribution of the TM mode intensity for electrical power of 200 mW is given on Fig.2. The dependence of diffracted light for TM and TE modes on the electrical power is shown on Fig.3. The analysis of results has shown the fact that effective modulation of TM mode is possible in Rb:KTP waveguide by means of the direct excited SAW.

References:

- 1 Bierlein, J.D., Vanherzeele, H., *J. Opt. Soc. Am.*, 1989, 6, 622.
- 2 Buritskii, K.S., Dianov, E.M., Maslov, V.A., Chernykh, V.A., Shcherbakov, E.A., *Sov. Lightwave Communication*, 1991, 1, 107.
- 3 Stucky, G.D., Phillips, M.L., Gier, T.E., *Chem. Mater.* 1989, 1, 492.
- 4 Buritskii, K.S., Dianov, E.M., Kiselev, A.V., Maslov, V.A., Shcherbakov, E.A., *Electronics Letters*, 1991, 27, 1896.

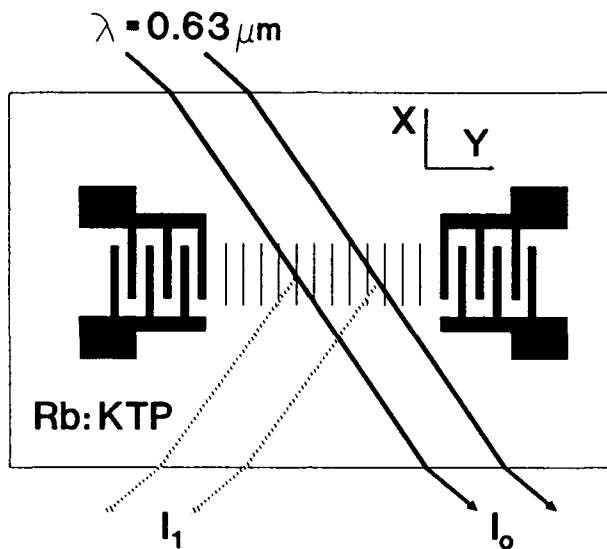


Fig.1. Acoustooptic modulator in Rb:KTP.

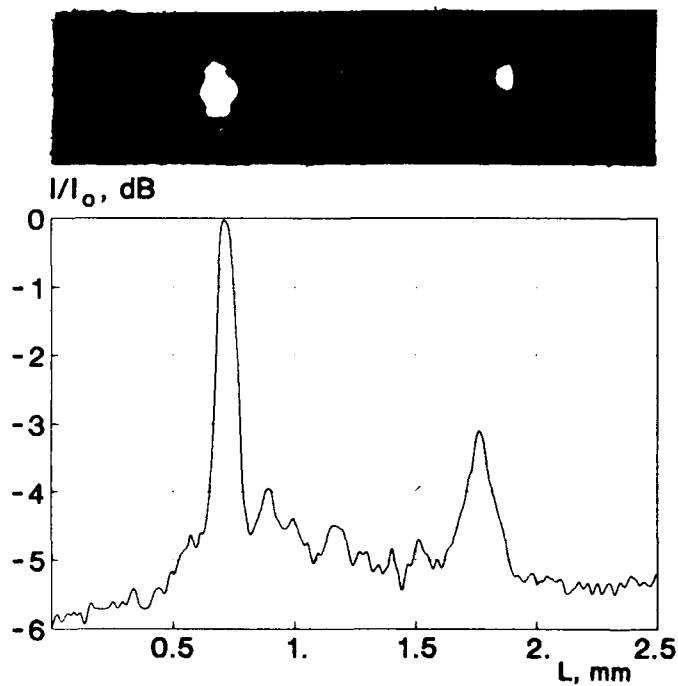


Fig.2. The distribution of TM mode intensity.

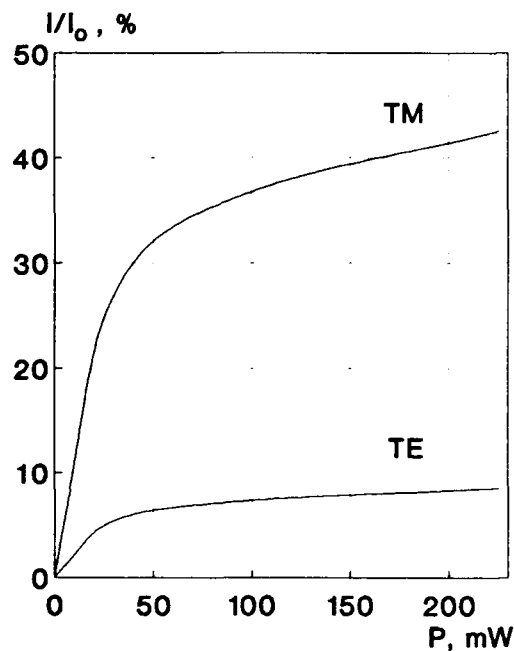


Fig.3. The dependence of diffracted light for TM and TE modes on the electrical power.

Electro-Optically Tunable General Polarization Transformer on GaInAsP/ InP Using "Analog" and "Digital" Control Voltage Patterns

M. Schlak, P. Albrecht, H. Heidrich, H.-P. Nolting, F. Reier
 Heinrich-Hertz-Institut für Nachrichtentechnik Berlin GmbH
 Einsteinufer 37
 D-1000 Berlin 10

Introduction

Polarization transformers are key components for future optical signal processing circuits e.g. in a coherent optical polarization diversity receiver OIC. Here the received TE- and TM-polarisation modes are splitted, heterodyned and detected separately. Since the integrated laser only emits in TE-polarization a TE/TM-mode converter is necessary to produce the required TM-polarization [1]. In the framework of the RACE project *Coherent Multichannel System* a TE/TM-mode converter in the GaInAs-InP-system for an operating wavelength of $1.56 \mu\text{m}$ has been developed and investigated. Fabricated devices showed a 45° mode conversion necessary in the OIC at a maximum voltage of 50 V.

Concept

The polarization transformer consists of the ridge waveguide oriented along the $[110]$ direction. TE/TM-mode conversion is achieved by an electrostatic field parallel to the $[1\bar{1}0]$ direction (fig. 1). The field can be generated by a deep p^+ -doping introduced into the n^- -layer beside the waveguide. For an applied reverse bias, the voltage drop is almost entirely in the depletion area created in the quaternary layer outside of the p^+ -doped region. The overlap of the optical field with the static electrical field determines the degree of TE/TM-mode

conversion and the overlap with the lossy p^+ -region yields the additional loss of the device [2].

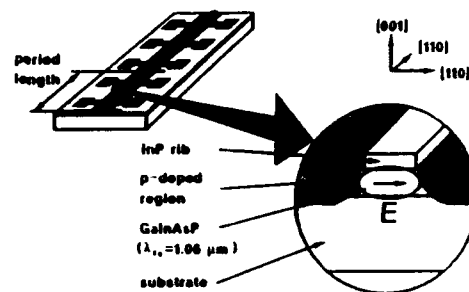


Fig.1: TE/TM-mode converter architecture

Device Structure

Usually the propagation constants β of rib waveguides differ for TE- and TM- polarization. Therefore, the control voltages for electro-optically induced mode conversion have to be matched to the TE/TM beatlength Λ_0 . In the ideal case the applied voltage has to change sign with a period of $\Lambda_0/2$. This is realized in our device by fabricating electrodes on both sides of the waveguide with the control voltage applied alternatively on the left and right side ($\Lambda_0/2$ structure).

In general, for actual devices Λ_0 will not coincide with the electrode period length given by the mask pattern. The use of electrodes consisting of a multiple of subelectrodes (in our case 4 subelectrodes per period) provides the possibility not only to

tune the control voltages to the actual TE/TM beatlength Λ_0 ($\Lambda_0/4$ structure), but also to vary the electrical phase η of the control voltage pattern resulting in a variation of the optical phase between TE- and TM-mode at the output of the device. In addition, this configuration allows a reset-free continuous operation of the device as an optical compensator for arbitrary polarization transformation ranging between pure phase-conversion and pure TE/TM-conversion [3] which could be shown in a simulation and in experiments. As an example in fig. 2 measured curves of the same device are shown operating as a polarization converter and as a pure phase shifter.

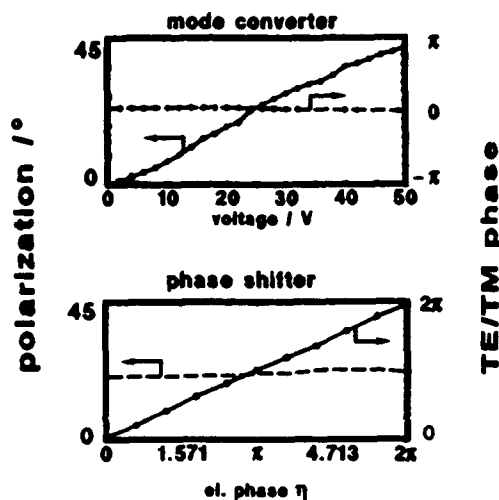


Fig. 2: mode converter: operation
a: pure polarization converter
b: pure phase shifter

As in general the control voltages have to be matched to the actual beatlength of the fabricated waveguide a large number of different voltages has to be controlled. This is a main drawback for practical applications. A new "digital tuning" technique using only a single voltage eliminates this problem. Here only the voltage pattern is varied with a constant maximum control voltage. The resulting curves of e.g. tuning experiments - although slightly "rougher" than the normally measured curves, due to the limited number of electrodes per period - seem to be sufficient even for polarization control experiments. Furthermore, the efficiency of the electro-optical mode conversion is a up to a factor of $\sqrt{2}$ higher due to control voltages of maximum heights. This has been shown in

simulations and in experiments as well (fig. 3).

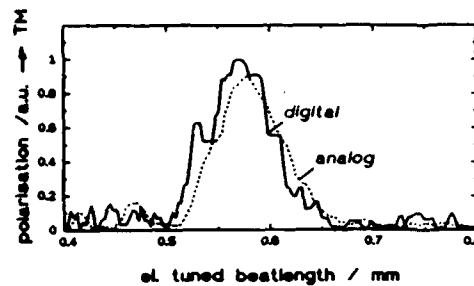


Fig. 3: tuning mode
period length: 0.8 mm
number of periods: 5
electrodes/ period: 4
beatlength: 0.57 mm

Conclusion

In conclusion we fabricated an electro-optically controllable general polarization converter and verified its versatility ranging from pure phase shift operation to polarization conversion. For practical use, a "digital" control voltage operation has been realized for the first time using only a single voltage with voltage patterns matched to the actual beatlength of the fabricated waveguide.

References

- [1] M. Schlak, H.-P. Nolting, P. Albrecht, W. Döldissen, D. Franke, U. Niggebrügge, F. Schmitt, *Electronics Letters*, Vol. 22, No. 17, August 1986
- [2] M. Schlak, C. M. Weinert, P. Albrecht, H.-P. Nolting, *IEEE Photonics Technology Letters*, Vol. 3, No. 1, January 1991
- [3] H.-P. Nolting, H. Heidrich, D. Hoffmann, *Patentanmeldung DE: P 36 798.5*, 18.9.1986 (US-PS 4 832 431)

MB21-1

Vertically Integrated AlGaAs Waveguide and GaAs Photodetector with Efficient Total-internal-reflection Coupling

R. W. Ade, D. E. Bossi, R. P. Basilica, and J. M. Berak

United Technologies Research Center
East Hartford, Connecticut 06108
(203) 727-7297

We present a new approach for monolithic optical waveguide-to-photodetector coupling that enables integration of photodetectors with active integrated-optic components. Several techniques for integrating *passive* waveguides with photodetectors have been reported [1-3], but to our knowledge integration of detectors with *active* waveguide modulators has not been demonstrated. This paper reports efficient monolithic coupling between low-loss AlGaAs channel waveguides and multi-GHz GaAs MSM photodetectors, using a device structure and fabrication process compatible with high-performance modulator integration. In combination with on-chip electronics [4], detector integration enables monolithic feedback control of analog external modulators and realization of taps for high-speed optoelectronic signal processing.

A cross-sectional profile of the integrated waveguide/photodetector is shown in Fig. 1(a). Optical radiation at $\lambda = 0.84 \mu\text{m}$ is incident from an AlGaAs single-mode strip-loaded waveguide onto an etched total-internal-reflection (TIR) mirror. The mirror redirects the optical beam upward through the transparent cladding, onto the backside of an overlying GaAs MSM photodetector. The AlGaAs waveguide and cladding are sufficiently thick to confine >99.9% of the guided mode within these transparent layers, ensuring low propagation loss, yet the optical path from the mirror to detector through the upper cladding is sufficiently short to prevent appreciable spreading of the unguided beam. Hence, the TIR mirror provides efficient coupling between a low-loss waveguide and small-area photodetector. A key feature of the structure in Fig. 1(a) is the ease of integrating an active p-i-n modulator into the waveguide without introducing significant propagation loss. In a similar structure, we have fabricated efficient ($V_{\pi} \sim 6 \text{ V}$), low-loss (<1 dB/cm) intensity modulators with monolithic drive electronics, by using Be implantation and electrode deposition to define the waveguide active regions [4].

Figure 1(b) shows a SEM photograph of an integrated waveguide/detector with a wet-chemical-etched TIR mirror. Devices are processed on MOCVD-grown heterostructures with $<2 \times 10^{14} \text{ cm}^{-3}$ residual n-type carriers in the undoped waveguide and detector layers. Interdigitated Ti/Pt/Au detector contacts (50- μm -long, 2- μm -wide fingers with 2- μm spacing) are patterned on the GaAs detector layer using a liftoff process, and successive wet etches are used to define the detector mesa and waveguide rib. The final fabrication step involves etching the retrograde mirror, whose surface must be angled greater than 17° from the wafer normal in order to satisfy the TIR condition. Both Cl_2 -assisted ion beam etching and wet chemical etching in 1 H_2SO_4 :8 H_2O_2 :1 H_2O have been used to produce suitably angled ($18^\circ - 22^\circ$) reflectors.

The photoresponse of a waveguide-integrated detector is shown in Fig. 2 for 36.5 μW of 840-nm optical radiation incident from the waveguide. The waveguide-incident power is derived from output power measurements on unterminated adjacent waveguides, adjusted by measured values of propagation (1-2 dB/cm) and output coupling losses. For an applied bias voltage of 8 V, the measured internal responsivity of waveguide-coupled photodetectors (i.e., photocurrent divided by optical power in the waveguide) is $0.56 \pm 0.03 \text{ A/W}$, corresponding to an average internal quantum efficiency $\eta_{\text{int}} = 0.83$. The calculated value of $\eta_{\text{int}} = 0.82$, which assumes unity carrier collection efficiency, is in close agreement with the measured value, indicating a low recombination velocity at the etched surface. Low dark currents (<1 nA at 10 V) and high breakdown voltages (>25 V) provide additional evidence that mirror etching does not degrade photodetector performance. The frequency response for these waveguide-illuminated photodetectors is measured using a 6-GHz-bandwidth GaAs laser diode and network analyzer.

The overall system response (laser plus packaged detector) is shown in Fig. 3 and exhibits a 5-GHz 3-dB bandwidth. The dip in frequency response around 4.4 GHz is due to the detector package, as confirmed by S_{21} measurements on the package alone. Currently, the photodetector bandwidth is limited by the $(150 \times 100 \mu\text{m}^2)$ bond pad-to-backplane capacitance. Reducing the bond pad area will readily extend the detector bandwidth to >10 GHz while maintaining high η_{int} .

The authors acknowledge Dr. W. D. Goodhue and G. A. Lincoln of MIT Lincoln Laboratory for Cl_2 -assisted ion beam etching of TIR mirrors.

References

1. S. Chandrasekhar, J.C. Campbell, F.G. Storz, A.G. Dentai, C.H. Joyner, G.J. Qua, T.J. Bridges, *Electron. Lett.* **24**, 1145 (1988).
2. R.J. Deri, N. Yasuoka, M. Makiuchi, H. Hamaguchi, O. Wada, A. Kuramata, R.J. Hawkins, *IEEE Photon. Technol. Lett.* **2**, 496 (1990).
3. R.J. Deri, T. Sanada, M. Makiuchi, A. Kuramata, H. Hamaguchi, O. Wada, S. Yamakoshi, *IEEE Photon. Technol. Lett.* **2**, 581 (1990).
4. D.E. Bossi, R.W. Ade, R.P. Basilica, J.M. Berak, R.N. Sacks, R.D. Carroll, T.C. Eschrich, 1992 Optical Fiber Communication Conference, Paper ThJ6.

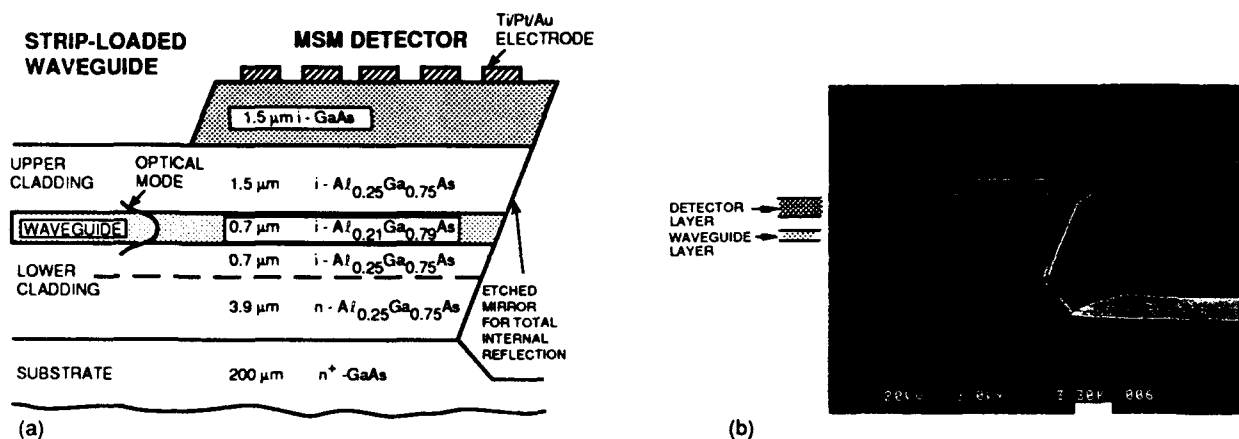


Fig. 1. (a) Cross-sectional profile of an integrated waveguide/photodetector utilizing a total-internal-reflection mirror. (b) SEM photograph of a fabricated device with wet-etched mirror.

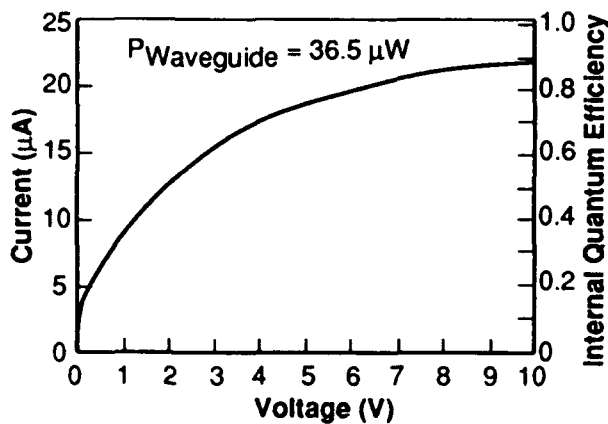


Fig. 2. Photoresponse of a waveguide-illuminated MSM photodetector at $\lambda = 0.84 \mu\text{m}$.

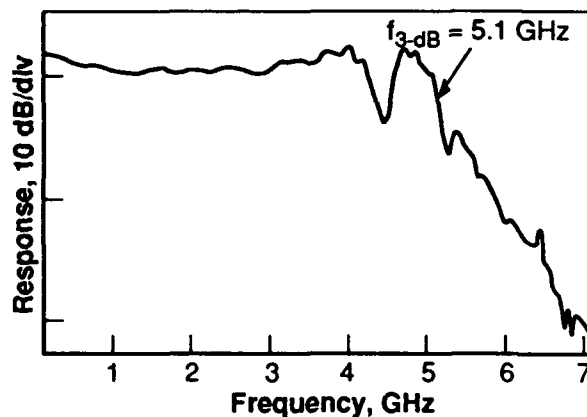


Fig. 3. Frequency response of a packaged waveguide-integrated photodetector. The dip around 4.4 GHz is due to the detector package.

Single layer structure supporting both HBT and modulator

K.W. Goossen, J.E. Cunningham, and W.Y. Jan
 AT&T Bell Laboratories, room 4B-519
 Crawfords Corner Rd.
 Holmdel, NJ 07733
 (908) 949-6979

Optical interconnection of electronic integrated circuit chips is currently of great interest. This would provide a much greater bandwidth of information flow on and off the chip, especially if surface-normal devices are used since then information may flow vertically from the chip and the entire area of the chip may be used rather than just the periphery. Modulators are attractive candidates for active optical input/output. We demonstrate here a simple, elegant scheme for producing a modulator and a heterojunction bipolar transistor (HBT) on the same chip.

Our layer structure is generally n-p-i-n from the surface downward, with the top layer forming the emitter, and the i region between base and collector. Separate HBT's and modulators are formed by etching mesas with or without emitter pads and without or with optical windows, respectively. This structure has been investigated previously in Ref. 1, wherein the i region was a GaAs/Al_{0.3}Ga_{0.7}As multiple quantum well (MQW). This MQW is pathological to the performance of a HBT, since the high barriers block carriers from leaving the base. Indeed, in Ref. 1 a 1000 Å i GaAs spacer was placed between the base and the MQW to allow electrons to accelerate over the barriers, which is pathological to the modulator, since this spacer is absorbing but not electroabsorptive at the operating wavelength. Even so, no HBT characteristics were shown in Ref. 1. In Fig. 1 a similar structure's (without a spacer) HBT curves are shown, demonstrating the severe reduction in performance caused by the i(MQW) region. Ideally, one would prefer a material for the i region which at the same time had strong electroabsorption and

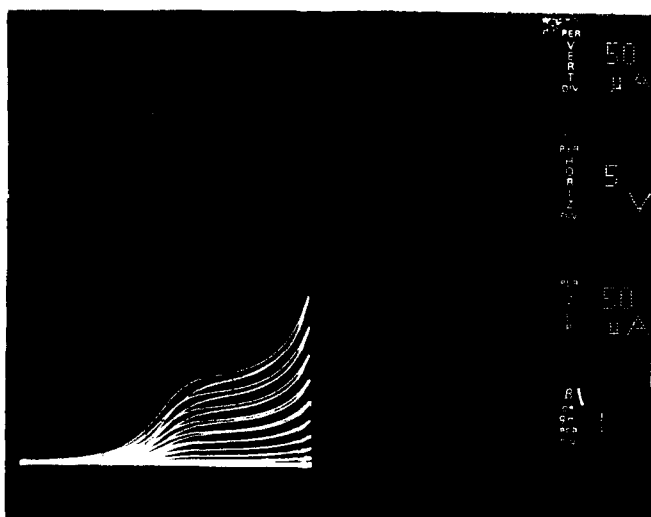


Fig. 1: CE characteristics of n-p-i(deep multi-quantum well)-n HBT.

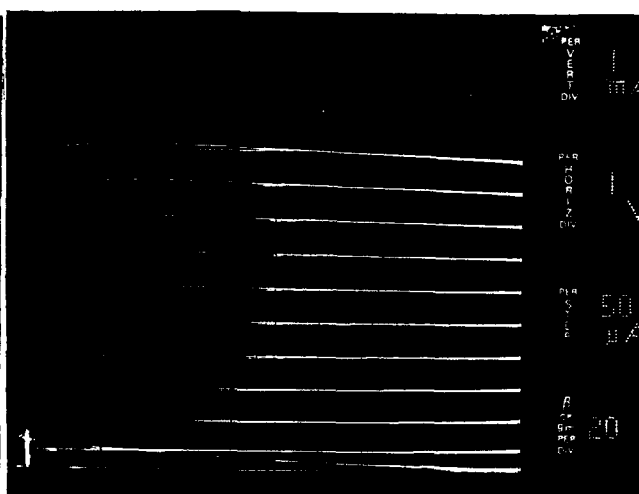


Fig. 2: CE characteristics of n-p-i(shallow MQW)-n HBT otherwise identical.

transport equivalent to bulk GaAs.

We have discovered such a material, the shallow MQW (SMQW) described in Ref. 2. There, we found that when the barriers of a GaAs/Al_xGa_{1-x}As MQW are lowered to $x=0.02$, a strong exciton remained, and the MQW actually had stronger low-field electroabsorption than deep MQW's because the exciton ionized under moderate biases. In Ref. 3 we found that for $x \leq 0.04$, transport in the MQW became equivalent to bulk GaAs because the work function to excite carriers out of the well becomes less than the LO phonon energy.

Here we present a n-p-i(SMQW)-n layer out of which both HBT's and surface-normal modulators are made. The structure and processing is essentially identical to that in Ref. 4, where we demonstrated a novel contacting scheme for HBT's, except that an intrinsic 50 period 100/100 Å GaAs/Al_{0.02}Ga_{0.98}As region is inserted between the base and collector. Also, the sub-collector is Al_{0.3}Ga_{0.7}As, which forms a stop-etch layer that allows the substrate to be removed for transmission measurements. The doped substrate forms the collector contact. The characteristics of the HBT are shown in Fig. 2. An enormous improvement is realized compared to the sample of Fig. 1, which is identical except that $x=0.3$ barriers are used in the MQW. We achieve good characteristics with our n-p-i(SMQW)-n structure with a gain of 15.

For the modulator only a base-contact was made. Shown in Fig. 2 are the transmission spectra at different base-collector biases. A strong exciton exists that decays rapidly and shifts slightly with bias, just as in Ref. 2. We obtain a change in transmission from 30.7 % to 50.1 % for a change in bias from +1 V to -3 V at 859.5 nm.

In conclusion, we have produced an HBT and a modulator on the same chip using a simple structure employing shallow quantum wells, neither of whose performance is affected by the other being present.

The inspiration for this work came during a discussion with A.L. Lentine.

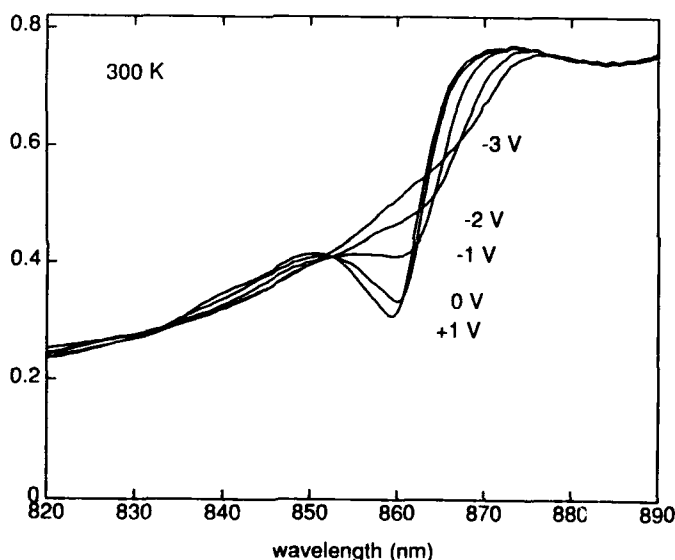


Fig. 3: Transmission spectra of n-p-i(SMQW)-n structure for various biases.

REFERENCES

- [1] W.Q. Li, S.C. Hong, J.E. Oh, J. Singh and P.K. Bhattacharya, *Electron. Lett.* **25**, 476 (1989).
- [2] K.W. Goossen, J.E. Cunningham and W.Y. Jan, *Appl. Phys. Lett.* **57**, 2582 (1990).
- [3] J. Feldmann, K.W. Goossen, D.A.B. Miller, A.M. Fox, J.E. Cunningham and W.Y. Jan, *Appl. Phys. Lett.* **59**, 66 (1991).
- [4] K.W. Goossen, T.Y. Kuo, J.E. Cunningham, W.Y. Jan, F. Ren and C.G. Fonstad, *IEEE Tran. Electron Dev.* **38**, 2423 (1991).

GaAs-Based Integrated Optic RF Signal Processor Modules Using InGaAs Photoconductive Receiver Array

T. Q. Vu and C. S. Tsai
Department of Electrical And Computer Engineering
And Institute For Surface And Interface Science
University of California, Irvine, CA 92717
(714) 856-5144; (714) 856-4152 (Fax)

SUMMARY

There has been a great deal of effort on the integration of various types of devices on a single GaAs or InP substrate to form monolithic optoelectronics and photonic integrated circuits. Utilizing acoustooptic (AO) Bragg cell as the basic modulator, specialized integrated optic functional modules such as RF spectrum analyzers (IOSA), convolvers and correlators[1], space-switches[2], and matrix algebra processors [3] can be realized. Toward this objective we had previously realized GHz AO Bragg cells in GaAs waveguide, and devised the ion-milling technique for fabrication of waveguide lenses and lens arrays of high efficiency and near diffraction-limited characteristics[4]. Most recently, we have succeeded in the integration of the ion-milled lenses and a photodetector array of the InGaAs photoconductive type in a common GaAs waveguide substrate. In this paper we report the first realization of an IOSA in a common GaAs waveguide which consists of a wideband AO Bragg cell, a pair of newly devised curved hybrid lenses, and an InGaAs photoconductive receiver array.

Fig. 1 shows the architecture of the IOSA module in a GaAs waveguide substrate $0.5 \times 6 \times 23 \text{ mm}^3$ in size. The waveguide consists of a $1.1 \mu\text{m}$ thick GaAs layer and a $2 \mu\text{m}$ thick $\text{Al}_{0.15}\text{Ga}_{0.85}\text{As}$ waveguide-substrate layer, both grown by MOCVD on top of a semi-insulating GaAs wafer. Both the collimating and Fourier transform lenses were fabricated using the ion-milling technique referred to above. This lens pair was of the newly devised curved hybrid Fresnel/Chirp grating type which did not incur any significant coma at a field of view up to ± 4 degrees. The collimating (input) lens had an aperture of 1.5 mm and a focal length of 7.5 mm . The Fourier transform (output) lens had an aperture of 1.7 mm and a focal length of 12.5 mm . Both lenses had an ion-milled groove depth of $0.3 \mu\text{m}$ in order to provide an index-change of 0.0149 at $1.3 \mu\text{m}$ wavelength.

Performance of the lenses measured individually on test samples had shown efficiency higher than 53% with -3dB focal-spot sizes ranging from 1.2 to 1.5 times the diffraction-limited spot sizes of 1.7 and $2.8 \mu\text{m}$ for the input and output lenses, respectively. The AO Bragg cell at 500MHz center frequency and octave bandwidth was chosen for this RF signal processor module.

The layer for fabrication of the photodetector array of the photoconductive $\text{In}_{0.53}\text{Ga}_{0.47}\text{As}$ type and the matching load resistor array was first grown by MBE over the waveguide, and except for the mesa areas ($6 \times 50 \mu\text{m}^2$ separated at $10 \mu\text{m}$) which defined each photodetector or load resistor element, was totally removed by ion-milling. Ohmic contacts to the photodetectors and the load resistors were then formed by evaporation of Aluminum and subsequent lift-off. The separation between the cathode and the anode contacts was $2.5 \mu\text{m}$, providing each photodetector with an active area of $2.5 \mu\text{m}$ by $50 \mu\text{m}$. The load resistors having the same structure as the photodetectors were placed 1 mm away from the photodetector array which coincided with the focal plane of the output lens. A second Al metalization layer were formed over a $1 \mu\text{m}$ thick ZnO interdielectric layer to bring the electrical signals out to the probe pads situated at the peripheral edges of the sample. Trench isolation between each receiver element was also formed by ion-milling all the epitaxial layers down to the SI-GaAs substrate. The absorption coefficient of the InGaAs layer at $1.3 \mu\text{m}$ was determined by measuring the transmission of the light through different lengths of the InGaAs layer. The absorption coefficient was measured to be $0.2 \text{ dB}/\mu\text{m}$; thus, the $50 \mu\text{m}$ long photodetector would absorb 90% of the light. The dark resistance of both the photodetectors and the matching load resistors were measured to be $1.24 \text{ k}\Omega$. The responsivity of the

photodetector was measured to be in the range of several thousand A/W at frequency up to 1MHz, but decreasing slowly at higher frequency and down to 1A/W at GHz. Since each photodetector was in series with a matching load resistor, the transimpedance photoresponse across the load resistor was measured as high as several megavolt per watt at 1MHz modulation frequency. This high responsivity of the photoreceiver at low frequency is desirable for AO-based devices because of the relatively low modulation frequency involved. Since the measured $1/e^2$ focal-spot size was roughly $6\mu\text{m}$, the IOSA was capable of 6MHz frequency resolution at $10\mu\text{m}$ photodetector spacing. With the measured AO-bandwidth of 250MHz, the IOSA has provided 41 resolvable frequency channels. The detailed performance characteristics of the IOSA will be presented.

REFERENCE

1. See, for example, the many references cited in C. S. Tsai, *Guided-Wave Acoustooptic Interactions, Devices, and Applications*, New York: Springer-Verlag, 1990.
2. C. S. Tsai and P. Le, "A 4x4 Asymmetric Nonblocking Acoustooptic Space-Switch in LiNbO_3 ," (To Appear in *Appl. Phys. Lett.*)
3. A. Kar-Roy and C. S. Tsai, "A New Integrated Acoustooptic Matrix Algebra Processor Architecture," (To Appear in *Appl. Phys. Lett.*)
4. T. Q. Vu, J. A. Norris, and C. S. Tsai, "Planar Waveguide Lenses In GaAs By Using Ion Milling," *Appl. Phys. Lett.* **54**, 1098 (1989).

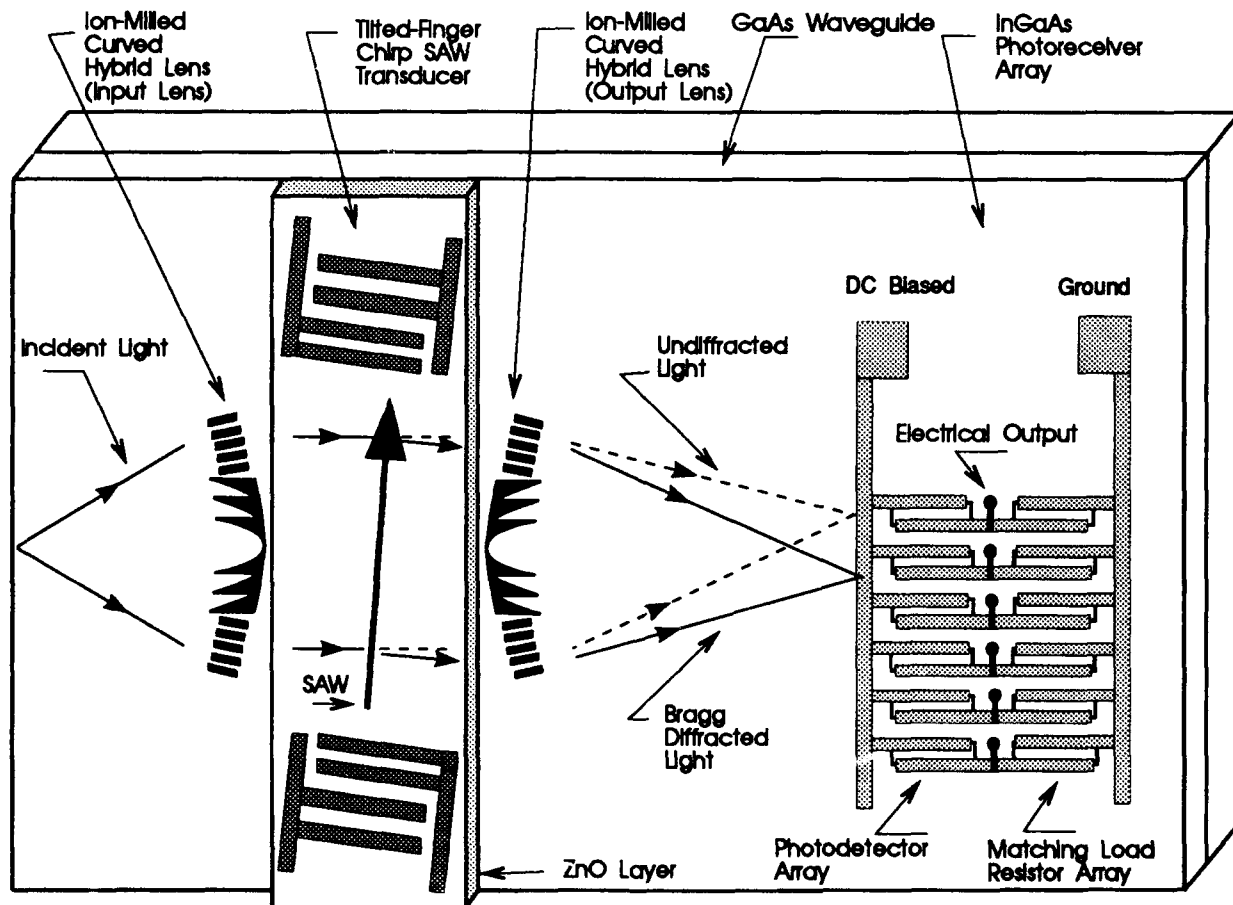


Fig.1 Integrated Optic RF Signal Processor Module In A GaAs Waveguide

Improved WKB phase shift via virtual turning points for waveguides with index discontinuities

F.XIANG and G.L.YIP

McGill University, Department of Electrical Engineering
3480 University, Montreal, Quebec, Canada H3A 2A7

The WKB method has been widely used to obtain approximate solutions of the guided mode propagation constants for optical waveguides with slowly varying graded-index profiles. One of the key features of the standard method, which is properly applied only to problems with isolated turning points, is the assumption of a constant phase shift ($\pi/4$) at a turning point. However, it has long been known that when turning points are not isolated, but are instead near some other transition points, the phase shift is no longer constant [1]. Here, we consider the presence of an index discontinuity near or at a turning point in an optical waveguide and present analytical expressions of the improved phase shift.

The principle of this phase shift correction is based upon two main points. The first consists of using Airy functions [2] as the field solutions at the discontinuity. The second point is that the introduction of virtual turning points (x_{t1} and x_{t3} in Fig.1b) makes the correction applicable to many types of discontinuities. For the index profile shown in Fig.1, the dispersion equation can be written as

$$k_0 \int_{x_{t1}}^{x_{t2}} \sqrt{n^2(x) - n_e^2} dx = M\pi + \phi_{t1} + \pi/4. \quad (1)$$

For $n^2(0^+) < n_e^2$ (Fig.1a) the phase shift ϕ_{t1} at $x = x_{t1}$ is given by

$$\phi_{t1} = -\pi/4 - \tan^{-1} \left[\frac{\eta D_3^{1/3} B_i(\xi_1) A_i'(\xi_3) - D_1^{1/3} B_i'(\xi_1) A_i(\xi_3)}{\eta D_3^{1/3} A_i(\xi_1) A_i'(\xi_3) - D_1^{1/3} A_i'(\xi_1) A_i(\xi_3)} \right] \quad (2)$$

where

$$D_1 = k_0^2 [n^2(x_{t1}) - n^2(0^+)]/x_{t1}, \quad D_3 = k_0^2 (n^2)'_{x=0-},$$

$\xi_1 = x_{t1} D_1^{1/3}$, $\xi_3 = x_{t3} D_3^{1/3}$, $\eta = 1$ for TE modes, $\eta = n^2(0^+)/n^2(0^-)$ for TM modes, and A_i and B_i are the Airy functions. For $n^2(0^-) < n_e^2 < n^2(0^+)$, the integration at the left side of (1) starts from the boundary $x=0$ and ϕ_{t1} in (1) is, then, replaced by

$$\tilde{\phi}_{t1} = -(2/3) |\xi_1|^{3/2} + \phi_{t1} \quad (3)$$

where ϕ_{t1} is given by (2) and D_1 is now given by $D_1 = k_0^2 (n^2)'_{x=0+}$. Eq.(3) actually gives a phase shift of a total internal reflection at $x=0$ in which the index slopes on both sides of the discontinuity have been taken into account. The detailed derivations are given in [3]. Important steps will be presented at the meeting.

Fig.2 shows an example of a given index profile with a significant improvement over the conventional WKB method, especially near the mode cutoffs, where b and v are the normalized propagation constant and frequency. The curves of the phase shift ϕ_t simplified from (2) for a symmetric cladded-parabolic profile are shown in Fig.3, which are very similar to those in [4], but computed numerically. At cutoffs ($b=0$), our result of the phase shift is $\pi/12$ instead of $\pi/4$ or zero for a waveguide with a truncated index profile.

REFERENCES

1. J. Heading, *An Introduction to Phase-Integral Methods*, Methuen, London, 1962.
2. M. Abramowitz and I. Stegun, *Handbook of Mathematical Functions*, Dover, 1972.
3. F. Xiang and G. L. Yip, to be submitted for publication.
4. R. Srivastava, C. K. Kao, and R. V. Ramaswamy, *IEEE J. Light. Tech.*, 5, 1605-9, 1987.

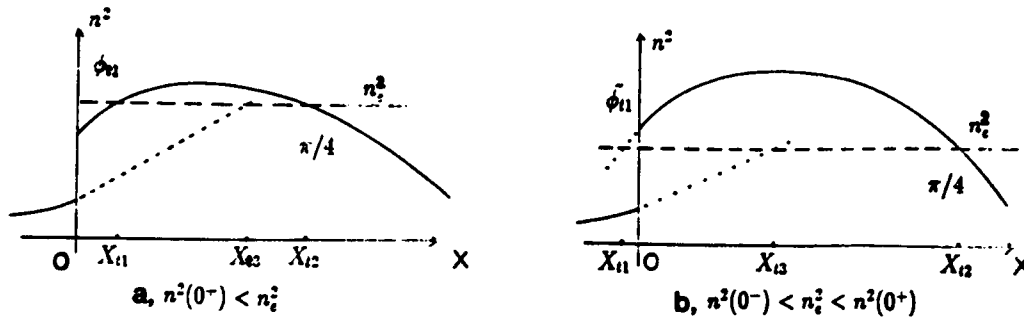


Fig.1 Schematic diagrams of a planar waveguide index profile $n^2(x)$ (solid lines) with a discontinuity at $x=0$ and its turning points x_{t1} , x_{t2} , and x_{t3} . The dashed lines indicate the n_e^2 value, and the dotted lines are tangents of $n^2(x)$ at $x=0$.

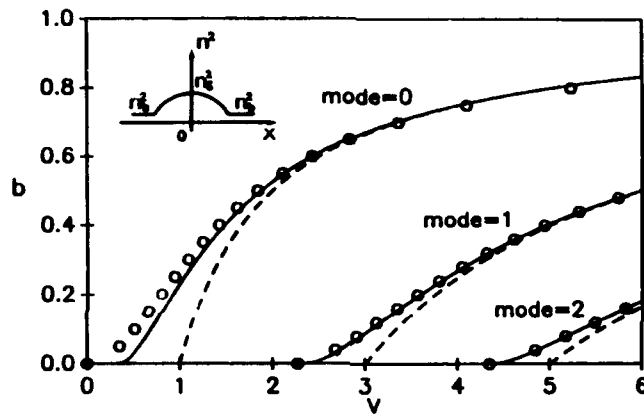


Fig.2 Normalized $b-v$ plots for a symmetric cladded-parabolic profile: \circ exact (staircase method), - - - WKB, — Improved WKB.

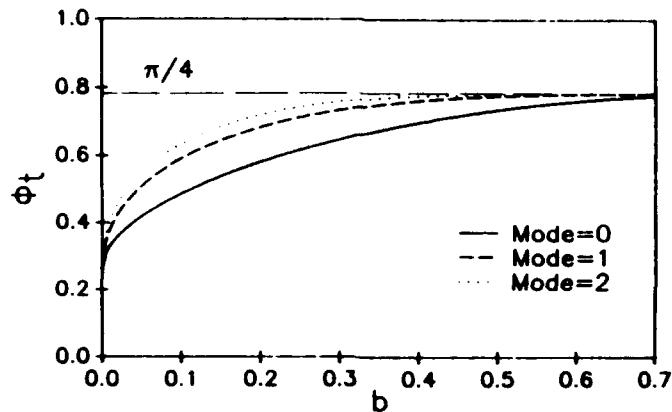


Fig.3 Phase shift dependence on b for the cladded-parabolic profile as in Fig.2.

Monday, April 13, 1992

Quantum-Confinement and Vertical Cavity Devices

MC 1:30 pm-3:30 pm
La Salle Ballroom B

Joseph C. Campbell, *Presider*
University of Texas at Austin

Quantum Optoelectronics based on Combined Quantum Control of Electron- and Photon-Systems in Semiconductors

Masamichi Yamanishi and Yong Lee

Department of Physical Electronics, Faculty of Engineering, Hiroshima University, Kagamiyama 1-chome, Higashihiroshima 724, JAPAN

Phone : 81-824-22-7111 (ext. 3422)

Fax : 81-824-22-7195

[Summary]

One of most attractive discoveries in cavity-quantum-electrodynamics in a past decade is that spontaneous emission of an atom can be controlled by squeezing zero-point fluctuations of the photon fields surrounding the atom in both spatial and frequency domains¹. Considering quantum optoelectronic device-applications, in addition to control of photon system, it is of great important to control electron system as well in order to alter spontaneous emissions. This can be easily realized, by up-date technologies, in semiconductor systems by use of distributed Bragg reflectors (DBRs) and the quantum confined Stark effect (QCSE) for control of photon and electron systems, respectively. The main purpose of this paper is to review our experimental results on physical phenomena originating from control of quantum electron- and photon-systems², and its possible device-applications.

We fabricated two kinds of devices with and without well-designed quantum microcavities, named quantum microcavity (QMC), shown in Fig.1, and weak microcavity (WMC), respectively. The QMC-device was designed so that a GaAs single quantum well (QW) was located at an antinode position of the standing wave of the zero-point fluctuations in a half-wavelength ($\lambda_r/2$) cavity. The WMC-device, in which replacement of p-doped DBR layer by a bulk p-doped $\text{Al}_{0.2}\text{Ga}_{0.8}\text{As}$ layer leads to free-space emissions, was made as a reference to the QMC-device. Fig.2 shows photoluminescence (PL) spectra, detected along the normal direction to the device surface, under different applied voltages in both devices at low temperature ($\sim 50\text{K}$). The GaAs QW's in both devices were selectively pumped by a dye laser (or $\text{Ti:Al}_2\text{O}_3$ laser) beam with a photon energy of 1.72eV . When the emission wavelength of the QW was tuned to the resonant wavelength of the cavity due to QCSE, the PL intensity was, as we expected, strongly enhanced up to about 40 times compared to that of the WMC-device. This clearly indicates that the coupling efficiency (β) of the spontaneous emission into the resonant mode of the cavity can be easily controlled by applied voltages.

A particular interest might be drawn by controllable beam steering of the spontaneous emission through the tuning of emission wavelength caused by QCSE, shown in Fig.3. When the emission wavelength: λ_p was shorter than the cavity resonant wavelength: λ_r , i.e., $\Delta\lambda < 0$, the conical beam pattern was observed. When $\Delta\lambda > 0$, the radiations were, on the other hand, focused around the axis normal to the device surface. Such alteration of the beam patterns results from whether or not the emission wavelength meets the resonant condition for the cavity.

In conclusion, we have demonstrated the possibility of β -switching by *dc*- applied voltages to microcavities involving a QW-active layer. Such a way of β -switching would lead us to an entirely new and advanced quantum optoelectronic devices with a variety of features including high efficiency, high speed, low power consumption and beam steering function. The switching speed of the modulation scheme based on the β -switching is expected to be extremely fast, $\sim 10^{11}\sim 10^{12}$ Hz, free of carrier life time limitation³. One of

concrete examples for an application of the above-described β -switching scheme to the existing devices is a simple incorporation of the microcavity structures into recently developed quantum confined field-effect light emitting triode⁴) which would realize a high speed as well as high efficient optical switching device. We believe that use of quantum control of both electron- and photon-systems would be main stream in next-generation quantum optoelectronic devices.

[References]

[1] See, for example, P.Goy, J.M.Raimond, M.Gross and S.Haroche, Phys. Rev. Lett. 50 (1983) 1903 for an atomic system. Y.Yamamoto, S.Machida, K.Igeta and G.Björk, Coherence, Amplification, and Quantum Effects in Semiconductor Lasers, Ed. Y. Yamamoto (Wiley, New York, 1991) pp.561-615 for a semiconductor system.
 [2] N.Ochi, T.Shiotani, M.Yamanishi, Y.Honda and I.Suemune, Appl. Phys. Lett. 58 (1991) 2735.
 [3] M.Yamanishi, Y.Yamamoto and T.Shiotani, IEEE. Photonics Tech. Lett. 3 (1991) 888.
 [4] Y.Kan, M.Okuda, M.Yamanishi, T.Ohnishi, K.Mukaiyama and I.Suemune, Appl. Phys. Lett. 56 (1990) 2059.

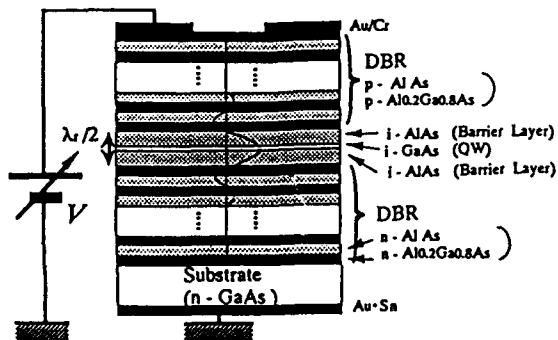


Fig.1 QMC-device structure.

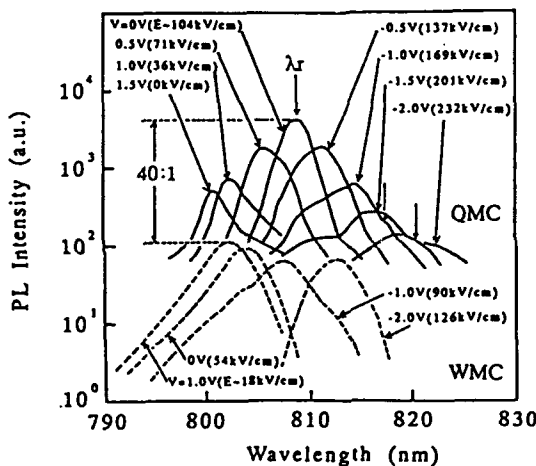


Fig.2 Spontaneous emission (PL) spectra for different applied voltages.

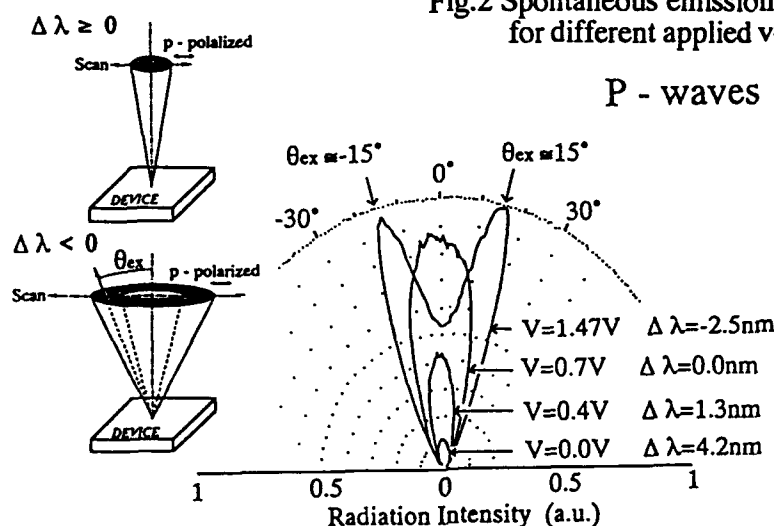


Fig.3 Radiation patterns for different applied voltages in a QMC-device.

Gain and Absorption Spectra of Quantum Wire Laser Diodes Grown on Nonplanar Substrates

*M. Walther, E. Kapon, A. Scherer, H. Song, D.M. Hwang and R. Bhat
Bellcore, 331 Newman Springs Road, Red Bank, NJ 07701
(908) 758-3370*

Quantum wire (QWR) semiconductor lasers, grown by organometallic chemical vapor deposition (OMCVD) on nonplanar substrates, exhibit two dimensional (2D) quantum confinement^{1,2} and sub-mA threshold currents³. The *in situ* formation of the wires in these lasers eliminates excessive nonradiative recombination at their interfaces, which is essential for the efficient operation of these devices. One of the expected advantages of QWR heterostructures is the enhanced optical gain and absorption resulting from the increased density of states at the quasi-1D subbands. This feature would make QWR heterostructures useful for applications in low power consumption integrated optoelectronics. Here, we report the first measured gain and absorption spectra of QWR lasers.

The multi-QWR lasers discussed here were grown by OMCVD on V-grooved substrates². Their active regions consist of 4 crescent-shaped GaAs wires, placed at the center of a 2D, graded index AlGaAs optical waveguide (see Fig. 1). A band structure model of these wires yields electron-heavy hole QWR subband transitions separated by 19meV, with an effective wire width of 15nm for the ground electron state. The subband structure was evident in the amplified spontaneous emission and lasing spectra of the devices, with observed transition energies in good agreement with the calculated values².

Modal gain and absorption spectra were evaluated from measured fringe visibility of the longitudinal modes⁴ in Fabry-Perot 4-QWR lasers. Devices of 260 μ m cavity length were cleaved and high-reflection (HR) coated using gold to ensure large spectral bandwidth of high reflectivity. Lasing occurred predominantly at 806nm (1.54eV), corresponding to the third ($l=2$) e-hh QWR subband transition², with threshold current of 6.5mA (see Fig. 2). The TE-polarized modal gain spectra (compensated for waveguide scattering and free carrier absorption losses) shown in Fig. 3 were obtained for the same device, at various diode currents below and above threshold. The calculated positions of the e-hh QWR subband transitions ($l=0,1,2,\dots, \Delta l=0$) are indicated by the arrows. Several absorption dips are evident at the QWR subbands, particularly at lower currents and higher energies. These absorption features reduce in depth with increasing current as the QWR subbands become populated by carriers. Above transparency level, the absorption dips turn into gain peaks whose magnitudes saturate at the cavity mirror loss value. A maximum modal gain of $\sim 20\text{cm}^{-1}$ was measured at 1.54eV ($l=2$) at or above threshold.

Using a two-dimensional waveguiding model, we calculated a total optical confinement factor of $6.8 \cdot 10^{-3}$ for the 4 wires. This yields an average *material* gain value of $\sim 3000\text{cm}^{-1}$ per wire, which is at least as large as reported gain constants in quantum well structures⁵. Furthermore, our models show that higher modal gains can be achieved by optimizing the waveguide structure to improve the optical confinement, and by minimizing the wire-to-wire variations to reduce inhomogeneous broadening. The combined effects of higher gain and extremely small active volume in such optimally designed QWR lasers should lead to threshold currents in the μA regime. In addition, The enhanced absorption features we have observed in these QWR structures should be useful for applications in low power consumption optical modulators and switches.

Optical Gain Properties of Serpentine Superlattice Quantum Wire Arrays

Jong Chang Yi and Nadir Dagli

Electrical and Computer Engineering Department, University of California, Santa Barbara, CA 93106 (805)893-4847

Quantum confinement in two dimensions, which results in quantum wires is likely to result in improved device characteristics due to density of states localization and anisotropic optical properties¹. However, to observe significant quantum wire effects at room temperature, the carriers should be confined to less than 100 Å in two dimensions, which is too difficult to fabricate even with the finest lithographic techniques developed so far. However, another fabrication technique which holds great promise is the direct growth of lateral superlattices on vicinal substrates^{2,3}. On the surfaces of such substrates uniform atomic steps are formed under proper conditions. The lateral superlattices are directly grown on such surfaces by the sequential deposition of two materials of different compositions. The end result is an array of quantum wires (QWR) with a period, T . The period is solely determined by the substrate tilt angle, α , and monolayer thickness, d , which is expressed³ as $T = d/\tan\alpha$. For example, when α is 2°, T becomes 81 Å, and when α is 1.5°, T becomes 108 Å in AlGaAs system. Amongst these lateral superlattices, a curved interfaced lateral superlattice named serpentine superlattice (SSL)^{4,5} has been developed to decrease the sensitivity of the fabricated structure to growth conditions and improve its uniformity. This makes SSL more desirable compared to tilted superlattices (TSL)^{2,3} which have rectangular cross sectional geometry.

The schematic cross sectional profile of an SSL is shown in Fig. 1. The curvature of the growth interface provides vertical confinement and the degree of vertical confinement depends on the intentional variation of the growth rate over the total thickness of SSL, D_0 . The growth interface can be expressed as $y = \frac{\Delta p}{\tan\alpha \cdot D_0} z^2$. p , the tilt parameter,

is defined as $p = m + n$ where m and n are the fractions of barrier and well material on a step. If the deposition or growth rate is adjusted such that $p = m + n = 1$ the amount of material deposited per monolayer exactly covers a step and the interface between the well and barrier material will grow vertically. If $p < 1$ or $p > 1$ interface will tilt one way or the other. $\Delta p = p - 1$, which is directly proportional to growth rate variation, indicates the intentional deviation from the nominal p value of 1 and determines the slope of the interface. Therefore, even though one cannot adjust and keep the p value to be 1 during the growth, by varying p from $1 - \Delta p$ to $1 + \Delta p$, one can obtain curved interfaces and somewhere within, one can surely obtain vertical interfaces where the carriers are confined as shown in Fig.1. The curvature plus the Al contents in the wires, barriers and the claddings, x_w , x_b and x_c , respectively, are the parameters that are available to optimize the structure.

In the analysis first the energy band diagram of SSL is calculated by solving the Schrödinger equation using the finite-element method. For conduction band calculations a single band model is used which is shown to be a good approximation even for $x \sim 0.4$ where Γ and L valleys cross over. For valence band calculations a 4 band $k \cdot p$ analysis is used to take into account the valence band mixing effects. In all the calculations finite potential barriers and periodic boundary conditions are utilized. The latter allows the analysis of the infinite array of QWR that exist in a SSL including the coupling between the wires due to their close spacing and finite barrier heights. Once the E-k diagram is generated density of state functions and other optical properties can be obtained.

Fig. 2 shows the modal gain spectra of SSLs on 1.5° vicinal GaAs substrate, i.e., when the lateral dimension of the wire and barrier region is $\frac{T}{2} = 54$ Å. The tilt parameter p is varied up to $\pm 20\%$ for the case when $x_w = 0$, $x_b = x_c = 0.5$, and $D_0 = 460$ Å. We assumed room temperature and a gaussian line shape function with $\Delta E = 6$ meV. The injected surface carrier density, n_s , is $5 \times 10^{12}/\text{cm}^2$ and the polarization of optical wave is parallel to wires. For $\Delta p = 0$ one broad spectrum is observed due to many closely spaced minibands. As Δp , hence confinement increases, one can clearly see the emergence of two gain peaks. The first peak corresponds to the transition from the first conduction band to the first valence band. The second peak indicated by arrows is due to the transition between the second minibands. As vertical confinement increases, the separation between these two peaks increases, the first gain peak becomes narrower and higher at a given carrier density, and the second peak diminishes significantly, hence one can obtain smaller threshold current and narrower linewidth.

Just like any fabricated structure SSL also deviates from the ideal structure considered so far. Presently the main problem in the SSL fabrication seems to be the incomplete segregation of the Al between the barrier region and wire

References:

1. E. Kapon, D.M. Hwang and R. Bhat, Phys. Rev. Lett. 63, 430 (1989).
2. E. Kapon, D.M. Hwang, M. Walther, R. Bhat and N.G. Stoffel, Surf. Sci. (in press).
3. S. Simhony, E. Kapon, E. Colas, D.M. Hwang, N.G. Stoffel and P. Worland, Appl. Phys. Lett. 59, 2225 (1991).
4. B.W. Hakki and T.L. Paoli, J. Appl. Phys., Vol. 46, No.3, 1299 (1975).
5. S.R. Chinn, P.S. Zory and A.R. Reisinger, IEEE J. Quantum Electron. QE-24, 2191 (1988).

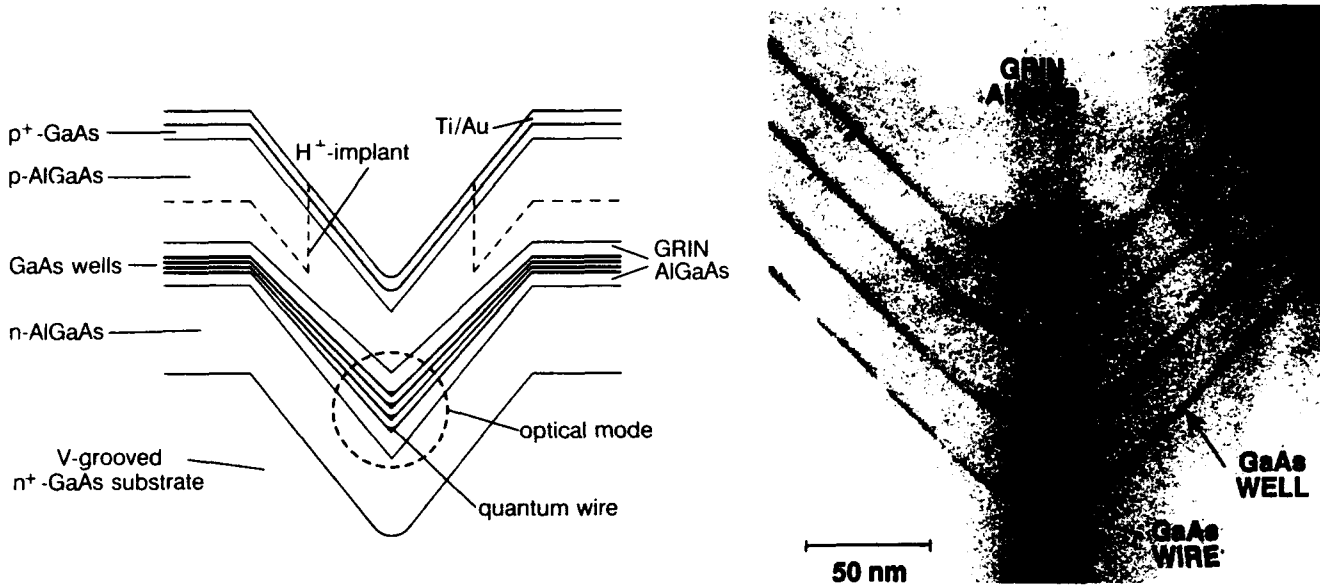


Fig.1: Schematic (left) and transmission electron microscope (right) cross sections showing the layer structure and the vertically-stacked, crescent-shaped wires at the core of the 4-QWR laser.

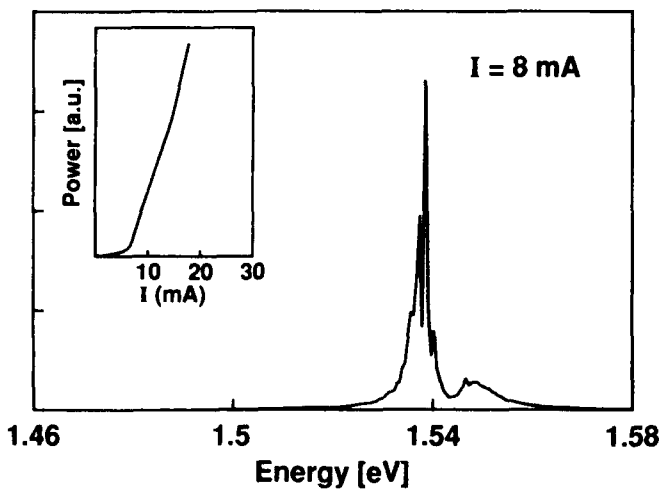


Fig.2: Spectrum of a 260µm long, HR coated 4-QWR laser above threshold. Inset shows the light versus current characteristic (pulsed operation).

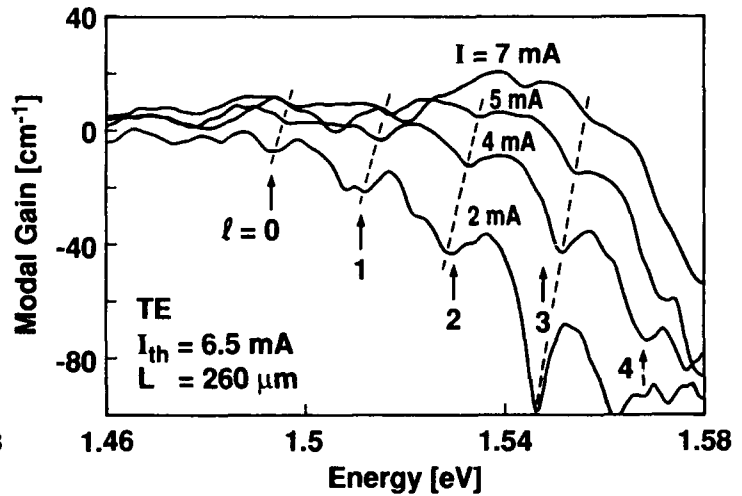


Fig.3: Measured modal gain spectra of the 4-QWR laser for TE polarization at various diode currents.

region⁵. If some of the Al intended to be in the barrier is incorporated in the wire region, the potential difference between barriers and wires decreases and consequently the lateral confinement becomes weaker. We studied this effect by using a model which assumes that the average Al concentration in the lateral superlattice region remains constant at $x_l = (x_b + x_w)/2$, hence $x_l = 0.25$, assuming equal wire and barrier widths. Furthermore, we define the degree of segregation as $\Delta x = x_b - x_w$ and assume that Al composition varies abruptly between x_b and x_w . Fig. 3 shows the maximum gain of a SSL grown on a 1.5° off substrate with $\Delta p = 0.20$ for different degrees of segregation, or Δx . These gain values are also compared with 54\AA thick GaAs/Ga_{0.5}Al_{0.5}As QW and 460\AA thick bulk GaAs structure. When $\Delta x = 0.50$, the maximum gain is higher than QW and bulk. As Δx decrease the maximum mode gain decreases due to the reduced lateral confinement hence increased coupling between wires. A dramatic gain reduction can be seen when Δx is reduced from 0.4 to 0.3. When Δx is smaller than 0.3, the maximum gain is even smaller than that of the single QW. Furthermore, as the x_w increases, the separation between Γ and L valley subband minima in the wire region decreases, consequently increasing carrier leakage from Γ to L valley. Therefore, to observe room temperature gain enhancement from QW, the lateral Al segregation should be greater than about 0.3.

In conclusion, the gain characteristics of serpentine superlattice quantum wire arrays grown on GaAs vicinal substrates were estimated including the valence band intermixing and miniband broadening effects. The effect of the imperfect Al segregation in the structure, which presently seems to be the main problem, was also investigated. Significant improvements in maximum and differential gain as well as in transparency carrier densities are expected provided that good Al segregation is realized.

References:

1. M. Asada, Y. Miyamoto, and Y. Suematsu, *Jpn. J. Appl. Phys.*, **24**, L95 (1985).
2. J. M. Gaines, P. M. Petroff, H. Kroemer, R. J. Simes, R. S. Geels, and J. H. English, *J. Vac. Sci. Technol.*, **B6**, 1378 (1988).
3. T. Fukui and H. Saito, *Appl. Phys. Letters*, **50**, 824 (1987).
4. M. S. Miller, C. E. Pryor, H. Weman, L. A. Samoska, H. Kroemer, P. M. Petroff and J. L. Merz, *J. Cryst. Growth*, **111**, 323 (1991).
5. M. S. Miller, H. Weman, C. E. Pryor, M. Krishnamurthy, P. M. Petroff, H. Kroemer and J. L. Merz, submitted for publication.

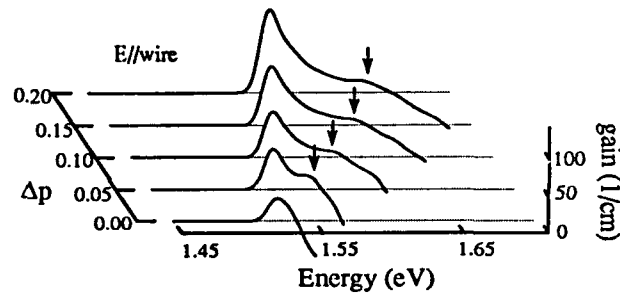


[Fig.2] Modal gain spectra of SSLs at different curvatures, or Δp . The arrows indicate second subband transitions.

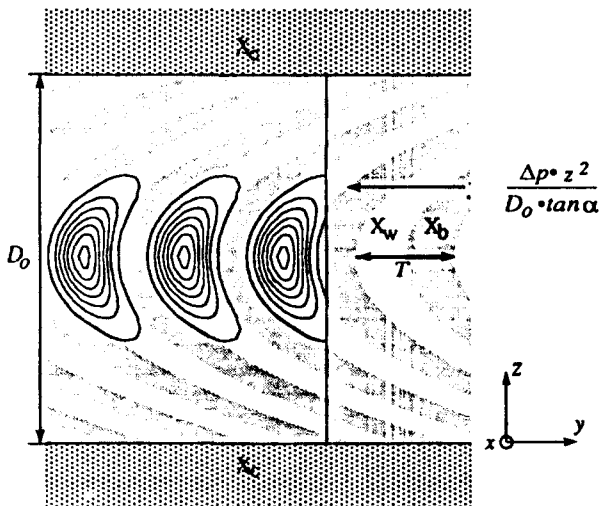


[Fig.1] Cross-sectional geometry of SSL and its conduction band electron density.

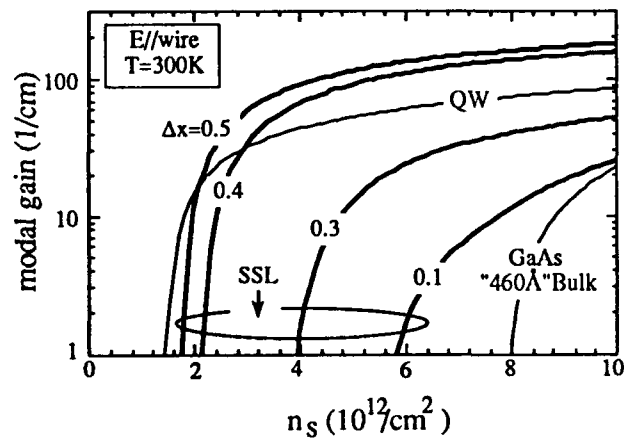


[Fig.3] Maximum modal gain of SSL at different degree of segregation. Inserted number denotes $\Delta x = x_b - x_w$.

Electro-Absorptive Optical Modulation by Wannier-Stark Localization in an InGaAs/InGaAsP Superlattice

N. Agrawal, C. Bornholdt, D. Franke, D. Hoffmann, F. Kappe, and K. C. Li
Heinrich-Hertz-Institut für Nachrichtentechnik Berlin GmbH.
Einsteinufer 37, D-1000 Berlin 10, Federal Republic of Germany, Tel. 49 30 31002 395

U. Clemens, L. Berger, and M. Wegener
Fachbereich Physik, Universität Dortmund, Otto Hahn Str. 4
D-4600 Dortmund 50, Federal Republic of Germany

Electro-absorptive long wavelength ($\lambda=1550$ nm) semiconductor modulators with low drive voltage are indispensable components for future high bit-rate communication networks. Recently, Wannier-Stark Localization (WSL) in an InGaAs/InAlAs superlattice was employed to achieve sub-volt operation combined with high extinction [1]. However, such devices are not readily integrable with the existing high quality InGaAsP/InP lasers. In this work we demonstrate for the first time electro-absorptive optical modulation by WSL in an InGaAs/InGaAsP superlattice. The WSL sample is grown as a p-i-n heterostructure (cf. Fig. 1) on an n^+ -InP substrate by low pressure (2×10^3 Pa) metalorganic vapor phase epitaxy. The intrinsic region consists of five Wannier superlattices each of them with five periods of quantum well and barrier layers. Moreover, quaternary spacer layers were employed to improve the quality of epitaxial growth. Superlattice formation was verified by the observation of satellite peaks in the double crystal x-ray diffraction rocking curves. Photoluminescence peak (300 K) for the Wannier superlattice was seen at 1450 nm without any traces of ternary signal.

Due to thin barriers in a Wannier superlattice the adjacent quantum wells are strongly coupled. Therefore, the original discrete energy levels broaden to form minibands with density of states given by arcsine function. In the presence of field F , additional oblique transitions $E_{QW} + p e F d$ ($p = \pm 1, \pm 2, \dots$) are obtained, corresponding to interaction between electron and hole states in the n th and $n+p$ th quantum well, respectively (cf Fig. 2a). From the tight binding method, the widths of electron and hole minibands were estimated to be 65 meV and 2 meV, respectively. To study WSL, we measure differential absorption spectra $\Delta T/T$ as field induced changes (cf. Fig. 2b). Mesa structures were defined by photolithography and then reactive-ion-etched (CH_4/H_2) down to the substrate. Since the p-i-n junction is formed between the p and n doped InP cladding layers, the flat-band condition is obtained at + 1.3 V and a localization of the electronic states occurs at - 6.3 V ($F \approx 10^5$ V/cm). At low bias voltages the characteristic spectra due to WSL is seen close to the primary absorption edge with changes on the order of 10^{-2} [2]. The first three peaks (1,2,3) in the range of $\lambda=1350$ -1600 nm correspond to red, blue, and red shifts due to $p=-1$ transition, WSL, and quantum confined Stark effect, respectively. Somewhat unexpectedly, a similar spectra is also observed around the quaternary gap of the barrier layers in the superlattice. Such resonant effects arise, perhaps, from a correlation between the continuum states of the isolated quantum wells. Note that as expected of WSL, whereas the spectral widths of peaks 1,4 increase continuously with the applied field, the widths of peaks 2,5 saturate to a nearly constant value indicating a complete localization of the electronic states.

Electro-absorptive optical modulators were fabricated by forming straight ridge (width=3 μm) waveguides with sputtered Ti/Pt/Au contact layers on top and bottom of the wafer. The relative transmission (on/off ratio) is shown in Fig. 3 as a function of wavelength (at -4V) and voltage (at 1515 nm). We measure both TE and TM polarizations using a tunable external cavity laser for a 500 μm long device. It is seen that the on/off ratio is considerably better for the TM as compared to the TE mode.

In conclusion, we have demonstrated for the first time electro-absorptive optical modulation by WSL in an InGaAs/InGaAsP superlattice grown by metalorganic vapor phase epitaxy. Moreover, we observe a novel electroabsorption feature related to the barrier layers.

- [1] F. Devaux, E. Bigan, M. Allovan, J. C. Harmand, P. Voisin, M. Carré, A. Carrenco, 17 th European Conference on Optical Communication 1991, Paris, France, Post-Deadline Papers, pp. 56-59.
- [2] I. Bar-Joseph, K. W. Goosen, J. M Kuo, R. F. Kopf, D. A. B. Miller, and D. S. Chemla, Appl. Phys. Lett. 55, 340 (1989).

No.	Function	Material	Band-Gap (nm)	Thickness (nm)	Doping (cm ⁻³)
	Substrate	InP(S)			n ⁺
	Cladding	n-InP		1000	5.0x10 ¹⁷
1.	Core (Aux.)	Quat	1250	36	n.i.d.
2.	Superlattice	Quat, Tern	1250, 1670		n.i.d.
3.	Core (Aux.)	Quat	1250	36	n.i.d.
	Cladding	p-InP		1000	5.0x10 ¹⁷
	Contact	p-Tern	1670	200	2.0x10 ¹⁹

No.	Function	Material	Band-Gap (nm)	Thickness (nm)
2.1.	Spacer	Quat	1250	36
2.2.	Well	Tern	1670	3
2.3.	Barrier	Quat	1250	3
2.4.	Spacer	Quat	1250	36

Fig. 1: a) Structure of the MOVPE grown InGaAs/InGaAsP/InP WSL waveguide modulator with layer(s) 2 repeated five times. b) Details of the Wannier superlattice with layers 2.2-2.3 repeated five times.

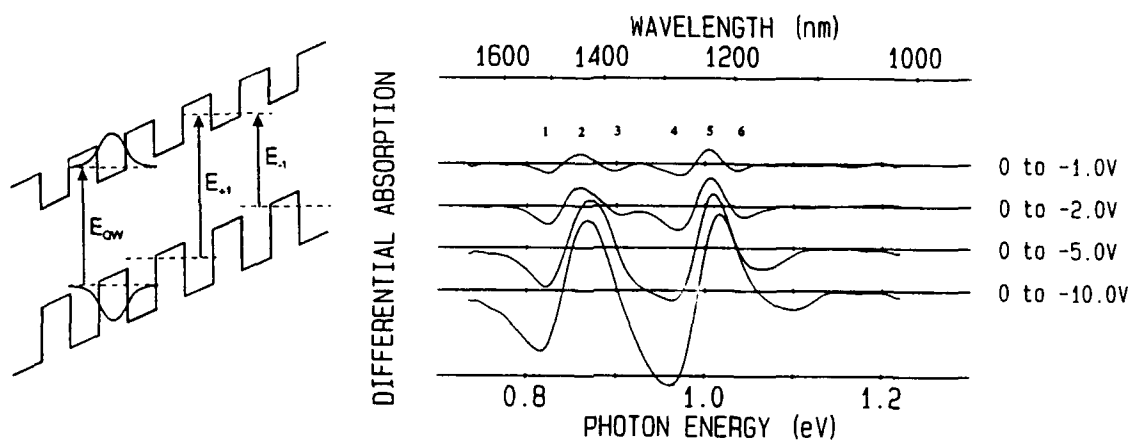


Fig. 2: a) Optical transitions and b) differential absorption spectrum of the InGaAs/InGaAsP Wannier superlattice.

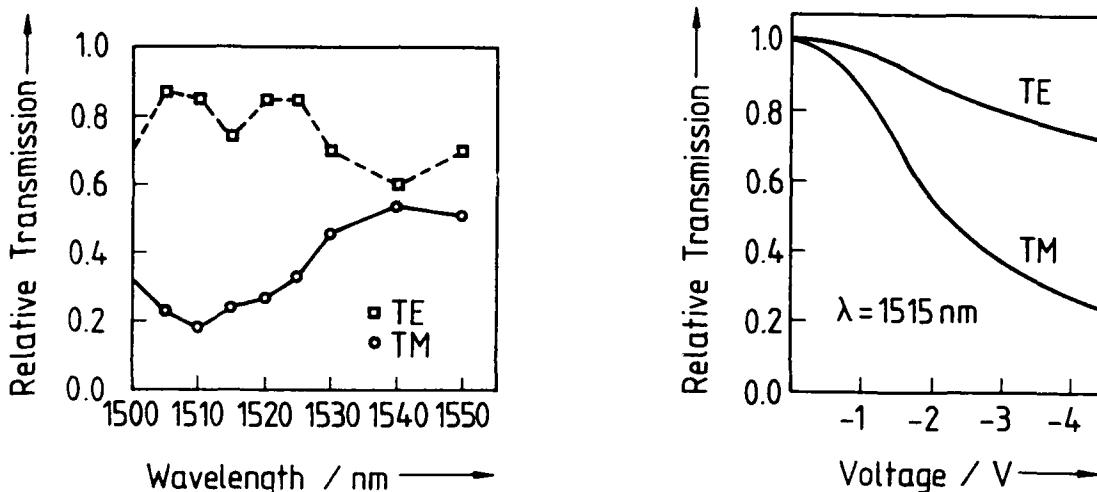


Fig. 3: Measured relative transmission as a function of a) wavelength and b) applied bias for a 500 μ m long WSL intensity modulator.

Stress Effect on Polarization of Surface Emitting Lasers

T. Mukaiharu, F. Koyama and K. Iga

Tokyo Institute of Technology,

Precision and Intelligence Laboratory

4259 Nagatsuta, Midoriku, Yokohama 227, Japan

Phone: 81-45-922-1111 X 2064

For polarization-sensitive applications such as magneto-optic disks and coherent detection systems, the polarization state of surface emitting (SE) lasers must be well defined. From the measured polarization characteristics, it was found that the output of mesa-structure SE lasers were linearly polarized^{1,2} and homogeneous lasers were unstable in terms of polarization state³. Several polarization control methods were also suggested². However, the stress would affect the polarization state of SE lasers and it is necessary to clarify its effect for stable polarization control.

We have investigated the lasing mode of SE lasers with the elliptical etched well as shown in Fig.1. This elliptical hole may produce an anisotropic stress in the active region induced by the asymmetric shape of the well. A model of SE laser with the anisotropic holed region is shown in Fig.2. The epitaxial layers are bent due to the difference of the thermal expansion coefficient between GaAs and AlGaAs. This provides the tensile stress difference between the major axis and the minor axis of the holed region. There are two cases, TypeI and TypeII, which provide the differential gain along the major axis and the minor axis, respectively.

We examined the polarization characteristics of several SE lasers with the elliptical holed region. Fig.3 shows a typical I-L characteristics of two polarization states along the major axis and the minor axis. The output from this device was polarized along the major axis, $\langle 01\bar{1} \rangle$. However, we found some devices which were polarized to the minor axis. Then, we gave an external stress to the device which polarized along the minor axis, and the polarization direction switched to the major axis, as shown in Fig.4. It is considered that the differential gain was produced by the external stress. This shows that the stresses which come from the structure and bonding should be considered for stable polarization control of SE lasers. We are now designing the device by taking this into

account together with polarization-dependent loss mechanism².

References

1. M. Shimizu, F. Koyama and K. Iga, Jpn. J. Appl. Phys. 27(1988)1774.
2. M. Shimizu, T. Mukaiyama, F. Koyama and K. Iga, ECOC MoA1-4 (1991)
3. Y. H. Lee, T. Sizer, B. Tell, K. F. Brown-Goebeler and L. E. Leibenguth, LEOS Ann. Meeting PD9 (1990)

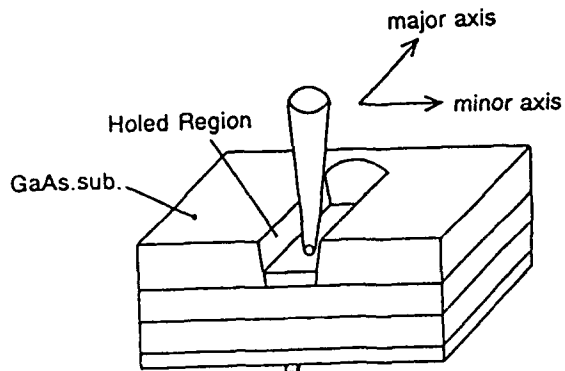


Fig.1. Device structure with the elliptical etched well.

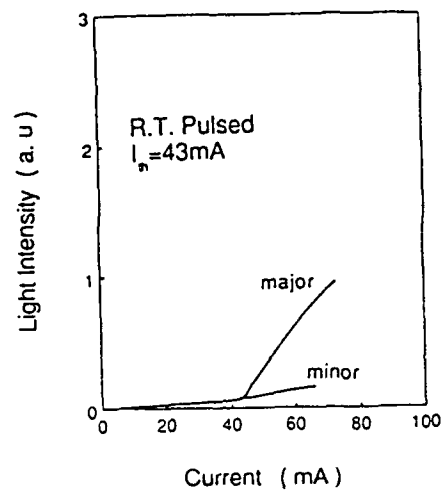


Fig.3. I-L characteristics.

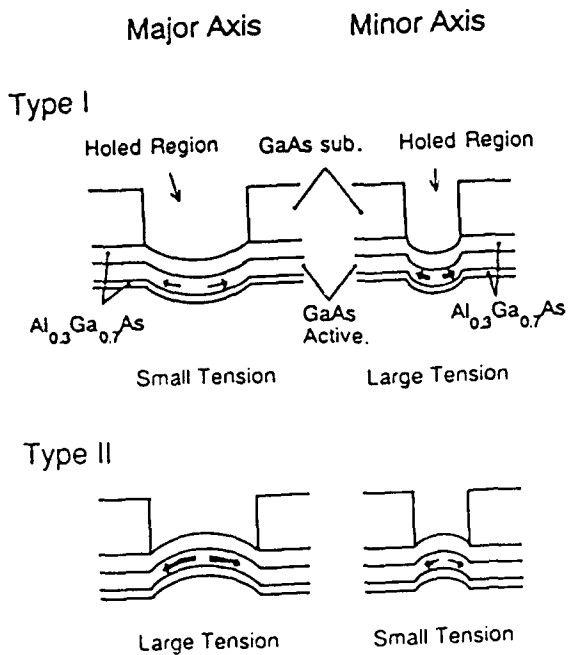


Fig.2. A model of SE laser with anisotropic holed region.

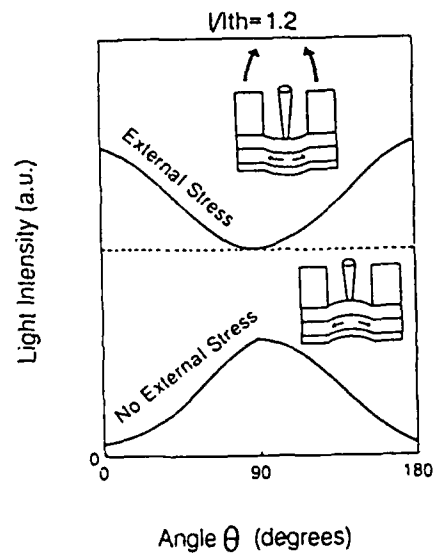


Fig.4. Polarization switching by the external stress.

MC6-1

Etched Vertical-Cavity Surface Emitting Laser Diodes

Kent D. Choquette, G. Hasnain, J. P. Mannaerts, J. D. Wynn,
R. C. Wetzel, M. Hong, and R. S. Freund
AT&T Bell Laboratories, Murray Hill NJ 07974 (908)582-3000

R. E. Leibenguth
AT&T Bell Laboratories, STC, Breinigsville, PA 18031

Vertical-cavity surface emitting lasers (VCSEL's) are promising light sources for optical computing and interconnection due to their unique topology and two-dimensional array capacity. To date, VCSEL's with monolithic distributed Bragg reflectors (DBR's) require current injection through the upper p-type DBR resulting in a large threshold voltage due to the concomitant series resistance. The voltage drop in the p-type DBR also leads to additional thermal effects which degrade the VCSEL performance.¹ Various methods, such as introducing extra layers with intermediate composition into the quarterwave DBR² or tapered doping in the p-type DBR,³ have provided a reduction in the series resistance, but have lead to complicated DBR designs. We have developed a novel VCSEL structure, utilizing dry etching, *in situ* metallization, and ion implantation, which can avoid current injection through the upper DBR, and thus simplifies the required epilayers. We report a comparison between our etched/implanted devices and VCSEL's formed by a planar ion implantation process,^{1,4} all fabricated from the same wafer.

In Figure 1(a) we sketch our etched/implanted VCSEL structure. The laser material is grown by MBE and is composed of a lower n-type staircase DBR (AlGaAs/AlAs multilayers), an undoped double heterostructure active region with five GaAs quantum wells, and a top p-type staircase DBR with graded doping. 10 μm diameter circular dots of SiO₂ are used as etching masks as well as protection layers over the top laser facets. Dry etching is done with an electron cyclotron resonance plasma system using SiCl₄ at a pressure of 1×10^{-3} Torr and 400 W of microwave power. These conditions yield a low damage anisotropic etch with a rate of 500 $\text{\AA}/\text{min}$. Accurate depth monitoring during etching is

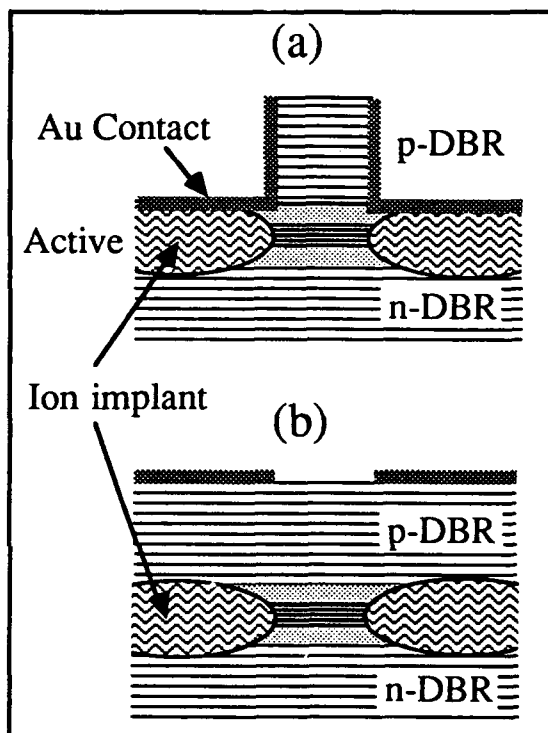


Figure 1. (a) Etched and implanted VCSEL; (b) planar implanted VCSEL.

accomplished by laser reflectometry in order to stop etching just after the last layer of the upper DBR, $\approx 800 \text{ \AA}$ from the GaAs quantum wells.

After etching, the samples are transferred in ultra high vacuum to a metallization MBE chamber. 300 \AA of Au is epitaxially deposited with the sample at an angle from the Au effusion cell and rotating to insure sidewall coverage. Another 1000 \AA of Au is deposited after atmospheric exposure in an evaporation system. The *in situ* deposited epitaxial Au⁵ insures excellent electrical contact, while the sidewall coverage encapsulates the exposed AlGaAs and AlAs layers of the upper DBR, eliminating potential corrosion problems. Lateral current confinement is achieved using two self-aligned O⁺ implantation steps, done

with ion energies of 300 and 600 keV, to produce approximately $0.5 \mu\text{m}$ of resistive material under the metallization. Finally, the Au is removed from the VCSEL tops by Ar^+ milling for front surface emission, and the individual lasers are isolated with a deep etch. For comparison, implanted planar lasers are fabricated,¹ as sketched in Fig. 1(b), from nearby pieces of the same wafer.

Fig. 2 shows a comparison of the cw light output and applied voltage versus injected current for a typical etched/implanted (Fig. 1(a)) and implanted planar (Fig. 1(b)) VCSEL at room temperature. The etched/implanted device exhibits lower threshold current as well as greater output power. It was expected that the series resistance would be lower since current no longer has to pass through the entire upper DBR. However, as seen in Fig. 2, no significant reduction was observed, likely due to a larger contact resistance. Note the confinement layer between the upper DBR and the quantum wells is 1000 \AA thick, and the etch depth extends only $\approx 200 \text{ \AA}$ into this region, which does not provide sufficient area for a low resistance contact. The roll over of the output power due to heating¹ occurs at nearly the same applied electrical power, implying that the thermal behavior of the etched device is the same as the unetched laser. We have previously observed dramatic thermal effects from etched and implanted VCSEL's due to the removal of heat sink material,⁶ and thus it appears that the thermal conductivity of the Au near the active region enhances the dissipation of heat.

The epilayer material used in this experiment is designed for the implanted planar VCSEL's, yet we find the etched/implanted devices function better. Further reduction of threshold and series resistance may be accomplished by incorporating a contact layer between the upper DBR and the laser active region, thus eliminating the current path through the upper DBR. This would also allow the use of a simple bilayer quarterwave DBR. A simplification of the epilayer material may lead to greater reliability and uniformity of VCSEL arrays and higher yields of suitable epilayer materials. Therefore this VCSEL device structure has the potential for superior VCSEL performance and manufacturability.

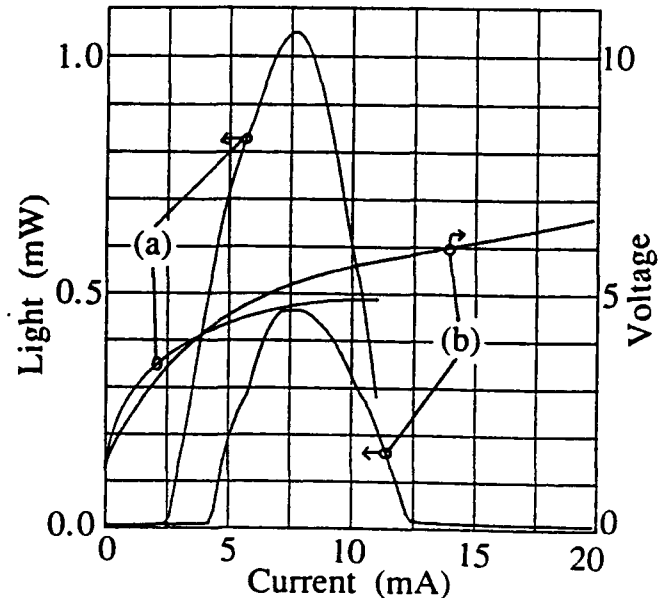


Figure 2. Continuous wave output and voltage versus injected current for (a) etched/implanted VCSEL and (b) implanted planar VCSEL.

References

- 1G. Hasnain, K. Tai, L. Yang, Y. H. Wang, R. J. Fisher, J. D. Wynn, B. E. Weir, N. K. Dutta, and A. Y. Cho, *IEEE J. Quantum Electron.* **QE-27**, 1377 (1991).
- 2K. Tai, L. Yang, Y. H. Wang, J. K. Wynn, and A. Y. Cho, *Appl. Phys. Lett.* **56** 2496 (1990).
- 3G. Hasnain, K. Tai, N. K. Dutta, Y. H. Wang, J. D. Wynn, B. E. Weir, and A. Y. Cho, *Electron. Lett.* **27**, 915 (1991).
- 4M. Orenstein, A. C. Von Lehmen, C. Chang-Hasnain, N. G. Stoffel, J. P. Harbison, L. T. Florez, E. Clausen, and J. E. Jewell, *Appl. Phys. Lett.* **56**, 2384 (1990).
- 5K. D. Choquette, M. Hong, J. P. Mannaerts, D. J. Siconolfi, R. P. Frankenthal, F. A. Baiocchi, R. C. Wetzal, and R. S. Freund, *J. Electron. Mat.* **21**, 17 (1992).
- 6K. D. Choquette, G. Hasnain, Y. H. Wang, J. D. Wynn, R. S. Freund, A. Y. Cho, and R. E. Leibenguth, *IEEE Photon. Tech. Lett.* **3**, 859 (1991).

Monolithic Integration of a Resonant Fabry-Perot Cavity p-i-n Photodiode with HBT's for 1.52 μm Optoelectronic Receivers

Ananth Dodabalapur, T.Y. Chang, and S. Chandrasekhar

AT&T Bell Laboratories, Holmdel, NJ 07733

The use of appropriately designed Fabry-Perot cavities has recently been shown to enhance the quantum efficiency of thin photodetectors. We describe our results toward utilizing such resonant detectors in integrated optoelectronic receivers for 1.5-1.6 μm .

The schematic layer structure of the as-grown material is shown in Figure 1. It essentially consists of a npn heterojunction bipolar transistor (HBT) with a multilayer InAlAs/InGaAlAs ($E_g \sim 1.06$ eV) subcollector. The thicknesses of the layers are carefully chosen such that the subcollector forms a quarter-wave stack (QWS) with a stop band at 1.52-1.55 μm . The total thickness of the other layers in the HBT (collector, base and emitter) are designed such that a Fabry-Perot cavity with a mode located at the peak of the stop band of the QWS is formed when a metallic reflector is deposited on the sample surface. This occurs when the total optical thickness of the layers, including a contribution due to the phase shift at the metallic mirror, is an odd multiple of $\lambda/4$. In the structure shown in Fig. 1, the total optical thickness of these layers is $7\lambda/4$. A resonant cavity p-i-n photodiode is formed by contacting the p^+ (base) and n^+ subcollector. The n-type layers which constitute the emitter in the HBT are electrically inactive in the resonant photodiode. Figure 2 shows the reflectance spectrum of the device structure, and an increase in absorption, relative to the average background, of more than 100 % is clearly observed at the resonance wavelength (1.52 μm). The photocurrent spectrum (Fig. 3) shows a corresponding increase in photocurrent at resonance. Thus, by employing a resonant structure we are able to enhance the quantum efficiency of the p-i-n diode formed with the base and collector regions of the HBT. The characteristics of the HBT devices are excellent and, as seen in Figure 4, DC current gains of around 1000 are obtained. The Gummel plot of the HBT devices shows that the current gain is 100 for base currents in the nA range, indicating that this material system is also suitable for high sensitivity applications.

We also experimented with a different structure in which the resonant cavity is shorter, consisting of only the collector and base regions of the HBT. The reflector metal is placed directly on the p^+ semiconductor, as shown in Fig. 5. For such a resonant p-i-n structure, with a cavity of thickness $3\lambda/4$, we also obtained similar resonant enhancement in the absorption as seen in Fig. 6. The HBT performance in this wafer is also good, and current gains of more than 100 were measured. The relative merits of these two approaches towards the monolithic integration of a resonant cavity p-i-n photodiode with HBT's and the high speed characteristics of such a receiver circuit will be discussed.

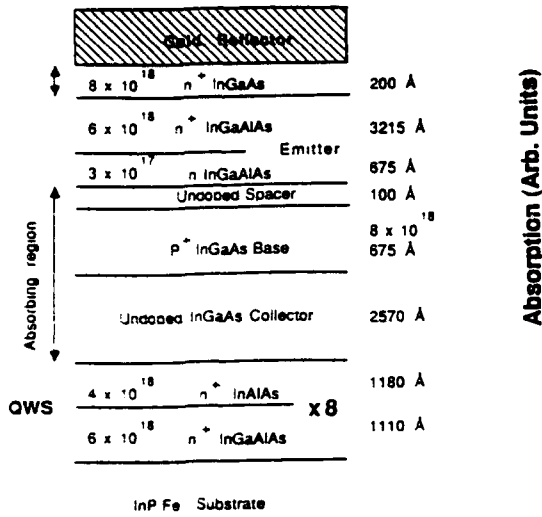


Fig. 1 Schematic layer structure for the monolithic integration of resonant p-i-n diodes with HBT's.

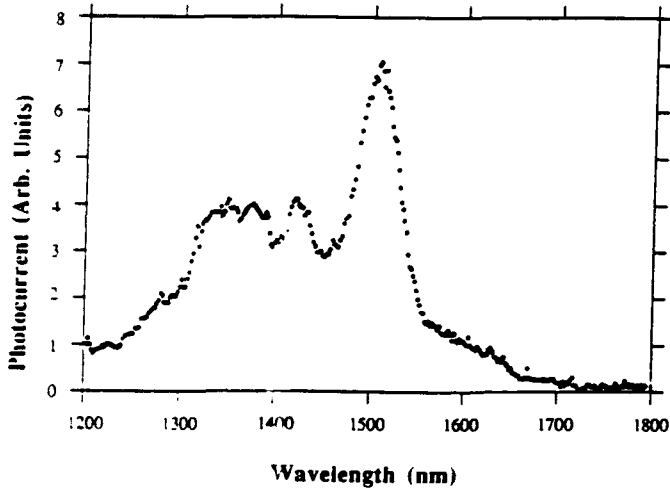


Fig. 3 Photocurrent spectrum of the resonant cavity device structure shown in Fig. 1 tested as a phototransistor showing a large enhancement in photocurrent at resonance.

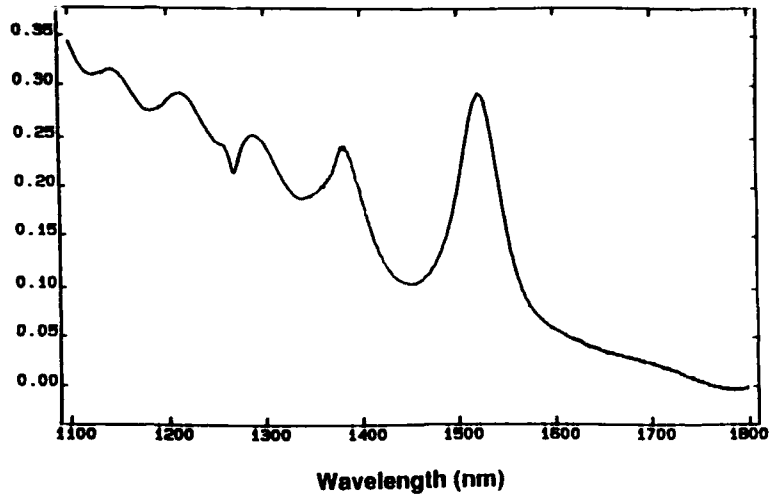


Fig.2 Reflectance spectrum of a resonant p-i-n photodiode structure showing a > 100 % increase in absorption at the resonance wavelength of 1.52 μm.

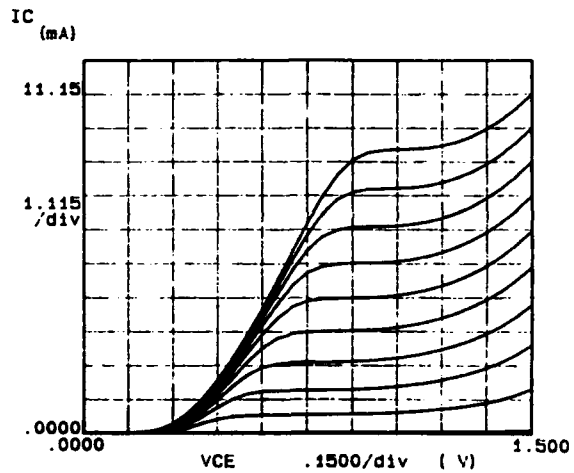


Fig.4 Common emitter DC I-V characteristics of a HBT device from the same wafer. The base current step is 1 μA, and the current gain is ~ 1000.

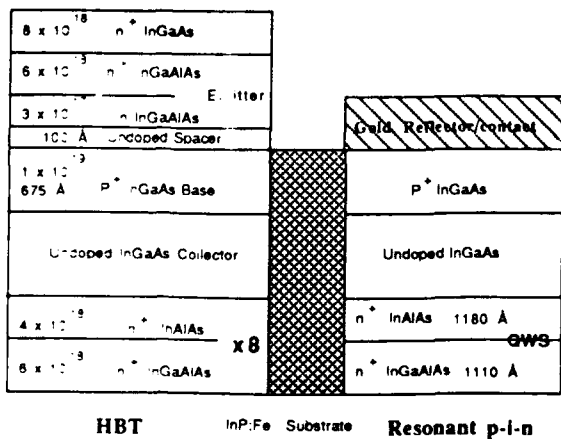


Fig. 5 Layer structure of a short-cavity resonant p-i-n photodiode/HBT.

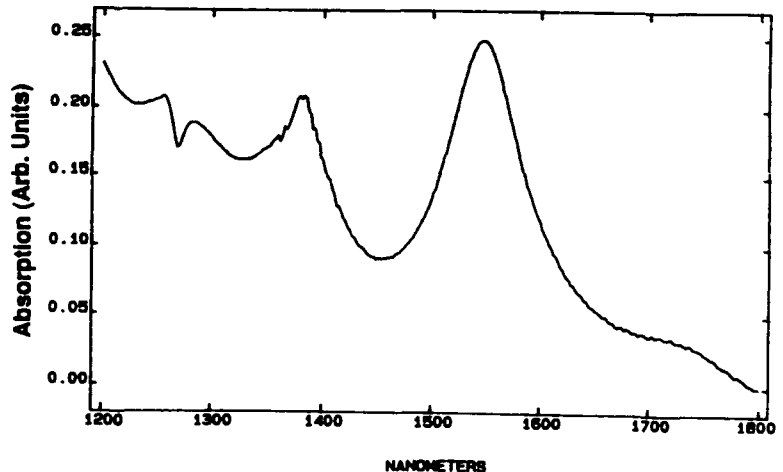


Fig. 6 Reflectance spectrum of a short cavity resonant p-i-n diode. The cavity length is 3λ/4.

Monday, April 13, 1992

Device Simulations

MD 1:30 pm–3:30 pm
La Salle Ballroom C

Shunji Seki, *Presider*
NTT, Japan

Electronic Device Simulation

A. Drobot
1710 Goodridge Dr.
McLean VA 22102

Summary was not available at the time of publication.

Ballistic electron diffractive switches: design and performance analysis

Gregory N. Henderson, Thomas K. Gaylord, and Elias N. Glytsis
 School of Electrical Engineering and Microelectronics Research Center
 Georgia Institute of Technology, Atlanta, GA 30332

Due to advances in nanostructure fabrication techniques, many devices have been fabricated that exhibit ballistic electron transport and quantum interference effects [1]. In addition, recent experiments have demonstrated the "optical like" characteristics of these ballistic electrons through refraction and diffraction experiments [2-3]. Based on these results, a class of ballistic electron grating diffraction devices was recently proposed [4]. Using the methods developed in Ref. [4], a ballistic electron diffractive switch and multiplexer are designed and analyzed in this paper. The present work contains the first systematic design and analysis of grating diffraction devices in which it is shown that over 90% of the ballistic input current can be diffracted into one or multiple outputs.

The ballistic electron diffractive switch (Fig. 1) and multiplexer (Fig. 2) were designed using a two-dimensional electron gas configuration [2]. In both devices, the electrons are emitted from contact E , collimated by contacts I_0 and I_1 , and diffracted by a potential grating Φ_g created by applying a voltage V_g to a periodic gate structure. Each diffracted order i propagates away from the grating in a unique direction (θ_i) [4] and is collected by gates G_i , G'_i and collector C_i . The kinetic energy KE of the i diffracted electrons is controlled by the potential Φ_{in} (Fig. 1a and 2a) as was done in Ref. [5].

The diffractive switch (Fig. 1) was designed to be in the Bragg regime [4] such that only the $i = 0$ and $i = 1$ diffracted orders have significant diffracted current. The diffraction efficiency (the percentage of the input current diffracted into order i) DE_i is shown in Fig. 1c as a function of the potential modulation for the design energy $KE = KE_D = 9meV$. If the device is to be used as a switch, the current at KE_D in the first diffracted order can be switched from 0% to 98% of the input current by applying a potential modulation of $\Phi_{g0} = 3.6meV$ ($V_g \sim 1V$). This device could also be biased in the linear region ($\Phi_{g0} = 1.8meV$) where the current in the first diffracted order is linearly modulated by V_g . The total diffraction efficiencies are found by evaluating $T_i = \int DE_i f(KE) dKE / \int f(KE) dKE$ where $f(KE)$ is the injected electron distribution. The function $f(KE)$ would be peaked about KE_D and would lie between a delta function $f_\delta(KE) = \delta(KE - KE_D)$ and the Fermi-Dirac function $f_{FD}(KE)$, yielding $T_0 = 0\%$ and $T_1 = 98\%$ for $f_\delta(KE)$ and $T_0 = 7.2\%$ and $T_1 = 91\%$ for $f_{FD}(KE)$.

In order to have significant current in multiple diffracted orders, the diffractive multiplexer (Fig. 2) was designed to be in the Raman-Nath regime [4]. The multiplexer diffraction efficiencies for KE_D are shown in Fig. 2c as a function of potential modulation. It is apparent that at $\Phi_{g0} = 3.8meV$, the multiplexer has an almost equal amount of current in 5 orders: $T_{\pm 2} = 18\%$, $T_{\pm 1} = 22\%$, and $T_0 = 16\%$ for $f_\delta(KE)$ and $T_{\pm 2} = 19\%$, $T_{\pm 1} = 21\%$, and $T_0 = 16\%$ for $f_{FD}(KE)$, yielding a total efficiency of 96%. Such a multiplexer can be designed for any odd number of output orders.

In conclusion, a ballistic electron diffractive switch and multiplexer have been designed that diffract over 90% of a ballistic current into one or multiple output ports. Such diffractive devices could become an integral part of future electron guided-wave integrated circuits for implementing high-speed integrated switches, modulators, and logic devices for computers and communications.

- [1] T. K. Gaylord, E. N. Glytsis, G. N. Henderson, K. P. Martin, D. B. Walker, D. W. Wilson, and K. F. Brennan, *Proc. IEEE* **79**, 1159 (1991).
- [2] J. Spector, H. L. Stormer, K. W. Baldwin, L. N. Pfeiffer, and K. West, *Appl. Phys. Lett.* **56** 1290 (1990).
- [3] K. Ismail, W. Chu, D. A. Antoniadis, and H. I. Smith, *Appl. Phys. Lett.* **52**, 1071 (1988).
- [4] G. N. Henderson, E. N. Glytsis, and T. K. Gaylord, *Appl. Phys. Lett.* **58**, 440 (1991).
- [5] U. Sivan, M. Heiblum, and C. P. Umbach, *Phys. Rev. Lett.* **63**, 992 (1989).

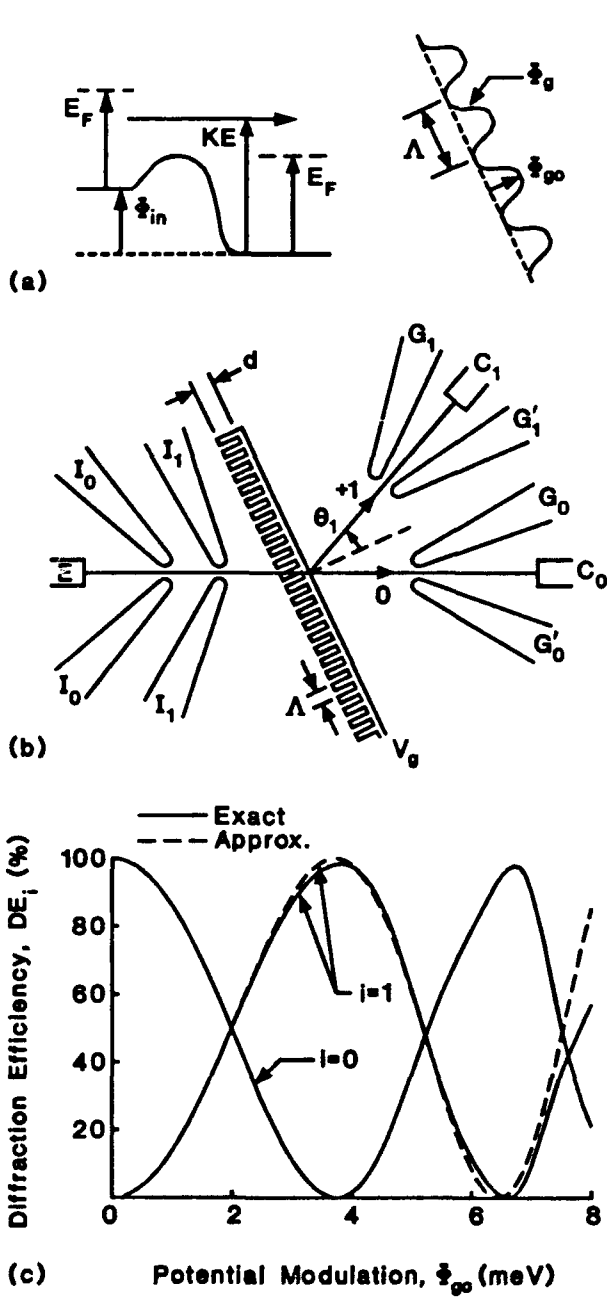


Fig 1. Bragg regime ballistic electron diffractive switch with $\Lambda = 60 \text{ nm}$, $d = 150 \text{ nm}$, and $E_f = 7.0 \text{ meV}$. (a) The conduction band profile of the injector and the grating. (b) The switch is designed in the 2DEG configuration, where electrons are injected by contacts E , I_0 and I_1 , diffracted by Φ_g , and collected by contacts G_i , G'_i and C_i for the $i = 0$ and $i = 1$ diffracted orders. (c) Diffraction efficiency of $i = 0$ and $i = 1$ diffracted orders as a function of potential modulation Φ_{g0} .

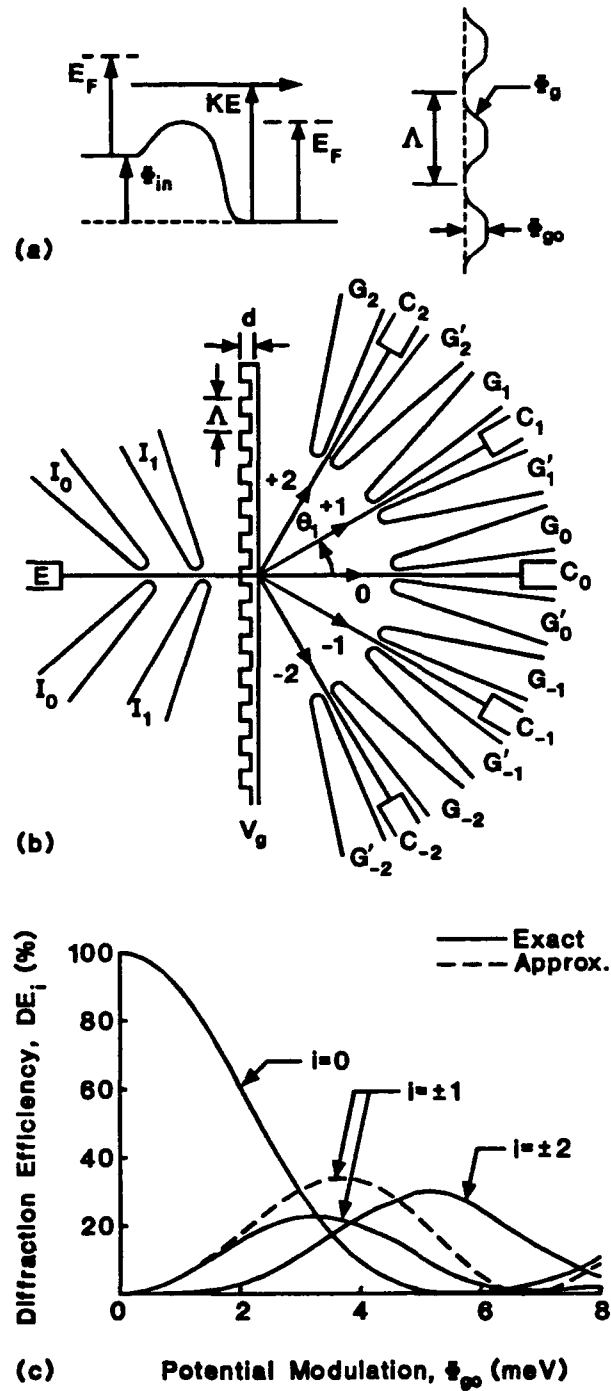


Fig 2. Raman-Nath regime ballistic electron diffractive multiplexer with $\Lambda = 250 \text{ nm}$, $d = 100 \text{ nm}$, and $E_f = 7.0 \text{ meV}$. (a) The conduction band profile of the injector and the grating. (b) The multiplexer is designed in the 2DEG configuration, where electrons are injected by contacts E , I_0 and I_1 , diffracted by Φ_g , and collected by contacts G_i , G'_i and C_i for the $i = 0, \pm 1, \pm 2$ diffracted orders (c) Diffraction efficiency of the i th diffracted order as a function of potential modulation Φ_{g0} .

MD3-1

SEMICONDUCTOR LASER DYNAMICS UNDER THE INFLUENCE OF WEAK EXTERNAL PHASE-CONJUGATE FEEDBACK

D. Lenstra, P. van der Linden and G.H.M. van Tartwijk
Department of Physics and Astronomy, Free University,
De Boelelaan 1081, 1081 HV Amsterdam, The Netherlands

The low facet reflectivity makes a diode laser very sensitive to external influences such as, e.g. weak feedback from a distant mirror. This sensitivity can successfully be used in stabilization and line-narrowing schemes based on delayed external optical feedback (see refs. 1-8 in [1]). Recently, successful frequency control of an AlGaAs diode laser using resonant phase-conjugate reflection was reported by Cyr *et al.* [2]. This experiment shows the possibility of locking the laser frequency through external optical feedback by the phase-conjugate reflection. A theory of phase-conjugate feedback in a semiconductor laser has been given by Agrawal and Klaus [1], but they formulated the problem for the case of a self-pumped mirror only. Therefore, in their theory the externally reflected signal does not provide a reference frequency to which the laser can lock.

We have formulated the problem for the case of a nearly-degenerate four-wave mixing model of phase-conjugate reflection. Representing the optical field within the laser as $\text{Re}E(t)\exp(i\omega_0 t)$ with $E(t)$ the slowly varying amplitude and ω_0 the solitary diode laser frequency (i.e. without feedback), our equations read

$$\begin{aligned} \dot{E}(t) = & \frac{1}{2}\xi(1+i\alpha)[n(t)-n_0]E(t) \\ & + \gamma e^{i\phi_{pcm}}E(t-\tau) e^{2i(\omega_p-\omega_0)(t-\tau/2)} \end{aligned} \quad (1)$$

$$\dot{n}(t) = -\left(\frac{1}{T_1} + \xi|E(t)|^2\right)[n(t)-n_0] - \Gamma_0(|E(t)|^2 - P_0) \quad (2)$$

where ξ is the gain parameter, α the linewidth enhancement parameter, n the carrier density and n_0 its value without feedback, T_1 the recombination time, Γ_0 the diode cavity decay time, γ the feedback rate (assumed to be small compared to Γ_0), P_0 is the stationary state power, i.e. the value of $|E(t)|^2$ without feedback, τ the feedback delay time, ω_p the reference (pump) frequency in the phase conjugate mirror and ϕ_{pcm} a fixed phase angle. It can be shown that our equations reduce to those formulated for the case of self-pumping in [1], after replacing ω_p by the laser output frequency.

In principle, the laser frequency can lock to ω_p provided $|\omega_p - \omega_0| \leq \gamma(1+\alpha^2)^{1/2}$, i.e. the solitary diode frequency should not deviate too much from the reference frequency ω_p . Results of numerical calculations confirm this behavior. A peculiarity related to the α parameter is that the locking situation leads not always to higher output intensity; lower intensity can occur as well. If the feedback is too weak for locking, the laser output oscillates at twice the difference frequency $|\omega_p - \omega_0|$. These oscillations can efficiently couple to the relaxation oscillation, providing a mechanism for unstable chaotic behavior.

[1] G.P. Agrawal and J.T. Klaus, *Optics Letters* 16(1991)1325

[2] N. Cyr, M. Breton, M. Tetu and S. Theriault, *Optics Letters* 16(1991)1298

Potential chirpless lasers with InGaAs/InGaAsP strained quantum well

Takayuki Yamanaka, Yuzo Yoshikuni, Wayne Lui, Kiyoyuki Yokoyama and Shunji Seki

NTT Opto-electronics Laboratories
3-1 Morinosato Wakamiya, Atsugi-shi, Kanagawa, 243-01 JAPAN

The boost on gain, differential gain and reduction of the linewidth enhancement factor in InGaAs on InP system due to compressive strain have recently been demonstrated theoretically [1-3]. The linewidth enhancement factor α (hereafter termed as the α parameter) is a key parameter in determining wavelength chirping and laser linewidth. Up to now, theoretical studies on strained quantum well (QW) lasers have been limited to lasing characteristics at gain peak, which implies the assumption of Fabry-Perot cavity. On the other hand, distributed feedback (DFB) lasers, which is an indispensable light source in optical transmission system, have the feature where the lasing wavelength can be tuned independent of the gain peak. The application of this feature is called detuning. In this paper, we discuss ways of designing lasers with extremely small α parameter (chirpless lasers) by detuning strained modulation doped (MD) QW lasers.

The detuning operation in DFB lasers is very sensitive to the wavelength dependence of the α parameter. The wavelength dependence of material gain and the α parameter of a non-strained QW structure are shown in Figure 1. By detuning away from the gain peak towards shorter wavelengths, the α parameter is reduced. To keep the operation point within the positive gain region, however, it is not always possible to achieve low α parameter even with detuning. As in the case shown in Figure 1, the region where $\alpha = 0$ lies within the absorption region, where the hole population is low. To boost the hole population, both compressive strain and modulation doping techniques will be utilized. In the following, we shall examine effects due to detuning of strained p-type MD laser structures.

A single QW structure consists of well material of $\text{In}_x\text{Ga}_{1-x}\text{As}$ sandwiched by barrier material of $\text{In}_{0.86}\text{Ga}_{0.14}\text{As}_{0.3}\text{P}_{0.7}$ (lattice-matched to InP) is analyzed. The well widths and the mole fraction x are determined so the lasing wavelength is about $1.55 \mu\text{m}$. To calculate accurately the heavy and light hole subband energy structure near the band edges, finite barrier height is assumed and the effective mass equations, described by the 4×4 Luttinger-Kohn (or $k \cdot p$) Hamiltonian with the axial approximation, are solved. Parabolic subbands are assumed for electrons. All the laser properties are derived based on the band structure obtained.

The density of states (DOS) of valence band are shown in Figure 2. Four cases of various compression are calculated. It is shown that as the strain increases, the DOS stretches into the high energy region. It is possible, therefore, for the hole quasi-Fermi level (E_{fp}) to penetrate into the valence band under relatively low injection carrier density. On top of this improved DOS characteristics by compressive strain, p-type modulation doping allows further penetration of E_{fp} into the valence band. As a result, the hole population is significantly increased.

To study the behavior of the α parameter through detuning of MD structure under strain, the material gain characteristics of various injection carrier densities are calculated. In these gain calculations, a Lorentzian line broadening with an intraband relaxation time of 0.1 ps is assumed. The gain characteristics versus the linewidth enhancement factor (using wavelength as a parameter) of three cases of interest are plotted in Figure 3. These three cases include (a) no strain, no doping, (b) 0.5% strain, no doping and (c) 0.5% strain with $2 \times 10^{17} \text{ cm}^{-2}$ background hole density by MD, which are used to illustrate the contribution due to strain and MD. It is found that in cases (b) and (c) the material gain is improved remarkably as compared to that in case (a). Because the α parameter at gain peak stays rather constant for all cases considered here, to improve the α parameter value, detuning is necessary. By doing so, the operation point is shifted along each curve towards the $\alpha = 0$ region. Since laser operation requires positive material gain, even by applying detuning, the best α parameter that can be obtained is -0.5 in case (a) and -0.2 in case (b). In case (c), however, it is possible to achieve the $\alpha = 0$ case via detuning, thereby realizing chirpless laser.

In summary, the effects of detuning on the α parameter are analysed for InGaAs/InGaAsP strained QW lasers. It has also been shown that significant reduction of the α parameter by detuning can be achieved in strained MD structure. As a result, chirpless lasers can be realized by techniques described in this report.

- [1] A. Ghati, W. Batty, U. Ekenberg and E.P. O'Reilly, "Low threshold current InP-based strained-layer 1.55 μm lasers," *SPIE Proceedings*, vol. 861, pp. 96-101, 1990.
- [2] S.W. Corzine and L.A. Coldren, "Theoretical gain in compressive and tensile strained InGaAs/InGaAsP quantum wells," *Appl. Phys. Lett.*, vol. 59, pp. 588-590, 1991.
- [3] T. Ohtoshi and N. Chinone, "Linewidth enhancement factor in strained quantum well lasers," *IEEE Photonic. Tech. Lett.*, vol. 1, pp. 117-119, 1989.

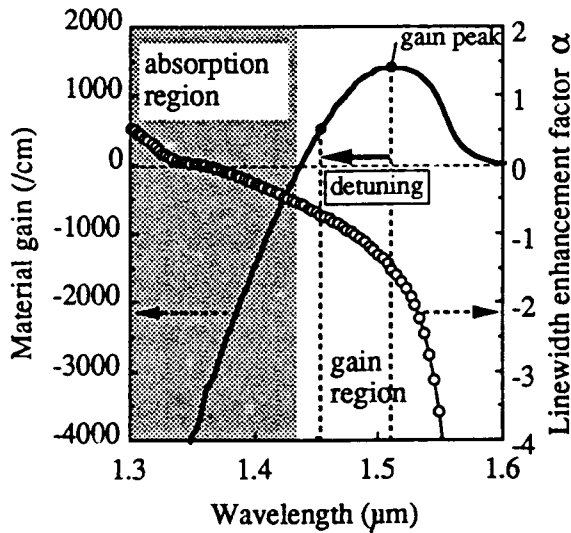


Figure 1 Wavelength dependence of material gain (solid line) and the linewidth enhancement factor(α)(circles) for the case of non-strained QW structure with well width of 90 \AA .

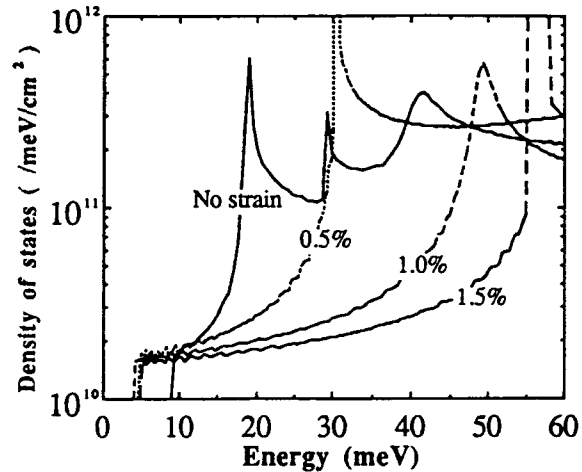


Figure 2 Density of states of valence band. Energy is measured from bulk valence band edge. Four cases of interest: (a) no strain with well width of 90 \AA ; (b) 0.5% compression with 50 \AA ; (c) 1.0% compression with 35 \AA ; and (d) 1.5% compression with 27 \AA are shown.

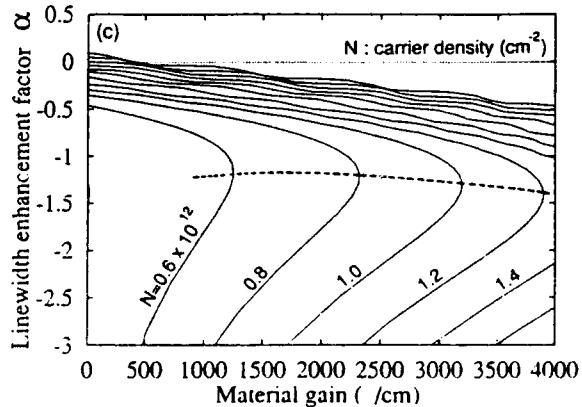
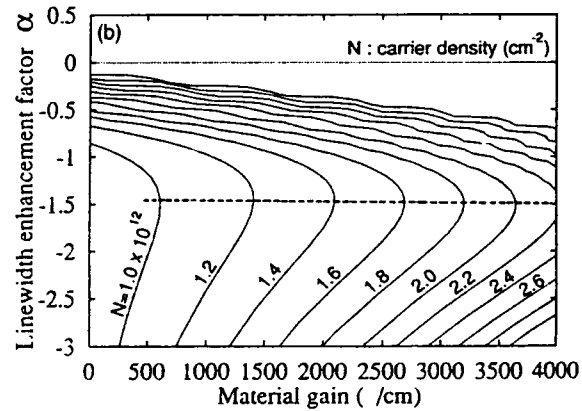
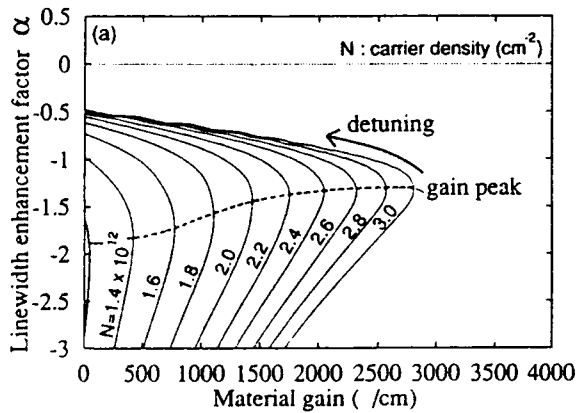


Figure 3 Plot of material gain versus the linewidth enhancement factor (α) using wavelength as a parameter for various carrier densities. Three cases of interest (a) no strain, no doping; (b) 0.5% compressive strain; and no doping, and (c) 0.5% compressive strain with $2 \times 10^{12} \text{ cm}^{-2}$ background hole density by MD density are shown.

EFFECTIVE NONLINEAR GAIN IN SEMICONDUCTOR LASERS

GUANG-HUA DUAN, PHILIPPE GALLION

Département Communications
Ecole Nationale Supérieure des Télécommunications
46, rue Barrault, 75634 PARIS CEDEX 13, France

GOVIND P. AGRAWAL

The Institute of Optics
University of Rochester
Rochester, N Y 14627, USA

Summary

The nonlinear gain is known to have an important influence on the dynamics and noise properties of semiconductor lasers [1,2]. The previous studies have used a form of the nonlinear gain derived from the consideration of the material properties alone such as spectral hole burning or carrier heating [3,4]. In every model, the nonlinear gain is a function of the local photon density. However, in most semiconductor lasers, the photon density is not uniform along the cavity due to the output coupling. A natural question is what is the effective nonlinear gain that should appear in the rate equations governing the laser dynamics and noise properties. The purpose of this paper is to clarify the influence of photon density distribution on the nonlinear gain.

The starting point of our analysis is the wave equation in the frequency domain. Assuming perfect transverse and lateral index guiding, we concentrate our attention to the longitudinal axis. The one-dimensional propagation equation is solved by using a modified Green's function method to include the material nonlinear gain. When the refractive index and the optical gain vary smoothly in the cavity, as in the case of Fabry-Perot, DFB and DBR lasers, the effective nonlinear gain can be written as :

$$g_{NL}^{EFF} = \frac{\langle Z_0^2(z) g_{NL}(N,P) \rangle}{\langle Z_0^2(z) \rangle} \quad (1)$$

where $Z_0(z)$ is the field distribution inside the cavity, g_{NL} is the material nonlinear gain, $N(z)$ the carrier density, $P(z)$ the photon density, $\langle \rangle$ denotes a spatial averaging over the cavity length L . The material nonlinear gain becomes complex when the nonlinear refractive index is included [2]. Thus the effective nonlinear gain is a spatial averaging of the material local nonlinear gain weighted by the squared field distribution rather than by the intensity. This newly defined nonlinear gain takes into account both material and structural dependences. It reduces to the material gain for an uniform intensity distribution. The effective nonlinear gain has the same origin as

the longitudinal spontaneous emission enhancement factor K_z [5,6]: the different longitudinal mode distributions $\{Z_m(z), m=0, 1, \dots\}$, forming a complete set, are not orthogonal in the Hermitian sense, due to the presence of optical gain in the cavity.

It can be predicted from this equation that for the same material, different laser structures can give rise to different values and forms of the effective nonlinear gain through field distribution $Z_0(z)$. Moreover, as the intensity distribution is usually not uniform and changes with the output power due to spatial hole burning, the effective nonlinear gain will have, in general, a different power dependence than the material nonlinear gain. Finally, as the field distribution generally includes a spatially dependent phase, the material nonlinear gain can result in an effective nonlinear index and *vice versa*.

The nonlinear gain can be approximated in the low output power regime by $g_{NL} = -g_L \epsilon P(z)$, where ϵ is referred to as the gain compression factor and g_L as the linear gain. It is assumed for the moment that the spatial variation of the linear gain due to spatial hole burning in the laser cavity could be neglected. By comparing this effective nonlinear gain with the material nonlinear gain corresponding to the average photon density in the cavity, a correction factor C of effective nonlinear gain can be introduced,

$$C = \frac{\langle Z_0^2(z) |Z_0(z)|^2 \rangle}{\langle Z_0^2(z) \rangle \langle |Z_0|^2(z) \rangle} \quad (2)$$

which relates the effective gain compression factor with the material gain compression factor. The real part of C represents the change in the material nonlinear gain, the imaginary part represents the contribution of the material nonlinear gain to the effective index.

We have calculated the correction factor for

different types of laser structure. For Fabry-Perot lasers with usual facet reflectivities, the real part of C is close to unity, the imaginary part is quite small compared to the real part. For a conventional DFB lasers with two AR coated facets, the real part of C increases from 0.87 for $\kappa L = 1.0$ to 1.3 for $\kappa L = 5.0$. The imaginary part changes from negative values to positive values with the increasing κL . The result for a AR-coated $\lambda/4$ phase-shifted DFB laser is shown in Fig. 1. The real part of the correction factor becomes larger than unity for $\kappa L > 1.25$ and attains 2 for $\kappa L = 4.0$. The imaginary part of the correction factor changes sign at $\kappa L = 1.25$ and becomes negligible for larger values of κL .

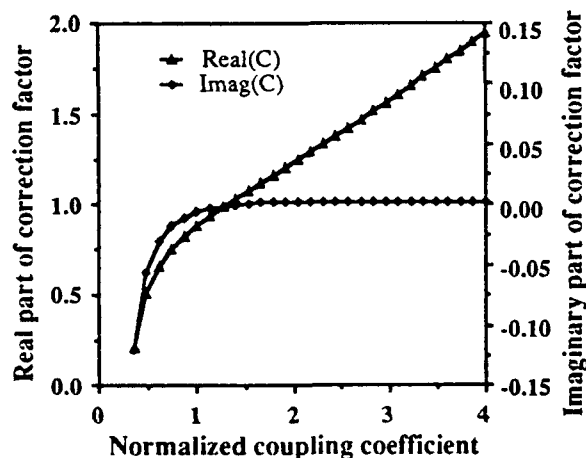


Fig. 1 The real and imaginary parts of the correction factor C as a function of the normalized coupling coefficient κL for a $\lambda/4$ phase-shifted DFB laser with AR-coated facets.

To evaluate its output power dependence, the effective nonlinear gain is calculated by using equation (1) for a AR-coated $\lambda/4$ phase-shifted DFB laser with $\kappa L = 3.0$. In our calculations, the field distribution and the linear gain are calculated by including the spatial hole burning. The material nonlinear gain is assumed to have the same form as in Ref. [3]. The real and imaginary parts of the effective nonlinear gain are plotted as a function of the output power in Fig. 2(a) and 2(b) respectively. The material nonlinear gain corresponding to the average photon density is also plotted in Fig. 2(a) for comparison. It can be seen that at low output powers, the effective nonlinear gain and the material nonlinear gain give a similar power dependence. The ratio of their values is represented by the correction factor C . At high output powers, the material nonlinear gain exceeds the real part of the effective

nonlinear gain, the imaginary part of the nonlinear gain tends to change sign.

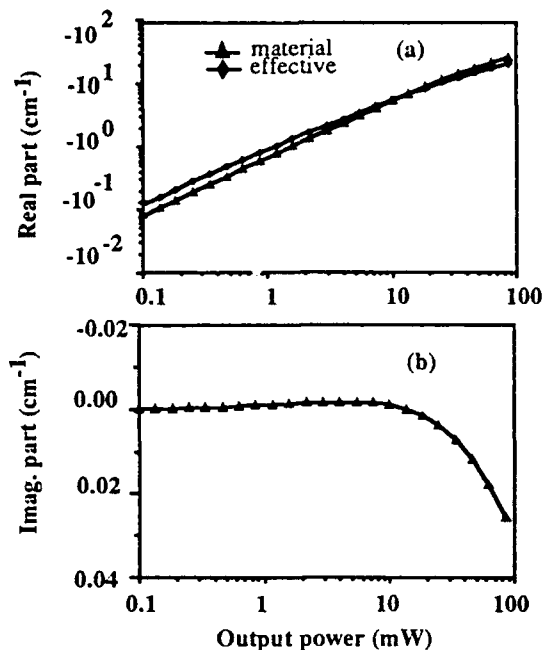


Fig. 2 (a) The real part and (b) the imaginary part of the effective nonlinear gain as a function of output power for a phase-shifted DFB laser with $\kappa L = 3.0$.

In conclusion, the concept of an effective nonlinear gain is introduced which takes into account both the material and structural dependences. The consequences of the effective nonlinear gain on laser dynamics and noise will be reported at the conference.

References

- [1] R. S. Tucker, vol. LT-3, pp. 1180-1192, Dec. 1985.
- [2] G. P. Agrawal, IEEE J. Quantum Electron., vol. QE-26, pp. 1901-1909, Nov. 1990.
- [3] G. P. Agrawal, IEEE J. Quantum Electron., vol. QE-23, pp. 860-868, June 1987.
- [4] B. N. Gommatam and A. P. DeFonzo, IEEE J. Quantum Electron., vol. 26, pp. 1689-1704, Oct. 1990.
- [5] C. H. Henry, IEEE/OSA J. Lightwave Technol., vol. LT-4, pp. 288-297, Mar. 1986.
- [6] G. H. Duan, P. Gallion, and G. Debarge, IEEE J. Quantum Electron., vol. QE-26, pp. 32-44, Jan. 1990.

QUENCHING of RESONANTLY ENHANCED ABSORPTION by MULTIMODE INTERFERENCE in VERTICALLY-COUPLED WAVEGUIDE PHOTODETECTORS

E.C.M. Pennings, R.J. Deri, and R.J. Hawkins^a

Bellcore, 331 Newman Springs Road, Red Bank, New Jersey 07701-7040, (908) 758-2972

a) Lawrence Livermore National Laboratory, Livermore, California 94550

Understanding optical propagation in lossy planar waveguides is important for photonic integration. "Steady-state eigenanalysis", ie: an analysis using *only the eigenvalues* (propagation constants $\beta_i + j\alpha_i$ for modes i) of the complex-index slab waveguide problem, is often used to model such structures,[1-5] and was recently used to optimize vertically-coupled detectors (fig. 1) by maximizing α_i . It predicts that α_i can be enhanced by adjusting the absorber thickness[1,3] or by inserting an additional, transparent "matching layer",[2] as indicated by a sharp resonance in the dependence of α_i on layer thickness (fig. 2, solid curve). However, recent experiments and BPM simulations indicate that steady-state eigenanalysis fails to adequately describe devices optimized with matching layers:[6,7] while enhanced absorption is observed, the predicted resonance is absent. Here we show that the resonance predicted by steady-state eigenanalysis for the conventional structure of fig. 1 is quenched by multimode interference associated with modal power non-orthogonality, and can be accurately simulated using an eigenmode-based propagation method.

We consider the previously-investigated[1,2,8-10] structure of fig. 1 with TE-polarized, 1.3 μm wavelength light incident from the left along z in the single-mode waveguide. Previous simulations employed "mode matching" for InGaAs absorber thickness $T \geq 0.2\mu\text{m}$ [10] or steady-state eigenanalysis for arbitrary T . [1] Fig. 2 shows steady-state eigenanalysis results $\alpha(T)$ (solid curves) and BPM results (asterisks). Since the optical power does not generally decay exponentially, we plot in fig. 2 an effective absorption $\alpha = 6.99\text{dB/L}$, where L is the length required for 80% (6.99dB) absorption. For thick absorbers ($T \geq 0.2\mu\text{m}$), BPM and steady-state eigenanalysis both predict similar behavior, which has been validated by experiment.[1,2,8-10] For thin absorbers, however, BPM predicts a much weaker resonant enhancement which can be more than three times smaller than the steady-state eigenanalysis prediction. We are confident that the BPM prediction is correct because this method has successfully described experimental data for non-exponential absorption in other multimode, vertically-coupled detectors.[6,7]

To explain why steady-state eigenanalysis does not correctly predict absorption and show how the eigensolutions can be used to correctly simulate such devices, we employ steady-state eigenmodes as computational basis functions for propagation calculations. This provides a rapid alternative to BPM as well as a simple conceptual picture for understanding propagation in terms of guided modes. Using normalized transverse modal fields $e_i(x)$ from the eigenanalysis, propagating fields are represented by a superposition of eigenmode contributions $E_i(x,z) = c_i e_i(x) \exp [(-\alpha_i + j\beta_i)z]$, where the exponential accounts for propagation and c_i is a complex amplitude coefficient obtained from overlap integrals. The total power in the detector is then $P(z) = \int dx \cdot \sum_{m,n} E_m(x,z) \times H_n(x,z)^*$, where $H_n(x,z)$ is the modal magnetic field corresponding to $E_n(x,z)$. Notably, $P(z)$ contains products of non-identical modes ($m \neq n$) due to modal power non-orthogonality in the absorbing structure. The absorption predicted by this eigenmode-based method agrees with BPM results (fig. 2), as well as with previous results for multimode waveguide detectors using matching layers.[6,7] Therefore, the modes themselves do form a useful basis for such simulations.

Having demonstrated that this method correctly describes vertically-coupled detectors, we can use it to understand why the resonance is weaker than predicted by steady-state analysis. For $T \geq 0.2\mu\text{m}$, all simulation methods agree with one another because nearly all incident light is coupled into a *single* guided mode of the absorbing region. For $T < 0.2\mu\text{m}$, however, *multiple* modes are excited within the absorbing $z > 0$ region. In this case, the absorptive decay $dP(z)/dz$ is not determined by modal eigenvalues α_i , but by the total integrated optical intensity $\int_{abs} |\sum_m E_m(x,z)|^2 dx$ within the absorber. The initial $z=0$ excitation minimizes this quantity, in that the modal fields interfere destructively to reduce the intensity inside the absorber, so that the initial absorption is slower than that predicted for an individual eigenmode alone. Constructive interference which increases absorption occurs after propagation over some distance. This interference is described by the $m \neq n$ terms in our expression for $P(z)$, which are nonzero due to modal power non-orthogonality. Quenching of the resonance is most pronounced for

E.C.M. Pennings et al., "Quenching of Resonantly Enhanced Absorption..."

thinner guides because more detector modes are excited. For $D=1.2\mu\text{m}$ guiding layers, the power is mostly coupled into two modes which are nearly equally excited. The resonance peak is reduced nearly twofold, consistent with the twofold absorption difference from steady-state predictions observed in bimodal detectors using matching layers.[7,8] For $D=0.9\mu\text{m}$, appreciable excitation of several guided and radiation modes reduces the resonant absorption by more than a factor of three. This decrease reflects a real change in dP/dz , rather than coupling to radiation modes; only $\sim 10\%$ of the incident power is never absorbed due to radiative loss in this structure.

In conclusion, we have demonstrated that the intermodal interference associated with power non-orthogonality quenches the resonant absorption exhibited by modal propagation constants for thin absorbing layers in waveguide-detectors.

This work was supported in part under the auspices of the U.S. Department of Energy under contract no. W-7405-ENG-48.

REFERENCES

1. J. F. Vinchant, F. Mallecot, et al., *Opt. Commun.* **67**, 266 (1988).
2. R. J. Deri and O. Wada, *Appl. Phys. Lett.* **55**, 2712 (1989).
3. G. M. McWright, T. E. Batchman, and M. S. Stanziano, *J. Quantum Electron.* **QE-18**, 1765 (1982).
4. S. Miyanaga and H. Fujiwara, *Opt. Commun.* **64**, 31 (1991).
5. R. E. Smith, S. N. Houde-Walter, and G. W. Forbes, *Opt. Lett.* **16**, 1316 (1991).
6. R. J. Hawkins, R. J. Deri, and O. Wada, *Opt. Lett.* **16**, 470 (1991).
7. R. J. Deri, W. Doldissen, et al., *Appl. Phys. Lett.* **58**, 2749 (1991).
8. C. Bornholdt, W. Doldissen, et al., *Electron. Lett.* **23**, 2 (1987).
9. R. Kaiser, L. Morl, and W. Rehbein, in *Tech. Dig. Integrated Photonics Res. 1990* **5**, p. 52 (1990).
10. M. C. Amann, *Electron. Lett.* **23**, 895 (1987).

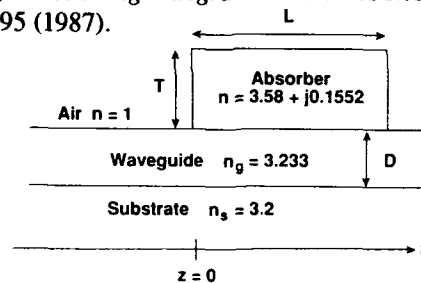


Fig. 1: Vertically-coupled Detector, with refractive indices at $\lambda=1.3\mu\text{m}$.

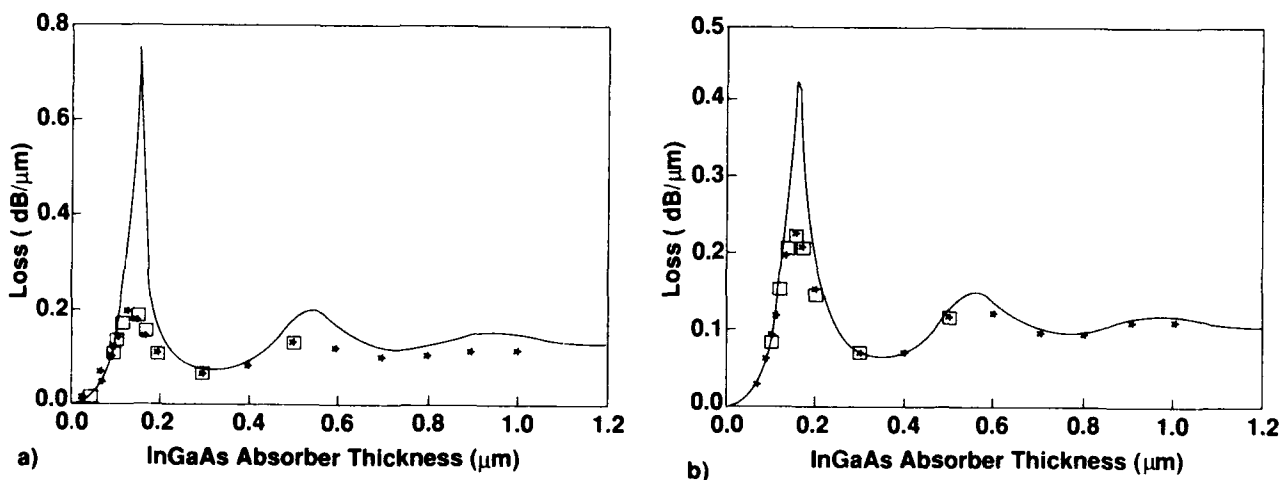


Fig. 2: Dependence of the absorption α characterizing guide-to-detector coupling on InGaAs absorber thickness T , for guide thicknesses $D=0.9\mu\text{m}$ (a) and $1.2\mu\text{m}$ (b). Predictions of steady-state eigenanalysis (lines), BPM (asterisks), and eigenmode-based propagation simulations (boxes) are shown.

Vectorial Simulation of Passive Mode Converter Devices on InP

C.M. Weinert and H. Heidrich,
Heinrich-Hertz-Institut für Nachrichtentechnik Berlin GmbH.,
Einsteinufer 37, D 1000 Berlin 10, Tel. + +30 31002 255

TE to TM converters with constant 45°-operation are required especially in coherent optical systems as for example, in a monolithically integrated polarization diversity receiver front-end OEIC. The following investigations were carried out within the RACE program, project "Subscriber Coherent Multichannel (CMC) System" (RACE 1010).

First passive TE/TM-mode converters on InP have been published recently [1] using InP/GaInAsP ($\lambda_Q = 1.3 \mu\text{m}$) rib waveguides periodically and asymmetrically loaded with a $\lambda_Q = 1.3 \mu\text{m}$ -layer on top of the waveguide (MC1) or on top and at one side of the waveguide (MC2). An alternative approach is to use a stepped waveguide layer (MC3) [2].

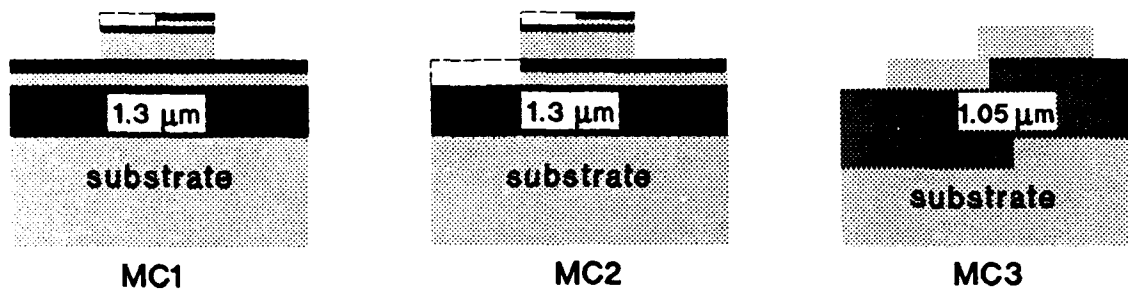


Fig. 1: Schematic cross-sections of MC1, MC2, and MC3; the dashed lines of MC1 and MC2 show the structure before etching.

The waveguide cross sections of the mode converter designs MC1, MC2, and MC3 are schematically shown in figure 1. Common to all structures are periodically arranged waveguide sections of length $\Lambda/2$ which alternatively have a perturbed geometry on the left and right hand side. Λ is the TE/TM-beat length of the structure. The change in geometry enables the coupling to the orthogonal polarization at the junction of two sections. For general structures polarization rotation cannot be simulated by the scalar approximation to the wave equation but can only be evaluated by the overlap integral S of the vector fields

$$S = \int (E_x(\text{TE},1)E_x(\text{TM},2) + E_y(\text{TE},1)E_y(\text{TM},2)) dx dy$$

where $E_i(\text{TE},1)$ and $E_i(\text{TM},2)$ are the ($i=x,y$) components of the normalized field vectors in the feeding waveguide of the converter ($E_x(\text{TE},1)$) and the converter section ($E_x(\text{TM},2)$), respectively. In order to obtain these fields the vectorial waveguide equation must be solved which is done by a vectorial 2-dimensional Finite-Difference scheme.

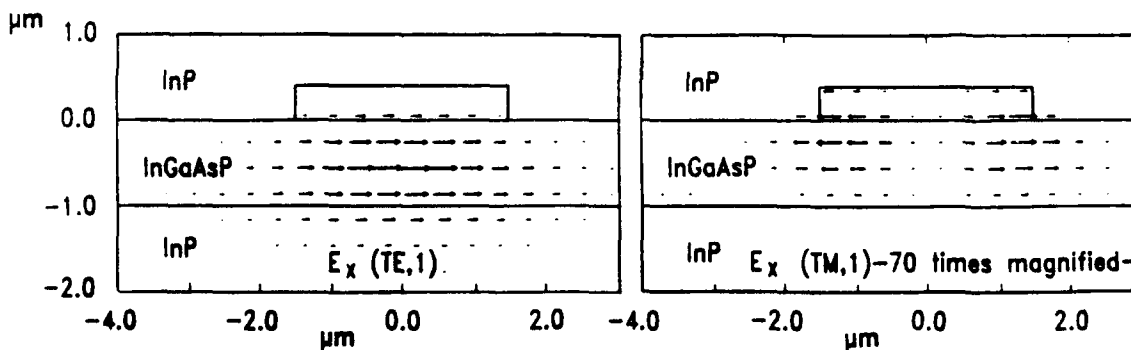


Fig. 2: E_x -field vectors of the feeding waveguide.

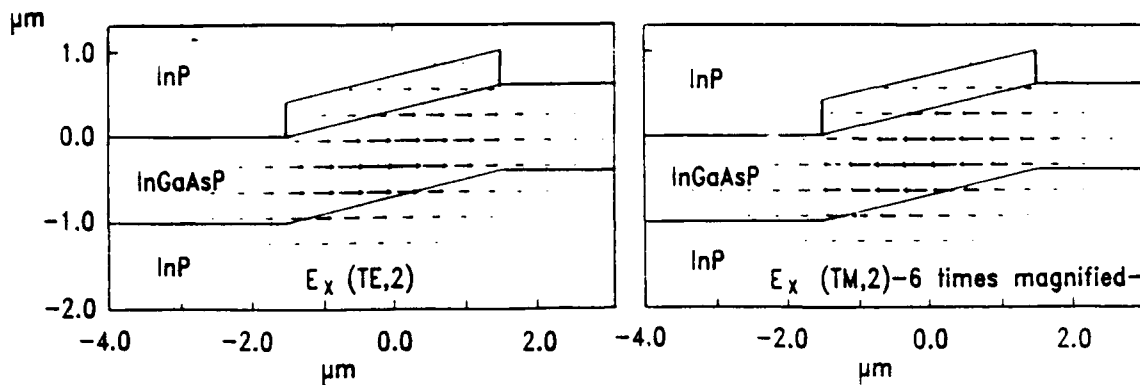


Fig. 3: E_x -field vectors of the tilted waveguide (MC3).

Vectorial solution of the guided modes of dielectric waveguide structures in general leads to modes which are not purely TE or TM polarized. As an example the calculated E_x components of the first and second eigenmodes of the feeding waveguide of MC3 are depicted in figure 2. For the first (TE-like) mode the E_x component is large whereas for the second (TM-like) mode E_x is the small (hybrid) component which has a node and a field maximum and minimum at the edges of the rib with only 1.3% field strength of the maximum E_x component of the TE mode. (For the E_y components the situation is interchanged. Here the E_y component is small for TE and large for TM.) Because of the antisymmetry of $E_x(TM,1)$ the TE-like and TM-like modes are orthogonal. Next, the E_x components of the tilted waveguide section of MC3 are depicted in figure 3. The E_x component of the TM mode has lost its antisymmetry in this coordinate system and therefore the TE mode of section 1 can couple to the TM mode of section 2.

The overlap between the feeding waveguide with MC1, MC2 and MC3 is calculated together with the beat length Λ of the device and the excess loss l per interface. Polarization rotation is expressed by the tilting angle α [2] which is found from S by $\alpha = \arctan(S)$.

	MC1	MC2	MC3
$\alpha(\text{calc}) [^\circ]$	0.36	1.7	9.8
$\alpha(\text{expt}) [^\circ]$	0.40	4.0	11
$\Lambda(\text{calc}) [\mu\text{m}]$	101	87	764
$l(\text{calc}) [\text{dB}]$	0.08	0.36	2.4

For MC1 the calculated value of α is five times smaller than for MC2. Loading of the waveguide rib only slightly perturbs the $E_x(TM,1)$ compared to the strong perturbation by etching besides the rib as in MC2. For MC3, the largest α results. Because of the hybrid character of the eigenmodes TE to TM conversion can be achieved either by shifting or tilting of one waveguide section with respect to the other but for optimization of devices losses also have to be considered.

The complete rotation Θ of a device with n sections is $\Theta = (-1)^n 2n \alpha$. The total excess losses $L = nl$ of all three structures are similar because n decreases from MC1 to MC3. However, MC3 is favoured since a large n acts as a wavelength filter.

Concluding, solution of the scalar approximation to the wave equation is insufficient for simulation of passive mode converter devices and solution of the vector equation is necessary. Eigenmode calculations with a two-dimensional vectorial Finite-Difference algorithm supply the design parameters necessary for fabrication of such devices.

[1] Y. Shani, R. Alferness, T. Koch, U. Koren, M. Oron, B.I. Miller, M.G. Young, Appl. Phys. Lett., 59, pp. 1278-1280, 1991.
 [2] H. Heidrich, P. Albrecht, M. Hamacher, H.-P. Nolting, H. Schroeter-Janßen, C.M. Weinert, to be published IEEE Photonics Technology Lett., Jan. 1992.

Monday, April 13, 1992

Acousto-Optic and Magneto-Optic Devices

ME 1:30 pm–3:00 pm
Pelican Room

Steven K. Korotky, *Presider*
AT&T Bell Laboratories

Sidelobe Suppression in an Acousto-optic Filter with a Raised-Cosine Interaction Strength

D. A. Smith and J. J. Johnson

Bellcore NVC 3X-233, 331 Newman Springs Rd., Red Bank, NJ 07701 (908)-758-3148

Introduction. The acousto-optic filter (AOF) is becoming increasingly important in optical communication research because of its unmatched potential in densely-packed WDM systems. In comparison to the Fabry-Perot, their main competitor, AOFs have a larger tuning range-to-bandpass ratio, are more than a thousand times faster, are free of hysteresis (a problem with all-fiber Fabry-Perots), are able to parallel process many wavelength channels at a time (the Fabry-Perot is a single-state device, unless ganged in a complicated and inherently lossy way) and are able to be configured as a 4-port switch [1] (the Fabry-Perot is a 1X1 filter, not a space-division switch) which makes the AOF a potential building block for large switch networks.

The notable weakness of the AOF has been the presence of secondary maxima (sidelobes) in its optical transmission spectrum, which results in interchannel crosstalk in dense WDM systems [2]. The sidelobe structure of the AOF is the direct consequence of an abrupt onset and cutoff of the AO interaction, which arises when the acoustic wave is generated at full strength at an interdigital transducer and propagates with little loss until terminated by an acoustic absorber. The Fourier transform of this rectangular interaction profile is a sinc-squared transmission function of wavelength, which falls off as $(\lambda - \lambda_o)^{-2}$. What we experimentally confirm in this paper is that significant suppression of the sidelobe skirt can be achieved by apodization of the interaction strength. In particular, we have gradually introduced (and later gradually removed) a surface acoustic wave (SAW) into a SAW guide containing the optical channel waveguide of an AOF (Fig. 1a). The tapered SAW beam profile was achieved by evanescent coupling to a launching SAW-guide, with the effect of producing a raised-cosine acousto-optic coupling strength. The Fourier transform of this interaction strength profile depends on detuning as $(\lambda - \lambda_o)^{-4}$: resulting in a much more depressed sidelobe spectrum than obtainable with an unapodized filter.

SAW-Guide Directional Coupler. The SAW-guide coupler [3] operates in a manner analogous to the optical directional coupler, by separating two SAW guides with a small-enough gap to maintain a weak evanescent coupling between the SAW-guide modes. If a SAW mode is generated in one SAW guide, the energy oscillates between the two guides so that the power in the adjacent guide P_{adj} is $P_{adj}(y) = P_{launch}(0)\sin^2(\pi y/2L_c)$, in which L_c is the coupling length for complete power transfer between arms of the coupler. The region of rise and fall of the first energy peak in the adjacent guide, $2L_c$, must be as long as possible to keep the power requirements ($\approx L^{-2}$) and the filter bandwidth ($\approx L^{-1}$) as small as possible. This means that the gap between SAW guides (upon which L_c exponentially depends) must be carefully selected. Truncating the AO interaction for $x > 2L_c$ is easily achieved by means of an acoustic absorber (a blob of rubber cement works for SAW powers less than 1 W/mm) placed at $L = 2L_c$.

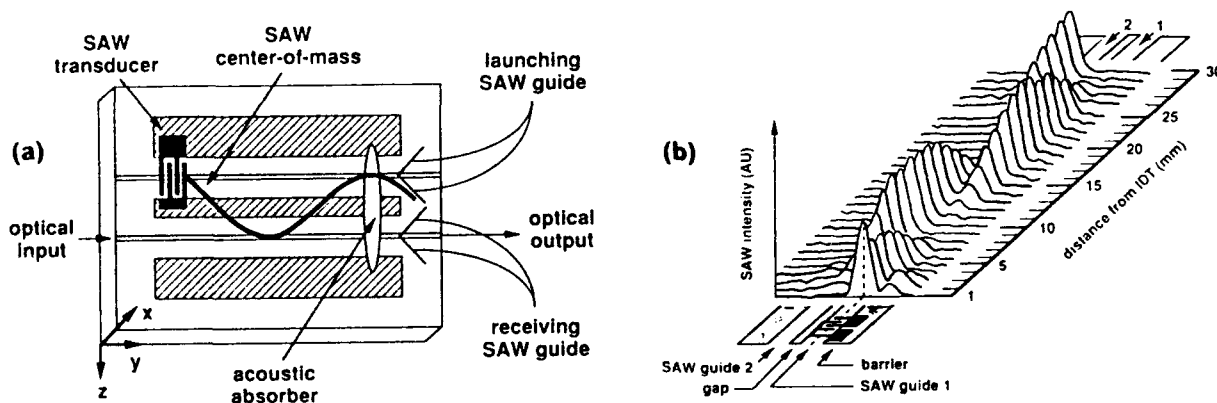


Fig. 1. (a) AOF imbedded in the receiving SAW guide of a SAW coupler. (b) SAW profilometer tracing of the acoustic intensity profile in a 20- μ m-gap SAW coupler.

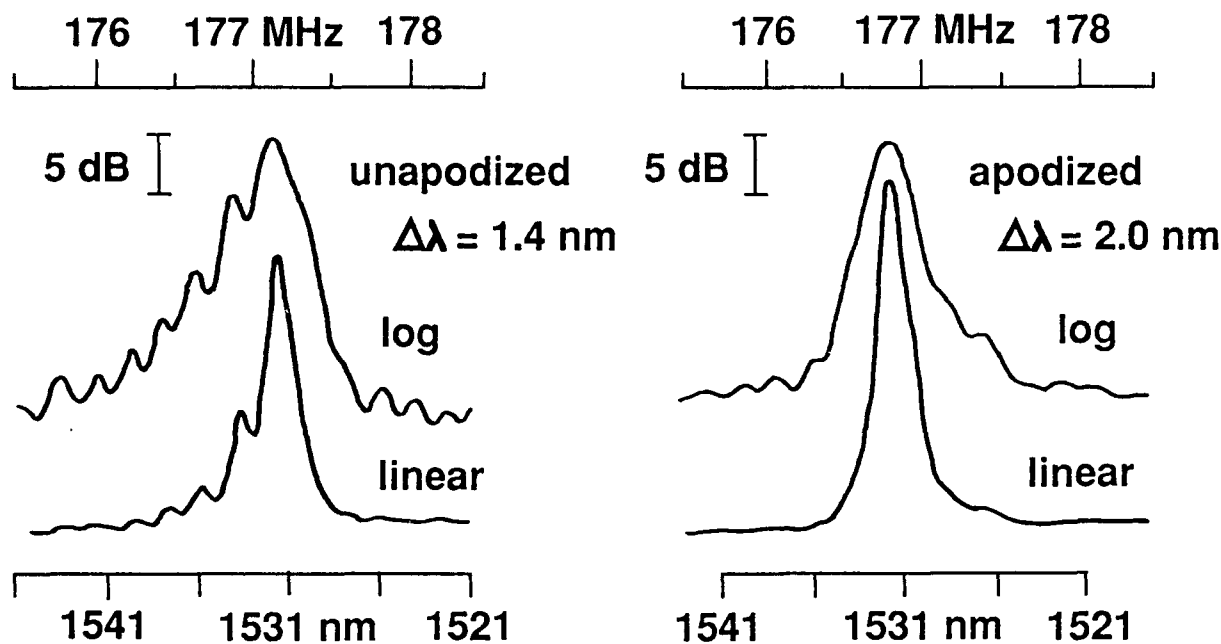


Fig. 2. (a) Linear and log traces of an unapodized AOF transmission and (b) transmission of matched AOF but with SAW-coupler apodization.

Device Fabrication. In our experiments, SAW guides were fabricated in x-cut y-propagating LiNbO₃, and consisted of 150- μ m-wide deeply-indiffused Ti metal barriers, separated by 100 μ m, supporting a monomode acoustic wave [4]. By reducing the barrier width between two SAW guides, a directional coupler was formed. The active optical waveguide was imbedded in the "receiving" SAW guide of the SAW coupler as shown in Fig. 1a. The SAW beam was generated by an 20-pair 20- μ m-period gold interdigital transducer. Fig. 1b is a profile of the acoustic intensity taken at 1-mm increments along the 20- μ m-gap SAW-coupler length, using a diffraction profilometer [3].

Results and Discussion. Fig. 2a shows the transmission of an *unapodized* filter, obtained from a simple SAW-guided AOF (actually the launch guide of a 150- μ m-gap SAW coupler). The probe was a fixed 1531-nm laser source, and the spectral scan was taken by sweeping the RF drive frequency imposed on the launching SAW transducer. The reference filter had very prominent sidelobe peaks (-5 dB secondary peak on the low-frequency or long-wavelength edge) and its linewidth was broadened from a theoretical value of 1.2 nm to 1.4 nm, presumably because the rough edges of the SAW guide caused degradation of the coherence of the SAW beam over the thousand acoustic wavelengths of this 19-mm-long device. The unapodized filter length was chosen to match the apodized filter interaction length $2L_c$.

Fig. 2b shows the transmission spectrum of an *apodized* filter, for which the active optical guide was in the receiving SAW guide of a 20- μ m-gap coupler with an interaction length of 19 mm. The worst-case sidelobe intensity for the apodized filter was -15 dB, *down 10 dB from the unapodized filter*. The filter width broadened to 2.0 nm, as expected from the decreased effective interaction length. Absorbers placed so as to make a shorter or longer AOF resulted in worse sidelobe levels, but the absorber placement was only critical to ± 1 mm.

Conclusion. We have shown that the SAW coupler provides an effective way to improve the sidelobe spectrum of acousto-optic filters, bringing this technology much closer to practical use in spectroscopy and dense WDM systems applications.

- [1] D. A. Smith, J. E. Baran, K. W. Cheung and J. J. Johnson, *Appl. Phys. Lett.* **56**, 209 (1990).
- [2] M. M. Choy, K. W. Cheung, D. A. Smith and J. E. Baran, *Photonics Technol. Lett.* **1**, 171 (1989).
- [3] D. A. Smith and J. J. Johnson, *IEEE Trans. Ultrason. Ferroelectr. and Freq. Control* (1992).
- [4] J. Frangen *et al.*, *Electron. Lett.* **25**, 1583 (1989).

Low-Sidelobe Integrated Acousto-optic Tunable Filter Using Focused Surface Acoustic Waves

A. Kar-Roy and C. S. Tsai

Department of Electrical and Computer Engineering
and Institute for Surface and Interface Science
University of California, Irvine, CA 92717.
Tel : (714) 856-5144; Fax : (714) 856-4152

Summary

Integrated acousto-optic tunable filters (AOTFs) have been shown to have potential applications in optical wavelength-division-multiplexed systems.¹ The single-stage integrated AOTFs reported previously² all use uniform coupling between the surface acoustic waves (SAWs) and guided-optical waves throughout the interaction length, resulting in best filter sidelobe levels of up to -9dB. It was recently suggested³ that the replacement of uniform-coupling with weighted-coupling would result in significant reduction of the sidelobe levels of the filter. In the weighted-coupling schemes, the coupling constant, κ , of the collinear AO interaction for mode conversion varies along the interaction length. Higher values of κ in the middle region of the interaction length with appropriate tapering of κ values in its end regions would result in significantly lower sidelobe levels.

In this paper, we report on a new weighted-coupling scheme for integrated AOTFs at the optical

wavelength of $1.31\mu\text{m}$ using focused SAWs produced by a compensated curved interdigital transducer (CIDT)⁴ on a Y-X LiNbO_3 substrate (see Fig. 1). An array of three single-mode optical channel waveguides, each $7\mu\text{m}$ in width, was first formed by titanium indiffusion. Subsequently, a compensated CIDT with a center frequency of 214MHz, a bandwidth of 32MHz, and an angular aperture (α) of 10.3-degree was fabricated. The interaction length of 6mm was delineated by using electric black tapes for SAW absorption. The lateral confinement of the SAW via focusing at the middle region of the interaction length results in power-efficient integrated AOTFs. The CIDT was designed with the intrinsic acoustic anisotropy taken into account. The on-axis intensity profile of the SAW generated can be determined by application of the Huygen's principle.⁴ It can be shown that the weighting of κ at any axial distance is directly proportional to the on-axis SAW intensity at that corresponding location. The weighted-coupled filter characteristics,³ obtained from the on-axis acoustic intensity profile referred to above, are plotted in Fig. 2. Fig. 2 also shows that the tunable range of the resulting integrated AOTF can exceed 300nm with only slight variations in sidelobe levels and filter bandwidths.

In the experiment, light source from a laser diode at a fixed wavelength of $1.31\mu\text{m}$ was used. Peak mode conversion between TM and TE modes was observed at the designed acoustic frequency of 214MHz. Fig. 3 shows the filter characteristics obtained by sweeping the acoustic frequency at RF drive power of 100mW, indicating an acoustic bandwidth (Δf) of 0.65MHz. The optical bandwidth ($\Delta\lambda$), obtained from the small signal relation $\Delta\lambda/\lambda = \Delta f/f$, was determined to be 4.0nm, in good agreement with the theoretical bandwidth for the interaction length of 6mm. Sidelobe levels of -15.1 to -17.6dB

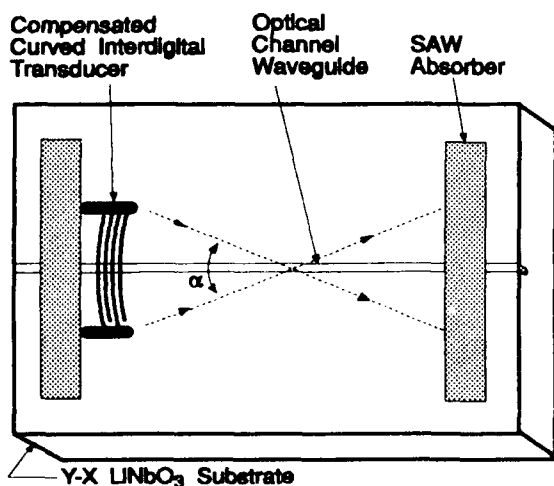


Fig. 1 : Schematic Of The Curved IDT Weighted-Coupled Integrated Acousto-optic Tunable Filter.

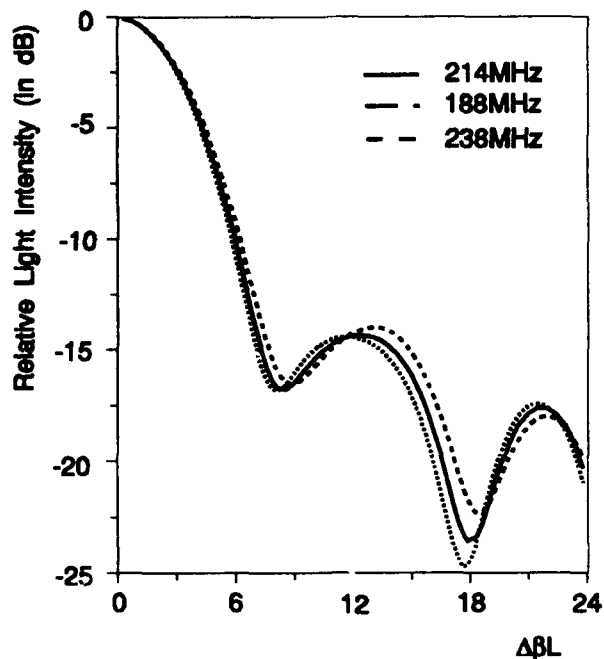


Fig. 2 : Weighted-Coupled Integrated AOTF Response Obtained With The CIDT On-Axis Acoustic Power Profile of Fig. 2 ($\Delta\beta$ is The Phase Mismatch). The Two Dashed Curves Are Responses For Acoustic Frequencies Corresponding To A Wavelength Tunability of 300nm.

were measured for the three optical channel waveguides. These measured sidelobe levels were in reasonable agreement with the theoretical estimate of -14.3dB. Cascading of two such filter stages should result in optical bandwidth reduction by a factor of 29% and sidelobe levels lower than -28dB. Peak mode-conversion efficiency of 45% for 1W of pulsed RF power was measured. This high power requirement was largely due to the low conversion efficiency (-16dB) of the transducer. Improved power efficiency and narrower optical bandwidth of the integrated AOTFs can be achieved by utilizing the CIDT of higher conversion efficiency and appropriate aperture and longer interaction length, respectively.

In conclusion, we have realized a weighted-coupled integrated AOTF at the optical wavelength of $1.31\mu\text{m}$ using a compensated CIDT that has provided the lowest sidelobe levels reported yet so far in any single-stage integrated AOTF. Further details of the weighted-coupling scheme, the design and fabrication of the resulting integrated AOTF, measured device results, and comparison to theoretical predictions will be presented.

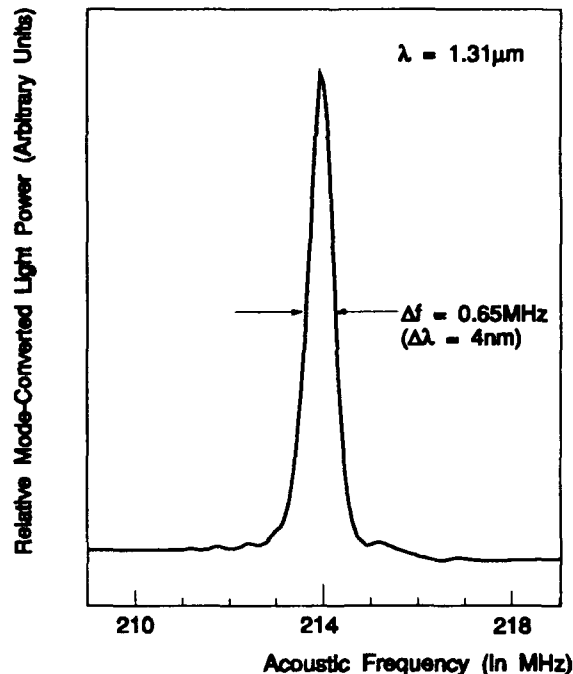


Fig. 3 : Acoustic Frequency Response Of The Weighted - Coupled Integrated AOTF Measured At Fixed Optical Wavelength of 1.31nm.

REFERENCES

1. D. A. Smith, J. E. Baran, J. J. Johnson and K. W. Cheung, *IEEE J. Sel. Areas Commun.*, vol. 8, 1151 (1990).
2. Y. Ohmachi and J. Noda, *IEEE J. Quantum Electron.*, vol. QE-16, 964 (1980); B. Kim and C. S. Tsai, *IEEE J. Quantum Electron.*, vol. QE-15, 642 (1979); L. N. Binh and J. Livingstone, *IEEE J. Quantum Electron.*, vol. QE-16, 964 (1980); B. L. Heffner, D. A. Smith, J. E. Baran, A. Yi-Yan, and K. W. Cheung, *Electron. Lett.*, vol. 24, 1562 (1988); J. Frangen, H. Herrman, R. Ricken, H. Seibert, W. Sohler and E. Strake, *Electron. Lett.*, vol. 25, 1583 (1989).
3. Y. Yamamoto, C. S. Tsai and K. Esteghamat, *Proc. Ultrasonics Symposium* (IEEE, New York, 1990), pp. 605.
4. J. B. Green, G. S. Kino, and B. T. Khuri-Yakub, *Proc. Ultrasonics Symposium* (IEEE, New York, 1980), pp. 69.

Integrated, TE- and TM-Pass, Acoustically Tunable, Double-Stage Wavelength Filters with Combined Optical/Acoustical Waveguides

H. HERRMANN, P. MÜLLER-REICH, V. REIMANN,
R. RICKEN, H. SEIBERT, AND W. SOHLER

Angewandte Physik, Universität-GH Paderborn,
Postfach 1621, W-4790 Paderborn, Germany

Introduction

Integrated optical, acoustically tunable wavelength filters are attractive due to their narrow-band filter characteristics, large tuning range, low drive power and simultaneous filtering capability. Such wavelength filters can be realized by combining acousto-optical mode converters with polarizers. In the mode converter a surface acoustic wave (SAW) with an appropriately chosen frequency yields a polarization conversion of a guided optical wave of specific wavelength to allow passing the subsequent polarizer. To improve the efficiency of the mode converter, acoustical strip waveguides can be used. We have demonstrated such an integrated optical filter with a tuning range of more than 100 nm and a filter bandwidth of less than 3 nm [1].

However, the single-stage structure has some drawbacks because of the high sidelobes of the filter characteristics and the frequency shift imposed on the filtered wave. Therefore, a double-stage configuration has been proposed [2]. It consists of two cascaded acousto-optical filters with an intermediate polarizer and complementary polarizers at the input and output as shown in Fig. 1. The filter characteristics of such a device is just the squared response of a single-stage filter. This yields a narrowing of the filter characteristics, a strong suppression of sidelobes and no net frequency shift. Double-stage acousto-optical filters have already been realized [3,4]. However, the demonstrated devices operated with unguided SAW's separately excited

with large aperture transducers in the two converters. In this contribution we present double-stage wavelength filters with acoustical guides. Moreover, we have investigated two different types as sketched in Fig.1. They differ by the arrangement of the polarizers. Filter performance is obtained via TE-TM-TE conversion (TE-pass filter) or TM-TE-TM conversion (TM-pass filter), respectively.

Mode converter and polarizers

The wavelength filters have been fabricated in X-cut, Y-propagating LiNbO₃. Monomode ($\lambda \approx 1.5 \mu\text{m}$), $7 \mu\text{m}$ wide optical waveguides were formed by Ti-indiffusion. They are embedded in $100 \mu\text{m}$ wide, monomode ($f_{ac} \approx 170 \text{ MHz}$) acoustical waveguides fabricated by Ti-indiffusion of the "claddings". Details are given in [1].

As *TE-pass polarizers* $20 \mu\text{m}$ wide, 1 mm long layer sandwiches of $25 \text{ nm Y}_2\text{O}_3$ and 50 nm Al were vacuum evaporated on the waveguide surface. In such a structure strongly damped surface plasma waves are excited by a TM-mode, whereas a TE-mode is only little affected [5]. We achieved a TM-extinction ratio of more than 20 dB with a TE excess loss of 0.3 dB.

As *TM-pass polarizers* proton exchanged 1 mm long regions, adjacent to the optical waveguide on both sides, have been prepared. As the extraordinary index of refraction is increased by the proton exchange, a TE-mode is no longer guided. On the other hand, a TM-mode can pass the structure with small additional losses [6]. We learned, that the outer boundaries of the proton exchanged regions should not be parallel to the waveguide axis to avoid total reflection of an outcoupled TE-wave with a subsequent coupling back into the waveguide. Using a structure as depicted in Fig. 2 we obtained TM-pass polarizers with more than 30 dB TE-extinction ratio and an excess loss of only 0.4 dB for the TM-mode. The proton exchange was performed at 250°C in

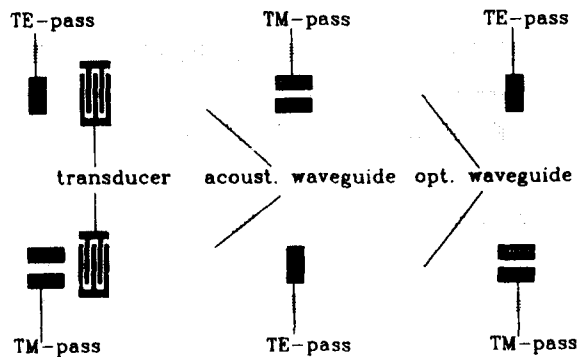


Fig. 1: Basic structure of TE-pass (above) and TM-pass (below) double-stage filters.

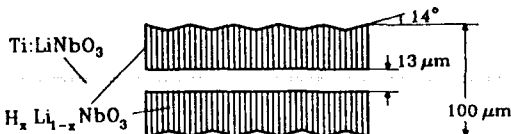


Fig. 2: Design of the TM-pass polarizer.

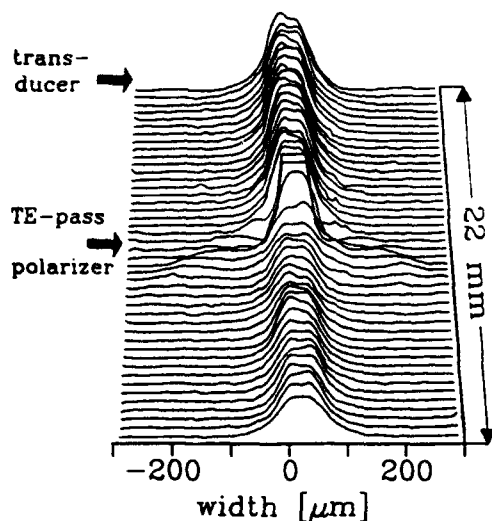


Fig. 3: Intensity profile of the SAW in the acoustical waveguide.

diluted (1% lithium benzoate) benzoic acid for 15.5 h followed by thermal annealing for 4 h at 330 °C.

Using the laser probing technique [7] the intensity distribution of the SAW propagating in the converters has been measured. The example, presented in Fig. 3, reveals monomode guiding of the acoustical wave with propagation losses of less than 1 dB/cm. Moreover, it can be seen, that the TE-pass polarizer induces only a weak distortion for the SAW resulting in a loss of only about 0.4 dB. Similar measurements for the TM-pass polarizer gave an excess loss of 2.5 dB. We are confident, that it can be reduced by using narrower proton exchanged regions.

Filter characteristics

Both types of filters have been investigated using a $\lambda = 1.554 \mu\text{m}$ DFB-laser as optical source. The optical power transmitted by the filter was monitored as function of the SAW-frequency.

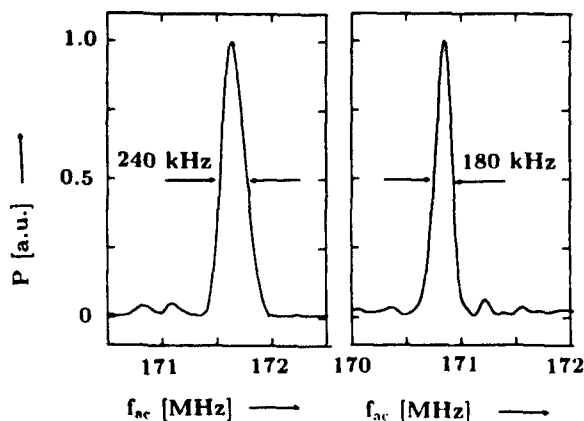


Fig. 4: Measured filter characteristics of TE-pass (left) and TM-pass (right) double-stage wavelength filters.

The 18 mm long TE-pass device was slightly modified in comparison with the original concept shown in Fig. 1. It required a second transducer behind the TM-pass polarizer; otherwise the SAW in the second section was to weak for a complete polarization conversion. Although the filter characteristics of the two sections considerably differed from ideal responses (due to inhomogeneities of the optical waveguide) a reasonable overall (double-stage) characteristics was obtained (see Fig. 4, left). It has a halfwidth of 240 kHz, corresponding to a wavelength width of 2 nm, and only small residual sidelobes.

The TM-pass device was built according to the concept of Fig. 1 without any modifications. It had two sections of 10.6 mm and 12.2 mm length with good single-stage filter characteristics. The SAW was excited by a single transducer tilted at about 5° with respect to the waveguide axis [8]. In this way, the acoustical drive power was minimized leading to optimum double-stage filter performance with 70 mW electrical RF-drive power. Fig. 4 presents on the right the double-stage filter characteristics with only weak sidelobes and a halfwidth of 180 kHz, corresponding to 1.5 nm. The overall insertion loss (without coupling losses) is about 3 dB.

Both filters have a tuning range of 60 nm, determined by the bandwidth of the unidirectional transducer of 8 MHz; it can be extended by an appropriate transducer design.

Conclusions

We have fabricated and investigated the first integrated TE- and TM-pass double-stage acoustooptical wavelength filters with a doubly confined optical/acoustical single-mode waveguide structure. They can be operated as tunable ($\approx 60 \text{ nm}$), narrow band ($< 2 \text{ nm}$) filters without frequency shift. By combining both types of filters with polarization splitters a polarization independent device can be fabricated using polarization diversity.

REFERENCES

- [1] J. Frangen et.al., *Electron. Lett.* **25**, 1583 (1989)
- [2] G.D. Boyd, F. Heismann, *J. Lightwave Technol.* **7**, 625 (1989)
- [3] D.A. Smith et.al., *Electron. Lett.* **25**, 399 (1989)
- [4] D.A. Smith et.al., *Techn. Digest Integrated Phot. Research*, Opt. Soc. Am. **5**, 164 (1990)
- [5] G. Stock, *Electron. Lett.* **24**, 899 (1988)
- [6] M. Papuchon, S. Vatoux, *Electron. Lett.* **19**, 612 (1983)
- [7] E.G.H. Lean, C.G. Powell, *Proc. IEEE* **58**, 1939 (1970)
- [8] D.A. Smith, J.J. Johnson, *IEEE Photon. Technol. Lett.* **3**, 923 (1991)

Acoustooptical Coupling of Guided to Substrate Modes in Planar Proton-Exchanged LiNbO₃-Waveguides

U. RUST AND E. STRAKE

Angewandte Physik, Universität-GH Paderborn, Postfach 1621,
W-4790 Paderborn, Fed. Rep. Germany

Introduction

The acoustically induced conversion of guided to substrate modes in optical waveguides has several attractive applications in integrated optics. One of them is an extremely simple RF-spectrum analyzer as presented in [1]. The principle setup is shown in Fig. 1.

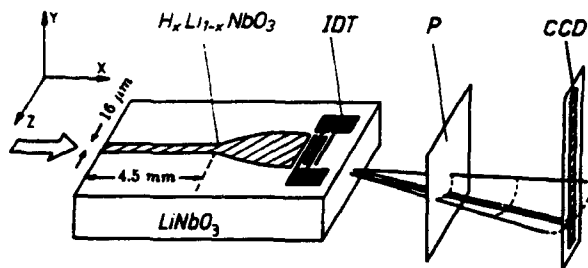


Fig. 1: Acoustooptical RF-spectrum analyzer [1]. IDT: interdigital transducer electrodes, P: polarizer, CCD: detector array. The coordinate system shows the orientation of the crystal's principle axes.

The generated radiation field leaves the waveguiding region and propagates into the substrate under a well defined angle, which is determined by the phase matching condition. This deflection angle can be controlled by the acoustical frequency. As guided and radiation modes may be chosen to have orthogonal polarizations, the converted light can easily be detected using a polarizer and an array of photodiodes.

We present a method that, for the first time, allows a rigorous numerical simulation of the device under the assumption that both, optical and acoustical waveguides are planar.

SAW and optical mode analysis

First of all the wave equation for surface acoustic waves in a layered, anisotropic, piezoelectric crystal is solved using a method outlined in [2]. Thus, the effect of the proton-exchanged waveguide on the properties of the SAW is taken into account. Due to the elasto-optic and electro-optic effects the SAW produces a modulation of the dielectric tensor in the form of a traveling wave.

Fig. 2 shows the calculated depth dependence of the modulation amplitude of the dielectric tensor element which is mainly responsible for the TE-TM mode conversion in a medium consisting of a H_xLi_{1-x}NbO₃ layer on LiNbO₃. It was assumed, that the elements of the piezoelectric and electrooptic tensors vanish in the proton-exchanged waveguide, as its structure tends to become cubic as reported in [3]. For comparison, the depth dependence of the relevant offdiagonal element of LiNbO₃ is presented as well.

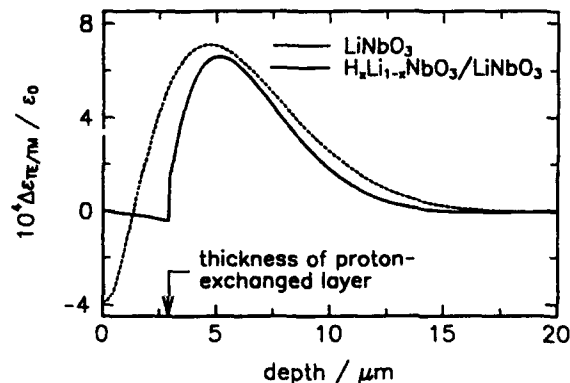


Fig. 2: Modulation amplitude of the offdiagonal dielectric tensor element $\Delta\epsilon_{TE/TM}$ which is mainly responsible for the conversion of guided TE modes to TM radiation modes in LiNbO₃ and H_xLi_{1-x}NbO₃ on LiNbO₃. The SAW power is taken as $P_{ac} = 100$ W/m. The values for the material parameters are taken from [4,5].

The optical field distributions of the interacting modes are calculated using a generalized version of a method reported in [6]. This technique works for guided and radiation modes of both polarizations in planar waveguides with arbitrary index profiles. It is not necessary to make any approximations.

Acoustooptical interaction

Using coupled mode theory [7,8], the longitudinal development of the radiation field is determined. Both, depletion of the guided mode and reconversion from radiation to the guided mode are taken into account.

The strength of the coupling process depends on the magnitude of the coupling factor, which is mainly the square of the overlap integral of the two interacting modes and the distribution of the acoustically induced modulation of the dielectric tensor. The overlap is small for low order guided modes, strongly localized within the proton-exchanged region; here the dielectric disturbance is practically zero. Only for higher order guided modes extending deeper into the substrate an efficient conversion process can be expected. This is demonstrated in Fig. 3 showing the coupling factor as a function of the effective index of the TM radiation mode for different guided TE modes in an annealed proton-exchanged waveguide. To get efficient coupling the acoustic frequency has to be chosen in such a way that a phase matched interaction with large coupling factor is induced:

$$\beta_{TE} \pm K_{ac} = \beta_{TM}$$

with β_{TE} , K_{ac} , β_{TM} being the wavevectors of the guided TE mode, the SAW, and the TM polarized radiation mode, respectively.

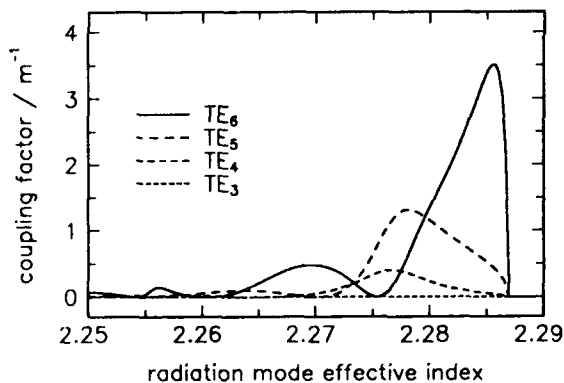


Fig. 3: Coupling factors for the conversion of guided TE modes to TM substrate modes in an annealed $H_xLi_{1-x}NbO_3$ waveguide as function of the effective index of the substrate modes. The SAW power is taken as $P_{ac} = 100 \text{ W/m}$.

The solution of the coupled mode equations yields the total radiation field at the waveguide end. This near field can be transformed into the desired far field by a simple Fourier transform, according to Fraunhofer diffraction. Additionally, the refraction at the rear sample end must be taken into account. As an example, the intensity distribution of the radiation far field obtained by acousto-optical coupling from

the guided TE_6 mode is shown in Fig. 4 for different acoustic frequencies. A good qualitative agreement with experimental results is observed [9]. In particular, a resolution of 0.4 MHz of the RF-spectrum analyzer has been evaluated in good accordance with the experimental figure of 0.5 MHz [1].

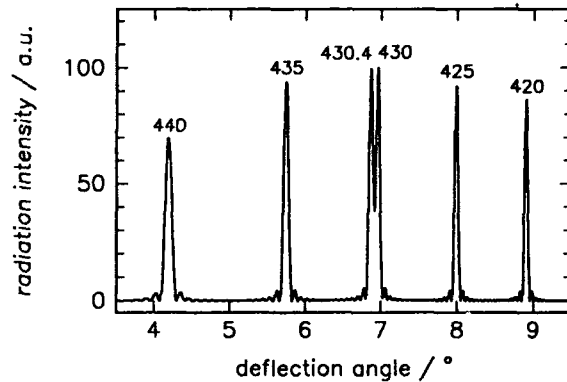


Fig. 4: Calculated far field intensity distribution of the radiation field converted from the TE_6 mode for different acoustic frequencies. The frequencies are given in MHz.

Conclusions

The rigorous numerical analysis of the acousto-optical coupling of guided to substrate modes, presented above, allows to study the influence of all parameters of the RF-spectrum analyzer in detail. This will help to further optimize the integrated acousto-optical device.

References

- [1] V. Hinkov, U. Nolte, W. Sohler, *Techn. Digest Integrated and Guided-Wave Optics*, Opt. Soc. Am., 4, 138 (1989)
- [2] G. W. Farnell, *IEEE Trans. Sonics Ultrason.* SU-17, 229 (1970)
- [3] C. E. Rice, J. L. Jackel, *Mat. Res. Bull.* 19, 591 (1984)
- [4] A. W. Warner, M. Onoe, G. A. Coquin, *J. Opt. Soc. Am.* 42, 1223 (1973)
- [5] E. M. Biebl, P. H. Russer, K. Anemogiannis, *Proc. IEEE Ultrasonics Symposium*, 281 (1989)
- [6] E. F. Kuester, D. C. Chang, *IEEE Trans. Microwave Theory Tech.* MTT-23, 98 (1975)
- [7] D. Marcuse, *Theory of Dielectric Optical Waveguides*, Academic Press (1974)
- [8] E. Strake, PhD-Thesis, University of Paderborn (1991)
- [9] H. Hu, H. Lausen, U. Rust, W. Sohler, E. Strake, to be published

Strictly Nonblocking 8x8 Integrated Acoustooptic Space-Division Switch Array on LiNbO₃

A. Kar-Roy and C. S. Tsai

Department of Electrical and Computer Engineering
and Institute for Surface and Interface Science
University of California, Irvine, CA 92717
Tel : (714) 856-5144; Fax : (714) 856-4152

Summary

A number of architectures for integrated optic (IO) space-division switching,¹ using guided-wave electro-optic (EO) switches² have been implemented in recent years. Unlike the guided-wave EO devices, guided-wave acoustooptic (AO) devices³ can facilitate a multiplicity of AO Bragg diffractions in the same interaction region of a planar waveguide by controlling the directivity of multiple input light beams, and the directivity and the carrier frequency of the surface acoustic waves (SAWs). Under such circumstances, proper design enables AO Bragg diffraction to take place between a designated pair of a light beam and a SAW without causing significant crosstalk to other similarly interacting pairs. In consummating the above idea, asymmetric⁴ and symmetric⁵ 4x4 nonblocking guided-wave AO space switches have been constructed recently. As shown in Fig. 1, the 8x8 AO space switch array to be reported here has been fabricated on a Y-cut LiNbO₃ substrate, 1.0x10.0x37.0mm³ in size, and consists of a titanium indiffused channel-planar-channel composite waveguide, a pair of titanium-indiffused proton-exchanged (TIPE)⁶ planar waveguide lenses, and a pair of four-element tilted SAW interdigital transducers (IDTs).⁷ Potentially, as the size of the switch array increases, these AO switch arrays incur considerably smaller increments in waveguide substrate size and number of on-chip switching elements as well as lower performance degradations such as differential crosstalk and differential insertion loss¹ than in the EO switch arrays.

The 8x8 AO space switch array, as shown in Fig. 1, is a significantly improved extension of the 4x4 symmetric switch array presented previously.⁵ In brief, light beam coupled into an input channel waveguide expands due to diffraction at the first input channel-planar waveguide interface and is collimated by a newly devised hybrid TIPE beam expanding-collimating lens.⁸ Appropriate displacement of the input channel waveguide from the lens axis tilts the collimated light beam w.r.t. the lens axis, such that efficient Bragg diffraction from SAWs generated by a single appropriately oriented IDT is facilitated. The

propagation direction of the Bragg-diffracted light is precisely switched into the apertures of the output channel waveguides situated in the back focal plane of a second TIPE lens by feeding in selected carrier frequencies for the IDT involved. The above mentioned example of 1xN space switch can be extended to an MxN switch array by appropriate off-axis displacement of M input channel waveguides, and assigning appropriate center-carrier frequency and propagation direction to SAWs of corresponding IDTs. Furthermore, the symmetric architecture employed in Fig. 1 also enables the allocation of identical switching bandwidths to the input channel-IDT pairs on either side of the lens axis, thus reducing the total carrier frequency bandwidth requirement by a factor of two. This architecture supports strictly non-blocking point-to-point switching, multicast switching (by multiplexing all the carrier frequencies to the corresponding IDT at the same time) and multipoint-to-point switching. These AO space switch arrays have also been shown to be capable of implementing optical computations such as highly-parallel matrix-vector and matrix-matrix multiplications.⁹

The four IDTs in the symmetric 8x8 AO space switch array had design center frequencies of 198, 300, 405 and 512MHz, and AO bandwidths of 90MHz each. Fig. 2 shows the switched light beam spots and their corresponding beam profiles obtained when light beam at the wavelength of 633nm was edge-coupled into the input channel waveguide #3 and switched to the eight output channel waveguides at frequency increments of 13.5MHz and an average RF drive power of 100mW. Average diffraction efficiency of 20% was measured at 100mW cw RF drive power. Other measured performances include throughput loss of -15 ± 2 dB at 50% diffraction efficiency, average crosstalk of -12.2 dB (primarily due to larger than expected focused spot size from the second TIPE lens) and a reconfiguration time of 0.4 μ sec. Details of the working principle, design, fabrication, and measured performances will be presented.

ME5-2

REFERENCES

1. See, for examples, R. A. Spanke, *IEEE Commun.*, 25, 42 (1987); H. Scott Hinton, *IEEE Commun.*, 28, 71 (1990).
2. R. C. Alferness, *IEEE J. Select. Areas Commun.*, 6, 1117 (1988); A. Selvarajan and J. E. Midwinter, *Optical and Quantum Electronics*, 21, 1 (1989).
3. See, for example, the many references cited in C. S. Tsai, *Guided-Wave Acousto-Optics : Interactions, Devices and Applications*, Springer Verlag, New York, 1990.
4. C. S. Tsai, and P. Le, to appear in *Appl. Phys. Lett.* (1992)
5. A. Kar-Roy and C. S. Tsai, in *Technical Digest of Integrated Photonics Research* (Optical Society of America, Washington, D. C., 1990), WG2.
6. D. Y. Zang and C. S. Tsai, *Appl. Phys. Lett.*, 46, 703 (1985).
7. C. S. Tsai, *IEEE Trans. Circuits and Syst.*, CAS-26, 1072 (1979)
8. A. Kar-Roy and C. S. Tsai, (To be published).
9. A. Kar-Roy and C. S. Tsai, to appear in *Appl. Phys. Lett.* (1991)

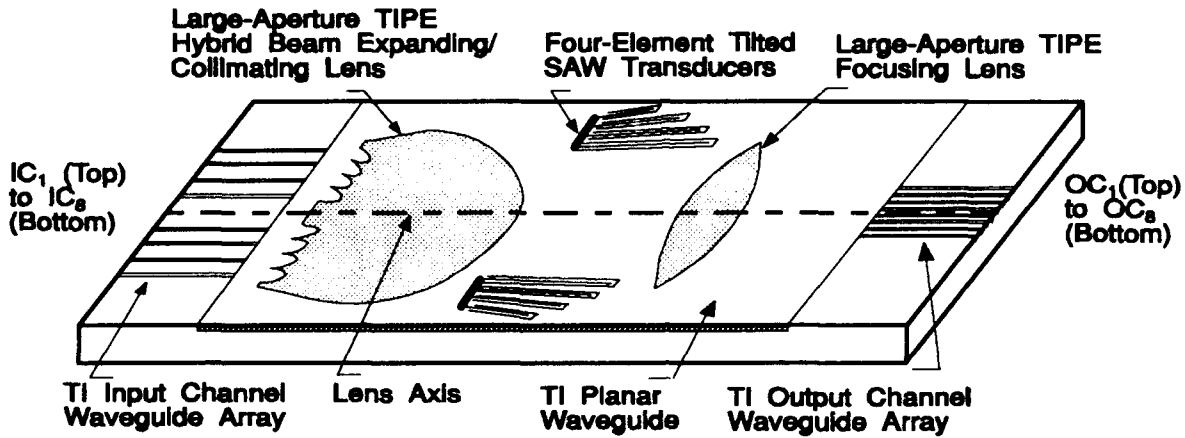


Fig. 1 : Schematic Of 8x8 Symmetric Nonblocking Integrated Acoustooptic Space Switch Module Using Bragg Diffractions In A LiNbO_3 Channel-Planar-Channel Composite Waveguide.

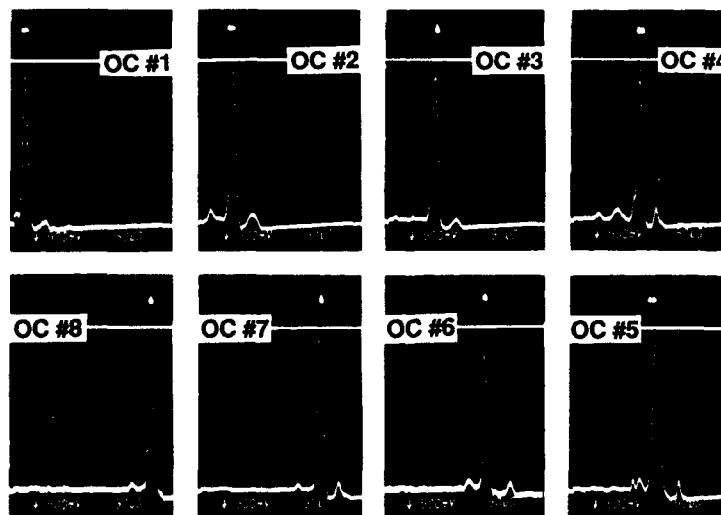


Fig. 2 : Typical Output Beam Spots And Corresponding Beam Profiles Obtained When A Light Beam Coupled Into Input Channel Waveguide #3 Was Switched To The Various Output Channel (OC) Waveguides (Scale = $30\mu\text{m}$ Per Major Division)

Integrated Magneto-optic Bragg Cell Module in Tapered YIG-GGG Waveguide

C.L. Wang and C.S. Tsai

Department of Electrical and Computer Engineering
and

Institute for Surface and Interface Science
University of California
Irvine, CA 92717

and T. Ryuo

Shin-Etsu Chemical Co.,
Isobe Annaka Gunma, Japan
(714)856-5144 (Tel) (714) 856-4152 (FAX)

Summary

Magnetostatic waves-based guided-wave magneto-optic (MO) Bragg cells in yttrium iron garnet-gadolinium gallium garnet (YIG-GGG) waveguide possess the unique capabilities of electronically tunable carrier frequency beyond X-band microwave frequencies and GHz bandwidth, and are therefore inherently capable of direct RF signal processing at the carrier frequencies from 0.5 to 26.5 GHz[1]. Other capabilities include multiport light beam scanning and switching at a speed one- to three-order of magnitude higher than that of acousto-optic (AO) Bragg cells[2]. Obviously, it is desirable to incorporate lenses and lens arrays in the same YIG-GGG waveguide substrate to realize integrated MO Bragg cell modules. Negative-index change waveguide lenses which combine analog Fresnel and chirp gratings were fabricated recently in LiNbO_3 , GaAs and YIG-GGG waveguide substrates using ion-milling technique[3]. It has been concluded that the thinner the waveguide, the smaller the required milled-depth in the gratings in order to produce desired index changes, and thus ensure high lens throughput. It has also been shown most recently that the MO Bragg bandwidth is approximately proportional to the thickness of the YIG waveguide[4]. Therefore, there exists contradictory requirements on the waveguide thickness for achieving both wideband MO interaction and high lens throughput.

In this paper, we report a tapered YIG-GGG waveguide structure to accommodate simultaneously the requirements for achieving both large MO Bragg bandwidth and high lens throughput, and thus enables the realization of high-performance integrated MO Bragg cell modules. As shown in the middle region of Fig.1, the initial thickness of the YIG waveguide layer was 6.550 μm . The two end regions of the tapered waveguide was ion-milled down to 2.735 μm in five steps in order to produce a gradual transition, and thus ensure a high transmission for the light beam. Newly devised curved hybrid lenses[5] with 4.0 mm focal length and 0.8 mm aperture were then fabricated onto the two end regions using ion-milling technique(Fig.1). Using this tapered waveguide structure, a milled-depth of only 0.47 μm was required for the gratings in the 2.735 μm waveguide in order to produce the required index change of 0.004, and still preserves the throughput efficiency to greater than 60 %. In contrast, a uniform waveguide structure of 6.550 μm in thickness would require a milled-depth as large as 2.86 μm for the gratings in order to produce the same required index change of 0.004 for the same curved hybrid lenses. The resulting throughput efficiency of the lens would be as low as 24 %. The measured -3 dB focal spot size for a single lens was 5.62 μm with a -12.3 dB sidelobe (Fig.2) as compared to the diffraction-limited spot size of 2.50 μm . For a pair of

identical lenses the measured -3 dB focal spot size was $10.27 \mu\text{m}$. The angular field of view was measured to be 2° on each side of the lens axis. The lens was practically coma free up to this angular field of view. The optical throughput efficiencies for the single lens and the lens pair were measured to be 69 and 49.4 %, respectively. The measured static mode conversion (TE to TM and vice versa) induced by the lenses and the tapered waveguide structure was as low as -37.4 dB.

High-performance MO Bragg cells with tunable center frequencies and large bandwidth for the carrier frequencies of 2.0 to 12.0 GHz were constructed recently[1]. The curved hybrid lens pair described above has also been incorporated with such high-performance MO Bragg cell in the tapered waveguide structure $6.0 \times 16.0 \text{ mm}^2$ in size to realize integrated optic module as shown in Fig.1. Placement of the MO Bragg cell in the middle region and the lens pair in the two end regions facilitated simultaneous realization of high-performance MO Bragg cell and high-performance lens pair. The middle section of the waveguide was set at 6.0 mm in order to enable usage of Bragg interaction length up to 5.0 mm. By changing the DC magnetic field from 1800 to 4900 Oe, the carrier frequency of the integrated MO Bragg cell module can be tuned from 2.0 to 12.0 GHz. A MO bandwidth of 350 MHz can also be obtained. Other modules that utilize the tapered waveguide structure but with the thickness of the middle region reduced to $3.25 \mu\text{m}$ have provided a MO bandwidth greater than 500 MHz.

In summary, guided-wave magneto-optic Bragg cell has been integrated with newly devised curved hybrid lenses in a tapered YIG-GGG waveguide structure to realize high-performance integrated optic device modules. Applications of such device modules to RF signal processing at X-band and high-speed optical scanning and switching have been demonstrated.

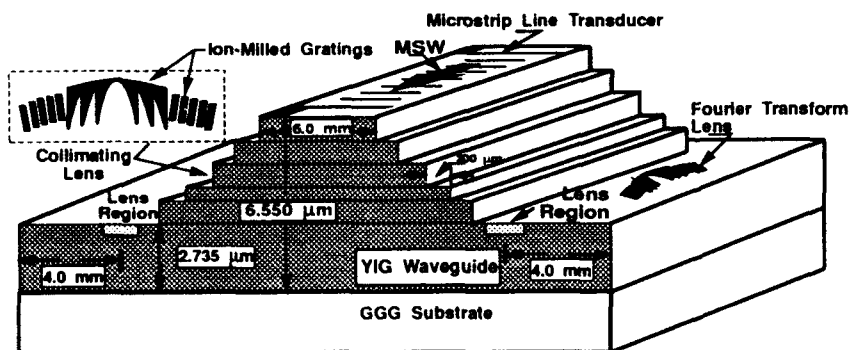


Fig.1: Integrated Magneto-optic Bragg Cell Module Using Tapered YIG-GGG Waveguide Structure

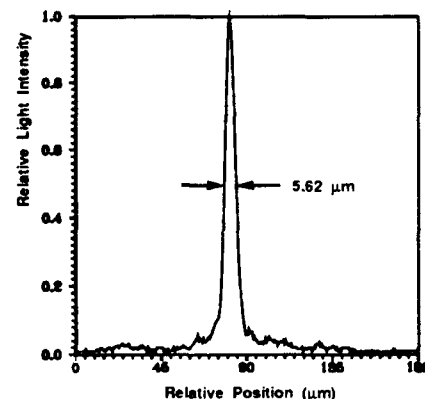


Fig.2: Measured Focal Spot Profile of Ion-Milled Curved Hybrid Lens in Tapered YIG-GGG Waveguide

References

- [1] C.S. Tsai and D. Young, *IEEE Trans. on MTT.*, **38**, 560-571 (1990).
- [2] See the many references cited in C.S. Tsai, *Guided-Wave Acousto-optic Interaction, Devices, and Applications*, New York: Springer-Verlag, 1990.
- [3] (a) T.Q. Vu, J.A. Norris, and C.S. Tsai, *Opt. Lett.*, **13**, 1141-1143 (1988);
 (b) T.Q. Vu, J.A. Norris, and C.S. Tsai, *Appl. Phys. Lett.*, **54**, 1098-1100 (1989);
 (c) T.Q. Vu, C.S. Tsai, D. Young, and C.L. Wang, *Appl. Phys. Lett.*, **55**, 2271-2273 (1989).
- [4] Y. Pu and C.S. Tsai, "RF Magnetization of Magnetostatic Forward Volume Wave in a YIG-GGG Layered Structure with Application to Design of High-Performance Guided-wave Magneto-optic Bragg Cell," (To appear in *International J. of High Speed Electronics*).
- [5] C.L. Wang and C.S. Tsai, "High-Performance Curved Hybrid Lenses in YIG-GGG Waveguide", (To be published).

Monday, April 13, 1992

Spatial Solitons and Planar Waveguide Phenomena

MF 1:30 pm–3:30 pm
Poydras Room

Mohammed N. Islam, *Presider*
AT&T Bell Laboratories

MF1-1

Spatial Solitons in a Self-Focusing Semiconductor Gain Medium

G. Khitrova, H.M. Gibbs, Y. Kawamura, H. Iwamura and T. Ikegami
NTT Optoelectronics Laboratories, 3-1 Morinosato-Wakamiya,
Atsugi, Kanagawa 243-01, Japan

The pulse broadening by group velocity dispersion can be balanced by the narrowing effect of self-phase modulation to form temporal solitons.¹ The identical nonlinear Schrödinger equation describes the one-transverse-dimension balancing of diffraction and Kerr-medium nonlinear refraction. Some evidence for spatial solitons has been published for planar waveguides of CS₂ and glass, both in Kerr (n₂) media.^{2,3} Here we report soliton formation in a semiconductor gain medium which is amplifying rather than lossy, is accumulative rather than instantaneous, and is near resonance instead of far from resonance.

The self-focusing semiconductor gain medium is obtained by current injection into the following planar waveguide structure. A crystal was grown by gas-source molecular beam epitaxy on an n-doped InP substrate: 1.0- μm -thick n-doped InP buffer; 0.6- μm -thick guiding layer consisting of n-doped In_{0.78}Ga_{0.22}As_{0.55}P_{0.45} and six 42- Å Ga_{0.47}In_{0.53}As/30- Å Al_{0.48}In_{0.52}As quantum wells in the center, p-doped In_{0.78}Ga_{0.22}As_{0.55}P_{0.45}; 2 μm of p-doped InP; and 0.1 μm of p-doped Ga_{0.47}In_{0.53}As contact layer. Photolithography and chemical etching were used to leave 80- μm -wide strips. This structure lases at $\approx 1.31 \mu\text{m}$ with a threshold current of 1.2 A for a length of 400 μm .

The laser source consisted of $\approx 2 \mu\text{s}$ pulses Q-switched at a 1 kHz rate from a cw Nd:YAG laser operating at 1.319 μm . The unexcited waveguide is almost completely opaque to this wavelength, so that only the peak portion of the 2- μs laser pulse is detected, by pulsing the injection current with a 0.1 to 1 μs square-top synchronized pulse.

Demonstration of a fundamental soliton is done by choosing a small enough input waist (5 μm) so that diffraction expands the low-power profile by almost 2.5 times during the 400- μm length. At high power the self-focusing nonlinear refraction largely overcomes the diffraction resulting in a 6- μm output waist and demonstrating *a semiconductor-gain-medium approximation to the fundamental spatial soliton of a Kerr medium*.

An example of a second-order soliton is shown in Fig. 1. The side peaks disappear if the intensity or gain is reduced sufficiently. These second-order spatial solitons are quite robust. To make sure that they were affected little by the feedback of the cleaved ends, we observed essentially identical solitons in an AR coated sample.

The computations were performed using a two-transverse-dimension beam-propagation code with the plasma theory for the gain medium optical nonlinearity. They agree very well with the observed dependence of the output profiles upon intensity and gain.

In two-transverse-dimension self-focusing sodium vapor with the input symmetry broken by minutial input aberrations, a stationary spatial pattern (transverse solitary wave) is formed that bifurcates as a function of input power or detuning.⁴ We searched for bifurcations of transverse solitary waves in our gain-medium planar waveguide but found none.

In summary, we have demonstrated that a semiconductor gain medium in a planar waveguide is almost ideal for the demonstration of fundamental and second-order spatial solitons.

The Arizona portion of this research was supported by NSF LWT, AFOSR, ARO, and the OCC. Computations were performed by L. Ming on the Kirtland CRAY.

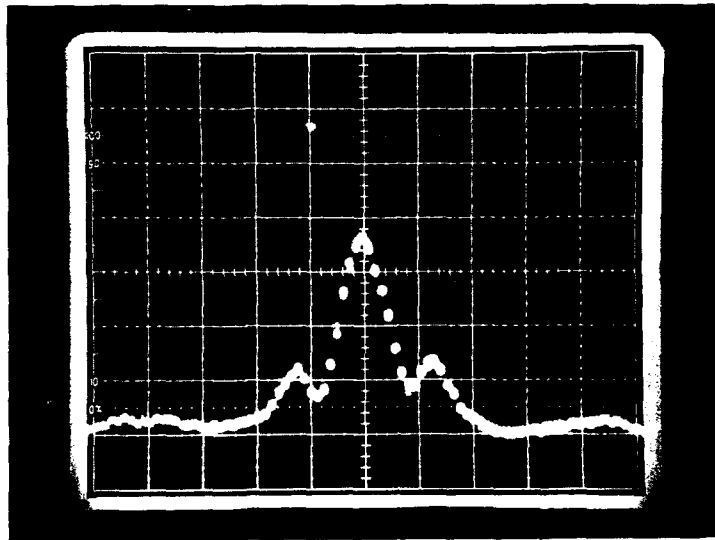


Figure 1. Second-order spatial soliton in a semiconductor gain medium. Approximately $5 \mu\text{m}/(\text{major division})$.

REFERENCES

1. A. Hasegawa and F. Tappert, *Appl. Phys. Lett.* **23**, 142 (1973) and L.F. Mollenauer, R.H. Stolen and J.P. Gordon, *Phys. Rev. Lett.* **45**, 1095 (1980).
2. S. Maneuf and F. Reynaud, *Opt. Commun.* **66**, 325 (1988). S. Maneuf, R. Desailly, and C. Froehly, *Opt. Commun.* **65**, 193 (1988).
3. J.S. Aitchison, A.M. Weiner, Y. Silberberg, M.K. Oliver, J.L. Jackel, D.E. Leaird, E.M. Vogel, and P.W.E. Smith, *Opt. Lett.* **15**, 471 (1990).
4. J.W. Grantham, H.M. Gibbs, G. Khitrova, J.F. Valley, and Xu Jiajin, *Phys. Rev. Lett.* **66**, 1422 (1991).

WAVE-GUIDES, Y-JUNCTIONS, AND OTHER STRUCTURES FORMED IN BULK MEDIA USING DARK SPATIAL SOLITONS

Barry Luther-Davies

Laser Physics Centre

Xiaoping Yang, Allan W. Snyder

Optical Sciences Centre

Australian National University

CANBERRA AUSTRALIA

All-optical devices are essential building blocks for the development of photonics as an advanced technology. In this context, there is considerable interest in spatial solitons and their interaction to provide a means for switching and guiding beams in bulk non-linear materials[1,2].

Here we consider self-guided beams of planar cross section in a bulk self-defocussing medium where the refractive index change in proportion to intensity. Such beams are also known as spatial solitons. However, only dark solitons are stable to perturbations in 3D, i.e. self-guided beams in a self-defocussing medium[3]. A dark soliton is the 2nd mode at cutoff of the profile it induces [4] whereas a bright soliton is the fundamental mode of the profile it induces[2].

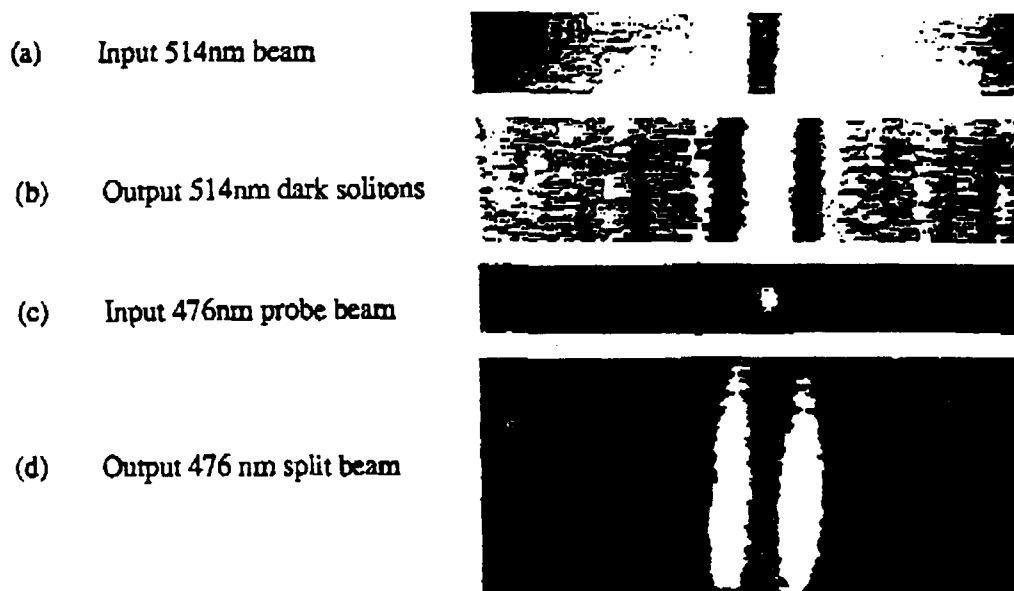
The fundamental dark soliton at wavelength λ_s induces an 'ideal' single mode, graded index profile fiber - ideal in the sense that it propagates a highly confined signal (low power) beam at wavelength λ_s , becoming multimoded for a signal with a wavelength shorter than λ_s . The crucial advantage of using dark solitons is that the induced waveguides are highly stable. Spatial solitons are here generated by a quasi-plane wave containing phase or amplitude perturbations.

The absence of a threshold power for dark soliton production, means that dark soliton waveguides can develop in a quasi-adiabatic fashion from perturbations on the input beam. For example, in appropriate conditions a beam containing a π -phase jump generates a structure akin to an adiabatically tapered waveguide which can efficiently couple a broad input beam into the narrow waveguide formed around the soliton. An amplitude discontinuity, generated by placing a narrow wire across the centre of the input beam, leads to the development of a pair of dark solitons whose structure is equivalent to that of a waveguide Y-junction. At high powers, multiple solitons and hence multiple waveguides are produced and the power in the different waveguides becomes distributed in an increasingly complex manner between them. Structures such as four-way splitters, for example, have been observed.

The formation of multiple solitons can be appreciated by a heuristic argument[5]: If the intensity of the dark soliton is increased, while holding its dimensions fixed, then the height of the induced refractive index profile is increased. This changes the induced waveguide from a single moded waveguide to a multimoded waveguide. When the intensity is increased sufficiently so that the waveguide supports the 2nd odd mode (at cutoff) then any perturbation can cause this second mode to be initially excited. The second odd mode of this induced linear structure is the one with two minima and appears like two dark self-guided beams.

The operation of a dark soliton induced waveguide Y-junction is shown in figure 1. Here a weak probe beam was generated by extracting radiation at 476.5nm from a multi-line argon laser and this beam was injected into the "dark" zone caused by blocking the centre of a 514nm soliton-forming beam at the input of a thermally defocussing non-linear medium by a 50 μ m diameter wire. The 476.5 and 514nm beams were combined using a polarizing beam splitter. Figures 1a,1b show the 514nm beam at the input and output of the non-linear medium. The intensity perturbation caused by the wire develops into a pair of diverging, 2-D dark solitons each one about 50 μ m wide. The probe beam diameter was chosen to approximately equal the wire diameter at the input since our numerical solution of the scalar version of the non-linear Schrodinger equation showed that this provided the optimum launch conditions for the dark solitons to split the probe into two output beams. The probe beam at the input and output of the non-linear medium is shown in figures 1c, and 1d respectively. Measurements have shown that in excess of 85% of the input power is transferred to the two guided output beams.

In this paper we discuss the formation and properties of structures such as these and their potential for the manipulation of light by light in bulk materials.



This figure shows the beam distributions at the input and output of a 100mm long cell containing a thermally defocussing non-linear liquid into which is launched both a 514nm soliton forming beam perturbed by a 50 μ m diameter wire, and a focussed Gaussian 476.5nm probe beam. (a): the 514nm beam at the input to the cell showing the region obscured by the 50 μ m diameter wire; (b): the 514nm beam distribution at the output of the cell where the input perturbation has split into two diverging dark solitons; (c): the probe beam distribution at the input to the cell; (d): the output probe beam pattern showing that the probe has been split into two output beams by the dark soliton induced waveguide Y-junction. The frames are 1mm wide.

References

1. R. De la Fuente, A. Barthelemy, C. Froehly, *Optics Letters* 16, 1472 (1991).
2. A.W. Snyder, D.J. Mitchell, L. Poladian, F. Ladouceur, *Optics Letters* 16, 21 (1991).
3. G.R. Allen, S.R. Skinner, D.R. Andersen, A.L. Smirl, *Optics Letters* 16, 156 (1991).
4. Y. Silberberg, personal communication.
5. A.W. Snyder, et al, "Stable black solitons of circular symmetry" submitted to *Optics Letters*.

High-Efficiency Excitation of Nonlinear Guided Waves Using Chirped and Tapered Gratings

Guifang Li

Department of Electrical and Computer Engineering
University of Wisconsin-Madison, Madison, WI 53706

Phone: (608) 262-7581; Fax: (608) 262-1267

All-optical computing and signal processing using nonlinear guided-wave devices potentially offer high speed and low energy consumption. Efficient control of light by light requires that the product of the nonlinear coefficient (of the waveguide) and the guided-wave intensity be significant. The wavenumber of a nonlinear guided wave, however, is a function of its intensity. The distributive excitation of nonlinear guided waves using a grating is a coherent process. Since the guided-wave amplitude builds up from zero, the local wavenumber of the nonlinear guided wave varies within the extent of the grating. The phase-matching condition for the coherent excitation process can only be satisfied at one location. Theoretical and experimental investigations[1,2] of the excitation of nonlinear guided waves demonstrate that the excitation efficiency decreases as the incident intensity increases for a fixed nonlinear coefficient. Therefore, even if very highly nonlinear optical materials are available, the above-mentioned product is still limited by the excitation process.

Consider the grating coupler, shown in Fig.1, and two schemes for improving the phase matching: chirping and tapering of the grating. Improving phase matching by chirped gratings can be understood intuitively. Let K be the wavenumber of the grating, k_z , the z component of the wavenumber of the incident wave, and $\beta(|a_g|^2)$ the intensity-dependent wavenumber of the nonlinear guided wave. The

phase-matching condition requires that

$$k_z \pm K = \beta(|a_g|^2). \quad (1)$$

Since the amplitude a_g is a function of z , the phase-matching condition, Eq.(1), cannot be satisfied if the wavenumber of the grating is a constant. By chirping the grating, K becomes a function of z . It is then possible to compensate the phase mismatch induced by the self-phase modulation of the nonlinear guided wave by adjusting $K(z)$ accordingly. The effect of tapering is more intricate and is discussed later.

We have investigated the excitation of the nonlinear guided wave using a uniform grating [$x(z) = \eta_0 \cos(K_0 z)$] with amplitude η_0 and wavenumber K_0 such that $k_z \pm K_0 = \beta(|a_g|^2 = 0)$, i.e., the phase-matching condition is satisfied in the linear limit.¹ For the chirped and tapered grating, the profile is given by

$$x(z) = \delta \eta_0 T(\delta^2 z) \cos\{[K_0 + K_1(\delta^2 z)]z\}, \quad (2)$$

where δ is a small parameter, T is the tapering function and K_1 is the chirping function. Both T and K_1 are slowly-varying functions of z as indicated. Using the same analytical technique as in Ref.[1], we deduce the set of canonical equations governing the excitation of the nonlinear guided waves using chirped and tapered grating as:

$$b_r = C_{rr}^0 a_i + C_{rg}(z) a_g, \quad (3)$$

$$i V_g \left(\frac{\partial}{\partial z} a_g + C_g(z) a_g + C_{gr}(z) a_i \right)$$

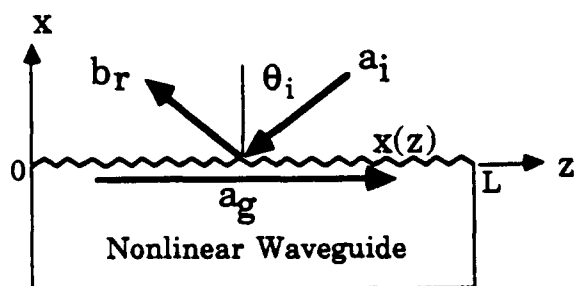


Figure 1: Geometry of grating excitation. a_i , b_r and a_g are the amplitudes of the incident, reflected and guided waves, respectively. θ_i is the incident angle and $x(z)$ is the grating profile.

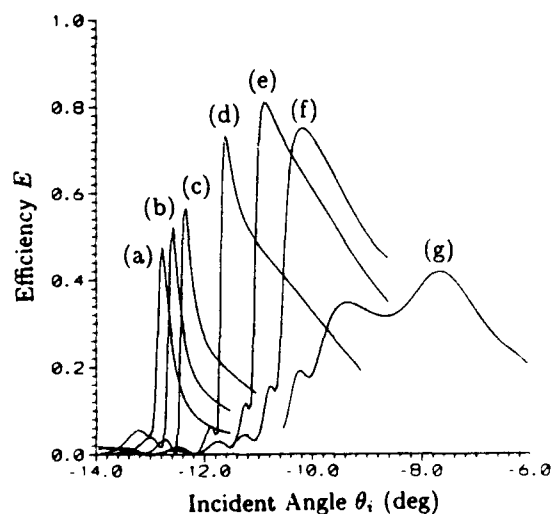


Figure 2: Resonance of E with respect to θ_i for linear chirping rates $\kappa =$ (a) 10^{-6} , (b) 0, (c) -10^{-6} , (d) -5.0×10^{-6} , (e) -8.0×10^{-6} , (f) -10^{-5} , (g) -5.5×10^{-5} . $|a_i|^2 = 10^{-3}$, $K_0 = 0.3415$ and $\eta_0 = 0.63$. Since a_i is already in the nonlinear regime, the maximum efficiency for $\kappa = 0$ is 52.1% rather than 81.45%.

$$+ P \frac{\partial^2}{\partial z^2} a_g = Q |a_g|^2 a_g, \quad (4)$$

with

$$C_{rg} = C_{rg}^0 T(\delta^2 z) \exp[-iK_1(\delta^2 z)z],$$

$$C_{gr} = C_{gr}^0 T(\delta^2 z) \exp[iK_1(\delta^2 z)z],$$

$$C_g = C_g^0 T^2(\delta^2 z),$$

where C_{rr}^0 , C_{rg}^0 , C_{gr}^0 and C_g^0 are the coupling constants for the uniform grating that depends on η_0 and K_0 .

The nonlinear surface polariton supported by the silver-vacuum interface was used as a specific example of the nonlinear guided wave. Our analysis and simulation show that appropriate chirping and tapering can both increase the efficiency of excitation. Linear chirping almost compensates the phase mismatch due to self-phase modulation at moderate incident intensities, as shown in Fig. 2.

Combined effects of chirping, tapering and adjustment of the grating extent result in even greater increase in the excitation efficiency. In a specific example, we improve the efficiency from 40.0% to over 81.45% (the maximum efficiency in the linear regime).

[1]G. Li and S.R. Seshadri, J. Opt. Soc. Am B. 7, 998 (1990).

[2]M.B. Marques, *et. al.*, Appl. Phys. Lett. 58, 2613 (1991).

MF4-1

Experimental and theoretical investigations of two-photon and free carrier absorption in a GaAs/AlGaAs Quantum Well Waveguide

F.R. Laughton and J.H. Marsh

Department of Electronics and Electrical Engineering, University of Glasgow, Glasgow G12 8QQ,
Scotland.

Tel: ++44-41-330-5220 Fax: ++44-41-330-4907

J.S. Roberts

Department of Electronic and Electrical Engineering, University of Sheffield, Sheffield, S1
3JD, England.

There have been many studies of two-photon absorption (TPA) in semiconductors¹⁻². In calculating the TPA coefficient, β , the effect of free carrier absorption (FCA) has often been neglected. However, it is relatively straightforward to include this by means of an intuitive theoretical model³. The model's use can be demonstrated in evaluating β from nonlinear absorption experiments carried out in GaAs/AlGaAs Multiple Quantum Well (MQW) waveguides using a Nd:YAG laser. When only linear absorption and TPA are considered and the experimental analysis carried out in the usual way, the TPA coefficient β is calculated to be $2.2 \times 10^{-10} \text{ m W}^{-1}$ for TM polarisation, and $2.7 \times 10^{-10} \text{ m W}^{-1}$ for TE polarisation. Including the effect of free carrier absorption in the waveguide, the model predicts β to be $1.5 \times 10^{-10} \text{ m W}^{-1}$ and $2.0 \times 10^{-10} \text{ m W}^{-1}$ for TM and TE polarisations respectively.

Pump-probe experiments have also been performed, and the change in probe transmission measured as a function of both pump intensity and pump-probe delay time. The results from these experiments can also be successfully fitted to the model, as shown in Figures 1(a) and 1(b). It may be seen from Figure 1(a) that, for relatively low peak pump input intensities of approximately $4.5 \times 10^{11} \text{ Wm}^{-2}$, there is a 35% decrease in transmission of the probe beam when the pump beam is present and overlapping in time. TPA is generally considered to have a deleterious effect on the performance of nonlinear optical switches, but for this low peak pump input intensity the recovery time of this absorption modulation is limited only by the laser pulsewidth. At higher peak pump input intensities of about $1.5 \times 10^{12} \text{ Wm}^{-2}$, as shown in Figure 1(b), there is a 70% decrease in the transmission of the probe beam when the pump beam is present and overlapping in time, but the recovery time of the modulation is now much slower, as it is limited by the carrier lifetime.

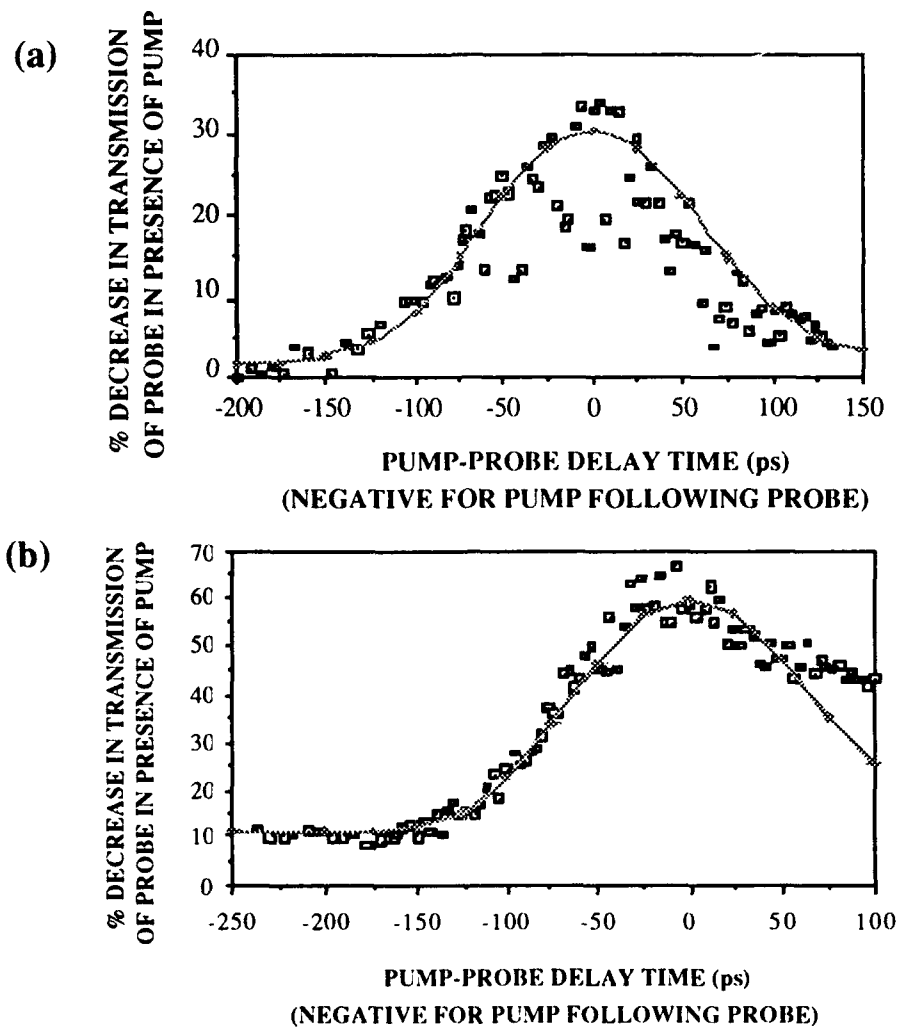


Fig. 1(a) and (b) Time-resolved nonlinear transmission of a TE probe due to a TM pump of peak input intensity (a) $4.5 \times 10^{11} \text{ Wm}^{-2}$ and (b) $1.5 \times 10^{12} \text{ Wm}^{-2}$. The solid lines are the theoretical fits.

We have also made nonlinear refractive index measurements at $1.06 \mu\text{m}$ using a time-division interferometer⁴, and measured n_2 to be about $-1 \times 10^{-16} \text{ m}^2\text{W}^{-1}$ for a TM pump and TE probe. When measured as a function of pump-probe delay time, the refractive index change is seen to contain a positive component when the pump and probe pulses are overlapped in time.

REFERENCES:

- ¹ J.H. Bechtel and W.L. Smith, *Phys. Rev. B*, **13**, 3515, (1976).
- ² E.W. Van Stryland et al, *Opt. Eng.*, **24**, 613, (1985).
- ³ F.R. Laughton, J.H. Marsh and J.H. Roberts, *to be published in Appl. Phys. Lett.*, Jan. 1992.
- ⁴ M.J. LaGasse, K.K. Anderson, C.A. Wang, H.A. Haus and J.G. Fujimoto, *Appl. Phys. Lett.*, **56**, 417, (1990).

Dynamics of Dissipative Optical Wave Structures

M. Haelterman, S. Trillo, and S. Wabnitz

Fondazione Ugo Bordoni, Via B. Castiglione 59, 00142 Rome, Italy

The onset of spatio temporal wave structures in macroscopic systems may often be understood in terms of universal dynamical descriptions. A concept which has been successful in diverse fields of application such as hydrodynamics and biology is that the behavior of a complex nonlinear system may be well described in terms of the interaction between a small number of normal modes. The evolution of the physical system is then represented by the finite set of coordinates of this modal expansion. The transition of the system from a steady state, which corresponds to closed curves in the phase space, to a weakly turbulent state follows the universal route of the development of nonlinear modulations [1].

In this work we discuss two important nonlinear guided optics examples of spatio temporal wave pattern generation and chaos. We consider optical feedback systems such as the fiber ring laser [2] and the nonlinear planar waveguide Fabry-Perot resonator (FPR) [3]. We show that the modulational instability laser (MIL) is the temporal analog of a FPR: pulse train generation in a MIL occurs from the nonlinear development of a dissipative stable temporal structure (see fig.[1]). This is in contrast with pulse train generation from the conventional MI in a fiber, where the pulses in the train continuously interact and the contrast ratio strongly depends on the longitudinal coordinate along the fiber [4].

We find however that if the pump power is large enough the generated pulse train loses its stability. As a result, temporal chaotic alternation between coexisting attractors is predicted. A similar behavior is observed in the nonlinear FPR: here the spatial coherence may be preserved by an appropriate choice of the boundary conditions.

We obtain considerable insight in the physical description of these phenomena by applying the following two steps. Consider first the case of the MIL laser (the nonlinear FPR may also be treated along similar lines). Under the hypothesis of small residual losses (which may result from the compensation of mirror losses by means of linear gain in the fiber), and small nonlinear phase shift or dispersive broadening on each passage of the train through the ring, we may replace the infinite dimensional Ikeda map [5] by a single averaged equation, in analogy with the case of long distance transmission with periodic amplification [6].

As a result, we describe temporal structure formation in the field U traveling in a nonlinear dispersive fiber ring cavity by means of the averaged driven and damped dimensionless nonlinear Schrödinger (NLS) equation

$$i \frac{\partial U}{\partial \zeta} - \frac{\eta}{2} \frac{\partial^2 U}{\partial \tau^2} + |U|^2 U = (\Delta - i)U + i\delta \frac{\partial U}{\partial \tau} + \beta \frac{\partial^2 U}{\partial \tau^2} + iV, \quad (1)$$

where η is the sign of the fiber group velocity dispersion, Δ is the phase detuning of the cavity, δ is the cavity group velocity detuning, β is the fiber gain dispersion, and V is the forcing term due to the external (quasi-cw) pulse.

The second step of our reduction procedure is to perform a modal truncation to the field U in eq.(1) to the frequency component of the pump and one or two adjacent sideband modes [7]. In this way we obtain ordinary differential coupled mode equations and we analyse and display the dynamics of stable or chaotic pulse generation by the MIL in terms of phase space trajectories. Note that eq.[1] predicts MIL oscillation both in the normal and in the anomalous dispersion regime of the fiber (i.e., $\eta = \pm 1$).

We show the perfect space time analogy between the dispersive and the diffractive wave structure formation processes in the MIL and the FPR. In the so called mean field approximation, the transverse structure of the optical field A that is transmitted by a nonlinear Fabry-Perot resonator in a planar waveguide geometry is described by the averaged NLS equation

$$i\frac{\partial A}{\partial t} + \frac{\partial^2 A}{\partial x^2} + \eta(|A|^2 - \Delta)A = iA + i\delta\frac{\partial A}{\partial x} + iE. \quad (2)$$

Here η is the sign of the nonlinearity, Δ is the cavity detuning, and δ represents the oblique incidence angle of the input beam E .

We also show that the above averaged descriptions (eqs[1-2]) may be extended to the period two regime in the cavity. In this case the MI may develop independent time shifted stable pulse trains over two consecutive transits. This is important in view of the possible use of the fiber ring as a recirculating optical memory.

References

- [1] P. Manneville, *Dissipative Structures and Weak Turbulence* (Academic, San Diego, 1990).
- [2] M. Nakazawa, K. Suzuki, and H.A. Haus, *Phys. Rev. A* **38**, 5193 (1988).
- [3] L.A. Lugiato and R. Lefever, *Phys. Rev. Lett.* **37**, 2209 (1988).
- [4] S. Trillo and S. Wabnitz, *Opt. Lett.* **16**, 1566 (1991).
- [5] K.J. Blow and N.J. Doran, *Phys. Rev. Lett.* **52**, 526 (1984).
- [6] A. Hasegawa, and Y. Kodama, *Opt. Lett.* **15**, 1443 (1990).
- [7] A. Bishop, G. Forest, D. McLaughlin, and E. Overman, *Phys. Lett. A* **144**, 17 (1990).

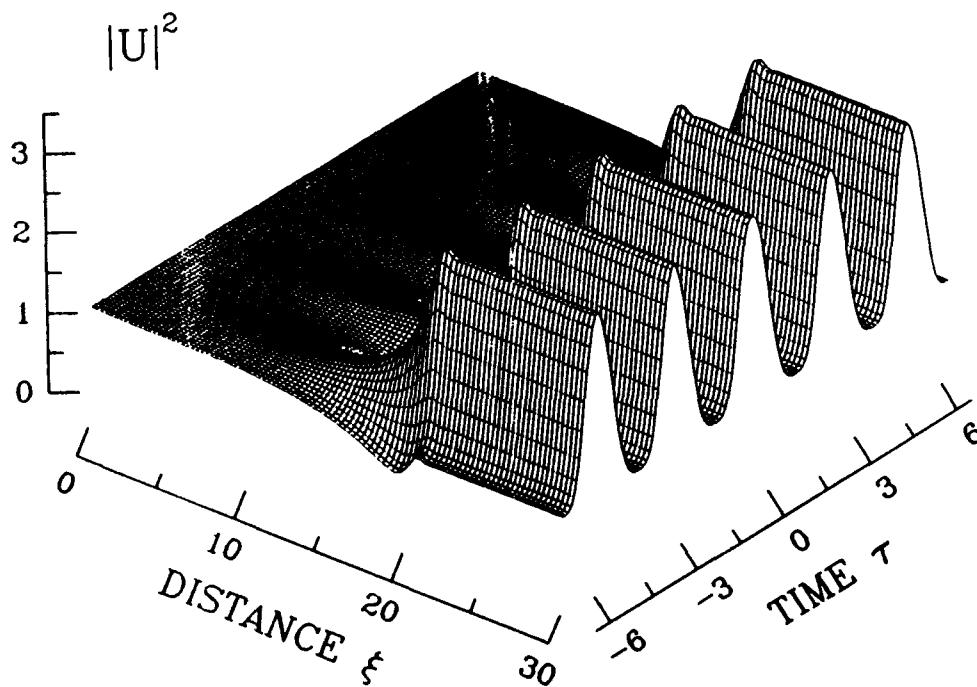


Figure 1: Pulse train generation from a MIL in the normal dispersion regime of the fiber.

MF6-1

Crystalline Organic Semiconductor Waveguide Optical Directional Couplers and Switches

D. Y. Zang and S. R. Forrest

National Center for Integrated Photonic Technology
Departments of Electrical Engineering and Materials Science
University of Southern California
Los Angeles, CA 90089-0241

In previous work [1, 2], we have successfully developed techniques to fabricate low-loss rib waveguides in a crystalline organic compound, namely, 3,4,9,10 perylenetetracarboxylic dianhydride (PTCDA). Here, we demonstrate apparently the first optical directional coupler using an index-matching layer in similar crystalline organic semiconductor waveguides. We also observed switching of the guided light between the waveguides in the PTCDA couplers by pumping the surface of one waveguide in the coupling region with 0.514 μm wavelength light.

A directional coupler typically consists of a pair of parallel channel waveguides with a gap between them. The gap width and the refractive index discontinuity between the guides and the gap are small enough to allow the guided light to couple from one waveguide to the other by the overlapping evanescent tails of the guided modes. However, there is a large refractive index discontinuity of 1.017 for TE modes at the interface between a PTCDA waveguide and an air gap at $\lambda = 1.06 \mu\text{m}$ [1]. The large index discontinuity causes a small coupling coefficient and a long coupling length. The best way to increase the coupling coefficient between two rib waveguides is to fill the gap with a layer whose index is only slightly lower than the adjacent guides. In our experiments, we employed AZ 1400 photoresist as the index-matching layer material for PTCDA couplers. AZ 1400 photoresist has a relatively high index of 1.61 and low absorption at $\lambda = 1.06 \mu\text{m}$. In this case, for a coupler having 0.5 μm thick, 2 μm wide waveguides and 1 μm gap, $\kappa \sim 0.50 \text{ mm}^{-1}$, which is about 40 times greater than that for the coupler without an index-matching layer. Correspondingly, the coupling length is 3.14 mm.

The coupler studied in these experiments has a 1.5 mm long coupled region and two 2 mm long guiding regions. In the coupled region, two 2 μm wide rib waveguides are separated by a 1 μm gap filled with AZ 1400 photoresist. The guiding regions consist of two S-bend waveguides separated by 50 μm at their input and output ends. According to calculations, the AZ 1400/PTCDA directional coupler is expected to have a coupling efficiency of $\sim 46\%$.

To fabricate the directional couplers, a 1 μm thick AZ 1400 photoresist layer was spin-coated onto the cleaned and polished surface of a (100) InP substrate. Next, an array of 2 μm wide directional coupler patterns were made onto the photoresist along the (110) direction using standard photolithographic techniques. A 0.5 - 0.7 μm thick crystalline PTCDA layer was then grown onto the InP substrate and the photoresist pattern surface using the process of organic molecular beam deposition under a $\sim 10^{-7}$ Torr base pressure [3]. After PTCDA deposition, a second 1 μm thick AZ 1400 photoresist layer was spun onto the wafer surface to form the index-matching layer.

To characterize the couplers, a 1.06 μm wavelength light beam from a YAG laser was end-fire coupled into one guide of the coupler to excite the TE_{00} mode using a microscope objective. Light emerging from the two output guides were reimaged onto a CCD camera using a second microscope objective. Two TE_{00} mode beam spots exiting from the coupler are clearly observed, as shown by the intensity profiles in Fig. 1 (dashed lines).

It was found that the refractive index of PTCDA can be changed by illumination with light at $\lambda = 0.514 \mu\text{m}$ due to the optical generation of excitons which subsequently dissociate into free electrons and holes creating a charged plasma [4]. This phenomenon has been utilized for observing all-optical switching in the PTCDA directional couplers by directly illuminating the surface of one guide of the coupler with a $0.514 \mu\text{m}$ wavelength light beam. The change of refractive index in one guide induced by this illumination alters the phase mismatch, δ , and the coupling coefficient, κ , thereby reducing the coupling efficiency. That is the light energy is switched back into the guide in which the waveguide mode was initially excited by end-fire coupling. A typical experimental result showing the output intensities exiting the two guides with short wavelength pumping is shown by solid lines in Fig. 1, in which the coupling efficiency was reduced by 8.3 % using a pump light intensity of $\sim 4 \text{ W/cm}^2$. Fig. 2 shows the measured relative output intensities from the two guides as a function of pump light intensity, together with the theoretical calculation. A resonant nonlinear coefficient of $n_2 = 5.4 \times 10^{-5} \text{ cm}^2/\text{W}$ [4] was assumed in the calculation. From Fig. 2, it is clearly seen that the measured data are in reasonable agreement with the calculation.

In the conclusion, we report the fabrication of a crystalline organic directional coupler with an index-matching layer grown by the high vacuum process of organic molecular beam deposition. All-optical switching between two arms of the coupler was also observed using wavelengths of $1.06 \mu\text{m}$ and $0.514 \mu\text{m}$ as the guided and pump light beams, respectively.

This work was supported by AFOSR and RADC.

References

1. D. Y. Zang, Q. Shi, F. F. So, S. R. Forrest, and W. H. Steier, *Appl. Phys. Lett.*, **58**, 562 (1991).
2. D. Y. Zang, F. F. So, and S. R. Forrest, *Appl. Phys. Lett.*, **59**, 823 (1991).
3. F. F. So, S. R. Forrest, Y. Q. Shi, and W. H. Steier, *Appl. Phys. Lett.*, **56**, 674 (1990).
4. D. Y. Zang and S. R. Forrest, to be published in *Appl. Phys. Lett.*, Jan. 13, 1992.

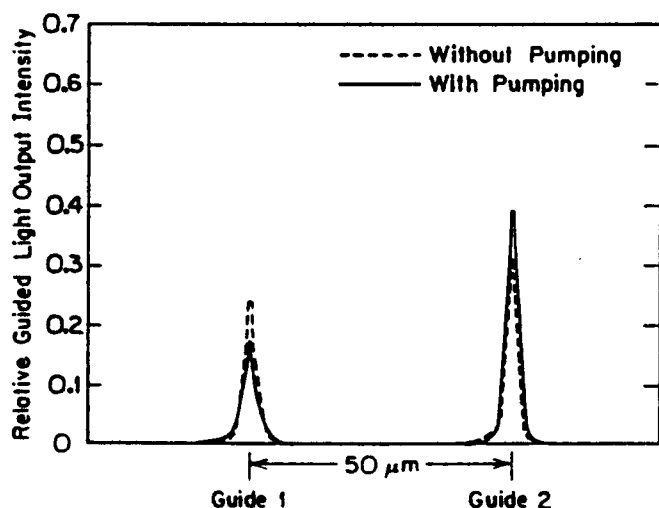


Fig.1: Output intensity distributions without (dashed lines) and with (solid lines) a $0.514 \mu\text{m}$ wavelength pump light beam intensity of $\sim 4 \text{ W/cm}^2$.

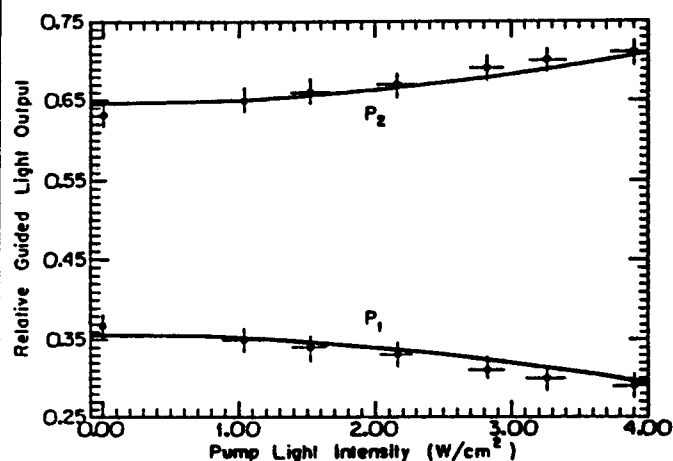


Fig.2: Measured relative light outputs (solid circles) from the PTCDA coupler as a function of $0.514 \mu\text{m}$ wavelength pump light intensity. The solid lines are theoretical fits to the data.

Tuesday, April 14, 1992

Optoelectronic Integrated Circuits

TuA 8:30 am–10:00 am
La Salle Ballroom B

Stephen Ross Forrest, *Presider*
University of Southern California

TuA1-1

VSTEP Technology for Optical Interconnections

Kohroh Kobayashi and Kenichi Kasahara

Opto-Electronics Research Laboratories
NEC Corporation4-1-1, Miyazaki, Miyamae-ku, Kawasaki, 216 Japan
81-44-856-2150

Optical interconnections have been expected to offer several advantages over conventional electronic interconnections. One of the most attractive advantages is the multi-channel capability. To fully utilize the advantage, parallel configuration is desirable, where two-dimensional array devices play an important role. If the device has some functions such as switching and memory, it will make the interconnections more attractive and flexible. VSTEP (Vertical to Surface Transmission Electro-Photonic device) has been studied to realize such an optical functional devices[1]. In this paper, recent advances in VSTEP will be reviewed.

A basic concept of VSTEPS is that electronic non-linearity is effectively combined with optical input/output interfaces in a device level. The electronic non-linearity will provide us a variety of functional operations with lower power consumption and higher uniformity compared with pure photonic non-linearity will do. These features are fairly important for large scale integration. In VSTEPS developed so far, a pnpn thyristor was utilized to attain the electronic non-linearity.

Fundamental properties of VSTEPS has been studied with LED-mode pnpn VSTEPS. By introducing laser diode structure into the VSTEPS, significant improvements in the performance will be expected, such as higher light output intensity, higher switching speed, higher electrical efficiency, and smaller device size. A laser-mode pnpn VSTEP or a vertical cavity (VC) pnpn VSTEP has been designed and investigated[2] based on the results of LED-mode VSTEPS and of surface emitting laser diodes[3].

A pnpn VC-VSTEP consists of pnpn thyristor layers sandwiched by the top and bottom mirrors for the vertical cavity. In designing the device, three factors should be considered: threshold gain, absorptivity of the active region and transmissivity of the output mirror. The latter two factors are closely related to the functional operation performances, such as low optical switching energy. Computer simulation was done for optimizing the mirrors with AlAs/GaAs quarter wavelength thick multi-layers. The AlAs/GaAs pair number was chosen to be around 15[4] for the top mirror to achieve a high reflectivity of 99.7%. The pair number for the bottom mirror was designed to be from 14.5 to 24.5[4].

The VC-VSTEP layers were grown on a GaAs substrate by molecular beam epitaxy. The active region consists of three 100 Å InGaAs quantum well layers and AlGaAs barrier layers. The quantum well was designed to emit laser light at around 950 nm, which is transparent at GaAs substrate. Mesa structure was fabricated by etching down through the lower mirror and the whole mesa was covered with plated gold.

The smaller bottom mirror reflectivity induces higher light output power slope efficiency. With a 14.5-period bottom mirror, the slope efficiency as high as 0.32 mW/mA was observed at pulsed operation. With increasing the period number, the threshold current decreases with the sacrifice of the slope efficiency. A VC-VSTEP with a 24.5-period bottom mirror showed threshold current as low as 2.4 mA at cw operation. In pulsed operation, it did not show clear lasing threshold kinking in the light output vs. current curve at below 40 °C[4], [5]. Even at fairly small current level, 0.5-1 mA, for example, it emitted linearly polarized light with high sub-mode suppression ratio of larger than 25 dB. The light beam divergence was as narrow as 7°. These indistinct threshold phenomena seem to appear by the carrier regeneration from the spontaneous emission strongly confined in a small cavity by the vertical cavity mirrors and high reflectivity plated gold. The indistinct threshold operation of the devices will lead to a very low power consumption operation, which is most significant for optical functional devices with a large scale two-dimensional array configuration.

Feasibility of VSTEPS in optical interconnections has been successfully demonstrated in experiments. For example, low optical power switching was achieved with a differential mode VSTEP configuration[6]. Four 2x8 array VSTEPS were coupled and cascaded sequentially, resulting in a shift resistor operation[6]. Flexible optical interconnection was designed[7] and tested in an ATM photonic packet switch routing fabric, where 3x3 matrix VSTEP array was used. According to the header optical signal, the path was switched[8].

Issues related to optical interconnections as well as devices will be discussed.

[REFERENCES]

- [1]K. Kasahara et al., Appl. Phys. Lett., 52, pp.679-681(1988).
- [2]T. Numai et al., Appl. Phys. Lett., 58, pp. 1250-1252(1991).
- [3]K. Iga et al., IEEE J. Quantum Electron., QE-24, pp. 1845-1855(1988).
- [4]T. Numai et al., LEOS'91, OE7.5(1991).
- [5]T. Numai et al., in preparation.
- [6]Y. Yamanaka et al., OSA Annual Meeting, FS3(1991).
- [7]S. Suzuki et al., Topical Meeting on Photonic Switching, ThA1 (1991).
- [8]M. Nishio et al., Study Group on Switching, EICE Japan(1991).

HIGH EFFICIENCY WAVEGUIDE-INTEGRATED 1.3 μm InGaAs/GaAs MSM DETECTOR AS AN OPTICAL DELAY LINE SWITCH FOR MICROWAVE PHASED ARRAYS

W. NG, A. NARAYANAN, R. HAYES, D. YAP
Hughes Research Laboratories
3011 Malibu Canyon Road
Malibu, CA 90265

In recent years, there has been much interest in the development of waveguide-integrated detectors for applications in wavelength division multiplexing and balanced heterodyne receivers in coherent systems⁽¹⁾⁻⁽³⁾. In this paper, we report the first integration of a strained layer ($\text{In}_{0.35}\text{Ga}_{0.65}\text{As}$ on GaAs) metal-semiconductor-metal (MSM) detector with a GaAlAs/GaAs rib-waveguide. By optimizing the thicknesses of the epitaxial layers, we achieved an estimated coupling efficiency of 99% from the incident mode in the rib waveguide to the guided modes in the integrated-detector section. We measured a DC responsivity ($\lambda = 1.3 \mu\text{m}$) as high as 0.6 mA/mW for 100- μm long detectors at a voltage bias of 6 V. In addition, we will present the advantages offered by this device for bias-switching waveguide delay lines designed for the optical control of microwave phased array radar.

The epitaxial structure of this device (see Fig. 1 for layer thicknesses) consists of $\text{Al}_{0.1}\text{Ga}_{0.9}\text{As}$ and GaAs layers from which the rib waveguide was fabricated. The growth of these layers was followed by that of a thickness-graded $\text{In}_{0.35}\text{Ga}_{0.65}\text{As}/\text{GaAs}$ superlattice buffer that enabled the strained $\text{In}_{0.35}\text{Ga}_{0.65}\text{As}$ detection layer to be grown on the GaAs substrate. Finally, a layer ($\sim 0.02 \mu\text{m}$) of $\text{In}_x\text{Ga}_{1-x}\text{As}$ ($\lambda \sim 1.1 \mu\text{m}$) was grown to enhance the Schottky barrier heights of metal electrodes in the MSM detector. All the epitaxial layers were grown by MOVPE in a single growth step. In fabricating the waveguide-integrated detector, we first etched a mesa from the detector layer down to the GaAs waveguiding layer. After definition of the rib waveguide, a window was opened in the passivating dielectric of the detector. The Ti/Pt/Au finger electrodes of the MSM detector were finally deposited inside the window. The finger widths and spacing were typically between 1 and 2 μm . An SEM photograph of a finished device is shown in Fig. 2.

By computing the overlap integrals, we estimated that 22.9% and 75.9% of the incident mode from the rib waveguide coupled, respectively, into the fundamental and first order mode of the integrated-detector section. The estimated absorption coefficients of these two modes at $\lambda = 1.3 \mu\text{m}$ were, respectively, $\sim 1280/\text{cm}$ (fundamental mode) and $539/\text{cm}$ (first order mode), giving a composite absorption coefficient of $\sim 702/\text{cm}$ for the device.

We observed dark currents as low as $\sim 250 \text{ nA}$ at a bias voltage of 6 volts for Si_xN_y passivated devices (100 μm long x 20 μm wide). When the rib waveguide was excited from a single mode optical fiber, we measured responsivities of 0.43 and 0.58 mA per milliwatt of incident power ($\lambda = 1.3 \mu\text{m}$) from the optical fiber for 50- and 100- μm -long detector integrated with 10- μm -wide rib waveguides. We characterized their microwave response (Fig. 3) with an optical heterodyne setup that mixed the optical outputs of two Nd:YAG lasers. At a bias voltage of 12 V, we measured a drop of only 3 dB in the RF response of a 50- μm -long, 10- μm -wide detector from 2 to 11 GHz. Their RF on/off ratio was better than 40 dB in that frequency range as the bias voltage was switched from ~ 8 to 0 V, making them an attractive candidate for delay line switching. Further details will be presented in the talk.

REFERENCES:

1. J.B. Soole et al. Appl. Phys. Lett. 56, 1518 (1990)
2. R.J. Deri et al. Appl. Phys. Lett. 58, 2749 (1991)
3. G.K. Chang et al. IEEE Photon. Technol. Lett. 3, 475 (1991)

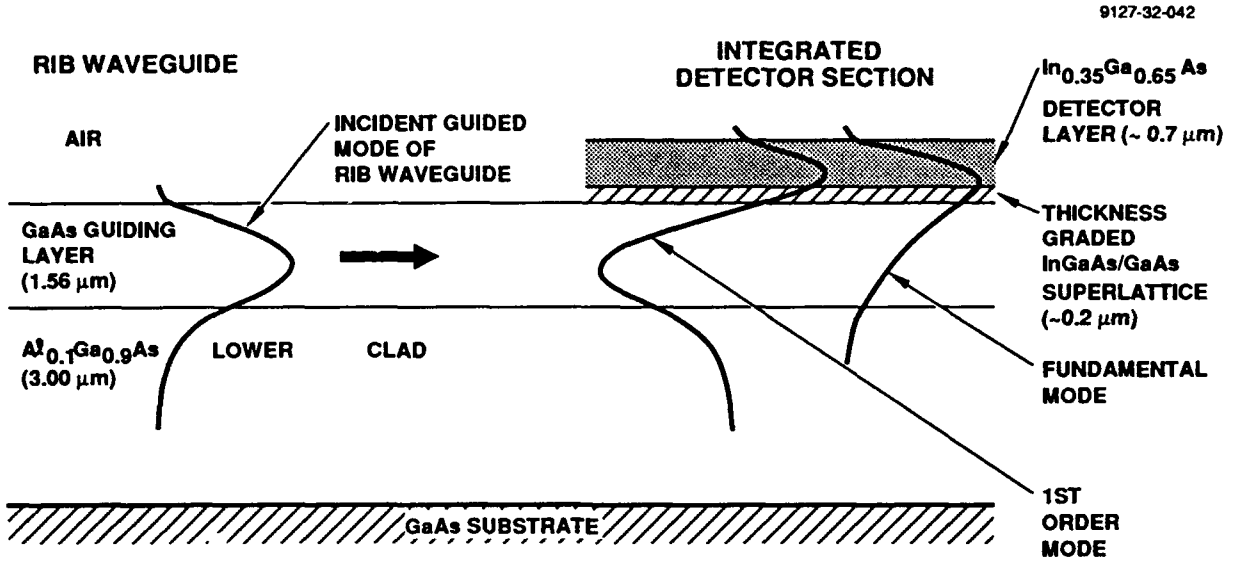


Figure 1. EPITAXIAL STRUCTURE AND GUIDED MODES OF WAVEGUIDE-INTEGRATED MSM DETECTOR

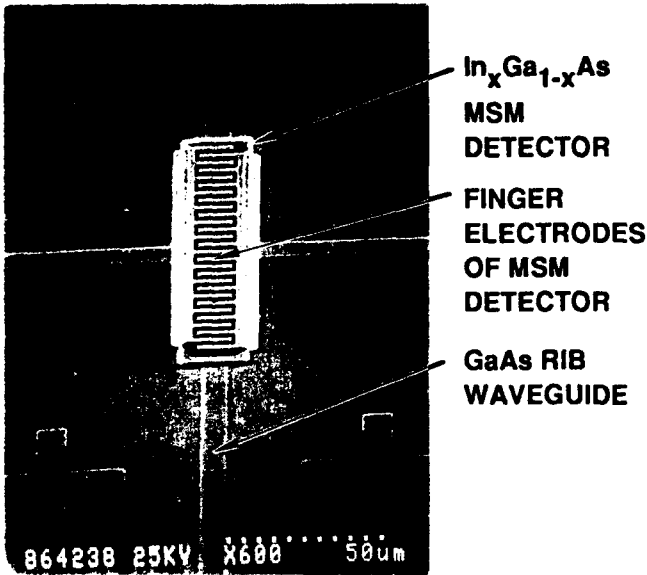


Figure 2. SEM PHOTOGRAPH OF FINISHED DEVICE

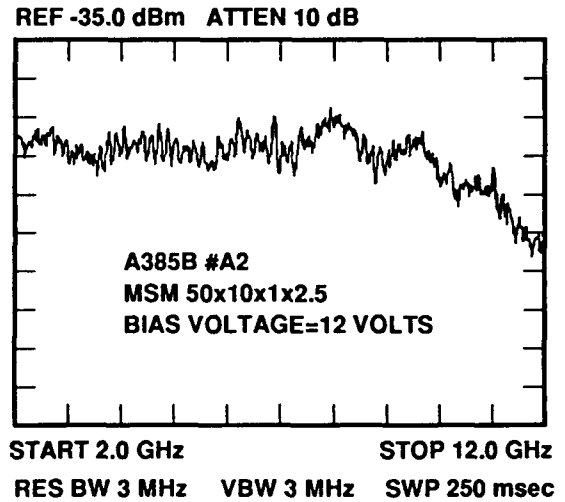


Figure 3. RF RESPONSE OF DEVICE OBTAINED BY OPTICAL HETERODYNING

TuA3-1

Butt-Coupled PIN Photodiode on InP Using Selective Refill MOVPE Growth

A. Umbach, O. Kayser*, D. Trommer, G. Unterbörsch

Heinrich-Hertz-Institut für Nachrichtentechnik Berlin GmbH
Einsteinufer 37, D-1000 Berlin 10, Germany

* Institut für Halbleitertechnik, RWTH Aachen,
Sommerfeldstraße, D-5100 Aachen, Germany

The integration of photodetectors with optical waveguides is a key element in the fabrication of optoelectronic integrated circuits (OEICs) for long wavelength communication techniques. For example, coherent heterodyne receivers or wavelength demultiplexer chips combine the optical information processing by waveguide devices with the highly sensitive photodetection by waveguide integrated pinFETs /1,2/. For the light coupling from the waveguide into the photodiode two different concepts are feasible, i.e. evanescent and butt-joint coupling /3/. The latter scheme provides several advantages as compared to the vertical integration. Firstly, the lateral detector dimensions may be smaller due to the higher absorption efficiency thus providing a reduced device capacitance and an increased cut-off frequency. Furthermore, light coupling does not depend on the waveguide structure enabling the separate optimization of the passive components. Finally, recessing the photodiodes leads to planar devices which facilitates the integration e.g. with field effect transistors.

These benefits, however, have to be paid for by a rather complicated three-dimensional device structure, which can only be achieved by advanced growth techniques. Metal organic vapour phase epitaxy (MOVPE) provides the possibility of selective material deposition on partially masked substrates taking advantage of the fact, that the epitaxial growth necessitates the catalytic decomposition of the group V reactants at the semiconductor surface /4/. In this work low pressure MOVPE was used for the growth of the absorbing InGaAs embedded in a semi-insulating InGaAsP:Fe waveguide layer ($\lambda_g = 1.05 \mu\text{m}$). Pyrolytically deposited SiO_2 served as a mask both for the reactive ion etching (RIE) of the $1.4 \mu\text{m}$ deep recesses and for the subsequent selective MOVPE growth of a S-doped InGaAs contact layer and an undoped absorption layer. The growth conditions had to be adjusted accurately to obtain a high selectivity and planar surfaces (see ref. /5/ for more details). The local non-depletion of reactants above the masked areas leads to lateral diffusion in the gas phase and thus to a strong dependence of the material composition on the mask geometry /6/. These effects had to be considered during mask design by including unmasked areas of the same size only, equally spaced for all devices on the wafer.

The pin diodes were fabricated in the selectively grown regions using masked ion implantation of Si and local Zn diffusion. AuGe/Ni/Au and Ti/Pt/Au were evaporated to form n- and p-type ohmic contacts, respectively. Device passivation was accomplished by plasma enhanced chemical vapour deposition of SiN_x , and finally ridge waveguides of 70 nm height and $3 \mu\text{m}$ width were etched using a CH_4/H_2 RIE process. The resulting device structure is sketched out in fig. 1.

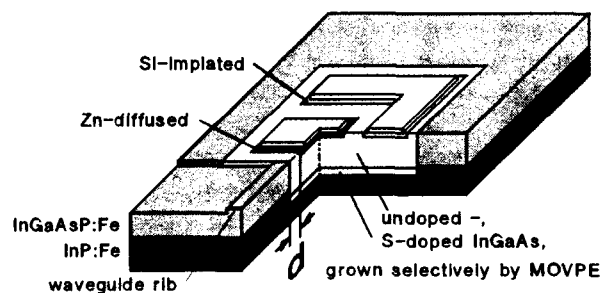
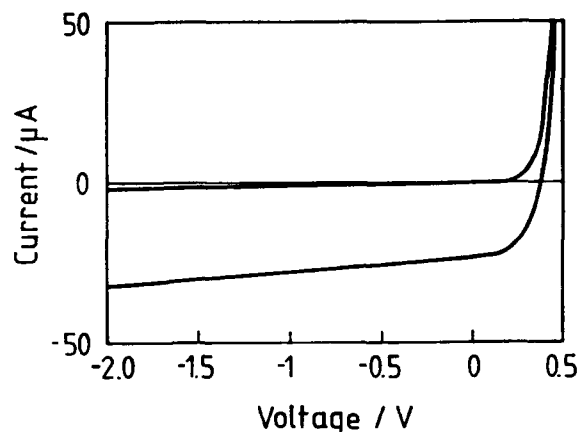


Fig. 1: Structure of butt-coupled photodiode

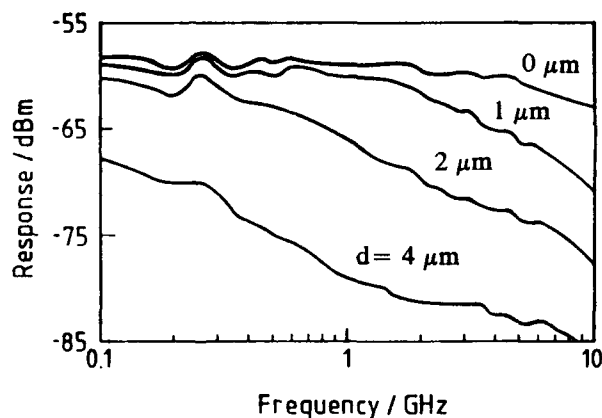
Fig. 2 shows the current-voltage characteristics of a $10 \times 11 \mu\text{m}^2$ photodiode with and without illumination. From the forward current a series resistance of 15Ω and an ideality factor of 1.8 were determined. The dark current of $1 \mu\text{A}$ at 1 V reverse bias may be due to non-ideal passivation properties of the SiN_x layer. The photo current considerably increases with applied bias voltage indicating loss mechanisms for carriers generated outside the space charge region, e.g. caused by crystal defects at the vertical InGaAs / InGaAsP interface. The amount of carriers diffusing to these recombination centers depends both on the lateral extension of the depletion region and on the spacing d between the p-area of the diode and the waveguide (cf. Fig. 2). We found an improvement of responsivity with increasing bias and decreasing distance from 4 to $0 \mu\text{m}$. For a device with $d = 1 \mu\text{m}$ a photo current of $60 \mu\text{A}$ was observed under 0.43 mW illumination at $\lambda = 1.55 \mu\text{m}$. Taking into account the insertion loss and the measured waveguide attenuation of 4 dB/cm an internal quantum efficiency of $\eta = 65\%$ was estimated.

Fig. 2: Current-voltage characteristics of a selectively grown photodiode with and without illumination



To characterize the high frequency performance of the detector, light of a $1.3 \mu\text{m}$ laser was modulated up to 10 GHz and end-fire coupled into the waveguide. Frequency analysis of the photodiode signal was carried out using on-wafer probing techniques and a spectrum analyzer. Fig. 3 shows the frequency response of four diodes with different distances d from the vertical interface at -1 V bias. The observed increase of the output power and the bandwidth with decreasing distance again results from the absorption in the undepleted region adjacent to the butt-coupled waveguide. For the device with zero spacing a 3 dB bandwidth of $\approx 8 \text{ GHz}$ was determined, which is to our knowledge the highest value reported for waveguide integrated photodiodes.

Fig. 3: Frequency response of photodiodes with different spacings between active area and vertical InGaAsP/InGaAs interface at -1 V



In conclusion we demonstrated the potential of selective growth techniques for optoelectrical integration by fabricating butt-joint photodiodes embedded in a semi-insulating waveguide. Quantum efficiency and frequency response strongly depend on the distance between the photodiode p-region and the waveguide. The measured bandwidth of 8 GHz is very promising for high speed communication applications.

References

1. D. Trommer, U. Feiste, R. Kaiser, G.G. Mekonnen, W. Passenberg, F. Reier and G. Unterbörsch, Proc. of the 17th European Conf. Opt. Commun. (ECOC, 1991, Paris, France) **2**, 497-500.
2. G. Unterbörsch, D. Trommer, C. Bornholdt, H.G. Bach, F. Kappe, A. Umbach and H. Venghaus, Conference on Optical Fiber Communication OFC '92, 3.-7.2.1992, San Jose, USA
3. M. Erman, Ph. Riglet, Ph. Jarry, B.G. Marti, M. Renaud, J.F. Vinchant and J.A. Cavallès, IEE Proceedings-J, **138**, 2, 101-108 (1991).
4. O. Kayser, J. Crystal Growth **107**, 989-998 (1991).
5. O. Kayser, B. Opitz, U. Westphalen, U. Niggebrügge, K. Schneider and P. Balk, J. Crystal Growth **107**, 141-146 (1991).
6. J. Finders, J. Geurts, A. Kohl, M. Weyers, B. Opitz, O. Kayser and P. Balk, J. Crystal Growth **107**, 151-155 (1991).

Waveguide/photodetector combination in SiGe for long wavelength operation

A. Splett, B. Schüppert, K. Petermann,

Institut für Hochfrequenztechnik, Technische Universität Berlin, Einsteinufer 25,
D-1000 Berlin 10, F.R.G., Tel. 49-30-314-22437

E. Kasper, H. Kibbel, H.-J. Herzog

Daimler Benz Forschungsinstitut, Wilhelm-Runge-Str. 11, D-7900 Ulm, F.R.G.

As silicon is a promising candidate for low cost integrated optical applications the monolithical integration of photodetectors is of major interest. Photodetectors for long wavelength operation have been realized on silicon as discrete devices [1] and in combination with SOI-waveguides [2], having waveguide losses around 1dB/cm. Recently, the losses of *SiGe*-waveguides already reported in [3][4] could be reduced to 0.5dB/cm [5]. In this work the efficient coupling between a *SiGe*-waveguide and a *SiGe*-detector is reported, which is a key component for integrated optics. Optical coherent applications, for example, then benefit from the low reflection coefficient at the waveguide/photodetector transition.

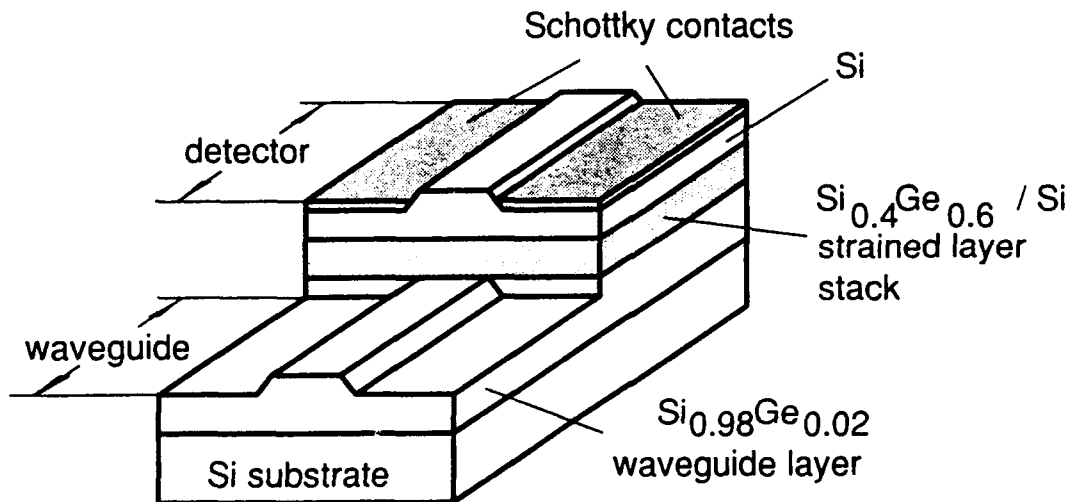


Figure 1: Principle view of a *SiGe*-waveguide/photodetector transition

All layers of the waveguide/detector combination shown in Fig.1 were pseudomorphically grown by molecular-beam-epitaxie(MBE) on (100)-silicon and are intentionally undoped. Waveguiding is obtained by a 2500nm thick strained $Si_{0.98}Ge_{0.02}$ -layer. In

the detector region an absorbing multilayer stack of $20 \times (30nmSi + 5nmSi_{0.4}Ge_{0.6}) = 700nm$ is added, covered by $700nm$ Si. The layer structure was analysed by X-ray diffraction and trans electron microscopy (TEM). The waveguide region and the ribs in both regions were defined by wet chemical etching. Two Schottky contacts placed on opposite sides of the detector rib are formed by evaporating *Ti* in high vacuum ($10^{-7}mbar$) directly after buffered HF treatment. The barrier height of the *Ti/Si*-contact is approximately half the bandgap of silicon, which is chosen for low leakage currents in the resulting MSM-diode.

Numerical simulations of the optical wave propagating from the waveguide into the detector are carried out in the vertical cross-section for TE-polarization using a novel finite-difference-beam-propagation-method(BPM) [6]. The refractive indices of the $Si_{1-x}Ge_x$ -layers were estimated to be $n(x) = 3.5 + 0.38x$ [4]. An optical absorption $\alpha = 500cm^{-1}$ of the strained $Si_{0.4}Ge_{0.6}$ material was assumed [1]. Numerical calculations yield 96 percent absorption of the power delivered by the waveguide for an infinite detector length. For a realistic detector length of $1mm$, however, only 20 percent absorption is obtained due to the indirect bandgap. A detector length of $3.5mm$ is required for 50 percent absorption. Optical near field measurements of the polished end face of a $10mm$ long detector match well with the results of the BPM-simulation.

Preliminary samples exhibited dark current densities around $500pA/\mu m^2$ at $5V$ bias and $T = 295K$, which are to be reduced by improved contacts. Responsivities of $0.2A/W$ were measured for a detector length of $1mm$ at $\lambda = 1.3\mu m$. Impulse response times of $10ns$ (presently limited by the wafer probes) were measured at $25V$ bias with a slightly modified device allowing higher electric fields normal to the multilayer stack. We believe, that high normal fields are required for improved tunneling of the holes being generated in the $Si_{0.4}Ge_{0.6}$ quantum wells.

References

- [1] H.Temkin, A. Antreasyan, N.A. Olsson, T.P. Pearsall, J.C. Bean: Appl.Phys.Lett., 1986, 49, pp.809-811
- [2] V.P. Kesan, P.G. May, E. Bassous, S.S. Iyer: in IEDM Tech.Dig., 1990, pp.637-639
- [3] B.Schüppert, J.Schmidtchen, K. Petermann: Electron.Lett., 1989, 25,pp. 1500-1502
- [4] A.Splett, J.Schmidtchen, B.Schüppert, K. Petermann, E. Kasper, H. Kibbel: Electron.Lett., 1990, 26,pp.1035-1037
- [5] J. Schmidtchen, A. Splett, B. Schüppert, K. Petermann: submitted to IPR 1992
- [6] A.Splett, M.Majd, K. Petermann: IEEE Photon.Techn.Lett., 1991, 3, pp.466-468

Small Signal and CW operation of the Lateral Current Injection Heterostructure Field Effect Laser

P. A. Evaldsson, G. W. Taylor, P. W. Cooke, P. R. Claisse, P. A. Kiely,
and C. A. Burrus

AT&T Bell Laboratories, Holmdel, New Jersey

Recently, we reported on a new Lateral Current Injection Laser suitable for optoelectronic integration, the Heterostructure Field Effect Laser (HFEL)[1]. This device utilizes the field effect at the heterointerface within the same structure used to make the Heterostructure Field Effect Transistor (HFET)[2], and the Bipolar Inversion Channel Field Effect Transistor(BICFET)[3]. The laser and the HFET can be fabricated from the same single epitaxial growth sequence using the same fabrication sequence. The properties of each device can be optimized simultaneously.

The HFET/HFEL structure was grown on a semi-insulating GaAs substrate by molecular beam epitaxy (MBE). The layer sequence consists of 5000Å of p-type GaAs for collector contact layer, 8000Å of p-Al_{0.35}Ga_{0.65}As and 2000Å of undoped Al_{0.35}Ga_{0.65}As for the lower cladding, 1800Å of p (undoped) Al_{0.15}Ga_{0.85}As for the lower optical waveguiding layer, two 80Å strained In_{0.2}Ga_{0.8}As quantum wells separated by 100Å GaAs barriers forming the active region of the laser and the channel of the FET, 20Å of undoped Al_{0.25}Ga_{0.75}As spacer layer, 80Å n+ Al_{0.25}Ga_{0.75}As to form the charge sheet, 1800Å of p-Al_{0.25}Ga_{0.75}As for the upper optical waveguiding layer, 1µm of p-Al_{0.35}Ga_{0.65}As for the upper cladding region, and 500Å of heavily p-doped GaAs to form the ohmic contact. The optical confinement factor for this structure was calculated to be 5.3%. Low temperature growth, 620C, was used for the Al_{0.35}Ga_{0.65}As regions and the InGaAs quantum wells were grown at 500C, as measured by an infrared pyrometer.

Figure 1 shows a schematic cross-section of the finished device. It is noted that the HFEL is a three-terminal laser since both the collector and the emitter(denoted gate for the FET) are available to inject holes into the quantum wells, and the source supplies electrons. Therefore, the device exhibits two modes of operation source/emitter and source/collector. In the source/emitter mode typical pulsed threshold currents for 5, 10, and 15 µm wide devices were 22mA, 32mA, and 34mA, corresponding to threshold current densities of 970, 710, and 500 A/cm² respectively. Under CW operation at room temperature they exhibited threshold currents of 29mA, 38mA, and 40mA respectively. Figure 2 shows the measured light output versus current characteristics in the source/emitter mode for a 10µm wide and 350µm long laser under pulsed operation. The external efficiencies were typically 45-50% for both pulsed and CW operation. The inset of figure 2 shows the far field angle parallel to the junction for a 10µm wide laser, which indicates that the lateral current injection is uniform. Figure 3 shows the small-signal modulation response for the source/emitter mode at different current levels for a 5µm wide and 400µm long laser. the maximum -3dB cut off frequency is 4GHz at an output power of 6.3mW, which translates to a current of $I = 2 I_{th}$.

The devices were also characterized in the source/collector mode with typical pulsed threshold currents of 22mA, 26mA, and 33mA for 5, 10, and 15µm wide devices respectively. CW operation was achieved with threshold currents as low as 23mA for a 10µm wide and 450µm long device. Typical lasing wavelengths for both modes were 1.02µm.

Figure 4a and 4b show the drain output characteristics for a 2µm long and 50µm wide HFET. A maximum transconductance of 95mS/mm was measured at a gate voltage of 1.3V. The peak source to drain current density is 120mA/mm, and the threshold voltage was $V_{th} = 0V$. The HFET may also be operated in bipolar mode(BICFET)[3], were the inversion channel may be considered the transistor base. Operated as BICFETs these devices exhibited current gains of 30 at a current density of $\sim 2 \cdot 10^4$ A/cm².

- [1] P. R. Claisse et. al., IEEE Lasers and Electro-Optics Society Annual Meeting, Paper SDL8.7,1990.
- [2] G. W. Taylor et. al., IEEE EDL. 10, 88 (1989).
- [3] G. W. Taylor and J. G. Simmons, IEEE Trans. Electron. Devices 32, 2345 (1985).

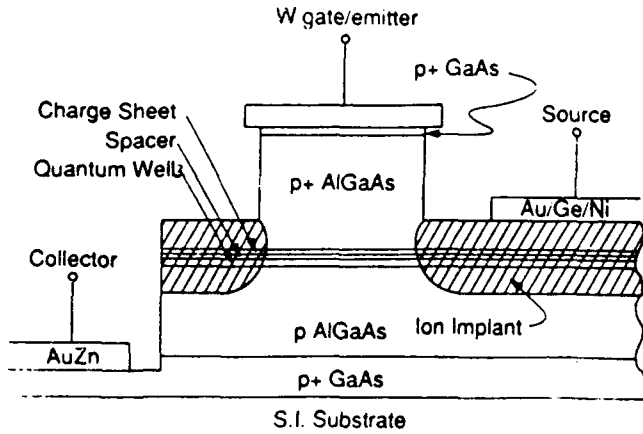
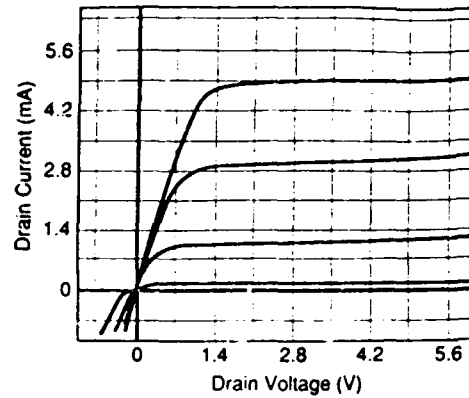


Figure 1: HFET/HELEL Device cross-section



(a)

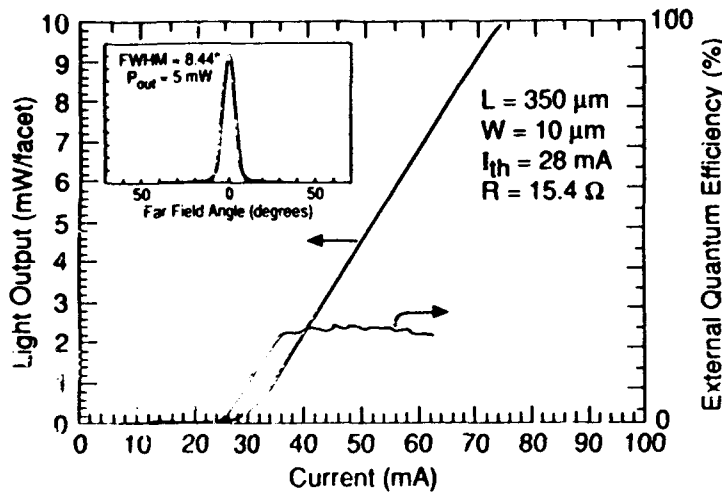
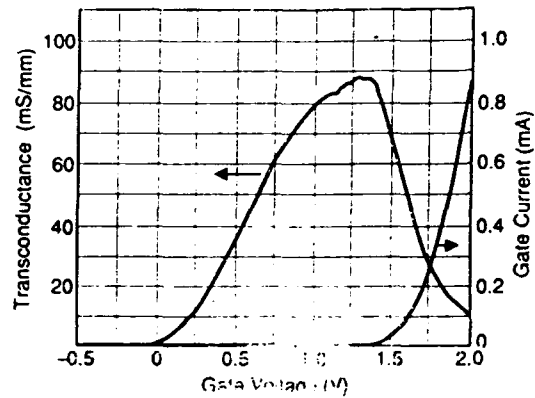


Figure 2: Light output versus current characteristics of a 10 μm wide and 350 μm long laser under pulsed operation. The inset shows the far field angle parallel to the junction.



(b)

Figure 4: 2 μm gate length HFET electrical characteristics. (a) Drain current output characteristics for gate voltages of 0, 0.4, 0.8, 1.2, and 1.6 V. (b) Transconductance (g_m) and gate conduction (I_g) as a function of gate bias V_{gs} .

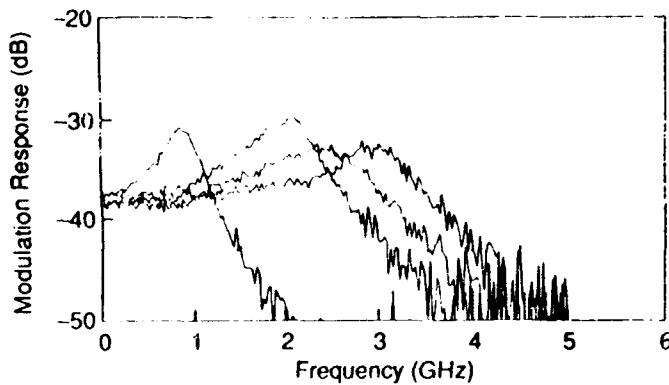


Figure 3: Modulation response of a 5 μm wide and 400 μm long device at 0.5, 2.5, 4.8, and 6.3 mW per facet. Maximum -3dB bandwidth is 4GHz at $I=2 I_{th}$.

Tuesday, April 14, 1992

Systems and Components

TuB 8:30 am–10:00 am
La Salle Ballroom C

A. Gopinath, *Presider*
University of Minnesota

TuB1-1

Theoretical Design Optimization for Multiple Quantum Well Electroabsorption Waveguide Modulator

Mee K. Chin, and William S. C. Chang
Electrical and Computer Engineering Department,
University of California, San Diego,
La Jolla, CA 92093-0407 Tel: (619)534-3627

An external waveguide intensity modulator must have low insertion loss and require low drive power. While high contrast ratio, high speed and low drive voltage have been achieved in many recent demonstrations of III-V semiconductor modulators, most modulators still suffer from large insertion loss^(1,2). A systematic approach has been developed to design a waveguide modulator which considers these four figures of merit: (1) throughput modulation depth, $\Sigma\Delta T$, where Σ is the coupling efficiency, and ΔT is the change in transmittance between the ON and the OFF states, (2) contrast ratio (CR), (3) bandwidth (Δf), and (4) voltage drive (V). Our approach addresses three important issues: (1) How does a waveguide designed to reduce coupling loss affect the other figures of merit? (2) How does the material design impact on the waveguide design? (3) What is the total performance limit?

In this approach, the waveguide is considered to be coupled directly from and to conventional single-mode optical fibers. We consider two cases of optimization for a given operating wavelength: (1) the minimization of V for a given Δf , and (2) the maximization of Δf for a given V. In addition, a required minimum CR and $\Sigma\Delta T$ must be satisfied. In a p-i-n waveguide modulator, CR and ΔT are given by

$$CR = \exp(\Delta\alpha\gamma L), \quad \Delta T = \exp(-\alpha_0\gamma L) [1 - \exp(-\Delta\alpha\gamma L)]$$

where $\Delta\alpha$ is the change in material absorption coefficient, α_0 is the residual material absorption coefficient at zero bias, γ is the filling factor of the MQW with respect to the optical mode, and L is the electrode length. The design parameters for the material structure are the well width (L_z) and the material composition (x). For a given operating wavelength λ , $\Delta\alpha$ and α_0 are calculated from L_z and x by the usual QW models. The drive voltage is given normally by $V=Fd_i$, where F is the electric field, and d_i is the thickness of the intrinsic region. Finally, the bandwidth is assumed to be RC time constant limited. It is thus proportional to $d_i/(wL)$, where w is the electrode width. Optimization of all the figures of merit in terms of material and waveguide parameters are in general very complex. We have devised a scheme that will significantly simplify the design procedure.

A simplification of the relationships between CR and ΔT and the various material and waveguide parameters is obtained by first defining two equivalent parameters

$$m = \Delta\alpha/\alpha_0, \quad X = \exp(-\alpha_0\gamma L)$$

m is a material parameter which depends on the applied electric field. In terms of the material and waveguide, the contours which satisfy a given CR and ΔT are shown in Fig. 1. The upper axis shows the propagation loss corresponding to X. The shaded area in Fig.1 represents the combinations of (m,X) which satisfy the requirements $\Delta T \geq 0.7$ and $CR \geq 20$ dB. The minimum required m for this case is 13.3. We will show that the optimal Δf and V are obtained with combinations of (m,X) that lie along the constant-CR curve which bounds the relevant (m,X) region. Along this curve, L is given by $L = -\ln(CR)/(\gamma\Delta\alpha)$. Using this fact, we will show that the optimum V and Δf are related by

$$\Delta f \ln(CR)/V = \gamma \Delta \alpha / F$$

This expression says that the optimum material structure should use x and L_z that give the maximum $\Delta \alpha / F$ ratio. At the same time, the $\Delta \alpha / \alpha_0$ ratio achievable by the material structure at that F value must also be greater than the minimum value determined by the ΔT and CR requirements.

To maximize $\Delta f / V$ for a given CR, the waveguide structure should have a maximum γ . The waveguide design must also have large coupling efficiency, which is determined by mode matching with the fiber. We will show that, for modest bandwidths (< 50 GHz) and for reasonably large $\Delta \alpha$ ($> 1000 \text{ cm}^{-1}$), the required γ is fairly small. These factors allow us to adopt a simple design which has small coupling loss, i.e. a *generic* strong passive waveguide with a large waveguide core (i.e. d_c and w). Fig. 2 illustrates the waveguide parameters. In order to have good coupling efficiency, typical values for d_c and w are $3 \mu\text{m}$. d_q is the thickness of the MQW layer. The index step (Δ_c) can be controlled by appropriate choice of the passive material composition. Only the fundamental mode is excited by a well-positioned fiber. Since γ is relatively small, the modal properties of the fundamental mode is insensitive to the active QW material structure. Thus, the QW design can be independently optimized without affecting the coupling efficiency.

Finally, d_i, d_q ($d_q \leq d_i$) and L are the waveguide parameters which, along with the optimum material structure, are designed to achieve the desired performance. For instance, to minimize V for a given Δf , d_i should be made equal to d_q . d_q must be designed to yield the γ which satisfies the condition $\gamma d_i (\mu\text{m}) = \Delta f (\text{GHz}) \ln(CR) / \Delta \alpha (\text{cm}^{-1})$. The known F and d_i determine the minimum V , $V = F d_i$. A similar algorithm applies for the case of maximizing the bandwidth. Theoretical results show that for an InGaAsP/InP modulator with $\Sigma = 1.5 \text{ dB}$ (neglecting reflection loss), $CR = 20 \text{ dB}$ and $\Delta T \geq 0.7$, (1) the minimum V can be as small as 1.5 V for $\Delta f = 20 \text{ GHz}$, (2) the maximum bandwidth is as large as 60 GHz for $V = 3 \text{ volts}$. If $CR = 10 \text{ dB}$ and $\Sigma \Delta T = 5 \text{ dB}$, $\Delta f = 40 \text{ GHz}$ for $V = 1.5 \text{ V}$.

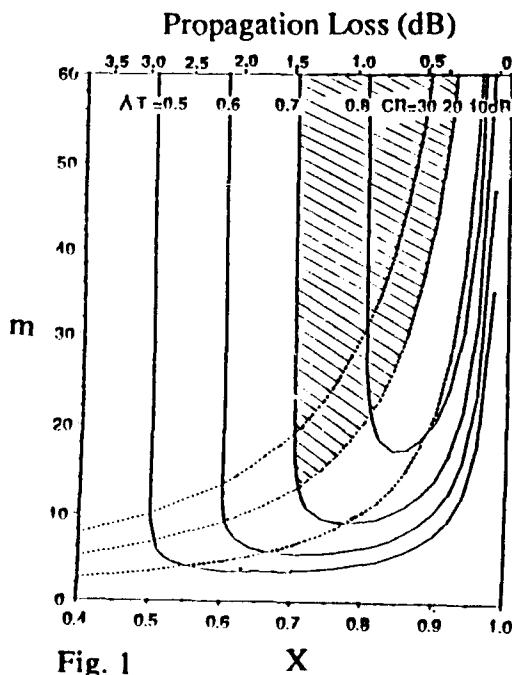
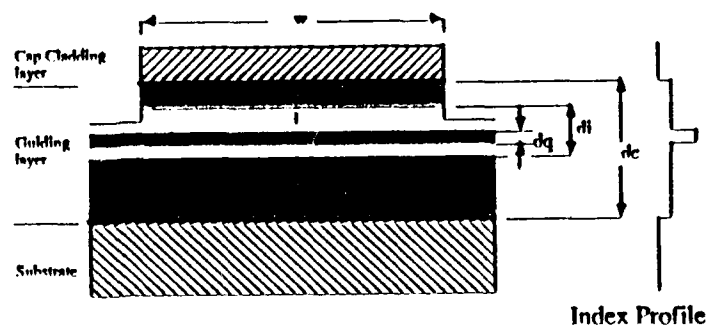


Fig. 1



- w = width of the ridge of the waveguide
- d_i = undoped intrinsic layer thickness
- d_c = high index guiding layer thickness for the waveguide
- d_q = thickness of the quantum well active layer

Fig. 2

This work is supported by RADC, ONR and DARPA.

Reference:

1. K. Wakita, I. Kotaka, O. Mitomi, H. Asahi, and Y. Kawamura, *Proc. CLEO*, vol. 7, p. 77, 1990.
2. T. Watanabe, T. Ikeda, H. Soda, and H. Ishikawa, *LEOS '91*, OE8.2, p.73, 1991.

Theoretical Investigation on Coupling Behaviour of Semiconductor / Glass Meander Coupler

H.-P. Nolting

Heinrich-Hertz Institut für Nachrichtentechnik Berlin GmbH,
Einsteinufer 37, 1000 Berlin-10, Germany, ++ 30 31002 427

The possibility to enhance the spectral performance of the recently developed meander coupler [1] as narrow band wavelength sensitive multiplexer/ demultiplexer is investigated. The device is a strongly asymmetric codirectional coupler with a periodic waveguide variation (grating) for phase matching for one center-wavelength. A narrow filter halfwidth (FWHM) can be accomplished by combining two waveguides with a large effective index and/or a large dispersion difference [2].

REFRACTIVE INDEX / FIELD DISTRIBUTION

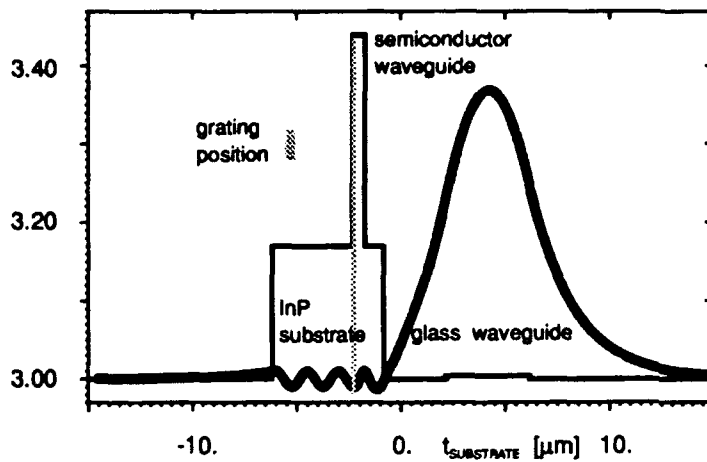


fig 1: refractive index model and field distribution of semiconductor / glass waveguide coupler

(fig. 1) is lower than the refractive index of the semiconductor substrate, leading to leaky modes. They cannot be normalized due to their infinite nature, so that overlap integrals and coupling coefficients cannot be calculated and BPM simulations fail since finite boundary conditions are required. Instead of using leaky modes, we can calculate the guided modes of the finite substrate, whose thickness is usually in the order of 100 to 300 μm , building a multimode waveguide with several hundreds of modes. We thus have to investigate the interaction of three modes: the semiconductor waveguide mode (ScM), the glass mode (GIM) and that substrate mode (SubM), whose eigenvalue is near to the eigenmode of the glass waveguide. For specific values of the substrate thickness we have phase matching between GIM and SubM and 100% energy transfer occurs. To demonstrate the fundamental behaviour in a BPM calculation, I have used the refractive index configuration shown in fig.1. Here I have chosen a reduced substrate thickness of a few μm and a high value of the refractive index of the "glass" material for more convenient calculations. The essential properties of the results are unaffected by this choice of parameters. The wave propagation for resonant coupling to the substrate is shown in fig. 2.

A narrow filter halfwidth (FWHM) can be accomplished by combining two waveguides with a large effective index and/or a large dispersion difference [2]. A FWHM reduction from 4 to 1 nm per mm device length is possible by adding a glass waveguide to the bulk InGaAsP/InP material system.

For calculating the characteristics of a vertically stacked layer structure [2], a 1D eigenvalue and BPM analysis is a well established approach. In the present case, however, the problem arises that the effective index of the glass waveguide

SUBSTRATE MODE COUPLING

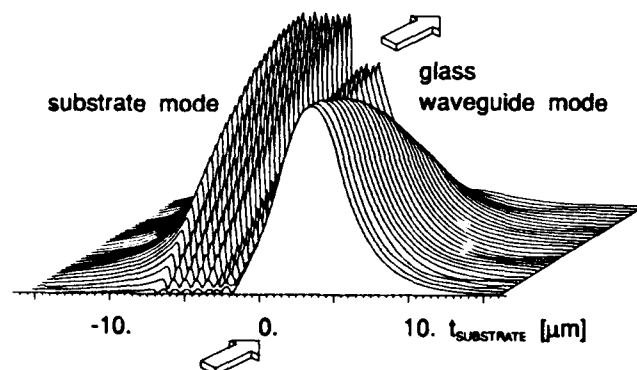


fig. 2: wave propagation illustrating resonant glass waveguide to substrate coupling (without grating)

The wave propagation for resonant coupling to the substrate is shown in fig. 2.

Due to the Fabry-Perot effect of the reflected wave from the backside of the substrate, a periodic behaviour of the phase shift as a function of the substrate thickness occurs and leads to resonances of the coupling behaviour. This is shown (dashed line) in fig. 3 for one period for the simple (without grating) waveguide combination. In between strong phase mismatch with almost no coupling occurs.

To design an efficient square meander coupler insensitive to substrate dimensions, we have to choose a substrate thickness corresponding to a phase mismatch of SubM and GIM, which is equivalent to the leaky mode situation, and to place the grating at a position of maximum field amplitude of the SubM/GIM mode. This can be done by adding a properly designed InP cladding layer on top of the ScM waveguide and placing the grating into the InP / quaternary layer (indicated in fig.1). It is

COUPLING EFFICIENCY

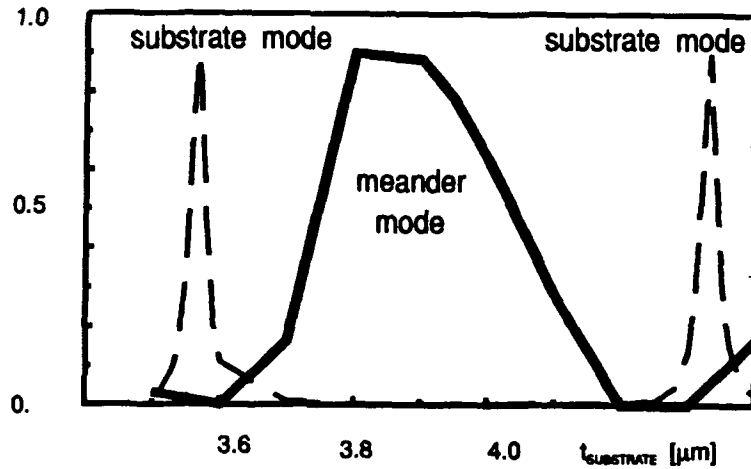


fig. 3: efficiency for substrate mode and meander mode coupling as function of substrate thickness

SQUARE MEANDER COUPLER

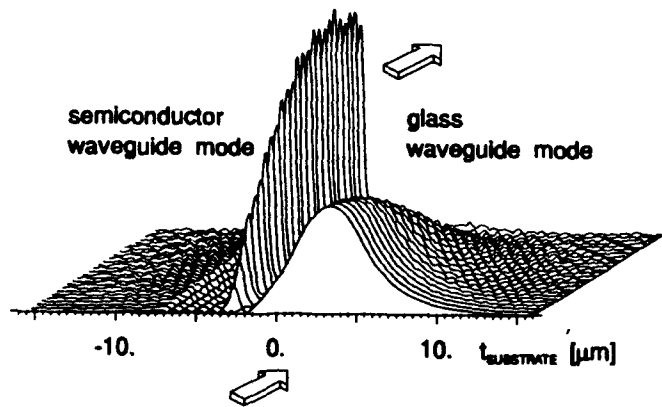


fig.4: wave propagation illustrating resonant meander coupling from glass to semiconductor waveguide

worthwhile to note, that the grating efficiency depends strongly on the substrate thickness, which controls the phase shift of the reflected wave and so the field strength at the position of the grating. Successful design is demonstrated for the same refractive index profile by grating coupling with a period length of 5.032 μm and a grating depths of 80 nm in a BPM simulation shown in fig. 4 The coupling efficiency as a function of the substrate thickness is shown in fig.3 (thick line). For a well defined interval of thickness values, complete meander coupling is possible and in the intermediate region coupling to ScM and SubM are both nearly

suppressed. Calculations of the eigenmodes for thick substrates (300 μm) and realistic refractive index values (1.5) show the same coupling behaviour. Nevertheless non parallel substrate end faces to suppress the resonant back reflections are considered to be helpful. If back reflection is not present meander coupling is always possible for the described architecture.

[1]C. Bornholdt, F. Kappe, R. Müller, H.-P Nolting, F. Reier, H. Venghaus, C. M. Weinert, Appl. Phys. Lett. 57 (24), p.2517-2519 (1990)
 [2] H.-P. Nolting, ECOC/IOOC '91, 9./12.Sept. 91, Paris, France, paper Mo.B2.4, page 65

Investigations of fabrication tolerances of narrow bandwidth directional coupler filters in InP

Remigius Zengerle and Ottokar Leminger

Deutsche Bundespost Telekom, Forschungsinstitut beim FTZ

Postfach 10 00 03, W-6100 Darmstadt, Germany

Phone: +49 6151 83-5037 Telefax: +49 6151 83-4988

Wavelength filters of narrow bandwidth are essential components of future photonic integrated circuits to be used, for example, in dense WDM systems. Based on the principle of asymmetrical directional couplers, there exist several studies and demonstrations in the InGaAsP/InP system ^{1, 2}.

In order to achieve the desired wavelength selectivity in the nanometer range, filters with a length of several millimeters will be needed. The epitaxial layers for these structures are fabricated preferably by metal organic vapor phase epitaxy (MOVPE) to obtain a good homogeneity of the optical waveguide parameters. However, even with this technological process (and using a rotating susceptor) there exist parameter fluctuations across the substrate surface with possibly significant influence on the transmission characteristic of the filter itself. For example, the thickness of the individual layers varies across the wafer. On the other hand, the material composition of the quaternary epitaxial layers changes, too, resulting in a spatial variation of their refractive indices.

We investigated theoretically the influence of waveguide parameter variations on the filter transmission characteristic with an appropriate model including the wavelength dispersion of the refractive indices. As shown in Fig.1, we use an asymmetrical directional coupler (not grating-assisted) completely buried in InP. Its planar waveguides have a different geometry and material composition so that the transmission bandwidth is reduced by enhanced material dispersion according to ³.

We assumed a linear variation of the thickness along the whole coupler length of either the upper waveguide with a large bandgap wavelength ($\lambda_g = 1450\text{nm}$) or the lower waveguide with a small bandgap wavelength ($\lambda_g = 1270\text{nm}$). Some results are plotted in Fig.2. Ideally, the untapered coupler 6 mm in length has a 3-dB bandwidth of 1.5 nm and a minimum sidelobe suppression of 9 dB (dashed line). The introduction of the thickness variation reveals three significant effects. The transmission maximum is reduced, the bandwidth is increased and the sidelobe suppression is clearly worse. In detail, a small thickness variation of only 0.4% of the lower waveguide results in a bandwidth broadening of 40 % and a remaining sidelobe suppression of only 4.7 dB. The influence of the same thickness variation of the upper waveguide is even stronger.

Small variations of the waveguide refractive indices may also cause severe distortions in the transmission characteristic. According to Fig.3, a linear variation of only 0.8 nm of the bandgap wavelength along the length of the upper waveguide results in a very pronounced distortion of the whole filter response.

With our simulation results we can deduce the stringent tolerance requirements on the homogeneity of epitaxial layers for the production of narrow-band directional-coupler filters suitable for system applications.

REFERENCES

1. A.Wakatsuki, *et al.*, *Electron.Lett.* 26, 1573 (1990)
2. R.C.Alferness, *et al.*, *Technical Digest OFC'91 (San Diego,1991)*, 143
3. Chi Wu, *et al.*, *Technical Digest OFC'91 (San Diego,1991)*, 144

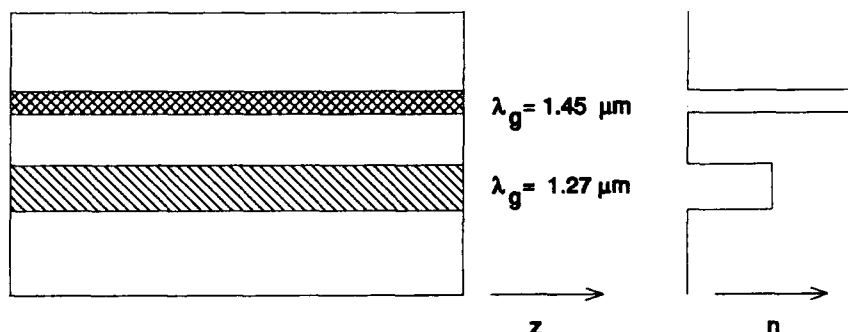


Fig.1. Device structure of the asymmetrical directional coupler filter

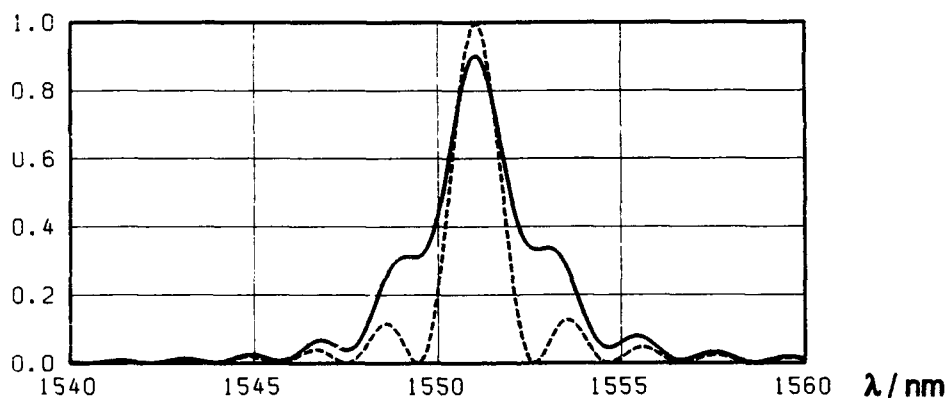


Fig.2. Transmission characteristic of the filter assuming a linear thickness variation of 0.4% for the upper waveguide along the whole coupler length

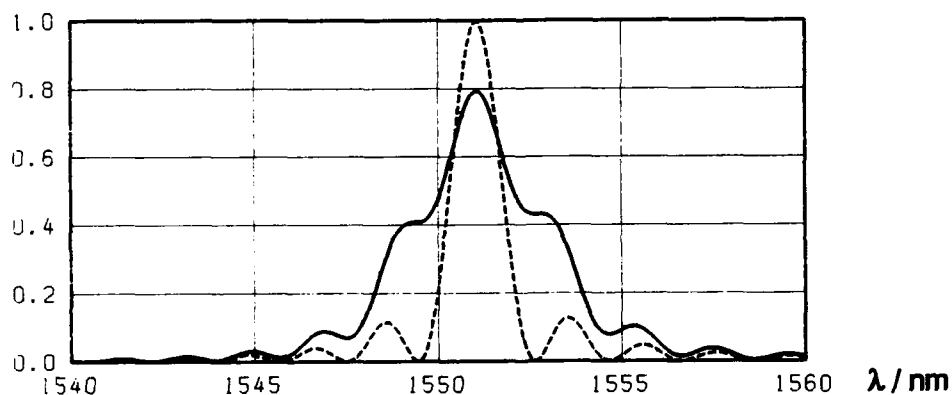


Fig.3. Transmission characteristic of the filter assuming a linear bandgap wavelength variation of 0.8 nm for the upper waveguide along the whole coupler length

A Bidirectional Propagation Algorithm for Large Refractive Index Steps and Systems of Waveguides Based on the Mode Matching Method

Georg Sztefka

Heinrich Hertz Institut für Nachrichtentechnik

Einsteinufer 37, 1000 Berlin 10, Germany

(tel. ..49-30-31002255, FAX ..49-30-31002213)

An accurate and fast propagation method for dielectric passive and active waveguides is a useful tool for OEIC design. The propagation constant, the intensity distribution, optical transmission/ reflection and the coupling efficiency characterize a device and can be calculated with several methods. However, large refractive index steps both in the propagation direction (gratings, BUTT-coupling), as well as in the transverse direction (multi waveguide structure, vertical coupler) lie above the common calculation limits of most optical modelling methods.

A standard Transfer-Matrix-Method (TFM) [1] takes into account one forward and one backward travelling wave so that the reflection and transmission characteristics can be obtained even for large refractive index steps and for any quantity of sections in the propagation direction. However, the standard TFM assumes lateral homogeneous sections and hence neglects the lateral structure, which is essential for the function of many devices (e.g. couplers).

The method presented here combines the advantages of an extended Transfer-Matrix-Method [2] for the propagation of a set of travelling waves and the accurate handling of Maxwell's boundary condition by the Mode-Matching-Method (MM-Method)[3]. Neither paraxial approximations nor restriction on the polarization (TE or TM modes) are applied.

The calculations present here are focussed on structures in one transverse and the longitudinal dimension and hence propagation through arbitrary piecewise constant slab waveguides is supposed (Fig.1). In some device applications two dimensional crosssections can be reduced by the Effective Index Method to a one dimensional problem. For more complex structures a full two dimensional treatment is aswell possible.

The extended TFM presented here includes all guided eigenmodes. An additional set of discrete radiation modes (discretized by introducing metal walls) represents the lateral structure in the presence of longitudinal discontinuities more accurately. (The extended TFM of Ref.[2] for comparison includes only the first two guided modes). All modes are propagating in forward and backward direction over the whole section length by one simple (and fast) matrix multiplication. In this way systems of parallel waveguides or other complex lateral structures can be taken into consideration.

Maxwell's boundary conditions here are satisfied by the continuity of the tangential electric and magnetic fields at the interface of adjacent sections. On the contrary other methods apply a Fresnel approximation at the boundaries [4] [5]. Any distribution of the electrical or magnetical field in a section is a superposition of all propagating modes. The continuity is attained by mode matching of the adjacent set of modes with respect to the local refractive indices at each point of the interface.

The Mode Matching Method takes into account the orthogonality of eigenmodes and matches the eigenmodes by analytically solved overlap integrals. Using eigenmodes is a very efficient way to increase the accuracy without solving a large equation system, because wave equation solutions are based on the thicknesses and the refractive indices of the layer stack. Thus, a propagating eigenmode carries a maximum of information of the lateral structure through the device and guarantees a more moderate number of propagating functions than other simple functions (sin and cos) [6].

A standard Method [1] is applied to calculate the eigenmodes and the discrete set of radiation modes automatically. By a suitable positioning of the ideal metal walls the influence on the eigenvalues and the guided mode shapes is practically eliminated.

The figures demonstrate the Method and show the calculated intensity distributions for devices with lateral and longitudinal discontinuities. A device with 21 piecewise constant sections is shown in Fig.1. The additional periodic longitudinal discontinuities of the asymmetrical (meander) coupler in Fig.1 match the phase difference of the propagating waves for complete power transfer into the output waveguide. The standing wave pattern in Fig.2 are due to the reflection from the cleaved waveguide facet.

In conclusion, a (fast) bidirectional propagation method for lateral and longitudinal discontinuities with an accurate treatment of large refractive index steps is presented. The method combines the advantages of the TFM for propagation and the Mode Matching Method for the boundaries and is applicable to passive (directional coupler, BUTT-coupling) as well as active (DBR-,DFB-,VCSE-Laser) devices.

References

- [1] J.Chilwell et al., J.Opt.Soc.Am, A-1, (1984) p742
- [2] R. März, H.-P. Nolting, Optical and Quantum Electronics 19, (1987) p273
- [3] M.C.Amann, IEEE J.Quant.El., QE-22 (1986) p1992
- [4] D. Yevick et al., IEEE J.Quant.El., Vol.26 (1990) p109
- [5] P. Kaczmarek et al., Electronics Lett., Vol. 24 (1988) p675
- [6] C.H. Henry et al., IEEE J.Quant.El., Vol.27 (1991) p523

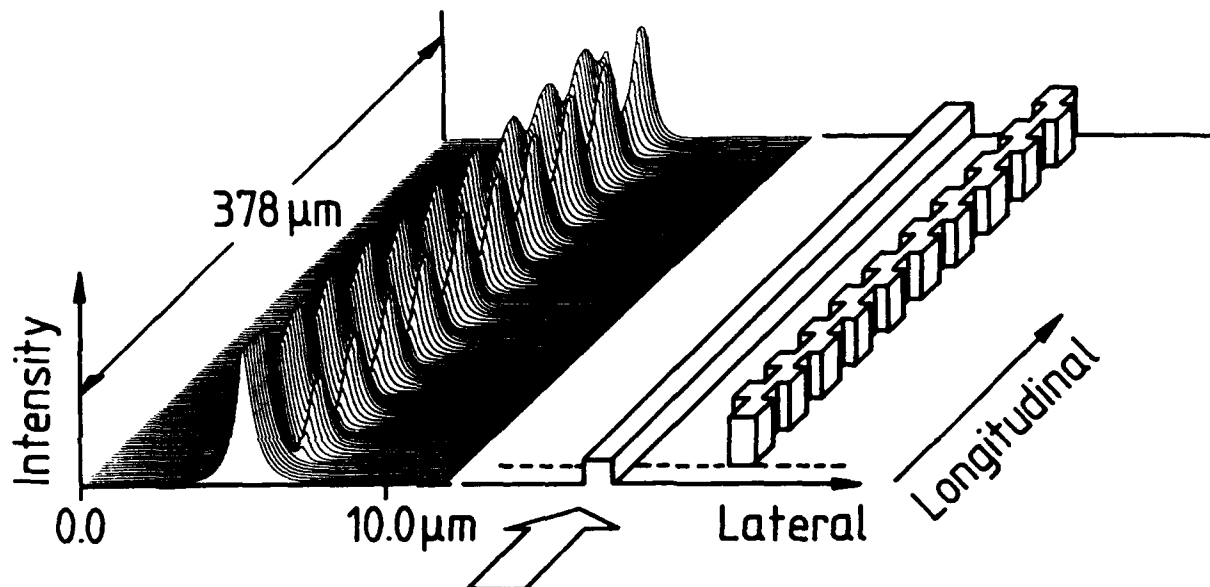


Fig.1: Intensity distribution of an asymmetrical meander coupler

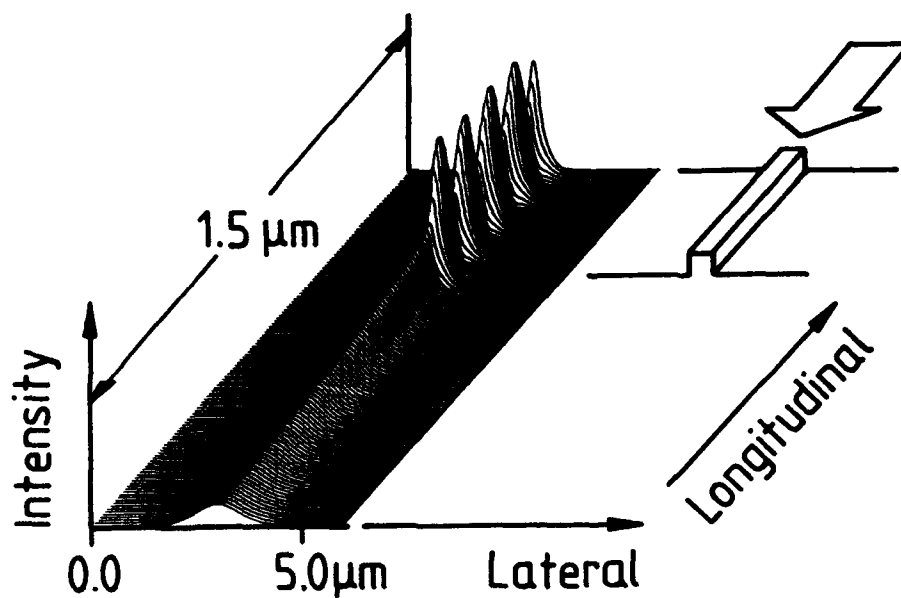


Fig.2: Reflection from the cleaved waveguide facet

TuB5-1

Analysis of Finite Beam Contributions to Waveguide Wavelength Division Demultiplexer Design

M.R. Wang and G.J. Sonek

Department of Electrical and Computer Engineering
University of California, Irvine
Irvine, CA 92717
(714) 856-6421

Micrograting devices have recently been implemented in chalcogenide [1], polymer [2], GaAs [3], and InP [4] based materials for multichannel wavelength multiplexer/demultiplexer applications. In waveguide grating demultiplexers, the micrograting length/beam width ratio ($q = d/\omega_0$) is an important parameter in determining device performance. Finite beam Bragg diffraction effects have previously been considered in the case of thick planar gratings [5,6], but should also be accounted for in the design of waveguide demultiplexers, if beam profiles, efficiencies, and channel selectivities are to be optimized in such devices.

Herein, we report on the results of a numerical study, using an impulse response technique in conjunction with coupled mode theory, that show the effects of Gaussian beam diffraction on the demultiplexer parameters of efficiency, wavelength and angular selectivities, and channel crosstalk. In the regime $1 < d/\omega_0 < 5$, with $d = 300 \mu\text{m}$, and a center wavelength $\lambda_c = 632.8 \text{ nm}$, several basic results are predicted, including: (1) a departure from the plane wave behavior of $(\text{sinc})^2$ dependence for the diffraction efficiency, with a corresponding modification in the sidelobe features; (2) beam profile distortion for given d/ω_0 ratios and diffraction angles α_d ; (3) a decrease in diffraction efficiency η with increasing q and diffraction angle α_d ; and, (4) an increase in channel crosstalk for increasing q at given detunings from the center wavelength. These results are summarized in Figs. 1 - 4, respectively, for TE - polarized light.

Fig. 1 shows the demultiplexer diffraction efficiency η as a function of both q and diffraction angle α_d , for $q = 1, 3, \text{ and } 5$, respectively. We note that $q = 0$ corresponds to the plane wave diffraction case. An increase in q is seen to result in a significant decrease in overall device efficiency and a shift in the maximum possible diffraction angle to smaller α_d . At the same time, each of the curves for q show a turning point in their α_d dependence, a region which defines the transition from single to multiple diffraction peaks and, therefore, distortion of the original Gaussian beam profile. Single peak behavior is maintained for values of $\eta > \sim 60\%$ in all cases. The regions of minimal beam distortion are the desirable regions of operation for efficient demultiplexing and fiber coupling of the diffracted beams. Angular selectivity behavior is shown in Fig. 2 for the same values of q under normal incidence conditions. For the case when the beam size is comparable to the grating interaction length ($q = 1$), the efficiency response is similar to that of the plane wave case, with nearly identical $(\text{sinc})^2$ dependence and a peak efficiency which approaches 100%. As q increases, the peak η decreases, while the sidelobe features decrease and eventually disappear, signifying the greater finite beam contributions to the diffraction process. This behavior is accompanied by a slight broadening of the curves, as measured from the full-width half-maximums (FWHM).

Demultiplexer wavelength selectivity is summarized in Fig. 3 for three values of q and the micrograting lengths of 100 and 300 μm , respectively. As expected, larger grating interaction lengths and diffraction angles are required to produce better wavelength selectivities and narrower channel spacings. For example, at $\alpha_d = 40^\circ$, $d = 300 \mu\text{m}$, and $q = 3$, a channel spacing of $\sim 4 \text{ nm}$ can be achieved. The channel bandwidth must, however, be designed with η , and the regions of minimal beam distortion, in mind. Fig. 4 shows the resulting channel crosstalk for $d/\omega_0 = 1, 3, \text{ and } 5$, respectively. A greater finite beam contribution, as shown for $d/\omega_0 = 5$, results in an increase in crosstalk for specified shifts in wavelength, primarily due to the disappearance of the diffraction

sidelobe features, as shown in Fig. 2. A change of up to -12 dB in channel crosstalk is possible, for example, when the wavelength shift, $\lambda - \lambda_c$, is 5 nm.

In summary, an analysis of finite beam diffraction effects, and their contributions to waveguide demultiplexer design parameters, have been presented. Designs that address efficiency and channel bandwidth should also account for the possibility of Gaussian beam distortion, limited ranges of diffraction angle, and variations in crosstalk, as a function of the micrograting length/ beam width ratio.

References

1. T. Suhara, Y. Handa, H. Nishihara, and J. Koyama, Appl. Phys. Lett. 40, 120 (1982).
2. M. R. Wang, G. J. Sonek, R. T. Chen, and T. Jansson, IEEE Photon. Technol. Lett. 3, 36 (1991).
3. J. Hryniewicz and Y. J. Chen, Top. Meeting Microfab. for Photon. and Optoelectron. 1991 (IEEE LEOS, Newport Beach, CA 1991), 53.
4. J. B. D. Soole, A. Scherer, H. P. LeBlanc, N. C. Andreadakis, R. Bhat, and M. A. Koza, Integrated Photonics Research 1991, Tech. Digest Series (Opt. Soc. Am., Washington, DC 1991), 123.
5. R. S. Chu and T. Tamir, J. Opt. Soc. Am 66, 220 (1976).
6. M. G. Moharam, T. K. Gaylord, and R. Magnusson, J. Opt. Soc. Am. 70, 300 (1980).

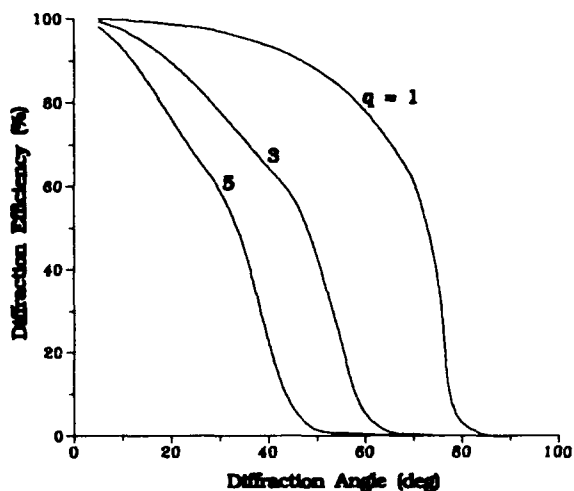


Fig.1 Diffraction efficiency as a function of q and α_d .

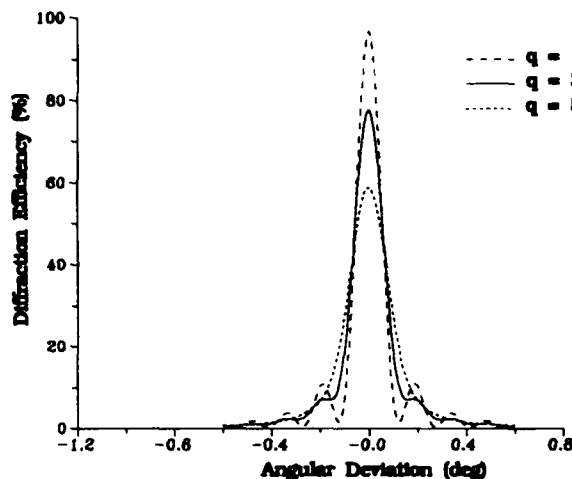


Fig.2 q dependent angular selectivity.

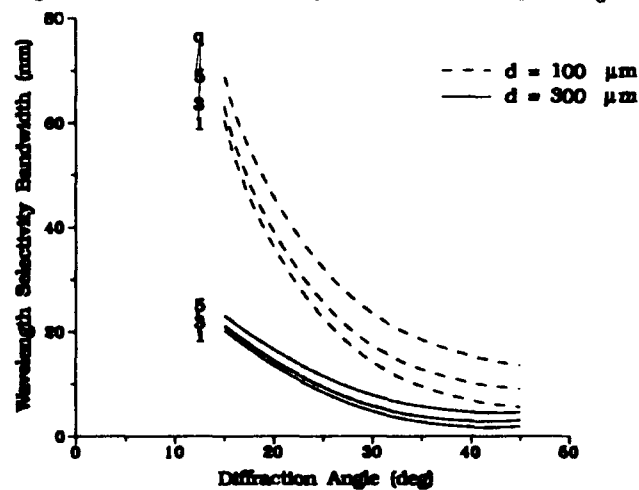


Fig.3 Effects of q, d, and α_d on wavelength selectivity bandwidth.

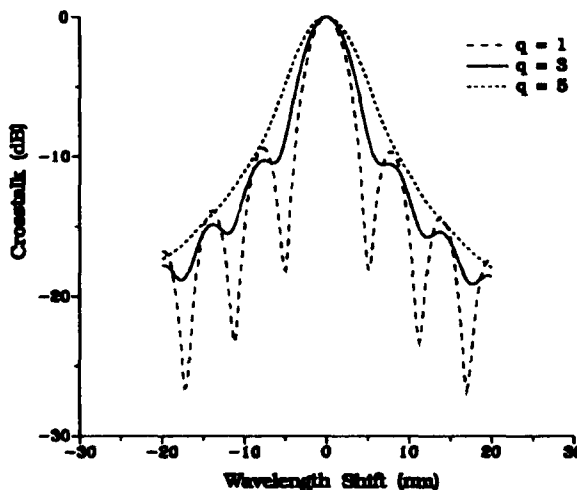


Fig.4 Crosstalk vs. q and $\Delta\lambda$.

REQUIREMENTS TO THE OPTICAL SIGNALS IN FULLY DIFFERENTIAL OPTICAL COMPUTER INTERCONNECTS

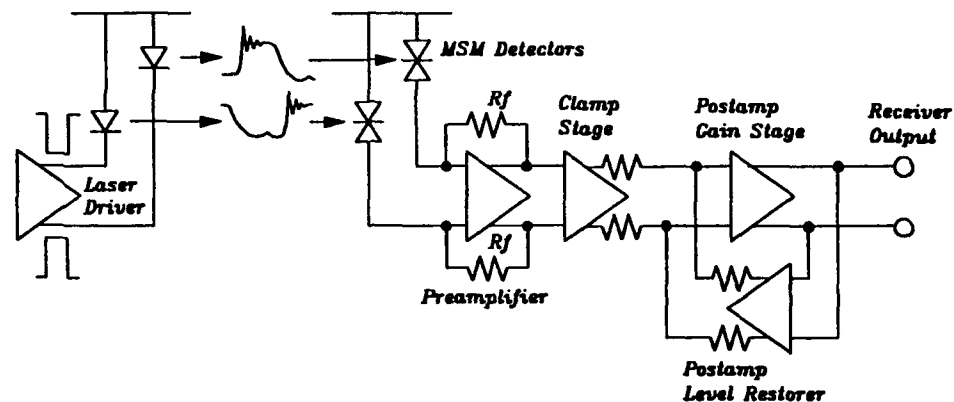
C. M. Olsen and C.-S. Li

IBM T.J. Watson Research Center, P.O. Box 704, Yorktown Heights, NY 10598

Telephone: (914) 784-7354

In dense parallel optical interconnects it is of highest importance to minimize the switching noise arising in the sharing of a common power supply through bonding wires with finite lead inductance at the driver array chip or the receiver array chip [1,2]. In general the noise increases with the number of channels. This problem can be overcome by using a fully differential transmission scheme [3] as outlined in Fig. 1. In the following we assume the complementary optical signals are generated by modulating two 825 nm laser diodes with ideal complementary drive currents. Laser parameters for a typical BH laser were used in the simulations.

Fig. 1. Schematic of fully differential optical link.



The receiver (see Fig. 1) consists of a pair of monolithic integrated metal-semiconductor-metal (MSM) photodetectors, a differential transimpedance preamplifier, a clamp stage, two gain stages and a level restoration circuit. The receiver has a dynamic range from +3 dBm to -23 dBm with a nominal bandwidth of 700 MHz (at -23 dBm). The responsivity of the photodetectors are 0.35 A/W. To minimize the latency the receiver is dc-coupled to avoid bit encoding/decoding.

We calculated the eye pattern on the receiver output for different values of the average incident power, $P_{av,1}$ and $P_{av,2}$, and extinction ratios, $R_{e,1}$ and $R_{e,2}$, on the two photodetectors to determine to what extent the receiver design can tolerate variations in the laser threshold current, laser quantum efficiency, coupling losses and detector responsivity. As a reference we show in Fig. 2 the 1 Gb/s eye pattern obtained for $P_{av,1} = P_{av,2}$ and $R_{e,1} = R_{e,2}$ using the bit sequence '1010010111000111111100001000010' in arm 1 and its complement in arm 2.

First we consider $P_{av,1} = 0$ dBm while $P_{av,2}$ is gradually reduced. Simulations were done for the extinction ratios, $R_{e,1} = R_{e,2} = R_e = 5, 10$ and 15 dB. It was found that an upper limit existed for the difference, $\Delta P_{1,2}$, between the incident power on the two detectors. $\Delta P_{1,2} = 3, 6$ and 11 dB could be tolerated for $R_e = 5, 10$ and 15 dB, respectively. Exceeding these levels results in

"spikes" on the receiver output as is shown in Fig. 3 for the case of $R_e = 10$ dB. The spikes arise due to the off-level laser relaxation oscillations, $f_{r,off}$, (typically 500-1500 MHz) in detector arm 1. Thus, the detector current in arm 1 may temporarily exceed the (reduced) on-level in arm 2 and therefore give rise to the spikes occurring at the off-level relaxation peaks. Using faster lasers reduces the problem as $f_{r,off}$ is increased further beyond the receiver bandwidth. In addition, an increase in the timing jitter with increasing $\Delta P_{1,2}$ was observed. At the maximum values of $\Delta P_{1,2}$ a half-width timing jitter of $\Delta t_{jit,max} = 85, 70$ and 170 ps for $R_e = 5, 10$ and 15 dB, respectively, was observed. This jitter is mainly caused by the finite preamplifier rise time. In computer interconnects $\Delta t_{jit,max} < 100$ ps (10% of a bit period) is required. At $\Delta P_{1,2} = 0$ dB $\Delta t_{jit,max} = 8, 25, 50$ and 105 ps for $R_e = 5, 10, 15$ and 40 dB, respectively. The increase in jitter with R_e is due to the increased delay of the optical leading edge in arm 2 when the laser bias level is decreased. Keeping $P_{av,1} = P_{av,2}$ and gradually increase the difference between $R_{e,1}$ and $R_{e,2}$ gives rise to an increasing timing jitter. For example, for $R_{e,1} = 5$ dB and $R_{e,2} = 40$ dB (this scenario could arise due to variations in the laser threshold) we estimated $\Delta t_{jit,max} = 365$ ps.

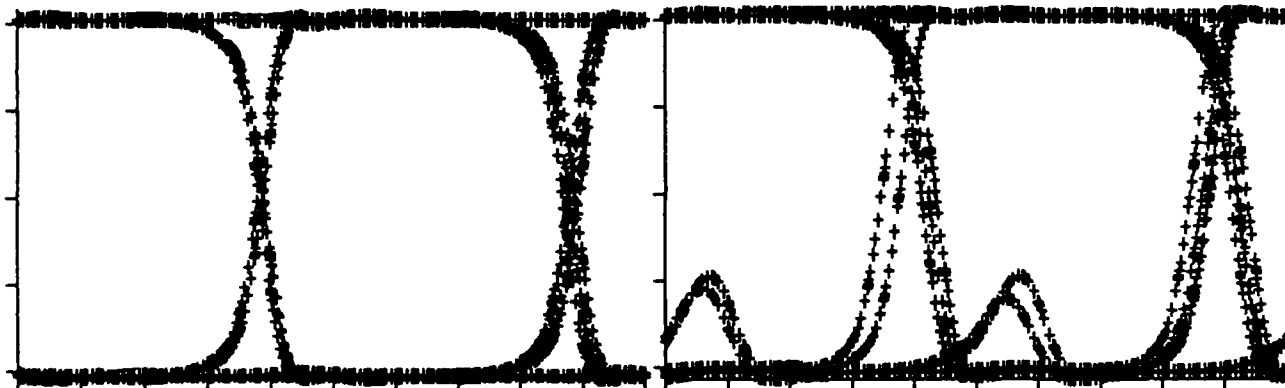


Fig. 2. 1 Gb/s simulated eye-pattern on the receiver output for $P_{av,1} = P_{av,2} = 0$ dBm and $R_{e,1} = R_{e,2} = 10$ dB (vertical: 0.5 V/div, horizontal: 200 ps/div).

Fig. 3. 1 Gb/s simulated eye-pattern on the receiver output for $P_{av,1} = 0$ dBm and $P_{av,2} = -7$ dBm and $R_{e,1} = R_{e,2} = 10$ dB (vertical: 0.5 V/div, horizontal: 200 ps/div).

It has been shown that the maximum acceptable power difference, $\Delta P_{1,2}$, is clearly smaller than the extinction ratio of the strongest signal. Ideally, optical signals with as large R_e as possible should be used such that even very large variations in the two power levels can be tolerated. However, to reduce "spikes" in the logical levels as well as timing skew we need (1) faster lasers or external modulation to increase or eliminate off-level relaxation oscillations and to reduce or eliminate bit-pattern dependent delays of the optical leading edge, and (2) high-bandwidth preamplifiers to reduce the timing range for possible switching.

[1] C.-S. Li, "Packaging Requirements ...", Proc. of OFC'91, p. 74.

[2] C.-S. Li et al, "Electrical Crosstalk ...", Proc. of LEOS'91 Annual Meeting, Paper OE6.1.

[3] C.-S. Li, "Chapter 11: Fully Differential ...", Ph.D. Dissertation, U. C. Berkeley, 1991.

Tuesday, April 14, 1992

Second Harmonic Generation in Waveguides

TuC 8:30 am–10:00 am
Pelican Room

Martin M. Fejer, *Presider*
Stanford University

TuC1-1

Blue Second-harmonic Generation in Waveguides

Hitoshi Tamada

Sony Corporation Research Center

174 Fujitsuka-cho, Hodogaya-ku, Yokohama 240 Japan (Tel:045-334-6868)

Summary

Blue second-harmonic generation (SHG) in waveguides has been investigated intensively over the past five years and has progressed significantly. Now it is thought one of the most promising candidates for a compact blue laser that is necessary for higher density optical disk systems. Cerenkov radiation SHG from a proton exchanged LiNbO_3 waveguide opened up such research stream in 1987¹⁾. Although it demonstrated a mW-level blue output using a laser diode, it unfortunately had a serious drawback of poor focusing characteristics because of its large (16°) Cerenkov angle. Then quasi-phase matching (QPM) SHG from a LiNbO_3 waveguide followed²⁾³⁾⁴⁾. The QPM SHG has progressed very rapidly with the improvement in the fabrication process for a periodic domain inversion structure. In particular, a segmented KTiOPO_4 waveguide⁵⁾ and a proton exchanged LiTaO_3 waveguide⁶⁾ reported $>10\text{mW}$ blue output with the normalized efficiency of around $100\%/ \text{Wcm}^2$. LiNbO_3 might catch up soon since various methods to fabricate a periodic domain inversion structure with a large aspect ratio have been investigated⁷⁾. However, the small tolerances in temperature ($2\text{-}3^\circ\text{Ccm}$) and a fundamental wavelength ($0.1\text{-}0.2\text{nmcm}$) are serious problems for a mass production of SHG using a laser diode. In this respect, a Cerenkov radiation SHG is still very attractive because of its large tolerances owing to automatic phase-matching characteristics.

The author and co-workers have found that a $\text{Ta}_2\text{O}_5/\text{KTiOPO}_4$ waveguide could generate an efficient Cerenkov radiation blue SHG particularly with low ($<1^\circ$) Cerenkov angles⁸⁾. The normalized efficiency is around $50\%/ \text{Wcm}$ and the blue output up to 5mW has been observed. It has been confirmed that such blue light with low Cerenkov angles can be focused to a nearly diffraction limited spot because of its small wavefront aberration.

In the presentation the recent advances for blue SHG in waveguides are reviewed with the emphasis on QPM and Cerenkov radiation SHG. And the remaining important problem of the stable, efficient coupling between a laser diode and a SHG waveguide is stated.

References

- 1) T.Taniuchi and K.Yamamoto, presented at the conf.Lasers Electro-opt., Apr.26-May1, 1987, Baltimore, MD, paper WP6.
- 2) E.J.Lim, M.M.Fejer, R.L.Byer, and W.J.Kozlovsky, Electron. Lett. 25, 132 (1989).
- 3) J.Webjorn, F.Laurell, and G.Arvidsson, IEEE/OSA J.Lightwave Technol. LT-7, 1597 (1989).
- 4) N.Nada, O.Kawakubo, and K.Watanabe, presented at the conf.Lasers Electro-opt., May12-17, 1991, Baltimore, MD, paper CTuV7.
- 5) J.D.Bierlein, C.J.van der Poel, and J.Brian Brown, presented at the conf.Lasers and Electro-opt., May12-17, 1991, MD, paper CMH3.
- 6) K.Mizuuchi, K.Yamamoto, and T.Taniuchi, presented at 52 Annual Meet., Japan Soc.Appl.Phys., 1991, paper 11p-ZN-8.
- 7) M.Yamada and K.Kishima, Electron. Lett. 27, 828 (1991).
- 8) H.Tamada, C.Isobe, and M.Saitoh, in Integrated Photonics Research 1991, Technical Digest Series, (Optical Society of America, Washington,DC 1991), pp.95-96.

TuC2-1

Fabrication of periodically reversed domain structure for second-harmonic-generation in LiNbO₃ by applying voltage

M.Yamada, N.Nada, and K.Watanabe

Applied Magnetic Research Department, Corporate Research Laboratories, Sony Corp.

141, Kita-Shinagawa 6-7-35, Shinagawa-ku, Tokyo, Japan

Tel; 81-3-3448-2547, Fax; 81-3-3448-4308

Recently there has been much interest in quasi-phase-matched(QPM) second harmonic generation (SHG) to obtain coherent blue light in LiNbO₃ waveguide¹⁾. Several techniques for the domain reversal of LiNbO₃ have been proposed^{2),3)}. By using these techniques, the domain shape is triangle and the domain region has the change in refractive index. This shape is not enough for making a fine and deep periodical domain structure of the QPM-SHG, so the conversion efficiency can not become so high⁴⁾.

We had reported that we could succeed to reverse the domain of LiNbO₃ by the electron beam bombardment⁵⁾. We have been investigating the mechanism of the domain reversal. We do not know clearly about the mechanism, but we know the charge on the positive c surface of the LiNbO₃ substrate is important for the domain reversal. So we conjectured that the domain reversal was caused by the electric field from the charge on the surface.

To confirm this, we made the electrode on the both surfaces of the positive and negative c faces, and applied the voltage. We observed the domain was reversed. Fig.1 shows the cross section of y face of this sample which was etched by HF. The domain shape is different from that made by the Ti diffusion technique or the Li₂O outdiffusion technique. This domain shape is similar to that made by an electron bombardment.

Usually, the breakdown voltage of LiNbO₃ is lower than the domain reversal voltage. We investigated about the I-V characteristic of LiNbO₃. Fig.2 shows the I-V characteristic. In this graph, in a high voltage area (I) there is the region where the current through the sample increases rapidly for a small increase in voltage and the substrate is broken. The substrate may be broken by the electron avalanche when the voltage is applied to the LiNbO₃.

Using this domain reversal technique, we have realized the 1st order QPM-SHG in the annealed H⁺ exchanged slab waveguide. The period of the periodical domain structure was 2.8 μm. The maximum SH power was 4.5 μW when the fundamental power was 77 mW. The interaction length was 0.6 mm. The normalized conversion efficiency was 28 %/W cm².

REFERENCE

1. N.Nada, O.Kawakubo, and K.Watanabe, CLEO '91, CTuV7 (1991)
2. J. Webjorn, F. Laurell, G.Arvidsson, Phot.Tech.Lett., 1,316(1989)
3. E.Lim, M.Fejer, and R.Byer, Electron. Lett., 25,174(1989)
4. F. Laurell, J. Webjorn, G.Arvidsson, IPR, Tul2 (1990)
5. M.Yamada and K.Kshima, Electron. Lett., 27, 828 (1991)

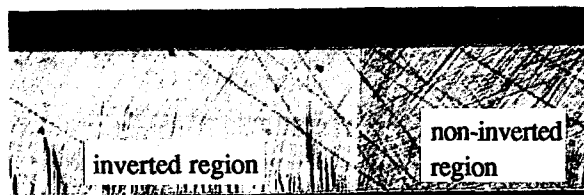


Fig.1 The cross section of the y-face of the LiNbO₃ substrate which was applied voltage. The domain was reversed. (x 83.7)

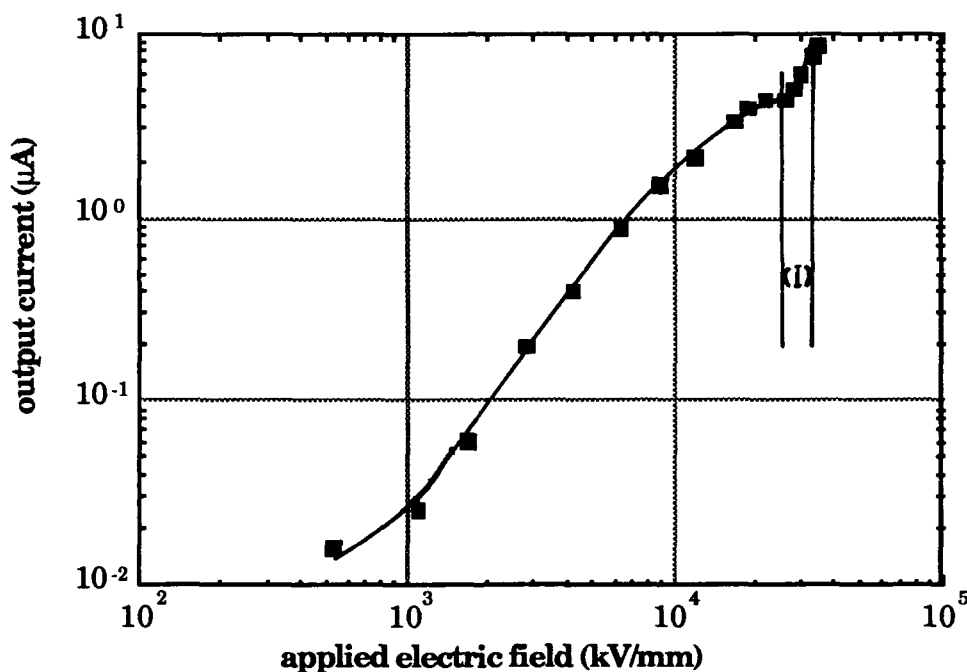


Fig.2 The I-V characteristic of LiNbO₃.

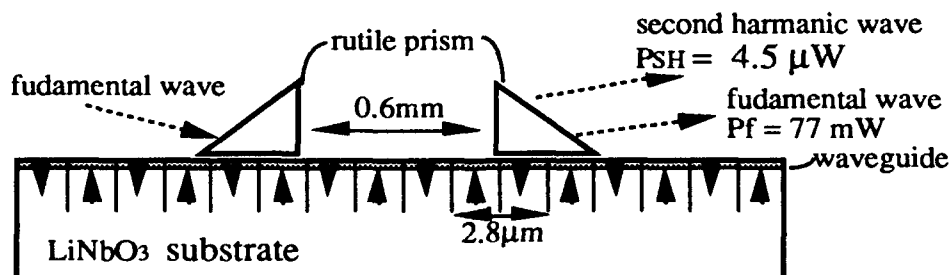


Fig.3 The outline of the 1st order QPM-SHG.

TuC3-1

Generalized Dispersion Relations for Waveguide Frequency Doubler

G.Khanarian and G.Hunte
Hoechst Celanese Corporation
86 Morris Ave.
Summit, N.J. 07901
(908) 522 7918

The optimum design of an efficient waveguide frequency doubler depends on many parameters such as the refractive indices of the guide n_2^ω and cladding n_1^ω materials, their respective dispersions from ω to 2ω ($\omega=2\pi/\lambda$), the thickness of the waveguide t , and the fundamental wavelength λ . Furthermore, it is desirable that the waveguide be noncritically phase matched with respect to a) random thickness fluctuations which arise from the fabrication process, b) variations of fundamental wavelength due to characteristics of the laser source and c) changes in ambient temperature. Otherwise additional components may have to be added to stabilize the output of the frequency doubler. Since phase matching depends critically on $(\sin x/x)^2$, where $x=2\pi\Delta N L/\lambda$ (L = length of waveguide), we have developed a theory for the dispersion $\Delta N=N^{2\omega}-N^\omega$ (N is effective index at ω) of the waveguide frequency doubler based on the generalized waveguide parameters $V^\omega, V^{2\omega}$ where $V^\omega=2\pi t/\lambda\sqrt{(n_2^\omega)^2-(n_1^\omega)^2}$. We consider the case where both the fundamental and harmonic are zeroth order modes, since this results in the most efficient type of waveguide doubler. The characteristic equation for a zeroth order mode in a symmetric slab waveguide is solved according to the formulation of Botez [1] and we find that the generalized dispersion D is,

$$D(V^\omega, \alpha) = \frac{\Delta N - \Delta n_2}{(n_2^\omega - n_1^\omega)} = \cos(\psi^\omega/2)^2 - \cos(\psi^{2\omega}/2)^2 (\alpha/2)^2 \quad (1)$$

where $\psi^\omega, \psi^{2\omega}$ are the solutions to the symmetric guide equation $\psi^\omega/V^\omega = \cos(\psi^\omega/2)$ at ω and 2ω , $\alpha = V^{2\omega}/V^\omega$ and $\Delta n_2 = n_2^{2\omega} - n_2^\omega$ is the dispersion of the guide material, respectively. Fig. 1 is a plot of D versus V^ω for different values of α . We find three interesting cases; 1) $\Delta N \neq 0$. Phase matching (P.M) occurs only with a grating (quasi phase matching[2]), 2) $\Delta N = 0, D < 0, \alpha > 2$, P.M. occurs in a uniform waveguide with a normal dispersive guide and an anomalously dispersive cladding, 3) $\Delta N = 0, D > 0$, P.M. occurs with an anomalously dispersive guide and a normal dispersive cladding. The special case $\Delta N = 0, D = 0$, occurs when the guide medium has zero dispersion. These three cases can be realized with organic and polymeric materials.[3]

Next we consider noncritical phase matching i.e when the phase matching condition is insensitive(to 1st order) to changes in a waveguide parameter, such as thickness t , wavelength λ and temperature T ; so that

$$\frac{d}{d\xi} \left(\frac{\Delta N}{\lambda} \right) = \frac{d}{d\xi} \left(\frac{\Delta n_2}{\lambda} \right) + \frac{d}{d\xi} [(n_2^\omega - n_1^\omega) D] = 0 \tag{2}$$

where $\xi = t, \lambda, T$. Let us consider the relatively simple case of $\xi = t$ [4]. Then (2) reduces to

$$\frac{d}{dt} \left(\frac{\Delta N}{\lambda} \right) = (n_2^\omega - n_1^\omega) \frac{\partial D}{\partial V^\omega} \frac{\partial V^\omega}{\partial t} \tag{3}$$

since α is independent of t . Noncritical phase matching with respect to thickness fluctuations occurs when $d/dt(\Delta N/\lambda) = 0$ i.e when $\partial D/\partial V^\omega = 0$. Fig. 2 shows the pairs of values($V^\omega, \sqrt{2}\omega$) so that $\partial D/\partial V^\omega = 0$. Noncritical phase matching with respect to λ and T occurs when $d/d\xi(\Delta n_2/\lambda)$ is less than a critical value so that (2) is satisfied. Thus it should also be possible to design frequency doubling waveguides which are not so sensitive to fluctuations in laser sources and ambient temperature.

References:

- [1] D.Botez , RCA Rev. 39, (1978) 577
- [2] C.J.van Der Poel, J.D.Bierlein, J.B.Brown and S.Colak, Appl. Phys. Lett. 57 (1990) 2074
- [3] R.A.Norwood and G.Khanarian, Elect. Lett. 26(1990) 2105
- [4] E.J.Lim,S.Matsumoto and M.M.Fejer, Appl. Phys.Lett. 57(1990) 2294

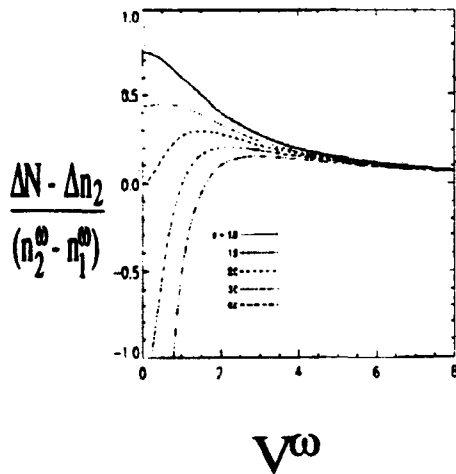


Fig. 1 Generalized dispersion $D(V^\omega, \alpha)$ versus V^ω , for different values of α .

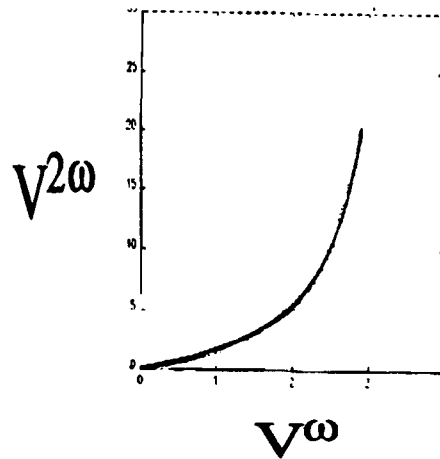


Fig.2 Pairs of values ($V^\omega, \sqrt{2}\omega$) for which $\partial D/\partial V^\omega = 0$.

Dynamic Properties of Contra-Directional Second-Harmonic Generation in Periodically Nonlinearity-Modulated Structures

Masayuki Matsumoto and Kohsuke Tanaka

Osaka University, Faculty of Engineering, Department of Communication Engineering

2-1, Yamada-Oka, Suita, Osaka 565, Japan
Tel.+81-6-877-5111 ext.4753, Fax.+81-6-875-0506

Quasi-phase-matched (QPM) second-harmonic generation (SHG) in periodically domain-inverted ferroelectric waveguides has been extensively studied in recent years for use in efficient frequency doubling of infrared radiation emitted from laser diodes[1]-[4]. The period of the domain inversion is usually chosen to be $\Lambda = m\lambda/\{2|n_1 - n_2|\}$, where λ is the fundamental wavelength, m is the order of QPM, and n_1 and n_2 are the effective indices of fundamental and second-harmonic waves, respectively. When the period is shortened to $\Lambda = m\lambda/\{2(n_1 + n_2)\}$, the incident fundamental wave excites the second-harmonic wave propagating in the direction opposite to the fundamental wave[5],[6]. The feedback provided by the counterpropagation of the second-harmonic wave gives rise to the appearance of interesting properties such as bistability and switching in the output second-harmonic power. In this work we analyze numerically the dynamic properties of the contra-directional SHG in periodically domain-inverted structures(Fig.1).

The coupled-wave equations governing the contra-directional SHG are

$$\begin{cases} \frac{\partial e_1}{\partial z} + \frac{1}{v_{g1}} \frac{\partial e_1}{\partial t} = \kappa e_1^* e_2 \exp(j \Delta k z) \\ \frac{\partial e_2}{\partial z} - \frac{1}{v_{g2}} \frac{\partial e_2}{\partial t} = \kappa e_1^2 \exp(-j \Delta k z) \end{cases}$$

where e_i 's and v_{g_i} 's are the normalized electric-field envelopes and group velocities of the fundamental ($i=1$) and second-harmonic ($i=2$) waves, $\Delta k = 4\pi(n_1 + n_2)/\lambda - 2m\pi/\Lambda$, and κ the coupling coefficient ($= 2\sqrt{2}\omega d(\mu_0/\epsilon_0)^{3/4}/(m\pi n_1 \sqrt{n_2})$ for the case of plane-wave interaction). Effect of the group-velocity dispersion is neglected here. We make the variable transformations $u = z + v_{g2}t$ and $v = z - v_{g1}t$, and integrate the equations along the u and v axes using the predictor-corrector algorithm.

Fig.2 shows the SHG efficiency versus normalized input intensity in steady state ($\partial/\partial t=0$) for $\Delta kL=15$, which is obtained by analytical calculation using Jacobian elliptic functions[5],[6]. Bistable feature is seen in the fundamental branch in the range $14 < I_1(0) < 19$. Fig.3 shows the response of the SHG efficiency η to step inputs. After experiencing transient variations for $T < 15$, the efficiency becomes constant. The values of η at $T=40$ correspond to those of the points indicated by C,D,E, and F in Fig.2 for $I_1(0) = 20, 30, 40$, and 50 , respectively. Fig.4 demonstrates a bistable operation of the structure. The output second-harmonic intensity is switched between two states A and B by narrow triggering pulses applied on the dc bias of the input intensity. The normalized intensity $I_1 = 15$ corresponds to $\cong 60 \text{ mW}/\mu\text{m}^2$ for LiNbO_3 with $L = 1 \text{ cm}$, $m = 1$, and $\lambda = 0.84 \mu\text{m}$.

Realization of the contra-directional SHG requires the fabrication of a fine nonlinearity grating which has a period of the order of a fraction of μm . Such a fine grating may be holographically produced with self-organization mechanism in optical fibers[5].

References

- [1] E.J.Lim, M.M.Fejer, R.L.Byer, and W.J.Kozlovsky, *Electron.Lett.*, 25,11,731(1989).
- [2] J.Webjörn, F.Laurell, and G.Arvidsson, *IEEE Photon.Technol.Lett.*,1,10,316(1989).
- [3] C.J.van der Poel, J.D.Bierlein, J.B.Brown, and S.Colak, *Appl.Phys.Lett.*,57,20,2074(1990).
- [4] K.Mizuuchi, K.Yamamoto, and T.Taniuchi, *Appl.Phys.Lett.*,58,24,2732(1991).
- [5] P.St.J.Russell, *IEEE J.Quantum Electron.*, 27,3,830(1991).
- [6] M.Matsumoto, K.Tanaka, and T.Kimura, National Convention Record, IEICE, C-202(1991).

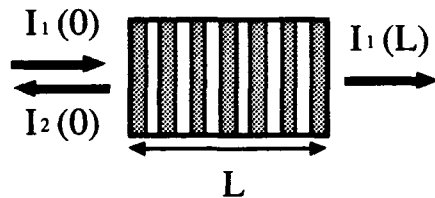


Fig.1. Contra-directional second-harmonic generation in a periodically nonlinearity-modulated structure.

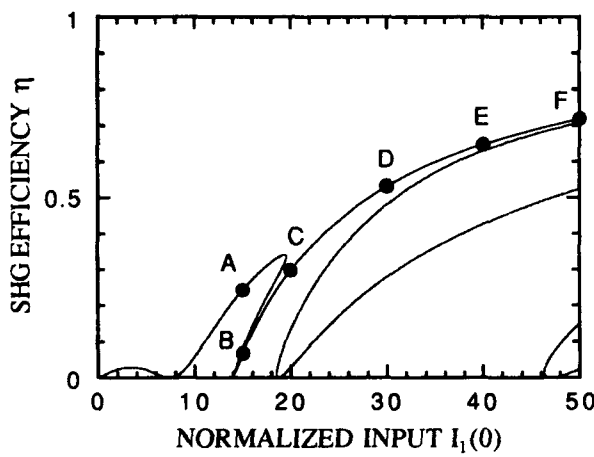


Fig.2. SHG efficiency $\eta = I_2(0)/I_1(0)$ versus normalized input intensity $I_1(0)$ in steady state for $\Delta kL=15$. I_i 's are defined by $|\kappa L e_i|^2$.

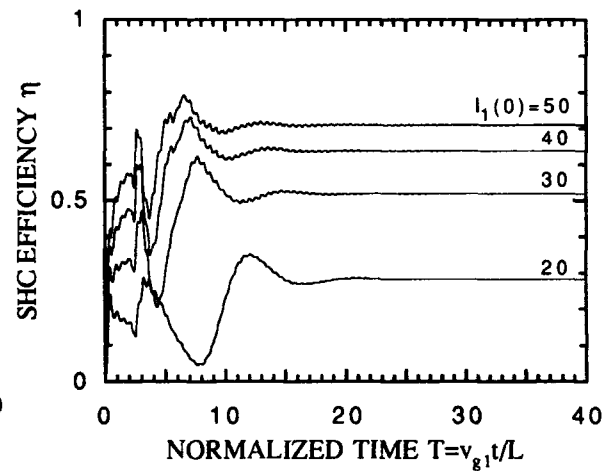
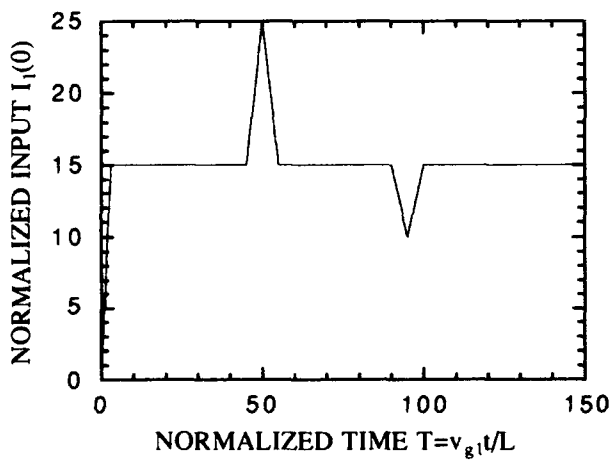
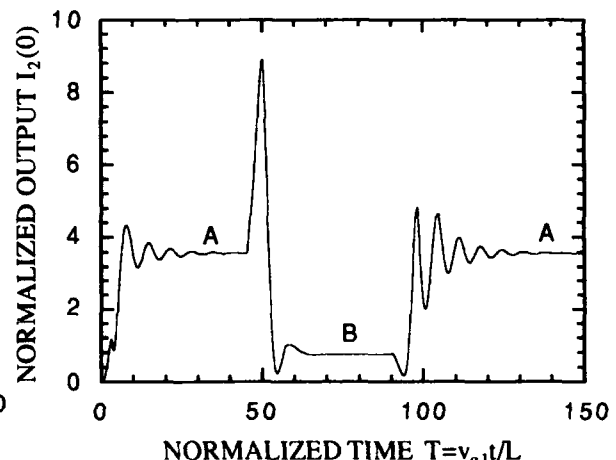


Fig.3. Response of SHG efficiency to step inputs ($\Delta kL=15$).



(a) Input intensity $I_1(0)$.



(b) Output intensity $I_2(0)$.

Fig.4. Bistable operation ($\Delta kL=15$).

Second Harmonic Generation at 1.3 μ m Wavelength in InGaAsP Waveguide

M. Cada

Department of Electrical Engineering, Technical University of Nova Scotia, Halifax, Nova Scotia, B3J 2X4, Canada; Presently with SiemensAG, ZFE ME FKE32, Postfach 830953, Otto-Hahn Ring 6, 8 München 83, Germany. Tel. (49) 89-636 44677

M. Svilans

Advanced Technology Laboratory, Bell-Northern Research (BNR) P.O. Box 3511, Station C, Ottawa, Ontario, K1Y 4H7 Canada. Tel. (613) 763 3598

S. Janz

National Research Council (NRC) and Solid State Opto-Electronics Consortium(SSOC) Ottawa, Ontario, K1A 0R6, Canada. Tel. (613) 993 4449

R. Bierman

Department of Engineering Physics, McMaster University, Hamilton, Ontario, L8S 4M1, Canada

R. Normandin

National Research Council (NRC) and Solid State Opto-Electronics Consortium(SSOC) Ottawa, Ontario, K1A 0R6, Canada. Tel. (613) 993 4449

J. Glinski

Advanced Technology Laboratory, Bell-Northern Research (BNR) P.O. Box 3511, Station C, Ottawa, Ontario, K1Y 4H7 Canada. Tel. (613) 763 3598

Abstract.

We report the first surface emission of red light from an InGaAsP/InP waveguide, generated by non-linear mixing of counter-propagating guided 1.3 μ m waves.

SUMMARY

Introduction

The non-linear mixing of counter-propagating guided waves was predicted, and demonstrated in non-semiconducting materials [1]. The theoretical prediction [2] that large cross-sections can be obtained in semiconductors if losses at the harmonic wavelength are controlled has been subsequently verified [3] and many interesting demonstrations and applications proposed [5], mostly using the GaAs-based material system. We present our latest results in the InGaAsP/InP system, which is of particular interest to the fiberoptics communications field.

Theory and design

In the InP-based material system, the second order susceptibility non-linear coefficient is at least four times larger than that of GaAs, but with the disadvantage of higher absorption losses in the visible spectrum. In fact, as it was demonstrated in [2], an AlGaAs/GaAs structure can be designed to have negligible losses for wavelengths above about 550nm. This is not the case with the InP system where the quaternary layers of InGaAsP have even higher absorption loss than those of InP.

The design procedure followed basically that of [6,7] except that a more rigorous model was employed by including the exact phase contributions of all interfering SHG plane waves and multiple reflections within the multilayer. In some configurations this model yielded very different results for an AlGaAs-based structure from those obtained with the approximate calculations of [4]. Details of the theoretical our new model will be published elsewhere.

The designed structure comprised 9 alternating layers of InGaAsP ($\lambda_g=1.23\mu\text{m}$) and InP, each 94nm thick (Fig. 1). The calculated non-linear cross-section, A_{NL} , was on the order of $10^{-8} - 10^{-9} \text{ W}^{-1}$ at $\lambda=1.3\mu\text{m}$, depending on the value of d_{36} which is not experimentally known for InGaAsP. Values of $5.5\mu\text{m}^{-1}$ and $6.5\mu\text{m}^{-1}$ were used for the absorption coefficients of InP and InGaAsP, respectively, at $\lambda=650\text{nm}$.

Experimental Results

Nine layers of alternating InGaAsP and InP were grown on <100> InP substrate by low pressure MOCVD were n-doped with silicon to a level of $\sim 10^{17} \text{ cm}^{-3}$. The thicknesses of the layers were 102nm and 108nm for InP and InGaAsP, respectively.

TuC5-3

The material was transparent at the fundamental wavelength and of excellent quality. Ridge waveguides of various widths, nominally 2–7 μm , were etched in order to compare the slab and the ridge guide performance.

Two sources were used to pump the structures: a YAG laser oscillating at 1.32 μm in CW and Q-switched modes through a single mode fiber; and a CW semiconductor laser diode, a BNR standard ridge guide structure, coupled through two 40x objectives and polarisation control elements. In both cases power levels of ~1mW were achieved in the waveguide.

Since a counter-propagating beam was supplied by the reflection at the cleaved edge of samples (~30%), unilateral pumping was sufficient. A silicon CCD camera with a computerized readout system was used to image and detect the SHG signal. Infrared as well as visible filters were employed to select the desired signal. Figure 2 shows a typical arrangement used in the experiments.

Figure 3 is a photograph of the generated SHG signal. The beaded streak running across the whole length (0.5mm) of the sample exhibits a spatial periodicity of about 100 μm due to the beating of the TE and TM fundamental modes.

About 0.1pW CW of very directional SHG signal radiated at $\lambda=650\text{nm}$ (red light) from a ridge waveguide. From the measured total SHG CW power, the estimated fundamental coupled power and the dimensions of the radiating area, A_{NL} was determined to be $\sim 4 \cdot 10^{-9} \text{ W}^{-1}$ and $\sim 6.5 \cdot 10^{-10} \text{ W}^{-1}$ for the ridge and slab waveguides respectively, excellent agreement with the theory. It should be noted that the average SHG signal scales approximately as the inverse duty cycle when the pump power is pulsed at an average power the same as CW.

As the waveguide supports both the $\text{TE}_{0,1}$ and $\text{TM}_{0,1}$ modes with different wave vectors propagating in opposite directions, four modes of different polarizations mixed to give a total of eight SHG beams radiating at slightly differing angles from the structure. These correspond to the eight lines in the symmetrical Fourier plane image of the SHG radiation (Fig.4). The faint lines near the center of the figure arise from the mixing of the TE_0 and TM_0 modes; the two brightest ones, due to the TE_1 and TM_1 modes, are the most intense because the first-order mode peak field is nearer the surface of the guides than for the zero-order mode. The

outlying set of lines results from the mixing of the TE_1 with TM_0 , and TM_1 with TE_0 modes.

It is also worth mentioning that all samples including a single InGaAsP slab waveguide produced measurable SHG signals with the CW operated YAG laser as well as with a $1.3\mu\text{m}$ semiconductor laser.

Conclusions

The first surface emission of second-harmonic red light from an InGaAsP/InP waveguide structure was obtained from the non-linear mixing of two counter-propagating guided modes at $1.3\mu\text{m}$. A multi-layer embedded in a waveguide was employed to dramatically enhance the total radiated power. Pumping with a semiconductor laser yielded observable SHG signals, which is significant for potential applications in monolithic integration

References

- [1] R. Normandin, G.I. Stegeman, *Optics Letters*, 4,58 (1979).
- [2] P.J. Vella, R. Normandin, G.I. Stegeman, *Appl. Phys. Lett.*, 38, 759 (1981).
- [3] D. Vakhshoori, J. Walker, S. Digaili, S. Wang, J.S. Smith, *Appl. Phys. Lett.*, 55, 1164 (1989)
- [4] R. Normandin, S. Létourneau, F. Chatemond, R.L. Williams, *IEEE J. Quantum Electron.*, 27,6 (1991).
- [5] J. P. van der Ziel, M. Ilegems, *Appl. Phys. Lett.*, 28, p.437 (1976)
- [6] R. Normandin, F. Chatemond, R.L. Williams, *Electron. Letters*, 26,25 (1990).
- [7] R. Normandin, F. Chatemond, R.L. Williams, paper WP29, *Digest Nonlinear Optics: Materials, Applications & Devices*, Kanai, Hawaii, July 1990.

Acknowledgments

M. Cada and R. Bierman wish to acknowledge support for this work from Natural Sciences and Engineering Research Council of Canada and from Bell-Northern Research, Ltd. in Ottawa. R. Bierman also wishes to acknowledge the support of Prof. J. Simmons and Prof. D. Thompson. Use of National Research Council Solid State Optoelectronic Consortium facilities is also appreciated. The crystal growth of the structures by C. Larocque are also gratefully acknowledged.

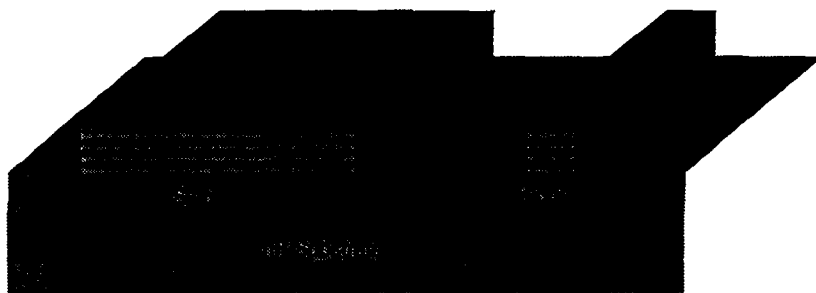


Fig. 1 Diagram of the InP/InGaAsP waveguide structure

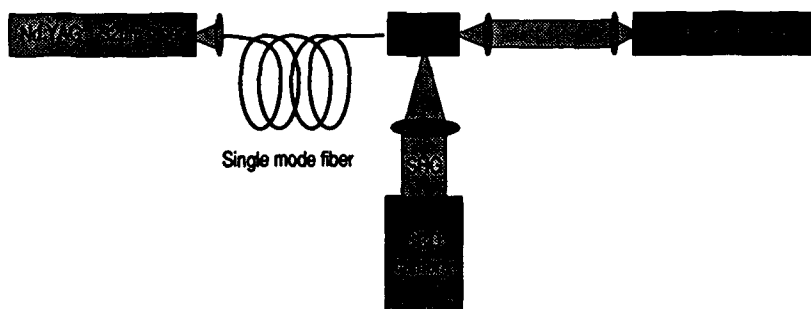


Fig. 2 Experimental set-up



Fig. 3 Photograph of the surface emitting second-harmonic signal



Fig. 4 Photograph of the Fourier transform of the second-harmonic signals

Tuesday, April 14, 1992

Dielectric Waveguides and Devices

TuD 10:30 am–12:00 m
La Salle Ballroom B

Joe Lorenzo, *Presider*
Hanscom Air Force Base

A Novel Vertical Directional Coupler Made by Graded-index Ion-exchanged Slab Waveguides

P.C. Noutsios, G.L. Yip, and J. Albert*

McGill University, Department of Electrical Engineering
3480 University, Montreal, Quebec, Canada H3A 2A7

Passive waveguide components fabricated by $K^+ - Na^+$ ion-exchange in glass have demonstrated great potential for low-loss single-mode integrated optical devices. Recently, active components made by combining these ion-exchanged guides with overlayers of semiconductor have received considerable interest for optical detection applications¹. In this waveguide-detector geometry, single-mode surface guides are used, which are not adequate for efficient fiber-guide coupling. An improved configuration would allow for fiber coupling to a buried guide (with minimal insertion loss) and efficient power transfer to a surface guide through a vertical directional coupler (see Fig. 1). Here, we report, for the first time, the fabrication and measurement of vertical directional couplers made by field-assisted K^+ -ion exchange in glass with comparison to modelled results.

The vertical coupler, comprised of two parallel slab waveguides (see Fig. 2), was fabricated by a three-step electric field-assisted K^+ -ion exchange in soda-lime glass². The buried guide 2 was made by a two-step exchange, using an applied field of 50 V/mm in the first step and 75 V/mm in the second step with exchange times varying from 5 to 10 min, while the single-mode surface guide 1 by a one-step exchange with 50 V/mm and exchange times ranging from 5 to 15 sec at 385°C. The TE and TM effective indices of the even (N_{even}) and odd (N_{odd}) mode m-lines (see Fig. 3(a)) were measured by prism-coupling at $\lambda = 0.633 \mu m$. The relative intensities of the normal modes were measured with an IR vidicon and oscilloscope. An input lens was used to excite both modes simultaneously yielding a streak of periodic dots, representing power transfer, as shown in Fig. 3(b).

The modelling of the coupler graded-index (GRIN) profile was accomplished by solving the planar non-linear ion-exchange equation³. Surface and buried concentration profiles were modeled using appropriate initial and boundary conditions. The equation was solved by a finite difference scheme with the resultant GRIN profile shown in Fig. 4.

The directional coupler was analyzed by the normal-mode method. Using the measured N_{even} and N_{odd} and the power ratio between them, key properties such as the coupling coefficient κ , length L_c , transfer efficiency F , and the individual slab indices (N_{e1}, N_{e2}) were deduced⁴. With the modelled coupler configuration (Fig. 2), the depth d_2 was chosen at the $1/e$ point of the maximum peak of the diffusion simulated buried guide, whereas d_1 was taken as the effective surface guide depth². The indices n_2 and n_4 were deduced by constructing an equivalent step-index (ESI) profile such that the step-index guides have effective indices equal to (N_{e1}, N_{e2}). Then, κ and L_c are calculated using the coupled-mode formalism⁵ and compared to the measured results (see Table 1). The discrepancies could be due to the fields not being accurately provided by the ESI model. Improved results based on the GRIN profile and the BPM method will be presented at the meeting.

REFERENCES

1. A. Yi-Yan *et al*, IEEE Photon. Tech. Lett., 1, 379-380, 1989.
2. G.L. Yip *et al*, Opt. Lett., 15, 789-791, 1990.
3. H.J. Lilienhof *et al*, IEEE J. Quant. Elect., 18, 1877-1883, 1982.
4. E. Marom *et al*, IEEE J. Quant. Elect., 20, 1311-1319, 1984.
5. D. Marcuse, IEEE J. Light. Tech., 5, 113-118, 1987.

* Communications Research Center, Ottawa, Ontario, K8H 8S2, Canada

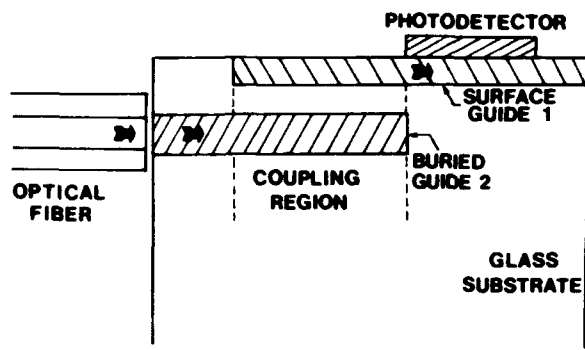


Fig. 1 Vertical directional coupler used in waveguide-detector geometry

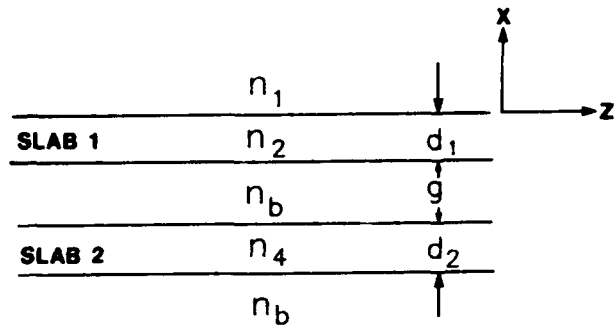


Fig. 2 Schematic of the slab directional coupler



Fig. 3(a) Output m-lines of even and odd modes



Fig. 3(b) Periodic variation of coupled power; period = $2L_c$ (Scale: 7.18:1)

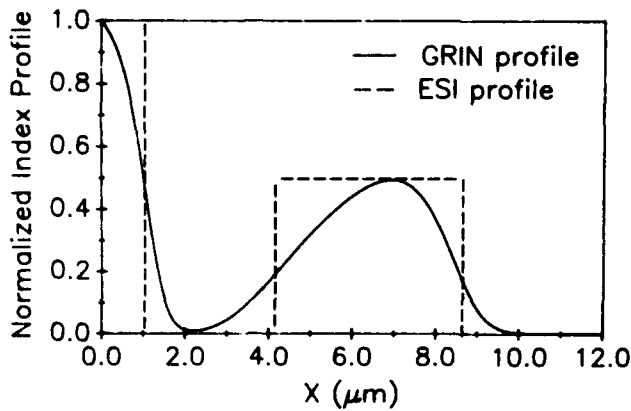


Fig. 4 Simulation of the coupler GRIN and ESI profile

	$\kappa(1/\mu m) \times 10^{-3}$	$L_c(\mu m)$	$F(\%)$
TE (Meas.)	6.7	233	97
TE (Calc.)	3.4	447	92
TM (Meas.)	6.5	236	95
TM (Calc.)	3.2	449	82

Table 1 Comparison between measured and calculated coupler properties

TuD2-1

Micro-Mechanical Structures As Integrated Optical Sensor Elements

S. Wu and H. J. Frankena

*Delft University of Technology, Dept. of Applied Physics
Lorentzweg 1, 2628 CJ Delft, The Netherlands (31) 15-784287*

Introduction

As optical channel waveguides and part of sensor circuits, micro-mechanical cantilevers and bridges have been fabricated upon Si substrates. The waveguides have a sandwiched layer structure of $\text{SiO}_2/\text{Al}_2\text{O}_3/\text{SiO}_2$ and possess very good optical wave-guiding properties¹. Typical dimensions of such channel waveguides are 25–200 μm in length, 5–30 μm in width, about 2.5 μm in thickness and 10 μm in the separation distance between waveguide and substrate. A schematic drawing of such structures is shown in Fig. 1. Such micro-mechanical structures

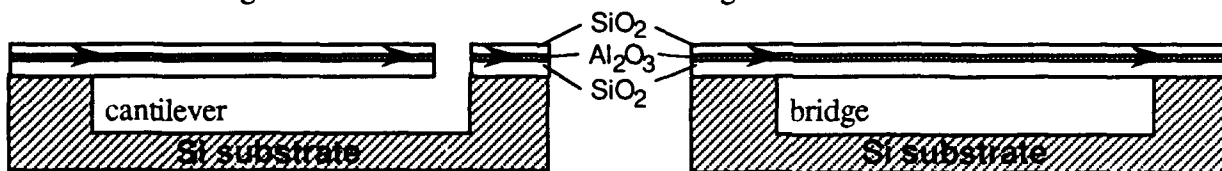


Fig. 1. Schematic drawing of micro-mechanical structures.

provide new possibilities to realize integrated optical transducer components for detecting force-related quantities such as sound, vibration and acceleration. Shifts at a cantilever's free end or bending of a bridge will change the out coupled beam in relation to the driving forces.

Fabrication Process

A silicon substrate not only offers an excellent surface for further optical thin-film deposition, but also for an already advanced micro-fabrication technology since single crystal Si possesses optimal properties for realizing miniaturized mechanical structures². Fig. 2 shows a cantilever made from a SiO_2 layer on a Si substrate. Its dimensions are $100\mu\text{m}\times 20\mu\text{m}\times 1.7\mu\text{m}$.

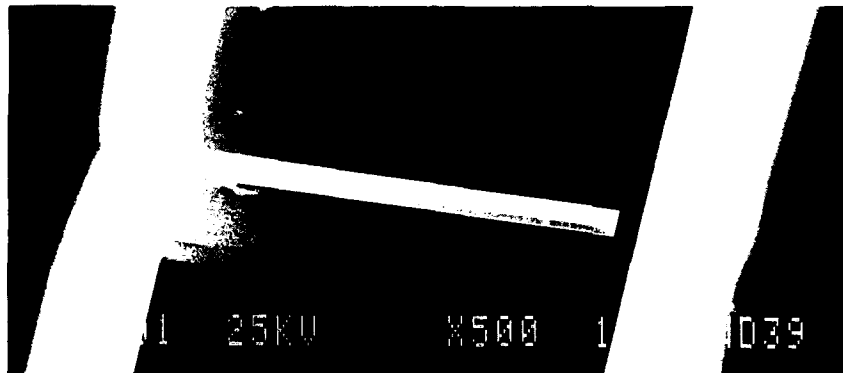


Fig. 2. SEM photograph of a SiO_2 cantilever on a Si substrate.

Because Al_2O_3 is hard to be etched, fabrication of the channel waveguides is accomplished by etching Si and SiO_2 . First, a SiO_2 layer is obtained on a Si substrate by thermal oxidation. Next, photoresist is applied and stripped according to the designed pattern of cantilevers and

bridges. Then, this pattern is transferred to the SiO_2 layer by HF buffered etching. An additional Si etching is needed to prevent covering already exposed Si surface by a sputtered Al_2O_3 layer in the next step. Finally, after depositing another SiO_2 layer, a $\text{SiO}_2/\text{Al}_2\text{O}_3/\text{SiO}_2$ sandwiched waveguide structure is formed. An etching process follows to remove the silicon underneath the channel waveguides, leaving waveguides in the form of cantilevers or bridges suspended above the Si surface at a distance determined by the etch rate and duration.

Results

Actual optical channel waveguides in the shape of cantilevers and bridges have been produced. Fig. 3 shows two SEM photographs of a cantilever and a bridge, both with a

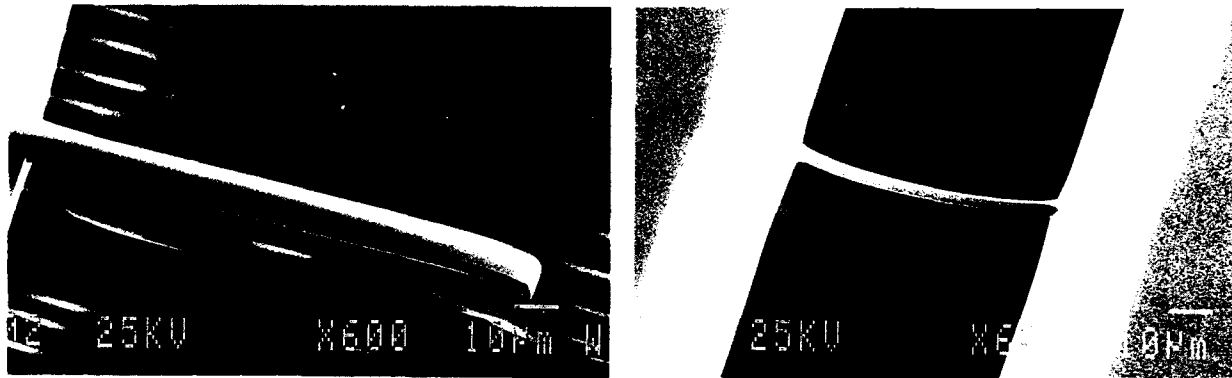


Fig. 3. SEM photographs of optical waveguides in the form of cantilevers and bridges.

$\text{SiO}_2/\text{Al}_2\text{O}_3/\text{SiO}_2$ sandwiched structure. The cantilever's dimensions are $100\mu\text{m}\times 30\mu\text{m}\times 2.5\mu\text{m}$ and the bridge's are $50\mu\text{m}\times 10\mu\text{m}\times 2.5\mu\text{m}$. Wave-guiding through them is presented in Fig. 4. The bright spots indicate scattered waves occurring when guided waves meet discontinuities. As the pictures show, the waveguides themselves appear to cause no serious scattering loss.

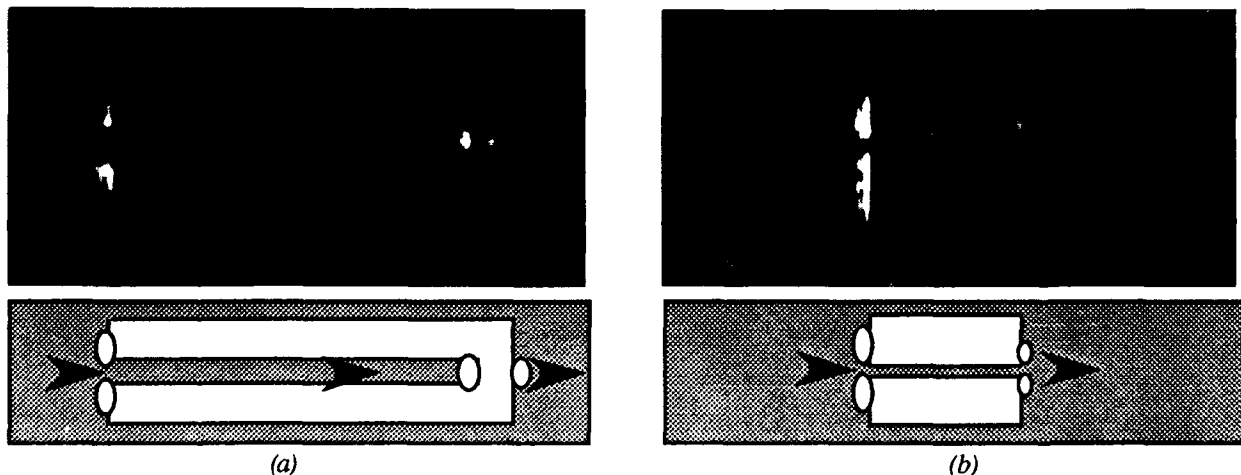


Fig. 4. Wave-guiding observation through the optical waveguides, (a) cantilever, (b) bridge.

References

1. M. K. Smit, A. Acket and C. J. VAN DER Laan, *Thin Solid Films*, **138**, pp.171–181, 1986.
2. K. E. Petersen, *Proc. of the IEEE*, **70**, pp.420–457, 1982.

TuD3-1

**A Hybrid Proton-exchanged/ Titanium-indiffused
2 × 2 Polarization Splitter in $LiNbO_3$**

J.E. Baran and D. A. Smith

Bellcore NVC-3B-207, 331 Newman Springs Road, Red Bank, NJ 07701
(908) 758-3374

Introduction. An integrated-optic polarization splitter is a necessary component in many integrated photonic devices, particularly in those devices, such as coherent receivers and optical filters, which achieve polarization independence by employing a polarization-diversity configuration [1-3]. A very versatile structure is the 2 × 2 beamsplitter which separates each of two input ports into orthogonally-polarized output ports.

Integrated 2 × 2 polarizing beamsplitters (PBS) which have been demonstrated include a (tunable) directional-coupler PBS [4], and a passive interferometric X-junction PBS [5]. Recently, two different groups demonstrated passive polarization splitting using adiabatic Y-branches, or 1 × 2 structures [6-7]. The adiabatic 2 × 2 polarization splitter has the advantage of greater fabrication tolerance, unlike the critical length dependence of interferometric designs. Goto fabricated a 1 × 2 polarization splitter in lithium niobate which used a titanium-indiffused (Ti) optical waveguide to carry the ordinary-index polarization and a proton-exchanged (PE) branching section to extract the extraordinary-index polarization [6]. This splitter operated by adiabatic evolution of the fundamental mode into that output waveguide which had the highest effective index for a given polarization. Since we have used an x-cut $LiNbO_3$ substrate, the TM (ordinary) mode stays in the Ti guide, while the TE mode transfers to the PE waveguide.

The device described here (Fig. 1), incorporates four adiabatic Y-junctions in a crossing waveguide configuration to couple two parallel Ti waveguides. The TE light is exchanged between inputs, but TM light remains in the input side. The crossing PE waveguides were designed to have different widths in order to form an asymmetric X-junction. The advantage of this asymmetry is that there is very little crosstalk (i.e. power splitting) between PE waveguides because the shallow junction angle guarantees mode sorting in the region of the crossover [8-9]. Since the start of the PE transition is crucial to proper mode coupling in the junction, we varied the gap W_{gap} , PE waveguide widths W_{PE} , and maximum junction width W_{max} of the Y-branch as shown in Fig. 1 inset. We varied the gap between the PE and Ti branches due to the observation that lateral diffusion of an annealing PE waveguide can attenuate TM transmission in a Ti waveguide [10]. The PE transition consisted of wedge and taper segments. The outer edge of the wedge was opened up at a 4.0 mrad angle while the gap was held constant. For the taper, the inside edge was held at a constant angle of 4.0 mrad while the outer edge was flared over a distance of 1 mm to attain the desired PE waveguide width. The total device length was 9 mm. All Ti waveguides were kept at an 8 μm width.

Device Fabrication and Evaluation. The Ti-indiffused waveguides were formed by diffusing 700 Å of titanium into an x-cut, y-propagating substrate in a closed platinum crucible, at a temperature of 1050° C for 8.5 hours. Afterward, the sample was repatterned with an aluminum mask which created openings for the sections requiring proton exchange. Proton exchange was carried out at 212° C in a pure benzoic acid melt for 30 minutes. The sample was annealed at 360° C in an air ambient in several steps. The ends of the device were cut and polished for fiber coupling.

The polarization splitting properties of the device were evaluated using a 1531 nm laser diode and a pair of fiber polarization controllers. Light was

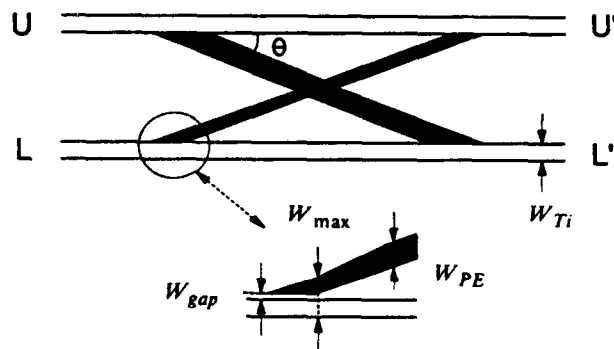


Fig. 1. Layout of 2 × 2 PBS. The shaded waveguides are proton-exchanged (PE). All inputs and outputs are 8 μm Ti waveguides. Inset provides enlarged view of PE taper.

fiber-coupled at the input. The output image was periodically scanned across a slit on the front of a germanium detector by using an oscillating mirror. An oscilloscope displayed the peak heights of the transmitted light in each branch for an established eigenpolarization, providing an instantaneous measurement of the extinction ratio (i.e. the ratio of the two peak intensities).

Scope traces displaying polarization splitting performance of the best device are shown in Figure 2. The pair of uppermost traces correspond to the TE (UL' path) and TM (UU' path) power distribution when light of the respective eigenpolarizations was coupled into the upper branch of the switch. Likewise, the middle pair of traces display the TE (LU' path) and TM (LL' path) performance when coupling into the lower branch of the polarization splitter. The third pair of traces, located in the lowermost right corner of the scope photo, show the TE and TM intensities for a straight 8 μ m Ti-indiffused waveguide which served as a reference for determining excess loss. Excess loss was defined as the ratio of the PBS peak heights to the reference waveguide. It is clear from the traces that when a pure TE or TM state is launched, the extinction ratio is excellent. In addition, one can see that the peak intensities for both polarization states in the upper and lower branches are comparable to that of the 8 μ m reference waveguide.

Extinction ratios and excess loss for all paths of the best device, which had a gap of 1 μ m, a maximum junction width of 14 μ m, and 9 and 7 μ m width PE waveguides, are summarized in Table I. The optimum anneal time of 11 hours was reached in eight anneal steps. The lower, 7 μ m, branch of the 2 \times 2 had extinction ratios in the 25-dB range with excess loss less than 1-dB. The 9 μ m PE path had worse extinction and loss. Perhaps this is because the 9 μ m waveguide was multimoded, resulting in partial mode conversion in the upper lefthand junction, while the 7 μ m waveguide was singlemoded. The highest loss in the worst case junction could be due to some lateral diffusion of the PE region into the Ti waveguide. Two other 2 \times 2s with the 9,7 μ m PE waveguide combination, but with zero gap, exhibited 20-dB extinction ratios; however, the excess loss for the TM polarization in both branch was 3-dB or greater.

[1] B. Glance, *J. Lightwave Technol.*, **LT-5**, 274 (1987).
 [2] W. Warzanskyj, F. Heismann, and R.C. Alferness, *Appl. Phys. Lett.*, **53**, 13 (1988).
 [3] D. A. Smith, J. E. Baran, K. W. Cheung, and J. J. Johnson, *Appl. Phys. Lett.*, **56**, 209 (1990).
 [4] R. C. Alferness, and L. L. Buhl, *Opt. Lett.*, **10**, 140 (1984).
 [5] A. Neyer, *Appl. Phys. Lett.*, **55**, 927 (1989).
 [6] N. Goto and G. L. Yip, *J. Lightwave Technol.*, **7**, 1567 (1989).
 [7] Y. Shani, C. H. Henry, R. C. Kistler, R. F. Kazarinov, and K. J. Orlowsky, *Appl. Phys Lett.*, **56**, 120 (1990).
 [8] W. K. Burns, and A. F. Milton, *J. Quant. Electron.*, **11**, 32 (1975).
 [9] M. Izutsu, A. Enokihara, and T. Sucta, *Opt. Lett.*, **7**, 549 (1982).
 [10] M. De Micheli, J. Botineau, P. Sibillot, D. B Ostrowsky, and M. Papuchon, *Opt. Comm.*, **42**, 101 (1982).

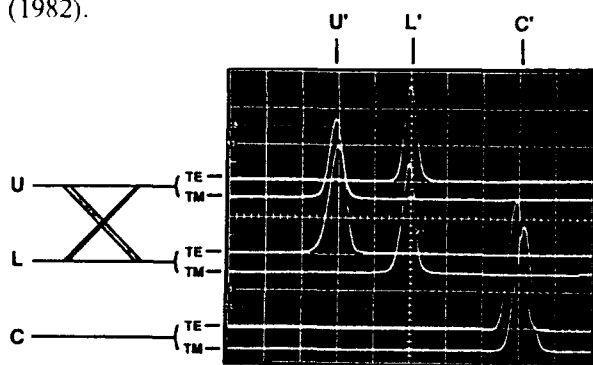


Fig. 2. Scope traces showing polarization splitting for upper and lower branches of 2 \times 2. Lower right corner displays TE and TM behavior for straight waveguide.

Input Branch	Upper (U)		Lower (L)	
Output Branch	L'	U'	U'	L'
Polarization	TE	TM	TE	TM
Extinction ratio (dB)	20.2	25.5	24.8	26.0
Excess Loss (dB)	1.2	1.8	0.6	0.7

Table I. Extinction and excess loss measurements of the 2 \times 2 PBS. Guide widths are: UL' = 9 μ m (PE), LU' = 7 μ m (PE), UU' = LL' = 8 μ m (Ti).

Ge-diffused passive optical waveguide structures in silicon

J.Schmidtchen, B.Schüppert, A.Splett, K.Petermann

Technische Universität Berlin
 Institut für Hochfrequenztechnik
 Einsteinufer 25, D-1000 Berlin 10, Germany

Summary

For the fabrication of complex integrated optical devices such as a coherent optical receiver the separate investigation of its components like directional couplers, S-bends and Y-branches is a necessity. A promising material for its realization is silicon since it exhibits an optical absorption of below 0.1cm^{-1} in the infrared regime ($\lambda > 1.2\mu\text{m}$) provided that waveguides with equally low losses can be produced. The goal is achieved by indiffusing Ge from a stripe containing an alloy of germanium and silicon as proposed in [1,2] thus minimizing losses due to free carriers. Silicon also offers the potential of being the most developed material for electronic applications making it suitable for an opto-electronic integration.

To characterize the waveguides the number of propagating modes and the waveguide losses were determined. Applying a Cut-Back technique the loss was evaluated by measuring the insertion losses of the system polarization maintaining fibre/chip/detector for three different sample lengths. Waveguides with a Ge-indiffusion depth of $1.54\mu\text{m}$ and a maximum Ge concentration at the surface of 4.5% at $1.3\mu\text{m}$ have been made.

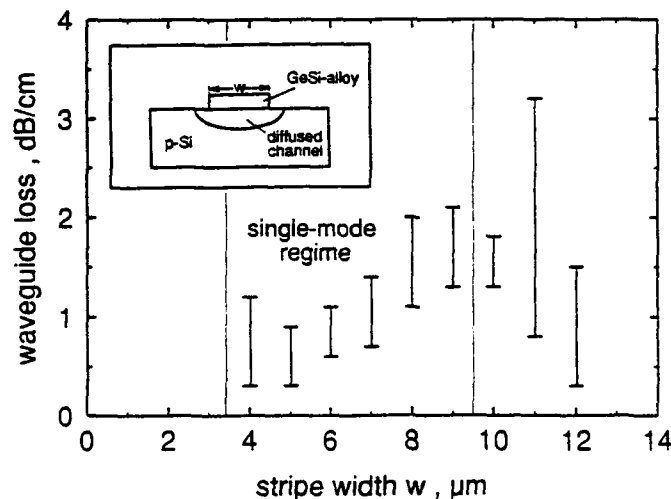


Fig.1 : Losses for Ge-indiffused waveguides at $1.3\mu\text{m}$

Fig.1 shows that waveguide losses below 0.5dB/cm in the single-mode regime could be achieved. These are the lowest losses reported so far for this material system and they are comparable to those in III/V semiconductors. No dependence on polarization could be observed.

Passive optical components were made with the same process and same Ge-concentration for stripe widths between $4\mu\text{m}$ and $6\mu\text{m}$ for single-mode operation.

In the case of directional couplers the coupling length and separation between the waveguides were varied. According to theory the power splitting ratio between the two arms can be described by /3/

$$P/P_0 = \sin^2(k \exp(-ad)L)$$

with d being the distance between the waveguides and L the coupler length. The remaining two variables k and a are coupler dependent constants. As can be seen from Fig.2 the measured results are represented by this formula to a good accuracy. Fig.2 shows that the coupling ratio is polarization independent.

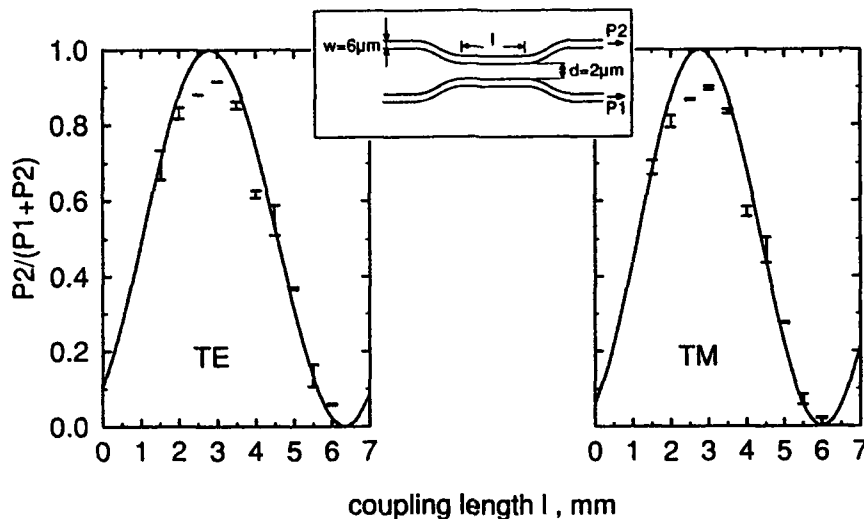


Fig.2 : Coupling ratio

S-bends with bending radii between 1mm and 35mm were also realized. Without any optimization an excess loss of less than 1dB could be observed for radii $R \geq 20\text{mm}$.

For power splitters like Y-junctions with angles between 0.4 and 2.0 degrees losses of less than 1dB for branching angles below 1.5 degree could be obtained.

References

- /1/ B.Schüppert, J.Schmidtchen, K.Petermann
"Optical channel waveguides in silicon diffused from a GeSi alloy"
Electron.Lett., 1989, 25, 1500-1502
- /2/ K.Petermann, J.Schmidtchen, B.Schüppert, A.Splett
"Integrated Optical Waveguides in Silicon"
Arch.f.Elektr.u.Übertr. AEÜ-45, 1991, 5, 273-278
- /3/ H.F.Schlaak, A.Brandenburg, G.Sulz
"Integrated optical circuits with curved waveguides"
SPIE's International Conference on Integrated Optical Circuits Engineering III
16.-18.April 1986, Innsbruck, Austria

Electric Field Induced Ferroelectric Microdomain Inversion on X- and Y-Cut Lithium Niobate

G. Janzen, H. Seibert, and W. Sohler

Angewandte Physik, Universität-GH-Paderborn, Postfach 1621
W-4790 Paderborn, Fed. Rep. Germany

Introduction

Ferroelectric microdomain inversion in LiNbO_3 has been demonstrated as an important means for integrated optics technology allowing quasi-phase-matching of second order nonlinear processes such as second harmonic generation in optical waveguides. Most of the processes investigated up to now for the generation of inverted microdomains are applicable only on $\pm Z$ -faces of LiNbO_3 [1,2,3]. For $\pm Y$ -cut material we recently demonstrated periodical domain reversal by pyroelectrically generated electrical fields across a small gap between comblike electrodes [4]; the depth of the microdomains was about $0.25\mu\text{m}$. In this contribution we present a new approach using again electrical fields between similar, photolithographically defined electrodes; however, now the electrical field is generated by applying a well defined external voltage (see Fig.1). The new method gave a better control of the process and was successfully applied not only to Y-cut, but also - for the first time - to X-cut crystals. The depth of the domains could be increased up to $1.8\mu\text{m}$.

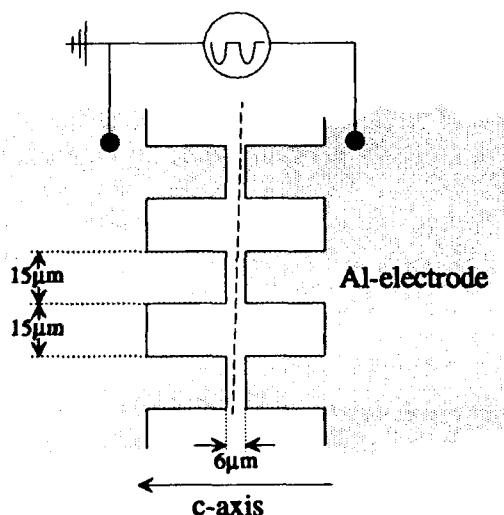


Fig.1: Scheme of the electrode structure and voltage supply for the domain inversion process.

Sample Processing

A comblike Al-electrode structure of $30\mu\text{m}$ periodicity and $6\mu\text{m}$ gap between the electrodes was deposited by vacuum evaporation on the (X- or Y-) face of LiNbO_3 with the Z-axis normal to the gap (see Fig.1). After contacting and short-circuiting the electrodes the sample was heated in a crystal oven to the processing temperature ranging between 220°C and 330°C . The electrode on the $+c$ side of the sample was grounded; to the other a 700Hz pulsating voltage (one halfwave of a sinusoidal) with $-140\text{V} \leq U_{\text{max}} \leq 70\text{V}$ was applied for times longer than or equal to five seconds. The field strength across the gap was close to electrical breakdown (some 10^7V/m); this was sufficiently high to achieve domain inversion in a very controlled and reproducible manner. Afterwards the electrodes were short-circuited again and the sample was allowed to cool down to room-temperature. Finally, the electrodes were chemically removed.

Domain Characterization

To ascertain a successful domain inversion different techniques have been applied. The domain structure became visible by using the voltage contrast in a scanning electron microscope (SEM), or - even simpler - by developing the potential differences on the sample with a (liquid) toner. Both methods are non-destructive, but have very limited spatial resolution and do not supply any information on the inversion depth.

Therefore, also anisotropic etching in HF:HNO_3 [5] was used. This etchant preferably attacks $-Y$ and $-Z$ -faces. By cutting and polishing the sample along the dashed line in Fig.1, also the cross-section - being a Z-face - was anisotropically etched.

The $\pm X$ -faces of an X-cut sample are not attacked by the etchant; however, differential etching of the cross-section (Z-face) reveals the details of the domain shape in this case, too. Optical and/or scanning electron microscopy was used to investigate the microdomain structure.

Results

Complete domain reversal of the area between the 'fingers' of the electrode structure on X- and Y-cut LiNbO_3 could be achieved for various sets of temperature and voltage between $220^\circ\text{C}/140\text{V}$ and $330^\circ\text{C}/70\text{V}$. Fig.2 shows as an example the domain structure on a -Y-cut sample prepared by processing at $290^\circ\text{C}/100\text{V}$ as described before. The domain structure became visible by differential etching. An analysis of such SEM-micrographs allowed to determine not only the maximum depth of the domain (here $1.1\mu\text{m}$), but also its full (3-dimensional) shape. E.g. along the crystalline Z-axis the lower domain boundary roughly follows a line of constant fieldstrength E_z as expected from simple physical arguments. Similar results have also been obtained with +Y-cut samples; in that case differential etching preferably attacked the microdomains themselves producing an inverse representation (in comparison with Fig.2) of the domain structure.



Fig.2: SEM micrograph of an etched -Y-cut surface of LiNbO_3 . The +Z-face of the sample has been polished prior to etching, revealing the depth profile of the domain. (5000 \times ; tilt angle 75°)

As an example of successful microdomain inversion on $\pm\text{X}$ -cut samples Fig. 3 presents a SEM-micrograph of a Z-face inside a microdomain fabricated by processing at $300^\circ\text{C}/100\text{V}$. Differential etching revealed the shape of the domain not visible from the surface. The maximum depth of a microdomain was $1.5\mu\text{m}$ ($300^\circ\text{C}/100\text{V}$) on -X-cut and $1.8\mu\text{m}$ ($300^\circ\text{C}/110\text{V}$) on -Y-cut LiNbO_3 .



Fig.3: SEM micrograph of a microdomain on -X-cut LiNbO_3 ; the depth is $1.5\mu\text{m}$. (5000 \times ; tilt angle 60°)

Conclusions

We demonstrated a new and well controllable, reproducible technique to obtain microdomain inversion on X- and Y-cut LiNbO_3 . It should be capable to enlarge the inversion depth to more than $2\mu\text{m}$. This is sufficient to allow fabrication of nonlinear quasi-phase-matched waveguide devices. Experiments with structures of $7.6\mu\text{m}$ periodicity for third-order quasi-phase-matched second harmonic generation in H^+ -exchanged waveguides are in progress.

References:

- [1] E.J. Lim, M.M. Fejer, and R.L. Byer, 'Second-harmonic generation of green light in periodically poled planar lithium niobate waveguide', *Electron. Lett.* **25**, 174 (1989)
- [2] J. Webjörn, F. Laurell, and G. Arvidsson, 'Fabrication of periodically domain-inverted channel waveguides in LiNbO_3 for second harmonic generation', *IEEE J. Lightwave Technol.* **7**, 1597(1989)
- [3] M. Yamada and K. Kishima, 'Fabrication of periodically reversed domain structure for SHG in LiNbO_3 by direct electron beam lithography at room temperature', *Electron. Lett.* **27**, 828 (1991)
- [4] H. Seibert and W. Sohler, 'Ferroelectric microdomain reversal on Y-cut LiNbO_3 Surfaces', *Int. Conf. on Physical Concepts of Materials for Novel Optoelectronic Device Applications II: Device Physics and Applications*, Aachen, Germany, 28.Oct.-2.Nov. 1990, *Proc. Soc. Phot. Instr. Eng.*, **1362**, 370 (1991)
- [5] N. Ohnishi and T. Iizuka, 'Etching study of microdomains in LiNbO_3 single crystals' *J. Appl. Phys.* **46**, 1063 (1975)

TuD6-1

**Low-loss coupling of ribbon fibres to silica-on-silicon integrated optics
using preferentially etched V-grooves**

M.F. Grant, S. Day, R. Bellerby
BNR Europe Limited, London Road, Harlow, Essex CM17 9NA, England
Telephone + 44 279 429531

Introduction

Future advanced communication systems are likely to require complex passive optical components with many input and output ports. Such components include $M \times N$ couplers, high density wavelength multiplexers, optical amplifiers etc. Traditionally, these components have been constructed using fused fibre coupler or micro-optic technology. These devices tend to be "hand made" and therefore expensive. Integrated optics technologies are more suitable for low cost mass production using fabrication technologies developed for the silicon integrated circuit industry. The most expensive part of the production of integrated optics devices is then fibre interfacing and packaging.

A wide range of devices have been demonstrated using silica-on-silicon integrated optics technology¹. We have developed a process in which etched V-grooves are precisely defined in a silicon substrate on which silica waveguides and integrated optics devices are formed². Alignment tolerances of better than $1 \mu\text{m}$ are achieved, leading to low loss passively aligned coupling. To our knowledge, we are the first group to achieve this result. This paper reports the fabrication technique and the results of single and multiple fibre coupling.

Experimental results

A fabrication route has been developed which uses only processes and technology currently standard in the silicon integrated circuit industry. Precisely defined V-grooves are first formed in the silicon substrate using a KOH/IPA based etchant. Waveguide layers are then formed using Plasma Enhanced Chemical Vapour Deposition (PECVD). The refractive index is precisely controlled using either fluoride doping, which depresses the refractive index, or phosphorus doping, which raises the index. Channel waveguides are formed using an additional Reactive Ion Etching (RIE) step. The dimensions and refractive index of the waveguides are chosen to achieve interface losses with standard fibres of $< 0.3 \text{ dB}$. After formation of the waveguides and V-grooves, the endfaces of the waveguides are prepared using a standard wafer dicing saw. Total alignment tolerances of $< 1 \mu\text{m}$ are achieved. A schematic of the final structure is shown in figure 1.

Interface losses are measured by first measuring the fibre-device-fibre loss with a single mode output fibre, and then repeating the measurement with a multi-mode output fibre. The difference between the two measurements then gives the total interface loss, including modal mismatch, misalignment and scattering loss. Figure 2 shows measurements of total interface loss (64 interfaces over 2 wafers). Mean interface loss is $< 0.3 \text{ dB}$, demonstrating excellent reproducibility of the passive alignment technique.

Work on fibre attachment has concentrated on the use of eight-way ribbon fibre. This enables large numbers of input and output fibres to be rapidly and simply attached to waveguides. The use of ribbon fibres also significantly reduces fibre preparation costs, leading to a low cost production process.

The integration of V-grooves and waveguides on the same substrate results in excellent temperature stability. Figure 4 shows a typical example of temperature cycling of epoxied ribbon fibre coupling. The total loss variation is better than $\pm 0.2 \text{ dB}$ over the temperature range $-40 \text{ }^\circ\text{C}$ to $+70 \text{ }^\circ\text{C}$.

Conclusions

A process for integrating etched fibre alignment V-grooves and waveguides has been developed for silica-on-silicon integrated optics. Average interface losses of < 0.3 dB/interface has been achieved. Ribbon fibre coupling with excellent temperature stability has been demonstrated.

The use of self-aligned multiple fibre coupling is expected to result in very low cost, complex passive optical components.

Referencies

1. C.H. Henry, G.E. Blonder and R.F. Kazarinov, "Glass waveguides on silicon for hybrid optical packaging", J. Lightwave Tech., Vol 7, No. 10, October 1989, pp 1530 - 1539
2. M.F. Grant, R. Bellerby, S. Day, G.J. Cannell and M. Nelson, "Self aligned multiple coupling for silica-on-silicon integrated optics", Proc. EFOC-LAN, London, June 19-21 1991, pp 269-292

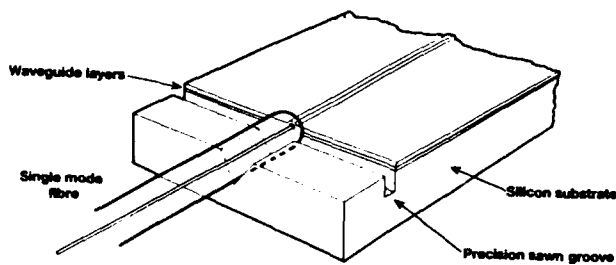


Figure 1 - Schematic of the final structure

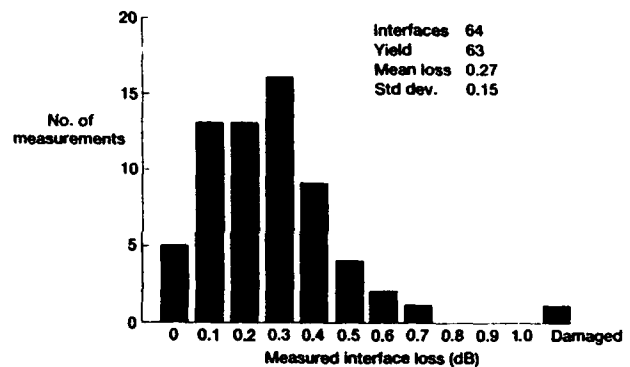


Figure 2 - Passive fibre-guide coupling using V-grooves

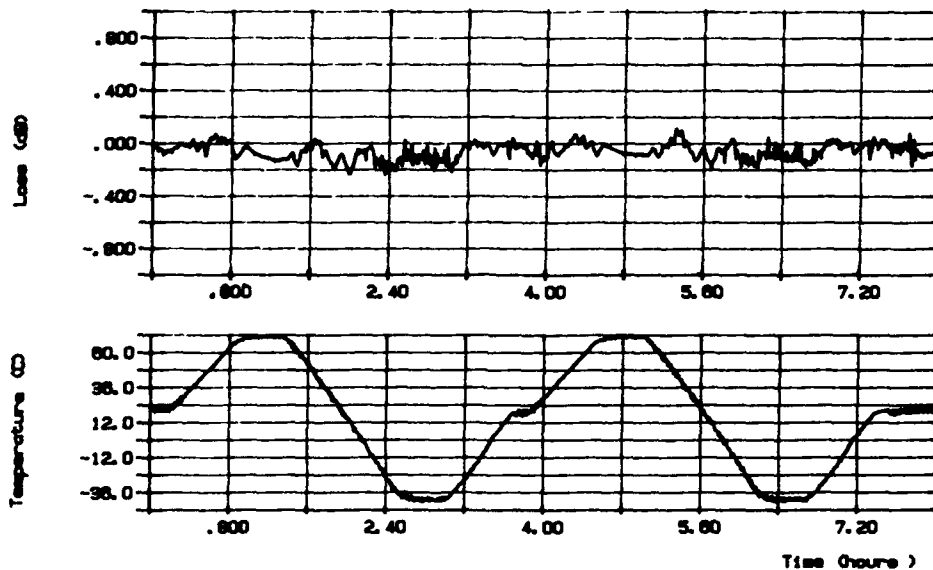


Figure 3 - Typical fibre-device-fibre loss variation during temperature cycling

Tuesday, April 14, 1992

Guided Wave Structures

TuE 10:30 am–12:00 m
La Salle Ballroom C

Daan Lenstra, *Presider*
Vrije University of Amsterdam, The Netherlands

Application of the Discrete Spectral Index Method to the Design of Coupled Ridge Waveguides with Carrier Injection

S.V.Burke* M.J.Adams† P.C.Kendall P.N.Robson G.J.Rees

Dept. of Electronic and Electrical Engineering
University of Sheffield, Mappin St., Sheffield, S1 3JD, UK.
Tel: (0742) 768555

*Present address: Dept. of Physics, University of Wales College of Cardiff, Cardiff, UK

†BT Laboratories, Martlesham Heath, Ipswich, IP5 7RE, UK.

The discrete spectral index (DSI) method has proved successful for modelling single rib waveguides, symmetric and asymmetric couplers [1]. For couplers, the method produces propagation constants for the lowest-order symmetric and antisymmetric supermodes, β_s and β_{as} , and generates accurate field profiles. A necessary feature of the DSI method is that the layers below the ribs must be of uniform refractive index, n . However, for example a twin-guide laser amplifier, consisting of two coupled ridge waveguides, experiences small non-uniform changes in n in the active layer as a result of carrier injection. In this work, a technique, which is a combination of the DSI method and a perturbation approach, has been developed to model such structures.

The following approximate perturbation formula is well known for single guides [2]

$$\beta_p^2 - \beta_0^2 = k_0^2 \int_{-\infty}^{\infty} \{n_p^2 - n_0^2\} E_0^2 dA / \int_{-\infty}^{\infty} E_0^2 dA \quad (1)$$

Here, β_0 and E_0 are the propagation constant and field for the mode of the unperturbed guide and n_0 is the corresponding refractive index profile. Similarly β_p , E_p and n_p will refer to the perturbed guide. The wave number in vacuum is k_0 and A refers to the cross-sectional area. For couplers, eqn.(1) is valid for each supermode individually only if both guides are perturbed equally. Otherwise we must employ a degenerate perturbation technique [3] by expressing the perturbed field E_p as a linear combination of the two unperturbed supermodes, E_s and E_{as} .

$$E_p = aE_s + bE_{as} \quad (2)$$

where a and b are constants. A quadratic equation, yielding the propagation constants of the perturbed supermodes β_{ps} and β_{pas} , is constructed by substituting eqn.(2) into the Helmholtz equation, multiplying by E_s and E_{as} in turn and integrating over all A . The resulting integrals, $E_s^2 \Delta(n^2)$, $E_{as}^2 \Delta(n^2)$ and $E_s E_{as} \Delta(n^2)$ (where $\Delta(n^2) = n_p^2 - n_0^2$) summed over the perturbed regions, can be evaluated efficiently in Fourier space using the DSI method. Finally, a and b in eqn.(2) can then be determined, permitting the calculation of perturbed field profiles.

For the InP/InGaAsP ridge waveguide coupler, symmetric before perturbation, shown in Fig.1, real negative index changes Δn_1 , and Δn_2 were modelled in regions R_1 and R_2 . In Fig.2, β_{ps}/k_0 and β_{pas}/k_0 , calculated individually using eqn.(1) and also using the revised approach of eqn.(2), are plotted against $\Delta n_1/\Delta n_t$, where $\Delta n_t = \Delta n_1 + \Delta n_2 = -0.036$. Also shown is β_p/k_0 from eqn.(1) for each isolated guide. The trends are in close agreement with [4], and with the curves shifted significantly, the need for the revised approach can be clearly seen.

In conclusion, this presentation will describe a perturbation technique for couplers which is applicable to both active and non-linear devices.

References

- [1] P.N.Robson and P.C.Kendall (eds), Rib Waveguide Theory by the Spectral Index Method, Research Studies Press and Wiley, 1990.
- [2] A.W.Snyder and J.D.Love, Optical Waveguide Theory, Chapman and Hall, 1983.
- [3] L.I.Schiff, Quantum Mechanics, McGraw Hill, 248, 1968.
- [4] I.Paiss and A.Hardy, IEEE J.Quantum.Electron, QE-25, 1609, 1989.

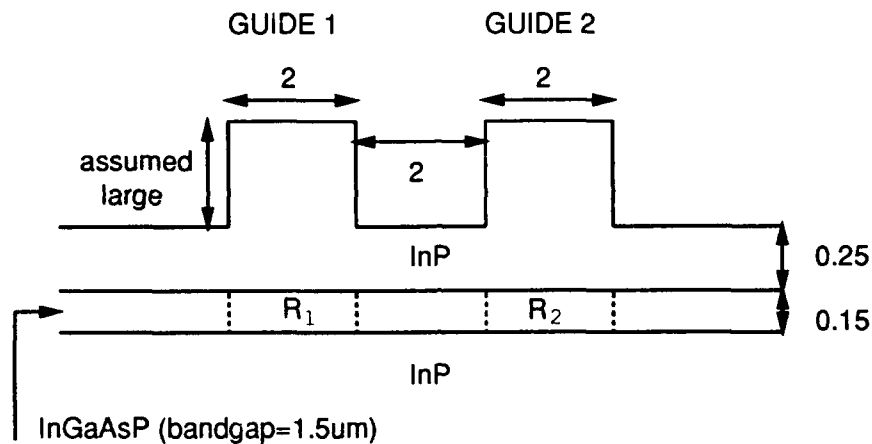


Figure 1: Cross-section through an InP/InGaAsP ridge waveguide coupler. All dimensions are in microns. Wavelength = 1.5 μm .

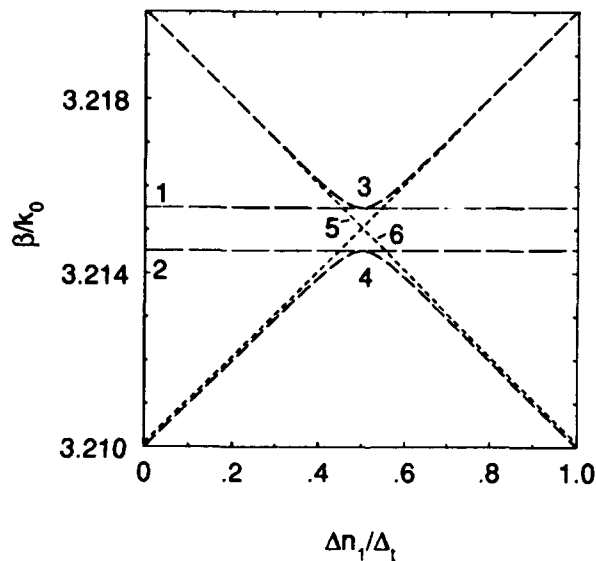


Figure 2: β/k_0 against fractional index change in region R_1 , for structure in Fig.1

- (1),(2): β_{ps}, β_{pas} , calculated using eqn.(1).
- (3),(4): β_{ps}, β_{pas} , calculated with revised approach, eqn.(2).
- (5),(6): β_p for modes of isolated guides 1 and 2 respectively.

Effective Index Series Analysis of Ridge Waveguides with Arbitrarily Sloped Sidewalls

J. P. Donnelly* and S. D. Lau*†

*Lincoln Laboratory, Massachusetts Institute of Technology
P. O. Box 73, Room C-331
Lexington, MA 02173
(617) 981-4423, FAX (617) 981-5793

†Research Laboratory of Electronics and the Department of Electrical Engineering
and Computer Science
Massachusetts Institute of Technology
Cambridge, MA 02139

Semiconductor ridge waveguide structures are widely used in many integrated optical circuits and devices, including low threshold current, single-mode diode lasers. Although computer-intensive numerical techniques are required to completely analyze these structures, reasonable accuracy can be obtained with simple effective index methods, in cases where the ridge is not etched into the guiding layer. However, effective index methods to date have been restricted to ridges with vertical sidewalls, while many actual structures have sloped sidewalls. In this paper, an effective index series technique for analyzing ridge waveguide structures with arbitrarily sloped sidewalls is presented.

A simple ridge waveguide with sloped sidewalls is illustrated in Fig. 1. For this ridge structure, the effective index at each position in the lateral direction, y , is calculated assuming a slab waveguide of infinite extent with upper cladding thickness, h . The square of the effective index of a typical four-layer slab guide as a function of the upper cladding thickness, h , is shown in Fig. 2. Once the effective index is known as a function of y (as illustrated in Fig. 3), another slab waveguide analysis is used in the transverse y -direction. For quasi-TE modes in the ridge structure (i.e., predominant electric field in the y -direction), TE boundary conditions are used to calculate the effective index as a function of h , and TM boundary conditions are used in the transverse direction. For quasi-TM modes, the boundary conditions used in the two parts of the solution are reversed. Since TM boundary conditions are more difficult in the presence of graded indices, the quasi-TE mode case is treated here.

For TM boundary conditions in the transverse direction, the reduced wave equation for H_x in each region of Fig. 3 is given by:

$$\frac{\partial^2 H_x}{\partial y^2} - \frac{1}{\epsilon} \frac{\partial \epsilon}{\partial y} \frac{\partial H_x}{\partial y} + (\omega^2 \mu \epsilon - \beta^2) H_x = 0 \quad (1)$$

where $\epsilon = \epsilon_0 n^2$ (ϵ_0 being the dielectric constant of free space and n the refractive index) and β is the propagation constant. In Regions 1 and 3, n^2 is a constant: so, H_x is assumed to be a cosine (symmetric mode) or sine function (antisymmetric mode) in Region 1 and an exponential in Region 3. In Region 2, n^2 is curve fit to a polynomial function of $z = y-d$:

$$n^2(z) = \sum_{i=0}^p \Delta_i z^i \quad (2)$$

The number of terms used depends on the actual structure and the accuracy desired. In the graded region, H_x can be written as a series $H_x(z) = \sum_{n=0}^{\infty} a_n z^n$. By substituting $n^2(z)$ and $H_x(z)$ into the scalar wave equation, an iterative expression for the coefficients a_n is obtained:

$$a_n = - \frac{\left\{ \sum_{j=1}^{n-1} j(2j-n-1) \Delta_{n-j} a_j + k_0^2 \sum_{j=0}^{n-2} \sum_{m=0}^{n-2-j} \Delta_m \Delta_{n-2-j-m} a_j - \beta^2 \sum_{j=0}^{n-2} a_j \right\}}{n(n-1) \Delta_0} \quad (3)$$

where $\Delta_i = 0$ for $i < 0$ or $i > p$ and $k_0 = 2\pi/\lambda$. The only unknowns are a_0 and a_1 and these can be determined by matching boundary conditions at $y=d$ ($z=0$). Matching boundary conditions at $y=d+s$ ($z=s$) then gives the eigenvalue equation

$$-\gamma \sum_{n=0}^{\infty} a_n s^n = \sum_{n=0}^{\infty} n a_n s^{n-1} \tag{4}$$

where $\gamma = (\beta^2 - k_0^2 n_e^2)^{1/2}$. This equation is a function of the mode propagation constant β only.

Many actual structures contain quantum wells and graded-index layers in the guiding region. These can be treated in a manner similar to the simple waveguide shown in Fig. 1 using a series solution analysis for the GRIN layers similar to that described for the transverse direction. Results for various ridge waveguide structures will be presented. In addition, coupled two- and three-guide ridge structures with sloped sidewalls will be discussed.

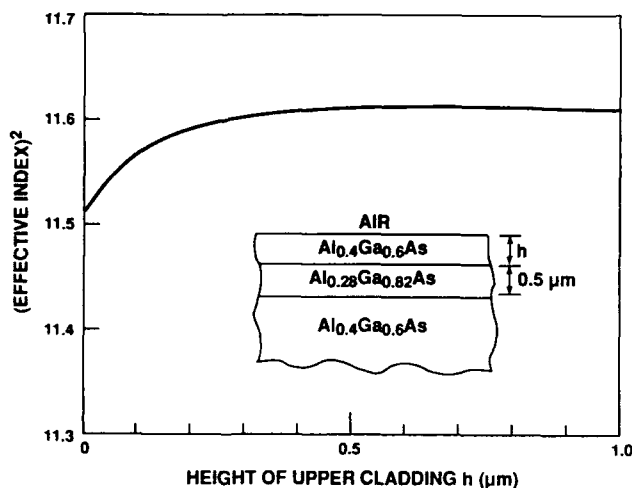


Figure 1. Schematic illustration of a simple ridge waveguide with sloped sidewalls.

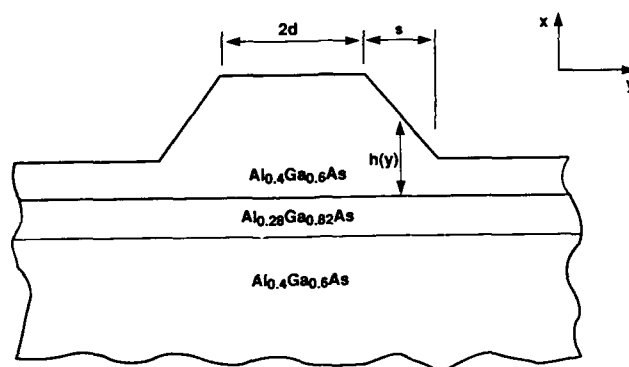


Figure 2. Plot of the square of the effective index of a typical four-layer slab guide as a function of the upper cladding thickness h .

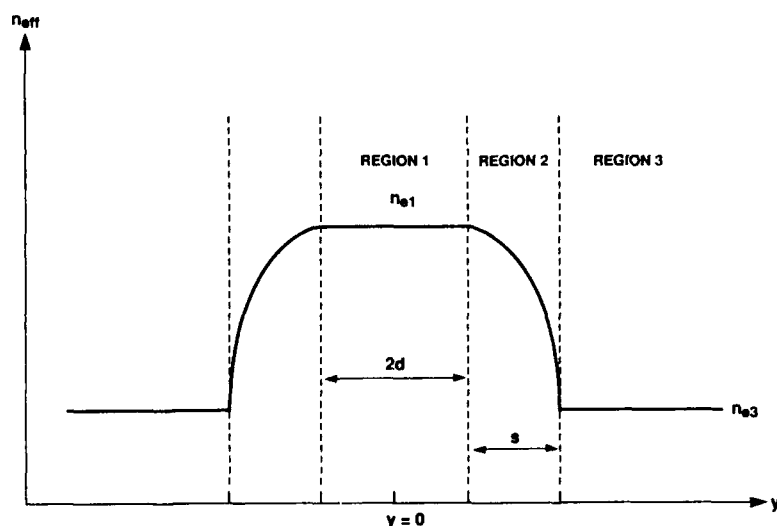


Figure 3. Illustration of the effective index of the ridge waveguide with sloped sidewalls as a function of position y .

S-Bend theoretical profile for minimum radiation losses

F.J.Mustieles, E.Ballesteros, P.Baquero
 Telefónica, Investigación y Desarrollo
 Emilio Vargas 6, 28043 Madrid (Spain)
 Phone: 34-1-3374598 Fax: 34-1-3374212

Curved waveguides are a key element in optical integrated circuits. High density circuits require that the total length of curved waveguides is minimized. However, radiation losses limit practical length. This radiation is the sum of transmission losses α_t (at the entrance and the exit of the bend) and bending losses α_b .

Transmission losses can be evaluated from overlap integral between optical fields in straight and curved waveguides [1]. Bending losses can be expressed as

$$\alpha_r = \int_{\Gamma} \alpha(R) ds$$

where $\alpha(R)$ is the bending losses per unit length and R is the curvature radius of the curve Γ to be optimized. Baets and Lagasse [1] obtained a suboptimal S-bend profile considering an approximation expression for $\alpha(R)$ ($\alpha(R) = C \cdot R^{-n}$). We have considered a more general expression proposed by Marcuse and Marcatili [2,3]:

$$\alpha(R) = C_1 e^{-C_2 R}$$

In order to find the optimal curve Γ , we consider a x-y coordinate system, in which curve Γ can be written as a function $y = y(x)$, $0 \leq x \leq L$. In this case the curvature radius can be expressed as:

$$R(x) = \frac{(1 + y'(x)^2)^{\frac{3}{2}}}{|y''(x)|}$$

Considering the hypothesis of "low-slope" S-bends:

$$1 + y'(x)^2 \approx 1$$

we have $R(x) = |y''(x)|^{-1}$. So, our problem is to minimize

$$\alpha_r = \int_0^L C_1 e^{-\frac{C_2}{|y''(x)|}} dx ; \text{ with } y(0) = 0, y(L) = h, y'(0) = y'(L) = 0 \quad (1)$$

From variational calculus theory [4], the function $y(x)$ which minimizes the functional α_r is solution of the following differential equation

$$\frac{d^2}{dx^2} \left[\frac{\partial F}{\partial y''} \right] = 0$$

where F is the subintegral function of (1).

We have found that the solution of this fourth-order differential equation admits the following parametric analytical representation:

$$x = -\frac{L}{2} \left[\frac{\text{sgn}(t)}{\text{sgn}(t_0)} \frac{t_0^2}{t^2} e^{-c_2 \left[\frac{1}{|t|} - \frac{1}{|t_0|} \right]} - 1 \right]$$

$$y = \frac{h}{2} + \frac{L^2 t_0^4}{4 t^2} \text{sgn}(t) \left[\frac{1}{C_2} - \frac{1}{|t_0|} \right] e^{-c_2 \left[\frac{1}{|t|} - \frac{1}{|t_0|} \right]} - \frac{L^2}{4} t_0^4 e^{-2c_2 \left[\frac{1}{|t|} - \frac{1}{|t_0|} \right]} \left[\frac{-1}{2 t^3} + \frac{3 \text{sgn}(t)}{4 t^2 C_2} - \frac{1}{4 t C_2^2} - \frac{\text{sgn}(t)}{8 C_2^3} \right]$$

with $t_0 \leq t \leq -t_0$, where t_0 is solution of the algebraic equation:

$$\frac{16 h C_2^3}{L^2} = 4 t_0 C_2^3 - 2 \text{sgn}(t_0) t_0^2 C_2^2 - 2 t_0^3 C_2 - \text{sgn}(t_0) t_0^4$$

On the other hand, we have developed a numerical optimization method, based on cubic spline interpolation, which allows us to find the minimum radiation losses profile for arbitrarily curved waveguides. This procedure includes both transmission and bending losses, without the "low-slope" hypothesis.

In Table I, we present the bending losses for two LiNbO₃ waveguides [5]. We compare three typical S-bend profiles (I:cos(x) profile, II:double circular arc profile, III:sin(x) profile; see [1]) with the analytically and numerically optimized ones. Experimental verification of the bending losses for profile III are available in [5].

C ₁ (mm ⁻¹)	C ₂ (mm ⁻¹)	L (mm)	h (mm)	Theo. (dB)	Num. (dB)	I (dB)	II (dB)	III (dB)
8.64	0.105	4.0	0.1	1.70	1.83	1.87	2.225	4.25
10.83	0.231	3.0	0.1	0.60	0.64	0.71	0.78	1.91

Table I: Bending losses for different S-bend profiles.

From these results we can see that the theoretical profile has actually the minimum losses. On the other hand, the cos(x) profile seems to be close to the optimal one, under the "low-slope" assumption.

References:

[1] R.Baets, P.E.Lagasse, J.Opt.Soc.Am. 73, No.2, p.177 (1983).
 [2] D.Marcuse, B.S.T.J., 50, No.8, p.2551 (1971).
 [3] E.A.J.Marcatili, B.S.T.J., 48, No.7, p.2103 (1969).
 [4] L.Elsoltz, Ecuaciones Diferenciales y Cálculo Variacional, Ed. MIR (1977).
 [5] W.J.Minford et al., IEEE J.Quantum Electron. QE-11, p.1802 (1983).

ACCURATE FINITE ELEMENT ANALYSIS OF POLARIZATION-MAINTAINING OPTICAL FIBERS

B.M.A. Rahman, P.A. Buah, K.T.V. Grattan

City University

Department of Electrical, Electronic and Information Engineering

Northampton Square,

London EC1V 0HB U.K. Tel: +44-71-253-4399 Fax: +44-71-490-0719

Single-mode polarization-maintaining optical fibers that can maintain a state of polarization over a long length play an important role in coherent optical communications [1] and optical fiber sensing systems [2]. These fibers are realized by using axially nonsymmetrical refractive-index distribution [3] or by a nonsymmetrical stress distribution [4] to reduce mode coupling between two orthogonally polarized modes. Eigenmodes of these special fibers cannot be found analytically, they must be determined by approximate methods. So far some numerical techniques have been tried to analyze such fibers among them point-matching method [5], mode-matching method [6] and finite element method [7] can be mentioned. In this paper some polarization-preserving optical fibers are investigated rigorously using an accurate vector H -field finite element method. The finite element method is particularly suitable for the analysis of arbitrarily shaped waveguides hence it is a very flexible analysis tool for fibers with axially nonsymmetrical cross-section or refractive-index distribution. The present finite element formulation is made via a full H -vector field [8], which is particularly suitable for optical waveguides as field continuity is automatically satisfied at dielectric interfaces. By contrast, in the previous E_z/H_z formulation [7] continuity conditions needed to be specifically imposed. The present H formulation is also valid for general anisotropic refractive indices (lossless) without destroying the canonical form of the eigenvalue matrix and this formulation is accurate for the analysis of high-birefringence fibers. A divergence free constraint is imposed by using a penalty technique to eliminate spurious modes. A highly efficient sparse matrix solver has been developed using subspace iteration along with adaptive remeshing techniques to optimize the computer resources. An user-friendly pre- and post-processing package is also used to define a specific waveguide cross-section, and to interpret the results [9].

The normalized birefringence B is defined as

$$B = \frac{\beta_x - \beta_y}{\beta_x + \beta_y} = 2 \frac{(\beta_x - \beta_y)}{(\beta_x + \beta_y)}$$

where β_x and β_y are the propagation constant of the H_{x11} and H_{y11} modes. These are the two orthogonal dominant modes with magnetic field vector along x -axis and y -axis respectively. Figure 1 illustrates the variation of normalized propagation constant and power carried by core, bow areas, and cladding for a bow-tie fiber with normalized frequency. The bow-tie fiber is shown inset in Fig.1. Refractive indices are, for core $n_1 = 1.54$, for cladding $n_2 = 1.5246$, and for bow-areas $n_3 = 1.5230754$. The fiber core radius is $a = 5 \mu\text{m}$, inner and outer radii of bow are $15 \mu\text{m}$ and $25 \mu\text{m}$ respectively. Half of the bow angle (each side) is $\theta = 45$ degree. Figure 1 also shows the variation of the spot size with normalized frequency. The normalized birefringence B was 6×10^{-6} at $\lambda = 6.0 \mu\text{m}$.

Figure 2 illustrates the variation of normalized propagation constant, and power carried by different regions of a side-pit fibers. The figure is shown inset Fig. 2. Refractive indices are, for core $n_1 = 1.458$, for cladding $n_2 = 1.45$, and for side-pit $n_p = 1.436$. The fiber radius is $a = 4 \mu\text{m}$ and core width $W = 4 \mu\text{m}$. Figure 2 also shows the variation of spot size with the normalized frequency. The normalized birefringence B is 4×10^{-5} at $\lambda = 1.4 \mu\text{m}$.

In this paper two simple examples have been analyzed for axially nonsymmetrical fibers. The main strength of the finite element method is its easy applicability to arbitrarily shaped fibers and arbitrary refractive index profiles (including graded index). A further advantage of the vector H formulation [8] adopted here is that it is valid for anisotropic optical materials such as the case of Electro-optic guided wave devices or high-birefringent fiber showing large anisotropy caused by thermal stress. This formulation is also convenient to characterize nonlinear optical waveguides with any nonlinearity

including saturations [9]. Vector finite element methods with pre- and post-processing facilities have become very useful for accurate analysis of more complicated fibers increasingly used in optical engineering [9]. Most of these modal analyses takes 5-10 seconds on a Sun Sparcstation 2.

References

- [1] T. Okoshi, "Heterodyne and coherent optical fiber communications: Recent Progress," IEEE Microwave Theory Tech., MTT-30, pp.1138-1149, 1982.
- [2] R. Ulrich and M. Johnson, "Fiber-ring interferometer: Polarization analysis," Opt. Lett., 4, pp.152-154, 1979.
- [3] V. Ramaswamy, W.G. French, and R.D. Standley, "Polarization characteristics of noncircular core single-mode fibers," Appl. Opt., 17, pp.3014-3017, 1978.
- [4] R.H. Stolen, V. Ramaswamy, P. Kaiser, and W. Pleibel, "Linear polarization in birefringent single-mode fibers," Appl. Phys. Lett., 33, pp.699-701, 1978.
- [5] T. Miyamoto, "Accurate numerical analysis of polarisation-preserving optical fibre with three-layer elliptical cross-section," IEE Proc. part J, 138, pp.1-6, 1991.
- [6] K. Okamoto, T. Hosaka, and Y. Sasaki, "Linearly single polarization fibers with zero polarization mode dispersion", IEEE Trans. Microwave Theory Tech., MTT-30, pp.342-349, 1982.
- [7] K. Oyamada and T. Okoshi, "Two-dimensional finite-element method calculation of propagation characteristics of axially nonsymmetrical optical fibers," Radio Sci., 17, pp.109-116, 1982.
- [8] B.M.A. Rahman and J.B. Davies, "Finite-element solution of integrated optical waveguides" IEEE/OSA J. Lightwave Technology, LT-2, pp.682-688, 1984.
- [9] R.D. Ettinger, F.A. Fernandez, B.M.A. Rahman, and J.B. Davies, "Vector finite element solution of saturable nonlinear strip-loaded optical waveguides", IEEE Photonics Technology Letters, 3, pp.147-149, 1991.

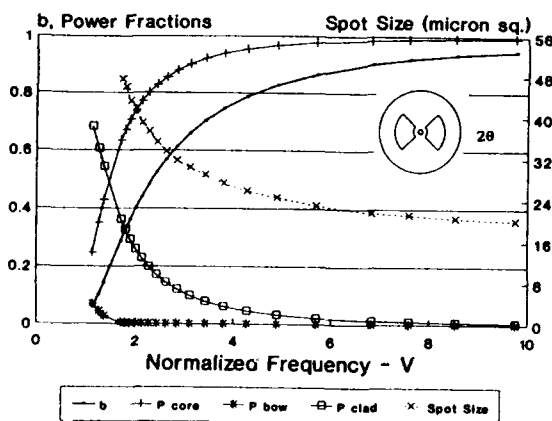


Fig.1 Variation of normalized propagation constant, power fractions and Spot Size with normalized frequency for a Hx11 mode in a bow-tie optical fiber.

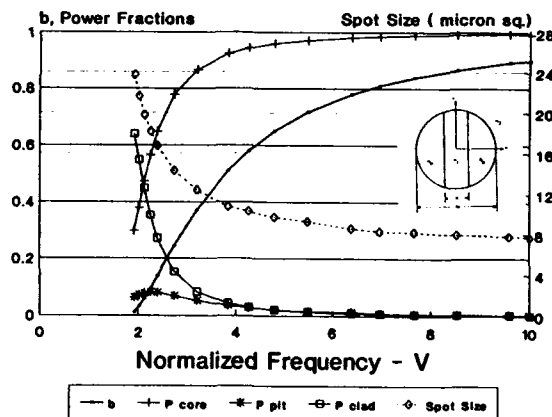


Fig. 2 Variation of normalized propagation constant (b), power fractions in different regions and spot size with normalized frequency (V) for Hy11 mode in a side-pit optical fiber.

Semiconductor Ballistic Electron Reflection, Refraction, Interference, and Diffraction Effects: Modeling and Quantum Device Applications

T. K. Gaylord,¹ G. N. Henderson,¹ E. N. Glytsis,¹ D. W. Wilson,¹ P. N. First,² and D. B. Walker¹

Microelectronics Research Center,

¹and School of Electrical Engineering, ²and School of Physics
Georgia Institute of Technology, Atlanta, GA 30332

Semiconductor growth techniques such as molecular beam epitaxy have been refined so that nanostructures can be grown with precise monolayer and compositional control [1]. This has produced semiconductor materials in which ballistic (collisionless) electron transport lengths of over a micron have been observed [2-4]. That is, the electrons traverse the sample as quantum mechanical plane waves experiencing no elastic or inelastic scattering events. Ballistic electrons can account for more than half of the current in small devices [3]. Since ballistic electrons are quantum mechanical deBroglie waves, they can be reflected, refracted, interfered, and diffracted [5] in a manner analogous to electromagnetic optical waves [6]. Recently, it has been shown that these electron wave optical effects are exactly analogous to electromagnetic waves in general dielectrics (lossless materials with arbitrary permittivity ϵ and permeability μ) [7]. Electron wave interference effects have been observed experimentally for electron energies below the barriers in double-barrier and multi-barrier resonant tunneling devices and for electron energies above the conduction band edges in $Ga_{1-x}Al_xAs$ heterostructures [5]. In addition, by combining growth techniques with nanolithography, electron wave refraction has been experimentally demonstrated through the fabrication of electron lenses and prisms [8,9] in a two-dimensional $GaAs$ electron gas.

For conduction electrons in a single band for which there is no zero-field spin splitting, the envelope wave function ψ is described by the effective mass time-independent Schrödinger equation

$$-\frac{\hbar^2}{2} \nabla \cdot \left(\frac{\nabla \psi}{m^*(\vec{r})} \right) = [KE(\vec{r})] \psi, \quad (1)$$

for electron wave propagation in a region of spatially varying effective mass $m^*(\vec{r})$ and spatially varying kinetic energy $KE(\vec{r})$, where \hbar is Planck's constant divided by 2π . This results in the boundary conditions at an interface being the conservation of the electron wave amplitude, ψ , and the conservation of the product of the inverse effective mass and the normal component of the gradient of the electron wave (EW) amplitude, $\nabla \psi \cdot \hat{n}/m^*$. If the spatial variation is confined to a plane, Eq. (1) has exactly the form of two wave equations occurring for electromagnetic waves (EMW) in general dielectrics. One is for TE polarization (electric field \vec{E} perpendicular to plane of variation) in which ψ is analogous (\sim) to the magnitude of the electric field E , $KE \sim \epsilon$, and $m^* \sim \mu$. The other is for TM polarization (magnetic field \vec{H} perpendicular to the plane of variation) in which $\psi \sim H$, $KE \sim \mu$, and $m^* \sim \epsilon$. For most dielectrics μ is equal to the permeability of freespace and so in electromagnetics μ is seldom treated as a variable. However a variable μ is clearly required in the present case. Somewhat similarly, in the quantum mechanics of heterostructures m^* is often taken to be a constant. However, recent experimental work has shown the importance of effective mass differences on electron transport in heterostructures [10-11]. The inclusion of variable μ in electromagnetics and variable m^* in quantum mechanics requires that separate phase and amplitude indices of refractions be defined for both. The phase refractive indices may be defined in terms of the relative permittivity $\epsilon_r = \epsilon/\epsilon_{ref}$, relative permeability $\mu_r = \mu/\mu_{ref}$, relative kinetic energy $(KE)_r = (KE)/(KE)_{ref}$, and relative effective mass $m_r^* = m^*/m_{ref}^*$ as

$$n_{ph}^{TE} = n_{ph}^{TM} = \sqrt{\mu_r \epsilon_r}, \quad n_{ph}^{EW} = \sqrt{m_r^* (KE)_r}, \quad (2)$$

where the reference region is chosen to be an arbitrary dispersionless region. These indices are used in phase-matching calculations such as in Snell's law and total internal reflection (critical angle). The reflectivity and transmissivity for EMW's and EW's are given by Fresnel's equations which result from applying the boundary conditions. The reflectivity of the electric field for TE polarization r_E^{TE} , of the magnetic field

for TM polarization r_H^{TM} , and of the electron wave r_ψ^{EW} are all given by a common Fresnel equation if the amplitude indices of refraction are given by

$$n_{am}^{TE} = \sqrt{\epsilon_r/\mu_r}, \quad n_{am}^{TM} = \sqrt{\mu_r/\epsilon_r}, \quad n_{am}^{EW} = \sqrt{(KE)_r/m_r^*}. \quad (3)$$

Similarly, using these indices of refraction allows the transmissivities t_E^{TE} , t_H^{TM} , and t_ψ^{EW} all to be calculated from a second Fresnel equation. In addition to reflectivity and transmissivity, these indices are used to calculate Brewster angles. For $Ga_{1-x}Al_xAs$ it has been shown that all interfaces will have both a critical angle and a Brewster angle [7]. Complex multilayer structures such as superlattices can be modeled using a combination of phase refractive indices (for propagation effects) and amplitude refractive indices (for reflectivity and transmissivity).

Quantum electron wave optical effects as described here occur for submicron device dimensions. The semiconductor industry in its continuing effort to produce faster and more integrated microcircuits has been steadily decreasing device dimensions since the time of the first integrated circuit. This decreasing of the size has now reached a point where quantum effects are important. Therefore further development of present-day devices will require an understanding of these effects. Beyond existing devices, these quantum electron optical effects suggest a new class of devices that utilize these above-conduction-band-edge propagation effects to advantage. An example of such a device is a heterostructure narrow-band Fabry-Perot interference filter – an electron half-wavelength layer surrounded by reflective quarter-wavelength layers [12]. These filters have the capability of being voltage tunable. Further they could serve as narrow-band emitters in electroluminescent devices, photodetectors, and subpicosecond ballistic transistors. Similarly, electron impedance transformers could be constructed between dissimilar materials [13] such as from a $GaAs$ base of a bipolar transistor to the $Ga_{1-x}Al_xAs$ collector. Beyond improving the efficiency and speed of existing devices, however, is the concept of “guided electron wave integrated circuits.” These very small integrated circuits would be comprised of quantum wave devices interconnected with electron slab waveguides (quantum wells with a two-dimensional electron gas) and channel waveguides (quantum wires with a one-dimensional electron gas) [14]. An element of these circuits might be electron gratings [15] that could serve as single-pole and multiple-pole switches, energy multiplexers, energy spectrometers, and electron waveguide couplers. In addition to high speed, these circuits would potentially have the advantages of “optical-like” processing – parallelism, interconnectivity, and bandwidth (but with a wavelength typically 100 times smaller than that of visible light).

- [1] L. Esaki and R. Tsu, *IBM J. Res. Dev.* **14**, 61 (1970).
- [2] A. F. J. Levi, J. R. Hayes, P. M. Platzman, and W. Wiegman, *Phys. Rev. Lett.* **55**, 2071 (1985).
- [3] M. Heiblum, M. I. Nathan, D. C. Thomas, and C. M. Knoedler, *Phys. Rev. Lett.* **55**, 2200 (1985).
- [4] J. Spector, H. L. Stormer, K. W. Baldwin, L. N. Pfeiffer, and K. W. West, *Surface Sci.* **228**, 283 (1990).
- [5] See references in T. K. Gaylord, E. N. Glytsis, G. N. Henderson, K. P. Martin, D. B. Walker, D. W. Wilson, and K. F. Brennan, *Proc. IEEE* **79**, 1159 (1991).
- [6] W. van Haeringen and D. Lenstra (eds.), *Analogies in Optics and Micro Electronics*. (Kluwer Academic Publishers, Dordrecht, Netherlands, 1990).
- [7] G. N. Henderson, T. K. Gaylord, and E. N. Glytsis, *Proc. IEEE* **79**, 1643 (1991).
- [8] U. Sivan, M. Heiblum, C. P. Umbach, and H. Shtrikman, *Phys. Rev. B* **41**, 7937 (1990).
- [9] J. Spector, H. L. Stormer, K. W. Baldwin, L. N. Pfeiffer, and K. W. West, *Appl. Phys. Lett.* **56**, 1290 (1990) and 2433 (1990).
- [10] H. Ohno, E. E. Mendes, and W. I. Wang, *Appl. Phys. Lett.* **56**, 1793 (1990).
- [11] L. D. Bell and W. J. Kaiser, *Phys. Rev. Lett.* **61**, 2368 (1988).
- [12] E. N. Glytsis, T. K. Gaylord, and K. F. Brennan, *J. Appl. Phys.* **70**, 3920 (1991).
- [13] T. K. Gaylord, E. N. Glytsis, and K. F. Brennan, *J. Appl. Phys.* **67**, 2623 (1990).
- [14] D. W. Wilson, E. N. Glytsis, and T. K. Gaylord, *Appl. Phys. Lett.* **59**, 1855 (1991).
- [15] G. N. Henderson, E. N. Glytsis, and T. K. Gaylord, *Appl. Phys. Lett.* **59**, 440 (1991).

Tuesday, April 14, 1992

Nonlinear Fiber Phenomena

TuF 10:30 am–12:00 m
Pelican Room

M. Cada, *Presider*
Technical University of Nova Scotia, Canada

Squeezed Optical Solitons

Robert M. Shelby
IBM Almaden Research Center, K34/803
650 Harry Rd.
San Jose, CA 95120-6099
(408) 927-2423

An optical fiber is a dispersive nonlinear waveguide. Short pulses in single-mode fibers broaden temporally due to the dispersion in the group velocity, and broaden spectrally due to the intensity-dependence of the index of refraction of fused silica which leads to self-phase modulation. Classical optical solitons avoid this distortion because the phase shifts due to these two effects are made to balance each other. This balance is achieved by the proper choice of pulse shape and duration for a given pulse energy. The resulting soliton pulses propagate long distances, limited only by fiber losses and are Fourier-transform-limited pulses characterized by a single nonlinear phase shift and well-defined central frequency and pulse position in time. They often can be thought of as interacting with each other in a particle-like way, and these properties give soliton pulses in fibers or in other waveguides great potential for applications in communications and optical logic.

However, this ideal classical picture no longer obtains when the quantum nature of the optical field is considered. Quantum fluctuations associated with a coherent soliton do not undergo stationary propagation, and a number of effects are predicted including the evolution of vacuum noise associated with the input coherent pulse into squeezed fluctuations, and the temporal spreading of the soliton pulse due to dispersion acting on quantum fluctuations of the pulse frequency. It is of interest to understand whether these quantum noise effects will disturb soliton propagation, and if so over what propagation distances they may become important. We have begun experimental investigation of the quantum propagation of initially coherent solitons (i.e. pulses corresponding to a classical mean optical field superimposed on fluctuations due to the zero-point or vacuum noise of the quantum field) by measuring the evolution of phase-independent vacuum noise into phase-dependent, squeezed quantum noise.

Squeezed states of light are nonclassical optical fields. A mode of the electromagnetic field has two degrees of freedom: the two quadratures of the field. Following the analogy between the quantized field mode and a mechanical harmonic oscillator, the two quadratures correspond to the position and momentum, and they obey a corresponding uncertainty principle. This quantum quadrature noise is responsible for the equal phase and amplitude noise of a coherent pulses, and is responsible for the shot noise limit when coherent light is detected. Squeezed light has less uncertainty in one quadrature than that of coherent light and correspondingly greater uncertainty in the other. If the squeezed quadrature is in phase with the mean field, reduced intensity noise and photocurrent noise less than the shot noise limit results. Although only prototype applications of squeezed light have been demonstrated, squeezed light generation may one day provide a practical means of reducing fundamental photodetector noise to below the shot noise.

In an optical fiber fluctuations in the intensity acting via the intensity-dependent refractive index impose correlated fluctuations in the phase of a light pulse as it propagates. This correlation can be used to produce a destructive interference of the intensity noise of the pulse, i.e. a pulse with squeezed amplitude quadrature results. To date we have observed reduction in quantum noise to a factor of two below the vacuum noise level after propagation of 200 fsec pulses through 5 meters of fiber held at liquid nitrogen temperature. The low temperature is used to reduce thermal fluctuations in the fiber refractive index which can swamp the quantum noise after only a few meters of propagation. This thermal noise originates physically from localized two-state-like modes in the amorphous silica material, from acoustic waves that are guided by the glass fiber, and from Raman scattering by the silica matrix. The thermal fluctuation spectra due to these mechanisms have been extensively investigated, and a full colored noise theory of quantum soliton propagation in the presence of these thermal fluctuations has been developed, more than 90% elimination of the quantum noise in one quadrature is predicted compared with the observed 50%. Current research strives to understand the source of this discrepancy.

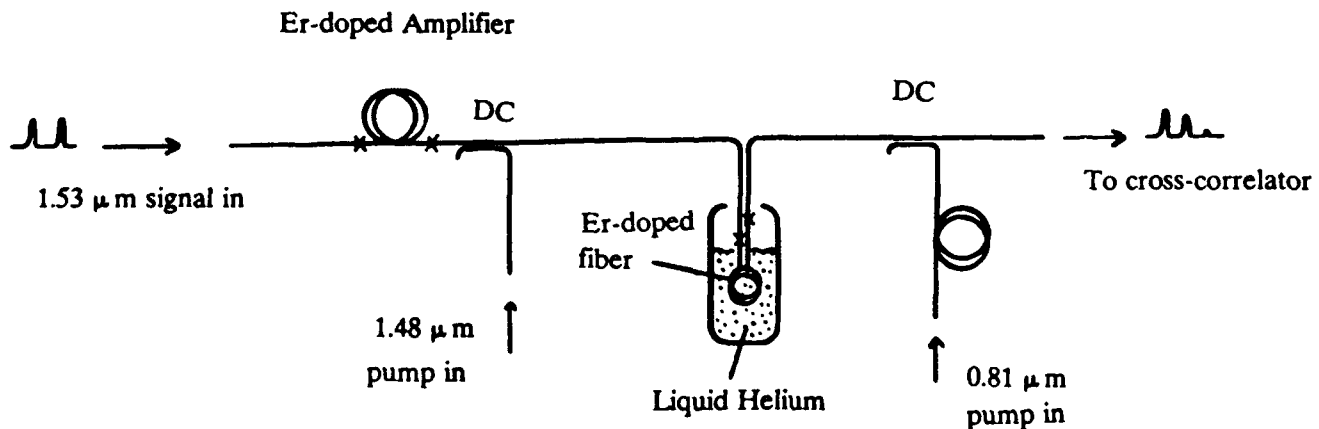
Photon-Echoes in a Pumped Er-Doped Fiber

V. L. da Silva, Y. Silberberg

Bellcore, 311 Newman Springs Rd., Red Bank, N.J. 07701-7040

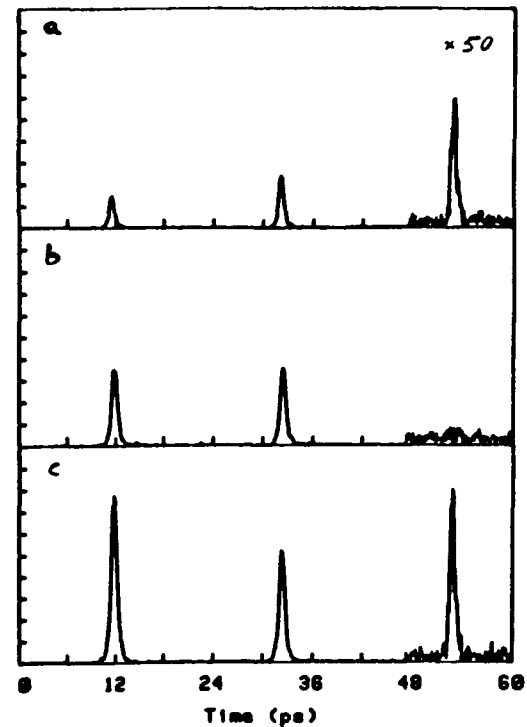
Recently we reported the first photon echo experiments in Er-doped fibers, and described their application to ultrafast time domain signal processing [1]. Our previous results were obtained with absorbing Er-doped fibers at 4°K, and our signals at 1.53 μ m were attenuated by the fiber. In this paper we report photon echo experiments with Er-doped *amplifiers*. We expect the photon echo process in amplifiers to yield strong echoes, perhaps stronger than the input signal. This could be important for signal processing applications. To our knowledge this is the first demonstration of photon echo in any inverted system.

Photon echo is a coherent optical effect which is observable on time scales shorter than the homogeneous dephasing time of the system. The dephasing time of the 1.53 μ m $^4I_{15/2} \rightarrow ^4I_{13/2}$ erbium transition in silica at 4.2°K is about 1 nsec. At this temperature the transition is inhomogeneously broadened, with a width which is about 1000 times that of the homogeneous width. The main difficulty in this experiment is to pump the entire inhomogeneous line. Most pump sources used to pump room-temperature Er-doped fibers are much narrower than the 10 nm wide inhomogeneous line, and therefore they will pump only a small fraction of the population in a cooled fiber. In our experiment we have used a modelocked Ti:Sapphire laser at 810 nm. The 1.2 psec pulses from the laser are about 0.5 nm wide, however, after propagating through a few meters of optical fiber they are broadened through self-phase-modulation to more than 15 nm. A few hundreds milliwatts could be coupled to the cooled fiber.



1. Outline of the experimental setup. DC - dichroic couplers.

2. The time resolved signal emerging from the fiber for three different pumping situations. (a) No pump, signal is attenuated. (b) Partial pumping, system at transparency. (c) Inverted system, signal is amplified.



The $1.53\mu\text{m}$ signal coupled to the fiber consisted of an 82 MHz train of 1 psec, equal-amplitude pulse-pairs separated by 20 psec. Fig. 2 shows the cross-correlation between the output signal from the fiber and a single short pulse. The traces are shown for (a) no pump, (b) pump adjusted for transparency, and (c) inverted system. The echo was observed to decrease as the pump power is increased, until it completely disappears when transparency is reached. The echo increased again as inversion is induced. Fig. 2 also shows coherent coupling between the excitation pulses. Note that due to the 10 msec lifetime of the transition there is practically no population changes on the picosecond time scale shown. The change in the relative strength of the excitation pulses are all due to coherent coupling.

Finally, we note that the echo generated in the amplifying system can be stronger than that generated in the absorbing system, but its relative strength compared with the transmitted excitation pulses is actually reduced. In our presentation we will explain the physics behind these effects and discuss their possible implications on signal processing systems.

REFERENCE

- [1]. V.L. da Silva, Y. Silberberg, J.P. Heritage, E.W. Chase, M.A. Saifi, and M.J. Andrejco, *Opt. Lett.* 16, 1340 (1991).

Soliton-Dragging Logic Gate with an Erbium-Doped Fiber Amplifier

M.N. Islam, C.E. Soccolich, B.J. Hong, C.-J. Chen, J.R. Simpson, D.J. DiGiovanni
AT&T Bell Laboratories, Holmdel, N.J. 07733

We place an erbium-doped fiber amplifier (EDFA) in the interaction region between orthogonally polarized control and signal pulses to widen the timing window for a soliton-dragging logic gate (SDLG). In general, the two inputs to an SDLG must overlap within a pulse width to obtain a time shift at the device output. However, by introducing gain during the interaction between the two pulses, we can asymmetricize the walk-off and, thereby, broaden the timing window [1].

To understand the expected timing broadening, we first solve numerically the coupled nonlinear Schrödinger equations. In the simulations we assume a several walk-off length section of moderately birefringent fiber followed by a discrete amplifier and then a longer length of moderately birefringent fiber (insert in Fig. 1). Figure 1 shows the calculated shift of the control pulse ΔT (with and without the signal) versus initial separation between pulses ($\delta t = t_{\text{signal}} - t_{\text{control}}$) when the same moderately birefringent fiber is used on both sides of the amplifier and the control pulse is along the fast axis. Curves are plotted for a discrete gain of 1.5 placed at 1, 1.5 and 2 walk-off lengths, l_{wo} , down the fiber. We find that the timing window can be broadened, although the shape is quite asymmetric. The peak near $\delta t=0$ arises from the interaction between the control and signal pulses at the beginning of the first fiber. A second feature (at $\delta t < 0$) arises from collision of the pulses in the amplifier, and its magnitude is proportional to the increase in the signal amplitude (i.e. proportional to the gain minus one).

The deviation from the ideal case, which would have a broadened rectangular-like curve for the timing shift, occurs because we assume identical fiber properties on both sides of the amplifier. If the control pulse is an $N=1$ soliton in the second length of the fiber, then the amplifier limits the control to $N < 1$ in the first fiber. Consequently, the control and signal pulses broaden while propagating in the first fiber. Since the peak intensity of the pulses decreases by the time the two pulses collide in the amplifier, the strength of the shift also decreases. To achieve the optimal timing relaxation requires the use of different fibers on each side of the amplifier; i.e., we need to adjust the fiber core sizes and/or dispersions so that the control pulse is an $N=1$ soliton in both sections. For example, if we neglect the pulse shape changes associated with propagation [1], then we can obtain a nearly flat-topped broadening of the timing window with a 3dB amplifier placed $1.54l_{\text{wo}}$ down the fiber.

To verify the widening of the timing window, we performed experiments using an EDFA in the apparatus of Fig. 2. The first section is 25 m of moderately birefringent fiber with a polarization dispersion of 33 ps/km, which for $\tau=0.5$ ps pulses corresponds to about $1.6l_{\text{wo}}$. The output from this fiber is coupled into a 1.77 m length of polarization-maintaining EDFA (1660 ppm doping level and ends beveled to prevent lasing). The EDFA is pumped at 980 nm by a Ti:Sapphire laser through a dichroic beam splitter that transmits both polarizations at 1.56 μm while reflecting the pump. Finally, the amplified beam is coupled into a 30 m ($\sim 2l_{\text{wo}}$) length of the same moderately birefringent fiber, which is then fusion spliced to a 480 m length of polarization-maintaining fiber.

We obtain sub-picosecond pulses at $\lambda \sim 1.56\mu\text{m}$ from a passively modelocked NaCl color-center laser. The control and signal energies in the first fiber were ~ 12.3 pJ, and the gain in the EDFA was adjusted so that the control energy out of the last fiber was ~ 20 pJ, which corresponds approximately to the $N=1$ soliton. Therefore, the net gain between the fibers was ~ 1.6 including the coupling and beam splitter losses. One serious complication in the experiment is that the EDFA is not a linear amplifier at these power levels; i.e. in the partially saturated amplifier the gain for the control pulse decreases when the signal pulse is added. Since there is some soliton self-frequency shift in the fiber (the control pulse alone experiences a spectral shift less than one-sixth of its spectral width), changes in the control pulse amplitude lead to a time shift. The EDFA has long lifetimes for the excited state (0.1-1 ms), so the gain saturation is a slow effect that can be compensated for.

The experimental time shift curve is plotted in Fig. 3 for $\tau=0.5ps$ pulses from the laser, and at least qualitatively we see similar behavior as in Fig. 1. We compensate for the amplifier saturation by subtracting out the background shift caused by the signal pulse when the control and signal are separated by many pulse widths. Differences in the shape between theory and experiment may arise from: (a) the pulses from the laser are not hyperbolic secant pulses as used in the simulations; and (b) the simulations assume a discrete amplifier, while our EDFA has a finite length, which means that the pulses will shift their relative positions somewhat (less than a pulse width).

In summary, we show that pulse amplification during the soliton-dragging interaction can increase the timing window. The results can be improved by using different fibers on the two sides of the EDFA and using an EDFA with a higher saturation energy.

[1] M.N. Islam, C.R. Menyuk, C.-J. Chen, and C.E. Socolich, Opt. Lett. 16, 214 (1991).

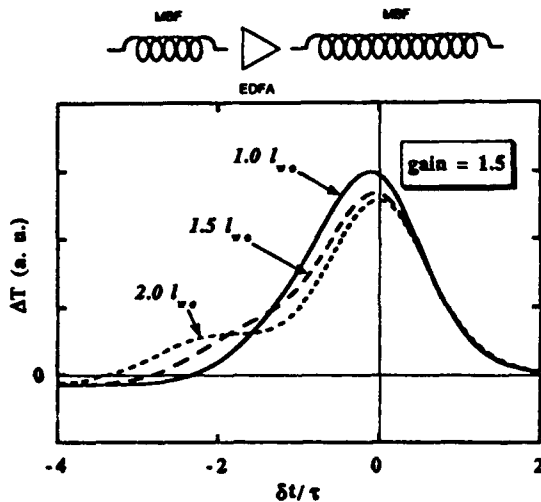


Fig.1 Calculated shift of the control pulse ΔT versus initial separation between control and signal pulses δt with a net gain of 1.5 and the EDFA located at 1, 1.5 and 2 l_{wo} down the fiber.

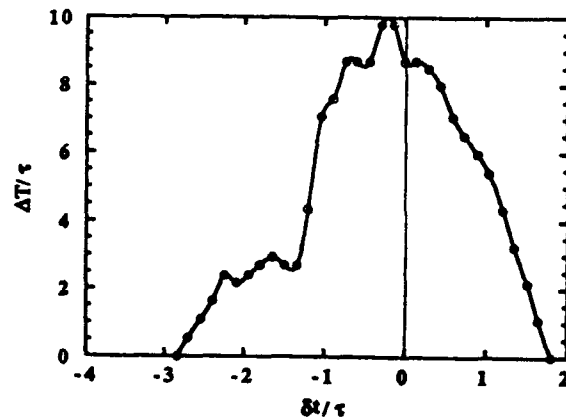


Fig.3 Experimentally measured timing shift of the control pulse versus initial pulse separation for a net gain of 1.6 and the amplifier about 1.6 walk-off lengths down the fiber.

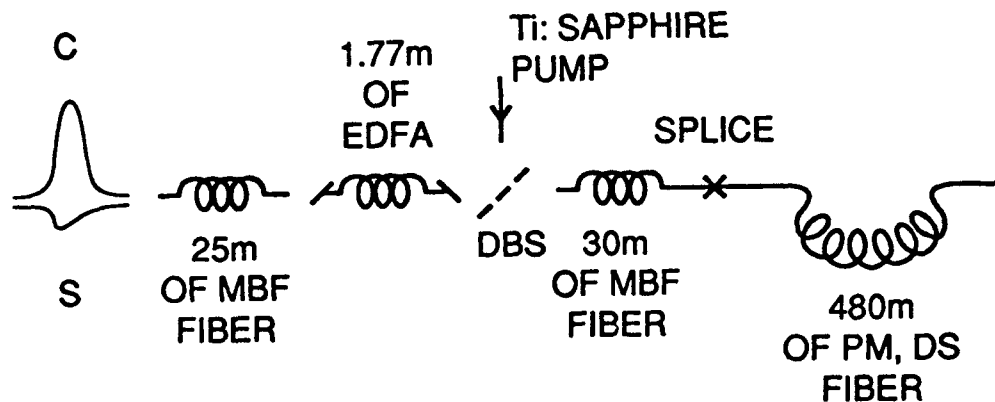


Fig.2 Experimental configuration for testing the timing relaxation when introducing an EDFA (MBF = moderately birefringent fiber, DBS = dichroic beam splitter, PM-DS = polarization-maintaining, dispersion-shifted).

Soliton Interactions in Periodically Amplified Fiber Systems

Y. Kodama

Department of Mathematics, Ohio State University, Columbus, OH 43210, USA

S. Wabnitz

Fondazione Ugo Bordoni, Via B. Castiglione 59, 00142 Rome, Italy

The transmission of optical solitons over transoceanic distances by means of dispersion shifted fibers and periodic all-optical amplification by erbium doped fibers has been recently demonstrated. Soliton transmission in the fiber link is described by the averaged nonlinear Schrödinger (NLS) equation [1-3]

$$\frac{\partial V}{\partial Z} - \frac{i}{2} \frac{\partial^2 V}{\partial T^2} - i|V|^2 V = \delta V - \beta \frac{\partial^2 V}{\partial T^2} \equiv R. \quad (1)$$

Here δ is the excess amplifier gain, and β ($\beta < 0$) is the mean value of the gain dispersion. Note that β may be controlled by inserting Fabry-Perot filters after each amplifier. Based on the dynamics of single solitons in the perturbed eq.(1), Kodama and Hasegawa have predicted the suppression of the Gordon-Haus effect [3], which has been recently confirmed experimentally [4].

In this work we consider the interaction between a soliton pair of the form

$$V(T, Z = 0) = \text{sech}(T - X_0/2) + \text{sech}(T + X_0/2). \quad (2)$$

A preliminary analysis has shown that the collision distance between the two pulses in eq.(2) may be more than doubled by the insertion of the filters [5]. Here we optimise the choice of the parameters in eq.(1) in order to obtain the largest bit rate improvement, without introducing net amplification or compression of the solitons owing to the excess gain δ .

First we consider a two soliton perturbation analysis of eq.(1) with the condition (2). The real eigenvalues η_ℓ , $\ell = 1, 2$ of eq.(2) move in the complex plane according to

$$\frac{d\eta_\ell}{dZ} = i \frac{\int_{-\infty}^{\infty} \{R\psi_2^2(\eta_\ell) + R^*\psi_1^2(\eta_\ell)\} dT}{\int_{-\infty}^{\infty} \{\psi_1(\eta_\ell)\psi_2(\eta_\ell)\} dT}; \ell = 1, 2 \quad (3)$$

where $\psi_{1,2}$ are the two soliton eigenfunctions of the NLS equation. By solving eqs.(3) we may determine the optimal values of δ, β in eq.(1).

In the real transmission system a filter is described by the complex transfer function

$$H(\omega) = \frac{1}{(1 + \frac{2i(\omega - \omega_0)}{B})} \quad (4)$$

This introduces higher order dispersive terms in eqs.(1). We determine the influence of these higher order effects on the soliton interaction by comparing analytical and numerical results. We obtain that even when a balance exists between the excess gain and the high frequency loss due to the filter, still it is possible to double the collision distance and hence the bit rate of the transmission (see fig.(1)). We give an interpretation of these results in terms of the nonlinear dynamical properties of the single (in the case of weak overlapping) and two soliton solutions of the perturbed NLS equation (1).

References

- [1] A. Hasegawa, and Y. Kodama, *Optics Lett.* **15**, 1443 (1990); *Phys. Rev. Lett.* **66**, 161 (1991).
- [2] L.F. Mollenauer, S.G. Evangelides, and H.A. Haus, *J. Lightwave Technol.* **9**, 194 (1991).
- [3] Y. Kodama, and A. Hasegawa, *Generation of asymptotically stable optical solitons and suppression of the Gordon-Haus effect*, submitted to *Optics Lett.* (1991).
- [4] L.F. Mollenauer *et al.*, *Electronics Lett.* **27**, 2055 (1991).
- [5] Y. Kodama, and S. Wabnitz, *Electron. Lett.* **27**, 1931 (1991).

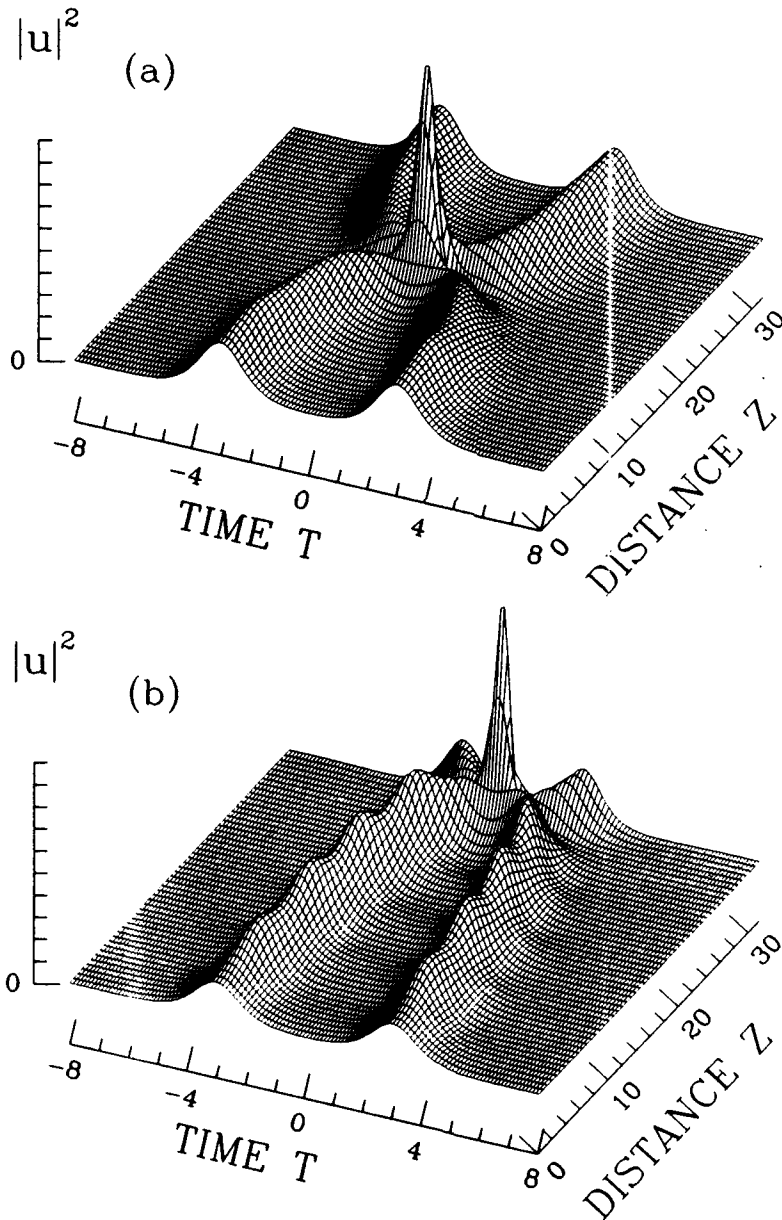


Figure 1: Two soliton collision (a) without the insertion of filters; (b) with properly designed filters ($\delta = 0.04$, $B = 30$, and $X_0 = 6$). The input pulse width is 50 ps, and the total distance is equal to 20,000 km.

TuF5-1

Sideband Formation in Soliton Lasers and Transmission

N.J. Smith, K.J. Blow

BT Laboratories, Martlesham Heath, Ipswich IP5 7RE, UK; Tel. 0473 643417

I. Andonovic

Strathclyde University, 204 George Street, Glasgow G1 1XW, UK; Tel. 041 552 4400

1 Introduction

Both optical communication systems and erbium doped fibre lasers have been developed in which the pulses are thought of as being solitons. The propagation is insensitive to periodic changes in the pulse energy occurring on length scales, Z_a short compared with the soliton period, Z_0 , as formalised in the Average Soliton Model[1]. Such energy variations are caused by the lumped amplifiers in transmission schemes, or output couplers in a fibre laser cavity.

Mode locking processes in fibre lasers can force operation into regimes where the cavity length (and hence energy variations) are comparable to the soliton period. In this situation sidebands have been observed in the output spectrum [2].

To explain these sidebands, we describe the mechanism as a two stage process. The energy perturbations cause dispersive wave radiation to be emitted from the pulse over a broad band of frequencies. A phase matching process then selects individual wavelengths which grow into sidebands.

2 Numerical Simulations

The Nonlinear Schrodinger Equation (NLSE) describing the nonlinear pulse dynamics can be implemented numerically to provide accurate simulations of the system's behaviour. We did not incorporate the effects of a mode-locker, considering only nonlinear propagation, including gain and loss terms. The results showed multiple sidebands in the spectra, as illustrated in figure 1. Both the amplitude and position in wavelength of these sidebands was found to be a function of the amplifier spacing.

3 Dispersive Wave Formation

It is well known that a perturbed soliton will emit dispersive radiation from the main pulse. Blow and Doran have shown [1] that the full NLSE can be rescaled into a lossless version for small z_a , thus confirming stability in the face of energy variations. By following the same approach we have derived extra terms that must be considered for significantly large amplifier spacings. These take the form of concatenated self phase modulation and dispersion. Intuitively this is correct, for at some stages of the gain/loss cycle the power level results in an excess of nonlinearity over dispersion, and vice versa at other positions.

These terms form a continuous source of extra frequency components produced by the pulse every amplification cycle. Their spectrum extends well beyond the bandwidth of the original soliton. In non modelocked situations, this eventually leads to temporal collapse of the pulse. Modelocking results in an equilibrium by constantly removing the dispersive radiation.

4 Phase Matching

The dispersive wave radiation is formed coherently with the soliton, but has different phase velocity. Consequently interference may take place between generation from different amplification cycles. Sideband formation will only take place at wavelengths phase matched to the soliton over an amplifier spacing (or cavity length in the case of a laser).

The nonlinear phase, ϕ , of a soliton and the linear phase, ψ of a sideband separated by $\Delta\omega$ are,

$$\phi = \frac{|\beta|Z}{2\tau^2}; \quad \psi = -\beta\Delta\omega^2 Z/2 \quad (1)$$

From the phase matching criteria, $\psi(Z_a) - \phi(Z_a) = 2m\pi$, the wavelength at which sidebands form may be derived:

$$\Delta\lambda = \frac{\pm\lambda^2}{2\pi c\tau} \sqrt{\left\{1 + \frac{8mZ_0}{Z_a}\right\}} \quad (2)$$

This is a selection criterion only, the amplitude of the oscillation will be substantially determined by the strength of the driving force, namely dispersive wave generation at that wavelength.

5 Discussion

The sidebands are not evenly spaced in wavelength, the offset varying approximately with \sqrt{m} . This is reflected in figure 1, which shows the sidebands predicted by this theory marked on the spectrum from a full numerical simulation.

The $m = 1$ sideband is in most cases dominant, lying near the spectral peak of the dispersive radiation. In figure 2 we show the excellent agreement between prediction and numerical simulation as a function of amplifier spacing.

In conclusion we have identified the mechanism responsible for sideband formation in mode locked fibre lasers. The theory is equally applicable to soliton transmission systems, allowing the effect of amplifier spacing to be quantified for the first time.

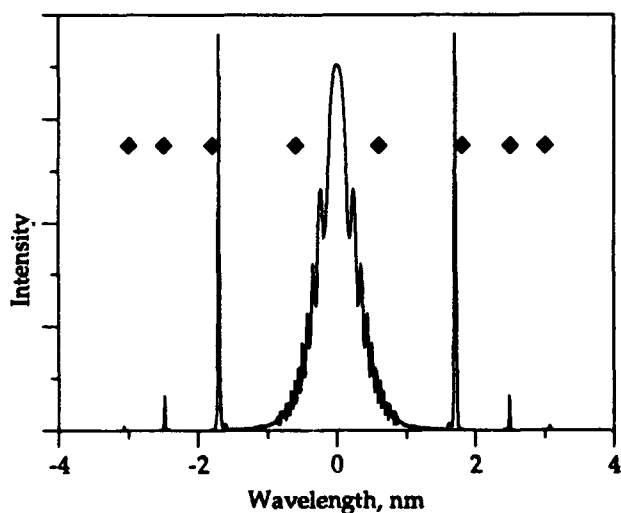


Figure 1: Spectra showing high order sidebands, predictions marked by diamonds

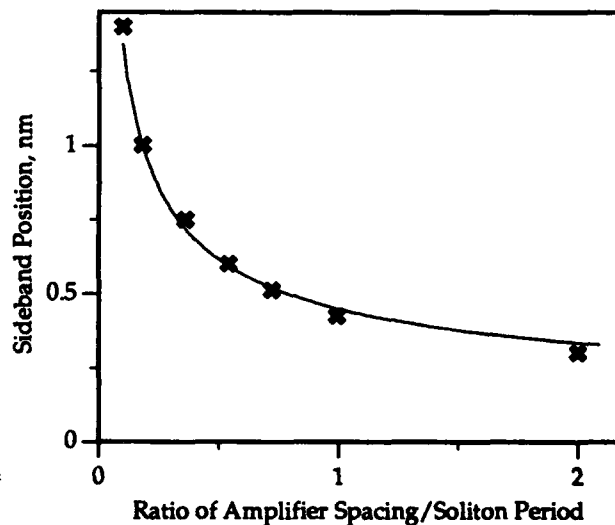


Figure 2: Phase matching criterion as a function of amplifier spacing. Simulation results are marked with crosses.

References

- [1] Blow, K.J., Doran, N.J., IEEE Photonics Techn. Lett., 1991, 3, pp. 369-371
- [2] Richardson, D.J., Laming, R.I., Payne, D.N., Matsas, V.J., Phillips, M.W., Electron. Lett., 1991, 27, pp. 1451-1453

Tuesday, April 14, 1992

Electro-Optic Devices

TuG 1:30 pm–3:00 pm
La Salle Ballroom B

D. A. Smith, *Presider*
Bellcore

FAST AUTOMATIC POLARIZATION CONTROL SYSTEM

F. Heismann and M. S. Whalen

AT&T Bell Laboratories, Crawfords Corner Road, Holmdel, NJ 07733, Tel. (908) 949-6343

Automatic polarization controllers are of great interest for fiberoptic communication systems to compensate for the random polarization fluctuations in standard optical fibers, thus allowing the use of polarization-dependent components, such as coherent optical receivers, high-speed modulators, or photonic switches. Here, one requires polarization controllers with effectively endless transformation ranges and control speeds of the order of 1000 rad/sec to continuously track the large and rapid changes in the optical phase retardation of the fiber [1]. Previous systems for endless polarization control have not exceeded speeds of 50 rad/sec [2], limited by the slow response of mechanical actuators and complicated drive algorithms.

In this paper, we demonstrate an inherently fast polarization control system using a waveguide *electrooptic* polarization transformer and a simple electronic feedback circuit, which presently operates at speeds of up to 6300 rad/sec. The integrated-optic controller, shown schematically in Fig. 1, is fabricated on low-birefringent z-propagation LiNbO₃ with a titanium-indiffused single-mode waveguide designed for 1.5 μm wavelength.

It employs three cascaded electrode sections, which are driven by sinusoidal voltages of the form shown in Fig. 1, where the two phase angles α and γ are the only independent variables. With α and γ endlessly adjustable, the controller allows endless transformations from any arbitrarily varying general input polarization state into any arbitrary output state, as we have previously demonstrated in [3]. The voltages are generated by four digital sine-wave synthesizers with a step resolution of 5.6°.

A conventional polarization splitter at the output of the controller serves as the polarization discriminator and allows simultaneous detection of the optical powers in the two orthogonal output polarization states. However, the feedback circuit however monitors only the power in the desired output and searches for a maximum by continuously dithering the output polarization via α and γ using quadrature modulation at a frequency of 88 kHz. The dither is converted into intensity modulation by the polarization splitter and is then analyzed by two phase-sensitive detectors, which re-adjust α and γ after each dither cycle by one step increment to minimize the modulation component at the fundamental dither frequency.

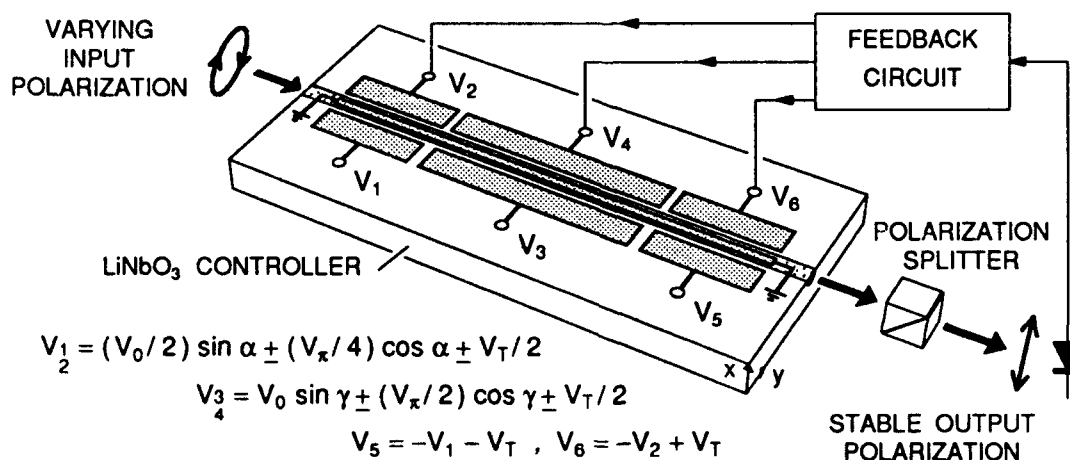


Fig. 1. Schematic diagram of the polarization control system ($V_0 \approx 19$ V, voltage for complete TE \leftrightarrow TM mode conversion; $V_\pi \approx 26$ V, voltage for TE-TM phase shift of π ; $V_T \approx 54$ V, bias voltage to compensate for residual birefringence; α and γ , endlessly adjustable parameters).

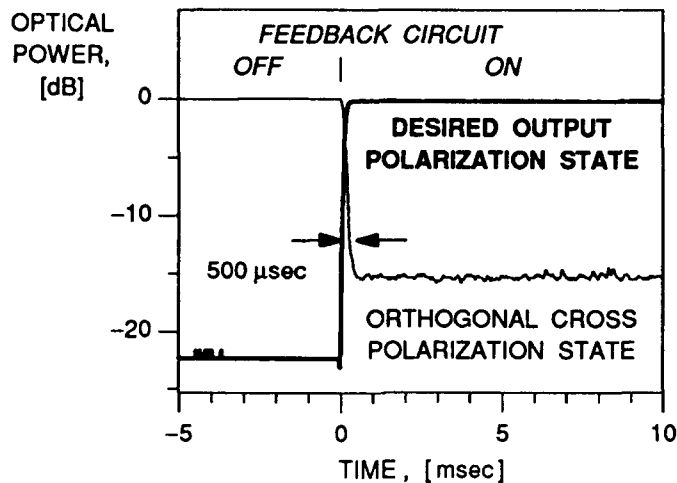


Fig. 2. Response time of the automatic control system, producing general elliptical phase retardation at 6300 rad/sec.

To measure the response time of the entire system, we have first turned off the feedback circuit and adjusted the input polarization of the controller such that all output light is in the undesired orthogonal cross polarization state, as shown in Fig. 2. The light source here is a 1.52- μm DFB laser diode. When the feedback circuit is now turned on, it takes the system less than 500 μsec to induce the π phase retardation required to transform the output light into the desired polarization state. Note that the phase retardation changes linearly with time at a record rate of 6300 rad/sec, which is more than 100 times faster than any previously reported speed. As a result of the finite polarization dither, about 2.5% of the output light remains in the undesired cross polarization state. This level could be reduced, at the expense of control speed, by decreasing the step increments in the sine-wave synthesizers.

In a second series of experiments, we have transformed various rapidly fluctuating input polarization states into a stable output state, as shown in the example of Fig. 3. Here, we have initially turned off the feedback circuit to show the large variations in the input polarization, which change periodically at rates of up to 4900 rad/sec and are generated by a second LiNbO₃ polarization transformer. With the feedback circuit turned on, the power in the desired polarization state stabilizes at a level of -0.18 dB

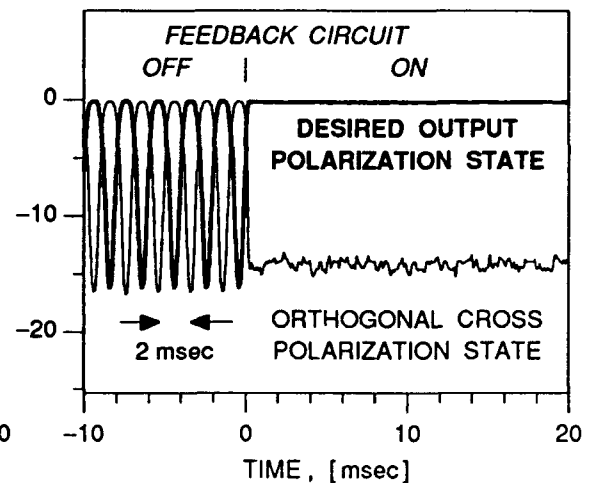


Fig. 3. Automatic stabilization of a rapidly varying polarization state, changing periodically at up to 4900 rad/sec.

of the total output light. The optical power in the undesired cross polarization state is about 4% and slightly higher than in Fig. 2, indicating that the system operates close to its speed limit.

We believe that the present control speed is sufficient for practical applications in fiberoptic communication systems. It is about two orders of magnitude faster than the polarization fluctuations in a submarine fiber cable during installation [4] and about one order of magnitude faster than the fastest polarization changes that we could generate by rapidly bending and twisting a fiber having only a thin plastic jacket. However, if necessary the speed could be increased further by employing a faster feedback circuit.

REFERENCES

- [1] G. R. Walker and N. G. Walker, *J. Lightwave Technol.* **8**, pp. 438-458, 1990.
- [2] H. Shimizu, S. Yamazaki, T. Ono, and K. Emura, *J. Lightwave Technol.* **9**, pp. 1217-1224, 1991.
- [3] F. Heismann and M. S. Whalen, *Electron. Lett.* **27**, pp. 377-379, 1991.
- [4] Y. Namihira, Y. Horiuchi, S. Ryu, K. Mochizuki, and H. Wakabayashi, *J. Lightwave Technol.* **6**, pp. 728-738, 1988.

TuG2-1

**"Very high speed polymeric external modulator with more than
40 GHz of 3-dB electrical bandwidth and low drive voltage"**

C. C. Teng, M. G. Scaturro, and T. K. Findakly

Hoechst Celanese Corp.
86 Morris Ave.
Summit, NJ 07901
Tel: 908-522-7681

Nonlinear optical (NLO) polymers offer unique advantages for high speed device applications by virtue of their low dielectric constants and the near perfect velocity matching between the optical and microwave wavevectors^{1,2}. In this paper, we report on the demonstration of a very high speed (> 40 GHz of 3-dB electrical bandwidth) electrooptic Mach Zehnder intensity modulator in a nonlinear optical polymer developed by Hoechst Celanese.

The optical Mach Zehnder circuit was formed by spin coating a three layer NLO polymer structure (two claddings and waveguide) to a total thickness of 6.5 μm on an electroplated Si wafer, and subsequent photo-bleaching³ for the definition of the optical guiding circuit yielding single mode operation at 1.3 μm . To induce the electrooptic effect, the device is poled⁴ (in the TM polarization) at a high electric field near the glass transition temperature of the polymer. The device utilizes a 12mm long gold-plated microstrip line applied to one arm of the Mach-Zehnder modulator. RF power is coupled in and out of the microstrip line through two 5mm long tapered coplanar waveguides and K connectors. The measured RF input coupling loss to the microstrip line was below 0.9 dB up to 40 GHz.

The index mismatch between the optical and the RF waves in the travelling -wave electrode $\Delta n = \sqrt{\epsilon} - n$, where ϵ is the effective dielectric constant and n is the effective refractive index of the medium, is about -0.03 for the used NLO polymer yielding excellent velocity matching for a wide bandwidth which becomes limited primarily by conductor losses. The modulator frequency response was measured with a calibrated direct detection system. The modulator was biased at the linear portion of the modulation transfer curve and a leveled RF power output from a microwave synthesizer was connected directly to the input K connector. The measured 3-dB electrical bandwidth of the modulator is more than 40 GHz, as shown in Fig. 1, which is very close to the theoretical prediction with the measured input coupling loss and conductor loss ($0.75 \text{ dB/cm} \cdot \sqrt{\text{GHz}}$). The characteristic impedance of the transmission line was close to 50 Ω yielding an RF return loss below -17 dB from DC to 40 GHz as shown in Fig. 2. Additionally, the current design

is expected to have extremely small phase distortion¹, which is essential for direct time domain modulation such as in short pulse applications.

The drive voltage V_{π} of the modulator depends on the poling field applied during the poling process. For the demonstrated device, V_{π} was 6 V, with an extinction ratio > 20 dB, achieved with a poling field of 160 V/ μm . The corresponding electrooptic coefficient (r_{33}) is 26 pm/V. The drive voltage could be reduced by a factor of 2 with a push-pull operation in which the polymeric waveguides are poled in opposite directions in the two arms of the interferometer. This was performed and demonstrated at low frequencies. Demonstration of push-pull operation at high speed is in progress.

In summary, we have demonstrated an NLO polymeric wideband external modulator with > 40 GHz electrical bandwidth, < -17 dB return loss, a drive voltage of 6V, and an extinction ratio of > 20 dB. Additional data related to fabrication and performance will be reported at the meeting.

REFERENCES

- [1] C. C. Teng, "Travelling-wave polymeric optical intensity modulator with more than 40 GHz of 3-dB electrical bandwidth", submitted for publication to Appl. Phys. Lett. .
- [2] D. G. Girton, S. L. Kwiatkowski, G. L. Lipscomb, and R. S. Lytel, Appl. Phys. Lett. 58, 1730 (1991).
- [3] K. W. Beeson, K. A. Horn, M. McFarland, and J. T. Yardley, Appl. Phys. Lett. 58, 1955 (1991).
- [4] H. T. Man, K. Chang, D. Haas, C. C. Teng and H. N. Yoon. SPIE, 1213, Photopolymer Device Phys. Chem. and applications, (1990).

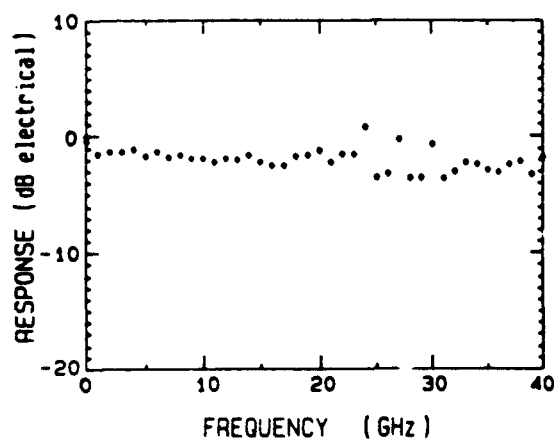


Fig. 1: Frequency response of the small-signal optical modulation.

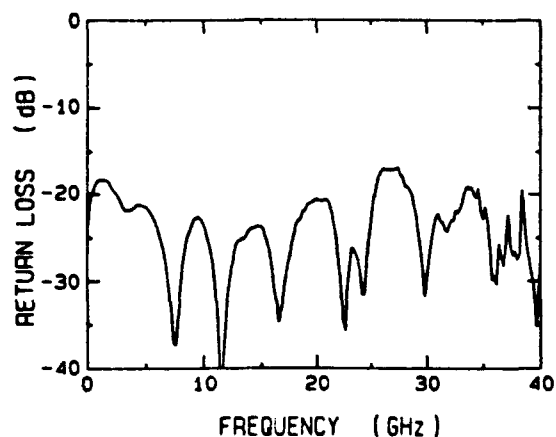


Fig. 2: RF return loss vs. frequency.

TuG3-1

Electrical and Optical Characteristics of 20 GHz Ti:LiNbO₃ Traveling Wave Intensity Modulator

G.K. Gopalakrishnan*, C.H. Bulmer[†], W.K. Burns[†], R.W. McElhannon* and A.S. Greenblatt[†]

[†]Naval Research Laboratory, Code 6571, Washington D.C. 20375-5000

*Maryland Advanced Development Laboratory, Greenbelt MD 20770

The bandwidth of Ti:LiNbO₃ traveling wave (TW) optical modulators may be enhanced by improving the phase match between the microwave and optical signals. This has been accomplished in the coplanar waveguide (CPW) configuration by use of a shielding plane [1] and in the coplanar strips (CPS) configuration by use of thick electrodes [2]. In the phase matched condition, the device bandwidth would be limited by only the resistive electrode loss, provided that there is no power leakage from the fundamental coplanar mode to the dielectric substrate modes of LiNbO₃. We have observed and modeled this leakage that occurs in LiNbO₃ traveling wave modulators. Below we describe our model and demonstrate a 20 GHz bandwidth optical modulator in the CPW configuration with thick electrodes without any power leakage over a 40 GHz span. The V_{π} for this device was 5 V at an operating wavelength of 1.3 μm .

The fundamental mode of a coplanar waveguide can become leaky by coupling to substrate modes (surface waves) when the effective index of the substrate mode is larger than that of the coplanar mode [3]. Phase match is achieved in the process by a tilt of the substrate mode wavevector relative to the axial direction of the coplanar mode and leakage occurs to both sides of the coplanar guide. To model this leakage, we consider c-cut slabs of LiNbO₃ which may or may not have a conductive layer (electrode) on top. The slab has a thickness h and is considered to be semi-infinite in width. The dispersion curves for the substrate modes are shown in fig. 1. Plotted is the effective index (n_m) vs. h/λ_0 where λ_0 is the free space wavelength. For CPS or CPW traveling wave devices with a microwave-optical phase match we expect the effective index of the coplanar mode to be near 2.15, the extraordinary index of LiNbO₃ at 1.3 μm . For CPW waveguides with semi-infinite ground planes, the first substrate mode which could cause leakage is the TM₀ (cond) mode, whose effective index exceeds 2.15 for $h/\lambda_0 > 0.04$. The asymmetric CPS (semi-infinite ground plane on one side) results in a substrate mode seeing a dielectric slab on one side of the strip and a conductor coated dielectric slab on the other side of the strip. We simply use the dispersion curve (TE₀(die)) for the uncoated dielectric slab which will cause leakage for values of $h/\lambda_0 > 0.015$. Hence leakage would occur at a lower frequency for CPS as compared to CPW implying better bandwidth for the CPW devices.

We fabricated Mach-Zehnder interferometric modulators using thick electrode (10-18 μm) CPS and CPW structures on c-cut LiNbO₃ with a 0.9 μm thick SiO₂ buffer layer. Strip widths were 8 μm , gap widths were 15 μm and ground planes were 2 to 3 mm wide. Finite element calculations indicated that these geometries should result in microwave indices between 2.4 and 2.2. Devices were fabricated on substrates 0.5-0.16 mm thick and 8 mm wide. The electrode interaction length was 24 mm. The devices were tested on an automatic network analyzer with the electrical transmission (S_{21}) shown in fig. 2. The variation of loss dips with device type and substrate thickness shown in fig. 2 confirms the mode coupling model presented above. The CPW device on a 0.16 mm thick substrate showed no leakage at all out to 40 GHz. The optical response of this device is shown in fig. 3 indicating a bandwidth(3 dB-electrical) of 20 GHz; this coincides with the approximately -6 dB point of the electrical response, indicating a near phase match between the microwave and optical signals.

We have, for the first time, explained the anomalous power leakage occurring in LiNbO₃ traveling wave modulators. Based on the model, CPW devices have been shown to be superior to CPS devices and electrical performance to 40 GHz without any power leakage in a CPW device has been demonstrated. The device has an optical bandwidth (3 dB-electrical) of 20 GHz and a V_{π} of 5 V.

REFERENCES

- [1] K. Kawano et al.: 'New traveling-wave electrode Mach-Zehnder optical modulator with 20 GHz bandwidth and 4.7 V driving voltage at 1.52 μm wavelength', Electron. Lett., 1989, 25, pp. 1382-1383.

- [2] M. Seino et al.: '20 GHz 3 dB bandwidth Ti:LiNbO₃ Mach-Zehnder modulator', ECOC, 1990, paper ThG1-5.
- [3] D.P. Kasilingam and D.B. Rutledge: 'Surface-wave losses of coplanar transmission lines'. IEEE International MTT-S Digest, 1983, pp. 113-116.

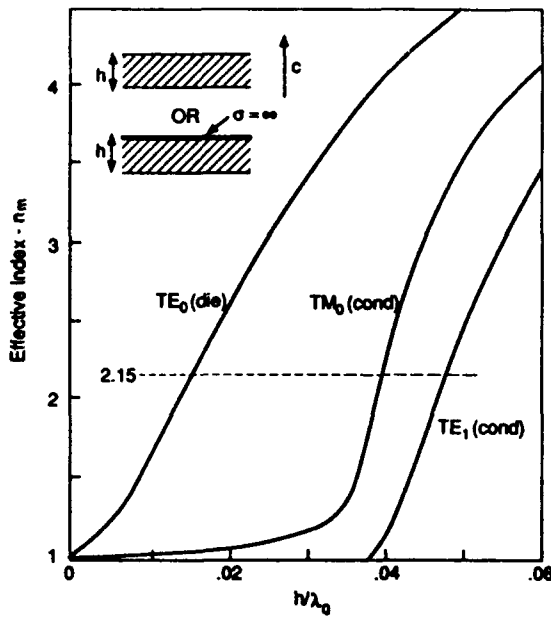


Fig. 1

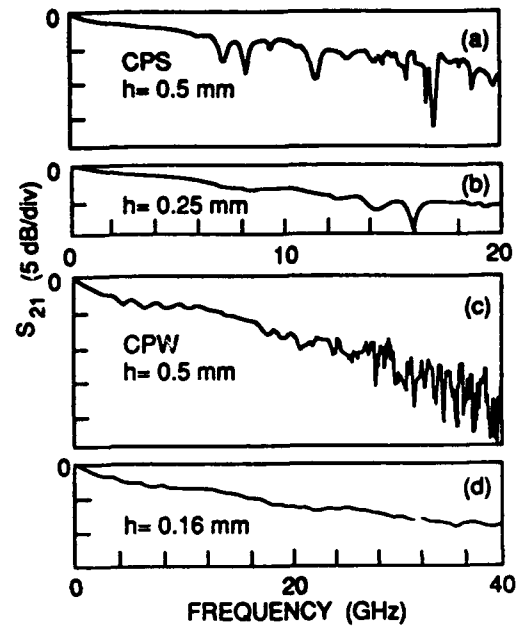


Fig. 2

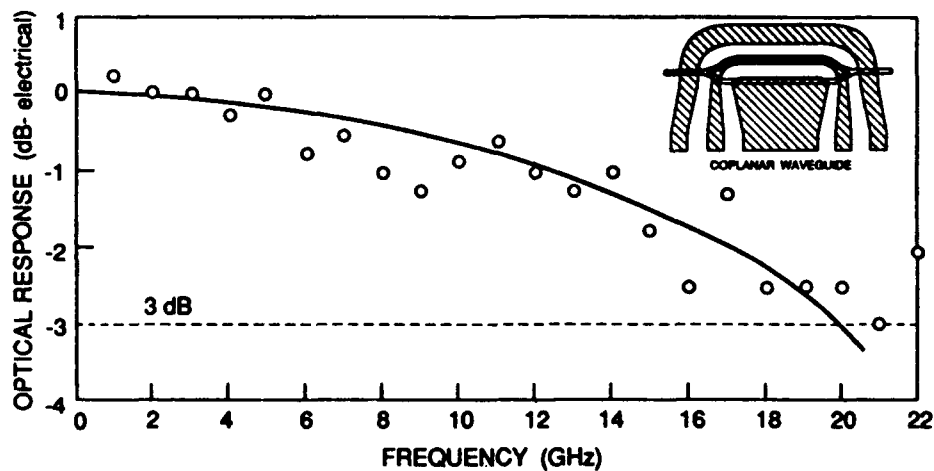


Fig. 3

Sensitivity to RF Drive Power and the Temperature Stability of Mach-Zehnder Modulators

J.J. Veselka, S.K. Korotky
AT&T Bell Laboratories

Room HO 4D-507, Crawfords Corner Road, Holmdel, NJ 07733-1988, 908-949-5213

C.T. Kemmerer, W.J. Minford, D.T. Moser, R.W. Smith
AT&T Bell Laboratories

Solid State Technology Center, Route 222, Breiningsville, PA 18031-9359

Waveguide electrooptic modulators usually require a DC bias voltage that is used to set an optical phase relation between waveguides to attain proper operation. In practice, the DC bias voltage consists of intrinsic and extrinsic components. The intrinsic component is that voltage necessary for an ideal device, which may be zero by design, while the extrinsic component is required to compensate for materials and fabrication imperfections and/or environmental influences. As the power supplies allowable for applications will place strict bounds on the bias voltage range, it is essential to prepare materials and formulate designs for maximum stability. In this work we concentrate on the temperature stability of traveling-wave Mach-Zehnder modulators, and, in particular, those fabricated in LiNbO_3 . We present results of experiments on the sensitivity of the bias point to RF drive power that emphasize the importance of structural symmetry in achieving environmentally stable devices.

High-speed electrooptic modulators may be exposed to changes in temperature for a variety of reasons. The changes may be caused by a change in the ambient environment, or, for example, a change in the temperature of the active region caused by the dissipation of RF power in the electrode and/or substrate. Such temperature changes may act directly, or through changes in stress and the photoelastic effect, to change the index of refraction of the material, and therefore the bias phase and operation of the device. Additionally, if the material is pyroelectric, as is LiNbO_3 , the index may be changed through changes in the internal field acting through the electrooptic effect. Because of the latter phenomenon it is normally assumed that devices fabricated on z-cut LiNbO_3 will be more sensitive to temperature variations than those fabricated on the x-cut orientation, and that LiNbO_3 modulators will be more sensitive than semiconductor devices [1]. However, it should be clear that most devices based on single-mode waveguides, such as the Mach-Zehnder interferometer, are mainly sensitive only to changes of the differential index between two waveguides. Therefore, it is the symmetry of the device structure and the drive configuration that will greatly effect the manifested thermal sensitivity of the device.

Using a dual-drive traveling-wave Mach-Zehnder modulator fabricated on z-cut LiNbO_3 [2] we have experimentally investigated the *structural* component of the temperature sensitivity of the electrode/waveguide configurations commonly used for LiNbO_3 traveling-wave modulators, Fig. 1. We have found the asymmetric configuration to result in a bias point sensitivity to temperature that is inherently 10-20 times larger than a balanced design and that the dual-drive design on z-cut is virtually identical in sensitivity to typical x-cut modulators using the symmetric coplanar waveguide (CPW) electrode geometry. Previously reported large differences between the temperature sensitivity of z-cut and x-cut LiNbO_3 interferometric modulators [1] can be understood based on the built-in asymmetry of the electrode/waveguide configuration of the z-cut device tested.

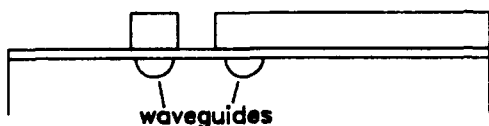
The present experiments were conducted by driving the two electrodes of the dual drive modulator, Fig. 2, in anti-phase at 1 GHz and recording the bias point for optimum modulation linearity, i.e. minimum second harmonic, for TM light as a function of the electrical drive powers delivered to the two inputs. In Fig. 3 we plot the observed bias point shift versus the drive power to electrode B for various ratios of the drive powers. Under balanced drive conditions the sensitivity is approximately 1 V/W. This is similar to that of x-cut devices we have tested [3]. When only one electrode is driven, the rate of change of

bias with drive power is an order of magnitude higher. This is comparable to ACPS devices we have tested [3]. It is worth noting that for the present device, which requires 2 V peak-to-peak (10 mW @ 50 Ω) delivered to each electrode to fully switch at 1 GHz, the bias point shift for 100% optical modulation depth is only 0.003 of the switching voltage.

REFERENCES

1. P. Skeath, C.H. Bulmer, S.C. Hiser, and W.K. Burns, "Novel electrostatic mechanism in the thermal instability of z-cut LiNbO₃ interferometers," *Appl. Phys. Lett.* **49**, 1221 (1986).
2. S.K. Korotky, *et al.*, "High-speed low drive power optical modulator with adjustable chirp," in *Tech. Dig. Top. Meet. Integrated Photonics Research, Monterey, 1991*, paper TuG2.
3. S.K. Korotky and J.J. Veselka, unpublished.

Fig. 1a) ACPS Electrode on Z-cut



b) CPW Electrode on X-cut

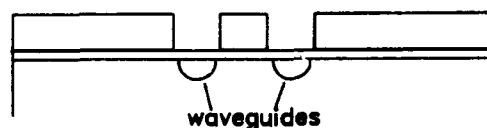


Fig. 2

Dual CPW on Z-cut

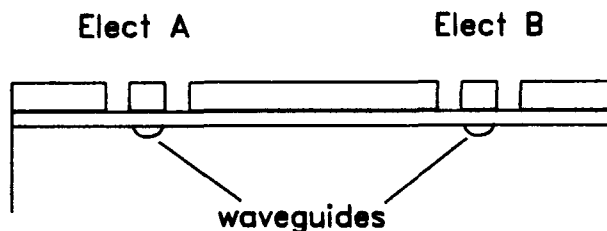
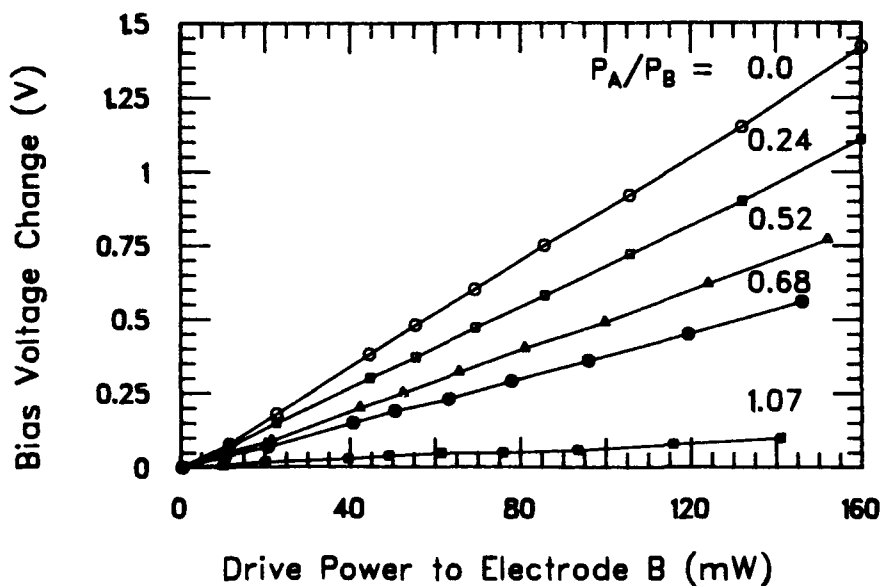


Fig. 3



CMOS-Compatible Interconnect With Poled Polymer Integrated Optic Switch

T. E. Van Eck, G. F. Lipscomb, A. J. Ticknor, J. F. Valley, and R. Lytel
Lockheed Palo Alto Research Laboratory
3251 Hanover St., O/97-02, B/202, Palo Alto, CA 94304
(415) 424-2309

In advanced microelectronic systems in which system performance is limited by interconnections between integrated circuits, optical interconnects can potentially improve system performance. An optical interconnect consisting of an electrical-to-optical transmitter, optical waveguide, and optical-to-electrical receiver can operate with lower power than an electrical interconnect in systems with high clock rates and long interconnects. Optical interconnects can also offer lower noise, lower crosstalk, higher interconnect density, and reduced impedance mismatch, in comparison with electrical interconnects. For optical interconnect networks to be attractive to electronic system manufacturers, the network should mass-produced with low cost and high reliability, and should be compatible with standard microelectronic manufacturing processes. A network of integrated optic switches and routing channels integrated into a multichip module substrate can be compatible with these requirements.¹ We describe here the demonstration of an elementary optical interconnect system which is compatible with CMOS electronic logic, and in which a poled polymer integrated optic switch on a silicon substrate serves as the transmitter.

The integrated optic switch was fabricated by evaporating a metal ground plane onto a silicon wafer, successively spin-coating the wafer with three polymer layers to create an active waveguiding layer sandwiched between two passive cladding layers, and evaporating a metal layer on top. The two metal layers were used for parallel-plate poling of the active polymer layer at elevated temperature to create an electro-optic effect. The top metal layer was patterned and used as a mask for photobleaching with UV radiation. The UV radiation alters the dye molecules in the active layer, reducing the refractive index in the unmasked area, so that light can be laterally confined in the masked area. A balanced Mach-Zehnder interferometer with drive electrodes over the arms of the interferometer was used as the electro-optic switch.

The experiment is illustrated schematically in Figure 1. An external CW laser provided optical power to the integrated optic switch, and an external receiver converted the optical signal to an electrical signal. The switch was driven by a pseudorandom data stream with a 4 V swing, provided by a bit error rate tester, and the received output signal was amplified back to the 4 V level, with a signal-to-noise ratio of 10 at low frequency. Eye diagrams of the received signal are shown in Figure 2, with two clock frequencies, 100 MHz and 200 MHz. The measured bit error

rates were 10^{-10} at 100 MHz and 10^{-8} at 200 MHz. The interconnect is compatible with CMOS integrated circuits by virtue of the 4 V logic level at both input and output, and faithful reproduction of digital signals at frequencies at the upper limit of commercially available CMOS components.

By means of some straightforward modifications, the interconnect described here could also be made compatible with ECL or GaAs MESFET integrated circuits. Switching speed could be increased by using low-capacitance electrical connections. The drive voltage could be reduced to a 1 V swing by increasing the device length or the electro-optic coefficient. Reducing the drive voltage to a 1 V swing would ease receiver requirements. A practical interconnect system would be more integrated than the one presented here. Receivers could be integrated into the silicon substrate, switching and routing networks could be integrated into polymer layers, and a large number of switches could be operated with the power from a single laser.

¹ R. S. Lytel, G. F. Lipscomb, and A. J. Ticknor, Proc. SPIE 1563 (to be published).

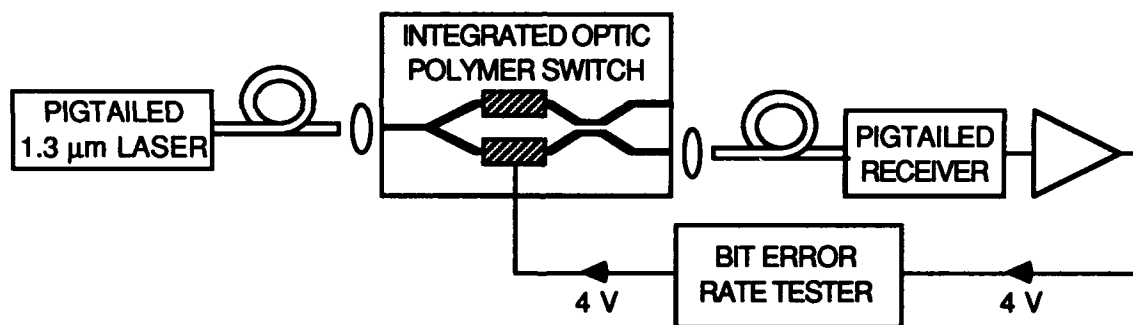


Figure 1.



Figure 2.

TuG6-1

Performance and Modeling of Proton Exchanged LiTaO₃ Branching Modulators

M.M. Howerton

SFA Inc., 1401 McCormick Dr., Landover, MD 20785 (202) 767-3826

W.K. Burns and R.P. Moeller

Naval Research Laboratory, Code 6571, Washington, D.C. 20375-5000

1x2 branching modulators^{1,2} and 2x2 digital switches³ are of interest due to their step-like response. We report results on branching modulators at 0.83 μm which were made by the annealed proton exchange process in LiTaO₃ in order to take advantage of its superior photorefractive behavior.⁴ The modulators are intended for use in a space communications program. Adiabatic devices have been modeled by direct calculation with step models, the beam propagation method, Fourier analysis, and by approximate methods using normal modes represented from coupled mode theory (CMT).⁵ We focus on the latter approach here as it is simple to use and required CMT parameters can be experimentally obtained. We show that the model gives a reasonable description of the experimental results. We also demonstrate that crosstalk in these devices (with linear branches) is linearly proportional to the voltage-length product.

Coupled amplitude equations between symmetric and antisymmetric local normal modes can be used to describe propagation in a branch. By using a CMT representation of the local normal modes, these equations can be converted into a set that depends only on the parameter $\Delta\beta/2\kappa$, where $\Delta\beta$ is the difference in propagation constants of the separated branch arms and κ is the coupling coefficient. $\Delta\beta$ is obtained analytically as a function of voltage V and an overlap integral δ . δ and κ are obtained experimentally. To describe the branch behavior at a given V the equations are integrated by computer.

We fabricated devices as shown in Fig. 1 with the parameters of Table I. Waveguides were formed in X-cut LiTaO₃ by a benzoic acid exchange and subsequent anneal. Guide mask width and electrode gap were 6.5 and 8 μm , yielding $\delta=0.55$. We obtained κ and γ (transverse momentum component) from 2x2 couplers on the same substrate.

The experimental branch arm output vs. V is shown in Fig. 2 along with the calculated response for the three devices, without adjustable parameters. The model consistently overestimates the performance by a small amount, likely due to the CMT approximation. In Fig. 3 the same quantity is plotted against the normalized parameter $\Delta\beta/\theta\gamma$, which removes the branch angle (θ) dependence. Crosstalk vs. V -L product is shown in Fig. 4, and is also independent of θ . We see that the theory predicts this to be a linear relationship, with experimental agreement degrading somewhat at low crosstalk. In terms of voltage the best performance is obtained from the smallest angle device ($\theta=0.06^\circ$), which also produces the lowest crosstalk (<-20dB for $V\geq 17\text{V}$).

We have shown that a simple theory, requiring only CMT parameters, can give a reasonably accurate description of a branching modulator or digital switch. We have also demonstrated, for linear branches, that crosstalk is linearly dependent on the voltage-length product. These results should be useful in device design.

References

- 1.W.K. Burns, A.B. Lee, and A.F. Milton, Appl. Phys. Lett. 29, 790 (1976).
- 2.L. Thylen et al., Proceedings of ECOC (1989).
- 3.Y. Silberberg, P. Perlmutter, and J.E. Baran, Appl. Phys. Lett. 51, 1230 (1987).
- 4.M.M. Howerton and W.K. Burns, J. Lightwave Tech. (1992), to be published.
- 5.W.K. Burns, IEEE J. Lightwave Tech. 8, 990 (1990).

Table I

θ (deg)	L (cm)
0.24	0.36
0.12	0.72
0.06	1.43

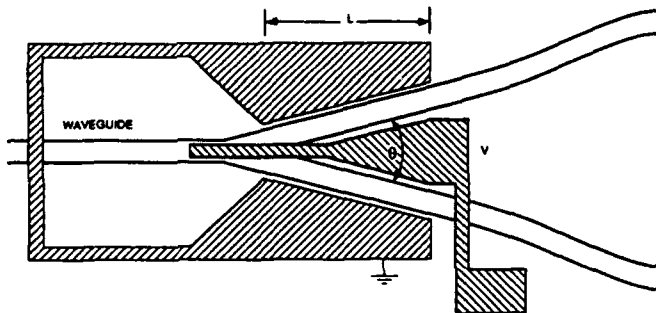


Fig. 1

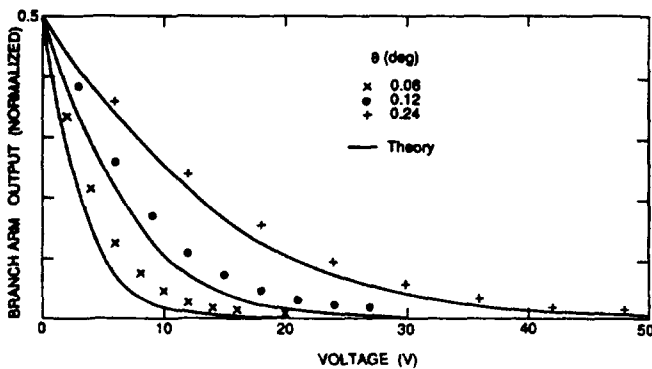


Fig. 2

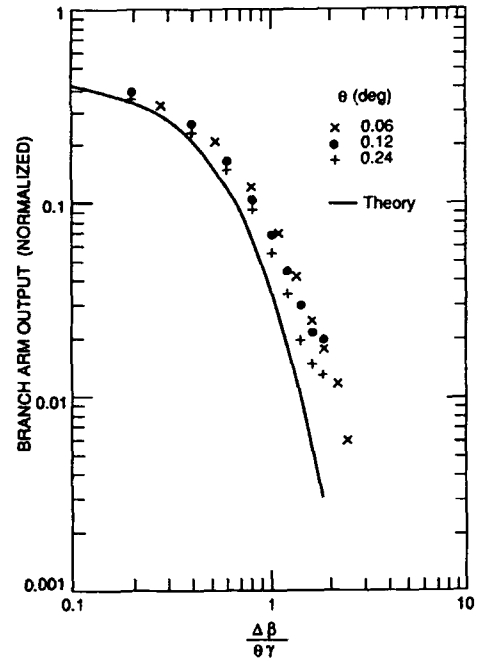


Fig. 3

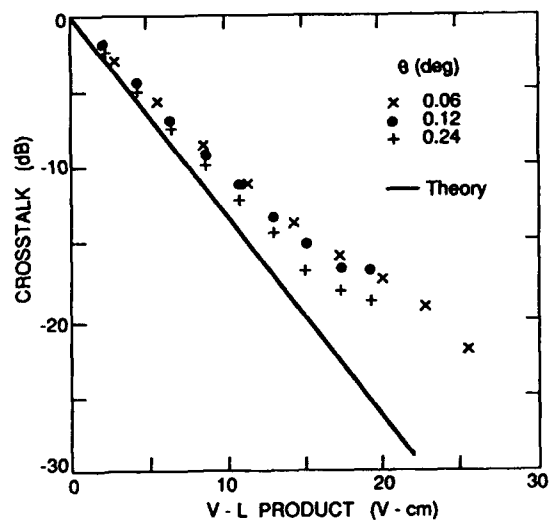


Fig. 4

Tuesday, April 14, 1992

Novel Materials and Processing

TuH 1:30 pm-3:30 pm
La Salle Ballroom C

Won-Tien Tsang, *President*
AT&T Bell Laboratories

Blue and green diode lasers and LEDs in ZnSe-based quantum wells. A. Nurmikko, *Brown Univ.*; R. L. Gunshore, *Purdue Univ.* Summary was not available at time of publication.

TuH2-1

CHEMICALLY-INDUCED SHIFTS IN THE PHOTOLUMINESCENCE SPECTRA OF POROUS SILICON

K.-H. Li, C. Tsai, and Joe C. Campbell
Microelectronics Research Center
Department of Electrical and Computer Engineering
The University of Texas at Austin, Austin, Texas 78712
and
B. K. Hance and J. M. White
Department of Chemistry and Biochemistry
The University of Texas at Austin, Austin TX 78712

The realization of practical, Si-based light-emitting devices would have a significant impact on numerous key technologies such as optoelectronic integrated circuits, optical interconnects, optical memories and logic, and advanced display systems. Previously, Si has exhibited extremely weak emission owing to its indirect bandgap. Recently, however, observations of efficient room-temperature, visible photoluminescence (PL) from porous silicon [1-3], have stimulated research and extensive debate on the physical mechanisms responsible for this luminescence. To date, the explanations that have been proffered include (1) quantum size effects in highly porous Si [1,2], (2) the formation of wide-bandgap material such as a-Si:H_x [4] or siloxene [5] during anodization, and (3) a local increase in the bandgap energy due to the presence of dihydride species on the surface [6]. Previously, we have utilized photoluminescence (PL) and transmission Fourier-transform infrared (FTIR) spectroscopy to demonstrate that hydrogen desorption from the dihydride surface species on porous Si is correlated to a decrease in the emission intensity [3,7]. In this paper, we show that changes in the surface chemistry achieved by changing the composition of the electrolyte in which the anodized wafer is immersed result in large shifts in the PL spectra. Using this approach we have repeatedly cycled the emission between red and green. These results are inconsistent with a quantum-confinement interpretation for the emission process.

The porous Si layers were formed on boron-doped (100) single-crystal Si wafers (resistivity = 7 Ωcm) using a Teflon sample holder in contact with a copper anode. The anodization area was defined by a one-inch-diameter circular opening in the fixture. The sample holder was immersed in 12.25% HF electrolyte (H₂O : acetic acid: 49% HF=2:1:1) at 10mA/cm² for 15 minutes under light illumination. Prior to removing the samples from the electrolyte, they were illuminated with a UV lamp and green luminescence was observed (curve A in Fig. 1). After the samples were exposed to air, the PL gradually (< 1 min.) changed from green to red (Fig. 1, curve B). Since the samples oxidize in air, the Si feature size would be expected to decrease. If two-dimensional quantum confinement were responsible for the luminescence, the reduction of pillar size by oxidation should cause a blue shift instead of the observed red shift. Subsequent immersion in an HF:H₂O solution produced little change in the PL spectrum (Fig. 1, curve C). This is consistent with the fact that one of the primary functions

of the acetic acid in the solution is to supply protons to the wafer surface which enhances the formation of a dihydride passivated surface. Finally, returning the wafer to the original solution of water, 49% HF, and acetic acid resulted in green luminescence within a few seconds (Fig. 1, curve D). This change in the luminescence can not be attributed to a change in feature size since this solution etches Si only 20Å to 100Å per hour. Finally, when the sample is blown dry in air the spectrum shifts back to the red (Fig. 1, curve E). This procedure for switching the peak emission wavelength can be repeated many times without a degradation in the PL intensity. Transmission Fourier-transform infrared (FTIR) spectroscopy shows that the spectral shift correlates with changes in the surface silicon hydride concentration. The concentration of the silicon hydride surface species was determined by from the integrated intensity of the SiH-SiH₂ stretch modes (2135 cm⁻¹ to 2089 cm⁻¹) and the SiH₂ scissors mode (907 cm⁻¹).

REFERENCES

1. L. T. Canham, *Appl. Phys. Lett.* **57**, 1046 (1990).
2. A. Halimaoui, C. Oules, G. Bomchil, A. Bsiesy, F. Gaspard, R. Herino, M. Ligeon, and F. Muller, *Appl. Phys. Lett.* **59**, 304 (1991).
3. C. Tsai, K.-H. Li, J. Sarathy, S. Shih, J. C. Campbell, B. K. Hance and J. M. White, *Appl. Phys. Lett.* **59**, 2814 (1991).
4. R. W. Fathauer, T. George, A. Ksendzov, T.-L. Lin, W. T. Pike, and R. P. Vasquez, *MRS Meeting Fall 1991, Symposium AA*, 12 (1991).
5. J. Weber, M. S. Brandt, H. D. Fuchs, and M. Stutzmann, *MRS Meeting Fall 1991, Symposium AA*, 12 (1991).
6. J. I. Pankove and D. E. Carlson, *Appl. Phys. Lett.* **29**, 620 (1976).
7. C. Tsai, K.-H. Li, D. Kinosky, R.-Z. Qian, T.-C. Hsu, J. Irby, S. Banerjee, A. Tasch, and J. C. Campbell, B. K. Hance and J. M. White, unpublished.

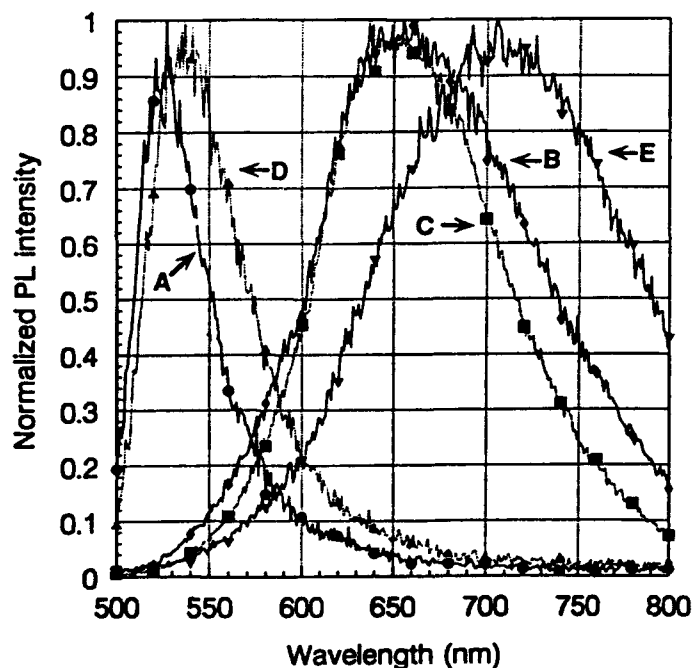


Figure 1

**Luminescence, Spectroscopy and Composition Fluctuations
in (110) Cross Sections of AlGaAs Multilayers**

S.F. Alvarado, H.W.M. Salemink and O. Albrektsen*

IBM Research Division, Zurich Research Laboratory, 8803 Rüschlikon, Switzerland

**Telecommunications Research Laboratory, DK-2970 Hørsholm, Denmark*

The controlled growth of semiconductor (ternary and quaternary) compound layers and their interfaces is a key concern in epitaxial technology. Ultimately both crystallographic and elemental accuracy on the atomic scale is required. In the analysis of such multilayers, however, 'large-scale' techniques such as transmission electron microscopy and exciton luminescence are usually employed, which retrieve their signals from a large number of crystalline unit cells (typically 10^2 to 10^6). Therefore their analysis gives averaged data.

In this work we report on how the STM technique can be used to display the atomically resolved lattice sites in UHV-cleaved (110) cross sections of epitaxially grown III-V multilayers [1]. The tip of the STM also works as a source of ultra-low energy electrons to excite luminescence with nanometer resolution [2].

Our main results on model multilayers demonstrate the following:

- 1) Luminescence imaging and spectroscopy with nanometer resolution within single quantum wells [2]
- 2) Mapping the conduction band energy profile across GaAs/AlGaAs interfaces. The conduction band offset appears to occur typically within 2.0 nm or less [3].
- 3) The different alloy layers are readily observed on atomic flat (110) cross-sections. The heterojunctions can be identified in either the group-III or group-V sublattice and are defined to ± 1 unit cell accuracy [4].
- 4) Tunneling spectroscopy across GaAs/AlGaAs junctions displays a transition in the valence band which occurs over a length-scale of approximately 3.5 nm. The extent of this electronic transition is discussed and a quantitative interpretation of the I-V curves is given [5].
- 5) Under regular MBE growth conditions, we frequently find extended terraces and associated step-bunching, 2-8 monolayers high. Such steps are readily identified with this cross-sectional STM technique and demonstrate the potential to study vicinality and quantum layer roughness.
- 6) Atomic-resolution topographs of the group III (Al-Ga) sublattice in AlGaAs and of the group V (As-P) sublattice in InGaAsP are generated for the first time. The charge-density corrugations reflect composition fluctuations on the atomic scale.

[1] H.W.M. Salemink *et al.*, J. Vac. Sci. Technol. B 9, 779 (1991).

[2] S.F. Alvarado *et al.*, J. Vac. Sci. Technol. B 9, 409 (1991)

[3] P. Renaud and S.F. Alvarado, Phys. Rev. B 44, 6340 (1991)

[4] O. Albrektsen *et al.*, Appl. Phys. Lett. 57, 31 (1990)

[5] P. Koenraad *et al.*, Phys. Rev. B 45, March 15, 1992 (in print)

TuH4-1

Dielectric Cap Disordering of InGaAs Quantum Well Structures on InP and GaAs

S.A. Bradshaw, A.C. Bryce, E. Tozowonah, J.H. Marsh

Department of Electronics and Electrical Engineering, University of Glasgow, Glasgow G12 8QQ, Scotland. Tel: ++44-41-330-5220 Fax: ++44-41-330-4907

R. Bradley, R. Nicklin

GEC-Marconi Materials Technology Ltd, Caswell, Northants NN12 8EQ, England.

R.W. Glew

BNR Europe Ltd, London Road, Harlow, Essex CM17 9NA, England.

Many InGaAs Quantum Well (QW) structures have limited thermal stability and this limits the use of QW intermixing techniques. Rapid thermal processing (RTP) can overcome some of these restrictions. Here we report the use of RTP with dielectric capping layers of SiO₂ and Si₃N₄ to initiate QW intermixing in strained InGaAs on GaAs substrates and unstrained InGaAs on InP substrates. The first structure contained a single 90 Å QW, with GaAs barriers with the wells under tension. The second structure contained four 100 Å InGaAs quantum wells, with 120 Å InGaAsP barriers embedded in 0.18 µm InGaAsP guiding region. The InP based system also has 1 µm InP above the QW structure and a 0.17 µm layer of InGaAs. 1000Å dielectric caps were deposited by plasma deposition on both sets of samples. To prevent Group III desorption during annealing proximity capping with either GaAs or InP was used throughout.

GaAs/InGaAs

First samples were annealed at 800 and 850 °C for 15 s. This produced small blue shifts in all samples with no significant difference between capped and uncapped samples. However it was found (Figure 1) that selective disordering of the samples could be achieved by repetitively heating the sample at 850°C, holding for 15 s and then allowing the sample to cool. It can be seen from Figure 1 that after the first cycle small blue shifts are observed in all samples with little difference between the capped and uncapped samples. However, after six repetitions blue shifts of up to 20 meV can be observed in the capped samples while little shift is seen in the uncapped samples.

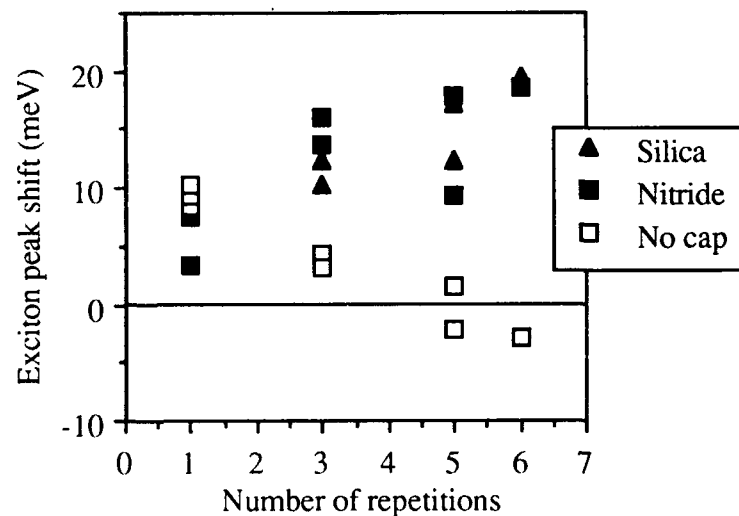


Figure 1 Exciton peak shifts for repetitive annealing at 850 °C for 15 s

InP/InGaAs/InGaAsP

The thermal stability problem of the InGaAs/InGaAsP system has been reported previously^{1,2}, and here we report on the effect of SiO₂ and Si₃N₄ caps on QW intermixing.

Figure 2 shows results of annealing capped and uncapped samples at 700°C for 10 to 60 s. It can be seen that there is little difference between the uncapped and SiO₂ capped samples. The Si₃N₄ capped samples show a significant increase in exciton shift especially at short anneal times, 15 meV compared to 4 meV for the oxide and uncapped samples. Samples with the InGaAs removed and annealed at 700°C for 60s show an average shift of 15 meV.

Figure 3 shows the results of annealing at 650°C, for 10 to 60 s. Again there is little difference between the oxide capped and uncapped samples and relatively small shifts for the nitride capped samples (7 to 10 meV). However, on cycling the annealing process six times (40 s at 650°C) a significant difference was observed. The uncapped and nitride capped exciton shifts both increased to 20 meV and 6 meV whilst the oxide capped sample showed only a very small increase in energy of approximately 3 meV. Cycling with a 10 s plateau had only a very small effect on all samples.

By using dielectric capping and RTP we can selectively obtain 20 meV exciton shifts in InGaAs QWs with both GaAs and InGaAsP barriers without the need to implant impurities into the wells. This process could be useful in applications where only a small change in exciton energy is required, whilst retaining most of the properties of the original structure e.g. modulators and nonabsorbing mirrors.

Acknowledgments

This work has been funded by DTI and SERC under the Optoelectronics Systems LINK Programme (GR/F/93913) and by SERC (GR/G/13488).

References

- 1 J.H. Marsh, S.A. Bradshaw, A.C. Bryce, R. Gwilliam and R.W. Glew, *J. Electron. Mat.*, **20**, 973-978, 1991
- 2 R.W. Glew, J.P. Stagg, P.D. Greene, A.T.R. Briggs, S.A. Bradshaw, J.H. Marsh, *Third International Conference on Indium Phosphide and Related Materials*, pp515-518, Cardiff, Wales 1991

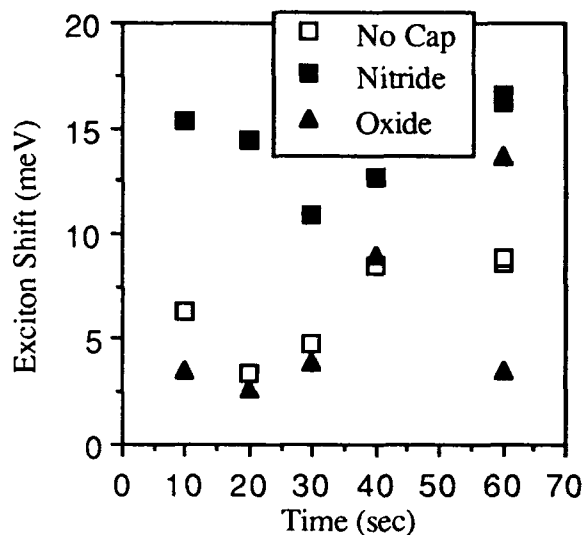


Figure 2 Exciton Shifts for Dielectric Capped Material at 700°C

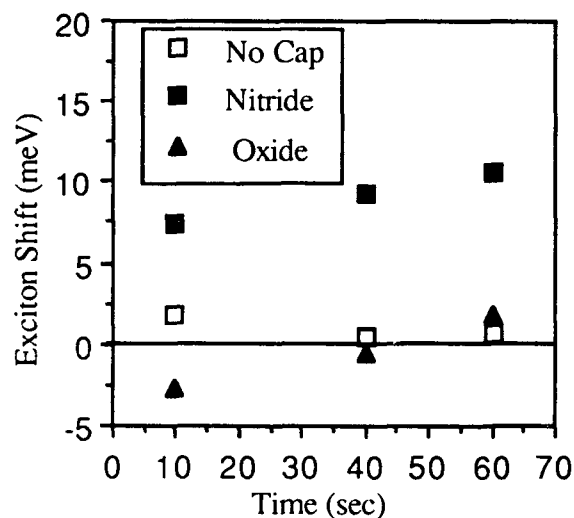


Figure 3 Exciton Shifts for Dielectric Capped Material at 650°C

TuH5-1

Use of Novel Periodic Multi-Layers for Highly Accurate Etch Depth Control of Ridge-Waveguide Directional Couplers

G.A. Vawter, G.R. Hadley, J.F. Klem, S.H. Kravitz
Sandia National Laboratories
Albuquerque, NM 87185-5800
(505)846-8985

Fabrication of large-area photonic integrated circuits (PICs) in III-V compound semiconductors presents many fabrication complexities. One difficulty is precise and reproducible etching of ridge waveguides for accurate control of optical mode shape and coupling length (distance required for full power transfer) of optical directional couplers. Directional couplers are an important element in PICs due to their utility as power taps, splitters, and combiners. However, the exponential relationship between the depth of the etched-rib waveguide and coupling length makes these structures very difficult to fabricate with precise control of coupling. This inability to precisely control the coupling purely through tight process control has led to the use of electrically biased couplers¹ where an electric field is applied across the waveguide to force the coupler into the desired switch state. Although biased couplers have proven successful, they are not desirable for large PICs due to the requirement of electrical contact to each coupler and careful custom tuning of the bias voltage across each coupler. In this talk, we disclose a new technique for fabrication of directional couplers with precisely controlled coupling lengths that no longer require bias-tuning after fabrication.

Careful control of etch depth and coupling length is achieved through the use of in-situ reflection monitoring of the sample surface during nonselective Cl₂ reactive-ion-beam etching (RIBE) and incorporation of a periodic multilayer stack into the upper-cladding layer of the waveguide material. To demonstrate the process, ridge-waveguide directional couplers were designed and fabricated according to figure 1. The three-waveguide power-splitter was designed to operate at 1.06 μ m wavelength with a theoretical coupling length of 650 μ m according to beam propagation analysis. The epitaxial layers were grown by molecular beam epitaxy according to table 1. In order to monitor and control the etch depth of the ridge waveguide, the entire thickness of the upper cladding layer intended to be removed outside the rib consisted of Al_{0.4}Ga_{0.6}As with 5 nm AlAs layers placed every 45 nm to create a periodic refractive index discontinuity. The effect of these periodic AlAs layers is to establish a sharply defined periodicity in the optical reflection magnitude vs. etch depth as shown in figure 2. The periodic reflection vs. depth relationship allows the nonselective etch to proceed at a measured rate with well-defined reflection peaks occurring every 50 nm in depth. Without these periodic layers the reflection vs. etch depth resembles that shown for the lower cladding layer in figure 2 where the periodic reflection oscillations created by the single GaAs/Al_{0.4}Ga_{0.6}As interface and the sample surface are highly damped by absorption in the material. The flatness of the reflection vs. etch depth near the top of the layer makes endpoint detection at a specified distance above the interface very difficult since extremely small peaks are easily missed. Use of the periodic layers permits etching to any point within the layer stack with an error of only ± 10 nm.

Coupling length of the as-etched devices was measured using comparison of near-field optical mode profiles from cleaved devices of various interaction lengths between 100 and 1000 μ m. The final measured coupling length was 570 μ m. This compares well with the 650 μ m design value. The shift in coupling length is due largely to errors in linewidth caused by the optical contact print process used to expose the photoresist etch mask. However, even this 80 μ m reduction in coupling length results in only a 0.2 dB penalty per guide in our power-splitter design. Thus, neglecting scattering and absorption, a three-guide power splitter with a 650 μ m interaction length operates with a 0.4 dB insertion loss.

In conclusion, we have developed a new technique for monitoring of ridge waveguide etching in real time with endpoint depth precision of $\pm 100\text{\AA}$ independent of total depth. This method has been applied to the fabrication of ridge-waveguide directional couplers in GaAs/AlGaAs and shown to yield coupling lengths within $80\ \mu\text{m}$ of the desired $650\ \mu\text{m}$ value. The added loss due to error in coupling length was only 0.2 dB per guide. This technique is directly applicable to PICs employing complex optical routing of waveguides, directional couplers, and y-junctions where total height of the waveguide plays a key role in performance of the circuit.

Layer Description	Material	Thickness	Number of Periods
Cap Layer	GaAs	75 nm	1
Upper Waveguide Cladding with Periodic Multi-layer	$\text{Al}_{0.4}\text{Ga}_{0.6}\text{As}/\text{AlAs}$	45nm/5nm	26
Upper Waveguide Cladding	$\text{Al}_{0.4}\text{Ga}_{0.6}\text{As}$	200 nm	1
Waveguide Core	GaAs	250 nm	1
Lower Waveguide Cladding	$\text{Al}_{0.4}\text{Ga}_{0.6}\text{As}$	1500 nm	1
Substrate/Buffer	GaAs	-	-

TABLE 1: Composition of epitaxial layers for etched ridge waveguide directional couplers using periodic multilayers for extreme control of etched rib height and coupling length.

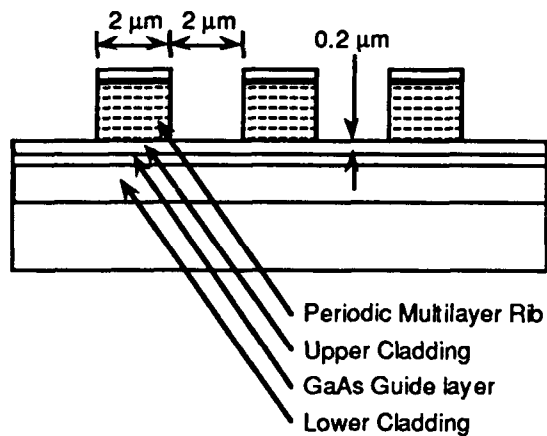


FIGURE 1: Cross-section view of three waveguide power splitter. Strength of interguide coupling is determined by etch depth between ribs.

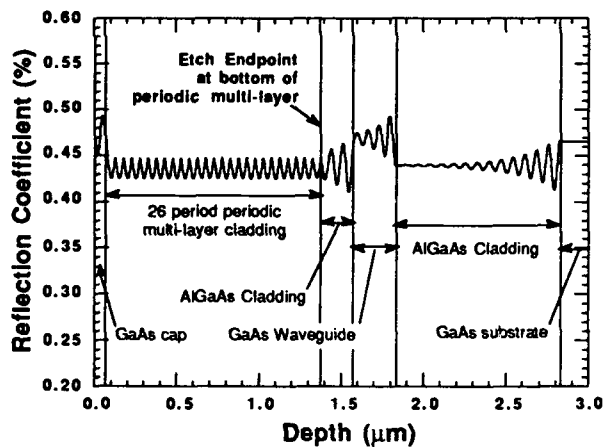


FIGURE 2: Reflection coefficient vs. etch depth for 543.5 nm light at 40° from normal incidence. Curve is calculated for etch through all epitaxial layers and into substrate. Desired endpoint for waveguide etch is at the bottom of the last AlAs layer.

References:

¹Alferness, R.C., "Guided-Wave Devices for Optical Communication," IEEE J. of Quantum Electronics, Vol. QE-17, No. 6, pg. 946, June 1981.

InGaAsP/InP OPTICAL WAVEGUIDE TAPERS by SELECTIVE OMCVD

R. J. Deri, C. Caneau, E. Colas, L. M. Schiavone, N. C. Andreadakis, G. H. Song and E. C. M. Pennings
Bellcore, 331 Newman Springs Road, Red Bank, New Jersey 07701-7040, (908) 758-2894

Small optical mode size ($\leq 2\mu\text{m}$) is essential for high-performance waveguide-based devices [1] and lasers on III-V semiconductors. High efficiency fiber coupling to small modes, however, requires additional mode-matching elements and submicron alignment tolerances,[2] resulting in costly packages and reliability concerns. These problems can be alleviated by monolithically tapering small modes to larger dimensions at chip edges, for which several techniques have been proposed.[2-8] Selective epitaxy, in which locally enhanced epitaxial growth rates are achieved in regions adjacent to dielectric masks, is particularly attractive because of its process simplicity, which requires no epitaxial regrowth nor complicated etch procedures. While selectively grown tapers were previously suggested,[7,8] actual spot-size tapering using this technique has not been reported. Here we describe selectively grown InGaAsP/InP tapers with low-loss and threefold spot-size increase.

We employ selective, low-pressure (30 torr) OMCVD [7] in which diffusion of reactants from low-growth, SiO_x -masked regions to open (unmasked) areas causes epilayer thickness to increase in narrow stripes opened in large masked areas. Thin layers are grown in regions far from the mask edges. Fig. 1 shows the growth profile, simulated by a diffusion model, which accurately describes experimental results. Since we cannot lattice-match InGaAsP in both the narrow stripes and the broad areas, we lattice match in the broad open areas. Thin waveguides in this region of high material quality provide small mode sizes for integration with additional optoelectronics. Mismatch within the narrow stripes affects only taper insertion loss, but not active devices integrated in the broad areas. Use of thick guides for large modes improves tolerances to fabrication and operating wavelength. The multi-mode character of the thick, uptapered guides does not affect operation due to minimal intermode coupling (adiabatic taper) and filtering by single-mode structures (fiber, thin guides) on each taper end. Thick guides do, however, introduce nonplanarities which may complicate subsequent device processing; to avoid this problem, we employ gas-phase etching to taper the substrate prior to growth.[7]

We fabricated tapers on (100) InP:Fe using the mask geometry of Fig. 1 with $100\mu\text{m}$ -wide open stripes. Some masked samples were etched by HCl gas inside the OMCVD reactor to taper the substrate for reduced nonplanarity. Epilayers were then grown, comprising a 50nm InP buffer followed by a waveguide of either bulk InGaAsP ($\lambda_g = 1.1\mu\text{m}$) or an InGaAsP ($\lambda_g = 1.3\mu\text{m}$)/InP multiple quantum well (MQW) structure, chosen for index difference $n_{\text{guide}} - n_{\text{InP}} \approx 0.1$. The guide thickness tapered from $1.2\mu\text{m}$ to $\approx 6\mu\text{m}$ (Fig. 2a). Taper length is $\approx 2\text{mm}$, which might be reduced using higher growth pressure and modified mask geometry. Last, waveguide ribs parallel to/centered in the growth stripes were etched (RIE). The rib width was laterally tapered from 4 to $6.5\mu\text{m}$ with $2\mu\text{m}$ rib etch depth. This provides moderate optical confinement and large spot size in the thick guides, and strong confinement for the small mode thin guides, which are suitable for compact waveguide bends.[1]

We characterized tapers by transmission measurements at $\lambda = 1.52\text{--}1.54\mu\text{m}$. Thin guides are monomode, whereas thick guides are multimode. Fundamental mode sizes (full-width at $1/e$ field) were estimated from near-fields (Fig. 2b) which clearly show mode size tapering. Spot size tapers from $2.9\mu\text{m} \times 1.6\mu\text{m}$ (lateral \times vertical) in broad, open areas to $6.2\mu\text{m} \times 4.5\mu\text{m}$ in the narrow stripes, a vertical increase of $\approx 300\%$. Propagation losses α of untapered thick and thin guides were determined by Fabry-Perot (FP) methods. Thin guides exhibit $\alpha = 1\text{--}4\text{dB/cm}$, comparable to the best losses achieved for such deeply-etched guides, which are predominantly due to rib sidewall roughness.[1] Thus, our selective growth process does not affect the quality of small mode waveguide structures far from the mask edge. Measuring fundamental mode losses in our multi-mode thick guides by careful input excitation and output spatial filtering to select only the fundamental mode, we observe losses as low as 1.4dB/cm . Correlation with sample growth details, photoluminescence and white light measurements will be discussed.

We evaluated taper losses for $\approx 3\text{mm}$ long samples containing tapers plus lengths of untapered guides. FP data show total on-chip taper losses as low as 0.4dB , which correspond to propagation loss with negligible contribution from the tapering. Losses associated with butt-coupling to conventional single-mode fiber (polished flat end, $10\mu\text{m}$ mode full-width) were determined from transmission data using fiber-in/objective-out coupling, after AR coating. A low coupling loss of 2.6dB was achieved for MQW guides on etched substrates, which is 0.4dB greater than the modal mismatch calculated from the measured spot size. Butt-coupling into the small-mode end of the same tapers results in 6.5dB coupling loss, showing that the tapers improve input coupling by $\approx 4\text{dB}$.

R.J. Deri et al, "InGaAsP/InP Optical Waveguide Tapers..."

In summary, we fabricated low-loss optical waveguide tapers by selective OMCVD of InGaAsP/InP which alter the vertical mode size by $\approx 300\%$. Total taper loss (on-chip plus coupling) is only 3dB for coupling to flat-end single-mode fiber. Their high performance and fabrication simplicity make selectively grown tapers suitable for widespread application to improve coupling to lasers and other waveguide-based III-V optoelectronics.

REFERENCES

1. R. J. Deri and E. Kapon, *J. Quantum Electron.* 27, 626 (1991)
2. U. Koren, T. L. Koch, et al., *Photonics Technol. Lett.* 2, 88 (1990).
3. D. E. Bossi, W. D. Goodhue, et al., *Appl. Phys. Lett.* 56, 420 (1990)
4. R. A. Pattie and M. W. Austin, *Electron. Lett.* 24, 284 (1988).
5. A. Shahar, W. J. Tomlinson, et al., *Appl. Phys. Lett.* 56, 1098 (1990).
6. H.-P. Nolting, in *Integrated Photonics Research 1991* (OSA; Washington, DC; 1991). p. 111.
7. E. Colas, C. Caneau, et al., *Appl. Phys. Lett.* 59, (1991).
8. B. Kim, Y. Kwon, and Y. S. Kwon, *Electron. Lett.* 22, 806 (1986).

Fig. 1: Selective growth spatial variation vs. position (x, y) for mask with 100 μ m growth stripe.

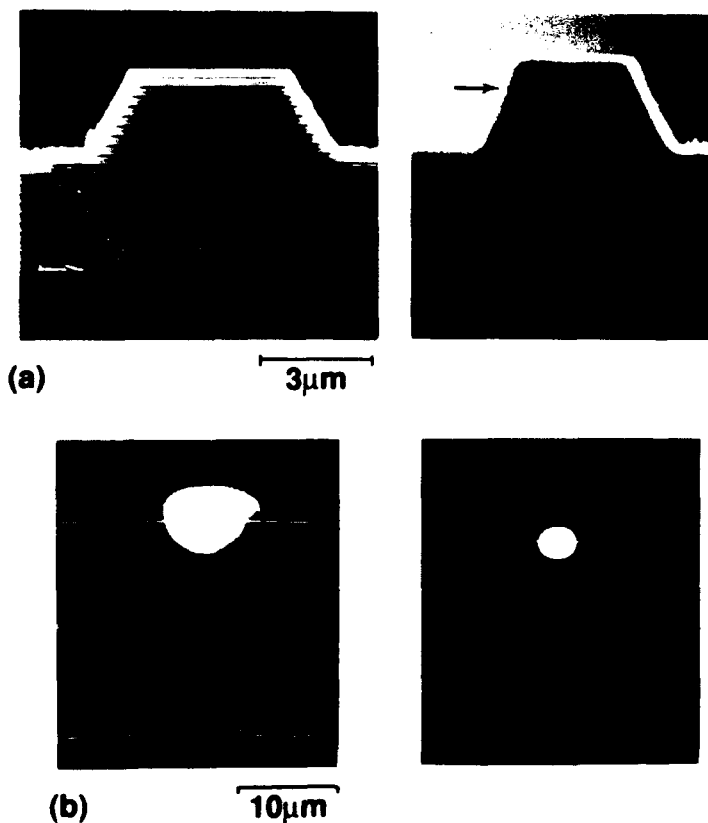
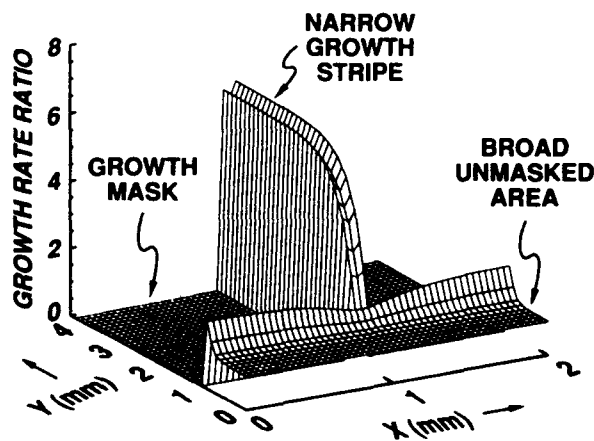


Fig. 2: Guide cross-section SEM (a) and optical near fields (b) for both endfacets of a selectively grown, MQW waveguide taper. Arrows in (a) show guide/InP interfaces.

Tuesday, April 14, 1992

Optical Fiber Solitons

TuI 1:30 pm–3:00 pm
Pelican Room

Govind Prasad Agrawal, *Presider*
University of Rochester

POLARIZATION MULTIPLEXING WITH SOLITONS

S. G. Evangelides Jr., L. F. Mollenauer, and J. P. Gordon

AT&T Bell Laboratories

Holmdel, NJ 07733

We have examined, through numerical simulations, experiment, and analytic theory, the behavior of the polarization state of a stream of solitons in a long distance, all optical transmission system consisting of spans of dispersion shifted fiber having a small (-0.2ps/km^2) randomly varying birefringence and periodically spaced Erbium doped fiber amplifiers. From the theory and simulations we find that a stream of solitons, all launched into such a system in the same polarization state, will emerge with all the solitons approximately in a common, well defined, polarization state. The pulse-to-pulse deviations from this average polarization state are small, as they are determined only by the component of the amplifier ASE noise in the polarization mode orthogonal to the soliton itself. An extinction ratio of 23 dB is predicted at 10,000 km, and we have confirmed this experimentally by using a 2.5 GHz stream of 50 ps solitons in a 75 km recirculating loop (Figure 1). Numerical simulations show that solitons launched in orthogonal polarization states maintain their orthogonality as they traverse the system. This is confirmed by the analytic theory. Based on this fact, we propose a polarization/time multiplexing scheme whereby two orthogonally polarized soliton bit streams are interleaved in time (Figure 2). Further simulations indicate that this technique should be able to double the bit rate of any single frequency soliton channel, with no significant increase in bit error rate.

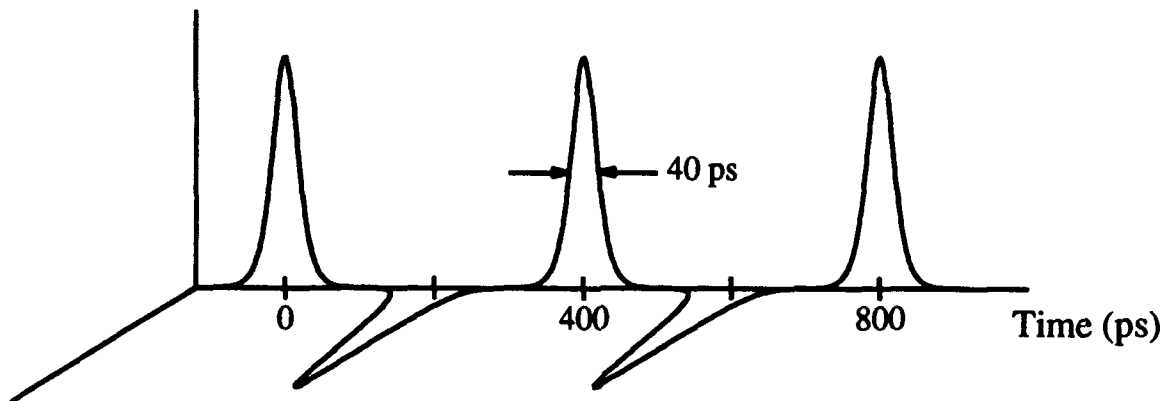


Figure 1 Plot of extinction ratio for a polarized soliton bit stream versus distance along the transmission fiber. We show simulation, experimental and theoretical results for 50 ps. solitons in a fiber with $D=1.36$ ps/nm/km, loss of .21 db/km and 28 km amplifier spacing.

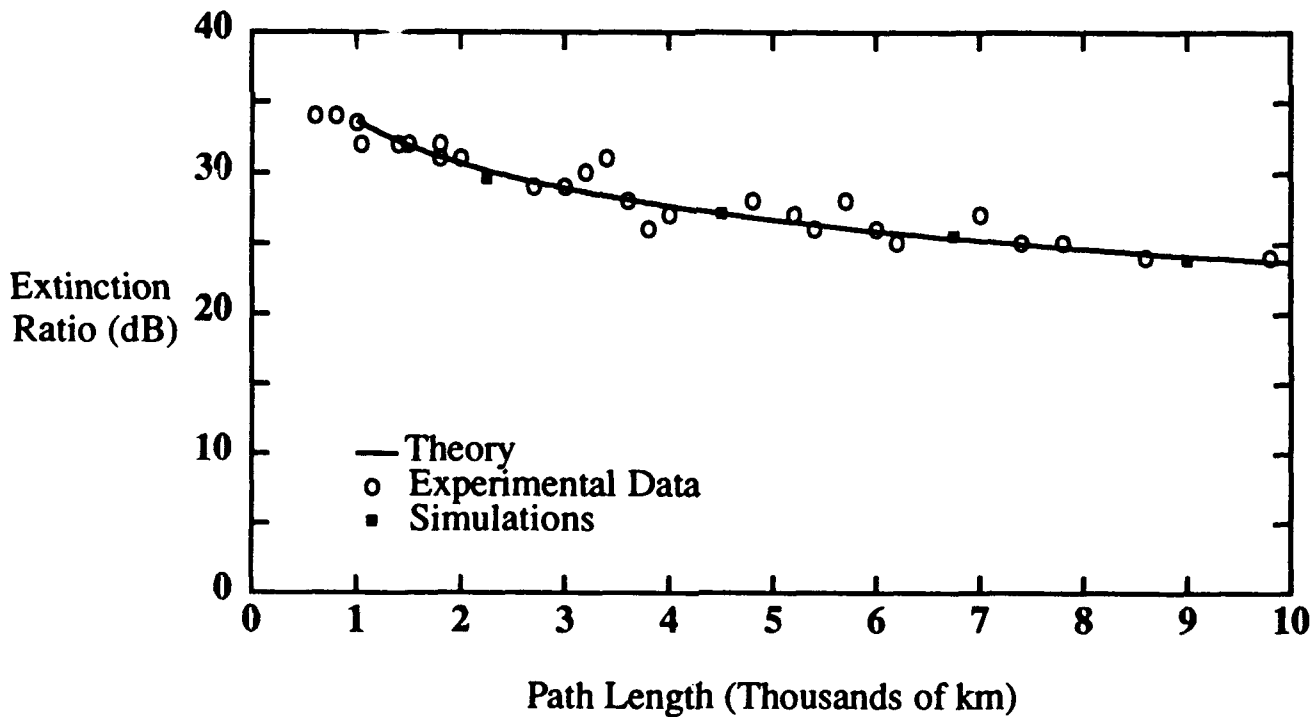


Figure 2 A depiction of the proposed time/polarization multiplexing scheme showing the multiplexing of two orthogonally polarized 2.5 Gbit/s soliton bit streams.

Tul2-1

LOCAL CARDINAL INTERPOLATION SPLINE METHOD FOR SOLVING COUPLED NONLINEAR SCHRÖDINGER EQUATIONS: A COMPARISON WITH BPM

A.K. Chan, C.K. Chui, Jun Zha and Jieren Bian
 Department of Electrical Engineering
 Texas A&M University
 College Station, Texas 77843-3128
 Telephone: (409) 845-7458

SUMMARY

In terms of computational speed, BPM is faster than finite difference method by an order of magnitude or more to achieve a given accuracy^[1,2]. However, it requires relatively small propagation steps and large computing window for artificial absorption on the boundary. A large transverse index change can also jeopardize the method. In solving coupled wave equations, BPM iterates between the equations until a converged solution is obtained. The total efficiency of this algorithm is greatly reduced.

In this paper, we present a numerical algorithm which uses the Local Cardinal Interpolation Spline (LCIS) method developed by Chui and Chan^[3,4] to solve the nonlinear Schrödinger equation and the coupled nonlinear Schrödinger equations that are frequently encountered in the analyses of integrated photonic circuit elements and nonlinear optical fiber devices. A comparison with the FFT-BPM is given to demonstrate that our method is about 3 to 4 times faster than BPM for uncoupled nonlinear Schrödinger equation and about 8 times faster for coupled nonlinear Schrödinger equations to achieve a given accuracy. Furthermore, the LCIS method does not have the disadvantages of BPM mentioned above. Our method has potential for fast and accurate simulations of integrated optical devices.

Because of the interpolatory property of LCIS, the solution to a nonlinear differential equation can be expressed as a series of the LCIS function $\psi(t)$ as following:

$$S_h f(t) = \sum_i f(2hi) \psi\left(\frac{t}{h} - 2i\right), \quad (1)$$

where h is the step-size. The LCIS method inherits the simple formulation of finite difference method, however, the higher order approximation of the LCIS increases the accuracy by two order of magnitude comparing with normal FDM. Thus, the LCIS method achieves both higher speed and accuracy. The complete procedure on constructing the LCIS function can be found in [3]. The LCIS function $\psi(t)$ is shown in Figure 1.

Our method is applied to nonlinear Schrödinger equation that governs the soliton propagation in nonlinear planar waveguides and optical fiber. Four cases have been tested and comparisons have been made with BPM under the same conditions. The convergence criterion for iteration is $\Delta < 10^{-8}$ where Δ is the maximum error. These four cases are: Case 1, Fundamental soliton $u_{initial}(x) = \text{sech}(x)$. Case 2, Third order soliton $u_{initial}(x) = 3\text{sech}(x)$. Case 3, Two solitons with relative phase 0. $u_{initial}(x) = \text{sech}(x - 3.5) + \text{sech}(x + 3.5)e^{i0}$. Case 4, Two solitons with relative phase π . $u_{initial}(x) = \text{sech}(x - 3.5) + \text{sech}(x + 3.5)e^{i\pi}$.

This method is also applied to coupled nonlinear Schrödinger equations which governs the pulse propagation in birefringence fibers and fiber couplers.

$$\begin{aligned} i \frac{\partial u}{\partial \xi} + i\delta \frac{\partial u}{\partial \tau} + \frac{1}{2} \frac{\partial^2 u}{\partial \tau^2} + [|u|^2 + \frac{2}{3}|v|^2]u &= 0, \\ i \frac{\partial v}{\partial \xi} - i\delta \frac{\partial v}{\partial \tau} + \frac{1}{2} \frac{\partial^2 v}{\partial \tau^2} + [|v|^2 + \frac{2}{3}|u|^2]v &= 0, \end{aligned} \quad (2)$$

where u and v are two fields with different polarizations. Initial fields are $u(x) = A \operatorname{sech}(x) \cos(\phi)$ and $v(x) = A \operatorname{sech}(x) \sin(\phi)$. For case 5, we choose $A = 1.1$, $\phi = 30^\circ$, $\delta = 0.5$. The simulation results for this case are shown in Figure 2. The parameters $A = 0.8$, $\phi = 30^\circ$, $\delta = 0.15$ are used in case 6. Table 1 and Table 2 summarize the step size and CPU time of each case for both LCSI method and BPM methods.

Table 1

Case	Window size and grid points	ξ and steps	error Δ	CPU time	
				BPM	CISM
1	20(μm), 1024	$\pi/2$, 4980	$< 10^{-8}$	11 min. 23 sec.	3 min. 29 sec.
2	20(μm), 1024	$\pi/2$, 4980	$< 10^{-8}$	16 min. 24 sec.	4 min. 49 sec.
3	20(μm), 1024	16.4π , 4980	$< 10^{-8}$	17 min. 58 sec.	5 min. 17 sec.
4	20(μm), 1024	16.4π , 4980	$< 10^{-8}$	15 min. 34 sec.	4 min. 36 sec.

Table 2

Case	Window size and grid points	ξ and steps	error Δ	CPU time	
				BPM	CISM
5	160(μm), 1024	12π , 4980	$< 10^{-8}$	1 hr. 43 min. 3 sec.	13 min. 08 sec.
6	160(μm), 1024	12π , 4980	$< 10^{-8}$	1 hr 36 min. 21 sec.	12 min. 19 sec.

In conclusion, we have presented a LCIS method to solve coupled and uncoupled nonlinear Schrödinger equations. Our method has simple architecture similar to the finite difference scheme, but with higher efficiency and stability than the widely used BPM.

REFERENCES

1. J. Van Roey, J. van der Donk, and P. E. Lagasse, Vol.71, No.7, J.Opt.Soc. Am, July 1981.
2. Govind P. Agrawal, "Nonlinear Fiber Optics", Academic Press (1989) and reference therein.
3. C.K. Chui, in Computation of Curve and Surface, W. Dahmen, M. Gassa and C.A. Michelli(eds), Kluwer Academic Publishers, pp 137-186, 1990.
4. A.K. Chan, C.K. Chui and J. Zha, Proceeding of PIERS, pp 765, Cambridge, MA, 1991.

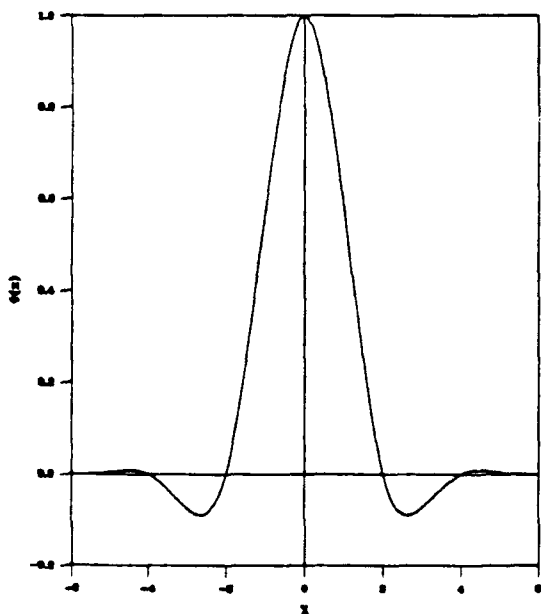


Fig.1. Cubic LCIS basis $\Psi(x)$.

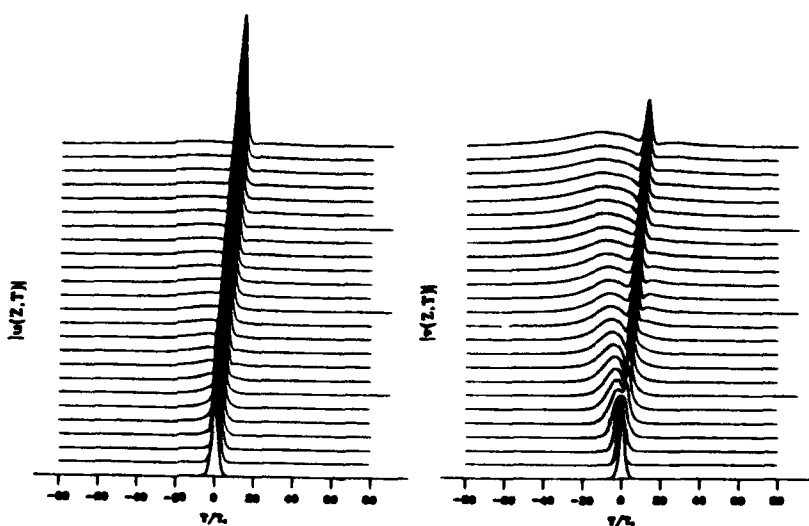


Fig. 2. Soliton propagation in birefringence fiber.

Direct Time Integration of Maxwell's Equations in Nonlinear Dispersive Media for Propagation and Scattering of Femtosecond Electromagnetic Solitons

Peter M. Goorjian
Mail Stop 258-1
NASA-Ames Research Center
Moffett Field, CA 94036
(415) 604-5547

Allen Taflove
EECS Department
McCormick School of Engineering
Northwestern University
Evanston, Illinois 60208-3118
(708) 491-4127

In this paper, we introduce a finite-difference time-domain (FD-TD) algorithm for direct solution of Maxwell's *nonlinear* vector-field equations suitable for modeling the propagation, scattering, and switching of optical pulses, including solitons. The new algorithm, a generalization of our work in [1] on femtosecond pulse propagation in linear dispersive media, should eventually provide a modeling capability for millimeter-scale integrated optical circuits beyond that of existing techniques that use the generalized nonlinear Schrodinger equation (GNLSE) since it retains the optical carrier wave and can rigorously treat the electromagnetic field physics of inhomogeneous nonlinear dispersive media in the context of a vector-field boundary value problem.

The algorithm employs an elegant way to reduce to coupled time-dependent ordinary differential equations (ODE's) the linear *and* nonlinear convolutions needed to specify quantum effects in the context of Maxwell's equations. These ODE's are then integrated in time concurrently with the Maxwell's curl equations. A critical factor, the backstorage in time, is now dimensionally very small, only that needed by the time-integration algorithm for the ODE's. The new level of required storage is as much as *10,000 times less* than that needed to implement the convolutional time integrations via brute force by storing the complete time-history of the kernel functions of the convolutions. For a 2-D or 3-D full-vector nonlinear optics model, this reduces the computer memory required for a first-principles Maxwellian computation from an *impossible* level in the order of 1000 Gwords to a *presently-feasible* level in the order of 1 Gword.

The FD-TD direct time integration of Maxwell's equations can now incorporate nonlinear instantaneous and dispersive effects as well as linear dispersive effects, thereby permitting the modeling of optical solitons having very large instantaneous bandwidths. The algorithm, described in detail in the full paper, assumes that the electric polarization consists of a linear part and a nonlinear part [2]. The linear part is characterized by a Lorentz dispersion [1]. The nonlinear part is characterized by the single nonlinear time convolution [3] used for modeling silica optical fibers. This includes the physics of Kerr nonresonant virtual electronic transitions (an instantaneous nonlinearity) and transient Raman scattering (a dispersive nonlinearity). The Raman interaction is modeled by a single Lorentzian line centered on the optical phonon frequency.

The modeling capabilities of this new algorithm are demonstrated by 1-D calculations of propagating and colliding solitons. The calculations are for a propagating pulse with a carrier frequency of $1.37 \cdot 10^{14}$ Hz, and a hyperbolic secant envelope having a characteristic time constant of 14.6 fs. The first calculation simulates Lorentz linear dispersion alone. As Fig. 1 shows, the pulse undergoes predicted [2,4] pulse broadening, amplitude diminishing and carrier frequency modulation, including asymmetrical shifting of the envelope, a higher-order dispersive effect.

The second calculation simulates the effects of the full linear and nonlinear polarizations. As shown in Fig. 2, the propagating pulse now has the features of a soliton with the retention of its

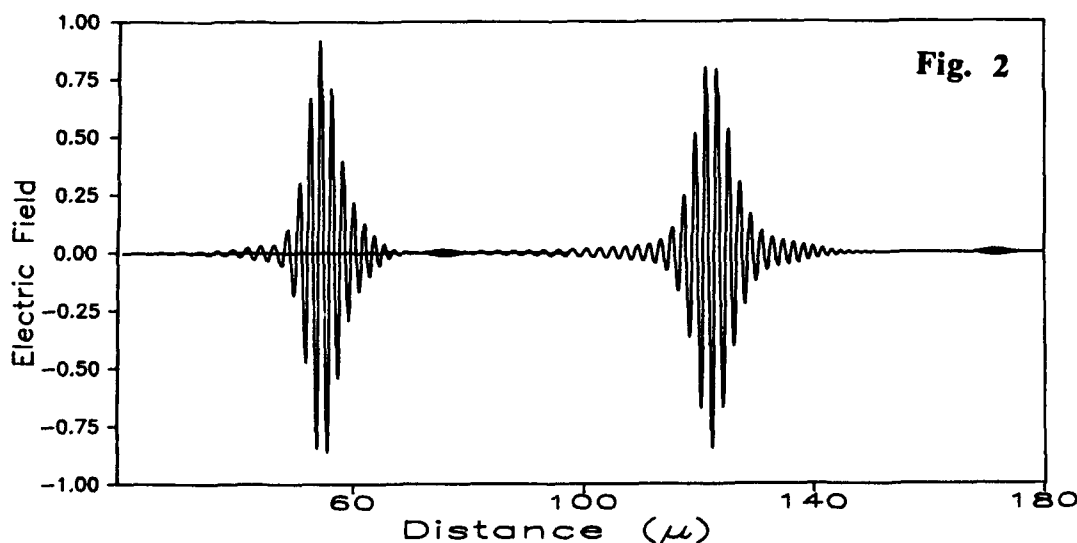
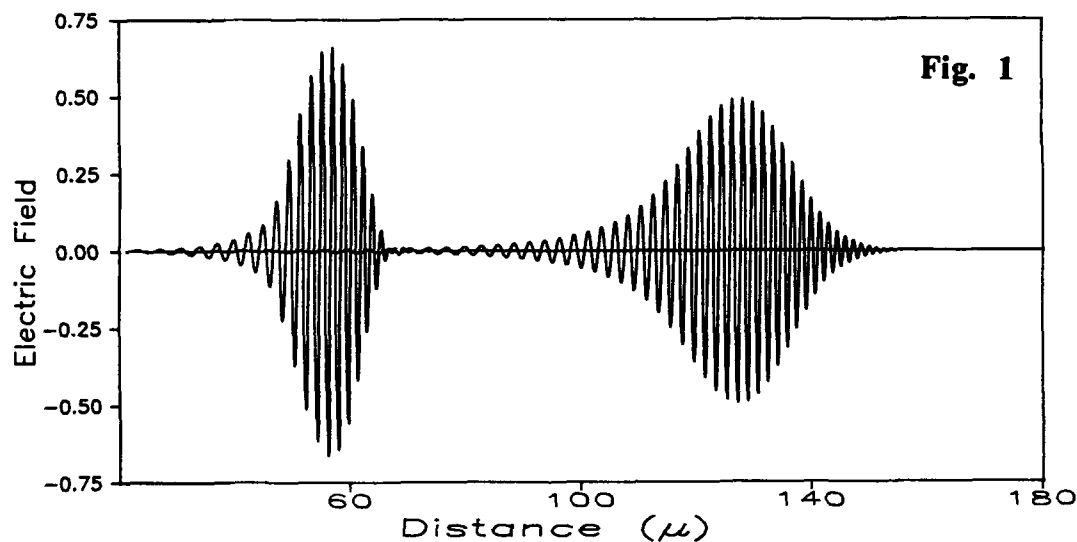
width and amplitude. In addition, a second, low-amplitude, high-frequency, "daughter" soliton forms and moves out ahead of the main soliton. A spectral red shift, generated by the Raman effect [2,3], has been obtained and will be discussed in the presentation.

The third calculation simulates the collision of two equal-amplitude, counter-propagating solitons, each with a daughter soliton. The results show the solitons interacting during the collisions and then separating without general changes [4]. However, by comparing the carriers of the collided main-daughter soliton pair with those of the non-collided pair, precise carrier phase lags of the collided main and daughter solitons are measured.

The presentation also includes a video of these calculations showing pulse evolution in time.

References

- [1] R. M. Joseph, S. C. Hagness, and A. Taflove. *Optics Letters* **16**, 1412 (1991).
- [2] G. P. Agrawal. *Nonlinear Fiber Optics*. Academic Press, New York, 1989.
- [3] K. J. Blow and D. Wood. *IEEE J. Quantum Electron.* **25**, 2665 (1989).
- [4] D. Marcuse. *Theory of Dielectric Optical Waveguides*, 2nd ed. Academic Press, 1991.



Tul4-1

A Recipe for Soliton Robustness in Optical Fibers

C. R. Menyuk
Department of Electrical Engineering
University of Maryland
Baltimore, MD 21228-5398
tel. no. (410)-455-3501

It is often claimed in the literature that solitons in optical fibers are well-described by the nonlinear Schrödinger equation. The evidence for this claim is the remarkable series of experiments, dating from the original work of Mollenauer, et al. [1], which clearly show that *single solitons in isolation* act in accordance with the nonlinear Schrödinger equation in the presence of significant fiber nonidealities—physical effects not included in the nonlinear Schrödinger equation. The most important of these are attenuation, the Raman effect, higher order dispersion, and birefringence. A clear qualitative difference in the effects of attenuation and the Raman effect on the one hand and higher order dispersion and birefringence on the other hand is visible in both experiments and numerical simulations. In the case of attenuation, a steady decrease of the soliton amplitude is observed [1] and in the case of the Raman effect, a steady decrease of the soliton central frequency is observed [2]. This steady change in the soliton parameters will ultimately destroy the soliton if it is uncompensated. In the former case, the soliton will ultimately become undetectable, while in the latter case, the soliton will be shifted into a wavelength regime where attenuation dominates, the amplitude falls, and, once again, the soliton becomes undetectable. By contrast, both higher order dispersion and birefringence change the soliton shape somewhat and shift its parameters, but lead to no steady change in these parameters [3] – [4]. As a consequence, their effect is hard to detect experimentally unless they become quite large.

What is responsible for the remarkable robustness of optical fibers, and why are higher order dispersion and birefringence so much more benign in their effects on solitons than attenuation and the Raman effect? The key to understanding these results is that the nonlinear Schrödinger equation is an *integrable Hamiltonian* system, and higher order dispersion and birefringence are *Hamiltonian deformations* of this system, while attenuation and the Raman effect are *non-Hamiltonian deformations*. Here, I will briefly explain the meaning of these terms, and I will be giving a recipe which allows one to quickly and simply determine whether a physical effect is Hamiltonian or not and, thus, whether its impact on solitons will be benign or not. This recipe is the result of two physical *hypotheses*. These hypotheses are *induced* from what is known about the behavior of finite-dimensional dynamical systems, rather than *deduced* from a rigorous mathematical theory. These hypotheses are thus subject to disproof from simulations and experiments, but, to date, these hypotheses have been extremely successful.

The first hypothesis is as follows:

Sufficiently small Hamiltonian deformations of soliton systems lead to soliton robustness.

One finds under these circumstances that when the initial conditions are close to being correct for the generation of solitons, soliton-like pulses appear. It is a matter of some controversy whether these soliton-like pulses should be called solitons. In principle, as long as they are not solutions

of integrable equations, there should be some emission of a dispersive wave continuum when they collide even if it is undetectably small. Hence, they do not satisfy the usual mathematical definition of a soliton. Nonetheless, from an experimental standpoint, these pulses will be indistinguishable from solitons.

How do we know when deformations are Hamiltonian? Often it is obvious. In the case of both higher order dispersion and birefringence, it is possible to write down the Hamiltonian by inspection. Often, however, the Hamiltonian is *not* obvious and a complicated change of variables may be needed. Because of the possibility that a complicated transformation will bring a deformation into the correct form to be obtained from a Hamiltonian, it is difficult to give a definitive answer to the question—when is this deformation Hamiltonian? However, there is a working hypothesis which appears thus far to be reliable in practice and which allows us to give a precise recipe for when deformations will be Hamiltonian and when they will not be. Kodama [5] has shown that when a deformation term satisfies the following rules,

$$\frac{P - P^*}{2} = 1, \quad \frac{I + D}{2} = \text{integer}$$

where P = the number of powers of the field envelope in the deformation term, P^* is the number of powers of the complex conjugate of the field envelope in the deformation term, D is the number of derivatives in the deformation term, and I is the number of powers of i in the deformation term, then a formal solitary wave solution for the deformed equation can be found, as a power series in the amplitude strength, in which the amplitude and frequency do not evolve in time. We now arrive at the hypothesis:

The conditions just given imply that a deformation term is Hamiltonian.

In this presentation, we will discuss the experimental evidence supporting these hypotheses. This work was supported by the Department of Energy.

REFERENCES

1. L. F. Mollenauer, R. H. Stolen, and J. P. Gordon, Phys. Rev. Lett. **45**, 1095 (1980).
2. J. P. Gordon, Opt. Lett. **11**, 662 (1986).
3. P. K. A. Wai, C. R. Menyuk, H. H. Chen, and Y. C. Lee, Opt. Lett. **13**, 628 (1987).
4. C. R. Menyuk, Opt. Lett. **12**, 614 (1987).
5. Y. Kodama, J. Phys. Soc. Japan **45**, 311 (1978).

Tul5-1

Noise effects on long distance propagation of solitons, James P. Gordon, *AT&T Bell Laboratories*. Summary was not available at time of publication.

Wednesday, April 15, 1992

All-Optical Switching

WA 8:30 am–10:00 am
La Salle Ballroom B

Yaron Silberberg, *President*
Bellcore

Energy Contrast from Cascaded Soliton Logic Gates

C.E. Socolich^{a)}, M.N. Islam^{a)}, M.W. Chbat^{b)} and P. Prucnal^{b)}

a) AT&T Bell Laboratories, Holmdel, New Jersey 07733

Tel: (908) 949-5361 Fax: (908) 949-2473

b) Princeton University, Princeton, N.J. 08544

We cascade an ultrafast, all-optical soliton dragging logic gate (SDLG)[1] with a soliton trapping AND-gate (STAG)[2] and measure an energy contrast of $\sim 12:1$ at the output. SDLG's exhibit fan-out and cascability; however, the output is in time-shift-keyed format. STAG's are sensitive to the timing of the input pulses and provide an energy contrast at the output. Therefore, STAG's convert the time-shift-keyed signal to an amplitude-shift-keyed output that can be measured with a detector.

Figure 1 shows the experimental configuration for testing the cascade of logic gates, and the inset provides a schematic of the logic circuit. A passively modelocked color-center laser ($\tau \sim 335$ fs and $\lambda \sim 1.695\mu\text{m}$) provides the control, signal and clock pulses. The SDLG consists of a 350 m length of moderately birefringent fiber surrounded by two polarizing beam splitters. The STAG is implemented in a 20 m length of moderately birefringent fiber followed by a polarizer and a narrow band frequency filter, and the output is detected with a germanium detector.

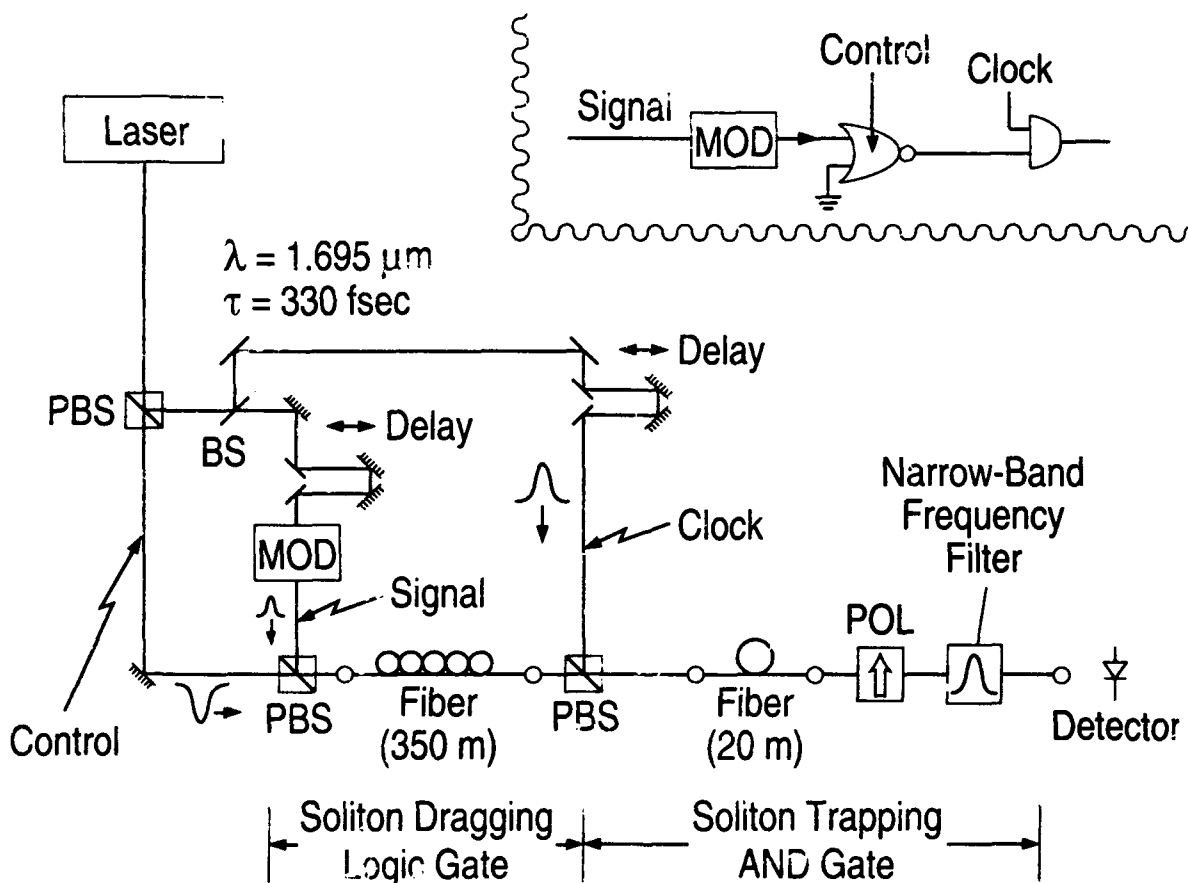


Figure 1. Experimental apparatus for testing the cascaded soliton gates (MOD = modulator, POL = polarizer, BS = beam splitter, PBS = polarizing beam splitter). The inset shows a schematic of the logic circuit.

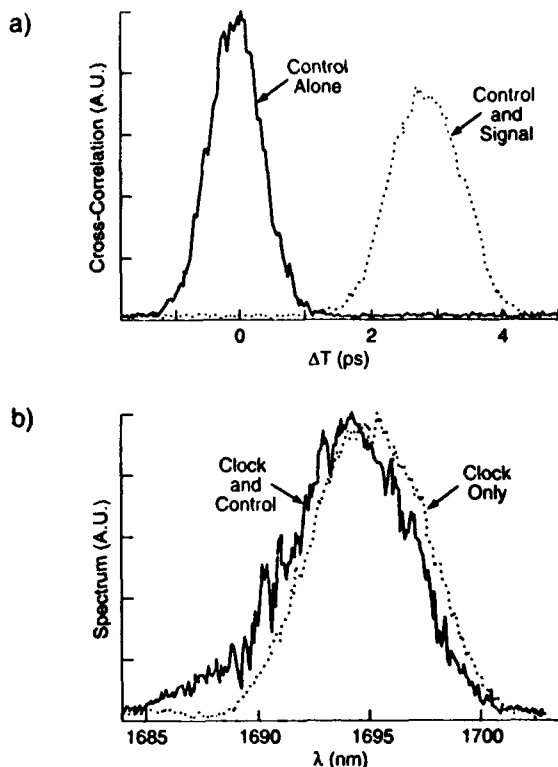


Figure 2. (a) Cross-correlation of control and clock pulse at the output of the soliton-dragging logic gate with and without the signal pulse ($E_{\text{control}} = 49 \text{ pJ}$, $E_{\text{clock}} = 44 \text{ pJ}$, $E_{\text{signal}} = 10 \text{ pJ}$). (b) Spectrum at the output of the soliton trapping AND-gate along the clock axis with and without the control present.

In the SDLG the propagation time for the control changes when the signal is added. For example, Fig. 2a shows the cross-correlation of a 49 pJ control pulse with a clock pulse at the output of the SDLG device; by adding a 10 pJ signal pulse at the input the control is shifted by ~ 3 ps. In soliton trapping two temporally coincident, orthogonally polarized solitons shift their frequencies so that through group-velocity dispersion they compensate for the polarization dispersion. Figure 2b shows the spectrum after the polarizer for a 44 pJ clock pulse with and without the temporally coincident 25 pJ control pulse. An AND-gate having a high output only when both inputs are temporally coincident is obtained by adding a narrow band frequency filter at 1688 nm at the fiber output. Figure 3 shows the detector output with the signal modulated by a chopper. The zero level is at the bottom of the scale, and the contrast

ratio is $\sim 12:1$ after the cascade of the two gates.

Although the contrast ratio from a STAG alone can be as high as 22:1 [3], timing jitter and coupling losses between the two gates degrade the cascade performance. Timing jitter results from soliton self-frequency shift (SSFS), which couples laser amplitude noise into propagation delay changes in the SDLG. In addition, SSFS shifts the control to longer wavelengths and thereby limits the maximum control power allowed in the first fiber. This limited power level combined with a 40% coupling loss between the two gates restricts the control pulse energy to $\sim 1/2$ of the clock energy in the STAG. The differences in pulse energy and wavelength reduce the frequency shift and lower the contrast ratio from the optimum case of identical 42 pJ pulses. Numerical simulations of the coupled nonlinear Schrödinger equation including Raman and pulse shape effects yield close agreement with the experimental results. Further details of the simulations will be presented.

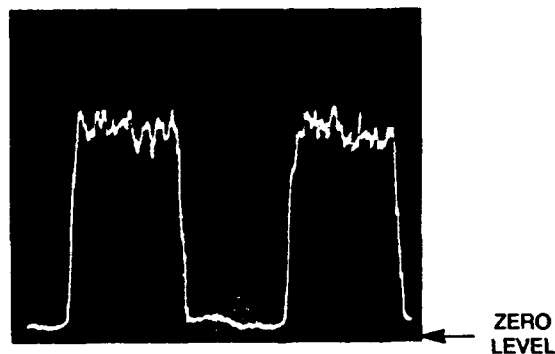


Figure 3. Output from the cascade after a frequency filter centered at 1688 nm with signal modulated at a 50% duty cycle (zero at bottom of scale).

In summary, SDLG's with cascability permit several levels of logic operations, while STAG's eliminate the need for a cross-correlator to measure the output. Numerical simulations agree with experimental results and indicate that the overall performance is limited by SSFS and coupling losses.

1. M.N. Islam, C.E. Socolich and D.A.B. Miller, *Opt. Lett.* 15, 909 (1990).
2. M.N. Islam, *Opt. Lett.* 14, 1257 (1989).
3. M.W. Chbat, B.J. Hong, M.N. Islam, C.E. Socolich, P.R. Prucnal and K.R. German, (submitted to *J. Lightwave Tech.*)

WA2-1

Nonlinear Switching and Pulse Breakup in a Semiconductor Directional Coupler with Multi-Photon Absorption

A. Villeneuve¹, J.S. Aitchison², C.C. Yang^{1,3}, P.G.J. Wigley¹,
C.N. Ironside² and G.I. Stegeman¹

1. CREOL, University of Central Florida, Orlando, FL, USA, (407)-658-6800
2. Dept. of Electronics and Electrical Eng. Univ. of Glasgow, Glasgow, U.K.
3. on leave from The Pennsylvania State University

Recently much interest has been placed in ultrafast all-optical switching in semiconductors near half the band gap¹. In this spectral range, the problem associated with two-photon absorption (2PA) can be avoided, while the relatively large nonlinear refractive index (n_2) can still be utilized. Here we report for the first time a complete characterization of a near half beat length AlGaAs/GaAs quantum well (QW) nonlinear directional coupler (NLDC) and show the effects of multi-photon absorption (MPA) on nonlinear switching and pulse breakup. The NLDC used was made of 4 AlGaAs/GaAs QW's. A NaCl color-center laser with additive pulse mode-locking was used to produce 450 to 800 fsec pulses at $\lambda=1.55 \mu\text{m}$. In Figure 1, we show the switching fraction of the NLDC as a function of input intensity before the input waveguide. The solid lines represent numerical simulations with $n_2=1.25 \times 10^{-13} \text{ cm}^2/\text{W}$, β_2 (2PA)=0.033 cm/GW, and β_3 (three-photon absorption) =0.16 cm³/GW². To show the effects of MPA, the dashed lines are drawn with $\beta_2=\beta_3=0$. It can be seen that MPA increases the switching intensity. Effects of MPA can also be clearly seen in Figure 2 in which the throughput as a function of input intensity is plotted. At high input intensity a change of transmission of about 30% occurs owing to MPA

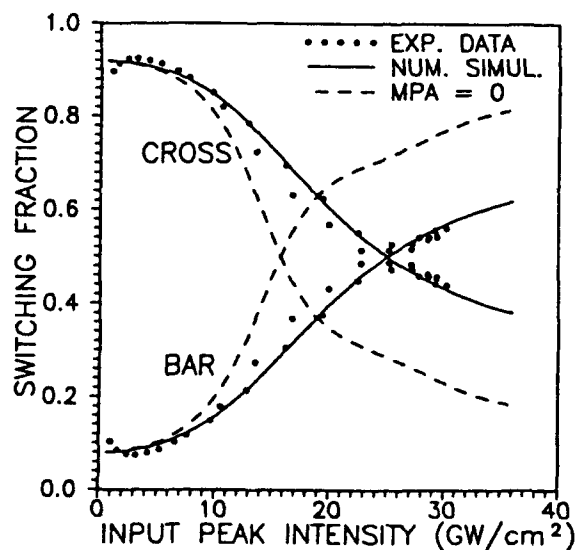


Fig. 1 Switching fraction vs. input intensity

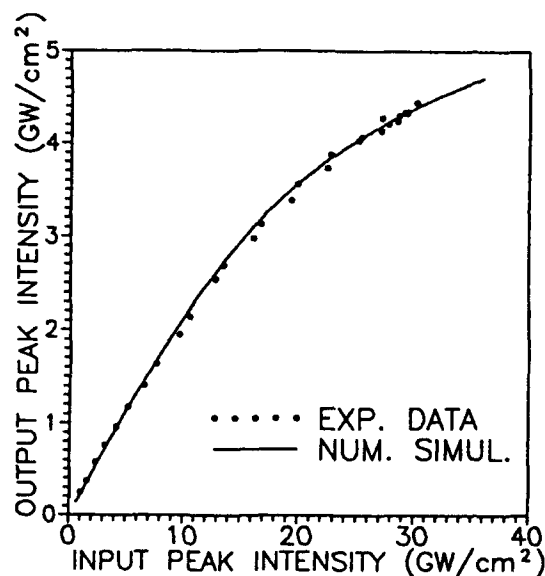


Fig. 2 Throughput

Figures 3(a)-(d) show the autocorrelations along with corresponding numerical simulations (N.S.). Figure 3(a) shows the experimental data and numerical simulations of the input pulse and the output pulse in the bar state

for the input peak intensity (inside the guide) of 12.4 GW/cm^2 . The pulse narrowing owing to nonlinear coupling and MPA can be seen². It was found that MPA has a strong effect on the output pulse shape³, however it is difficult to observe this effect on the autocorrelations. Figures 3(b)-(d) show the autocorrelations of the cross state output for input intensities (inside the guide) of 5.5, 6.9, and 9 GW/cm^2 , respectively. The three-peak feature in (d) clearly indicates pulse breakup through nonlinear coupling. The numerical result for zero MPA is also plotted in (b) for comparison. This curve (long dash) is similar to those in (d) confirming the effects of MPA on switching intensity and output pulse shape. The evolution from (b) through (d) shows that the two peaks in the cross state are further spaced as the input intensity increases. This is expected from nonlinear coupling as a larger central part of the input pulse remains in the bar state when a higher peak intensity is used. The features shown in Figure 3 also imply an ultrafast response of the nonlinearity employed in the nonlinear coupling.

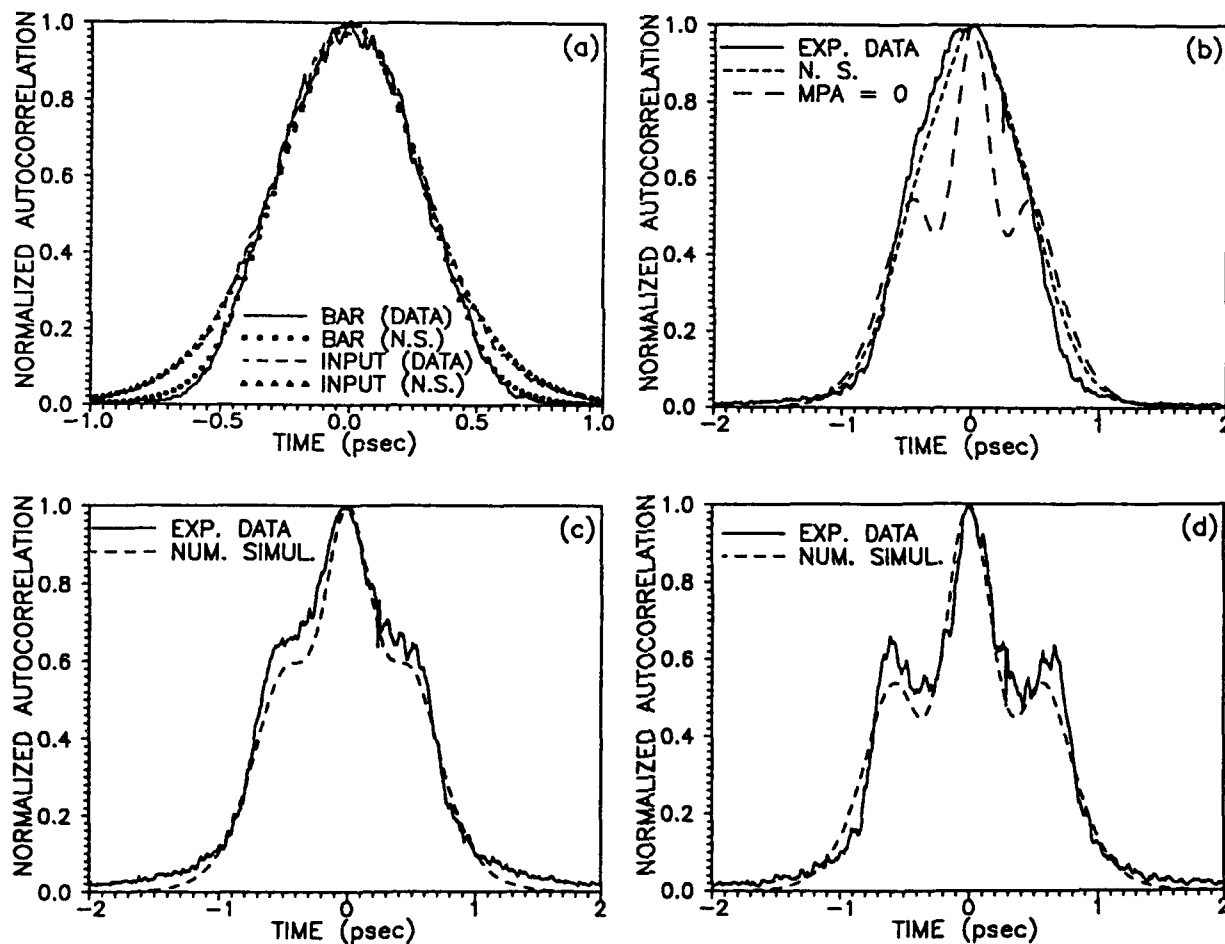


Fig.3 Autocorrelations of the pulses in the bar and cross states.

References:

1. J. S. Aitchison, A. H. Kean, C. N. Ironside, A. Villeneuve, and G. I. Stegeman, *Electron. Lett.*, **27**, 1709, 1991.
2. K. Kitayama and S. Wang, *Appl. Phys. Lett.*, **43**, 17, 1983.
3. C.C. Yang, A. Villeneuve, and G.I. Stegeman, submitted to *Appl. Phys. Lett.*, 1991.

WA3-1

Nonlinear optical properties of a GaAs/GaAlAs integrated asymmetric Mach-Zehnder interferometer.

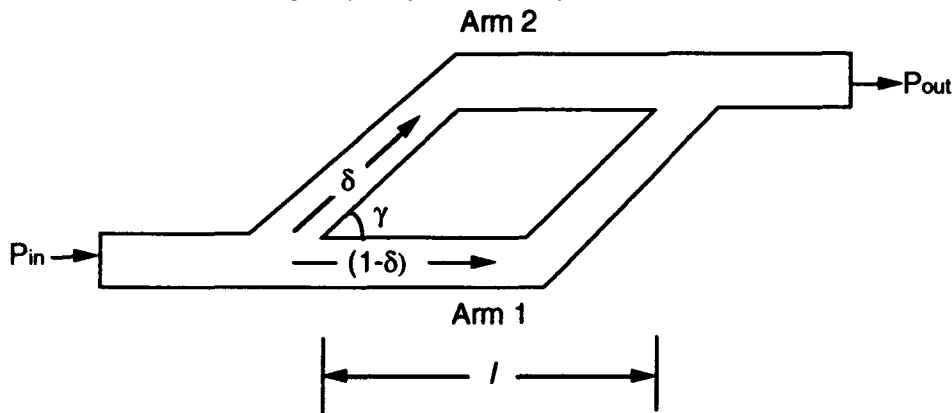
C.N. Ironside, K. Al-hemyari and J.S. Aitchison, Department of Electronics and Electrical Engineering, University of Glasgow, Glasgow G12 8QQ, U.K.

and G. T. Kennedy, R. Grant and W. Sibbett, Department of Physics, North Haugh, University of St. Andrews, St. Andrews, Fife, U.K.

Summary

The layout of an integrated asymmetric Mach-Zehnder interferometer (AMZI) is illustrated in figure (1). The device is an all-optical switch or modulator. It is based on the more familiar electro-optic integrated Mach-Zehnder where a phase change is produced in one arm of the interferometer by an applied electric field. In the all-optical version of the integrated Mach-Zehnder the phase change is produced by the light via the intensity dependent refractive index. The intensity of light in one arm of the interferometer has to be larger than in the other if there is to be a differential phase change therefore in the AMZI device asymmetric Y junctions are employed to split the light unevenly between the arms of the interferometer. The device is conceptually similar to the fibre loop mirror all-optical switches (1) and the same formalism can be applied to both. The key advantage of the interferometric devices over the directional coupler devices for switching applications are that the interferometric devices require half the phase change for full switching.

Figure (1) Layout of the Asymmetric Mach-Zehnder interferometer



Caption Fig. (1) Schematic diagram of a single mode asymmetrical Mach-Zehnder interferometer. The Y-junction full angle is γ and the power splitting in arm 1 and arm 2 are $(1-\delta)$ and δ respectively.

The device has been fabricated in two types of semiconductor waveguide a single quantum well waveguide (SQW) and an Al_{0.18}Ga_{0.82}As waveguide. The SQW waveguide is designed for operation with a resonant nonlinearity (i.e operating with photon energies close to the excitonic resonance of the SQW material). The Al_{0.18}Ga_{0.82}As waveguide is designed for operation with a nonresonant nonlinearity with photon at just below half the band gap. The same material previously employed in a nonlinear directional coupler which operated with the nonresonant nonlinearity()

The AMZI device consists of a single mode input waveguide, a Y-junction which splits the input intensity into two parts in the single mode waveguides 1 and 2 as a function of the Y-junction angle γ and a second Y-junction to recombine the two optical fields into a single mode output waveguide. Using the local normal-mode description, the output power density of the AMZI depends on the phase difference between the two beams incident on the output Y-junction. This phase difference ($\Delta\phi = \phi_1 - \phi_2$) is achieved by means of intensity dependent refractive index in the waveguide material. Using the scattering matrix model, the output transmission of a lossless AMZI is given by;

$$T = 4\delta(1-\delta)\cos^2(\Delta\phi/2 + \theta) \quad (2)$$

θ takes account of any built-in phase difference in the device due to slightly different optical paths in the arms caused by fabrication inaccuracies. The differential phase change between the two arms, $\Delta\phi$, due to the optical nonlinearity, is given by;

$$\Delta\phi = \frac{2\pi n_2 I_{in} l(1-2\delta)}{\lambda_0} \quad (3)$$

Where n_2 is the nonlinear coefficient, I_{in} is the pump beam intensity, δ and $(1-\delta)$ are the optical power splitting between the two arms and l is the length of the interferometer arms. The output response of the AMZI with the pump beam intensity is a \cos^2 function with amplitude and oscillating strength dependent on the Y-junction split ratio between the two arms.

With the resonant nonlinearity in GaAs/GaAlAs SQW waveguide, absorption and absorption saturation have to be taken into account and the output response of AMZI is given by;

$$T = \delta(1 - \delta) \left[\exp(-\alpha_1 l) + \exp(-\alpha_2 l) + 2 \exp\left(-\frac{(\alpha_1 + \alpha_2)l}{2}\right) \cos(\varphi_1 - \varphi_2 + \theta) \right] \quad (4)$$

where the phase changes in arm1 and arm2 of the AMZI (i.e. the intensity dependent refractive index change) are;

$$\varphi_1 = \frac{2\pi n_2(1 - \delta)I_{in} l_{eff}}{\lambda_o(1 + (1 - \delta)I_{in} / I_{nsat})} \quad \varphi_2 = \frac{2\pi n_2 \delta I_{in} l_{eff}}{\lambda_o(1 + \delta I_{in} / I_{nsat})} \quad (5)$$

The resonant intensity dependent refractive nonlinearity saturates and by analogy with the absorption saturation (14) we have chosen a two-level saturation law. and the intensity dependent absorption change in arm1 and arm2 are;

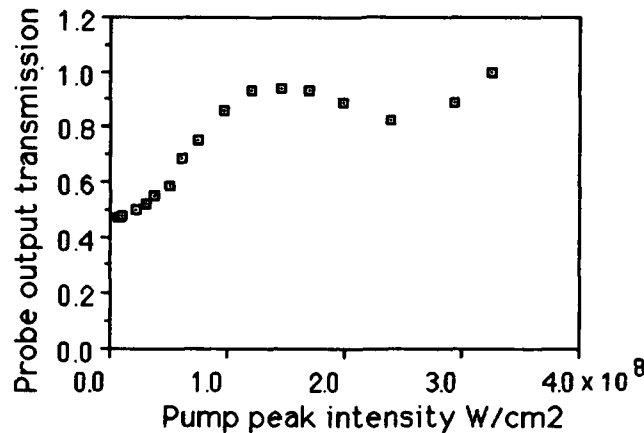
$$\alpha_1 = \frac{\alpha_0}{1 + \frac{(1 - \delta)I_{in}}{I_s}} \quad \alpha_2 = \frac{\alpha_0}{1 + \frac{\delta I_{in}}{I_s}} \quad (6)$$

where α_0 is the linear absorption coefficient and I_s is the absorption saturation power. I_s is estimated from the experimental results of the absorption saturation in the straight waveguide, the saturation mechanism maybe different for the refractive nonlinearity and therefore we have included a different saturation intensity for the refractive nonlinearity I_{nsat} .

The asymmetric Mach-Zehnder interferometer is fabricated in the GaAs/GaAlAs SQW material using the standard optical lithography and liftoff. The rib width was 3 μ m and the etching depth 1 μ m, the Y-junction angle γ was 2°. The interferometric arm length is 1 mm. The split ratio was measured, in the same manner as in ref. (15), $\delta = 0.3$. Note that, as can be seen from Fig. (1), the first Y junction splits the light in 0.3 : 0.7 ratio but the second Y junction recombines the light in the opposite ratio that is 0.7:0.3; this is important if a true null is to be achieved in the switch off state; it also means that the maximum possible transmission of the device (i.e. assuming no losses) is $4\delta(1-\delta)$, in this case 0.84.

The operation of the SQW device was investigated by employing a mode-locked Ti:sapphire laser. The laser output consisted of a train of ~ 50 ps pulses spaced by 13 ns with an average power ~ 350 mW. Therefore, the pulse energy was approximately 5 nJ and the peak power ~100 W. A pump-probe method was employed and figure (2) shows the normalised transmission of the device and zero delay between pump and probe.

Figure(2) Normalised transmission of the SQW AMZI (resonant nonlinearity)



Caption: Fig(2)The experimental results of the normalised probe-beam output transmission of the integrated. ASMZI as a function of the input pump-beam intensity.

The dip in the transmission is due to the nonlinear phase change producing destructive interference at the second Y junction. A true null in the destructive interference is not obtained because of the effect of saturation of the absorption which results in the relative intensity in the high powered arm increasing with respect to the original splitting ratio at the first Y junction. At the second Y junction the light in the low power arm cannot null out the high power arm. This effect would not be present in device operating with a nonresonant nonlinearity because were there is no significant nonlinear absorption.

In conclusion a nonlinear integrated interferometer has been fabricated which is the integrated optics analog of the nonlinear loop mirror. Its operation with a resonant nonlinearity has been characterised. Currently, the nonresonant nonlinearity operation is being investigated.

References

- (1) N. J. Doran, and D. Wood "Non-linear optical loop mirror" Opt. Lett., vol. 13, 56 1988.
- (2) J. S. Aitchison, A. H. Kean, C. N. Ironside, A. Villeneuve, and G. I. Stegeman "Ultrafast all-optical switching in Al_{0.18}Ga_{0.82}As directional coupler in 1.55 μ m spectral region" Electronics Lett., vol. 27, 1709 1991.

Ultrafast nonlinear transmission changes in a GaAs single quantum well waveguide structure suitable for ultrafast all-optical switches

P. Li Kam Wa, A. Miller[†], R. Bambha
Center for Research in Electro-Optics and Lasers,
University of Central Florida,
12424 Research Parkway, Orlando, Florida 32826

A. Cavailles
AT & T Bell Laboratories
Crawfords Corner, Holmdel, New Jersey 07733

A.L. Moretti, R.W. Wickman, K.A. Stair, T.E. Bird
Amoco Technology Company,
P.O. Box 3011, Naperville, Illinois 60566

We have previously demonstrated picosecond all-optical switching in a waveguide directional coupler⁽¹⁾. It was shown that cross-well carrier sweep-out could be used to increase the recovery speed of the device by over an order of magnitude by employing a p-i-n doped structure⁽²⁾. In this work, we report time resolved measurements of optical nonlinearities in a waveguide structure containing a single GaAs quantum well which exhibits a fast recovery without the need for an applied electric field. We observe phenomena associated with exciton absorption quenching and screening of the internal field resulting in a dynamic shift of absorption edge by the quantum confined Stark effect.

The structure studied in this work was grown on an n-type conducting GaAs substrate by molecular beam epitaxy. It consisted of a $0.25\mu\text{m}$ GaAs buffer doped $n\sim 1\times 10^{18}\text{cm}^{-3}$ followed by a $1\mu\text{m}$ lower cladding of undoped $\text{Al}_{0.4}\text{Ga}_{0.6}\text{As}$. The center of the $0.5\mu\text{m}$ waveguide core of undoped $\text{Al}_{0.3}\text{Ga}_{0.7}\text{As}$ contained a single GaAs quantum well 8nm thick. The upper cladding was $1\mu\text{m}$ of undoped $\text{Al}_{0.4}\text{Ga}_{0.6}\text{As}$ and was capped with a $0.1\mu\text{m}$ GaAs contact layer doped $p\sim 8\times 10^{18}\text{cm}^{-3}$. Lateral confinement was achieved by etching part way into the top $\text{Al}_{0.4}\text{Ga}_{0.6}\text{As}$ layer to leave ribs of widths $3, 5$ and $10\mu\text{m}$ and $0.75\mu\text{m}$ high. The device was finally cleaved to a length of $500\mu\text{m}$. By measuring the transmission spectrum of the waveguides, the absorption edge was found to be at 837nm for TE polarized light and 827nm for TM polarized light.

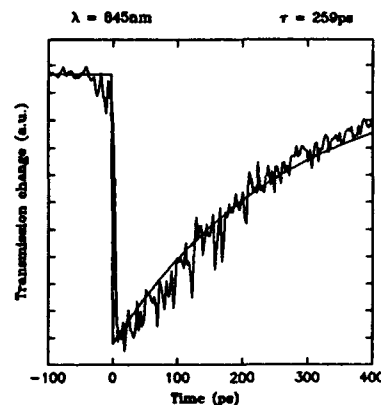


Fig. 1. Time resolved pump-probe transmission changes at 845nm

[†] Also with the Departments of Physics and Electrical Engineering

The nonlinear transmission characteristics were measured using a picosecond optical pump-probe technique. Picosecond laser pulses were split into pump and probe beams that could be temporally delayed with respect to each other. The pump beam passed through a half-wave plate whilst the probe beam was mechanically chopped. The two beams were then recombined on a beam-splitter and focussed onto the same spot of the input facet of the device. The pump beam excited the TE modes of the waveguide whilst the probe beam excited the TM modes of the waveguide. A cross-polarizer placed after the output collecting lens, ensured that only the TM polarized chopped probe beam was monitored using a photo-detector and lock-in amplifier. The temporal response was obtained by measuring the transmitted throughput of the probe beam as the probe timing was scanned past zero-delay. In fig.1 the nonlinear transmission measurements at a probing wavelength of 845nm, shows a fast decrease in probe throughput at zero delay due to the exciton broadening effects, with a fast recovery on a time constant of 250ps. At wavelengths closer to the light hole exciton, the nonlinear signal is due to the screening of the exciton which result in a fast positive signal that recovers with a fast time constant of 70ps (fig.2). However, in spite of the very small built in field, a self-electro-optic-effect is observed which results in the transmission going negative with long recovery time⁽³⁾. However, this negative signal in the transmission can be missed by probing at a very slightly shorter wavelength where the transmission is not sensitive to electric field changes as shown in fig.3. Here, the recovery time constant is 110ps.

In conclusion, it is believed that, due to the absence of recapture of carriers that would occur in a multiple quantum well system, very rapid carrier dissipation is obtained. Therefore, by employing structures containing a single quantum well (or only a few wells) instead of multiple quantum wells in all-optical switches, large reduction in switching times can be achieved. Measurements of all-optical directional coupler switching are currently under way and will be reported at the meeting.

REFERENCES

1. P. Li Kam Wa, A. Miller, C.B. Park, J.S. Roberts, P.N. Robson, *Appl. Phys. Lett.* 57, 1846, (1990).
2. P. Li Kam Wa, A. Miller, J.S. Roberts, P.N. Robson, *Appl. Phys. Lett.* 58, 2055, (1991)
3. T.H. Wood, J.Z. Pastalan, C.A. Burrus, B.C. Johnson, B.I. Miller, J.L. de Miguel, U. Koren, M.G. Young, *Appl. Phys. Lett.*, 57, 1081, (1990)

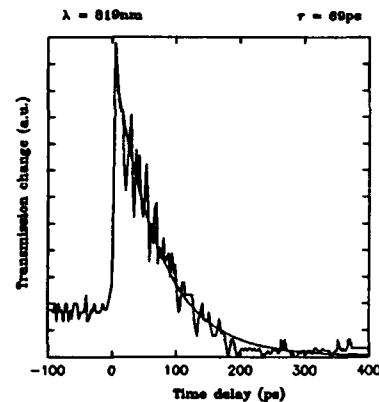


Fig.2. Time resolved pump-probe transmission changes at 819nm

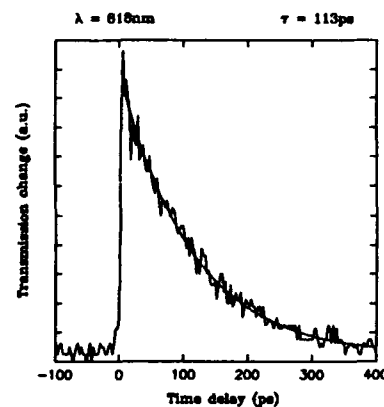


Fig.3. Time resolved pump-probe transmission changes at 818nm

AN ALL-OPTICAL SWITCH USING SPATIAL SOLITON IN LOSSY NONLINEAR MEDIUM

Jieren Bian and Andrew K. Chan
Department of Electrical Engineering
Texas A&M University
College Station, Texas 77843-3128
Telephone: (409) 845-7458

SUMMARY

In recent years, all-optical devices have attracted much attention both in theoretical studies and experimental verifications. After the experimental observation of soliton and their interactions in glass planar waveguide by J.S. Aitchison, A.M. Weiner, Y. Silberberg, etc.^[1] in 1991, optical switches using spatial optical solitons have been proposed by several authors^[2,3]. Since all types of nonlinear optical material exhibit some losses, the loss factor should be included in device designs and analyses. The loss factor is especially critical in devices using material with small nonlinear coefficient since it requires high threshold power to excite solitons in the material.

We have designed an all-optical switch using nonlinear coherent interactions between two spatial solitons with phase difference of π and demonstrated an improvement over our previous work^[3]. Since a small loss in the material will not adversely affect the operation principle of this device, we can choose to use those nonlinear material with relatively large loss factor and large nonlinear coefficient to reduce the threshold power requirement.

In a two-dimensional medium with a nonlinear refractive index n_n and loss factor α , the wave equation becomes

$$i \frac{\partial u}{\partial \xi} + \frac{1}{2} \frac{\partial^2 u}{\partial x^2} + N^2 |u|^2 u + i L_D \frac{\alpha}{2} u = 0.$$

where $\alpha = \frac{\epsilon_0''}{\epsilon_0'} k$, $\xi = z/L_D$, $x = x'/a_0$, $u = E'/\sqrt{P}$, and $N^2 = P_0 k^2 a_0^2 n_n^2 / 2n_l^2$. n_l represents the linear part of refractive index and n_n is the nonlinear part. It has been found both theoretically and experimently that when two spatial solitons with phase difference π are launched into a nonlinear medium, they repel each other. Our design is based on this principle.

The structural view of of the all-optical nonlinear switching device is shown in Figure 1. The length of the nonlinear region is 0.34(mm). Assuming the input signal is carried by the TE_0 mode propagating in waveguide No.2 with the control beams turn off, the TE_0 mode adjusts itself to form a spatial soliton after propagating for a short distance into the nonlinear region. The soliton moves directly toward waveguide No.6 with its shape unchanged. This case corresponds to the switch is set at the 'off' position. When the control channel No.3 is turned on and the signal channel 2 is on, the signal is pushed away from channel No.6 to channel No.5 if the relative phase of the fields in channels No.2 and No.3 is π . Two spatial solitons are formed in the nonlinear region, repelling each other as they propagate in the medium as shown in Figure 2.

A numerical simulation has been conducted to examine the effect of loss on the transmitted power. By varying the loss factor from 1.84×10^{-7} to 9.2×10^{-3} , Figure 3 shows the comparison on the transmitted power from the present work to that of our previous work [3]. It can be seen that for a given transmitted power level, the current design can tolerate material loss 3-4 times higher than that of previous design. By relaxing the small loss requirement, we may choose material with higher nonlinear coefficient to reduce the threshold power of the device. The model coupling in the waveguide has also been taken into account in this study.

REFERENCES

- [1]. J.S. Aitchison, A.M. Weiner, Y. Silberberg, D.E. Leaird, M.K. Oliver, J.L. Jackel, and P.W.E. Smith, "Experimental observation of spatial soliton interactions", Opt. Lett. Vol.16, No 1, 15 (1991).
- [2]. Tian-Tsorng and Sien Chi, "Nonlinear Photonic Switching by Using the Spatial Soliton Collision", Opt. Lett. Vol.15, No.20, 1123 (1990).
- [3]. J. Bian and A.K. Chan, "A Design of All-Optical Switch using Spatial Soliton Interactions", Microwave and Optical Technology Letters, to be published in December (1991).

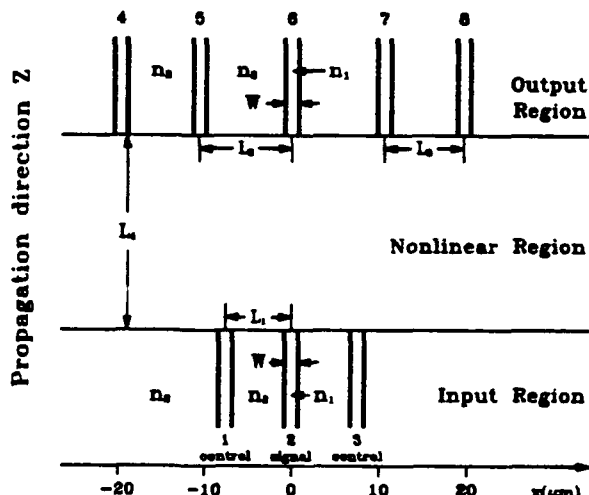


Figure 1 Structure of the All-Optical Nonlinear Switching Device

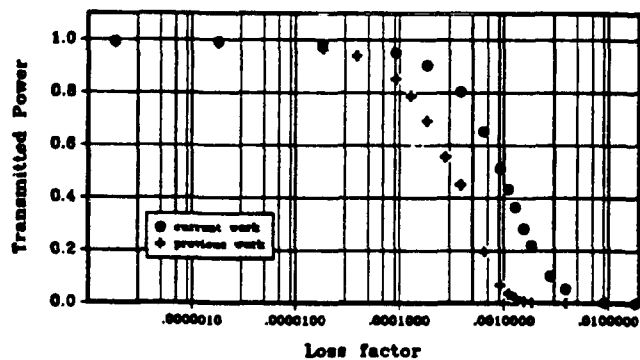


Figure 3 Transmitted power of the device

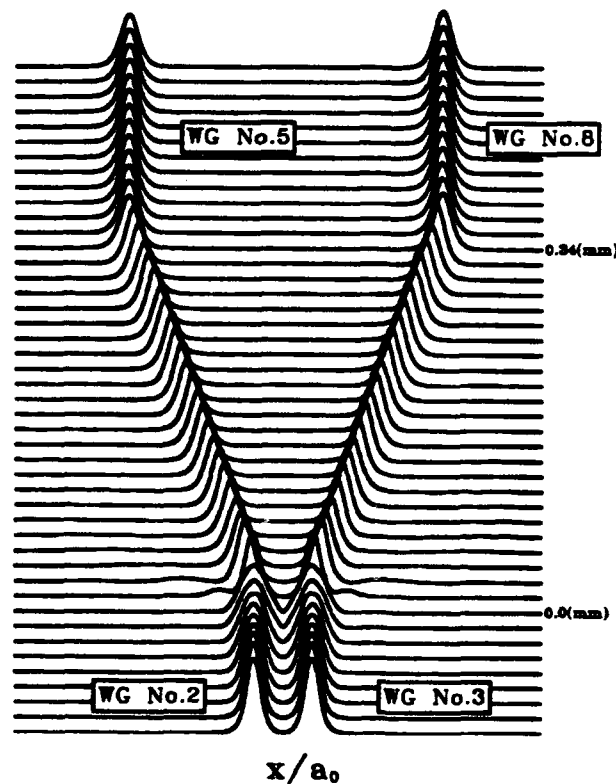


Figure 2 Signal and Control Beams in the device

**All-optical switching using dispersive nonlinearities
in InGaAs/GaAs single quantum well laser diodes**

P. Li Kam Wa, T.W. Kao, A. Miller⁺
Center for Research in Electro-Optics and Lasers,
University of Central Florida,
12424 Research Parkway, Orlando, FL 32826

M. Ogawa, R.M. Park
Dept. of Materials Science and Engineering
University of Florida, Gainesville, FL 32611

All optical switching due to nonlinear Fabry-Perot modulation has been obtained in laser diodes electrically biased below lasing threshold. The advantage of such devices over their passive counterparts is the realization of amplification of the input optical signal. This eliminates the problem of fan-out capabilities of all-optical switching devices. The mechanism for the nonlinear refraction arises through gain saturation by optical depletion of carriers.

The structure used in the measurements was grown on a n-doped GaAs substrate by molecular beam epitaxy and comprised a single 50Å thick undoped In_{0.2}Ga_{0.8}As quantum well layer sandwiched between undoped GaAs layers each 0.1μm thick. Due to the significant lattice mismatch between the In_{0.2}Ga_{0.8}As quantum well and the GaAs barrier, in plane biaxial compressive strain is present in the quantum well. The cladding layers of Al_{0.2}Ga_{0.8}As on either side of the core were doped n-type and p-type respectively. The top layer was capped by 0.1μm p⁺-GaAs layer. Gold stripes each 100μm wide were deposited on the surface and the laser diodes were cleaved to a length of 500μm.

A CW Ti-sapphire laser was used in conjunction with an acousto-optic modulator to provide wavelength tunable optical pulses that were end-fire coupled into the device. The latter was biased with electrical pulses of 2μs duration at a repetition rate of 1kHz, synchronized with the optical pulses such that the optical pulses passed through the device when the current injection has been established. Gain measurements at the wavelength of peak gain (965nm) as a function of input intensity, were performed in a device that was biased from 80% to 99% of lasing threshold. The plots of fig.1 clearly show evidence of gain saturation under these conditions. Similar measurements performed at other wavelengths

⁺ Also with the Departments of Physics and Electrical Engineering

indicate that gain is obtained over a relatively broad range of wavelength spectrum (around 30nm) with similar gain saturation characteristics.

As the wavelength of the Ti-sapphire laser was tuned carefully, the transmitted signal was found to go through strong oscillations due to Fabry-Perot effects. Triangular shaped optical pulses were then launched into the device and distinct optical switching in the transmitted pulse was observed. The switch-down in the transmitted power occurred at a slightly lower input power level than the initial switch-up thus showing evidence of bistability. The switching is hence consistent with the nonlinear detuning of the F-P transmission peak into resonance. The input-output characteristics of the device for two closely spaced wavelengths are shown in fig.2. A slight increase in the wavelength of the pump laser resulted in a shift of the switch points to higher input power levels. This is consistent with a positive optical nonlinearities which arises from saturation of the gain by carrier depletion.

Work is currently in progress on the measurements of optical nonlinearities in a single mode InGaAs strained layer quantum well laser as well as the characterisation of directional coupler switching under conditions of gain. The results of such measurements will be reported at the meeting.

References

1. T. Nakai, N. Ogasawara, R. Ito, Japan. J. Appl. Phys., 22, (1983)
2. W.F. Sharfin, M. Dagenais, Appl. Phys. Lett., 46, (1985)
3. M.J. Adams, H.J. Westlake, M.J. O'Mahony, I.D. Henning, IEEE J. Quantum Electron., QE-21, (1985).

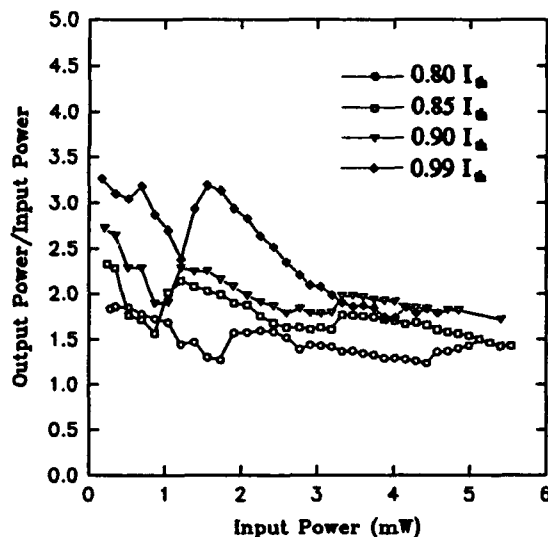


Fig.1 Gain characteristics of an InGaAs single quantum well diode

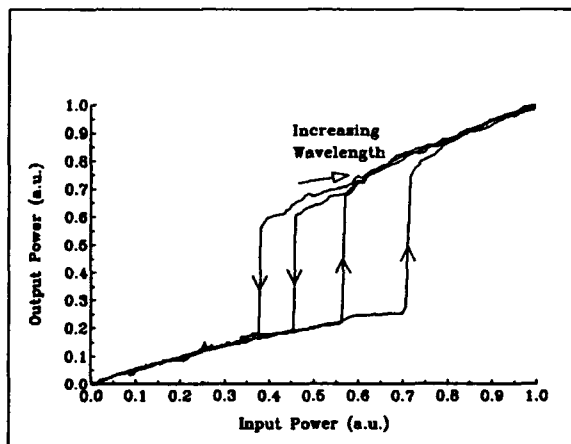


Fig.2. Bistable switching in the input-output characteristics

Wednesday, April 15, 1992

Waveguide and Device Technology

WB 8:30 am–10:30 am
La Salle Ballroom C

Talal K. Findakly, *Presider*
Hoechst Celanese Research Co.

WB1-1

Doped Optical Claddings for Electro-Optical Polymer Waveguide Devices

Paul R. Ashley
Weapon Sciences Directorate
Research, Development, and Engineering Center
U.S. Army Missile Command
Redstone Arsenal, AL 35898-5248
and
Elizabeth A. Sornsin
Physics Department
University of Alabama in Huntsville
Huntsville, AL 35899

With the continued development of electro-optic polymer devices, optical and electrical performance have become increasingly important issues. Higher r_{33} values and lower $V_{\pi}l$ are continually sought, and improvements have been reported [1,2]. In order to optimize these values, high electric field strengths must be achieved across the active polymer during both poling and device operation. Devices are generally constructed as a multilayer structure with upper and lower dielectric polymer optical buffer layers. The electric field strength across the EO polymer or active guiding layer is determined in large measure by the electrical properties of the cladding layers. If these properties for all layers are similar, then the field strength across the EO polymer is reduced by an amount determined by the relative thicknesses of the cladding and active layer. Reported here is a technique in which the buffer layers were doped in order to increase the field strength across the active polymer, thus reducing the required poling voltage as well as the operating voltage for the device.

The waveguide construction used is illustrated in Figure 1, and details of fabrication are reported elsewhere [3]. The substrate was conductive coated glass. A lower buffer layer (3 μm thick) was covered with a patterned cladding layer (3.5 μm thick). The patterned layer was formed by UV exposure and development. It was then backfilled with the active polymer. One of the polymers used was Hoechst Celanese PC6S. Above the upper cladding a gold electrode was patterned, and the entire structure was overcoated with an additional layer for electrical/mechanical isolation as well as an aid for end face polishing. The lower buffer layer, patterned cladding, and upper cladding consisted of a UV curing optical epoxy (Norland 61) doped with $[\text{CH}_3(\text{CH}_2)_3]_4\text{NCl}$ 1% by weight. The dopant was chosen from among several organic salts considered because of its high organic functionality, solubility, and observed conductivity increase in the cladding polymer. The measured resistivity of the doped polymer compared to the undoped polymer as a function of temperature is shown in Figure 2. At room temperature, over an order of magnitude increase in conductivity was observed with an increasing difference at higher temperatures.

Comparison of doped and undoped waveguide structures revealed no significant difference in propagation loss in both the poled and unpoled cases, respectively, at the operating wavelength of 1.32 μm . Intensity modulators were constructed using single mode waveguides fabricated as shown schematically in Figure 3. The devices contained common gold electrodes (7.4 mm long) for poling and device operation. A poling field of $70\text{V}/\mu\text{m}$ was applied with an external applied voltage corresponding to approximately $0.33V_0$ where V_0 is the required voltage for a similar undoped device. The measured r_{33} value of 2.5 agreed well with the value of 2.6 for an undoped device, and the $V_{\pi}l$ value was 2.8 times smaller than the equivalent undoped device.

Temperature stability and other effects of the doped materials have been investigated and will be discussed at the meeting. Also a comparison to other dopants, EO polymers, and cladding materials will be presented as well as an analysis of electrical properties which influence the composite two-dimensional field distribution in EO polymer devices.

References

1. Haas, D.R., and H.T. Man, Integrated Photonics Research, OSA Tech. Dig. Series, 8, 133 (1991).
2. Mohlmann, G.R., W.H.G. Horsthuis, A. McDonach, M.J. Copeland, C. Duchet, P. Fabre, M.B.J. Diemeer, E.S. Trommel, F.M.M. Suyten, E. Van Tomme, P. Baguero, and P. Van Daele, Proc. SPIE, 1337, 215 (1990).
3. Ashley, P.R., and T.A. Tumolillo, Jr., Appl. Phys. Lett., 58, 884 (1991).

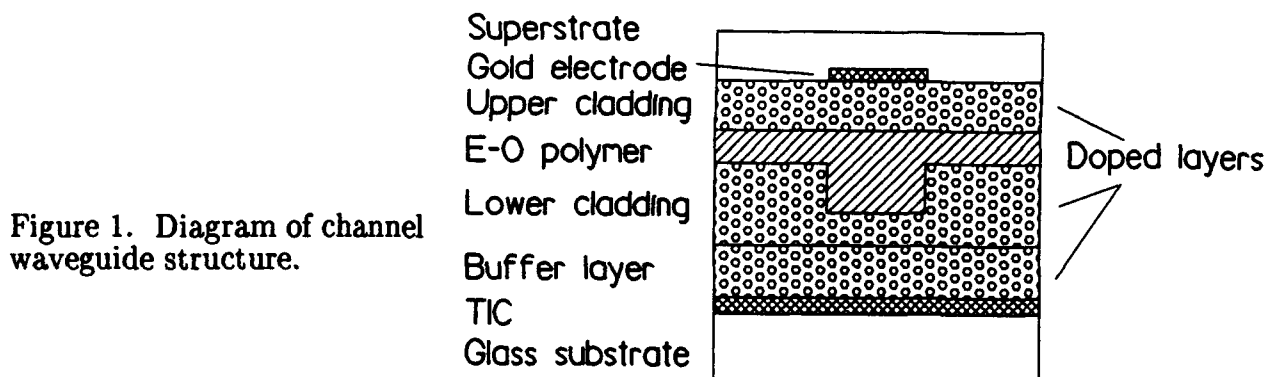


Figure 1. Diagram of channel waveguide structure.

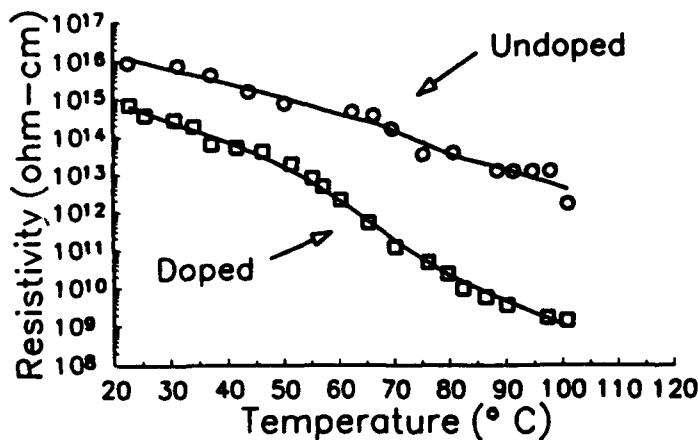
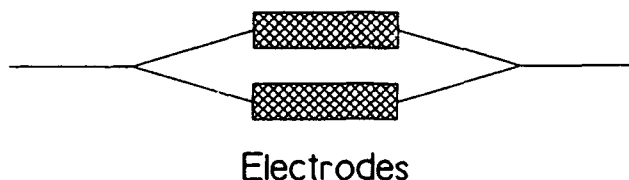


Figure 2. Resistivity of doped and undoped cladding as a function of temperature.

Figure 3. Intensity modulator device structure.



New Fabrication Technology for Polymer Optical Waveguides

A. Neyer, T. Knoche, P. Dannberg*, and L. Müller

**Lehrstuhl für Hochfrequenztechnik, Universität Dortmund
Postfach 500 500, W-4600 Dortmund 50, Germany**

***Institut für Angewandte Physik, Friedrich Schiller Universität Jena,
Max Wien Platz 1, O-6900 Jena, Germany**

Polymeric materials are very promising for a substantial cost reduction in the fabrication of guided wave devices, since mass fabrication technologies like molding, injection molding or casting may be applied. One of the greatest advantages of these technologies lies in the fact that the optical waveguide structures may be manufactured simultaneously together with fibre alignment grooves in one fabrication process.

Replication techniques using metal dies to generate waveguide structures have been studied already in 1974 /1/, but these techniques have not been further developed to a mass production level. Recently, OMRON has started an activity in structuring polymer waveguides and gratings by embossing metal dies into UV-curing polymer layers /2/. In this paper, the fabrication of buried single mode waveguides at 1300 nm is reported using injection molded PMMA waveguide substrates and UV-curing resins as higher refractive index waveguide materials.

The main fabrication steps for the realization of buried polymer strip waveguides are shown schematically in Fig. 1. The fabrication starts with the conventional UV-light lithographic structuring of photoresist layers. After the development of the resist, the waveguide structure is contained in the resist layer in form of rectangular grooves. The thickness of the resist will define the final waveguide thickness, whereas the width and the geometrical outline of the grooves - here straight lines - will determine the final waveguide width and the device structure. In the actual experiments, the resist thickness was 6 μm and the width of the grooves was between 2 and 10 μm . After this lithographic definition of the waveguide structure, the resist profil was replicated by electroplating into a nickel plate of 300 μm thickness. This metal mold of size 70x70 mm was then used as insert in an injection molding machine (type: Arburg 400-140). The resulting products of this fabrication step have been PMMA substrates of size 50x50x2 mm³ containing the waveguide structure in form of grooves. The waveguide grooves have been filled by liquid, highly transparent polymers (actually UV-curing resins), which had higher refractive indices than the substrate. Next, a plane plate of polymeric material (here the same as the substrate material) was pressed against the substrate to remove the surplus liquid polymer and to protect the waveguide from the top side. The last step in the fabrication of buried waveguides was the UV-curing of the liquid polymer.

After endface polishing, laser light of 1320 nm wavelength has been coupled into the strip waveguides by using polarisation maintaining fibres (York HB 1200). The total insertion loss (fibre-waveguide-fibre) of a 12 mm long single mode waveguide with a cross section of $6 \times 6 \mu\text{m}^2$ has been measured to 1.5 dB. Taking into account coupling losses by mode mismatch, angular mismatch, and reflexions in the order of 0.3 dB per interface, the pure waveguide loss is about 0.8 dB/cm. This figure may be reduced substantially down to values around 0.1-0.2 dB/cm by using deuterated and fluorated materials /3/.

- /1/ G.D. Aumiller, E.A. Chandros, W.J. Tomlinson, and H.P. Weber, "Submicrometer resolution replication of relief patterns for integrated optics", J. of Applied Physics, vol. 45, 1974, pp. 4557-4562
- /2/ H. Hosokawa, N. Horie, and T. Yamashita, "Simultaneous fabrication of grating couplers and an optical waveguide by photopolymerization", IPR 90, Hilton Head (1990), paper MF6
- /3/ S. Imamura, R. Yoshimura, and T. Izawa, "Organic channel waveguides with low loss at $1.3 \mu\text{m}$ ", OFC 91, San Diego (1991), paper TuF6

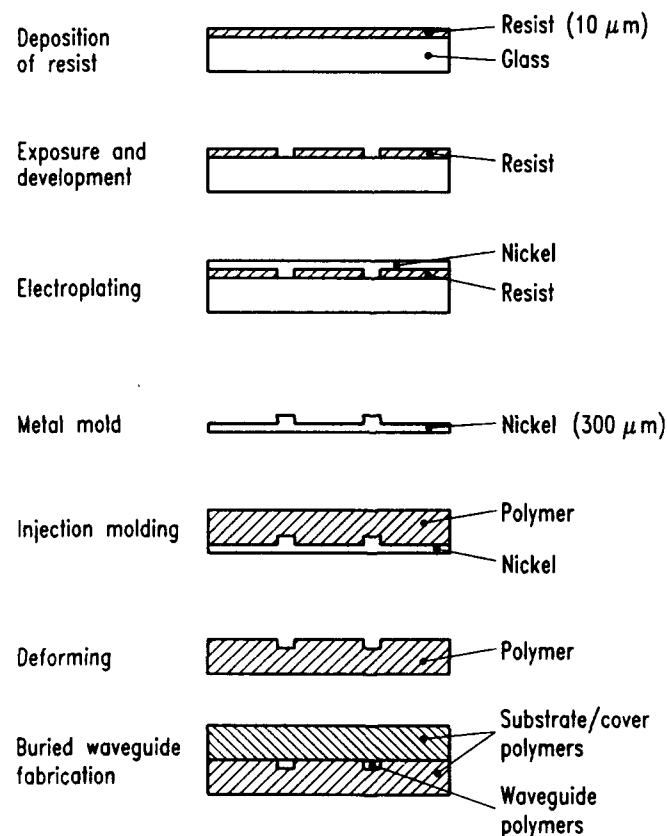


Fig. 1 Schematic illustration of the polymer waveguide fabrication process using injection molded waveguide substrates.

Electro-Optic Polyimide Thin Films for Integrated Photonic Interconnects on Silicon

J.F. Valley, J.W. Wu, S. Ermer, M. Stiller, D.L. Culbert, D.G. Girton,
A.J. Ticknor, T.E. Van Eck, E.S. Binkley, J.T. Kenney, G.F. Lipscomb, and R. Lytel
Lockheed Palo Alto Research Laboratory, O/9702, B/202
3251 Hanover Street, Palo Alto, CA 94304
(415) 354-5841

Using dielectric relaxation spectroscopy we have determined that commercially available polyimides exist which are highly suitable as hosts for nonlinear optical (NLO) molecules. In general, polyimides offer excellent thermal and mechanical properties as a host material but have, until now, presented some difficulties in the poling process.¹ We now process and pole polyimide thin films similarly to the techniques used in our successes with electro-optic waveguide devices made from methacrylate based material systems.² As seen in Fig. 1, the transition from glassy to rubbery states in the Hitachi LQ2200 optical quality polyimide (available for use in liquid crystal displays) occurs near 250 °C. We have found NLO molecules compatible with LQ2200 that shift the glass transition temperature, T_g , down (up) by plasticization (anti-plasticization) of the host correlating to the NLO molecules melting temperature being lower (higher) than the T_g of the pure host LQ2200. So far, the only NLO molecules which yield sufficiently strong poled response for the compact, complex integrated photonic interconnects we envision plasticize the host.

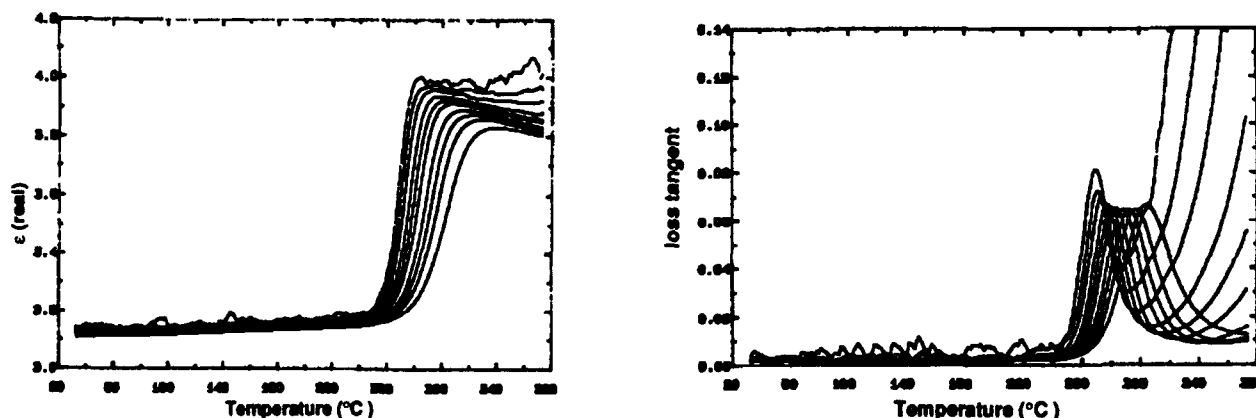


FIG. 1. The dielectric constant (a) and loss tangent (b) versus temperature for an LQ-2200 polyimide film cured at 370 °C for three hours prior to measurement. Ten frequencies make up the spectrum; from 100 Hz to 100 kHz in a 1-2-4 sequence. The thermoplastic alpha transition from glassy to rubbery states near 250 °C is apparent from the step increases in ϵ and the peaks in the loss tangent.

For the data we report here the NLO guest molecule is Disperse Red 1 (DR1).³ We selected DR1 as dopant for its availability, miscibility, large hyperpolarizability, nearly suitable thermal stability, and abundant published knowledge-base.⁴ The *in situ* measurement of poled EO response

for a DR1/2200 film as a function of temperature is shown in Fig. 2.⁵ This single layer film was prepared using an 11% solids by weight DR1 loading from a pre-mix in NMP (< 5% DR1) and poled at 190 °C with an applied field of 50 V/ μ m. The depoling knee-temperature of ~150 °C is significantly better than previously reported depoling temperatures for acrylate based polymer systems. Equally important for reliable EO devices is the flatness of the response for operational temperatures around room temperature. This is directly attributable to the superior properties of the dielectric response of the host polyimide, as seen by the curve flatness below 250 °C in Fig. 1 above.

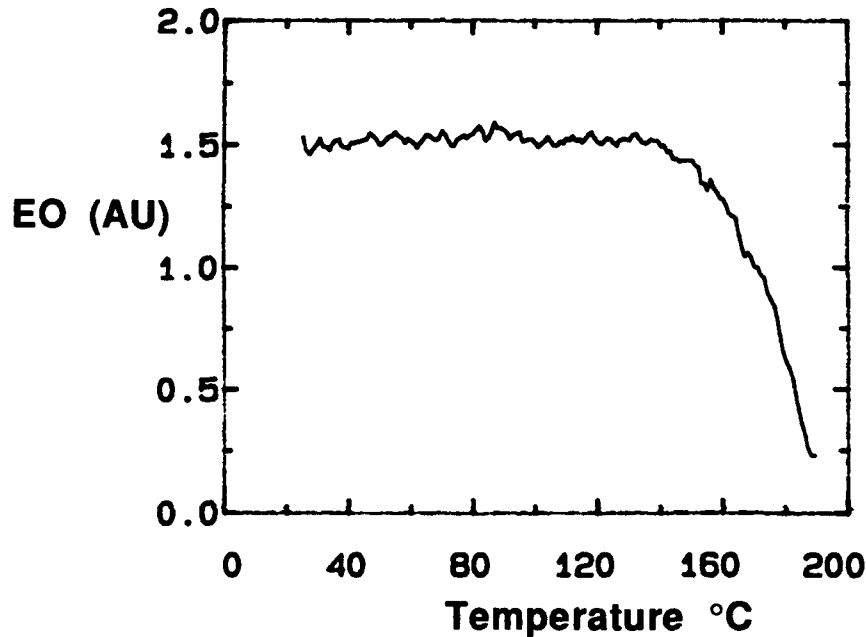


FIG. 2. Data taken of the electro-optic response r_{13} versus temperature for an 11% DR1 by weight version of DR1/2200. The temperature was ramped at 3 °C per minute and measurements taken every 20 seconds.

We are progressing on making and testing devices with modulating optical output by spinning three layer stacks with appropriate refractive indices.² Lateral definition of single-mode waveguides in DR1/2200 films using uv photobleaching of the DR1 through an etched metal mask has already been accomplished.

References

1. J.W. Wu, J.F. Valley, S. Ermer, E.S. Binkley, J.T. Kenney, G.F. Lipscomb, and R. Lytel, *Appl. Phys. Lett.* **58**, 225 (1991); J.W. Wu, E.S. Binkley, J.T. Kenney, R. Lytel, and A.F. Garito, *J. of Appl. Phys.* **69**, 7366 (1991).
2. J.I. Thackara, G.F. Lipscomb, M.A. Stiller, A.J. Ticknor, and R. Lytel, *Appl. Phys. Lett.* **52**, 1031 (1988). T.E. VanEck, A.J. Ticknor, R.S. Lytel, and G.F. Lipscomb, *Appl. Phys. Lett.* **58**, 1558 (1991); D.G. Girton, S. Kwiatkowski, G.F. Lipscomb, and R. Lytel, *Appl. Phys. Lett.* **58**, 1730 (1991).
3. J.F. Valley, J.W. Wu, S. Ermer, M. Stiller, E.S. Binkley, J.T. Kenney, G.F. Lipscomb, and R. Lytel, accepted *Appl. Phys. Lett.*, due Jan. 13, 1992.
4. K.D. Singer, J.E. Sohn, L.A. King, H.M. Gordon, H.E. Katz, and C.W. Dirk, *J. Opt. Soc. Am.* **B6**, 1339 (1989).
5. J.F. Valley, J.W. Wu, and C.L. Valencia, *Appl. Phys. Lett.* **57**, 1084 (1990).

WB4-1

Low-Loss PE:LiNbO₃ Waveguide Bends at $\lambda = 1.55 \text{ um}$

Indra Januar and Alan R. Mickelson
 University of Colorado
 Optoelectronic Computing Systems Center
 Boulder, CO 80309-0425
 Ph: (303) 492-2595

I. INTRODUCTION

Waveguide bends are essential elements in the design of integrated optical devices. Various bend configurations have been studied mostly for titanium-indiffused lithium niobate waveguides [1]-[4]. Among them, S-shaped bends as shown in figure (1a) have been widely used in integrated optical devices. The main goal of waveguide bend studies has been to achieve the minimum transition length that can be tolerated for acceptably low bend loss. Losses as low as 0.2 dB have been reported [4] in titanium-indiffused waveguides for a transition between offset parallel waveguides with a 0.1 mm lateral and 3.25 mm longitudinal separation. Here we report on very-low-loss PE:LiNbO₃ waveguide bend structures at $\lambda = 1.55 \text{ um}$.

II. EXPERIMENT

The waveguide bend structure used in this study is based on an S-curve made of two circular arcs with a constant radius of curvature R [2] specified by

$$R = \pm \frac{L^2}{4d} \left(1 + \frac{d^2}{L^2} \right) \quad (1)$$

where L is the transition length in the longitudinal direction and d is the lateral offset. A mask used to generate the curved transition was produced by MANN3600 system which wrote the curves as a succession of equal-length straight waveguide segments separated by 0.1° bends. On the mask, a straight waveguide was situated on the side of a set of curved waveguides with L varying from 1 to 4.5 mm for relative loss measurements. The waveguides were separated by 0.2 mm to prevent coupling between them. The lateral offset d was fixed at 0.1 mm.

The waveguides were fabricated on Z-cut Y propagating lithium niobate. Waveguide patterns were formed by immersing lithium niobate substrates in a melt of benzoic acid for the proton exchange process. The temperature of the melt was held constant at $175 \pm 0.5 \text{ }^\circ\text{C}$ for 90 minutes. After the proton exchange step, the substrate end faces were cut and polished to allow butt coupling.

All the substrates were then annealed in an oven at $360 \text{ }^\circ\text{C}$ in order to reduce the hydrogen ion concentration in the crystal, thereby restoring the electro-optical coefficients. Thermal annealing of substrates causes the step index profile of the proton exchange step to become a graded index profile. This additional annealing step has an added advantage in that the waveguide transverse nearfield distributions can be tailored to match those of single mode polarization maintaining fiber, thereby minimizing input and output coupling loss.

The waveguides supported only a single TM mode. Optical radiation of $\lambda = 1.55 \text{ um}$ wavelength from a color center laser was

launched into a single mode polarization maintaining fiber and then butt coupled to the waveguides. A Ge detector with a lock-in amplifier was used to monitor the output of the waveguides. Measurements of the waveguide output intensity were normalized to that of the fiber. The bend losses as a function of transition length are shown in figure (1b).

As can be seen from figure (1b), the bend losses were reduced as we annealed the substrates. This indicates that waveguides become more confined and at the same time, we also minimized the input and output coupling loss. The minimum transition length required for the PE:LiNbO₃ waveguide bends is 2.0 mm in order to have bend losses as low as 0.2 dB.

III. SUMMARY

We have presented the measurements of the bending loss for PE:LiNbO₃ waveguides at $\lambda = 1.55 \mu\text{m}$. The bend loss as low as 0.2 dB was achieved for 2.0 mm longitudinal transition length and 0.1 mm lateral offset. The losses for the waveguides using thermal annealing step show that the mode confinement is a critical factor determining bending loss.

REFERENCES

1. M.J. Taylor and E.R. Schumacher, "Measured losses in LiNbO₃ waveguide bends," *Appl. Opt.*, vol. 19, pp. 3048-3052, 1980.
2. L.D. Hutcheson, I.A. White and J.J. Burke, "Comparison of bending losses in integrated optical circuits," *Opt. Lett.*, vol. 5, pp. 276-278, 1980.
3. L.M. Johnson and F.J. Leonberger, "Low-loss LiNbO₃ waveguide bends with coherent coupling," *Opt. Lett.*, vol. 8, pp. 111-113, 1983.
4. W.J. Minford, S.K. Korotky and R.C. Alferness, "Low-loss Ti:LiNbO₃ waveguide bends at $\lambda = 1.3 \mu\text{m}$," *IEEE J. Quantum Electron.*, vol. QE-18, pp. 1802-1806, 1982.

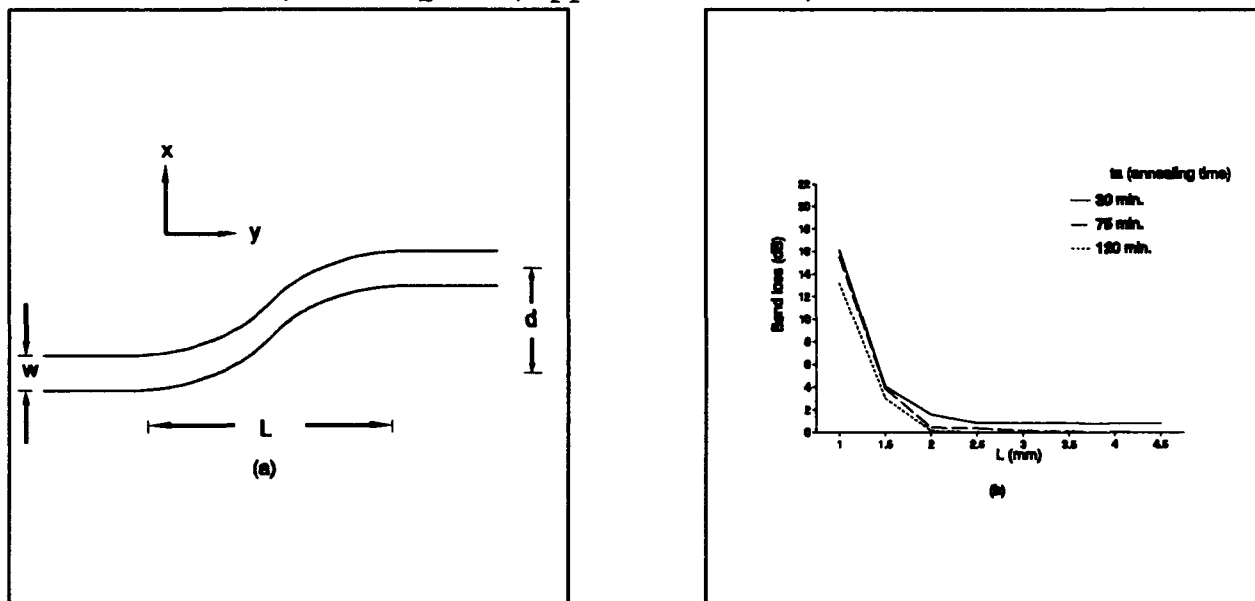


Figure 1: (a) The schematic of an S-shaped waveguide bend, (b) The measured bend losses as a function of transition length L at $\lambda = 1.55 \mu\text{m}$ for various annealing time.

Effects of Benzoic Acid Dilution on Proton-Exchanged LiTaO₃ Optical Waveguides

Toshiya YUHARA and Kunio TADA

*Department of Electronic Engineering, University of Tokyo,
Hongo 7-3-1, Bunkyo-ku, Tokyo, 113, Japan
+81-3-3812-2111 ext. 6677*

We have previously reported for the first time an increase of the surface extraordinary refractive index after annealing in H⁺:LiTaO₃ optical waveguides fabricated in benzoic acid or pyrophosphoric acid [1]. This anomalous index increase is thought to be caused by a movement of protons in a unit cell [2, 3]. Recently, we have also reported that the higher surface index was observed for waveguides proton-exchanged in diluted benzoic acid when compared with those fabricated using neat benzoic acid [3]. In this paper, we investigate the effects of melt dilution on the properties of H⁺:LiTaO₃ waveguides by examining the effective index, measuring the electrooptic coefficient r_{33}^T , and performing XRC analysis and IR absorption spectroscopy.

Proton-exchange was carried out on SAW-grade *z*-cut LiTaO₃ wafers using benzoic acid diluted with lithium benzoate at 250°C, and TM multi-mode planar waveguides were successfully fabricated. From the effective indices measured with a rutile prism coupler, the index profiles were calculated with the inverse WKB method [4] and step-like profiles were obtained. Although the surface index $\Delta n_e(0)$ of H⁺:LiNbO₃ is reported to decrease with dilution of benzoic acid [5], comparing the index profiles shown in Fig. 1, we note that $\Delta n_e(0)$ of H⁺:LiTaO₃ increased as a result of dilution up to 2 mole %. On the contrary, further dilution resulted in a decrease of $\Delta n_e(0)$.

The electrooptic coefficient r_{33}^T of the proton-exchanged region was measured at the wavelength of 632.8nm in a planar waveguide inserted into one arm of a Mach-Zehnder interferometer [6]. The r_{33}^T coefficient was found to decrease to 2.2pm/V after proton exchange in neat benzoic acid, but preserved to half of the bulk value of 30.5pm/V when diluted with 3 mole % lithium benzoate as shown in Fig. 2.

The double crystal X-ray rocking curve measurement was employed for the precise determination of lattice constant changes along the *c*-axis in the proton-exchanged layers of *z*-cut LiTaO₃ wafers [1, 3]. Fig. 3 shows $\Delta c/c$ obtained from the measured XRC data as a function of mole fraction of lithium benzoate. As $\Delta c/c$ decreases monotonously with dilution, it is inferred that the lattice constant change does not primarily determine the index change.

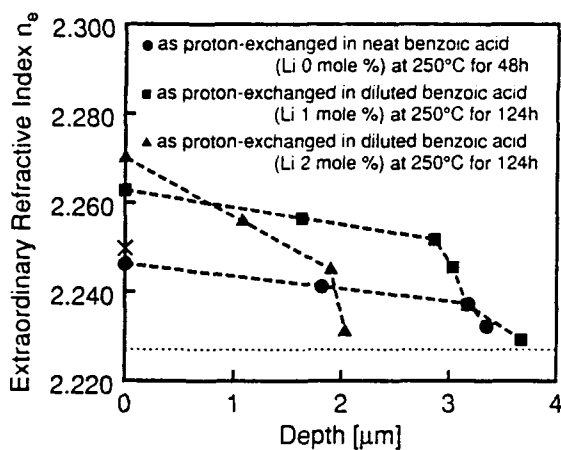
The IR absorption spectra corresponding to the OH stretching modes in proton-exchanged layers were measured using the FT-IR spectrometer. The spectra for samples proton-exchanged in benzoic acid diluted with 2 mole % lithium benzoate, shown in Fig. 4, exhibited almost no difference before and after annealing. In the spectrum for the *x*-cut sample as proton-exchanged in neat benzoic acid, not shown here, two peaks were observed: one was a sharp peak at 3495cm⁻¹ that was significant under the *E_{LZ}* configuration and the other was a broad peak at 3235cm⁻¹ that was observed not to be polarization-dependent [2, 7]. After annealing, the broad peak at 3235cm⁻¹ was quenched, whereas the sharp peak at 3495cm⁻¹ became remarkably stronger with an increase of annealing time [2, 8], and then saturated. This evolution of the spectrum indicates that a larger number of protons lie in the oxygen planes between TaO₆ octahedrons after annealing. In the case of dilution of benzoic acid, since proton exchange proceeds moderately, it is considered that a larger portion of the protons would be in the oxygen planes of the as proton-exchanged sample than in the case of no dilution.

The difference of proton site should affect the electronic polarization and would result in index increase. The r_{33}^T coefficient is considered to be preserved mainly because of a low proton exchange ratio *x* in the form of Li_{1-x}H_xTaO₃ as a result of dilution.

References

- [1] Y. S. Li, T. Yuhara, K. Tada and Y. Sakaguchi: Technical Digest of 1st Topical Meeting on Integrated Photonics Research, WE3 (1990).

- [2] T. Yuhara, K. Tada, Y. S. Li: Technical Digest of 2nd Topical Meeting on Integrated Photonics Research, WC4 (1991).
- [3] T. Yuhara, K. Tada, and Y. S. Li: Technical Digest of 3rd Microoptics Conference, D3 (1991).
- [4] J. M. White and P. F. Heidrich: Appl. Opt. 15, 151 (1976).
- [5] M. De Micheli, J. Botineau, S. Neveu, P. Sibillot, D. B. Ostrowsky and M. Papuchon: Opt. Lett. 8, 114 (1983).
- [6] Y. Kondo, L. Hu, and Y. Fujii: Trans. of the Institute of Electronics, Information and Communication Engineers of Japan E71, 1122 (1988).
- [7] I. Savatinova, M. Kunevea, Z. Levi, V. Atuchin, K. Ziling, and M. Armenise: SPIE Proceedings Vol. 1374, 37 (1990).
- [8] V. A. Ganshin, Yu. N. Korkishko, T. V. Morozova, and V. V. Saraikin: Phys. Status Solidi A 114, 457 (1989).



(x surface index of single mode waveguide (Li 3 mole %) measured with two wavelengths)

Fig. 1. Refractive index profiles of waveguides proton-exchanged with and without dilution ($\lambda=488\text{nm}$).

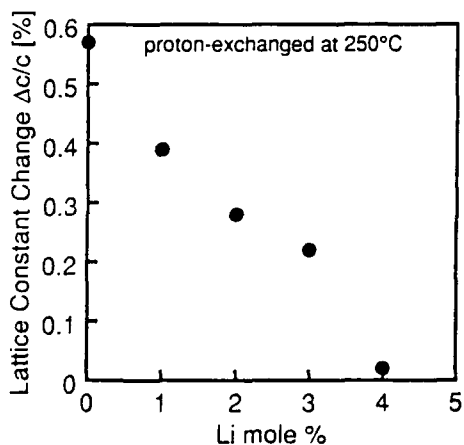


Fig. 3. Lattice constant change $\Delta c/c$ versus lithium concentration.

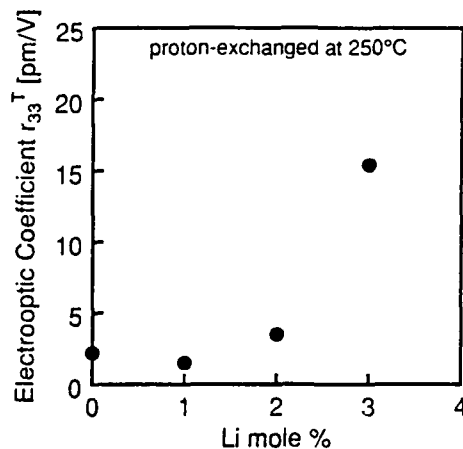


Fig. 2. Measured r_{33}^T coefficient at 632.8nm as a function of lithium concentration.

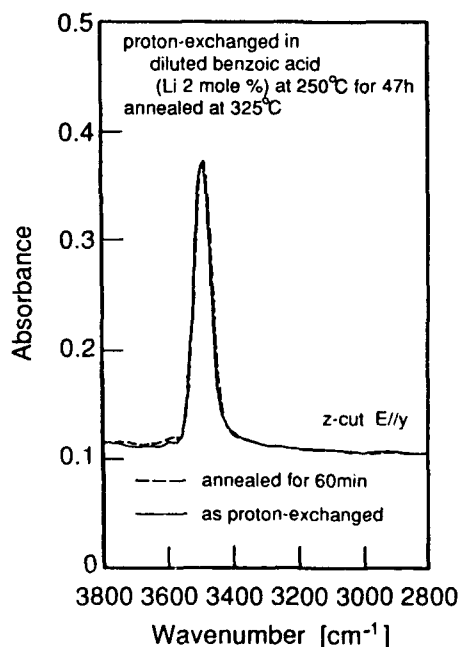


Fig. 4. IR absorption spectra for the sample proton-exchanged in diluted benzoic acid before and after annealing.

WB6-1

Characterization of Photorefractive Effect in Annealed Proton-Exchanged (APE) LiNbO₃ Waveguides in the Visible Region

Xiaofan CAO, Takumi FUJIWARA*, Ramu V. RAMASWAMY,
and Ramakant SRIVASTAVA

Photonics Research Laboratory
Department of Electrical Engineering
University of Florida
117 Larsen Hall, Gainesville, FL 32611
phone:(904)392-1049, fax:(904)392-4963

*permanent address : Electronics Materials Laboratory,
Sumitomo Metal Mining Co., Ltd., Tokyo, Japan

Annealed proton exchanged (APE) LiNbO₃ waveguides with recovered electro-optic/nonlinear coefficients and low propagation loss are widely used in integrated optics. Although it is known that the PE LiNbO₃ waveguides have higher resistance to photorefractive damage than Ti-diffused LiNbO₃ waveguides¹⁾, a feature which is quite attractive for nonlinear guided wave applications such as efficient diode laser doubling²⁾, a quantitative characterization of photorefractive effect in APE LiNbO₃ waveguides in the visible region has not yet been reported.

In this paper, we present a comparative study of the photorefractive effect in both PE and APE LiNbO₃ waveguides at several wavelengths (λ_{ir}) in the visible. Using a technique similar to that used for Ti-diffused waveguides³⁾, the temporal behavior of the index change caused by irradiation was measured by monitoring the phase change of an infrared probe beam at a modified Mach-Zehnder interferometer output. Fig.1 shows the time dependence of the photo-induced index change as a function of the irradiation time for $\lambda_{ir} = 488$ nm. The index change can easily be fitted to the equation,

$$\Delta n(t) = \Delta n_s (1 - e^{-t/\tau}), \quad (1)$$

where Δn_s is the saturated index change and τ is the buildup time constant. Hence, the saturated index change, build-up time constant, and photorefractive sensitivity (defined as $S = \Delta n_s / I_{ir} \tau$, I_{ir} = irradiation intensity) were determined and compared. The results for PE, APE and Ti-diffused waveguides are summarized in Table. 1 at several irradiation wavelengths.

A comparison of Δn_s and S shows that the photorefractive sensitivity of the APE waveguide is about 30% higher than that of the PE waveguide, and at least three orders of magnitude smaller than that of Ti-diffused guides. From a comparison of the time constants, it can be inferred that the conductivity of the PE LiNbO₃ waveguides is reduced slightly after the annealing.

REFERENCES

- 1) J. L. Jackel, A. M. Glass, G. E. Peterson, C. E. Rice, D. H. Olson, and J. J. Veselka, *J. Appl. Phys* **55**, 269 (1984)
- 2) E. J. Lim, M. M. Fejer, R. L. Byer, and W. J. Kozlovsky, *Electron. Lett.* **25**, 731 (1989)
- 3) T. Fujiwara, S. Sato, and H. Mori, *Appl. Phys. Lett.* **54**, 975 (1989)

Table 1. Comparison of the photorefractive effect between PE, APE, and Ti: LiNbO₃ waveguides

	λ_{ir} (nm)	I_{ir} (W/cm ²)	Δn_s (x10 ⁻⁶)	τ (min)	S (x10 ⁻¹⁰ cm ² /J)
PE guide	488	12.1	3.0	3.1	13.3
APE guide	488	3.6	3.0	13	10.7
	488	10.5	5.2	4.3	19.2
	532	1.1	4.0	82	7.6
	532	1.8	5.8	69	7.8
	633	7.1	-	-	-
Ti-diffused guide ³⁾	633	0.17	30.6	3.7	~8100
	633	2.6	223	1.6	~8900

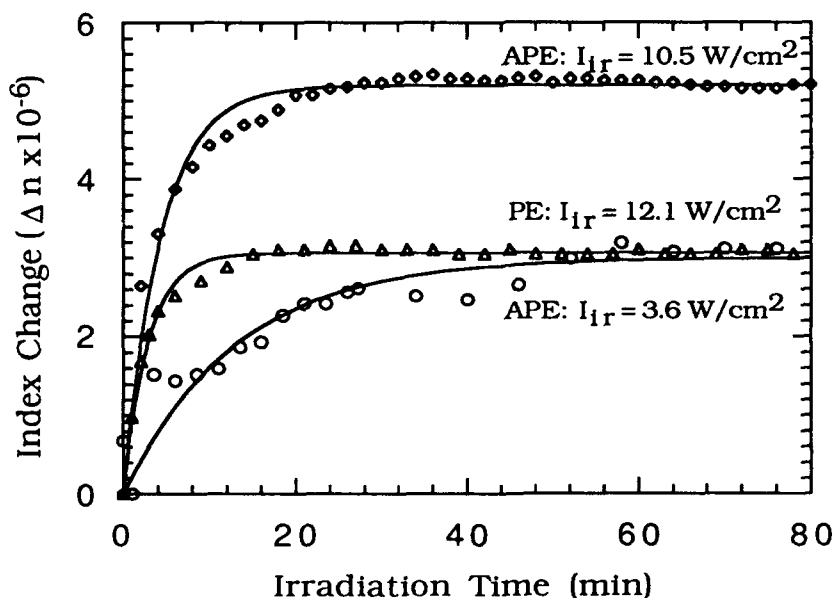


Fig. 1 Refractive index change as a function irradiation time ($\lambda_{ir} = 488 \text{ nm}$). PE waveguide was exchanged for 88 min at 220 °C in pure benzoic acid, APE guide was exchanged for 20 min at 220 °C and annealed at 350 °C for 6 hr. Solid curves represent fit to Eq.(1).

WB7-1

A Method for the Local Incorporation of Er^{3+} into LiNbO_3 Guided Wave Optic Devices by Ti Co-diffusion

D. M. Gill and L. McCaughan

Materials Science Program and Department of Electrical and Computer Engineering
University of Wisconsin-Madison, WI USA 53706 (608) 262-0311

Optical amplification has been demonstrated in waveguides fabricated in Nd-doped LiNbO_3 grown from a melt¹ and in planar diffused $\text{Er}:\text{LiNbO}_3$.² Such substrates are, however, not compatible with guided wave integrated optics since absorption will occur in every section of the waveguide which is not optically pumped to transparency. Lateral confinement of the gain medium is also necessary to avoid absorption of the evanescent field. We report a method for local incorporation of Er^{3+} which significantly enhances the diffusivity of the rare earth ion and is compatible with standard $\text{Ti}:\text{LiNbO}_3$ photolithographic processing.

Channel waveguides were photolithographically defined on z-cut LiNbO_3 . Er and Ti/Er thin films were deposited by ion beam sputtering onto a photoresist-patterned substrate. Er features could not be produced with this (lift off) technique due to its poor sticking coefficient. However, the films were easily processed if the Er was over-coated with Ti. Diffusion profiles were studied by electron microprobe scans of angle milled samples (Fig.1). Without Ti, Er is observed to diffuse to a depth of $D \sim 1 \mu\text{m}$ (Fig. 2, curve a) after a 20 h diffusion. With an 80 nm Ti overcoat, the effective diffusivity, $\mathcal{D} = D^2/4t$, is more than doubled (compare curves b and c). A 20 h co-diffusion of Er with 200 nm Ti produced a $4 \mu\text{m}$ e^{-1} diffusion depth (curve d), corresponding to an enhancement in Er diffusivity in excess of an order of magnitude.

The Er^{3+} concentration profile of, what we believe to be the first demonstration of a locally doped waveguide, is shown in Fig. 3. The e^{-1} concentration of Er is $\sim 2.7 \times 10^{19} \text{ cm}^{-3}$ at a depth of $\sim 3 \mu\text{m}$ with a maximum measurable ($\sim 5 \times 10^{18} \text{ cm}^{-3}$) penetration of $> 4.5 \mu\text{m}$. The e^{-1} diffusion width is $\sim 6 \mu\text{m}$. By comparison, the e^{-1} width of the Ti diffused waveguide is $\sim 18 \mu\text{m}$ (dashed line). Fluorescence of the $^4I_{13/2} \rightarrow ^4I_{15/2}$ transition from the waveguide shows a strong peak at 1.53 μm , with an ~ 7 ms lifetime and 3.3 nm width. Results from bulk doped 0.6 mol % single crystal $\text{Er}:\text{LiNbO}_3$ are nearly identical. High resolution fluorescence scans confirm that the Er in the codiffused sample is in the LiNbO_3 phase (Fig. 4). The observed upconverted fluorescence ($\lambda_{\text{fluor}} \sim 550 \text{ nm}$, $\lambda_{\text{pump}} \sim 656.5 \text{ nm}$) is probably due to efficient energy transfer between two excited Er^{3+} ions within the LiNbO_3 phase, as was shown for Er^{3+} doped fluorite.³

References

- ¹E. Lallier, J.P. Pocholle, M. Papuchon, M. de Micheli, M.J. Li, Quing He, D.B. Ostrowsky, C. Grezes-Besset, and E. Pelletier, *J. Quantum Electron.*, **27**, 618 (1991).
- ²R. Brinkmann, W. Sohler, and H. Suche, *Electronics Lett.*, **27**, 416 (1991).
- ³D.R. Tallant, M.P. Miller, and J.C. Wright, *The Journal of Chemical Physics*, **65**, 2, (1976).

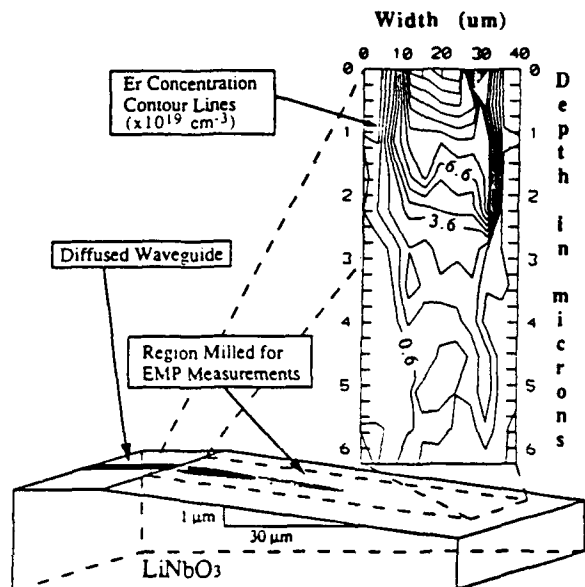


Fig. 1 Strip or planar Er or Er+Ti films are diffused into LiNbO₃ and mechanically milled at an angle of about 2 degrees (rise-to-run ~1:30) for electron microprobe measurements. Inset: Er concentration profiles ($\times 10^{19} \text{ cm}^{-3}$) from a 10 μm wide Er(12 nm)/Ti(80 nm) bilayer, diffused 40 h.

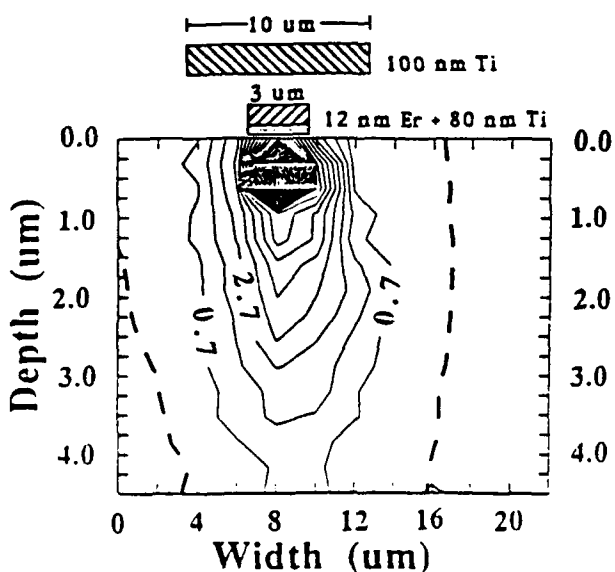


Fig. 3 Er concentration ($\times 10^{19} \text{ cm}^{-3}$) profile of a locally Er doped Ti:LiNbO₃ channel waveguide: 3 μm strip of Er (12 nm)/Ti (80 nm) diffused 40 h, plus 10 $\mu\text{m} \times 100 \text{ nm}$ Ti diffused (10 h). The dashed line shows the e^{-1} Ti concentration contour.

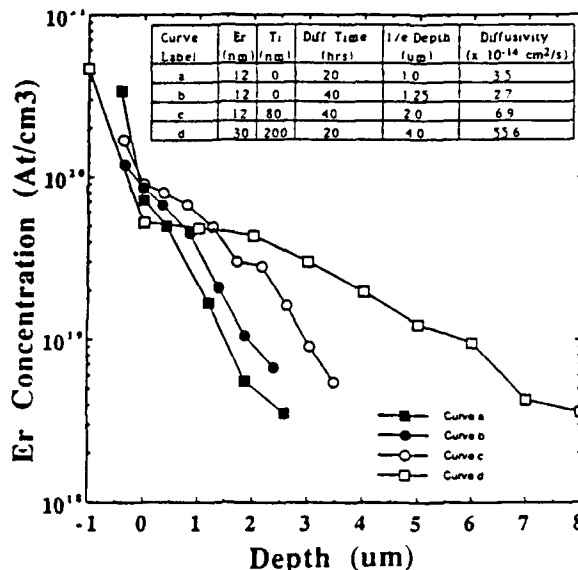


Fig. 2 One dimensional depth profiles from four Er diffusion experiments produced by averaging adjacent scans.

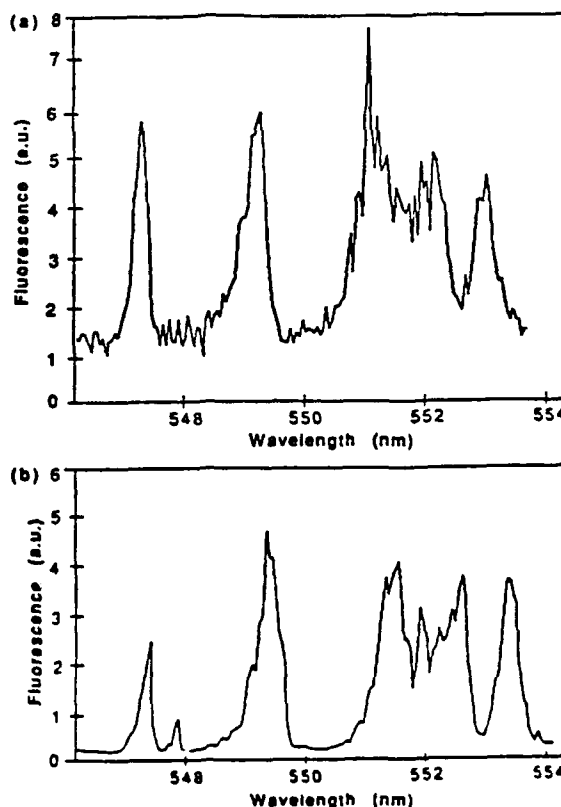


Fig. 4 Fluorescence spectra ($\lambda_{\text{excit}} = 453.4 \text{ nm}$) of the $^4\text{S}_{3/2} \rightarrow ^4\text{I}_{15/2}$ transition at 10 K in (a) co-diffused Er:Ti:LiNbO₃ and (b) bulk doped (0.6 mol %) Er:LiNbO₃.

WB8-1

Vertical integration of high-silica channel waveguides on Si

G. Barbarossa and P.J.R. Laybourn

University of Glasgow, Department of Electronics and Electrical Engineering
Glasgow, G12 8QQ, U.K.; Phone: +44 41 339 8855 Facsimile: +44 41 330 4907

The density of optical functions available on the same substrate and the complexity of the integrated optical circuits conceivable would benefit from the extension of the optical interaction to a third dimension. Recently, vertical integration of Si planar waveguides on Si has been reported¹. However, no experimental evidence of vertical integration of channel waveguides has been reported in the literature so far, to our knowledge.

In this work a multi-step fabrication process has been developed, which is based on a combination of flame hydrolysis deposition (FHD)², photolithographic patterning and reactive ion etching (RIE), making feasible the vertical integration of high-silica low-loss channel waveguides on the same Si substrate. Fig.1 shows the steps of the fabrication process. The fabrication parameters relative to each FHD step are listed in the table. The Si substrate used had a 10 μm thick, thermally grown, SiO₂ buffer layer to prevent coupling of the guided light from the first core into the highly absorbing Si. A first core layer was fabricated by depositing and sintering low density SiO₂-P₂O₅-GeO₂ glass soot synthesized by flame hydrolysis of SiCl₄-PCl₃-GeCl₄ vapours³ (a). Patterning of the first core layer was accomplished with a photolithographic process followed by RIE, where CHF₃ was used as etchant gas (b). A first cladding layer, thick enough to achieve perfect planarization (10 μm), was subsequently deposited by synthesizing low sintering point, soft SiO₂-P₂O₅ glass⁴ (c). The layer could be consolidated at 245°C below the sintering temperature of the first core glass, in order not to affect the guiding structure previously etched. At this stage, if coupling between the two levels of integration is required, the cladding thickness can be easily reduced by planar polishing or etching to the desired value to obtain effective optical coupling (d). In our case, the vertical separation between the guides was left at 6 μm . A second P₂O₅-GeO₂-doped silica core layer, richer in phosphorous but leaner in germanium than the first core, was afterwards deposited on the first cladding layer, which acted as a new substrate (e). The second core glass was sintered at higher temperature than the cladding glass, but still 120°C lower than the sintering temperature of the first core. Finally, after RIE of the second core structure (f), a second P₂O₅-doped silica cladding layer was deposited, which had a similar composition to the first one (g).

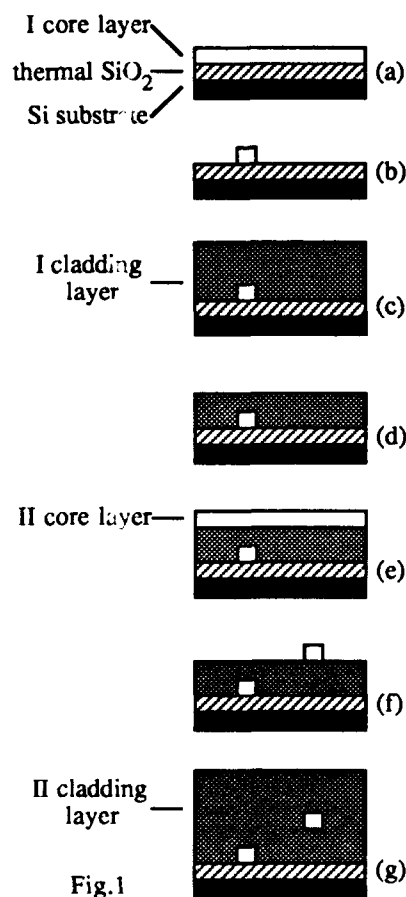
The refractive index step relative to the cladding was 0.6 % for both core glasses. The cross section of the integrated waveguides was 4x4 μm , achieving single mode operation at 1.55 μm . An optical microscope photograph in transmission relative to the cross section of the vertically integrated waveguides is shown in Fig.2. The difference in refractive index between core and cladding, as well as the preservation of the geometry of the first core structure after the subsequent heating treatments, are clearly visible. The two arrays of waveguides were deliberately misaligned to demonstrate the feasibility of a vertical integration structure which can not be obtained via a single deep etching of stacked planar guides. This means that different patterning can be etched onto the two levels. The heat treatment necessary to

consolidate subsequently deposited layers smoothed the waveguide sidewall roughness, caused by the dry etching, reducing the scattering losses and resulting in much lower propagation loss. The loss was estimated to be 0.08 dB/cm for both levels of waveguides.

This result opens up a wide range of interesting applications, which could possibly see the extension of the optical guided-wave interaction to three dimensions, and would certainly increase the density of guided-wave optical functions integrable on a single substrate.

References

- 1 Soref, R.A., Cortesi, E., Namavar, F. and Friedman, L., "Vertically integrated silicon-on-insulator waveguides," *IEEE Phot. Tech. Lett.*, 1991, 3, (1), 22-24
- 2 Kawachi, M., Yasu, M. and Edahiro, T., "Fabrication of SiO₂-TiO₂ glass planar waveguides by flame hydrolysis deposition," *Electron. Lett.*, 1983, 19, (15), 583-84
- 3 Kashyap, R., Maxwell, G.D. and Barbarossa, G., "Second harmonic generation in GeO₂ doped silica ridge waveguides", 1st Int. Ceramic Sc. and Tech. Congr., Anaheim, CA, 1989
- 4 Barbarossa, G. and Laybourn, P.J.R., "Fabrication and characterisation of SiO₂-P₂O₅ integrated optical waveguides by flame hydrolysis on Si substrate", *Ceram. Trans.*, 1991, 19, 313-19



Layer type	I core	II clad	III core	IV clad
Thickness [μm]	4	10	4	10
Sintering temperature [°C]	1385	1140	1265	1140
Sintering time [minutes]	120	30	10	30
PCl ₃ flow rate [cm ³ /min]	16	120	60	120
GeCl ₄ flow rate [cm ³ /min]	104	-	60	-

Deposition speeds - torch: 25 [mm/min], turntable: 25 [rev/min]

Flame flow rates H₂:4 [l/min], O₂:6[l/min] ; SiCl₄ flow rate: 120 [cm³/min]

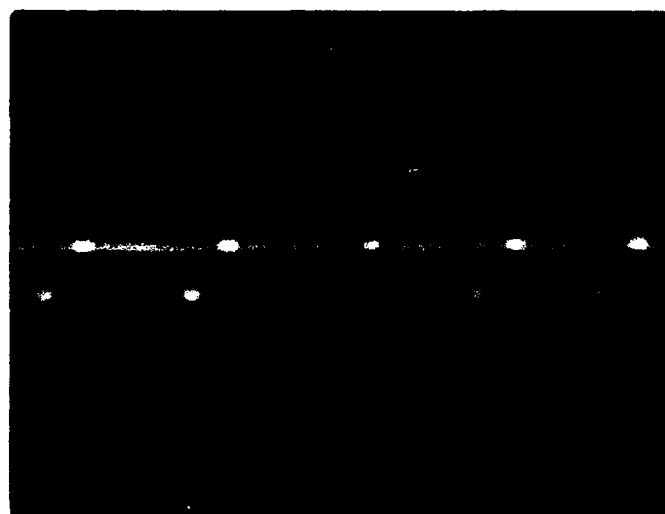


Fig. 2

Wednesday, April 15, 1992

Lasers:1

WC 8:30 am-10:30 am
Pelican Room

Willie Wing Ng, *Presider*
Hughes Research Laboratories

WC1-1

Surface Emitting Lasers for Integration**K. Iga, Tokyo Institute of Technology****4259 Nagatsuta, Midoriku, Yokohama, Japan 227**

A new field of optoelectronics including large capacity parallel lightwave communications, multi-access optical disks, optical computing, optical interconnects and so on, is accelerating the importance of surface emitting (SE) lasers¹. The research activity is now forwarded to monolithic integration of SE laser based optical circuits by taking the advantage of its small cavity dimension.

The importance of 1.3 or 1.55 μm devices is currently increasing, since parallel lightwave systems and optical interconnects are actually considered. However, the GaInAsP/InP system has some substantial difficulties for making SE lasers due to the Auger recombination, intra-valence band absorption, the index difference between GaInAsP and InP is relatively small, and so on. Pulsed operation has been obtained at near room temperature², and room temperature³. A polyimide buried structure device is fabricated by much simpler processes and pulsed operation at 66 °C has been obtained⁴. But, it is still difficult to operate CW at room temperature in this system.

A micro-cavity GaAlAs/GaAs SE laser of 5 μm long and 6 μm in diameter⁵ and room temperature CW operation⁷ was first realized among other systems. At present, devices exhibiting $I_{\text{th}} \cong 2 \sim 15$ mA and a few mW of output power are available in the laboratory level. A very high coupling efficiency to a single mode fiber ($\cong 90\%$) was reported⁷. The spectral linewidth of 50 MHz is obtained with an output power of 1.4 mW.

The GaInAs/GaAs strained pseudomorphic system grown on a GaAs substrate has been developed as a high power laser emitting $0.98 \mu\text{m}$. This material exhibits a high laser gain and has been introduced into surface emitting lasers together with using GaAlAs/AlAs multi-layer reflectors. A low threshold ($\cong 1\text{mA}$) has been demonstrated⁸. The single or multi-quantum wells are employed in the active region. The use of thin active layers which are much thinner than the wavelength can enhance the optical confinement factor by 2, if it is placed at the loops of standing waves. The minimum threshold reported so far is 0.7 mA using this system⁹. The minimum J_{th} is $8 \mu\text{A}/\mu\text{m}^2$, which is approaching to the similar level of stripe lasers.

By overcoming those technical problems, such as making tiny structures, ohmic resistance of electrodes and improving heat sinking, we believe that we can obtain a $1 \mu\text{A}$ device¹¹.

A lot of efforts toward improving the characteristics of surface emitting lasers have been made, including surface passivation in the regrowth process for buried heterostructure, micro-fabrication, and fine epitaxies.

Spontaneous emission control is considered by taking the advantage of micro-cavity structures. The spontaneous emission factor has been estimated on the basis of 3-D mode density analysis¹². The possibility of no distinct threshold devices is suggested. Another interesting topic for micro-cavity SE lasers is photon recycling. By covering the side-bounding surfaces of the cavity, some amount of spontaneously wasted photons can be recycled. It has been demonstrated that the device appears to have no distinct threshold¹³.

Densely packed arrays have also been demonstrated for the purpose of making high power lasers and coherent arrays. The coherent

WC1-3

coupling of these arrayed lasers has been tried by using a Talbot cavity¹⁴ and diffraction coupling. It is pointed out that 2-D arrays are more suitable to make a coherent array than a linear configuration, since we can take the advantage of 2-D symmetry¹⁵.

A stacked planar optics¹⁶ consists of planar microlens arrays¹⁷ and the stack of optical components is another important issue. For this purpose, in addition to surface emitting lasers, surface emitting laser-type optical devices such as optical switches, frequency tuners^{18,19}, optical filters²⁰, using ultra-minute structures such as quantum wells and super-lattices have become very active. Other wide variety of functions, such as polarization control, amplification, detecting, and so on can be integrated along with surface emitting lasers by stacking.

Some important technologies for integration related to surface emitting lasers are progressing, i.e., photonic integration, array formation, and OEIC. Moreover, a 2-D parallel optical logic system¹³ can deal with a large amount of image information with high speed. Vertical optical interconnection of LSI chips and circuit boards may be another interesting point. Further development of the SE laser may open up various applications and accelerate the integration of optical devices and optical circuits with freedom of 2-D arrays.

References

1. K. Iga, F. Koyama, and S. Kinoshita, IEEE J. Quant. Electron., QE-24, 9, p. 1845, Sept. 1988.
2. M. Oshikiri, H. Kawasaki, F. Koyama and K. Iga, Photo. Tech. Lett., 1, 1, p.11, Jan., 1989.
3. Y. Imajo, A. Kasukawa, S. Kashiwa and H. Okamoto, Jpn. J. appl. Phys., 29, 7, p.L1130, July, 1990.
4. H. Wada, D. I. Babic, D. L. Crawford, J.J. Dudley, J. E. Bowers, E. L. Hu, and J. L. Merz, Device Research Conference, Post Deadline Paper, III A-8, June, 1991.

5. K. Iga, S. Kinoshita and F. Koyama, *Electron. Lett.*, 23, 3, p.134, Jan. 1987.
6. F. Koyama, S. Kinoshita, and K. Iga, *Appl. Phys. Lett.*, 55, 3, p. 221, July 1989.
7. K. Tai, G. Hasnain, J. D. Wynn, R. J. Fischer Y. H. Wang, B. Weir, J. Gamelin, A. Y. Cho, *Electronics Letters*, 26, 19, p. 1628, Sept.1990.
8. J. L. Jewell, A. Scherer, S. L. McCall, Y. H. Lee, S. Walker, J. J. P. Harbison, L. T. Florez, *Electron. Lett.*, 25, 17, p.1123, Aug. 1989.
9. R. S. Geels and L. A. Coldren, 48th Device Research Conference, VIIIA-1, June 1990.
10. M. Oshikiri, F. Koyama, and K. Iga, *Electron. Lett.*, 27, 22, p.2038, Oct. 24, 1991.
11. T. Tamanuki, F. Koyama and K. Iga, *J. J. of Appl. Phys.*, 30, 4A, p. L593, April 1991.
12. T. Baba, T. Hamano, F. Koyama and K. Iga, *IEEE J. Quant. Electron.*, 27, 6, p. 1991.
13. T. Numai, M. Sugimoto, I. Ogura, H. Kosaka and K. Kasahara, *J. Appl. Phys.*, 30, 4A, p. L602, April 1991.
14. E. Ho, F. Koyama, and K. Iga, *MOC/GRIN'89*, J2, p. 242, Oct. 1989.
15. M. Orenstein, E. Kapon, N. G. Stoffel, J. P. Harbison, L. T. Florez, and J. Wullert, *Appl. Phys Lett.*, 58, 8, p. 804, Feb. 1991.
16. K. Iga, M. Oikawa, S. Misawa, J. Banno, and Y. Kokubun, *Appl. Opt.*, 21, 19, p. 3456, Oct. 1982.
17. S. Misawa, M. Oikawa and K. Iga, *Appl. Opt.*, vol. 23, No. 11, pp. 1784-1786, June, 1984.
18. M. W. Maeda, C. J. Chang-Hasnain, C. Lin, J. S. Patel, H. A. Johnson, and J. A. Walker, *IEEE Photonics Tech. Letts.*, 3, 3, p. 268, March 1991
19. N. Yokouchi, F. Koyama and K. Iga, *The Trans. of IEICE*, E73, 9, p.1473, Sept. 1990.
20. F. Koyama, S. Kubota, and K. Iga, *IEICE Trans.*, E74, 6, p.1689, June, 1991.

WC2-1

**3.0-mm diameter InGaAsP multiple quantum well ring laser
actively mode-locked at 9.0 GHz**

G. Raybon, P. B. Hansen, M.-D. Chien, U. Koren, B. I. Miller, M. G. Young,
J.-M. Verdiell and C. A. Burrus

AT&T Bell Laboratories
Crawford Hill Laboratory
Holmdel, NJ 07733
(908) 888-7221

Semiconductor ring lasers are attractive, by the nature of their geometry, for short pulse generation through active mode-locking and colliding pulse mode-locking (CPM) [1]. However, to date, only CW operation of small diameter ring lasers in GaAs has been demonstrated [2,3]. Recent advances in InP fabrication technology have enabled the realization of complex photonic integrated circuits using multiple quantum well (MQW) active regions and low-loss passive waveguides [4]. Using these techniques, we have fabricated an 3.0-mm diameter InGaAsP MQW ring laser which is actively mode-locked at 9.0 GHz producing nearly transform limited 27 ps optical pulses.

The ring laser, shown in Fig. 1, consists of a 3-mm diameter passive waveguide ring, two multiple quantum well (MQW) gain regions, and a tangential output waveguide with two output ports. MOVPE based growth and processing techniques are used to fabricate the laser [5]. The passive waveguide is a 3- μm wide buried rib waveguide structure, consisting of 1.3- μm quaternary material that is nearly transparent to 1.5- μm radiation. As shown in the insert of Fig. 1, the rib thickness is determined by the stop etch layer and is approximately 500 Å. Fe-doped semi-insulating InP is regrown over the waveguide to act as a cladding layer and to provide low capacitance blocking for the active regions. The two 500- μm long MQW active regions consist of 6 wells that are grown above the passive waveguide region. High quality transitions are achieved between the active and passive regions with coupling efficiency of approximately 90%. Guided optical output is obtained through evanescent coupling to the linear tangential waveguide, which is laterally separated from the ring by 1.5 μm . Nearly equal output power is measured from either port. Because the laser does not rely on facets for feedback or output coupling, great potential exists for monolithic integration with other guided wave optical components.

The laser exhibits a DC threshold current of 157 mA when both gain regions are biased simultaneously, and single longitudinal mode operation is achieved with a SMSR of 28 dB. Using the delayed self heterodyne method, the linewidth is measured to be 900 kHz at a combined bias current of 180 mA. Small signal and microwave noise measurements indicate a very strong resonance peak at \sim 9.0 GHz, which corresponds to the 9.5-mm optical path length around the ring. For high speed operation, only one gain region is modulated while the other is DC biased to provide amplification. The output is coupled into single mode fiber from both ports 1 and 2. Active mode-locking at the fundamental cavity resonance frequency is achieved by applying a 1-W sinusoid superimposed on a DC bias to the single gain region. Counter-propagating pulses collide in the modulated gain region and exit either side of the tangential waveguide. Figure 2 shows the pulses that exit port 1 as measured using a synchroscan streak camera with a resolution of 3-4 ps. Shorter pulses emerge from port 1 than port 2 when the drive conditions are optimized, supporting the notion of counter-propagating pulses. The measured FWHM of the pulses is 27 ps and 33 ps from ports 1 and 2, respectively. The corresponding mode-locked optical spectrum, measured using a high finesse Fabry Perot, has a FWHM of 17 GHz at port 1, as shown in Fig. 3. The spectra from either port are nearly identical, and consequently, a time-bandwidth product of 0.46 is measured from port 1 versus 0.63 from port 2. Similar average optical facet power of \sim 0.15 mW is measured from either port under modulation.

References

- (1): R. L. Fork, et. al., Appl. Phys. Lett., 1981, **38**, pp. 671-672.
- (2): N. Bar-Chaim, et. al., Appl. Phys. Lett., 1990, **57**, pp. 966-967.
- (3): T. Krauss, et. al., Elec. Lett., 1990, **26**, pp. 2095-2097.
- (4): T. L. Koch, et. al., IEEE J. Quantum Electron., 1991, **27**, pp. 641-653.
- (5): U. Koren, et. al., Integrated and Guided Wave Opt. Conf. Tech. Digest, 1989, Houston, TX, Paper MDD2.

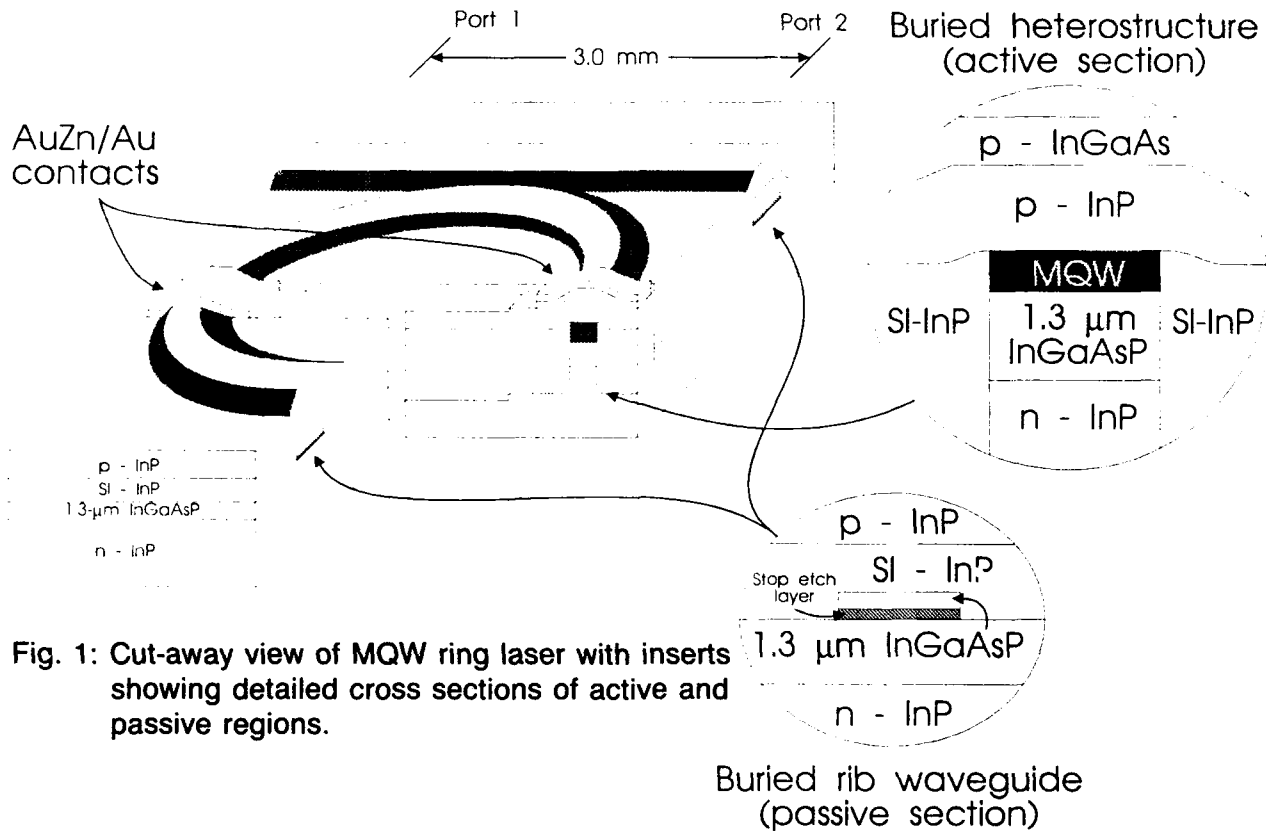


Fig. 1: Cut-away view of MQW ring laser with inserts showing detailed cross sections of active and passive regions.

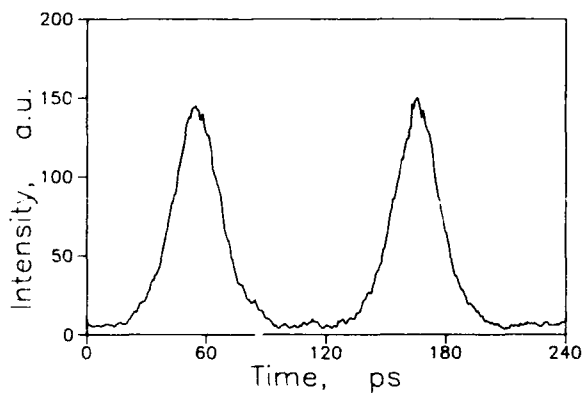


Fig. 2: Mode-locked optical pulses from port 1 with FWHM = 27 ps as measured on synchroscan streak camera.

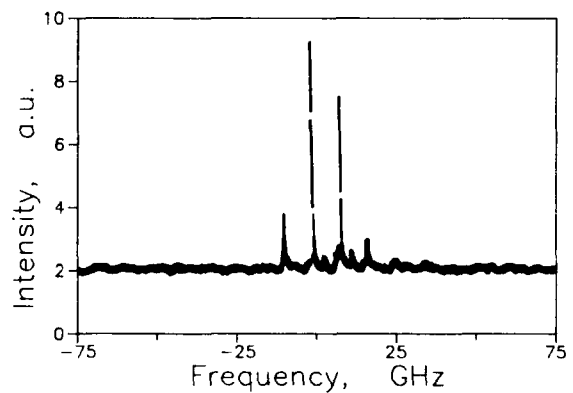


Fig. 3: Mode-locked optical spectrum of pulses from port 1 measured with high finesse Fabry-Perot.

Design of Multi-Section Mode-Locked Semiconductor Lasers With Intra-Waveguide Saturable Absorbers

D. J. Derickson, R. L. Helkey, A. Mar, J. G. Wasserbauer, and J. E. Bowers
ECE Dept. MS 172, University of California, Santa Barbara, Ca. 93106 (805)-893-4235

Monolithic and external cavity mode-locked semiconductor lasers with multiple contacts have produced excellent results [1-3]. The goal of this paper is to show how to optimize the design of these structures as a function of the free parameters in the design: (1) Active region composition and waveguiding, (2) segment lengths, and (3) electrical parasitics. The paper also explains how the effects of self-phase modulation in the saturable absorber and gain section interact with gain dispersion to limit the achievable pulse width. Figure 1 shows the types of structures that were fabricated and analyzed in this work. Both quantum well and bulk active region devices were tested at 0.85 μm and 1.55 μm . The functions of the various segments are: segment A provides the overall gain, segment B is reverse biased to form an intra-waveguide saturable absorber/photodetector, and segment C is used for active gain modulation or for repetition rate tuning.

The structure of Figure 1 was analyzed using the rate equations presented by Agrawal [4] and applied to both forward and reverse biased segments. Figure 2 shows the pulse shortening and net gain per pass through the mode-locked laser as a function of input power divided by the the saturation energy [4] of the amplifier. Increasing the input power increases the gain saturation of the amplifier which increases the amplifier's pulse broadening. The saturable absorber decreases the pulse width and the maximum net pulse shortening is found near the input energy for maximum net gain. Figure 3 shows the pulse shaping per pass and required unsaturated gain in the amplifier as a function of unsaturated gain in the saturable absorber for an assumed loss of 27 in the cavity. Longer saturable absorber lengths produce more pulse shaping but require a much larger amplifier gain. Longer saturable absorbers are also *much more susceptible* to self-pulsations. A good compromise is to choose an unsaturated absorber transmission value near 0.01 where the pulse shortening curve begins to rise quickly. Larger ratios of saturation energies between the gain and absorber segments produce larger pulse shortening and require less unsaturated amplifier gain levels. This ratio is found to be larger in quantum well devices than in bulk active region devices.

The minimum achievable pulse width and large time bandwidth product found in these these structures have been found to be a result of the interaction of self-phase modulation and gain dispersion. Figure 4 shows the output power and instantaneous frequency from a two section passively mode-locked laser. The output chirp shows an initial up-chirp in frequency due to saturable absorber saturation and then a down chirp in frequency caused by amplifier gain saturation. The magnitude of this self-phase modulation is controlled by the linewidth enhancement factor. Over much of the pulse, the chirp has a linear slope in time implying that pulse compression should be possible. Figure 5 shows autocorrelation traces before and after optical pulse compression that verify the sign of the chirp in figure 4. Figure 6 shows the pulse width versus pass through the laser starting with a 7.3 ps pulsewidth input for various values of the linewidth enhancement factor. The linewidth enhancement factor is very important in determining the ultimately achievable pulse width. Gain and absorption saturation induce a large frequency chirp and excess bandwidth beyond the Fourier transform limit. Gain dispersion (magnitude and especially phase) in conjunction with this excess bandwidth combine to limit the pulse width to values typically over 1 ps.

- [1] D. J. Derickson et al., Appl. Phys. Letts, **59**, Dec 23 (1991)
- [2] Y. K. Chen et al. Appl. Phys. Letts, **58**, 1253 (1991)
- [3] K. Y. Lau, IEEE J. Quantum Electronics, **QE-26**, 250 (1990)
- [4] G. P. Agrawal, IEEE J. Quantum Electronics, **QE-27**, [1991]

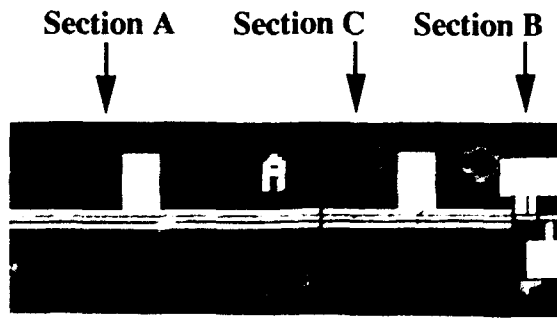


Figure 1: A multisection mode-locked laser design that is analyzed and tested in this work. Section A is the gain segment, section B is the saturable absorber/photodetector, and section C is the gain modulation/tuning section. Both monolithic and external cavity designs are examined.

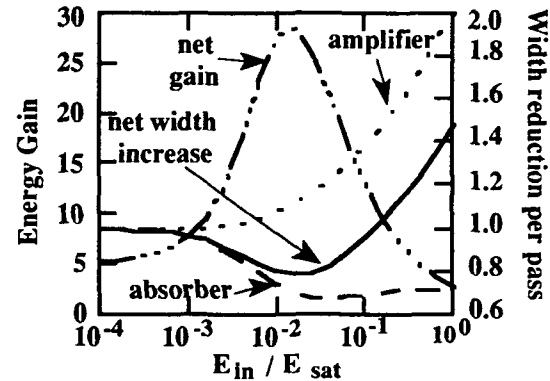


Figure 2: The net energy gain and pulse shortening per pass for a two section passively mode-locked laser vs. the input energy/saturation energy [4]. The unsaturated gain was 250 and the unsaturated absorber transmission was .02. The ratio of saturation energies is 3.

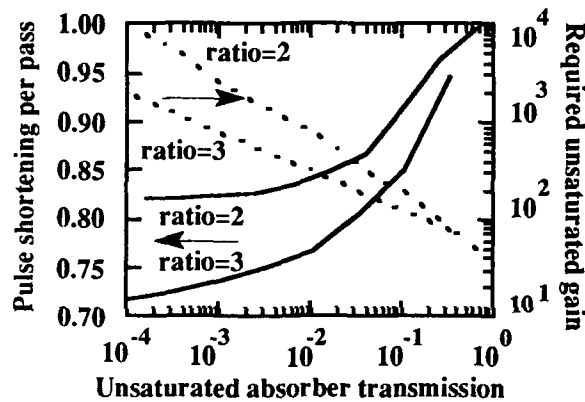


Figure 3: Pulse shortening per pass and required unsaturated gain versus the unsaturated absorber transmission. The plot is done for two ratios of saturation energies. The net gain through the two section passively mode locked device is 27 in all cases.

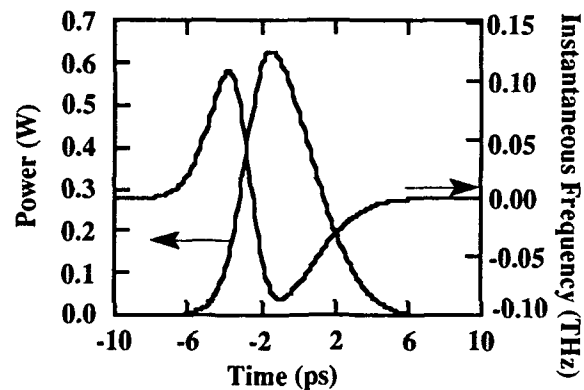


Figure 4: The output power and instantaneous frequency vs. time for one pass through a two section passively mode-locked laser. The ratio of saturation energies is 3, the linewidth enhancement factor is 3, and the net gain through the device is 27.

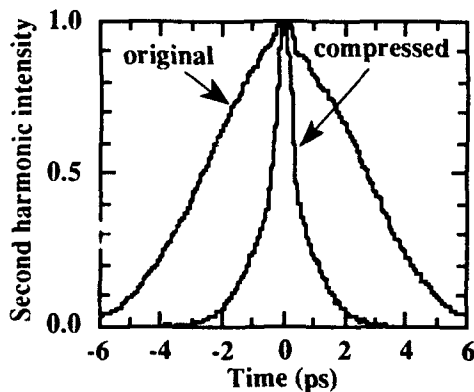


Figure 5: Experimental uncompressed and compressed auto-correlation traces from a two section passively mode-locked external cavity laser. The device had a bulk GaAs active region. The degree of compression indicates a quasi-linear frequency chirp across the optical pulse.

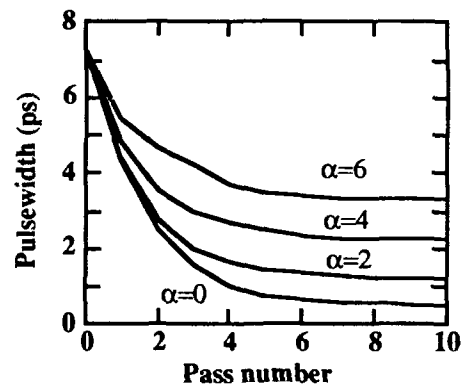


Figure 6: Pulse width versus round trip pass number through a two section passively mode-locked laser. The plot is done for 4 values of the linewidth enhancement factor. The bandwidth factor, t_2 , was equal to 0.1ps [4]. The ratio of saturation energies was 3 and the net gain through the device was 27.

WC4-1

Zero-Net-Strain InGaAsP/InP Multiple Quantum Well Lasers

C.P.Seltzer, S.D.Perrin, C.J.Gibbins, M.C.Tatham, J.R.Farr, D.M.Cooper

BT Laboratories,
Martlesham Heath, Ipswich, Suffolk, IP5 7RE, UK
Tel: +44 473 642508

In this paper, we compare results from zero-net-strain multiple quantum well lasers with similar devices having conventional strain (the barriers are lattice-matched to the substrate) and unstrained structures. Contrary to theoretical predictions, our initial results indicate that there is little difference between strained and unstrained lasers.

The optimum design of multiple quantum well (MQW) lasers for high speed applications has recently been shown to be a structure with 16 wells¹. This performance may be enhanced by incorporating strain in the quantum wells². However, if large numbers of strained wells are grown, the structure may reach the critical thickness for epitaxial growth³. This problem can be avoided by straining the barriers in the opposite sense to the wells to produce a zero-net-strain structure.

All device layers were grown by atmospheric pressure MOVPE. A zero-net-strain structure with 16 In_{0.7}Ga_{0.3}As wells has been grown with a mean MQW mismatch of only +90ppm. The same structure was grown with the barriers lattice-matched to the InP substrate for comparison. The mean mismatch for this wafer was +1332ppm which is close to the critical limit. All of the wafers were fabricated into broad area and buried heterostructure lasers.

Typical threshold current densities for 16 well broad area zero-net-strain lasers, 1000 μ m in length, were 1.2kA cm⁻² under pulsed conditions. Similar values were obtained from conventionally strained devices.

Buried heterostructure lasers of length 150 μ m had threshold currents as low as 6mA at 20°C. Output powers of over 30mW per facet were measured at 200mA drive current. The threshold current increases linearly with length to around 18mA for 1000 μ m long devices.

In Figure 1 we plot the characteristic temperature T_0 for zero-net-strain (ZNS), conventionally strained (CS) and unstrained (US) buried heterostructure lasers all with 16 quantum wells. The unstrained

lasers exhibit slightly higher values of T_0 than the strained devices in contrast to earlier theoretical predictions⁴.

Measurement of the relative intensity noise spectra has been shown to be an effective method of determining the intrinsic frequency response. RIN spectra for a 150 μm long zero-net strain device are shown in Figure 2. The resonance frequency at 8.7mW output power is about 15GHz. Extrapolation of the data gives a resonance frequency of over 30GHz at the maximum measured output power.

Zero-net-strain devices have a measured differential gain which is 40% larger than that of unstrained lasers with the same number of wells. However, this is offset by the reduction in optical confinement factor and internal loss leading to a lower increase in the measured D coefficient. The measured damping coefficient implies a potential modulation bandwidth of over 40GHz.

Reliability studies have been initiated on our strained layer lasers. The devices were subjected to a high temperature (125°C) burn-in screen for 24 hours at 50mA drive current. All showed only very small threshold current changes. The lasers were then biased to output 4mW per facet at 80°C. Drive currents are very stable after more than 1100 hours. Further progress on the lifetesting of these lasers will be presented.

References:

1. Lealman et al, Elec. Letts., 1991, **27**, pp.1191-1193
2. Suemune et al, App. Phys. Letts., 1988, **53**, pp.1378-1380
3. Matthews et al, J. Cryst. Growth, 1974, **27**, pp.118-125
4. Adams, Elec. Letts., 1986, **22**, pp.249-250

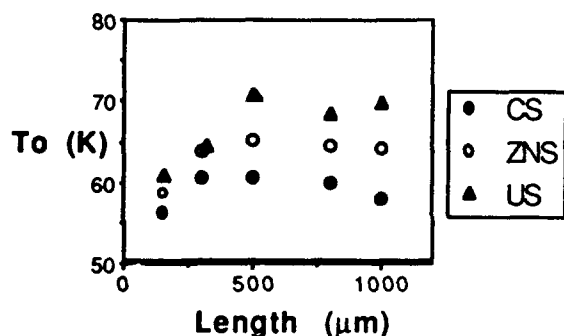


Figure 1: T_0 versus length for 16 well strained and unstrained BH lasers

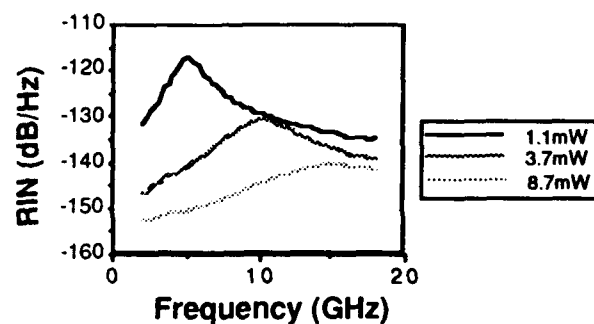


Figure 2: RIN spectra for 150 μm ZNS BH laser

LOW FREQUENCY RELATIVE INTENSITY NOISE IN SELF-PULSATING RIDGE-WAVEGUIDE QUANTUM WELL LASERS

Shlomo Ovadia

IBM East Fishkill Facility
Rt. 52, Z/71E
Hopewell Junction, N.Y. 12533

Kam Y. Lau

University of California at Berkeley
Electrical and Computer Sciences Department
Berkeley, CA 94720

Self-pulsating (SP) semiconductor lasers are used in optical systems in which optical coherence is undesirable. In particular, their short coherence length (< 10 mm) minimizes their sensitivity to modal noise in a multimode fiber link. In comparison, conventional diode lasers with increasing optical feedback can fall into the coherence collapse regime, characterized by a wide emission spectrum and huge relative intensity noise (RIN) fluctuations.¹ In this work, it is shown that predictions of the RIN of SP ridge-waveguide double quantum well graded-index separate-confinement heterostructure (RW DQW-GRINSCH) lasers can be made based on a simple conjecture for a dynamically unstable system, and yield good agreement with experimental data.

The SP RW DQW-GRINSCH lasers has been grown by molecular beam epitaxy as previously described in details.² The double contact laser cavity consisted of a $250 \mu\text{m}$ gain section with different absorber length sections ranging from $2.5 \mu\text{m}$ to $15 \mu\text{m}$. The measured RIN spectra of a typical SP laser with a $15 \mu\text{m}$ absorber at two different bias currents are shown in Fig. 1. Figure 2 shows the measured low frequency RIN ($\omega/2\pi = 400$ MHz) for SP lasers with $2.5 \mu\text{m}$, $5 \mu\text{m}$, $10 \mu\text{m}$, and $15 \mu\text{m}$ absorber length versus the normalized bias current. For comparison, the low frequency RIN for a similar laser without an absorber is also shown. Although the low frequency RIN of SP laser is relatively high (from -110 to -120 dB), it is still lower than the RIN of conventional laser in the coherence collapse regime (-103 dB).¹

To model the RIN behavior of these lasers, one starts from the single-mode rate equations for the carrier and the photon for the spatially uniform laser, which contains an optical saturable loss and is driven by a Langevin noise source. These stochastic rate equations are linearized in the small signal approximation, and solved in the frequency domain by Fourier analysis. The RIN spectrum of a single longitudinal mode is given by:

$$\text{RIN} = [2R_{\text{sp}}/S] \frac{\Gamma_{\text{N}}^2 + \omega^2 + (G_{\text{N}}S)^2[1 + (\gamma_{\text{e}}N)/(R_{\text{sp}}S)]}{(\omega_{\text{sp}}^2 - \omega^2)^2 + 2\Gamma_{\text{sp}}^2(\omega^2 + \omega_{\text{sp}}^2) + \Gamma_{\text{sp}}^4} \quad (1)$$

where $\omega/2\pi$ and $\omega_{\text{sp}}/2\pi$ are the measurement and the SP frequencies, $\Gamma_{\text{sp}} \equiv (\Gamma_{\text{N}} + \Gamma_{\text{S}})/2$ is the decay of the SP oscillations, $\Gamma_{\text{N}} = G_{\text{N}}S + N(\partial\gamma_{\text{e}}/\partial N) + \gamma_{\text{e}}$ is the small-signal carrier decay rate, N and S are the carrier and photon density, respectively, $\Gamma_{\text{S}} = R_{\text{sp}}/S - G_{\text{S}}S - [\alpha_0/S_p](S/[1 + S/S_p])^2$ is the small signal photon decay rate, R_{sp} is the spontaneous emission rate, G_{N} and G_{S} are the differential and the photon gain terms, respectively, α_0 is the unsaturated loss parameter, and S_p is photon saturation density. For an unstable laser system such as a SP laser, α_0 is always larger than a critical value α_{cr} , which leads to infinite RIN Q ($\cong \omega_{\text{sp}}/\Delta\omega_{\text{sp}}^{\text{FWHM}}$), and thus the conventional noise analysis does not apply. However, we found that as far as the the low frequency RIN is concerned, one obtains excellent agreement with the experimental data (Figs. 1 and 2) if one simply sets $\alpha_0 = \alpha_{\text{cr}}$ for a SP laser, regardless of what the real unsaturated loss is, as long it is above α_{cr} . This procedure gives excellent agreement with experimental RIN at low frequencies ($\omega < \omega_{\text{sp}}/2$), but fails to predict the RIN at or near $\omega = \omega_{\text{sp}}$. This model may be a useful design tool for predicting the low frequency RIN behavior of these lasers with different length absorber, which operate at any bias current.

REFERENCES:

1. K. Peterman, *Laser Diode Modulation and Noise* (Kluwer, London, 1988).
2. C. Harder, P. Buchmann, and H. P. Meier, *Electron. Lett.* 22, 1081 (1986).

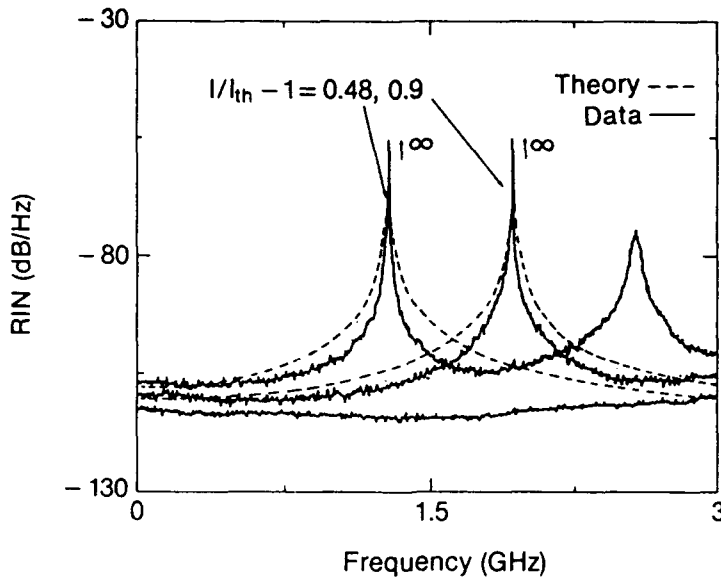


Fig. 1 The measured and calculated RIN spectra of SP RW DQW-GRINSCH laser with a 15 μm absorber length at $I/I_{th} - 1 = .48$, and $.9$ currents. The bottom trace is the instrument floor noise spectra.

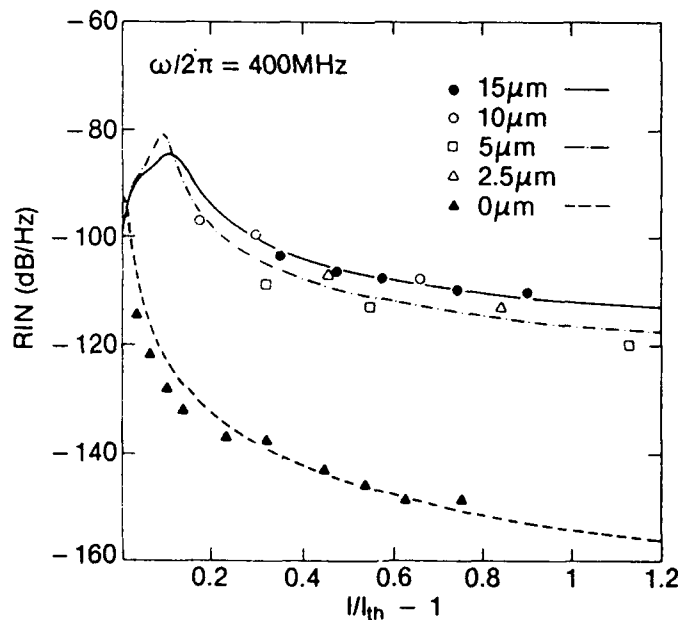


Fig. 2. The measured and calculated RIN at $\omega/2\pi = 400$ MHz for SP RW DQW-GRINSCH lasers with 2.5 μm , 5 μm , 10 μm , and 15 μm absorber length versus the normalized bias current. The symbols and the lines represent experimental data and theory respectively. The bottom trace is the measured RIN for a similar laser without an absorber. The calculated RIN uses $\beta = 5 \times 10^{-5}$.

WC6-1

GaAlAs/GaAs OPTICAL BEAM SCANNER USING PHASED ARRAY WAVEGUIDES**K. MORIKI, H. KATOH, Y. OHNISHI, T. HATTORI****Musashi Institute of Technology, 1-28-1 Tamazutsumi Setagaya-ku,
Tokyo 158, Japan****T. SAKAGUCHI, K. IGA****Tokyo Institute of Technology, 4259 Nagatsuta, Midori-ku
Yokohama 227, Japan**

The possible development of the electrooptic scanner with quick random access may find new applications in optical information processing, optical sensing and optical communications. The optical scanner using arrayed waveguides is one of the candidate devices because of its high speed operation and reliability^{1,2}. However, Optical power coupling into the arrayed waveguides has been one of the problems. In this paper, we describe an experiment to integrate the scanner with an optical branch on the substrate.

Figure 1 shows a schematic diagram of the integrated device. The optical beam launched from a three-dimensional waveguide propagates through a slab waveguide and is expanded in the one-dimensional direction by diffraction. The expanded beam is coupled into arrayed three-dimensional waveguides. In this manner, phase maintained optical power distribution can be achieved by a relatively short length device³. The divided optical waves propagate through the three-dimensional waveguides and are modulated phase relations by changing propagation constants by applying the reverse bias to one of the waveguides.

Figure 2 shows a cross sectional photograph of the fabricated device with MOCVD grown twin GaAlAs/GaAs ridge-waveguides. The branching loss depends on the width of three-dimensional waveguides, the spacing between those waveguides and the length of slab-waveguide. The estimated loss was about 40 percent for the fabricated device³.

Figure 3 shows the interference pattern from the device. The output light from the device is collimated using an objective lens and is projected directly on an IR-photoemissive detector surface. The pattern moves when applying the reverse bias to the pn junction in one of the waveguides. The deflection angle increases to about 1.1 degrees with increasing reverse bias up to 10 V. When a reverse bias is applied to the other waveguide, the optical beam also deflects in the opposite direction. Imperfect electric isolation between twin waveguides gives rise to small diffraction angle as compared with the calculated angle of 3.4 degrees. When the laser diode such as a monolithic DFB laser can replace the three-dimensional waveguide, a beam scanner integrated with a light source will be

realized.

References

- 1 K. Moriki, Y. Ohnishi, T. Hattori, and K. Iga: Electron. Lett. 27, (1991), pp. 450-451.
- 2 D. R. Wight, J. M. Heaton, B. T. Hughes, J. C. H. Birbeck, K. P. Hilton and D. J. Taylor: Appl. Phys. Lett., 59, (1991), pp. 899-901.
- 3 K. Moriki, K. Aizawa, Y. Ohnishi, T. Hattori, and K. Iga: Jpn. J. Appl. Phys., 30, (1991), pp. L1175-L1177.

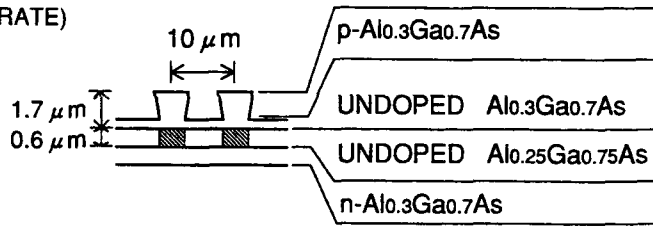
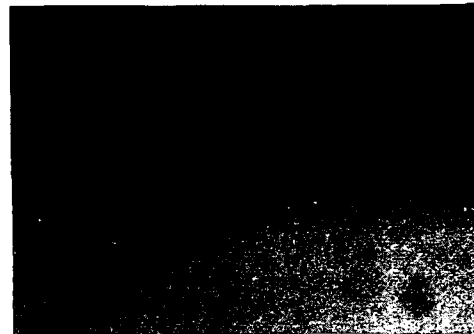
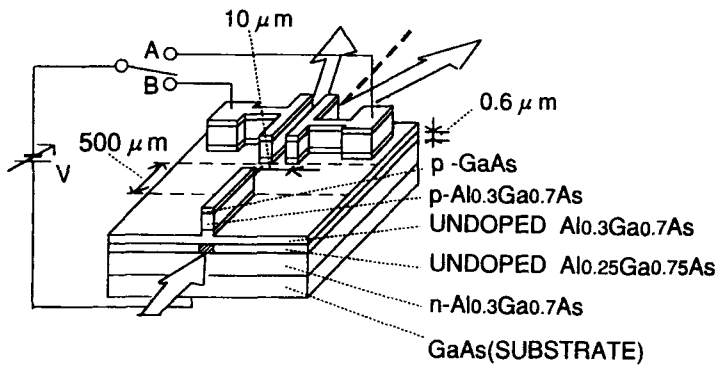


Fig. 1 A schematic diagram of the optical beam scanner which consists of twin GaAlAs/GaAs waveguides and an optical branch.

Fig. 2 A cross sectional photograph of the device.

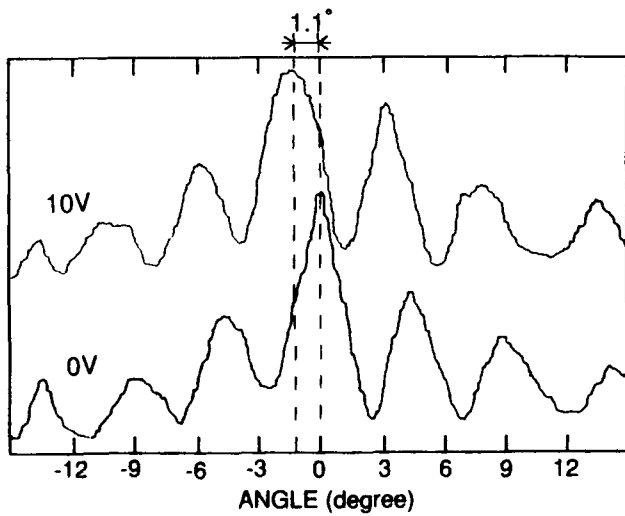


Fig. 3 An interference pattern of the lightwave from the device.

WC7-1

OptoElectronic Time Division Multiplexer(OETDM) using a Two Section Single Cavity(TSSC) switching scheme.

David McDonald, Ronan F. O'Dowd
Optoelectronics Research Centre
University College Dublin
Belfield
Dublin 4
Ireland
Tel. 353-1-7061852

Summary

Two Section Single Cavity semiconductor lasers have received a lot of attention with regard to being suitable sources for coherent transmitters or as local oscillators in coherent fiber-optic systems, where the tuning and FM response of such lasers is important[1],[2]. The two sections are driven by currents I_1 and I_2 which are independent but the resulting current densities interact optoelectronically. TSSC Fabry-Perot Lasers exhibit contours of constant power in the I_1, I_2 plane and whose threshold contour closely resembles the non-linearity typical of electrical multiplexers.

Fig. 1 shows the measured power contours for a P-side up InGaAsP/InGaAs TSSC-BH Fabry-Perot Ridge Waveguide laser. Superimposed on this characteristic are eight points A to H. These comprise the eight possible bias states that the laser may be in during each half cycle of the transmit clock. Fig. 2 details the signals and their timing relationships for two arbitrary input data streams.

I_1 is formed by the current summation of a scaled version of D1 and CLK, while I_2 is formed from D2 and CLK. STATE specifies at what operating point in the I_1, I_2 plane the laser resides during the data sequence shown, while O/P gives the relative optical output power waveform during the same data sequence.

On alternate half cycles of CLK channel D1 and then channel D2 are sampled; CLK effectively samples D2 and CLK samples D1.

Multiplexing action has been observed up to 34Mbits/s per channel, data throughput of 68Mbits/s(Fig. 3). Higher bit rates are limited at present only by the slew rate and rise time of the laser driver. The availability of P-side down TSSC lasers should alleviate this problem.

In conclusion, a novel data multiplexing scheme exploiting the nonlinear output characteristic of TSSC Fabry-Perot lasers has been reported. Reduction in transmitter complexity and absence of a multiplexer clock at twice the system clock greatly reduces driver/laser frequency response constraints.

This project is supported by Telecom Ireland.

References

1. R.F O'Dowd, M.G. Davis, Optical and Quantum Electronics,20,383,(1988).
2. M.J.Chawki, R.Auffret, D.Dumay, L.Berthou, Journal of Optical Communications,11,2,63,(1990).

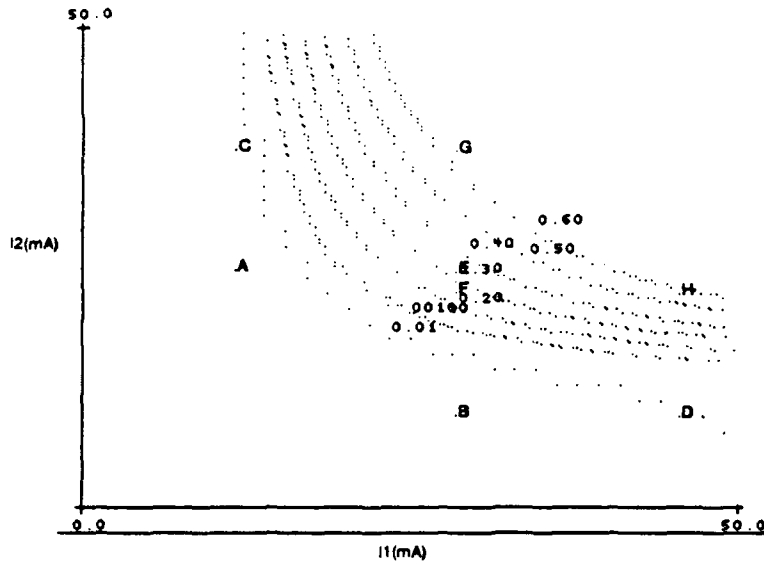


Fig. 1. Light output characteristics in the (I1,I2) plane for Fabry-Perot TSSC semiconductor lasers

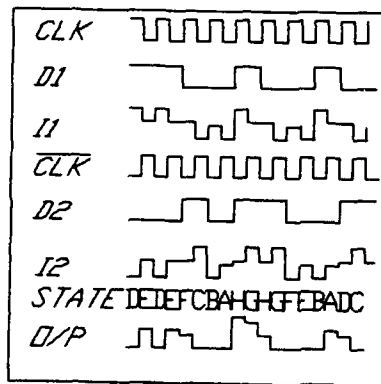


FIG.2. Input and output timing waveforms for the OETDM laser

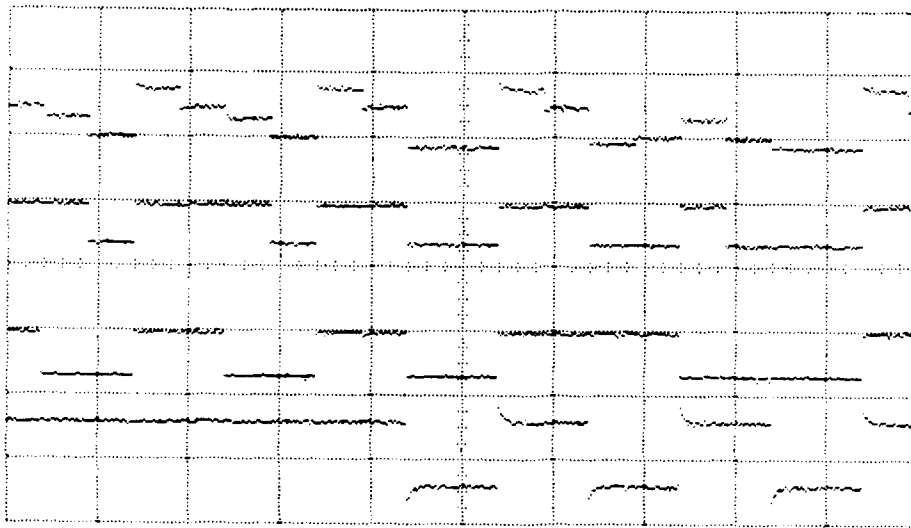


Fig. 3. Oscilloscope traces of (top to bottom): optical output, quantised output and input data channels D1 and D2 at 34Mbits/s.

Wednesday, April 15, 1992

Special Purpose
Glasses and
Fiber Amplifiers

WD 11:00 am-12:15 pm
La Salle Ballroom B

William Joseph Miniscalco, *President*
GTE Laboratories, Inc.

WD1-1

Highly Nonlinear and Photorefractive Glasses

N. F. Borrelli
 Research and Development Laboratory
 Sullivan Park SP-FR-03-1
 Corning Incorporated, Corning N.Y. 14831
 (607) 974-3155

Summary

The realization of all-optical devices, whether for high speed or for micro-opto-electronic applications, requires materials which possess large nonlinear optical coefficients. The compositional versatility of glass combined with the relative ease of manufacture and fabrication, make the study of its nonlinear properties for these applications important. A brief review of three areas of research activity will be discussed.

Glasses that exhibit a large real third order nonlinear susceptibility, χ_{ijkl} , defined from the third order nonlinear polarization,

$$P_i(\omega_4) = \chi_{ijkl}(\omega_4 = \omega_1 + \omega_2 + \omega_3) E_j(\omega_1) E_k(\omega_2) E_l(\omega_3)$$

have been found to be those glasses which contain a high concentration of ions with large linear polarizabilities, that is with high refractive indices. Measurement of χ_3 for a large number of glasses using such techniques as degenerate four wave mixing¹, where from eqn. 1, $\chi_3(\omega = \omega + \omega - \omega)$ is measured, or indirectly from the related DC Kerr effect², $\chi_3(\omega = \omega + 0 + 0)$ indicate this trend. Stable unconventional oxide glasses which contain only the heavy metal ions Tl, Pb, Bi, and Ga exhibit values of χ_3 of the order of 10^{-12} cgs-esu. Single mode optical fibers³ have been made of selected glasses of these compositions.

Glasses from which a microcrystalline phase of II-IV semiconductors can be thermally produced⁴ exhibit nonlinear optical behavior through a variety of mechanisms⁵. The most common is a band to band absorption saturation. The intensity dependence of the absorption leads to a refractive index change at a longer wavelength through anomalous dispersion. One can classify these phenomena as arising from $\text{Im}(\chi_3)$ as compared to the above which stem from $\text{Re}(\chi_3)$. Because the nonlinearity originates through absorption, the magnitude of the nonlinearity is resonance enhanced, but at the expense of the thermally limited data rate. Interest in these materials, particularly CdSe, was spurred⁶ by the observation of three dimensional quantum confinement effects⁶. The absorption edge could be tuned by controlling the quantum dot size. Unfortunately, the inability to control the particle size distribution precisely enough and the existence of competing trap dominated recombination processes have held these materials back.

The discovery of a nonlinear optical effect based on an oxygen vacancy in the standard $\text{SiO}_2/\text{GeO}_2$ waveguide material has led to a number of interesting optical manifestations. The change of the refractive index at longer wavelengths arises from the optical bleaching of the absorption corresponding to the oxygen defect, or Ge:Ge bond and the new absorption created by the trapped electrons. The intensity of this absorption can be correlated with the oxygen partial pressure of the consolidation. The induced refractive index change at $1.06\mu\text{m}$ measured by a Mach-Zehnder technique correlates well with the induced absorption. Aspects of the mechanism will be discussed in somewhat more detail. The major demonstration of this effect is in the ability to write Bragg gratings in fibers.

- 1) D. W. Hall, M. A. Newhouse, N. F. Borrelli and D. L. Weidman, *Appl. Phys. Lett.*, 54,1293, (1989)
- 2) N. F. Borrelli, B. G. Aitken, M. A. Newhouse and D. W. Hall, *J. Appl. Phys.*, 70(5),2774,(1991)
- 3) M. A. Newhouse, D. L. Weidman and D. W. Hall, *Opt. Lett.*, 15(21), 1185, (1990)
- 4) N. F. Borrelli, D. W. Hall, H. J. Holland, and D. W. Smith, *J. Appl. Phys.*, 61(12), 5399, (1987)
- 5) N. F. Borrelli and D. W. Hall, "Opt. Prop. of Glass", eds. D. R. Uhlman and N. J. Kreidl, Am. Ceram. Soc. Inc., 1991
- 6) B. G. Potter and J. H. Simmons, *Phys. Rev.*, 37B(18), 838, (1988)
- 7) K. O. Hill, Y. Fujii, D.C. Johnson and B. S. Kawasaki, *Appl. Phys. Lett.*, 32, 647, (1978)
- 8) G. Meltz, W. W. Morey, and W. H. Glenn, *Opt. Lett.*, 14(15), 823, (1989)

Gain and Noise Performance of Erbium-Doped-Fiber Power Amplifiers Pumped Between 960 and 1000 nm

Jagannath Chirravuri, W. J. Miniscalco and T. Wei, GTE Laboratories Incorporated, 40 Sylvan Road, Waltham, MA 02254.

B. Pedersen, Technical University of Denmark, Electromagnetics Institute, DK-2800 Lyngby, Denmark.

Pumping erbium-doped fiber amplifiers (EDFAs) near 980 nm has attracted much attention as a result of the lower noise characteristics and higher pump efficiency achieved compared to those obtained at 1480nm. The narrow absorption profile of the fiber at the 980nm pump band is generally believed to impose a tight constraint on the laser operating wavelength. Recent results for small-signal amplification with pump powers of ≈ 30 mW revealed a gain reduction of ≤ 3 dB for pump wavelengths varying by 30nm, a bandwidth which is significantly larger than that of the 980nm absorption band [1]. By reducing the cost of the pump lasers, this relaxed tolerance is expected to lower the overall cost of the EDFA as well as reduce the impact of temperature-induced wavelength drifts in the pump laser.

We present an investigation of the effect of pump wavelength, λ_p , on the signal output of a power amplifier. The experiments yield a 1dB gain-penalty bandwidth in excess of 30nm. A quantitative amplifier model is used to show that pump wavelength tolerance increases with pump power and fiber numerical aperture (NA). For the first time the tradeoff in noise performance associated with this relaxed tolerance in the pump wavelength is examined.

Figure 1 shows the signal output power as a function of λ_p for a Ge/Al/P/Er-doped silica fiber with NA of 0.18 and cut-off wavelength of 940nm. The signal input power used was -1.4dBm and the two sets of curves labelled 'a' and 'b' correspond to pump powers of 40 and 80 mW. The symbols represent the measured values for three fiber lengths at each pump power. The dashed curve in Figure 1 is the ground-state absorption (GSA) cross-section spectrum which peaks at 979nm. The solid lines were obtained using a numerical model [2] and are in good agreement with the experiment. From this figure it can be seen that under all conditions the maximum signal gain is obtained at 979nm, the wavelength corresponding to the peak of the

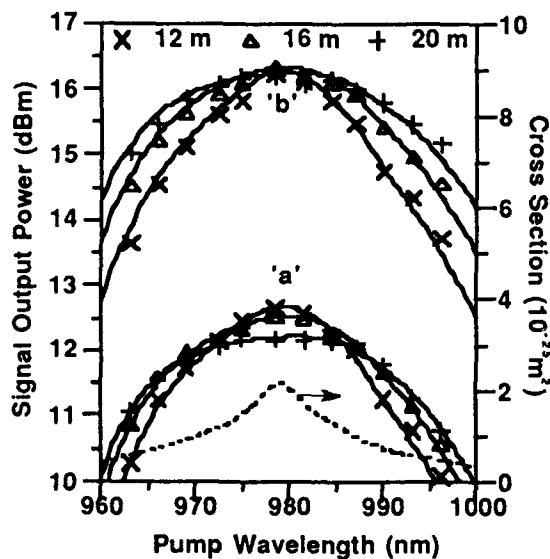


Figure 1: Signal output as a function of pump wavelength. The 'a' and 'b' represent measurements taken at pump powers of 40 and 80 mW, respectively. The dashed curve is the ground state absorption cross section.

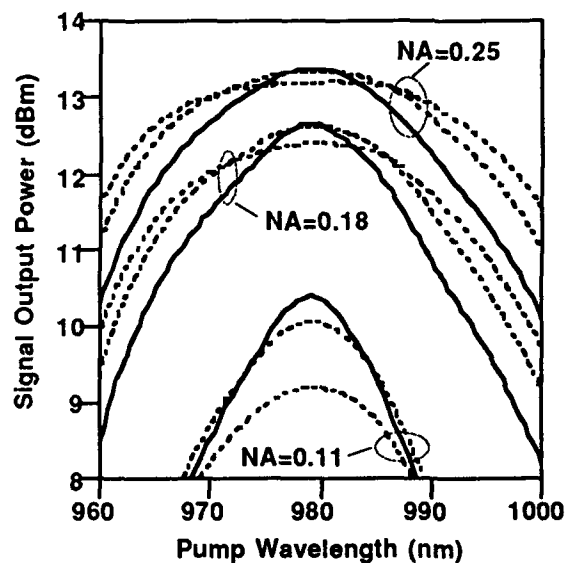


Figure 2: Calculated output signal as a function of pump wavelength for fibers with different NAs. For each NA, the output at 979nm decreases with increasing fiber length. The pump power is 40 mW.

GSA. The signal output is much less sensitive to fiber length for the higher power, the decrease in the maximum gain being only 0.1 dBm for 80 mW of pump power at 979nm when the fiber length is changed by $\pm 25\%$. Also, the sensitivity of gain to pump wavelength deviation from 979nm, $\Delta\lambda_p = (\lambda_p - 979)$ nm, decreases with increased fiber length. This decrease in gain is asymmetric with respect to $\Delta\lambda_p$, changing slower for $\Delta\lambda_p < 0$ compared to $\Delta\lambda_p > 0$. The effect of fiber design on the signal output power is illustrated in Fig. 2. The middle set of curves in this figure is the same as 'a' in Fig. 1, while the upper and lower sets are calculations for fibers with NAs of 0.25 and 0.12, respectively, all other fiber parameters being the same. Within each set of curves the one with highest gain at 979nm (solid line) represents the fiber with optimal length, L_0 , at this wavelength and pump power. The other two curves in each set have lengths of $1.33L_0$ and $1.67L_0$, respectively. It is apparent that the gain sensitivity to $\Delta\lambda_p$ decreases markedly with increasing NA. These effects are illustrated in a different way in Fig. 3 which shows the relationship between gain and noise figure (F) penalties and relative fiber length and pump wavelength. Fiber lengths are given relative to the optimum for $\lambda_p = 979$ nm and the filled-in circle at (979, 1.0) is the reference point of maximum gain and minimum F for all three NAs. The solid contours enclose regions with a gain penalty ≤ 0.5 dB while the area below the dashed curves corresponds to F penalties less than the indicated values. The shape of the gain penalty contours show that larger NAs and longer fiber lengths increase the range of pump wavelengths that can be tolerated. In contrast, the F penalty is relatively insensitive to NA and increases monotonically with fiber length. Diagrams such as Fig. 3 with a more complete set of curves can be used as an amplifier design guide. If the maximum gain penalty is specified and noise is not a consideration, fiber lengths ranging over the full height of the appropriate contour at the specified pump wavelength may be used. If a maximum F penalty is also specified, however, use of the longer fiber lengths may not be permitted.

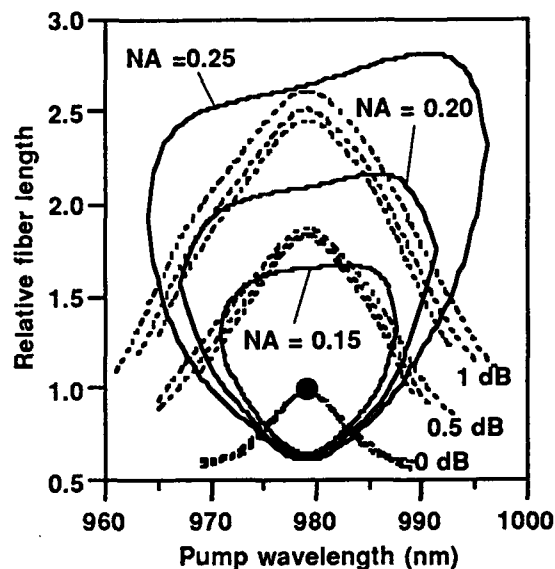


Figure 3: Gain penalty contours (solid lines) for fibers with the indicated NAs. Noise figure penalty curves (dashed lines) are grouped by magnitude of penalty and within each group the NA increases with relative fiber length. Pump and signal input powers are 17 and 0dBm. The gain at the reference point (filled-in circle) is 14, 14.5 and 14.7dB for NAs of 0.15, 0.20 and 0.25, respectively. F is 3.7dB, independent of NA.

In conclusion, we have examined the role of pump power and fiber design in expanding the range of useful pump wavelengths at the 980nm band for power EDFAs. The trade-offs between pump wavelength and gain and F have been quantified. For a high NA fiber the gain penalty is < 0.5 dB for pump wavelengths in a range of over 30nm centered at 979nm. For these conditions the noise figure penalty can be kept to ≤ 1 dB. We wish to thank R. Lauer for suggesting this investigation.

References

1. R.M. Percival *et al.*, Elec. Lett. **27** 1266 (1991).
2. Bo Pedersen *et al.*, Opt. Commun., vol **81**, 23 (1991)

WD3-1

Optimization of Pr³⁺-Doped Fiber Amplifiers

B. Pedersen (EMI, Technical University of Denmark, DK-2800 Lyngby, Denmark),
 W. J. Miniscalco (GTE Laboratories Incorporated, 40 Sylvan Rd., Waltham, MA 02254),
 R. S. Quimby (Department of Physics, Worcester Polytechnic Institute, Worcester, MA 01609)

Pr³⁺-doped fluorozirconate fiber amplifiers have been demonstrated to provide net-gains higher than 25 dB in a broad band centered on the 1300-nm communication window [1,2]. We have developed a quantitative numerical model and systematically analysed the performance improvements that can be achieved through fiber design or the use of host glasses providing a longer lifetime for the metastable state.

Figure 1 shows the cross sections for the relevant transitions used by the model. The ground-state-absorption (GSA) cross sections were determined from absorption measurements on bulk Pr³⁺-doped ZBLAN samples. The stimulated emission and excited-state-absorption (ESA) cross sections at the signal wavelength are those reported by Quimby and Zheng [3]. The stimulated emission cross sections at the pump band (≈ 1050 nm) were obtained from a McCumber analysis and scaled using the radiative rate of Ohishi *et al.* [1]. The numerical model was verified by trial calculations showing good agreement with the experimental results obtained by Ohishi *et al.* [1] and Miyajima *et al.* [2].

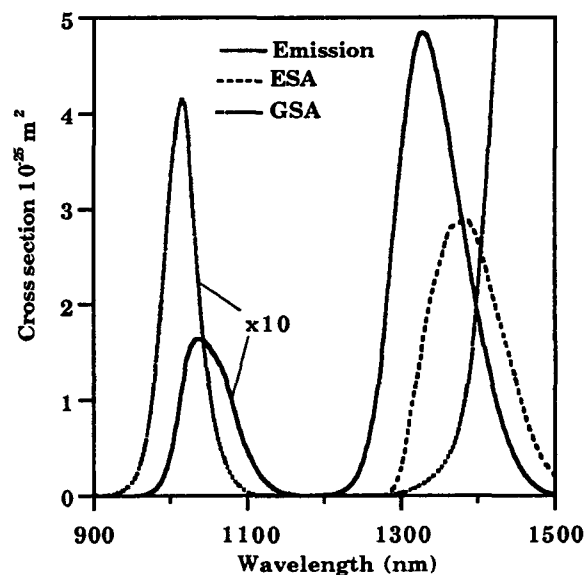


Figure 1 Cross section spectra for the transitions included in the model.

Figure 2 shows the maximum small-signal gain at 1310 nm versus the cut-off wavelength for step-index fibers pumped co-directionally at 1017 nm for pump powers of 100 and 250 mW. The fiber NAs range from 0.2 to 0.5 and the results indicated that the optimum cut-off wavelength is ≈ 800 nm almost independent of the NA and pump power. Figure 3 plots the maximum small-signal gain versus the NA for co-directional pumping with four different pump powers using the optimum cut-off wavelength. The gain increases with increasing NA due to the improved overlap between the Pr³⁺ ions and the pump and signal modes. For 50 mW of pump power gains higher than 10 dB are not practical since the NA would have to be > 0.4 . For pump powers of 100 and 200 mW the gain increases almost linearly with NA for NA < 0.35 . For 400 mW of pump power the biggest improvement is found when increasing the NA from 0.15 to 0.25, which roughly triples the gain in dB. It is observed that the gain curves bend over for high NAs. This occurs when the pump absorption rate, which increases with the NA and the pump power, becomes comparable to total relaxation rate of the ¹G₄ level.

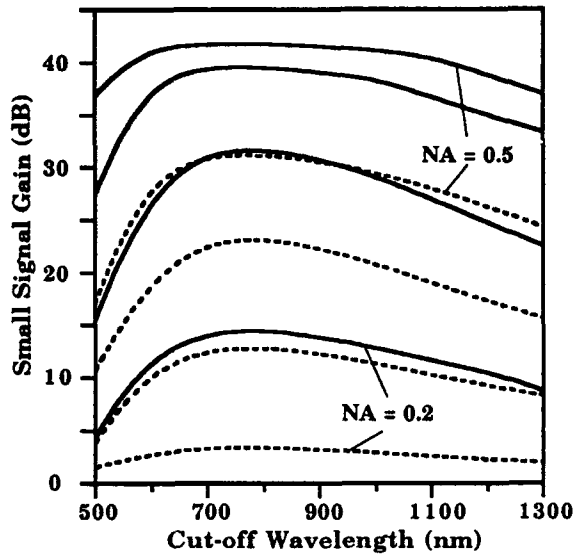


Figure 2 Gain versus cut-off wavelength for step-index fibers with NAs of 0.2, 0.3, 0.4, and 0.5. The pump power is 100 mW (dashed curves) and 250 mW (solid curves)

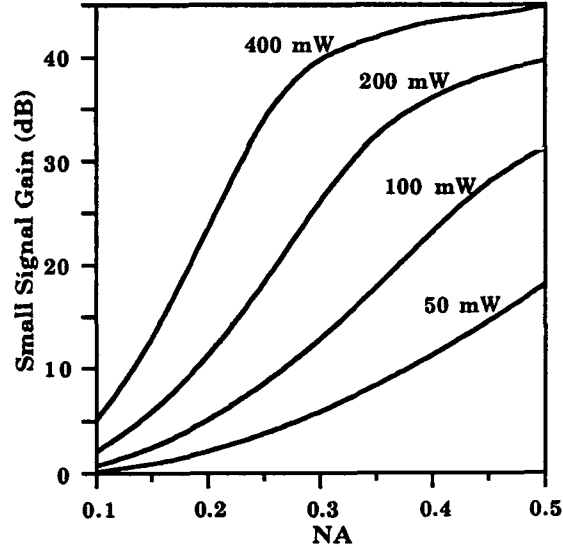


Figure 3 Gain versus NA for step index fibers pumped with different power. The cut-off wavelength is 800 nm.

The efficiency of $\text{Pr}^{3+}:\text{ZBLAN}$ fiber amplifiers is limited by the short lifetime of 110 μs for the metastable state. The nonradiative relaxation rate of the $^1\text{G}_4$ can be decreased through the use of other glass hosts with either a lower effective phonon frequency or weaker electron-phonon coupling. We have examined the potential improvement in amplifier performance that could be realized through the resultant increase in lifetime τ of the metastable state. Figure 4 plots the small-signal gain as function of τ for pump powers of 100 and 250 mW. The NA is 0.3 and the calculations represent the effect of changing only the nonradiative rate. As observed, the gain is very sensitive to τ for $20 < \tau < 400 \mu\text{s}$. If τ could be increased to 300 μs without changing the cross sections, only 100 mW of pump power would be required to obtain 30 dB gain compared to 250 mW for $\text{Pr}^{3+}:\text{ZBLAN}$ at room temperature.

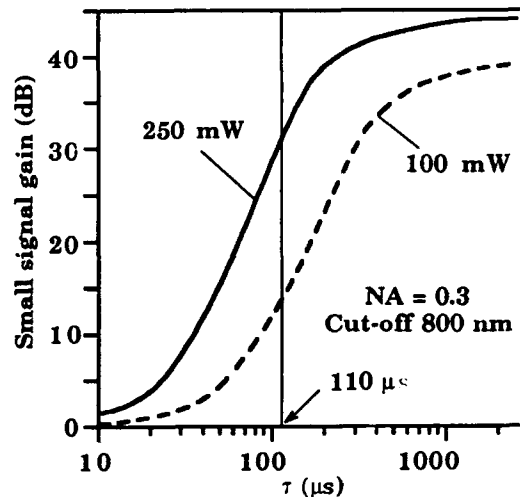


Figure 4 Small-signal gain versus the observed lifetime, τ , for the $^1\text{G}_4$ level. The launched pump powers are indicated.

References

- [1] Ohishi *et al*, Techn. Dig. of OFC'91, San Diego, CA, 1991, Paper PD2.
- [2] Miyajima *et al*, Proc. Optical Ampl. Appl., Snowmass V., Colorado, 1991, Paper PD1.
- [3] Quimby and Zheng, to be published

WD4-1

Femtosecond Soliton Amplification with the Pump Dependent Response Function of Erbium Doped Fibers

F.S. Locati, M. Romagnoli, M. Settembre, M. Tamburrini, and S. Wabnitz

Fondazione Ugo Bordoni, Via B. Castiglione 59, 00142 Rome, Italy

The process of femtosecond soliton amplification with erbium doped single mode fibers is determined by a complex interplay between fiber dispersion, the intensity dependent refractive index, the Raman effect and the finite bandwidth of the amplifier. Moreover, recent experiments have shown that the soliton evolution in the amplifier may be strongly affected by the depletion of pump light along the fiber. In particular, in contrast with the cw case, the spectral and temporal properties of the amplified femtosecond signal, and the degree of energy conversion from the pump are drastically different with either forward or backward pumping [1].

With constant inversion along the fiber, the femtosecond soliton amplification may be well reproduced by a simple two-level (or Lorentzian) model for the active transition [2]. In this work we show that this model is no longer valid in the presence of pump depletion. In fact, the spectral shape of the complex linear susceptibility of erbium doped fibers changes substantially with the level of inversion. In particular, the spectral width and the relative height of the two emission peaks depend on pump power. Moreover, gain and absorption may be simultaneously present in different regions of the pulse spectrum [3] (see fig.(1)).

By neglecting gain saturation effects, we describe the pulse amplification process in the erbium doped fiber amplifier by means of the perturbed nonlinear Schrödinger (NLS) equation

$$\frac{\partial E}{\partial Z} + \frac{i}{2} \frac{\partial^2 E}{\partial T^2} = iE \left(\rho |E|^2 + (1 - \rho) \int_{-\infty}^T |E(\tau)|^2 f(T - \tau) d\tau \right) + i \int_{-\infty}^T E(\tau) g(Z, T - \tau) d\tau$$

where $\rho \simeq 0.8$, $f(t)$ and $g(Z, t)$ are Fourier transforms of the experimental complex Raman and (pump dependent) erbium susceptibilities of the fiber. The above equation is coupled with the equation for the pump evolution along the fiber.

Figure (2) compares the calculated dependence of the total signal energy at the output of the amplifier versus the input pulse width (FWHM) with either forward or backward pumping. As can be seen, forward pumping strongly increases the extraction of energy from the pump with respect to backward pumping. In contrast, calculations with the two level model lead to nearly equal amplification curves for the two cases. When considering the output pulse shape and spectrum, however, in the forward case most of the energy is contained in a strongly chirped self frequency shifting Raman soliton. On the other hand, in the forward case the Raman self frequency shift is strongly reduced and the output pulses are much less distorted by the amplification process. These results are in agreement with the experimental observations, and may be easily physically interpreted by considering the changes along the fiber of the spectral dependence of gain in fig.(1).

References

- [1] K. Kurokawa, and M. Nakazawa, *Electron. Lett* **17**, 1765 (1991).
- [2] I.R. Gabitov, M. Romagnoli, and S. Wabnitz, *Appl. Phys. Lett.* **59** 1811 (1991).
- [3] E. Desurvire, *IEEE J. Lightwave Technol.* **8**, 1517 (1990).

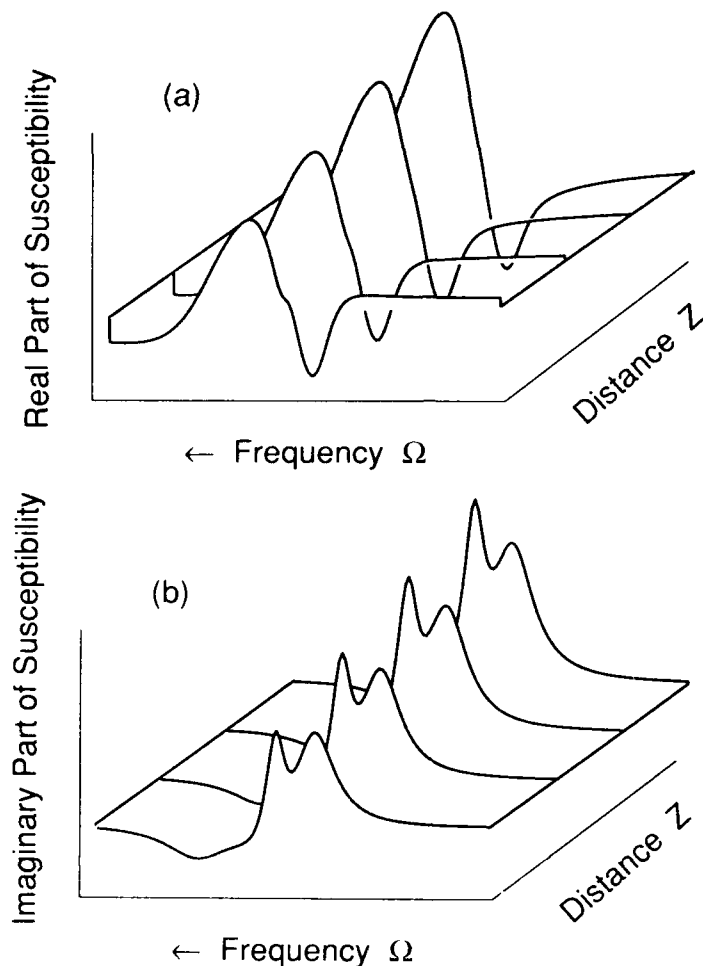


Figure 1: Fiber length Z dependence of (a) real and (b) imaginary parts of the linear susceptibility of erbium. Here the population inversion ΔN ($-1 \leq \Delta N \leq 1$) increases from 0.2 to 0.5 when Z grows from zero to 12.5 m. Host fiber dispersion is $-15ps^2/km$.

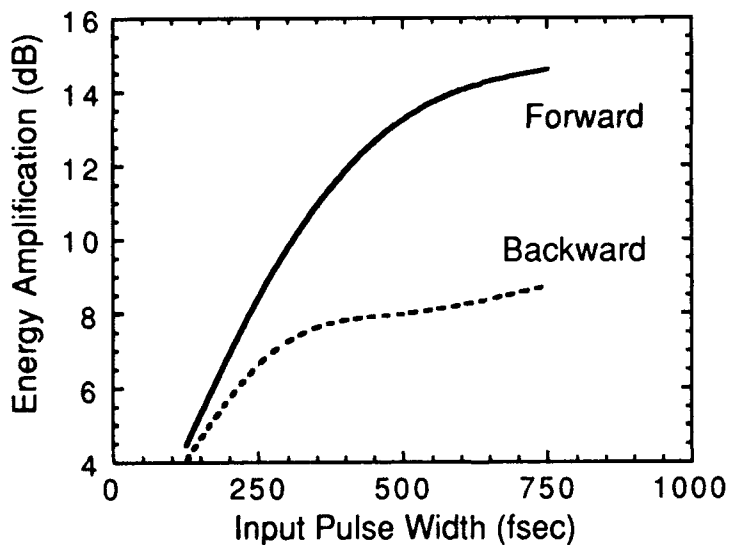


Figure 2: Energy amplification of femtosecond pulses versus input pulsewidth, with forward and backward pumping.

Wednesday, April 15, 1992

Beam Propagation Methods

WE 11:00 am-12:30 pm
La Salle Ballroom C

C. R. Menyuk, *Presider*
University of Maryland

Lanczos Propagation and Reflection Methods

David Yevick Department of Electrical Engineering, Queen's University, Kingston, ON, Canada K7L 3N6

Björn Hermansson Swedish Telecom, S-123 86 Farsta, Sweden

Witold Bardyszewski Department of Electrical Engineering, Queen's University, Kingston, ON, Canada K7L 3N6, and Institute of Theoretical Physics, Warsaw University, Hoza 69, Warsaw, Poland

Moses Glasner Department of Mathematics, Penn State University 221 McAllister Building, University Park, PA 16802

While wide angle algorithms have recently been developed to describe the propagation of highly divergent beams, only the first non-trivial wide-angle procedure, which is limited to beam half-widths below about $35-40^\circ$, can be efficiently implemented with standard numerical procedures.[1, 2] To circumvent this limitation, Lanczos recursion[3, 4] may be applied to project the propagation operator at a given cross-section of the refractive index profile onto a restricted subspace comprised of a limited number of Lanczos functions. The resulting matrix is diagonalized in this subspace and the representation of the electric field in the Lanczos basis is propagated through multiplication by the suitably transformed eigenvalues.

We have accordingly performed numerical simulations of light propagation through a strongly-guiding semiconductor rib waveguide Y-junction using both Fresnel and Helmholtz implementations of the Lanczos method. We find that while the first of these is comparable in speed and accuracy to standard Fresnel propagation techniques, the Helmholtz version converges so slowly for z -dependent problems as to be of questionable practicality. We then postulated that the source of this numerical difficulty originated from the finite radius of convergence of the Helmholtz operator $\sqrt{1+H}$ which precludes an accurate global description by a Taylor series formed from the Krylov vectors associated with H itself. To test our assertion, we constructed wide-angle algorithms by expanding the square-root operator in a power series. While our procedure then does not correctly describe highly evanescent fields, we observed that numerical computations based on our method are, at least as concerns the losses of lower-order modes, as accurate as the full Helmholtz approach but require orders of magnitude less computation time. Further, we have observed that an additional increase

in computational speed can be achieved by evaluating the transverse derivatives with the aid of a finite difference rather than the standard fast Fourier transform procedure. The combination of our wide-angle and finite difference methods reduces the computation time by several orders of magnitude from that required to perform a full Helmholtz simulation with little observable degradation in accuracy. This algorithm should enable the practical evaluation of many physically interesting effects in semiconductor rib waveguides and other integrated optic components.

Subsequently, we applied Lanczos decomposition to the evaluation of the reflection operator and compared our results with split-operator approximations.[5, 6] An advantage of the Lanczos procedure in this context is that the reflected electric field is automatically decomposed into a small set of Lanczos modes enabling a rapid approximation of the power flux. Unfortunately, while we generate correct results in the limit of many basis functions, convergence is extremely slow if modes with near-zero propagation are appreciably excited, presumably again because of the finite radius of convergence of the square-root operators.

References

- [1] D. Yevick and M. Glasner, "An analysis of forward wide-angle light propagation in semiconductor rib waveguides and integrated optic structures," *Electron. Lett.*, vol. 25, pp. 1611-1613, 1989. erratum: vol. 25, p. 1747.
- [2] D. Yevick and M. Glasner, "Forward wide-angle wave propagation in semiconductor rib waveguides," *Optics Lett.*, vol. 15, pp. 174-176, 1990.
- [3] T. Park and J. Light, "Unitary quantum time evolution by iterative Lanczos reduction," *J. Chem. Phys.*, vol. 85, pp. 5870-5876, 1986.
- [4] R. Ratowsky and J. Fleck, "Accurate numerical solution of the Helmholtz equation by iterative Lanczos reduction," *Optics Letters*, vol. 11, pp. 787-789, 1991.
- [5] P. Kaczmarek and P. Lagasse, "Bidirectional beam propagation method," *Electron. Lett.*, vol. 24, pp. 675-676, 1988.
- [6] D. Yevick, W. Bardyszewski, B. Hermansson, and M. Glasner, "Split-operator electric field reflection techniques," *Photon. Technol. Lett.*, vol. 3, pp. 527-529, 1991.

WE2-1

Accurate Solution of the Helmholtz Equation by Lanczos Orthogonalization for Media with Loss or Gain

R. P. Ratowsky, J. A. Fleck, Jr., and M. D. Feit

Lawrence Livermore National Laboratory, Livermore, California 94550
510-422-4127

The Helmholtz equation plays a central role in the description of propagation phenomena in optics and acoustics. The paraxial approximation to the Helmholtz equation, also known as the paraxial wave equation, has long been the instrument of choice for performing calculations because it is amenable to solution by accurate marching techniques. The generation of accurate solutions to the unapproximated Helmholtz equation by marching, on the other hand, requires the evaluation of a square root operator applied to some initial field. By using an orthogonalization procedure due to Lanczos one can generate a low-dimensional representation, valid over a sufficiently short propagation step, which accurately diagonalizes the square root operator.¹

A shortcoming of this Lanczos propagation scheme is that it is restricted to Hermitian operators, which prohibits its use with imaginary refractive indices, representing gain or loss. This restriction excludes a wide class of interesting propagation applications. Even when loss is not explicitly included in the problem, it is customary to include loss in a border region along the grid boundary to prevent power from reflecting from the boundaries back into the interior of the computational grid. We will describe a generalization of the previous Lanczos Helmholtz solver that allows general complex refractive index distributions to be considered.

After factoring out a complex monochromatic carrier wave, one can without loss of generality write the Helmholtz equation as

$$\frac{\partial^2 \psi}{\partial z^2} + 2ik \frac{\partial \psi}{\partial z} + H\psi = 0 \quad (1)$$

where the operator H is defined by

$$H = \nabla_{\perp}^2 + k^2 \left(\frac{n(x,y,z)^2}{n_0^2} - 1 \right) , \quad (2)$$

and where $n(x,y,z) = n'(x,y,z)[1 + i\delta(x,y,z)]$ is a complex refractive index that varies weakly with z . Equation (1) is satisfied by two independent solutions corresponding to waves propagating to the right and to the left. The rightward propagating solution can be written formally as

$$\psi(z) = \exp\{-iz[k - k(1 + H/k^2)^{1/2}]\} \psi(0) . \quad (3)$$

One can evaluate Eq (3) by introducing a low-dimensional diagonal representation of the operator H . First one constructs a basis from the N

Krylov vectors $\psi(0)$, $H\psi(0)$, \dots , $H^{N-1}\psi(0)$, where the components of the vectors are the function values on the computational grid, and the second derivatives in H are evaluated by expressing $\psi(0)$ as a finite Fourier series. These vectors are independent but not orthonormal. Since the operator H is nonHermitian, the standard Lanczos orthogonalization procedure² is not appropriate for deriving an orthonormal set of vectors from the Krylov vectors. We therefore generalize the standard Lanczos procedure as follows.

We define a set of "right" column vectors $|q_0\rangle, \dots, |q_{N-1}\rangle$ and a set of "left" row vectors $\langle q'_0|, \dots, \langle q'_{N-1}|$. The orthogonality for the different vectors is defined by the relation

$$\langle q'_n | q_n \rangle = \delta_{nn} \quad (4)$$

The lefthand side of Eq. (4) signifies an inner product between $\langle q'_n |$ and $|q_n\rangle$, where the components of $\langle q'_n |$ and $|q_n\rangle$ are in general not the complex conjugates of each other, as they are when H is Hermitian. The following pair of recursion relations generalizes the standard Lanczos orthogonalization procedure² and leads to a symmetric matrix representation of H :

$$\beta_n |q_{n+1}\rangle = H|q_n\rangle - \alpha_n |q_n\rangle - \beta_{n-1} |q_{n-1}\rangle \quad (5a)$$

$$\langle q'_{n+1} | \beta_n = \langle q'_n | H - \alpha_n \langle q'_n | - \beta_{n-1} \langle q'_{n-1} | \quad (5b)$$

where $|q_0\rangle = \psi(0)$, $\langle q'_0| = \psi^*(0)$, $\alpha_n = \langle q'_n | H | q_n \rangle$, $\beta_{-1} = 0$, and $\beta_n = \langle q'_n | H | q_{n+1} \rangle = \langle q'_{n+1} | H | q_n \rangle$. To compute $\langle q'_n | H$ in Eq. (7b) one makes use of the relation $\langle q'_n | H = \{H^\dagger [\langle q'_n |]^\dagger\}^\dagger$, where H^\dagger represents the Hermitian conjugate of the operator in Eq. (3), and the remaining \dagger symbols signify the complex conjugate transpose of the indicated vector.

The matrix elements $\langle q'_n | H | q_n \rangle$ form an N -dimensional tri-diagonal complex symmetric representation of the operator H . The matrix, which we call \mathbf{H}_N , can be reduced to diagonal form by the operation $\mathbf{B}' = \text{diag}[\beta'_0, \beta'_1, \dots, \beta'_{N-1}] = \mathbf{U} \mathbf{H}_N \mathbf{U}^{-1}$, where $\mathbf{U} \mathbf{U}^{-1} = \mathbf{1}$. Here $\mathbf{U} = [\mathbf{u}_0, \mathbf{u}_1, \dots, \mathbf{u}_{N-1}]$, where the \mathbf{u}_n are the eigenvectors of \mathbf{H} , and \mathbf{U}^{-1} is the transpose (without conjugation) of \mathbf{U} . In this representation Eq (3) can be evaluated using the relation

$$\psi(\Delta z) = \mathbf{U}^{-1} \exp\{-iz[k - k(1 + \mathbf{B}'/k^2)^{1/2}]\} \mathbf{U} \psi(0) \quad (6)$$

Equation (6) generates accurate numerical solutions to the Helmholtz equation, including either loss or gain, and is extendable to arbitrary order.

REFERENCES

1. R. P. Ratowsky and J. A. Fleck, Jr., *Optics Lett.*, **16**, 787 (1991)
2. N. S. Sehmi, *Large Order Structural Eigenanalysis for Finite Element Systems* (Halsted Press: a division of John Wiley and Sons New York, 1989) pp 48-69.

Wide-Angle Beam Propagation with a Transparent Boundary Condition

G. Ronald Hadley
 Sandia National Laboratories
 Albuquerque, New Mexico 87185-5800
 (505) 844-4015

SUMMARY

We present a new beam propagation algorithm based upon a Pade approximation of the propagation operator that is accurate at angles of up to 65 degrees from the propagation axis. Ours represents an alternate approach to previous work[1] in which the square root Helmholtz operator was first expanded and then approximated. In contrast, we define the various Pade approximants more directly (and accurately) from the recursion formula

$$\left. \frac{\partial}{\partial z} \right|_n = \frac{\frac{iP}{2k}}{1 - \frac{i}{2k} \left. \frac{\partial}{\partial z} \right|_{n-1}} \quad (1)$$

where P is the operator $\nabla^2 + k_0^2 \frac{\epsilon}{\epsilon_0} - k^2$, k_0 is the vacuum wave vector, and k is the input propagation constant. Centered difference equations based upon higher order (n,n) Pade approximants result in algorithms that allow larger off-axis propagation angles as shown in Fig. 1. The penalty incurred for their use is a matrix whose bandwidth is $2n+1$. However, such a matrix can be easily solved (for 2-dimensional problems) using a simple generalization of the common Thomas algorithm, which for $n=2$ runs at about 70% of the paraxial speed. More importantly, these schemes allow the use of general boundary conditions, and we have successfully implemented the transparent boundary condition algorithm reported previously[2] for the pentadiagonal formulation using a $(2,2)$ Pade approximation. The generalization of this scheme to 3D requires the solution of block pentadiagonal matrices, which will become more attractive with increases in available computational speed. In the meantime, 3D propagation can still be accomplished with split-step schemes if wide angles are expected in only one dimension.

We illustrate the utility of this scheme for 2D problems by calculating the energy transmission of a Y-guide made from a single-mode waveguide, using reflecting facets[3] to allow large angles and thus short device lengths. As can be seen in Fig. 2, large-angle devices can demonstrate reasonable transmissions provided the reflecting facets are deep-etched to produce total reflection. We expect even better performance after further optimization (impossible with a paraxial formalism) is completed using this $(2-2)$ Pade-based wide-angle scheme.

1. D. Yevick and M. Glasner, Opt. Lett. 15(3), 174(1990).
2. G. R. Hadley, Opt. Lett. 16(9), 624(1991).
3. F. S. Chu, P. L. Liu, S. L. Jia, and P. J. Cressman, Proc. of Conf. on Lasers and Electrooptics, Nov. 4, 1990, Boston, MA, paper ThY27.

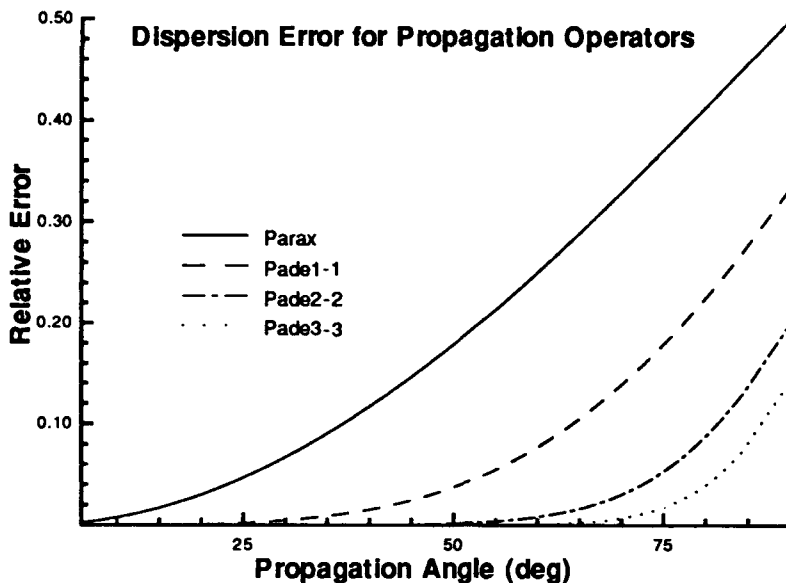


Fig. 1. Relative dispersion error incurred using various operators as a function of propagation angle relative to the propagation axis. These curves

assume that the input propagation constant is given by $k = k_0 \sqrt{\frac{\epsilon}{\epsilon_0}}$

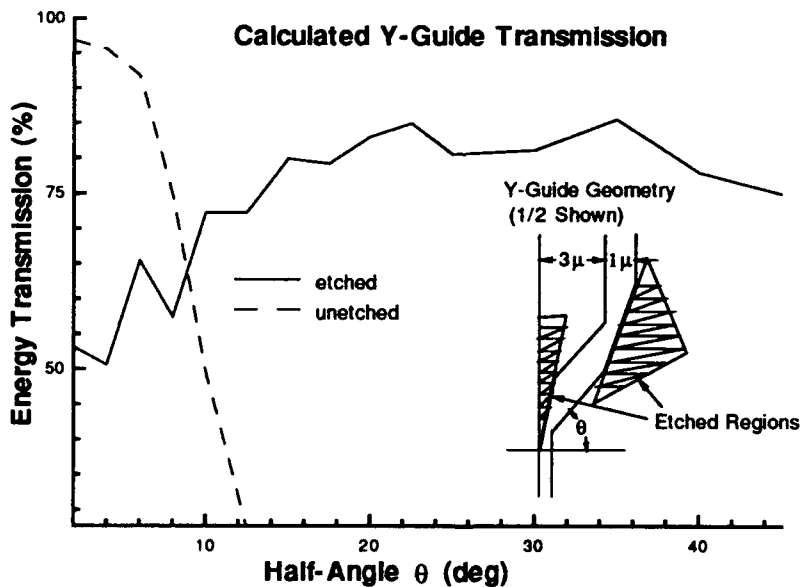


Fig. 2. Fraction of fundamental mode power remaining after traversing the Y-guide shown. The calculations assumed a simple rib waveguide with effective indexes of 3.4094 and 3.34 confining light of wavelength 1.55 micrometers. The curve marked "etched" refers to the use of highly reflective facets produced by etching through the active region in the shaded areas shown.

A non-iterative bidirectional beam propagation method

Youngchul Chung and Nadir Dagli
 Department of Electrical and Computer Engineering
 University of California, Santa Barbara, CA 93106 (805) 893-4847

For the analysis and optimization of guided-wave optoelectronic devices, efficient modeling techniques are essential. For this purpose the Beam Propagation Method (BPM) is widely used [1]. However, BPM has certain limitations, one of which is its applicability only to forward beam propagation. As a result, the BPM cannot handle structures with multiple discontinuities with strong reflections along the direction of propagation. To eliminate this difficulty a bidirectional BPM was introduced [2]. This is essentially an iterative scheme, in which multiple reflections are kept track of until a self consistent steady state is reached. Although this approach can analyze structures with limited number of discontinuities, it is not very suitable to analyze structures with multiple discontinuities, such as gratings both due to difficulty of implementation as well as large computational effort. The most commonly used method that can naturally include the reflection from discontinuities is the finite-difference time-domain (FDTD) method [3]. However, the FDTD method needs quite a lot of memory and computing time, which are usually an order of magnitude larger than the BPM. Therefore, it is very desirable to develop a beam propagation technique which can model backward optical wave as well as forward going wave in a simple way. The aim of this paper is to introduce such a method.

In our approach we propagate the beam from output back to input as schematically shown in figure 1. At the output of the structure we assume that there are no further longitudinal discontinuities, and only a forward traveling beam is present. This beam is propagated backwards until a longitudinal index discontinuity is encountered. The discontinuity is modeled with a transmission matrix, which relates the forward and backward traveling waves on either side to one another. Hence going right to left across this discontinuity we find the field amplitudes of forward and backward traveling waves on the left hand side of the discontinuity. It is well known that in an index distribution that doesn't vary longitudinally under paraxial approximation one obtains two decoupled paraxial wave equations each describing forward and reverse wave propagation. This allows us to trace the forward and backward traveling beams on the left side of the discontinuity back until the next discontinuity on the left is encountered. This process goes on until the input is reached. Then a simple argument reveals that if the structure is excited with the forward traveling beam obtained at the input, the reflection and the transmission due to this excitation are the backward traveling wave at the input and the forward traveling wave at the output respectively. As can be seen this approach doesn't require any iterations or keeping track of each multiple reflection, because going backwards from output to input at any point we calculate the steady state forward and backward traveling waves.

The transmission matrix for the longitudinal discontinuity involves the calculation of reflections from interfaces with inhomogeneous transverse index profiles, which usually consist of several homogeneous segments. This problem is studied by Yevick et. al. and it is shown that the reflections can be accurately calculated by reflecting the incoming optical field within each homogeneous transverse segment independent of the reflection in all the other segments [4]. This works very well when the dimension of the each segment is larger than the light wavelength[4]. We adopt this approach with a further simplification. Since the optical propagation in the practical waveguide is paraxial, we may ignore the transverse Laplacian operator in the reflection operator of reference 4 and treat the reflection as the normal incidence plane wave reflection. The bottom of Figure 1 schematically shows how this is implemented in a mesh configuration. The forward and backward traveling optical fields just in the left hand side of p- and q-th mesh point (E_{pq}^{+1} and E_{pq}^{-1} respectively) can be calculated by multiplying the forward and backward

traveling optical fields in the right hand side of p- and q-th mesh point (E_{pq}^{+r} and E_{pq}^{-r} respectively) by the transmission matrix as follows:

$$\begin{pmatrix} E_{pq}^{+1} \\ E_{pq}^{-1} \end{pmatrix} = \begin{pmatrix} P_{11} & P_{12} \\ P_{12} & P_{11} \end{pmatrix} \begin{pmatrix} E_{pq}^{+r} \\ E_{pq}^{-r} \end{pmatrix}$$

where $P_{11} = (n_{p,q-1} + n_{p,q})/2n_{p,q-1}$ and $P_{12} = (n_{p,q-1} - n_{p,q})/2n_{p,q-1}$. The propagation of forward and backward wave in the local continuous medium can be calculated using standard BPMs.

For the verification of the proposed method, the reflection from the volume index grating shown in the inset of Figure 2 was calculated using the present technique and the result was compared with semivectorial finite-difference

time-domain result [3]. At the beginning of the calculation we assume the eigenmode of the three layer slab guide with core index 1.55 as the outgoing wave at the output of the structure. Then we apply the proposed procedure until the input of the grating is reached. At the input the overlap integral of forward and backward waves with the eigenmode of the slab guide is performed to evaluate the reflection. The reflection coefficient obtained this way is found to be independent of the starting outgoing field profile at the output. As a beam propagation algorithm a finite difference BPM was used [5]. The comparison in Figure 2 shows the excellent agreement between the two methods. The extension of the present bidirectional BPM to the three dimensional structure is straight forward. As an example, we consider the volume index grating made of circular waveguides whose longitudinal sectional profile is the same as shown in the inset of Figure 2. As a beam propagation technique the split-step finite difference BPM was used [1]. The reflection as a function of wavelength is calculated and shown with dotted lines in Figure 2. The position of the peak is shifted toward shorter wavelengths. The magnitude of reflection is also reduced because the optical mode sees a smaller area of discontinuity than in the slab grating. All the 3-dimensional calculations are done on a SUN SPARC workstation and the reflection calculation at each wavelength takes about 25 minutes. The three-dimensional analysis is particularly suited to the analysis and design of surface emitting lasers and modulators, which is currently under investigation.

References

- [1] D. Yevick and B. Hermansson, *IEEE J. Quantum Electron.*, Vol. 26, pp. 109-112, 1990.
- [2] P. Kaczmariski and P. E. Lagasse, *Electronics Lett.*, Vol. 24, No. 11, pp. 675-676, 26th May 1988.
- [3] W.P. Huang, S.T. Chu, and S.K. Chaudhuri, *IEEE Photon. Technol. Lett.*, Vol. 3, No. 9, pp. 803-806, 1991.
- [4] D. Yevick, Witold Bardyszewski, B. Hermansson, and M. Glasner, *IEEE Photon. Technol. Lett.*, Vol. 3, No. 6, pp. 527-529, 1991.
- [5] Y. Chung and N. Dagli, *IEEE J. Quantum Electron.*, Vol. 26, pp. 1335-1339, 1990.

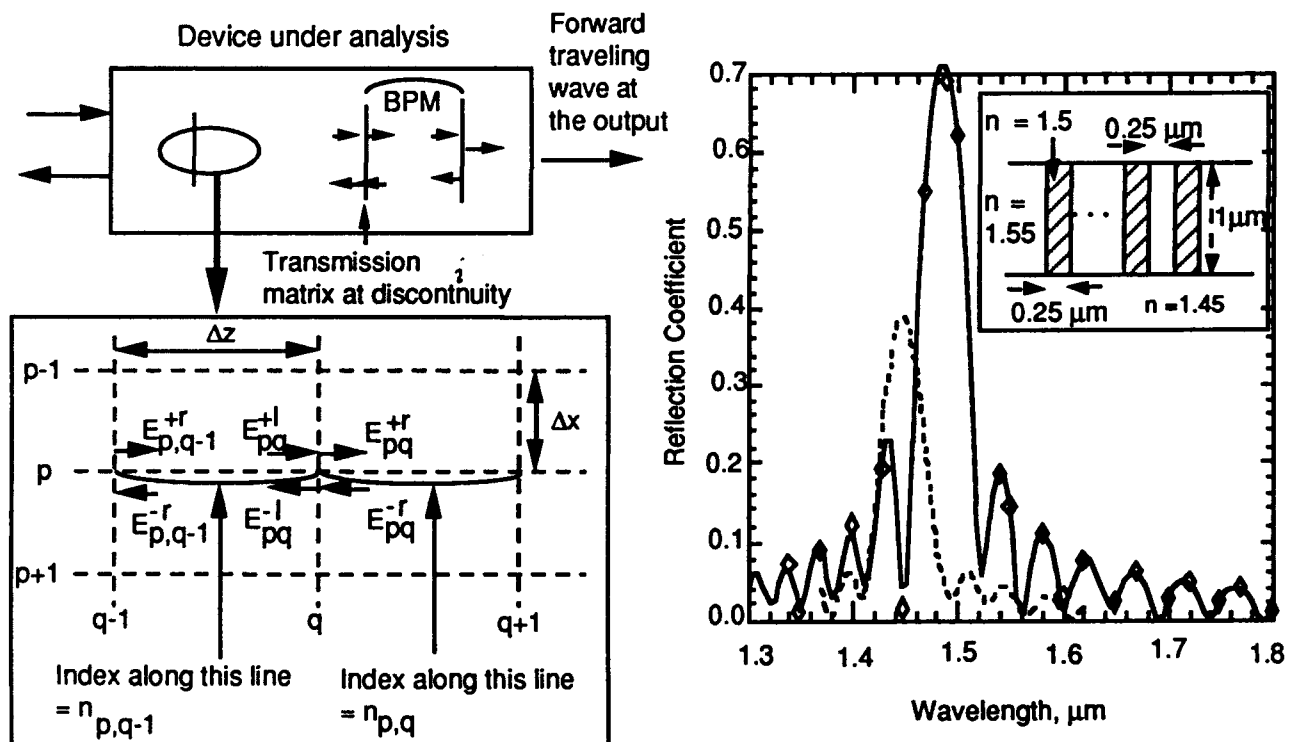


Figure 1 Schematic outlining the proposed algorithm.

Figure 2. The reflection coefficients calculated from the present technique and from the finite-difference time-domain method(diamonds). The dotted line shows the reflection coefficients for circular grating which is described in the text. The inset shows the configuration of the volume index grating analyzed. The grating has 40 periods.

Series-Expansion-Beam-Propagation-Method for the vector wave equation

M. Bothe, A. Splett, D. Uhlendorf, K. Petermann,

Institut für Hochfrequenztechnik, Technische Universität Berlin, Einsteinufer 25,
D-1000 Berlin 10, F.R.G., Tel. 49-30-314-22437

Recently, there has been much interest in solving the vector wave equation by beam-propagation-method-type algorithms [1][2][3][4]. Most of the proposed algorithms are based on scalar propagation algorithms which suffer from accuracy limitations for large propagation steps. Implicite formulations involving a Crank-Nicholson scheme[3] or similar methods[4] become more complex in a two-dimensional cross-section. In this work it is shown, that a recently proposed beam propagation method[5] using a rigorous Taylor-series expansion can be used to solve the vector wave equation with high accuracy and without major changes in calculation effort.

Starting with the vector wave equation for the magnetic field

$$\nabla \times (n^{-2} \cdot \nabla \times \mathbf{H}) = k_0^2 \cdot \mathbf{H} \quad (1)$$

two transversal components $H_x \cdot \exp(-jk_0 n_e z)$ and $H_y \cdot \exp(-jk_0 n_e z)$ describe the whole vector field. With the paraxial approximation $\partial_{zz} H_x \approx 0$, $\partial_{zz} H_y \approx 0$ we obtain

$$\partial_z \begin{pmatrix} H_x \\ H_y \end{pmatrix} = \underbrace{\begin{pmatrix} A_{xx} & A_{xy} \\ A_{yx} & A_{yy} \end{pmatrix}}_{\mathbf{A}} \begin{pmatrix} H_x \\ H_y \end{pmatrix} \quad (2)$$

with

$$A_{xx} = \frac{-j}{2k_0 n_e} [\partial_{xx} + \partial_{yy} + k_0^2 (n^2 - n_e^2) + n^2 (\partial_y n^{-2}) \partial_y] \quad (3)$$

$$A_{xy} = \frac{j}{2k_0 n_e} n^2 (\partial_y n^{-2}) \partial_x \quad (4)$$

$$A_{yx} = \frac{j}{2k_0 n_e} n^2 (\partial_x n^{-2}) \partial_y \quad (5)$$

$$A_{yy} = \frac{-j}{2k_0 n_e} [\partial_{xx} + \partial_{yy} + k_0^2 (n^2 - n_e^2) + n^2 (\partial_x n^{-2}) \partial_x]. \quad (6)$$

The solution of the first order differential equation

$$\begin{pmatrix} H_x \\ H_y \end{pmatrix} (x, y, z + \Delta z) = \exp(\mathbf{A} \Delta z) \begin{pmatrix} H_x \\ H_y \end{pmatrix} (x, y, z) \quad (7)$$

is explicitly evaluated by a rigorous Taylor expansion

$$\exp(\mathbf{A} \Delta z) = \sum_{\nu=0}^N \frac{\mathbf{A}^\nu}{\nu!} \Delta z^\nu + O(\Delta z^{N+1}) \quad (8)$$

where N is adaptively chosen for a certain required accuracy.

The series expansion requires the multiple application of the operator A during one propagation step, therefore a simple approximation of all transversal differential operators is important for a short calculation time. It can be shown, that the following approximations yield solutions which approximate the analytical solutions for small grid spacing $\Delta x, \Delta y$.

$$(\partial_{xx}H)_i \approx \frac{H_{i+1} - 2H_i + H_{i-1}}{\Delta x^2} \tag{9}$$

$$(\partial_x H)_i \approx \frac{H_{i+1} - H_{i-1}}{2\Delta x} \tag{10}$$

$$(n^2 \partial_x n^{-2})_i \approx \frac{n_{i-1}^2 - n_{i+1}^2}{(0.5n_{i+1}^2 + n_i^2 + 0.5n_{i-1}^2)\Delta x} \tag{11}$$

Here H_i applies to either $H_x(i \cdot \Delta x)$ or $H_y(i \cdot \Delta x)$. Equivalent expressions can be obtained for ∂_y and ∂_{yy} .

As an example the correct propagation with this finite-difference operators is shown for TM-polarization in the one dimensional case ($H_x = 0, \partial_y = 0$).

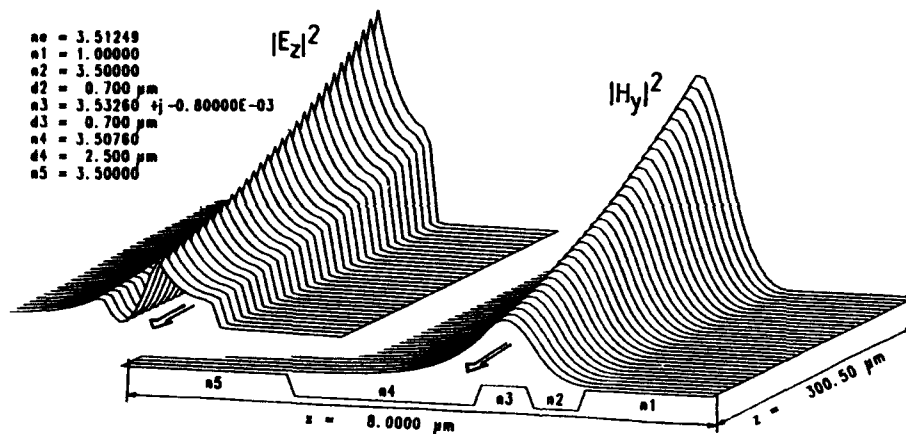


Figure 1: Propagation of the TM-eigenmode in an absorbing slab waveguide

The analytically calculated TM-eigenmode propagates stably in the slab waveguide with a high refractive index step at the surface. Even with absorbing layers and complex refractive indices the simulation behaves as expected. Instabilities are not observed.

References

- [1] J.S. Gu, W. Vogt, H. Melchior: ECOC 1991, pp.233-236
- [2] Y. Chung, N. Dagli, IEEE J.Quantum Electr., 1991, QE-27, pp.2296-2305
- [3] O.J.F. Martin, R. Clauberg, P. van Allmen: ECOC 1991, pp.281-284
- [4] W.P. Huang, C.L. Xu, S.T. Chu, S.K. Chaudhuri: IEEE Photon.Techn.Lett., 1991, 3, pp.910-913
- [5] A.Splett, M.Majd, K. Petermann: IEEE Photon.Techn.Lett., 1991, 3, pp.466-468

An Adaptive Approach to a Beam Propagation Method

F. Schmidt
Konrad-Zuse-Zentrum für
Informationstechnik Berlin
Heilbronner Straße 10
D-1000 Berlin 31
Tel. ++030 89604 170

H.-P. Nolting
Heinrich-Hertz-Institut für
Nachrichtentechnik Berlin
Einsteinufer 37
D-1000 Berlin 10
Tel. ++030 31002 427

1 Introduction

Most of the approaches to BPM use a fixed grid for the numerical discretization. In our opinion, it should be much more efficient in many cases, to generate a space grid during the simulation, which depends on the geometry of the structure and the actual computed field solution. In general, such adaptive generated grid will be highly nonuniform. As a first step to complete 3D adaptivity, an adaptive discretization of a 1D cross section is presented to investigate fundamental mathematical problems.

2 Algorithm

Like the conventional BPM, our algorithm is based on a stepwise calculation of a propagating field. But for the determination of the transverse field distribution the Finite-Element Method is used. Every new propagation step requires a complete new discretization of the cross section. The procedure starts with a very rough grid, containing only grid points (nodes) at positions, where the original structure has significant refractive index changes. For this fundamental grid, a first solution is computed. Now the errors belonging to every finite element are estimated by comparing solutions of different order. Elements with too large local errors are subdivided. The grid refinement is repeated, until the estimated discretization error is lower than a given tolerance.

3 Numerical Example

For a demonstration, we use the simple example of two butt coupled slab waveguides. The input waveguide has a thickness of 50nm and a refractive index $n_{in} = n_0 + 0.089$, the output waveguide has a thickness of $5.0\mu\text{m}$ and a refractive index $n_{out} = n_0 + 0.012$, where $n_0 = 3.169$ is the refractive index of the substrate ($\lambda = 1.55\mu\text{m}$, TE-polarization). Fig. 1 shows the simulated field distribution. The field propagates in z-direction, the butt coupling is located at $z = 50\mu\text{m}$. With a tolerance of $5 \cdot 10^{-3}$ our algorithm uses about 50 nodes in x-direction to propagate the field along the thin waveguide. An algorithm based on a uniform grid should need a minimum of 2800 nodes using a discretization of 25nm for the same result.

Fig. 2 shows the same simulation, but now only the position of nodes is plotted. It is seen, that the algorithm reacts very sensitively to the changing field distribution at the abrupt waveguide change. The nodes move with the locations of higher field intensities. Due to the adaptive realization, only nodes are used, which are necessary to fulfil the tolerance requirements.

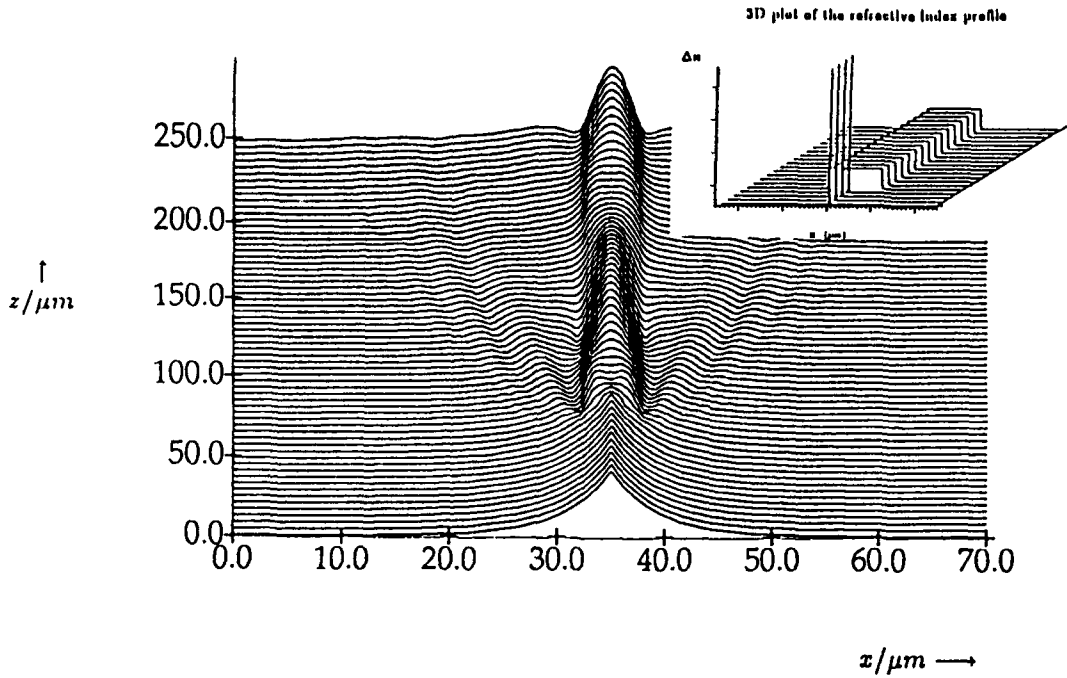


Fig. 1 Butt coupling of two different slab waveguides

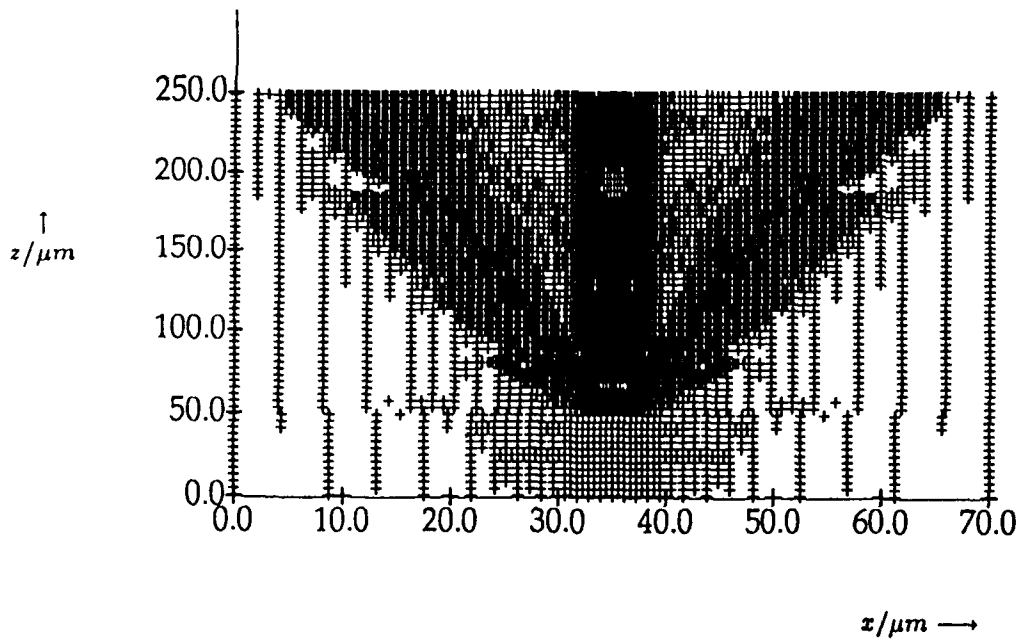


Fig. 2 Distribution of nodes generated by the adaptive algorithm

4 Reference

Bornemann, F.: *Adaptive multilevel discretization in time and space for parabolic partial differential equations*. Technical Report TR 89-7, Konrad-Zuse-Zentrum für Informationstechnik Berlin, November 1989

Wednesday, April 15, 1992

Lasers: 2

WF 11:00 am–12:15 pm
Pelican Room

Kam-Yin Lau, *Presider*
University of California at Berkeley

Wide Tunability and Large Mode-Suppression in a Multi-section Semiconductor Laser using Sampled Gratings

V. Jayaraman, L.A. Coldren, and S. Denbaars
Department of Electrical and Computer Engineering
University of California at Santa Barbara, CA 93106, (805) 893-8465

A. Mathur and P.D. Dapkus
Department of Electrical Engineering Electrophysics
University of Southern California, Los Angeles, CA 90089-0483, (213) 740-4390

Summary

We have recently proposed [1,2] a 4-section semiconductor laser which is capable of tuning over several tens of nanometers. A schematic of this device is shown in Fig. 1, along with the reflection spectra of the two mirrors which form the backbone of this device. These two mirrors consist of "sampled" gratings with mismatched periodic reflection spectra, as indicated in Fig. 1. Lasing in this structure occurs where two reflection maxima are aligned. By inducing index changes in one mirror relative to the other, adjacent reflectivity maxima can be brought into alignment, resulting in wide-range discontinuous tuning with very small index changes. Wavelength coverage between the maxima can be obtained by inducing identical index changes in the two mirrors, and adjusting the phase-shifter appropriately, much like 3-section lasers [3].

For our initial concept demonstration [2], we fabricated an all-active 2-section structure using liquid phase epitaxy (LPE). This device exhibited 29.3 nm of tuning but only 10 dB of mode suppression due to a weak grating. More recently, we have fabricated devices using metal-organic chemical vapor deposition (MOCVD). These devices incorporate a large kappa grating and show correspondingly large mode-suppression. A schematic of our device structure is shown in Fig. 2. The device (fabricated as a 50 μ m broad-area stripe) has two sections, a multi-quantum well active region using 4 wells, and sampled gratings etched in the upper 1.38 quaternary layer with two sampling periods in the two sections. The device was tested as-cleaved, with no anti-reflection coatings. This device is designed to exhibit discontinuous tuning in multiples of approximately 7 nm, which corresponds to the spacing of maxima in the reflection spectrum, for the sampling period indicated in Fig. 2.

Figure 3 shows time-averaged optical spectra of our best device under pulsed operation at 4 single-mode locations (on a log scale) over a tuning range of 22 nm. As can be seen, the single-mode locations are separated by approximately 7 nm, and the mode suppression for 2 of the 4 spectra exceeds 40 dB. The tuning range in this all-active device is limited by carrier clamping, which occurs at fairly low carrier densities due to the strong grating and uncoated facet reflections. Such would not be the case, of course, in the "ideal" active/passive structure of Fig. 1. Simulations for the active/passive device predict roughly 50 nm of tuning. Our calculations also indicate that the tuning range can be significantly increased even in an all-active structure, by reducing the mismatch between sampled gratings and incorporating 3 instead of 2 sections. Such all-active structures, in addition to providing easily fabricated test vehicles for the sampled grating concept, also offer promise of reduced spontaneous emission and narrow linewidth. In this paper we will present experimental tuning results in structures with both 2 and 3 sections, and with optimized sampled grating parameters.

References

1. V. Jayaraman, D.A.Cohen, and L.A.Coldren, *Leos '91*, paper SDL15.5, San Jose, CA.
2. V. Jayaraman, D.A.Cohen, and L.A.Coldren, *Appl. Phys. Lett.*, to be published.
3. K. Kobayashi and I. Mito, *IEEE JLT*, vol. 6, no. 11, November 1988.

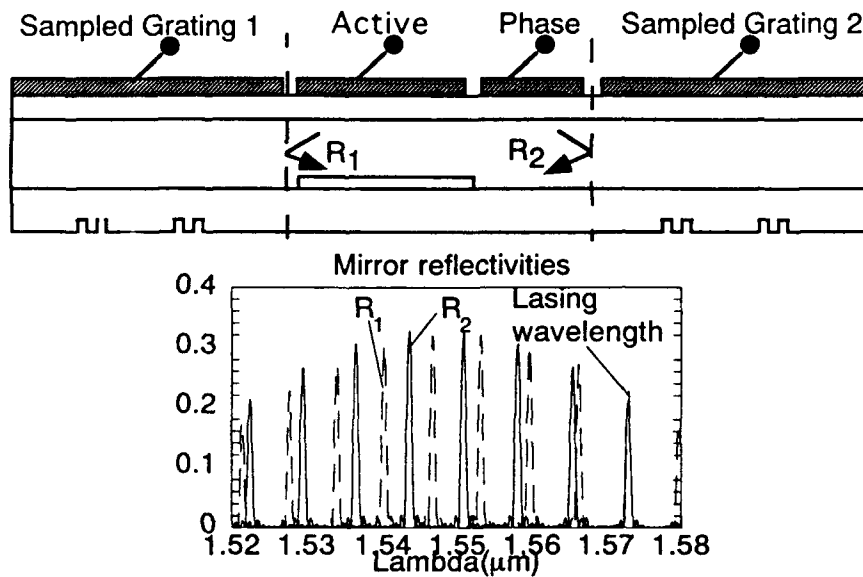


Figure 1: 4-section tunable laser and sampled grating reflectivity spectra

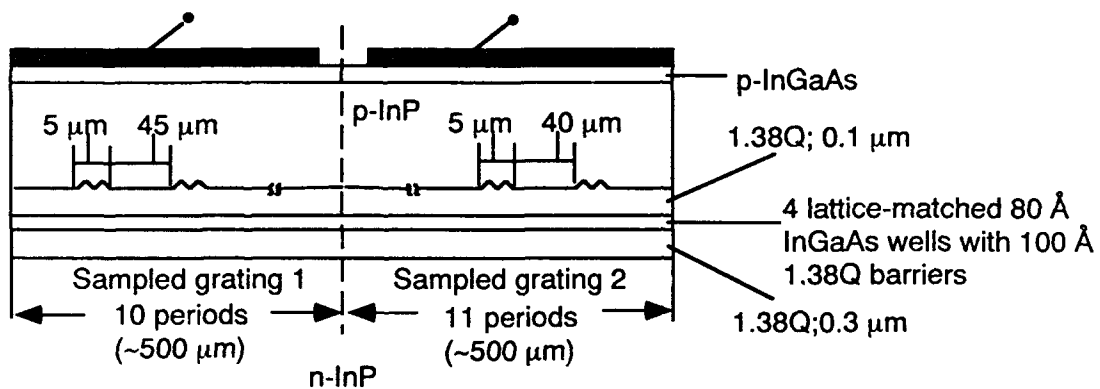


Figure 2: MOCVD-grown 2-section all-active sampled grating tunable laser

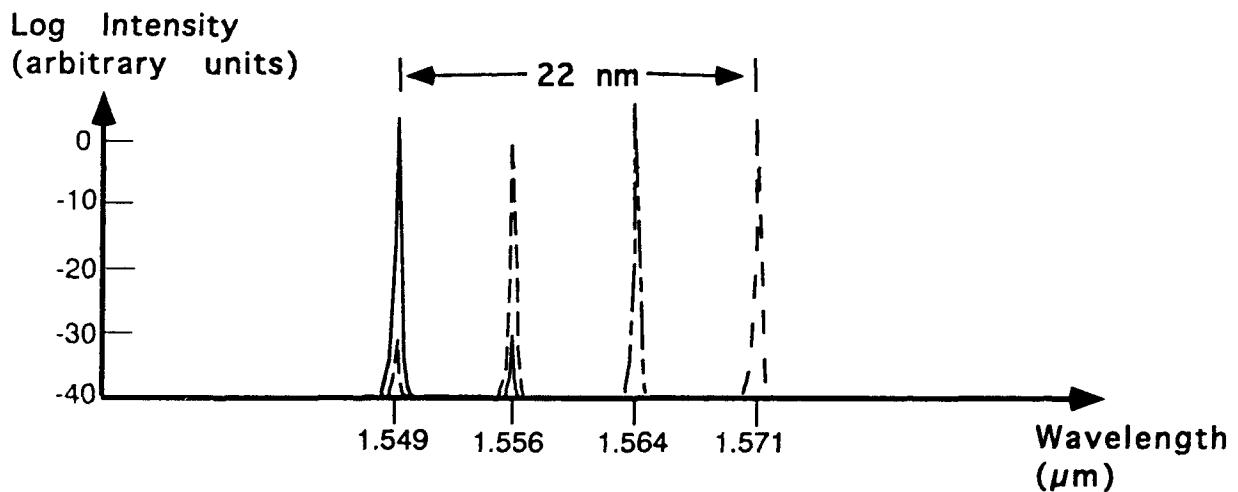


Figure 3: Time-averaged optical spectra for a broad-area device

WF2-1

Broadly Tunable InGaAsP/InP Laser Based on a
Vertical Coupler Filter with 57nm Tuning Range

by

R. C. Alferness, U. Koren, L. L. Buhl, B. I. Miller, M. G. Young,
T. L. Koch, G. Raybon* and C. A. Burrus*

AT&T Bell Laboratories
*Crawford Hill Laboratory
Holmdel, New Jersey 07733

Broadly tunable semiconductor lasers are important sources for a number of applications, especially wavelength division multiplexed networks and switching systems. Presently, the most developed monolithic tunable lasers, the distributed feedback (DFB) or distributed Bragg reflector (DBR), are limited to an $\sim 10\text{nm}$ electrical tuning range. By integrating a grating-assisted vertical coupler as a tunable intracavity filter in a novel active/passive monolithic laser, we have achieved a measured tuning range of 57nm.

A schematic of the novel tunable laser is shown in Fig. 1. It consists of a gain section (700 μm long) and monolithically integrated passive tunable filter (1.3mm long) and window (600 μm long) sections made with three metal organic vapor phase epitaxy (MOVPE) growth steps and processing similar to that previously described [1]. The upper waveguide of the vertical coupler filter (VCF) is a buried heterostructure formed with $\lambda\text{g} = 1.4 \mu\text{m}$ material (see Fig. 1 inset). This waveguide also forms the continuous buried rib waveguide upon which the multiple quantum well active layer (six 60 \AA thick InGaAs QWs separated by 80 \AA thick InGaAsP barriers) is grown to form the gain region. The MQW active layer is etched away in the other sections. In the window region following the filter this upper waveguide is terminated. The lower VCF waveguide is a buried rib made with $\lambda\text{g} = 1.1 \mu\text{m}$ core and rib material. This waveguide extends to the high reflection (HR) coated facet (Si/SiO₂). In the gain section (Fig. 1) the lower rib is not formed.

Wavelength selective coupling is achieved between the strongly asynchronous upper and lower waveguides in the VCF by the coarse phase match grating of $\lambda\text{g} = 1.4$ material above the upper waveguide [2]. The laser cavity is formed between the facet of the upper waveguide in the gain section and the HR mirror on the back facet of the lower waveguide. The lasing frequency is determined by that wavelength λ_0 which satisfied the forward coupling phase match condition, $\lambda_0 = \Lambda|N_2 - N_1|$ where Λ is the coarse grating period (16 μm) and N_1 are the effective indices of the two waveguides [2]. Light at this wavelength is coupled to the lower waveguide and reflected by the HR facet for the return trip. Wavelengths not coupled to the lower waveguide are strongly attenuated in the terminated upper waveguide. Tuning of the laser wavelength is achieved by either injecting current into or applying a reversed bias voltage to the upper waveguide of the VCF to decrease or increase, respectively, its index and change the coupled wavelength [3]. The filter center wavelength tunes continuously. The increased tuning range of this laser relative to a DFB or DBR laser results from the fact that the change in the filter center wavelength with induced index change for the VCF is much greater than it is for a reflection grating [3,2].

The CW light current characteristic of the laser with no tuning current is shown in Fig. 2. Threshold current of 85 mA with external quantum efficiency of about 7% and maximum output power higher than 6 mW were obtained. The below threshold spectrum clearly shows the vertical coupler filter response as a 30-50 \AA broad peak superimposed on the spontaneous emission spectrum, corresponding to the vertical coupler filter pass band transmission peak. The above threshold spectra at several tuning currents are shown in Fig. 3. Although the Fabry-Perot mode spacing of the entire cavity is only about 1.2 \AA , CW single mode operation could be maintained at most tuning currents. This might be aided by small internal reflections that help select some modes of the large cavity and depress others. The lasing wavelength as a function of the tuning current on the coupler electrode is

shown in Fig. 4. CW tuning currents as high as 0.95 A were used, but because the coupler section is 1.3 mm long, this does not lead to uncommonly high current densities. The tuning response shown in Fig. 4 for current injection is due to carrier induced index change. Thermal effects would cause an opposite (positive) tuning response. The temperature tuning of this laser was measured to be $+4.7\text{\AA}/\text{deg}$. The laser section was operated CW for most of the tuning range, but for the shortest wavelengths pulsed operation was used in order to obtain sufficient gain for lasing. Note that a total tuning range of 57 nm was obtained which is, to our knowledge, the highest yet reported for a monolithic device.

We note that very recently a tunable twin guide laser incorporating a vertical coupler filter was reported [4]. However, the short filter length ($200\ \mu\text{m}$) and rather coarse period ($\sim 40\ \mu\text{m}$) provides rather weak wavelength selectivity. Furthermore, the measured laser tuning to shorter wavelengths for current injection to the lower index waveguide and reversal to longer wavelengths for higher current is, we believe, inconsistent [3] with the expected tuning behavior of the VCF, suggesting that, perhaps, other effects may be operative.

In conclusion we have demonstrated a MQW tunable laser operating at $1.50\text{-}1.58\ \mu\text{m}$ wavelength with 57 nm tuning range. The laser employs an integrated, vertical coupler filter, using a built-in coarse grating to phase match between two different vertically separated waveguides.

REFERENCES

- [1] U. Koren, T. L. Koch, B. I. Miller, A. Shahar, Integrated and Guided Wave Optics (IGWO) Conference, paper MDD2, Houston, Texas, (1989).
- [2] R. C. Alferness, T. L. Koch, L. L. Buhl, F. Storz, F. Heismann, M. Martyak; *Appl. Phys. Letts.*, 55, pp. 2011-2013, 1989.
- [3] R. C. Alferness, L. L. Buhl, U. Koren, M. G. Young and T. L. Koch, Integrated Photonics Research, Monterey, CA, April, 1991.
- [4] S. Illek, W. Thulke, B. Borchert and M-C. Amann, IOOC'91/ECOC'91, 21 - 24, Paris, Sept. 1991.

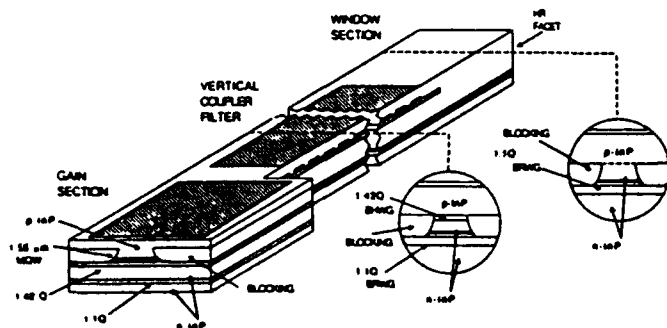


Fig. 1

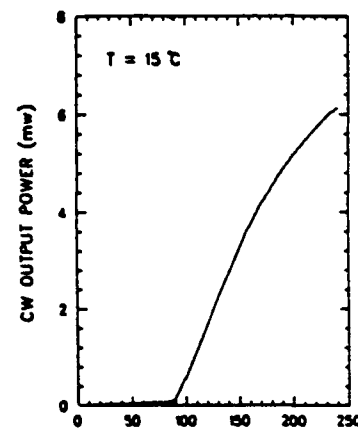


Fig. 2

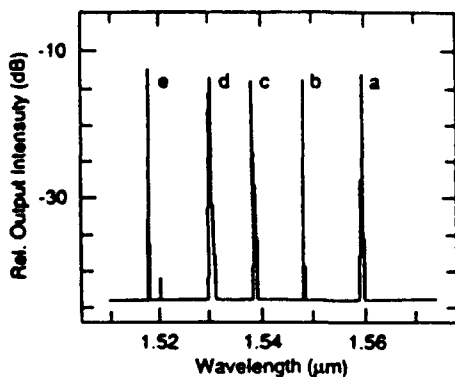


Fig. 3

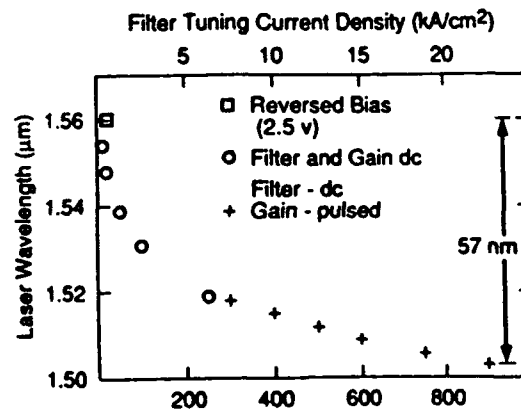


Fig. 4

Threshold Gain of a Grating-Assisted Codirectionally Coupled Twin-Guide Laser Diode

J. Willems, G. Morthier and R. Baets

University of Gent - IMEC, Laboratory of Electromagnetism and Acoustics
Sint-Pietersnieuwstraat 41, B-9000 Gent, Belgium (tel. : 32 91 64 33 16)

I. Introduction

Tunable lasers that cover a large wavelength range are important devices in wavelength division multiplexing applications. One promising structure is based on grating-assisted codirectional coupling [1] between two waveguides and has recently been fabricated [2]. This paper reports on the calculation of the threshold characteristics. An analytical expression has been derived, from which the threshold gain can be calculated. It turns out that lasing occurs at the wavelength of maximum coupling, only for not too large κL -values. This paper explains this behaviour. Furthermore the influence of the facet reflectivities is studied with respect to the threshold gain and the emission wavelength.

II. Threshold gain calculations

The structure of the analysed device is shown schematically in fig. 1. It consists of two asymmetric waveguides and a grating which performs a wavelength selective coupling between the two waveguide modes. Maximum coupling [3] occurs at the wavelength $\lambda_0 = \Lambda |n_{\text{eff}1} - n_{\text{eff}2}|$ with $n_{\text{eff}i}$ the effective refractive index of waveguide #i and Λ the grating period, typically 10-50 μm . This center wavelength can be tuned by changing the magnitude and the slope of the dispersion curve of the waveguides [4]. The potential tuning range is very large. Waveguide #1 is assumed to be active and can be biased by a current I. An absorber is placed at the right facet of waveguide #1 to prevent laser operation in waveguide #1. Using the coupled mode formulation for directional couplers with longitudinal perturbation [3], [5] an equation for the threshold gain is derived. The natural (i.e. non-grating-assisted) waveguide coupling is neglected. As pointed out in [3], this assumption is valid if the grating dominates the coupling process. With these assumptions we obtain :

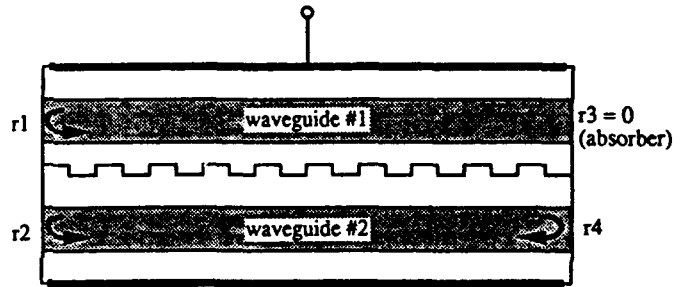


Fig. 1 Schematic of a codir. coupled laser

$$\left(r_1 r_4 \frac{\kappa^2}{p^2} \sin^2 pL - r_2 r_4 (\cos pL - j \frac{\gamma}{p} \sin pL)^2 \right) \exp(jL(\beta_0 + \beta_1)) = 1 \quad (1)$$

$$\text{with } \kappa = \sqrt{\kappa_{12} \kappa_{21}}, p^2 = \gamma^2 + \kappa^2, \gamma = \frac{1}{2}(\beta_1 - \beta_2) - \frac{\pi}{\Lambda} \text{ and } \beta_i = \frac{2\pi}{\lambda} n_{\text{eff}i} + \frac{1}{2}j(\alpha_{\text{int}} - \Gamma_i g_i)$$

κ_{ij} being the grating coupling coefficients from waveguide #i to #j, $\Gamma_i g_i$ and α_{int} being the modal gain and internal losses in waveguide #i. Obviously g_2 is zero and the gain in waveguide #1 is the threshold gain. We will focus on the amplitude of the LHS of (1). In order to calculate the exact lasing wavelength, one has to take into account the phase matching as well.

Two cases will be considered : $r_2 = 0$ and $r_2 \neq 0$. The other facets are assumed to be cleaved ($r_1 = r_4 = 0.566$).

If $r_2 = 0$, the second term in equation (1) vanishes. One would expect that the lasing wavelength is the wavelength λ_0 for maximum coupling. This is indeed the case if κL is small. Fig. 2a shows $g_{\text{th}}L$ versus δL , with $\delta L = \text{Re}(\gamma L)$ being a measure for the wavelength deviation from λ_0 . It is clear that the threshold gain will be smallest for $\kappa L = \pi/2$. The same curves are shown in fig. 2b for larger κL . At a certain κL -value the emission wavelength changes discontinuously : the lasing wavelength will strongly deviate from λ_0 , because the required

gain is smaller than for $\lambda = \lambda_0$. This behaviour can be explained by considering that three effects compete with each other in determining the threshold gain and the lasing wavelength :

1) the coupling efficiency is maximum at the wavelength where $\delta L = 0$; 2) the wavelength for which the coupling length equals the device length is favoured; 3) the optical field experiences gain only in waveguide #1. At low κL -values the coupling efficiency is relatively weak and any deviation from $\delta L = 0$ gives rise to a relatively large penalty in coupling to the active waveguide. Therefore the first effect dominates, explaining why the laser oscillates at the wavelength of maximum coupling. At higher κL -values however the coupling efficiency is strong and remains relatively strong even for deviations from $\delta L = 0$. Therefore effects 2 and 3 become more important now and lasing can occur at different wavelengths. The two minima in fig. 2b for high κL -values correspond to situations where the laser length equals approximately three coupling lengths. Considering the case of $r_2 \neq 0$, it turns out that for small κL -values the results are about identical to those for $r_2 = 0$ as can be seen by comparing fig. 2a and fig. 3a. From $\kappa L = \pi/2$ on, the effect of $r_2 \neq 0$ is apparent. Similar conclusions as for $r_2 = 0$ are valid : for large κL values the lasing wavelength will deviate from the maximum coupling wavelength (fig. 3b). But this occurs already for smaller κL -values.

III. Conclusions

We have calculated the threshold gain for a grating-assisted codirectionally coupled laser. It turns out that lasing does not necessarily occur at the wavelength of maximum coupling, especially if κL is large. This phenomenon has been explained by considering three competing effects that determine the threshold operation.

IV. Acknowledgement

This work is supported by the European RACE project R1069 (EPL0T).

V. References

- [1] Alferness R., Bul` L., Koren U., Miller B., Young M. and Koch T., Integrated Photonics Research, pp. PD8,1-PD8,7, Monterey, California, April 1991
- [2] Illek S., Thulke W., Borchert B. and Amann M.-C., Post-Deadline papers ECOC-IOOC '91, pp. 21-24, Paris, September 1991
- [3] Griffel G., Itzkovich M. and Hardy A., IEEE J. of Quantum Electronics, vol. 27, pp. 985-994, April 1991
- [4] Griffel G., Yariv A., IEEE J. of Quantum Electronics, vol. 27, pp. 1115-1118, May 1991
- [5] Huang W. and Haus H., J. of Lightwave Technology, vol. 7, pp. 920-924, June 1989

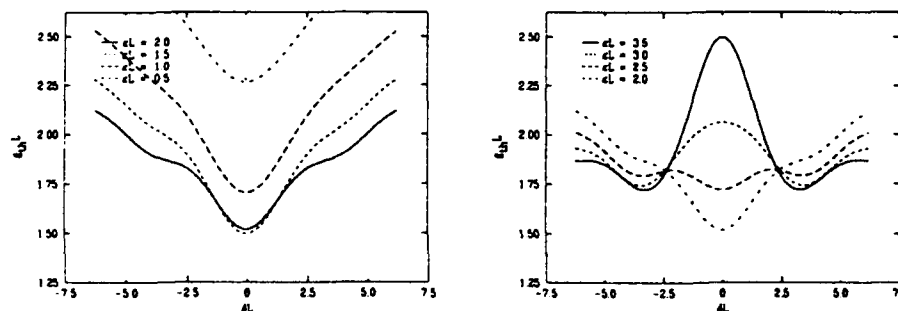


Fig. 2 Threshold gain versus $\delta L = \text{Re}(\gamma L)$ with κL as a parameter, for the case of $r_2 = 0$

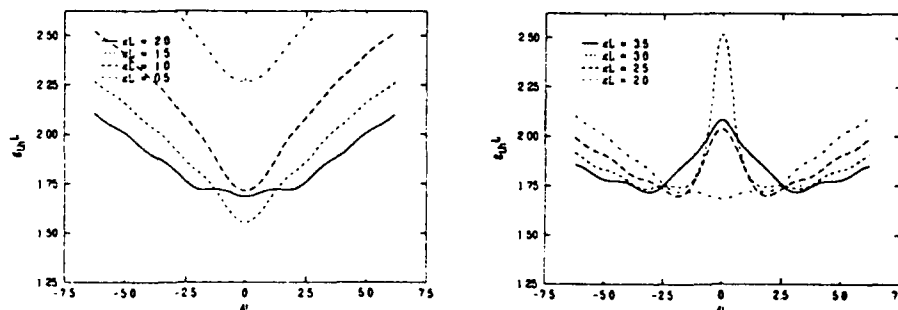


Fig. 3 Threshold gain versus δL with κL as a parameter, for the case of $r_2 = r_1 = 0.566$

A Compact 2X2 Amplifier Switch with Integrated DBR Lasers Operating at 1.55 Microns

M.G. Young, U. Koren, B.I. Miller, M. Chien, M.A. Newkirk, and J.M. Verdiell

AT&T Bell Laboratories, Holmdel N.J. 07733

The need for optical switching of data is becoming more apparent as fiber optical transmission is being used for telecommunication systems. Many groups have reported optical switching in semiconductor based devices, using either electro-optic effects[1] or optical amplifier gates[2]. Recently it has been shown, that by using an amplifier-based switching array, coupling losses can be recovered in addition to exhibiting high extinction ratios[3]. In this paper, we present the integration of a compact amplifier-based optical switch with distributed Bragg reflector lasers. This allows light from an integrated laser source to be spatially switched to one of two output ports.

The device was fabricated from a standard MOVPE-grown wafer used for long wavelength lasers[4]. An InGaAs/InGaAsP multiple quantum well stack with a wavelength of 1.55 μm was grown on top of 1.3 μm quaternary grating and waveguide layers. InP stop etch layers were placed at certain levels to allow selective wet chemical etching. After selectively removing the quantum wells in the passive sections, 3 μm wide buried-rib passive waveguides and DBR gratings were defined using standard photolithographic and holographic techniques. This was followed by two MOVPE regrowths. In the first regrowth, semi-insulating InP covered the passive waveguides and gratings and was used for current blocking in the active sections. In the second regrowth, p-type InP and InGaAs cladding and contact layers were grown. A schematic diagram of the device is shown in figure 1. The length of the DBR lasers and of the switch is 600 μm and 450 μm respectively. With the addition of the passive section, the total device length is 1200 μm . The total width of the device including the contact pads is 250 μm .

The device was tested under CW conditions using apparatused detectors and an infrared camera. Figure 2 shows the signal from one of the sources being switched between output ports, a separation of 30 μm . To achieve this switching, 50 mA bias current was used for either the "bar" amplifier, or the "cross" amplifier pair.

To investigate the characteristics of the device, the driving current of the lasers was varied while the current on the switching amplifiers was held constant. Figure 3 shows the L-I curve for one such device when operated in the "bar" (figure 3a.) and "cross" (figure 3b.) states. The laser was varied from 0 to 80 mA, while the amplifiers were held constant at 50 mA. Thresholds for the DBR lasers were typically 30 to 40 mA. When the lasers were operating below threshold, spontaneous emission from the amplifiers was still detected, leading to the non-zero baseline in the figures.

A plot of the output power as a function of current on the amplifier pair for the "cross state" is shown in figure 4 with the laser current held constant at 50 mA. Similar results were obtained for the "bar" state. A crosstalk, originating from scattered light, of approximately -12 dB is obtained for an applied current of 0 - 60 mA. In addition, it should be pointed out that the current applied to the amplifier pair to obtain 90% output is only 35 mA. This very low value, as well as the low current required for transparency, is due to the use of quantum wells in the amplifiers. These low current requirements make quantum well amplifiers useful for optical switching[5].

When 50 mA drive current is applied to the laser, approximately 3 mW was measured from the Bragg grating side on test samples. With 50 mA applied to the "cross" state amplifier pair, a total output power of 0.8 mW was measured (figure 4). Assuming a 2 dB gain in the amplifier, the insertion loss of the device is approximately 8 dB.

In conclusion, an amplifier based 2x2 switch monolithically integrated with two DBR lasers operating at 1.55 μm has been demonstrated for the first time. An insertion loss of approximately 8 dB in the device results in an output power of 0.8 mW when 50 mA is applied to the laser, and 50 mA is applied to the amplifiers. A crosstalk of -12 dB has been obtained, with switching from "bar" to "cross" states occurring at currents as low as 50 mA due to the use of quantum wells. In addition, the compact size allows for the realization of large scale switching arrays.

REFERENCES

- [1] Duthie et al., Proc. Topical Meeting on Photonic Switching, pp. 197-199, Salt Lake City, 1991
- [2] Eichen et al., Proc. Topical Meeting on Opt. Amp. and Their App., pp. 245-248, Snowmass Village, 1991
- [3] Janson et al., Post Deadline Proc. European Conference on Optical Communications, pp. 28-31, Paris, 1991
- [4] Koren et al., Integrated and Guided Wave Optics, paper MDD2, Houston, 1989
- [5] Koren et al., *Electron. Lett.*, 1991, 27, pp. 62-63

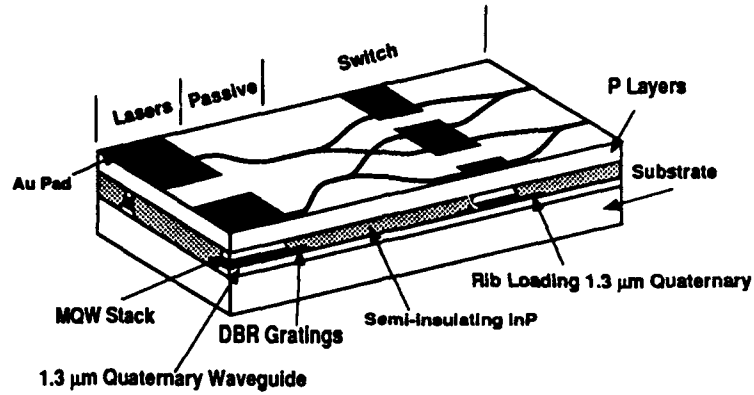


Figure 1. Schematic diagram of device. The lines indicate the paths of the waveguides.

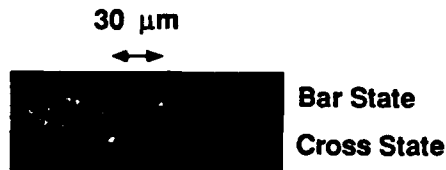


Figure 2. Operation of switch as seen by an infrared camera. Switching current was 50 mA.

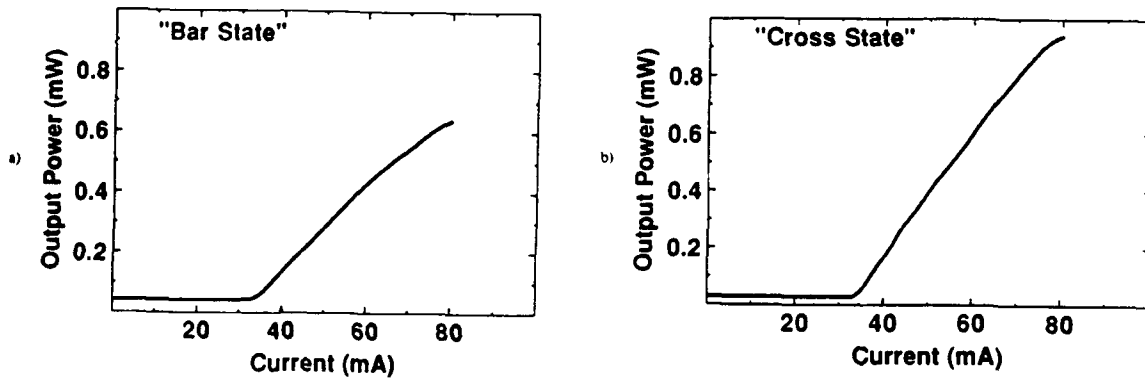


Figure 3. L-I curves of a DBR laser when current is applied to the a) "bar" amplifier b) "cross" amplifier.

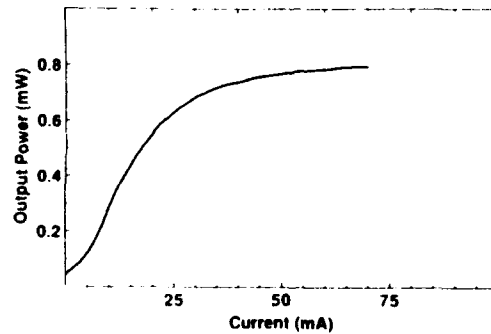


Figure 4. Gain curve of the multiple quantum well amplifier. 90% gain is achieved at approximately 35 mA.

Er-Diffused Ti:LiNbO₃ Waveguide Laser Emitting at 1563 and 1576nm Wavelength

P. BECKER, R. BRINKMANN, H. SUCHE, AND W. SOHLER

Angewandte Physik, Universität-GH Paderborn, Postfach 1621,
W-4790 Paderborn, Fed. Rep. Germany

Introduction

With Erbium-doped LiNbO₃ waveguides significant optical amplification in the wavelength range from 1.53 μ m to 1.62 μ m and lasing at 1.532 μ m have been demonstrated recently [1,2]. In this contribution simultaneous laser operation at 1563 and 1576nm wavelength is reported.

Waveguide and Cavity

Er-doping of Z-cut LiNbO₃ substrates has been done by indiffusion of an evaporated 10.9nm thick Er-layer at 1060°C during 41 hours. In the doped surface strip waveguides were subsequently fabricated by indiffusion of 8 μ m wide, 95nm thick Ti-strips at 1030°C for 9 hours. Diffusion at 1030°C (instead of 1060°C used earlier [2]) results in a single mode guide of significantly reduced effective mode area (26 μ m² for a TM-mode at λ =1.523 μ m instead of 39 μ m² [2]) and therefore in a better pump efficiency. At λ = 1.523 μ m an absorption coefficient of 0.6dB/cm and a waveguide scattering loss of about 0.1dB/cm were evaluated from transmission measurements with coherent (Fabry Perot method [3]) and incoherent light [4].

To develop a laser for longer emission wavelengths than the previously reported λ_s = 1.532 μ m, an appropriate cavity has to be designed with minimized round trip losses at the desired wavelengths. Simultaneously, increased losses at λ_s = 1.532 μ m are required to suppress laser action at this line of maximum gain (see the pump power dependent gain spectra presented in [1] and [4]).

Such a cavity was fabricated by depositing dielectric multilayer mirrors on the polished waveguide endfaces. Ion assisted reactive evaporation was used to improve the layer adhesion without degradation of the waveguide quality. To allow endfire pumping a dichroitic mirror of eight pairs of alternating SiO₂/TiO₂ layers, quarterwave at 1.8 μ m wavelength, was deposited onto the input face of the cavity. The output coupler consists of four pairs of SiO₂/TiO₂ layers, quarter-

wave at 1.48 μ m wavelength. The reflectance and transmittance of the input mirror is shown in Fig.1. The mirror transmittance is about 92% at 1.479 μ m and 83% at 1.484 μ m pump wavelength, respectively, whereas the reflectance at both laser emission wavelengths is about 98%. The output coupler has a reflectance of 93% around 1.48 μ m and about 92% at the laser emission wavelengths, respectively. Therefore about 75% of the output power is emitted in forward direction and the pump absorption is improved by a double pass in the cavity.

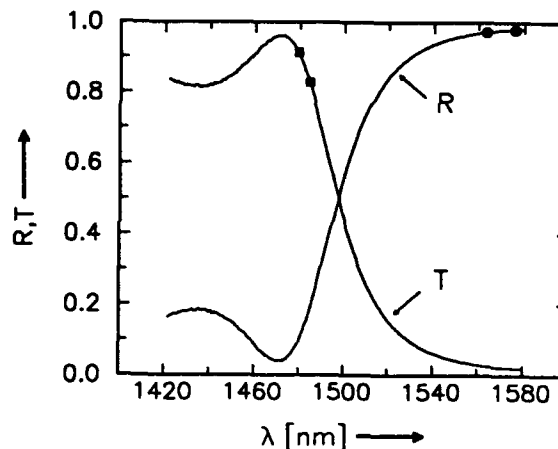


Fig. 1. Reflectance and transmittance of the dichroitic mirror on the input face of the laser. Pump (■) and emission wavelengths (●) are indicated.

Laser Operation

A tunable colour center laser was used to pump the Er-laser. The pump beam was launched into the waveguide cavity with an efficiency of about 50%.

As a result of the polarization dependent absorption of Er:LiNbO₃ the maximum laser efficiency was observed at 1479nm pump wavelength with TM- or π -polarized radiation whereas with TE- or σ -polarized pump light the maximum is slightly shifted to 1484nm. In Fig.2 a direct scan of the laser output power versus incident pump power is shown for cw operation and

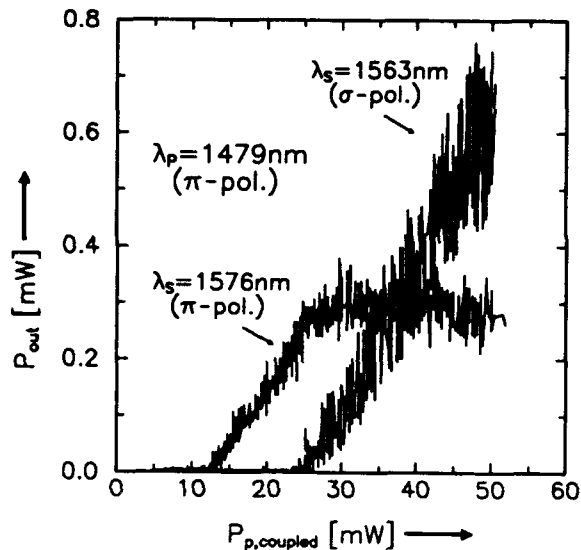


Fig. 2. Output power of the waveguide laser in forward direction versus coupled pump power ($\lambda_p=1479\text{nm}$; π -pol.).

π -polarized pumping. Lasing sets in at about 13mW coupled pump power with a π -polarized output at 1576nm wavelength. At about 25mW additional σ -polarized lasing at 1563nm starts. In the regime of simultaneous lasing at two wavelengths the output at 1576nm saturates. This behaviour is not yet understood and requires further investigations.

The "noise" of the laser power characteristics is mainly due to fluctuations of the emission spectrum of the pump laser during the power scan; the result is a frequency dependent resonant enhancement of the pump field in the waveguide cavity and therefore a frequency dependent pump absorption.

The spectrum of the waveguide laser at about 50mW coupled pump power is shown in Fig. 3. At this power level the σ -polarized output at 1563nm wavelength already exceeds the π -polarized output at $\lambda_s=1576\text{nm}$. By scanning the spectrum with a 5000 \times higher sensitivity the amplified spontaneous emission of the non-lasing transitions from the $^4I_{13/2}$ to the $^4I_{15/2}$ manifolds became apparent. At 1532nm (where lasing of the first Er:LiNbO₃ laser was demonstrated [2]), at 1547nm and 1602nm wavelength laser operation can be expected by an appropriate (wavelength selective) cavity design.

With σ -polarized pumping at $\lambda_p=1484\text{nm}$ a single line output at $\lambda_s = 1563\text{nm}$ is obtained with an even better efficiency. At about 115mW

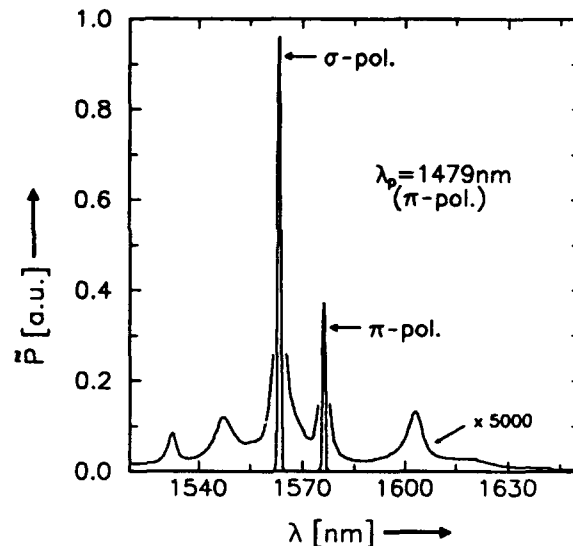


Fig. 3. Spectral power density \tilde{P} of the waveguide laser versus wavelength ($\lambda_p=1479\text{nm}$; π -pol.).

coupled pump power about 3mW output power were measured (cw) corresponding to a slope efficiency of 3% (the threshold pump power was about 22mW in this case).

The waveguide laser was also operated in a pulsed mode pumped with about 2 μs long (FWHM) pulses of the colour center laser. For π -polarized pulses of 1.6W peak power the waveguide laser emitted 110ns long (FWHM) pulses of up to 200mW peak power.

Conclusions

The cw-operation of an Er-doped waveguide laser in LiNbO₃ at new wavelengths and pulsed operation with a remarkable peak output power indicate a great potential for tunable and Q-switched lasers, respectively.

References

- [1] R. Brinkmann, W. Sohler, and H. Suche, *Proc. of the Intern. Conf. on Integr. Opt. and Opt. Comm.*, Paris 1991, pp. 157-160
- [2] R. Brinkmann, W. Sohler, and H. Suche, *Electron. Lett.*, **27**, 415 (1991)
- [3] R. Regener and W. Sohler, *Appl. Phys. B*, **36**, 143 (1985)
- [4] H. Suche, "Erbium-Doped LiNbO₃ Waveguide Amplifiers and Lasers", to appear in *NATO ASI series "Guided Wave Nonlinear Optics"*, R. Reinisch and D. B. Ostrowsky (eds.), Kluwer Academic Publishers, 1992

Diode Pumped, Garnet Channel Waveguide Lasers

A.C. Large, S.J. Field, D.C. Hanna, D.P. Shepherd, A.C. Tropper

Department of Physics and Optoelectronics Research Centre

University of Southampton

Southampton SO9 5NH, U.K.

Tel +44 703 595000

P.J. Chandler, P.D. Townsend, L. Zhang

School of Mathematical and Physical Sciences

University of Sussex

Brighton BN1 9QH, U.K.

Tel +44 273 606755

Summary

Ion implantation is a technique which can be used to form waveguides in a wide range of materials - including crystals of the garnet family for which no alternative techniques exist - by bombarding the material surface with high energy ions and altering the refractive index [1]. We report the use of this method to form channel waveguides in two Nd³⁺ doped materials; Nd:YAG and Nd:GGG both of which have operated as ion implanted planar waveguide lasers [2,3]. The additional confinement in the plane is achieved without any significant increase in propagation losses, which are comparable in the planar and channel guides. In the Nd:YAG system submilliwatt thresholds were observed.

The technique used here for guide formation was bombardment with He ions of energies about 3MeV. In some substances this creates a region of increased refractive index at the surface of the material which can be used as a waveguide. The size of this index increase is 0.2% for Nd:YAG and 0.06% for Nd:GGG. To form channel waveguides the surface of the material has to be masked to prevent the He ions penetrating in regions other than those where guides are to be formed. The first step in doing this was to evaporate a 120nm layer of Ni/Cr on to the crystal surface on top of which a 3 μ m layer of photoresist was spun and patterned to leave stripes. A 3 μ m layer of gold was then electroplated onto the exposed Ni/Cr and the remaining photoresist washed off to leave gaps ranging from 4-20 μ m in width. These were then made into channels by He ion bombardment the details of which are given below.

Material	Ion Energies (MeV)	Dose (ions/cm ²)
Nd:YAG	Multiple energies up to 2.8	6x10 ¹⁶
Nd:GGG	2.9	2x10 ¹⁶

The channels created had typical losses of 1.5dB/cm for YAG and 1dB/cm for GGG. In each

case a 2.5mm crystal length was pumped using a 810nm, 100mW single stripe laser diode. This was made into a cavity by attaching thin dielectric mirrors to the crystal ends using a small drop of fluorinated liquid, chosen because of its high thermal conductivity. Although this produces a more lossy cavity than if the mirrors were directly coated to the crystal end faces it has the advantage that the mirrors can be easily changed. Microscope objectives were used to launch light into the channels and to focus the output from them. Best laser performance was given by the 20 μ m wide channels in Nd:YAG and the 16 μ m channels in Nd:GGG. The actual values for absorbed power threshold and slope efficiencies are given in the following table.

	HR mirrors	16% output coupler	
	threshold	threshold	slope efficiency
Nd:YAG	500 μ W	1.6mW	29%
Nd:GGG	1.9mW	6.6mW	27%

Another feature of the Nd:GGG channels was that they lased in an extended cavity configuration where the output from one end of the channels was collimated onto an external mirror using a microscope objective. This allows for optical elements (such as a tuning device) to be placed in the cavity. Using this arrangement the absorbed power threshold was 8mW for one butted and one external HR mirror.

Ion implantation which has proved to be a versatile method for producing planar waveguide lasers has now been shown successfully to produce channel guides. Both host materials are important Cr hosts and the efficiency of the channel geometry should enable low threshold vibronic lasers to be constructed.

References

1. P.D. Townsend, Rep. Prog. Phys. **50**, 501 (1987).
2. S.J. Field, D.C. Hanna, D.P. Shepherd, A.C. Tropper, P.J. Chandler, P.D. Townsend and L. Zhang, IEEE J. Quantum Electron. **QE-27**, 428 (1991).
3. S.J. Field, D.C. Hanna, A.C. Large, D.P. Shepherd, A.C. Tropper, P.J. Chandler, P.D. Townsend and L. Zhang, Opt. Comm. **86**, 161 (1991).

Wednesday, April 15, 1992

Optical Fiber Devices

WG 1:30 pm–2:45 pm
La Salle Ballroom B

Vincent J. Tekippe, *President*
Gould Inc.

WG1-1

OPTICAL FIBER DEVICES IN LIGHTWAVE SYSTEMS

Juichi NODA*, Hiroaki HANAFUSA** and Taisuke OGUCHI**

- * NTT International Corporation
Mori-Bldg 21 Roppongi 1-4-33 Minatoku Tokyo 106 Japan
TEL 81-3-5562-7725 FAX 81-3-5562-7705
- ** NTT Opto-electronic Laboratories
Tokaimura Ibarakiken 319-11 Japan

INTRODUCTION

Fiber devices in fiber transmission systems became more important than micro-optic devices from view point of reliability, low insertion loss and price. Significant requirement in recent fiber transmission systems is high return loss close to 50 dB as well as low insertion loss and this accelerates importance of fiber devices. In this paper, fiber devices mainly in NTT systems are presented. Before reviewing them, it is necessary to define the fiber devices as follows; (a) they have no lens, and (b) they are alignment free devices even if bulk elements are attached to/or the fibers.

FIBER COUPLERS

In subscriber systems/1/ and remote automatic fiber testing system for trunk lines called FITAS (Fiber Transfer and Test System) /2/, cheap and low loss fiber couplers of 1.30 μm /1.55 μm WDM (Wavelength Division Multiplexing) commercially available are used. In this case, the influence of wavelength dependence of couplers and wavelength deviation of the laser diodes must be taken into account for system design. Other WDM couplers with 1.48 μm /1.54 μm or 0.98 μm /1.54 μm are very attractive for fiber amplifiers/3/. However micro-optic devices are still a strong candidate compared with fiber devices for fiber amplifier integration.

WICs (Wavelength Insensitive Couplers) are another important fiber devices in CATV systems and remote automatic fiber testing for subscribe lines called AURORA (Automatic Optical Fiber Operations Support System)/2/. WICs are made by fusion-elongation of two different fibers where cladding diameters, core diameters or core refractive indices are different/4/. In AURORA, WICs are installed in each subscriber line, of which characteristics has 20%/80% coupling ratio in the range of 1.2 μm to 1.6 μm in wavelength.

IN-LINE FIBER FILTERS AND ATTENUATORS

In-line fiber devices are fabricated by inserting thin films/5/ with filter or attenuator function into the slots which are made by cutting the fibers with a grinding machine. To reduce the gap loss as much as possible, i. e. less than 0.2 dB for the filters, the slot thickness must be less than 30 μm and the special diamond cutting machine is necessary/6/. This filter is installed in front of the transmission equipment of user's building in AURORA. In this system, the 1.55 μm light is used as OTDR light on the in-service fiber transmitting 1.31 μm light. The 1.31 μm /1.55 μm in-line filter is fabricated in the optical connector so as to reflect the 1.55 μm light and to pass 1.31 μm light with the reflection loss of 50 dB for the 1.31 μm light/2/.

In-line fiber attenuators are easier to fabricate than the filters. The insertion loss due to the slot gap can be included in the attenuator loss and consequently thicker film is available. The reflection loss of more than 50

dB is achieved by setting the film at 8 to 10 degrees from right angle. This kind of attenuators is also attached on the optical connectors of 5 dB, 10 dB, 15 dB and 20 dB with ± 0.5 dB deviations.

OTHER FIBER DEVICES

Water monitoring system using the bending loss increase is installed in water-blocking cables/7/. Fiber type water sensor is performed by bending the fiber due to the volume expand of polyacrylic acid polymer after absorbing water in the cable. The loss increase of about 2 dB yielded by fiber bending can be easily detected by OTDR.

Compact fiber polarizers are reported/8/. The structure is based on the similar concept as mentioned in fiber filters. Thin film polarizer called Lamipol with 20 μm thick is inserting the slot between the PANDA fiber taking into account the polarization direction of the Lamipol and the PANDA fiber. The crosstalk of -40 dB and insertion loss of 0.4 dB are obtained in the range of 1.3 μm to 1.6 μm wavelength.

New technology called TEC (Thermally-diffused Expanded Core) technology/9,10/ has been developed for new fiber devices. The core of end fiber heated by a micro torch is expanded twice or third larger than the initial core diameter without changing V value. Most available application of this technology is splicing of two different core fibers in assembling fiber amplifiers. The splicing loss of more than 1 dB between = 0.3 % and 2.3 % fibers decreased to 0.1 dB after TEC treatment/10/. Second application is in-line devices with TEC. In-line fiber filters and fiber isolators/9/ with low insertion loss are proposed. Third application is connection with high tolerance such as optical connectors between two different cores and laser module/11/.

Further fabrication technology for automation method and array fiber devices/12,13/ are necessary to reduce the fiber device price.

REFERENCE

- 1) H. Tsuji et al: Third IEEE Workshop on Local Optical Network, Digest 3.3 (1991 Tokyo).
- 2) N. Tomita et al: NTT Review, Vol. 3, p97 (1991).
- 3) M. Shimizu et al: J. Lightwave Technol., Vol. 9, p291 (1991).
- 4) H. Hanafusa et al: OFS'89 Digest Tu7-6 (1989 Paris).
- 5) T. Oguchi et al: Electron. Lett., Vol. 27, p706 (1991).
- 6) S. Matsui et al: J. Lightwave Technol. (to be published).
- 7) N. Tomita et al: J. Lightwave Technol. Vol. 8, p1829 (1990).
- 8) T. Arikawa et al: OFS'90 Digest p305 (1990 Sydney).
- 9) K. Shiraishi et al: J. Lightwave Technol., Vol. 9 p430 (1991).
- 10) H. Hanafusa et al: Electron. Lett., Vol. 27, p1968 (1991).
- 11) K. Kato et al: Photonics Tech. Lett., (to be published).
- 12) I. Yokohama et al: Electron. Lett., Vol. 24, p1147 (1988).
- 13) J. W. Arkwright et al: Electron. Lett., Vol. 27, p737 (1991).

A Birefringent Fiber 4x4 Wavelength Crossconnect

Sarah Cousins, W. John Carlsen
GTE Laboratories Incorporated
40 Sylvan Road
Waltham, Massachusetts 02254
(617) 466-2368, (617) 466-2728

A general technique for making all-fiber polarization-independent birefringent wavelength division multiplexers (BWDM) was introduced at this conference last year, and a first order 1x2 multiplexer with 0.2 nm channel spacing was presented.¹ This technique has now been extended, using birefringent filter synthesis,² to the design of a polarization-independent 4x4 wavelength crossconnect. This device has 0.78 nm channel spacing and is constructed from single-mode birefringent fibers and polarizing beam-splitters.

A 4x4 wavelength crossconnect³ can be used to distribute 16 signals at 4 different wavelengths as shown schematically in Figure 1. We have introduced a new design that is inherently simpler than conventional designs, and consists of a narrow channel BWDM in series with a wide channel flattened passband BWDM. The BWDMs are made from birefringent fibers (here 1.5 m and 3.0 m lengths) at appropriate angles (here 45° and -15°) between polarizing beam-splitters (PBSs). We planned to make an "all-fiber" crossconnect but our all-fiber polarizing beam-splitters had insufficient extinction (30 dB is desirable) so we replaced them with bulk PBSs. Figure 2 shows the layout used.

Fabrication of the birefringent fiber crossconnect involves two challenges: (1) getting the lengths of the 12 fibers to match within 0.1% (for 100:1 extinction) and (2) getting the angles of the fiber segments correct to within 1°. To solve the first problem, ovens were used to tune the fiber lengths. (If the lengths are cut simultaneously, these ovens may not be necessary.) The second task was avoided to a large extent by using quarter wave plates at the beam-splitters where a 45° split was called for. The remaining angles were aligned manually using a microscope.

An experimentally obtained curve of the transmittance function is shown in Figure 3. The channel spacing is 0.78 nm. This spacing is determined by the lengths of the fiber segments and can easily be made narrower with no additional loss simply by using longer fibers. The extinction is approximately 30:1 for the channel observed. This measurement is limited by the resolution of the spectrum analyzer, the angular orientation of the fibers and the extinction of the beam-splitters. The loss of the crossconnect is theoretically very low especially if fiber PBSs are used, but our bulk beam splitters exhibited 5 dB transmission loss. With four PBSs in series the total loss through the crossconnect was 20 dB. This project is ongoing, and we are pursuing a more efficient implementation of the device.

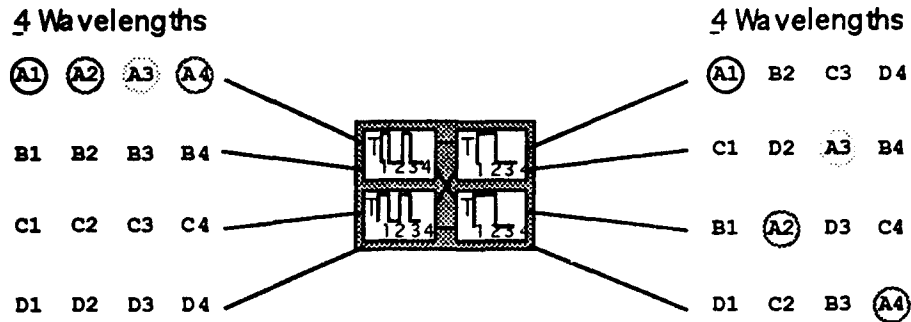


Figure 1: 4x4 Functional Schematic: 16 interconnects using 4 wavelengths.

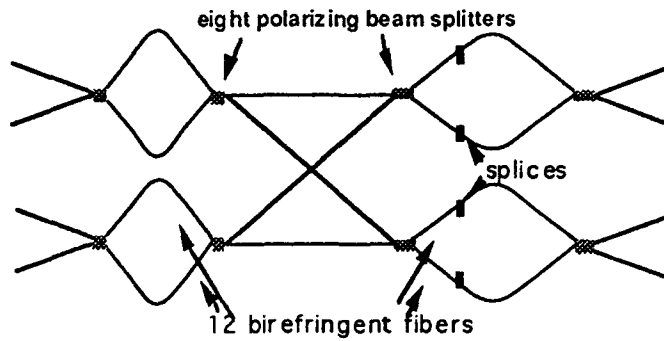


Figure 2: 4x4 Birefringent Fiber Implementation.

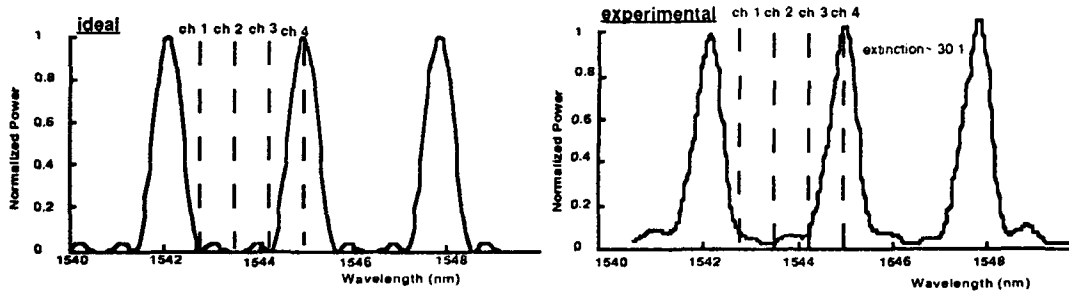


Figure 3: 4x4 Experimentally Obtained Passband.

References:

- ¹Cousins, S. and Carlsen, W. J.: "All-fiber Birefringent WDM Devices", *Workshop on Passive Fiber Components*, p. 147. 4/8/91
- ²Carlsen, W. J., and Buhner, C.: "Flat passband birefringent wavelength-division multiplexers", *Electron. Lett.*, 1987, 23, pp.106-107
- ³Kobrinski, *Electron. Lett.*, 23, p.975, 1987.

WG3-1

OPTICAL PHASE AND AMPLITUDE RESPONSE
OF AN IN-FIBER GRATING RESONATOR

David R. Huber

Jerrold Communications Division, General Instrument
2200 Byberry Road, Hatboro, PA 19040

Summary

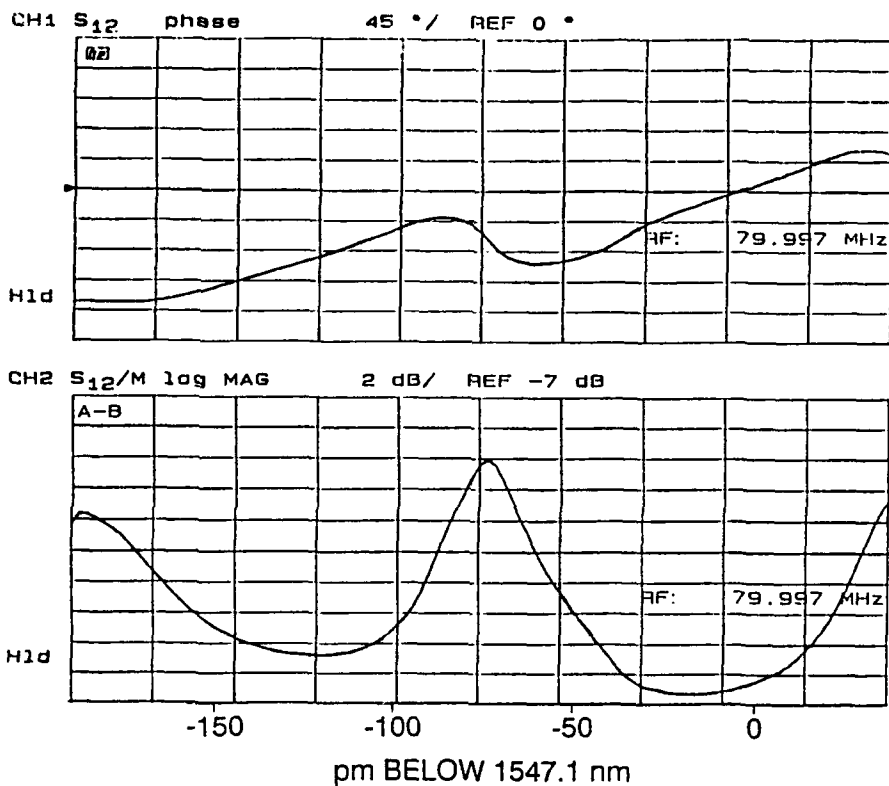
We report the measured phase and amplitude response of an in-fiber grating resonator¹. The optical bandpass resonator was formed in a single-mode fiber by a photo-refractive induced Bragg reflector². The grating length was about 22 mm with a 1 mm central gap to facilitate formation of the resonator. The resonant peak occurred at 1547.1 nm. The 3 dB optical bandpass is 4 GHz wide.

The optical phase and amplitude transmission response was measured by placing the resonator in one arm of a balanced heterodyne Mach-Zehnder interferometer. A laser was used to sweep through the grating resonance. The optical phase response is down converted to the electrical domain and detected by RF heterodyne techniques.

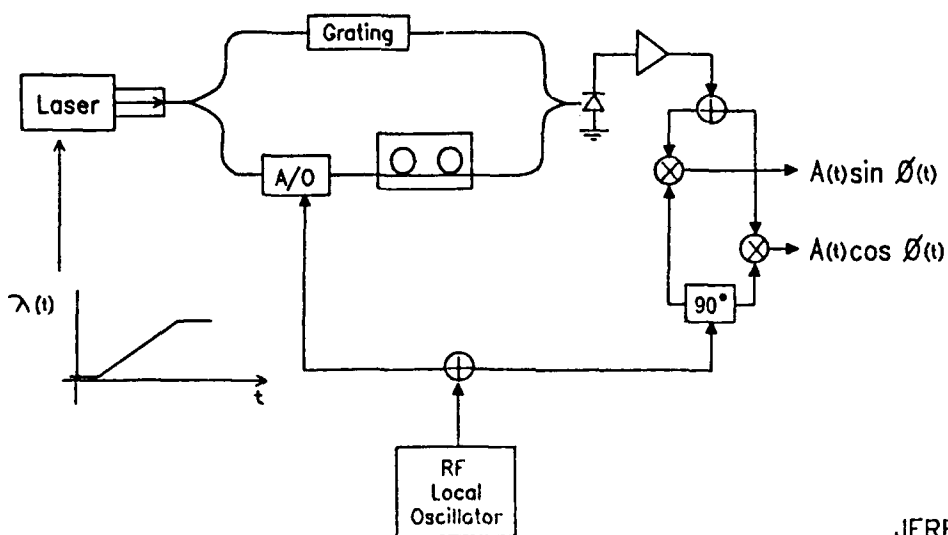
One application of this integrated silica component is the active frequency stabilization of a laser³. The linear portion of the grating phase response would provide the feedback signal for laser frequency stabilization. Precise temperature control of the grating resonator would provide an accurate optical frequency reference.

1. C.M. Ragdale, D.C.J. Reid and I. Bennion, Paper WI1, OFC (1991)
2. G. Meltz, W.W. Morey and W.N. Glenn, Opt. Lett. 14, p823 (1989)
3. T. Day, E.K. Gustafson and R.L. Byer, Opt. Lett. 15, p221 (1990)

GRATING PHASE AND AMPLITUDE RESPONSE



Grating Characterization Set-up



H20C9125

JERROLD COMMUNICATIONS

WG4-1

Photo-Effects in $\text{SiO}_2/\text{GeO}_2$ Waveguides

N. F. Borrelli
R. A. Modavis
J. W. H. Schreurs
Research, Development, and Engineering Laboratory
Corning Incorporated
Sullivan Park, SP-FR-03-1, Corning NY 14831
(607) 974-3155
(607) 974-3838
(607) 974-3148

Summary

The so-called photorefractive effect in $\text{SiO}_2/\text{GeO}_2$ waveguide materials¹ is initiated by exposure to ultraviolet radiation in the vicinity of 240nm. Absorption changes produced by this exposure contribute to a refractive index change at longer wavelengths, which can have device implications,² e.g., writing Bragg gratings in single-mode fibers for filters.

Some waveguide blank material exhibits an absorption band at the 240nm wavelength that is attributed to an oxygen vacancy defect of some type.³ This explanation is supported by two of our experimental findings; first, the strength of the 240nm absorption correlates inversely with the partial pressure of O_2 during the consolidation and second, the strength of the 240nm² band can be increased after consolidation by treatment of the blank in hydrogen above 500°C. The result after exposure to 249nm light (KrF excimer laser, 350mj/cm²) is the production of colors centers with absorption extending from 200-450nm. The model proposed is that an electron is excited from the oxygen deficient defect into the conduction band where it subsequently is trapped. The trapped electrons and holes provide the induced optical absorption. Electron spin resonance measurements can identify the various sites such as Ge-E', Ge(1) and Ge(2). A good semi-quantitative correlation has been established between the number of the trapped species and the induced optical absorption. In addition, one can relate the induced absorption, as measured on the blank to the measured refractive index change in the fiber at 1.3 μm . The refractive index change was measured by exposing one leg of a Mach-Zehnder fiber interferometer.

The thermal stability of the induced optical absorption and refractive index change was measured. The stability is proposed to be related to the electron trap depth. In general, it is proposed that the electron traps play a crucial role in the efficiency and stability of the photorefraction effect.

- 1) K. O. Hill, V. Fujii, D. C. Johnson, and B. S. Kawasaki, Appl. Phys. Lett., 32, 647, (1978)
- 2) G. Meltz, W. W. Morey, and W. H. Glenn, Opt. Lett., 14(15), 823, (1989)
- 3) D. L. Griscom, J. Noncryst. Sol., 73, 51, (1985)

Wednesday, April 15, 1992

Semiconductor Waveguides and Devices

WH 1:30 pm–3:30 pm
Pelican Room

Kohroh Kobayashi, *Presider*
NEC Corp., Japan

WH1-1

ULTRA-COMPACT PHOTONIC INTEGRATION of GUIDED-WAVE DEVICES on InPR. J. Deri, E.C.M. Pennings and R.J. Hawkins^aBellcore, 331 Newman Springs Road, Red Bank, New Jersey 07701-7040
(908) 758-2894

a) Lawrence Livermore National Laboratory, Livermore, California 94550

Monolithic, waveguide-based photonic integration offers the potential for enhancing functionality with on-chip optical signal processing and eliminating package complexity by reducing part count. A major drawback to integrated optics has been large device size, typically millimeters or more for directional couplers with their input/output branching guides, which is incompatible with the high cost of III-V materials. This paper describes ultra-compact (<1mm) directional couplers and their integration with photodetectors, for application to balanced, polarization-diversity coherent reception at wavelength of $\lambda=1.5\mu\text{m}$.

Fig. 1 shows schematically how all the front-end optics for this application could be integrated onto a single chip. The necessary components include a polarization-insensitive 3dB coupler for balanced operation,[1-6] polarization-splitting couplers based on metal-loading,[4,5] and four photodetectors for generating two IF signals associated with orthogonal optical polarizations. The particular design shown in fig. 1 eliminates difficult-to-define lithographic features (coupler gaps, Y-junctions) and epitaxial regrowths. The small size and simple processing of this photonic circuit render it ideal for high yield fabrication.

Use of self-imaging [7] in multimode interference couplers permits the use of tightly-confined branching guides, resulting in 3dB splitters of total length $\approx 800\mu\text{m}$ (fig. 1A).[8] The device does not require precise lithographic definition of either a coupling gap or Y-junction. Discrete multi-mode couplers exhibit excellent performance: they are polarization- and wavelength-insensitive for $\lambda=1.52\text{-}1.54\mu\text{m}$, show low excess loss (<0.5dB), and balance suitable for common-mode LO noise rejection >33dB (best values $\geq 40\text{dB}$).

Vertical couplers are used for polarization splitting to eliminate gap definition problems, reduce die size, and achieve broadband operation. Regrowth-free integration of extremely short detectors (21 μm TE, 31 μm TM) (to avoid degradation of polarization extinction) is achieved by "impedance matching." [9] Metal loading of the first coupler results in output from the first detector proportional to TE-polarized optical input, while the second coupler/detector pair captures the remaining TM-polarized light. This integration eliminates optical branching at coupler outputs to reduce device size. The complete polarization-splitting detector of fig. 1B is only $\approx 200\mu\text{m}$ long; thus this *optical* element is comparable in size to a typical *electronic* component (FET gate width). In addition to enhancing optical coupling to the absorbing InGaAs layer, the n^+ InGaAsP matching layer is integral to the *pin* detector structure and is essential for of large *pin* diode bandwidth. The n^+ matching layer anodes permit the use of semi-insulating, Fe-doped waveguide material, which is required for on-chip photocurrent subtraction and balanced operation.[6]

The polarization-selective detectors of fig. 1B have been fabricated and characterized.[10] Waveguide propagation loss is only 0.5dB/cm at $\lambda=1.52\mu\text{m}$, indicating that Fe-doping for high sheet resistance ($4 \times 10^8 \Omega/\text{sq}$) does not degrade material transparency. The detectors exhibit guide-to-detector coupling (quantum) efficiencies (87% TE, 76% TM), and typical polarization

extinction ratios of 10.6dB TE and 16.2dB TM; for these values, only 1dB total IF signal variation due to polarization fluctuation is expected. The short vertical coupler lengths (75 μ m TE, 54 μ m TM) result in wavelength-insensitive operation, which is predicted for $\Delta\lambda=\pm 35$ nm and observed for $\lambda=1.52$ to 1.55 μ m.

In summary, we have demonstrated techniques for ultra-compact photonic integration of directional couplers and photodetectors. Our results show how such integration can enhance photodetector functionality, by incorporating high-performance waveguide optics, *without compromising chip size or ease of fabrication.*

This research was performed, in part, under the auspices of the U.S. Department of Energy by the Lawrence Livermore National Laboratory under contract W-7405-ENG-48.

REFERENCES

1. S. Chandrasekhar, J.C. Campbell, et al., *Electron. Lett.* **24**, 1457 (1988).
2. H. Takeuchi, K. Kasaya, et al., *Photon. Technol. Lett.* **1**, 398 (1989).
3. T.L. Koch, U. Koren, et al., *Photon. Technol. Lett.* **2**, 577 (1990).
4. M. Erman, P. Riglet, et al., *15th European Conf. Opt. Commun.* (Gothenburg, Sweden; Sept. 1989). ThB20.
5. P. Albrecht, H. Hamacher, et al., *Photon. Technol. Lett.* **2**, 114 (1990).
6. R.J. Deri, N. Yasuoka, et al., *Photon. Technol. Lett.* **2**, 496 (1990).
7. R. Ulrich and G. Ankele, *Appl. Phys. Lett.* **27**, 337 (1973).
8. E.C.M. Pennings, R.J. Deri, et al., *Appl. Phys. Lett.* **59**, 1926 (1991).
9. R.J. Deri and O. Wada, *Appl. Phys. Lett.* **55**, 2712 (1989).
10. R.J. Deri, R.J. Hawkins, et al., *Appl. Phys. Lett.* **59**, 1823 (1991).

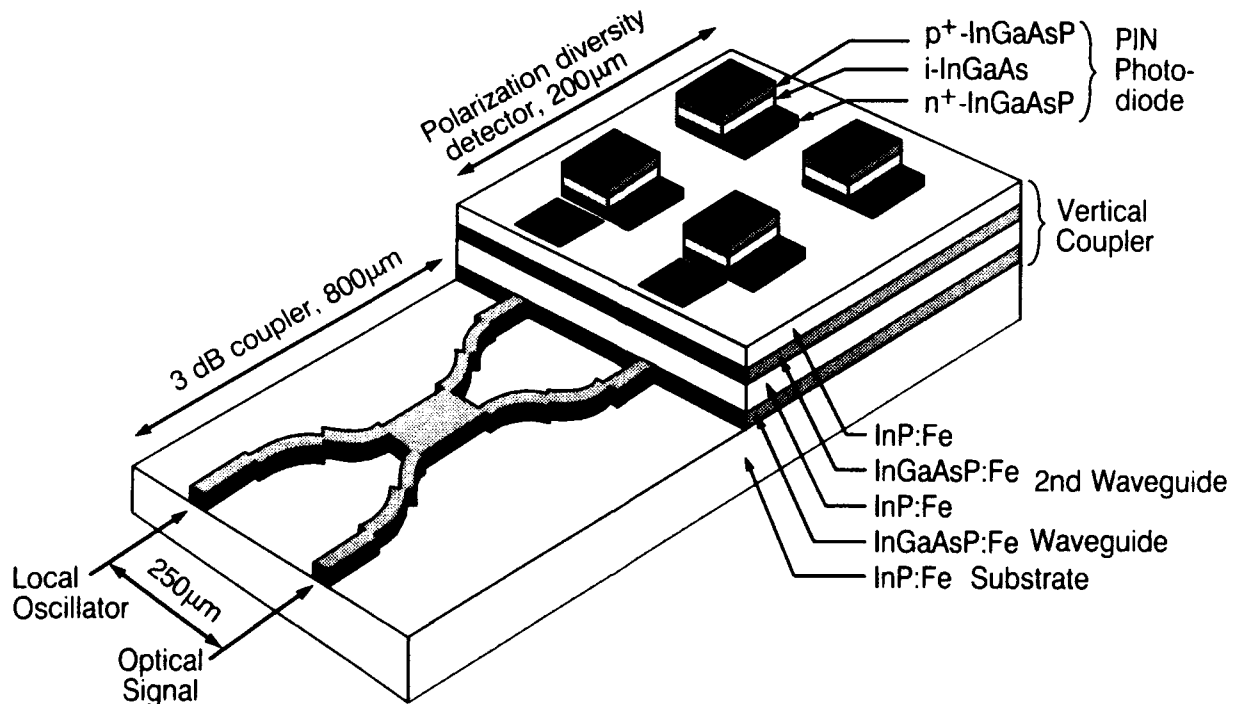


FIGURE 1: RECEIVER CHIP SCHEMATIC

WH2-1

GaInAs/GaAs Waveguide Modulators With Multiple Short-Period Strained-Layer Superlattice Quantum Wells

D. Yap, T.C. Hasenberg, T.Y. Hsu,
S.L. Bourgholtzer and A.R. Kost
Hughes Research Laboratories
3011 Malibu Canyon Road
Malibu, CA 90265

S.D. Koehler, M.H. Jupina and E.M. Garmire
Center for Laser Studies and
National Center for Integrated Photonics Technology
University of Southern California
Los Angeles, CA 90089-1112

InGaAs/GaAs multiple quantum well (MQW) structures with wells that consist of InAs/GaAs short-period strained-layer superlattices (SPSLS) have shown sharp excitonic absorption peaks at room temperature, despite the high degree of strain.¹ By using superlattices with multiple periods consisting of 2 monolayers of InAs and 5 monolayers of GaAs, dislocation-free InGaAs wells with 0.30 average In mole fractions have been obtained.² We report the first MQW waveguide modulators based on these InAs/GaAs SPSLS quantum wells. These modulators demonstrate significant electro-absorption and electro-refraction effects at wavelengths between 1.00 and 1.06 μm . An advantage of such modulators is that they can be monolithically integrated with low-threshold-current InGaAs lasers as well as low-loss GaAs waveguides for various optical circuit applications. In addition, stronger electric-field dependences are expected for the wider wells permitted by the use of SPSLS.³

The modulators have a standard PIN structure, illustrated in Figure 1, and were grown by migration-enhanced epitaxy. Their 0.3- μm thick, undoped active layers consist of quantum wells with 6 or 8 InAs/GaAs periods (resulting in thicknesses of 11 or 15 nm, respectively) and 20 nm thick GaAs barriers. The cladding and contact layers are comprised of lightly and heavily doped GaAs, respectively. Semi-insulating GaAs substrates were used so that high-speed devices could eventually be demonstrated. Fabrication of the modulators involved etching of 60-100 μm wide mesas, for wide-stripe devices, or 6 μm wide mesas, for narrow-stripe devices. An SEM micrograph of a narrow-stripe mesa is shown in Figure 2. Both wet-chemical etching, with $\text{H}_3\text{PO}_4:\text{H}_2\text{O}_2:\text{H}_2\text{O}$, and reactive-ion etching, with CH_4/Ar , have been used to form the mesas. The modulators have Mn/Au p-type and AuGe/Ni/Au n-type ohmic contacts. Both contacts are located on the top side of the device.

The modulators were cleaved into various lengths and placed in one arm of a Mach-Zehnder interferometer for the electro-refraction measurements. Figure 3 shows the change in refractive index at several reverse-bias voltages for 2-mm long devices with 6- or 8-period SPSLS wells. The measurements were obtained at a wavelength of 1.06 μm , which corresponds to detunings of 110 meV and 100 meV from the exciton resonance for the 6 and 8-period devices, respectively. Note that despite the large detuning, $V_\pi \times L$, for TE input polarization, is 6 V-mm for the 8-period device and 9 V-mm for the 6-period device.

The change in transmission due to an applied reverse-bias voltage has been measured at various wavelengths by using a tunable Ti:sapphire laser. Figure 4 shows measurements obtained from a 6-period device for wavelengths between 0.99 and 1.02 μm . A maximum transmission decrease of 95% was measured for TM polarized light at a wavelength of 1.01 μm , at which the residual absorption is expected to be quite low. These, and additional, results will be discussed in more detail at the conference.

1. T.C. Hasenberg, D.S. McCallum, X.R. Huang, M.D. Dawson, T.F. Boggess and A.L. Smirl, *Appl. Phys. Lett.*, **58**, 937 (1991).
2. T.C. Hasenberg, D.S. McCallum, X.R. Huang, A.L. Smirl, M.D. Dawson and T.F. Boggess, *J. Cryst. Growth*, **111**, 388 (1991).
3. S. Nojima and K. Wakita, *Appl. Phys. Lett.*, **53**, 1958 (1988).

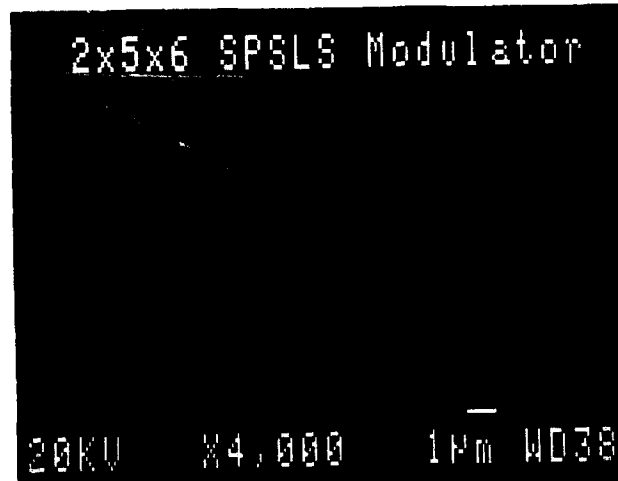
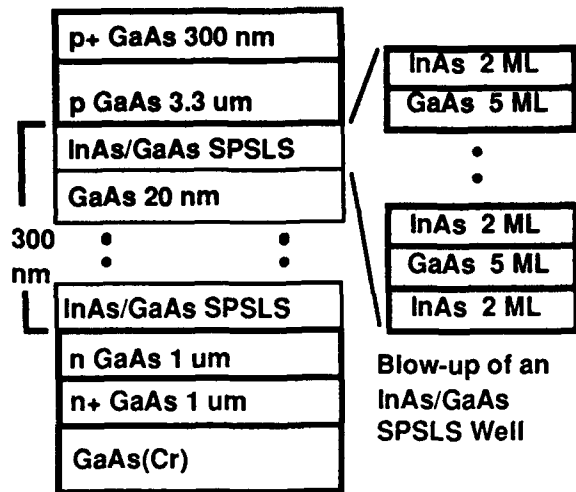


FIG. 1. Epitaxial structure of MQW waveguide modulator having SPSLS wells.

FIG. 2. SEM micrograph of narrow-stripe modulator; the endface has been stained to reveal the active MQW region.

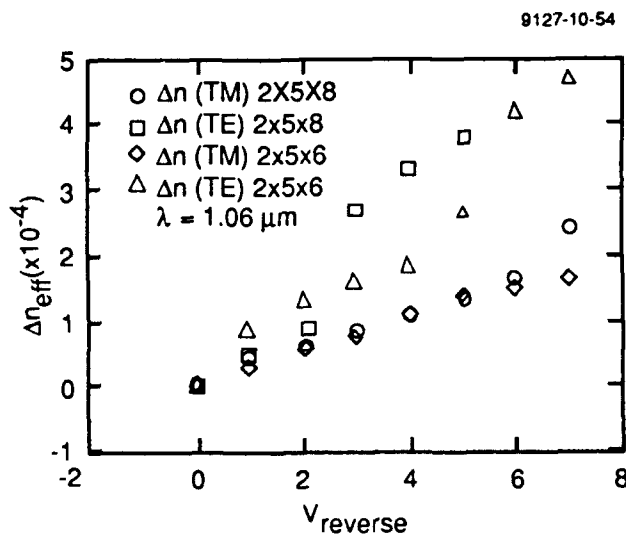


FIG. 3. Voltage-dependent change in guided-mode effective index measured at 1.06 μm for both TE and TM input polarizations.

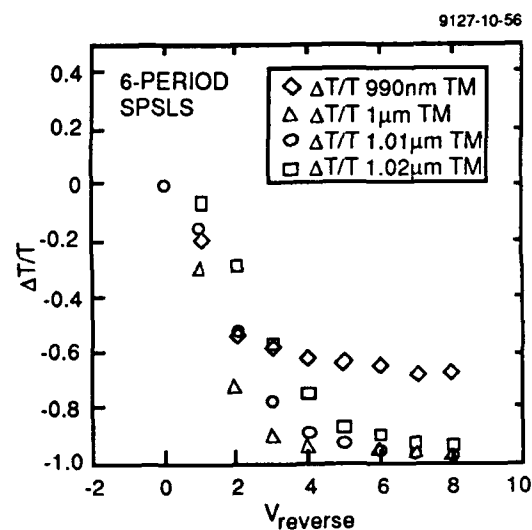


FIG. 4. Voltage-dependent transmission change measured at various wavelengths longer than the exciton resonance.

WH3-1

GaAs-on-Si modulator using a buried silicide reflector

K.W. Goossen, J.E. Cunningham, A.E. White ^a, K.T. Short ^a, W.Y. Jan, and J.A. Walker
 AT&T Bell Laboratories, room 4B-519
 Crawfords Corner Rd.
 Holmdel, NJ 07733
 (908) 949-6979
 a- AT&T Bell Laboratories, Murray Hill, NJ

Optical interconnection of electronic integrated circuit chips is currently of great interest. This would provide a much greater bandwidth of information flow on and off the chip, especially if surface-normal devices are used since then information may flow vertically from the chip and the entire area of the chip may be used rather than just the periphery. This capability is especially important for silicon very-large scale integrated circuits since input and output of information to the chip is a bottleneck.

The process of integrating surface-normal devices (either modulators or lasers) with silicon electronics is complicated by the necessity of thick mirror stacks. The resulting thick devices cause a large topography change, complicating processing due to reduced linewidth control and the necessity of wide depth-of-focus lithography for passivating and metalizing device sidewalls. A typical modulator on silicon is about 6 μm thick, 2-3 μm of which is the mirror layer, for devices operating at 850 nm. For longer wavelength devices, mirror stacks become even thicker, until at 1.55 μm they are prohibitive.

We present here a way to reduce this thickness by replacing the dielectric mirror with a buried silicide reflector. An epitaxial silicide layer buried under a thin layer of epitaxial silicon is formed by a implant/anneal technique called mesotaxy.¹ As an example of this technique, we present a GaAs modulator using a buried-silicide reflector. We obtain a change of reflectivity from 6% to 16% as the voltage on the device is ramped from 0 to 25 volts.

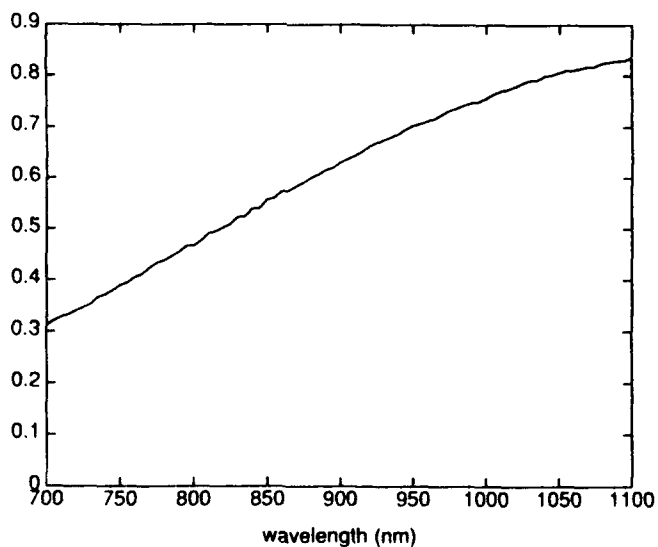


Fig. 1: Reflectivity of a mesotaxy-produced CoSi_2 layer.

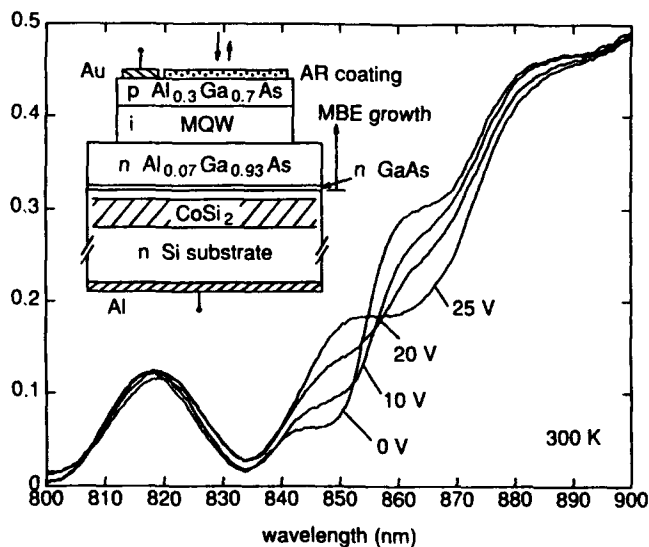


Fig. 2: Reflectivity of buried-silicide-reflector modulator at different biases.

Fig. 1 shows the reflectivity of an exposed silicide layer (CoSi_2) produced by mesotaxy. Its reflectivity is actually substantially higher at $1.06 \mu\text{m}$ than 850 nm (81 % vs. 56 %) so a silicide mirror is well suited to $1.06 \mu\text{m}$. Optically interconnected systems are moving toward $1.06 \mu\text{m}$ since the higher power Nd:YAG system is available. Other advantages of the silicide mirror include its broadband nature, rather than the narrowband nature of mirror stacks which place strict requirements on layer thickness control. Also, since silicides are used in silicon contact technology this paper demonstrates the possibility of growing a modulator (or detector) directly atop a contact for optimum integration with minimal stray capacitance.

For the sample presented here (Fig. 2, inset), an n-type (100) silicon wafer oriented 3° off-axis was implanted with cobalt atoms at 200 keV to a dose of $2.5 \times 10^{17} \text{ cm}^{-2}$. Then it was annealed at 600 C° for 1 hour, followed by 1000 C° for 1 hour. This causes the Co to coalesce into a layer of crystalline CoSi_2 about 1000 \AA thick buried beneath about 800 \AA of crystalline silicon.¹ The sample was then placed in a Gas source molecular beam epitaxy reactor after a brief HF dip. After a high temperature (850 C° for 10 minutes) oxide desorption a 500 \AA thick n-type GaAs layer was grown, followed by $0.5 \mu\text{m}$ of n $\text{Al}_{0.07}\text{Ga}_{0.93}\text{As}$, both at a substrate temperature of 350 C° . This was followed by $1.7 \mu\text{m}$ of n $\text{Al}_{0.07}\text{Ga}_{0.93}\text{As}$ grown at a substrate temperature of 550 C° . The buffer needed to have a small percentage of Al to make it transparent at 850 nm . Then an intrinsic 50 period $100/50 \text{ \AA}$ GaAs/ $\text{Al}_{0.3}\text{Ga}_{0.7}\text{As}$ multi-quantum well was grown, followed by 5000 \AA of p $\text{Al}_{0.3}\text{Ga}_{0.7}\text{As}$ and a 100 \AA p⁺ GaAs cap. Thus the total thickness of our sample is $3.5 \mu\text{m}$, substantially reduced from the usual $6 \mu\text{m}$.

The reverse breakdown of the diodes was typically 30 volts, indicating very good material quality, showing that the 3° off-axis orientation was preserved after implantation. The reflection of the device was measured with a lamp and monochromator. This is shown in Fig. 2 for reverse biases of 0, 10, 20 and 25 volts. Fabry-Perot fringes complicate the spectra, but they clearly show a red-shift of the absorption edge near 850 nm in accordance with the quantum-confined stark effect commonly observed for these standard QW's. This results in an increase of reflectivity near 850 nm and a decrease at longer wavelengths. At 848 nm the reflectivity changes from 6 % to 16 % with 25 volts bias. This is inferior to the modulator produced by us with a dielectric mirror, where a change from 14 % to 57 % was measured.² However, as a first try this result is very promising for this technique given the substantial reduction in modulator thickness. We achieve a contrast ratio of 2.5 at 848 nm .

In conclusion, we have produced a GaAs-on-Si surface-normal modulator that uses a buried silicide layer as an integral reflector. We achieve a change in reflectivity from 6 % to 16 % with 25 volts bias. The technology eliminates the requirement of mirror stacks and so reduces device thickness and provides a broadband mirror technology.

REFERENCES

- [1] A.E. White, K.T. Short, R.C. Dynes, J.P. Garno, and J.M. Gibson, *Appl. Phys. Lett.* **50**, 95 (1987).
- [2] K.W. Goossen, G.D. Boyd, J.E. Cunningham, W.Y. Jan, D.A.B. Miller, D.S. Chemla, and R.M. Lum, *IEEE Phot. Tech. Lett.* **1**, 304 (1989).

WH4-1

A Novel Device Structure of Vertical Multiple Quantum Well Directional Coupler Switch for Low Switching Voltage

Takeharu Yamaguchi, Kunio Tada,

Department of Electronic Engineering, University of Tokyo,
Hongo 7-3-1, Bunkyo-ku, Tokyo, 113, Japan, +81-3-3812-2111

and

Takuya Ishikawa

Opto-Technology Laboratory, Furukawa Electric,
6, Yawata-Kaigandori, Ichihara, Chiba, 290 Japan. +81-436-42-1773

The semiconductor directional coupler optical modulator/switch in vertical coupled-waveguide configuration [1] is one of useful components in integrated and guided-wave optics because of the less difficult fabrication process and small size. In recent years these devices with multiple quantum wells (MQW) were reported[2]-[5], where the large change in refractive index due to the quantum confined Stark effect(QCSE) were employed for reduction of the switching voltage V_s and the device length l . In this paper we report on a new device with very small V_s of 5V and l of 138 μm .

The novel device structure employed here is shown in Fig.1. This is designed on the basis of new concepts proposed earlier[6].

First, all three kinds of layers, i.e., clad, guide and separation layers, are superlattices (or MQWs) composed of $\text{Al}_{0.3}\text{Ga}_{0.7}\text{As}$ barriers and GaAs wells. The refractive index of each layer for TE mode light is known as $n_{\text{TE}} = \sqrt{(L_b n_b^2 + L_w n_w^2)/(L_b + L_w)}$ [7][8]. In the molecular beam epitaxy(MBE), growth thickness control is much easier than growth composition control. By using a fixed AlGaAs composition and by choosing barrier thickness L_b and well thickness L_w properly as shown in Fig.1, much better control of the refractive index profile across all the layers can be achieved. This leads to the improved control of the complete coupling length l_c than before. In our experiment, l_c was measured in a sample with tapered coupling region[3] as 170 μm , which is in good agreement with the designed l_c of 200 μm .

Second of the new concepts is that the refractive index modulation is carried out only in the undoped central region of the separation layer as shown in

Fig.1. The device length l is ideally equal to l_c at zero reverse voltage and the cross state is obtained. When the reverse voltage V is applied, the refractive index only in the central region of the separation layer increases due to the QCSE. This causes an increase of the coupling coefficient κ between the two guide layers and a decrease of l_c which is inversely proportional to κ . At $V = V_s$, l_c is reduced to $l/2$ and the bar state is reached.

By employing such a complete coupling length modulation scheme, a better extinction ratio at $V = V_s$ is expected than in the conventional phase coefficient modulation scheme. This is based on the fact that the symmetry of the refractive index profile is maintained even under the reverse voltage. Moreover, in our device structure, increase in optical absorption loss due to the QCSE under the reverse bias can be minimized because the optical confinement factor in the index-modulated region is small.

The key point of our new concept is as follows: By reducing the thickness ratio of the index-modulated region in the whole separation layer, V_s can be much reduced. A result of calculation indicating this finding is shown in Fig.2. The device model is the same as that in Fig.1, but the thickness t of the index-modulated region is varied at the center of the 1.2 μm thick separation layer. When t is decreased, the refractive index change needed for switching Δn increases, but $\Delta n \cdot t$ slightly decreases. Therefore, V_s should decrease even if the refractive index change is proportional to the applied electric field. Because of the quadratic change in the refractive index due to the QCSE, V_s is expected to decrease sharply as t is reduced.

On the basis of the two new concepts explained above, we designed and fabricated with MBE the sample as shown in Fig.1. In the optical modulation experiment, Ti-sapphire laser was used as the light source, and the end fire coupling method was employed. The optical output image was detected through an ($\times 100$) objective lens with an infrared CCD-TV camera, and the power ratio of light beams from each guide layer was analyzed using an image processor. The result in a sample with l of $138\mu\text{m}$ is shown in Fig.3. The sample length was apparently a little bit shorter than l_c at $V = 0$, but almost complete cross state was obtained at $V = 0$. At $V_s=5\text{V}$, the power ratio was reduced to 7% (extinction ratio of -11dB) and a fairly good bar state was reached. In addition, the main transition of power ratio occurred in a remarkably small voltage range between 1.5V and 3V .

In conclusion, we have proposed a novel device structure for vertical MQW directional coupler optical switch as shown in Fig.1 to lower the switching voltage and to get a better control of the device length in fabrication. In an actual sample with the length of $138\mu\text{m}$, a switching voltage as low as 5V has been measured. Both values are the lowest ever reported to our knowledge.

References

- [1] K.Tada and K.Hirose, Appl.Phys.Lett., vol.25, no.10, p.561, 1974
- [2] M.Cada, B.P.Keyworth, J.M.Glinski, C.Rolland, A.J.SpringThorpe, K.O.Hill, and R.A.Soref, J.Opt.Soc.Am.B, vol.5, no.2, p.462, 1988
- [3] J.A.Cavaillès, M.Erman, and K.Woodbridge, IEEE Photonics Technol.Lett., vol.1, no.11, p.373,1989
- [4] J.E.Zucker, K.L.Jones, M.G.Young, B.I.Miller, and U.Koren, Appl.Phys.Lett., vol.55, no.12, p.2280, 1989
- [5] M.Kohtoku, S.Baba, S.Arai and Y.Suematsu, IEEE Photonics Technol.Lett., vol.3, no.3, p.225, 1991
- [6] T.Ishikawa, T.Yamaguchi, and K.Tada, Extended Abstracts of the 51st Autumn Meeting, Jpn. Soc. Appl. Phys., 28-p-P-6, 1990
- [7] J.P.van der Ziel et al, M.Ilegems, and R.M.Mikulyak, J.Appl.Phys., vol.28, no.12, p.735, 1976
- [8] S.Ohke, T.Umeda and Y.Cho, Optics Comm., vol.70, no.2, p.92, 1989

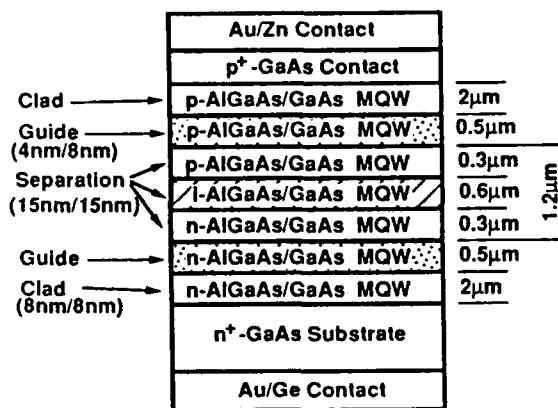


Fig.1: The novel device structure of vertical MQW directional coupler switch.

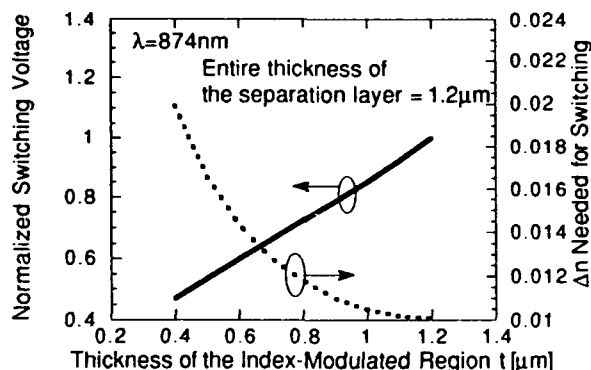


Fig.2: Calculated refractive index change needed for switching (dotted line) and normalized switching voltage (solid line) as functions of the thickness of the index-modulation region.

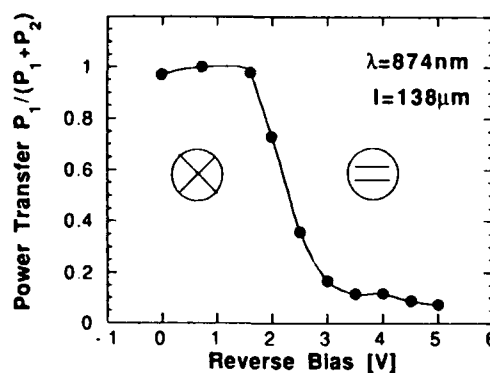


Fig.3: Measured switching characteristics in the sample.

WH5-1

Laser-Fabricated Electro-Optic Modulators in GaAs

L. Eldada, M.N. Ruberto, R. Scarmozzino, M. Levy, G. Scelsi, and R.M. Osgood, Jr.

Microelectronics Sciences Laboratory, Columbia University, New York, NY 10027, USA

Phone: (212) 854-8980 FAX: (212) 932-9421

1. INTRODUCTION

High-speed external modulators are necessary components for impressing signals onto lightwave carriers used in optical fibers for various transmission applications in telecommunications. III-V semiconductor waveguide electro-optic modulators offer the advantage of monolithic integration, which gives them an edge over lithium niobate modulators. We have used novel laser direct-writing techniques to masklessly define waveguide and electrode structures, and have fabricated an electro-optic polarization modulator in GaAs/AlGaAs. Our modulator exhibits a high extinction ratio and low value of V_{π} .

2. FABRICATION AND CHARACTERISTICS OF RIB-LIKE WAVEGUIDES

A detailed description of the experimental procedure and physical mechanism of laser-induced photoelectrochemical etching can be found elsewhere.¹ For these experiments, the substrate was a vertically single-mode waveguide structure consisting of a 1.3 μm layer of n-GaAs (10^{14} cm^{-3}) on a 2.7 μm layer of n-Al_{0.1}Ga_{0.9}As (10^{16} cm^{-3}). The IR wavelength used was 1.3 μm .

In a GaAs/AlGaAs heterostructure, IR light is confined vertically within the higher refractive index of the GaAs layer. By etching two grooves partway through the GaAs layer, we can confine light laterally in the region between the grooves by virtue of the greater effective index of the unetched region compared with that of the etched region.^{2,3} We have fabricated such rib-like waveguides and have measured their modal and loss properties as a function of geometric parameters. Lateral single-mode operation can be obtained by proper choice of etch depth and trench separation. Single-mode waveguides with losses as low as 0.6-0.9 dB/cm have been fabricated with our technique.

Several electro-optic devices, such as Mach-Zehnder-interferometer-based amplitude modulators and directional coupler switches, require various passive waveguiding structures such as tapers, bends, and branches. Such devices were easily fabricated with our novel maskless technique. Waveguide bend and branch loss has been measured and was found to be less than 1 dB for bend and branch angles less than 2°.

3. FABRICATION AND OPERATION OF THE MODULATOR

With our direct-write etching technique, we fabricated a straight waveguide on the GaAs/AlGaAs heterostructure described above. Aluminum electrodes were deposited on either side of the waveguiding region, using a combination of conventional lithographic procedures and UV direct-write patterning of photoresist.

In order to test the device, we launched light polarized at 45° to TE into the waveguide structure. The application of a voltage across the electrodes alters the polarization along the device via the electro-optic effect. By analyzing the output with an IR polarizer set at 90° to the input polarization, amplitude modulation is obtained. Figure 1 shows the transmission as a function of applied voltage, and demonstrates an extinction ratio of 17 dB and a V_{π} of 5 V.

4. CONCLUSION

In summary, the technique of laser-induced photoelectrochemical etching has been used to fabricate low-loss single-mode passive and active waveguiding structures and devices. In particular, we fabricated a polarization modulator which shows a high extinction ratio and a low value of V_{π} . These results indicate that our process offers a novel means for fabricating integrated optic device structures, and its maskless nature makes it a useful tool for prototyping integrated optic circuits.

This work was supported by the Defense Advanced Research Projects Agency / Air Force Office of Scientific Research and the National Center for Integrated Photonic Technology.

5. REFERENCES

1. M.N. Ruberto, X. Zhang, R. Scarmozzino, A.E. Willner, D.V. Podlesnik, and R.M. Osgood, Jr., *J. Electrochem. Soc.* **138**, 1174 (1991).
2. A.E. Willner, M.N. Ruberto, D.J. Blumenthal, D.V. Podlesnik, and R.M. Osgood, Jr., *Appl. Phys. Lett.* **54**, 1839 (1989).
3. M.N. Ruberto, R. Scarmozzino, A.E. Willner, D.V. Podlesnik, and R.M. Osgood, Jr., *SPIE Proc.* **1215**, 538 (1990).

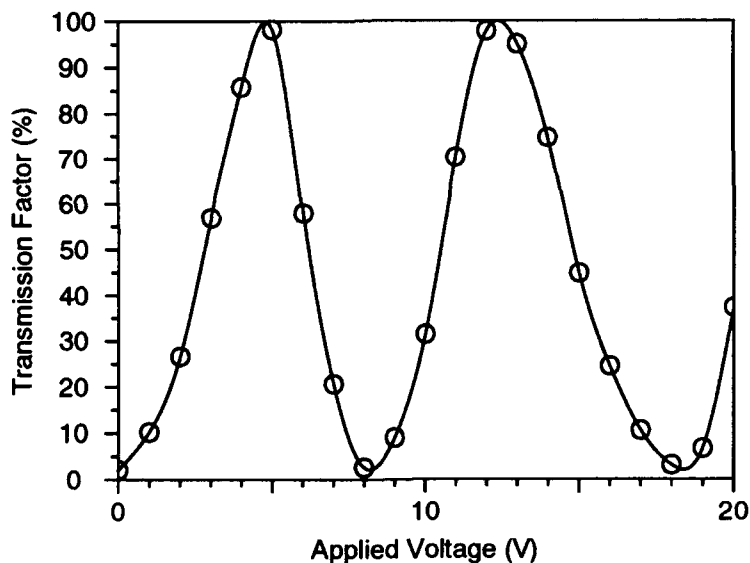


Figure 1. Transmission factor versus applied voltage for amplitude modulator described in text. The extinction ratio is 17 dB at $V_{\pi} = 5$ V for a device length of 8.5 mm.

WH6-1

Field-induced refractive index change dependence on incident light wavelength and polarization to an InGaAs/InAlAs multi-quantum well

Hiroaki Inoue, Hirohisa Sano and Shinji Nishimura

Central Research Laboratory, Hitachi Ltd.
Kokubunji, Tokyo 185, Japan
Tel: +81-423-23-1111

Field-induced refractive index change (Electro-refraction; ER) in multi-quantum well (MQW) structures arising from QCSE have become increasingly attractive for applications, especially in high speed, long-haul optical transmission systems. Because they have potential for low chirp, high speed modulation and for opto-electronic integration.[1,2]., Recently, highly efficient and small size MQW Mach-Zehnder(MZ) modulator had been reported[3]. However, the reports on the modulation characteristics had concentrated into the modulation characteristics for TE-like mode of the waveguide structure. Their polarization and wavelength dependences have not been fully revealed yet. In this paper, we describe an ER dependence on incident light wavelengths and polarizations to an InGaAs/InAlAs MQW MZ modulator operating at 1.55 μm wavelength region.

Figure 1 shows the structure of our modulator. The MQW was composed of 20 periods of InGaAs(60 \AA)/InAlAs(60 \AA), whose PL peak wavelength was 1.47 μm at room temperature. The absorption spectra showed the e-hh exciton absorption located at 1.47 μm and the e-lh at 1.40 μm , respectively. The device structures is the same as that of the previous report[3]. The MZ interferometer consisted of 2 Y-branches and 2 phase modulation arms having the ridge waveguides structures. The both facets of the modulator were anti-reflection coated by SiNx.

Figure 2 shows examples of the intensity modulation characteristics of the modulators with 1250 μm long arms. A wavelength tunable laser diode(1.50~1.60 μm) was used for the input light source with TE and TM mode polarizations. A set of 12 μm radius tapered fibers were coupled onto the input and output facets. The attenuation ratios including fiber-to-fiber coupling losses for various wavelengths are shown as a function of the voltage applied to only one of the modulation arms. The larger than 10dB of the extinction ratios were attained. The half wavelength voltage($V\pi$) for TE mode was 1.9V at 1.59 μm wavelength, and it reduced to 1.4V at 1.55 μm wavelength with 5dB increase of the insertion loss. And the values of $V\pi$ for TM mode were about 2.5 times larger than those of TE mode. Figure 3 shows the $V\pi$ and the phase modulation efficiency dependence on the incident light wavelengths for TE and TM modes. From this figure, we can see that the discrepancy between the phase modulation efficiencies for TE and TM modes coincides with the difference of the absorption peak wavelength difference between e-hh and e-lh exciton transition(~70nm).

In conclusion, we demonstrated the highly efficient field-induced refractive index change in InGaAs/InAlAs MQW MZ modulator for TE and TM modes. Its dependence on wavelength showed that ER characteristics for TE and TM modes almost depends on the detuning between the corresponding exciton absorption and incident light wavelengths, which suggests that the realization possibility of the polarization independent MZ modulator by introducing strain into MQW structures.

References

- [1] J.E.Zucker, et al., IEEE Photon. Technol. Lett., vol.2, p.32, 1990.
- [2] J.E.Zucker, et al., Top. Meeting on Integrated Photonics Research'91, WE4, 1991.
- [3] H.Sano, et al., Conference on Optical Fiber Communication (OFC'92), ThG4, 1992.

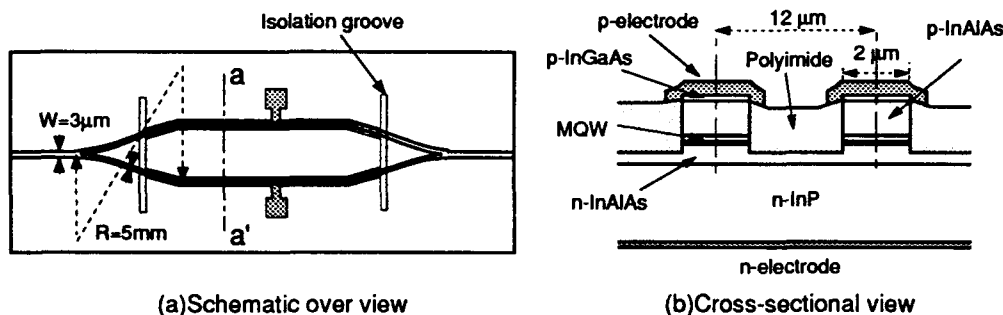


Fig.1 Device structure of MQW Mach-Zehnder optical modulator

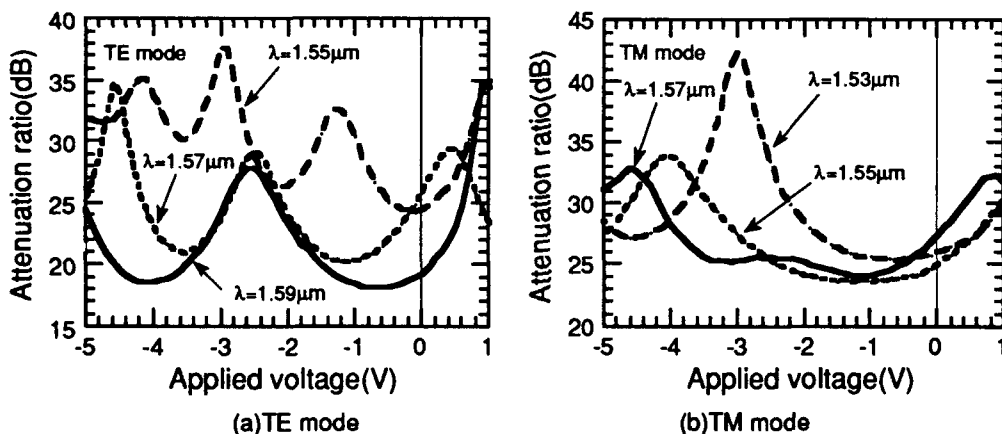


Fig.2 Examples of intensity modulation characteristics as a function of applied voltage

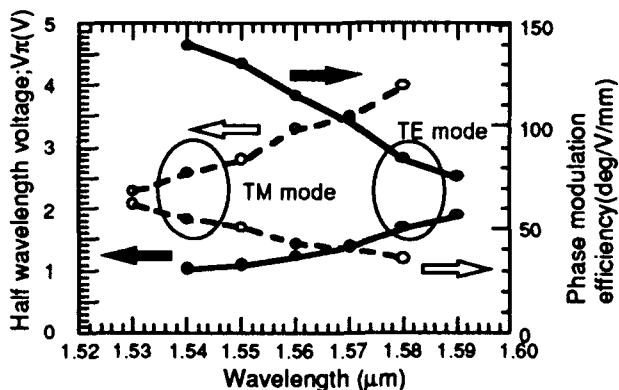


Fig.3 Half wavelength voltage and phase modulation efficiency as a function of wavelength

WH7-1

Geometry Dependence of the Field-Induced-Guide/Antiguide Modulator

T.C. Huang, T.C. Yang, Y. Chung, N. Dagli, and L.A. Coldren

Department of Electrical and Computer Engineering

University of California, Santa Barbara, CA 93106

Using the field-induced-guide (FIG) concept [1], guide/antiguide modulator with on/off ratio larger than 22dB, and optical bandwidth larger than 0.55 μm has been reported [2]. The device is formed with a central guide sandwich between two antiguides. For the on-state, a guide situation is created, and the input light will be confined and propagated in the central guide region. For the off-state, a antiguide situation is created, and the input light will be diffracted out of the central guide region [2]. It is obvious that the performance of the guide/antiguide modulator depends upon the geometrical dimensions of the gap G between the guide and antiguide electrodes, the active region length L , and the central guide width W . In order to understand the geometric dependence of the modulator, devices of different dimensions have been investigated, and both calculated and experimental results are reported here.

The measured on/off ratios for devices with $G=2\mu\text{m}$ (top data) and $G=5\mu\text{m}$ (bottom data) wide gaps are shown in Table 1. The devices are measured at 1.15 μm wavelength under push-pull operation, and the applied biases are $\sim -8\text{V}$. From the data in the same column, it can be seen that the modulators with longer modulation active lengths have larger on/off ratios. This is to be expected, since the diffraction loss increases with distance. Also, the data in the same row show that the modulators with narrower central guides have larger on/off ratios. This can be understood since the light can be diffracted out of the central guide more easily for a narrower guide. For devices with the same lengths and central guide widths, the device with a narrower gap size has larger on/off ratio, which indicates that when the gap becomes large, the propagating optical field has a lower overlap with the antiguide regions, which in turn decreases their function, and therefore, the on/off ratio.

L \ W	4 μm	6 μm	8 μm	10 μm
400 μm	~17.0dB ~11.6dB		~7.8dB	~8.2dB ~6.0dB
600 μm	~21.6dB ~13.5dB	~20.0dB ~9.8dB	~15.0dB	~10.8dB ~8.4dB
800 μm	~18.5dB	~18.1dB		~15.0dB ~13.2dB
1000 μm	~22.4dB ~21.9dB	~17.8dB	~17.0dB ~11.5dB	

Tab. 1 The measured on/off ratios of devices with different length L , different central guide width W for 2 μm (top data) and 5 μm (bottom data) wide gaps. The devices are measured at 1.15 μm wavelength under push-pull operation, and the applied biases are $\sim -8\text{V}$.

The dependence of on/off ratio on the device length is calculated using a finite difference BPM program [3], and the results are shown in Fig.1(a). The width of the center guide is $4\mu\text{m}$ for all gap sizes. Index changes of 0.0016 in the guide and antiguide are used in the calculation. To reach this index change, the applied bias has been found to be about -5V in our structure. In Fig.1(a), the dots are measured on/off ratios at -5V . The calculated results indicate that for lengths smaller than $800\mu\text{m}$ the on/off ratio for a gap size of $2\mu\text{m}$ increases faster than that for $3\mu\text{m}$ and $5\mu\text{m}$. However, the on/off ratio for a $2\mu\text{m}$ gap tends to increase sublinearly for a length longer than $800\mu\text{m}$, while that for $3\mu\text{m}$ and $5\mu\text{m}$ gap continue to increase slightly superlinearly. This is because the reflection at the gap region increases as the gap size decreases, so that off-state propagation for the smaller gap device would settle down to its leaky eignmode and as a result its off-state loss becomes relatively smaller as the modulation length becomes longer. Although the measured results are in relatively good agreement with the BPM calculation for short devices, there is discrepancy for lengths $>600\mu\text{m}$, especially for the $G=2\mu\text{m}$ case. We believe that the reason is because of relatively poor spatial filtering for this experiment.

In Fig.1(b), the dependence of on/off ratio on the guide width is plotted. The length of the modulation section is 1mm . The dots are measured on/off ratios at -5V . It is noted from the theoretical prediction that the optimum waveguide width for the on/off ratio varies as the gap size changes. To have a large on/off ratio, the light energy in the guide and antiguide regions should have an optimum distribution, if the waveguide is too small or too large, the light energy will be in the antiguide or guide region, which will reduce the modulation functions of the central guide or antiguide region and in turn reduce the on/off ratio. The optimum waveguide width becomes smaller as the gap size increases. Again, incomplete spatial filtering limits the on/off ratios of the experimental data.

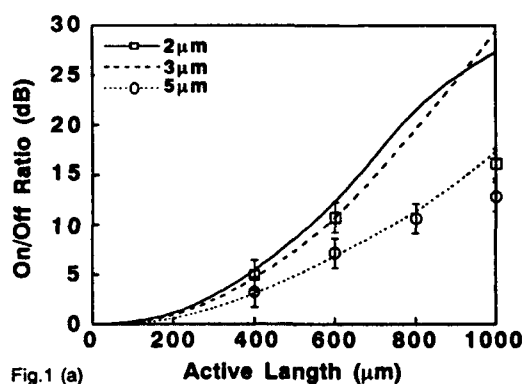


Fig.1 (a)

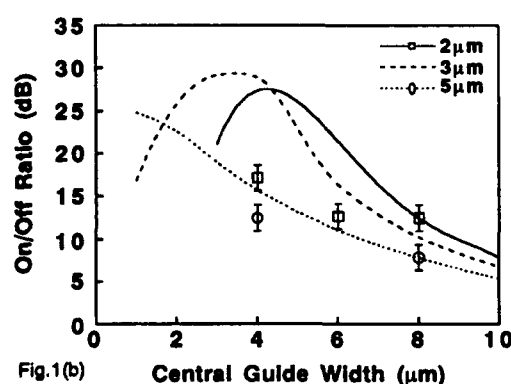


Fig.1(b)

Fig.1 Calculated (curves) and measured (dots) on/off ratios for three gap sizes vs. device length (a), as functions of the central guide widths (b) with the push-pull operation. An index change from 0 to 0.0016 is used in the calculations. The applied biases are -5V for the measurements.

Reference:

- [1] T.C. Huang, Y. Chung, N. Dagli, and L.A. Coldren, *Appl. Phys. Lett.*, 57 (1990)
- [2] T.C. Huang, Y. Chung, N. Dagli, and L.A. Coldren, *Appl. Phys. Lett.*, 58 (1991)
- [3] Y. Chung, and Dagli, *IEEE. J. Quantum Electron.*, Vol. QE-26, No.8, 1990

- Adam, P. — MB8
 Adams, M. J. — TuE1
 Ade, R. W. — MB21
 Agrawal, Govind Prasad — MD5, TuI
 Agrawal, N. — MC4
 Ahlers, E. — MB15
 Aitchison, J. S. — WA2, WA3
 Al-hemyari, K. — WA3
 Albert, J. — MB1, TuD1
 Albrecht, P. — MB20
 Alferness, R. C. — WF2
 Andonovic, I. — TuF5
 Andreadakis, N. C. — TuH6
 Andriesh, A. — MB9
 Ashley, Paul R. — WB1
- Baets, R. — WF3
 Ballesteros, E. — TuE3
 Bambha, R. — WA4
 Baquero, P. — TuE3
 Baran, J. E. — TuD3
 Barbarossa, G. — WB8
 Bardyszewski, Witold — WE1
 Basilica, R. P. — MB21
 Becker, P. — WF5
 Bellerby, R. — TuD6
 Berak, J. M. — MB21
 Berger, L. — MC4
 Bertolotti, M. — MB8, MB9
 Bhat, R. — MC2
 Bian, Jieren — TuI2, WA5
 Bierman, R. — TuC5
 Binkley, E. S. — WB3
 Bird, T. E. — WA4
 Blow, K. J. — TuF5
 Bornholdt, C. — MC4
 Borrelli, N. F. — WD1, WG4
 Bortz, M. L. — MB4
 Bossi, Donald E. — MB21
 Bothe, M. — WE5
 Bourgholtzer, S. L. — WH2
 Bowers, J. E. — WC3
 Bradley, R. — TuH4
 Bradshaw, S. A. — TuH4
 Brebner, J. L. — MB1
 Brinkmann, R. — WF5
 Bryce, A. C. — TuH4
 Buah, P. — TuE4
 Buhl, L. L. — WF2
 Bulmer, C. H. — TuG3
 Bulushev, A. G. — MB11
 Burke, S. V. — TuE1
 Burns, William K. — MA, TuG3, TuG6
 Burrus, C. A. — TuA5, WC2, WF2
 Burtiskii, K. S. — MB19
- Cada, M. — TuC5, TuF
 Campbell, Joseph C. — MC, TuH2
 Caneau, C. — TuH6
 Cao, Xiaofan — WB6
 Carlsen, W. John — WG2
 Cavaillès, A. — WA4
 Chan, Andrew K. — TuI2, WA5
 Chandler, P.J. — WF6
 Chandrasehkar, S. — MC7
 Chang, T. Y. — MC7
 Chang, William S. C. — TuB1
 Chaudhuri, S. K. — MB12
 Chbat, M. W. — WA1
 Chen, C.J. — TuF3
 Chien, M. D. — WC2, WF4
 Chin, Mee K. — TuB1
 Chirravuri, Jagannath — WD2
 Choquette, Kent D. — MC6
 Chui, C. K. — TuI2
 Chumash, V. — MB9
 Chung, Youngchul — WE4, WH7
 Classe, P.R. — TuA5
 Clemens, U. — MC4
- Colas, E. — TuH6
 Coldren, Larry A. — MA, MB, WF1, WH7
 Cooke, P.W. — TuA5
 Cooper, D.M. — WC4
 Cousins, Sarah — WG2
 Culbert, D. L. — WB3
 Cunningham, J. E. — MB22, WH3
- da Silva, V. L. — TuF2
 Dagli, Nadir — MC3, WE4, WH7
 Dannberg, P. — WB2
 Dapkus, P. D. — WF1
 Davidovitz, Marat — MB16
 Day, S. — TuD6
 Denbaars, S. — WF1
 Deri, R. J. — MD6, TuH6, WH1
 Derickson, D. J. — WC3
 DiGiovanni, D. J. — TuF3
 Dianov, E. M. — MB7, MB11, MB19
 Dodabalapur, Ananth — MC7
 Donnelly, J. P. — TuE2
 Drobot, A. — MD1
 Duan, Guang-Hua — MD5
- Eknoyan, O. — MB2
 Eldada, L. — WH5
 Ermer, S. — WB3
 Evaldsson, P. A. — TuA5
 Evangelides, S. G. Jr. — TuI1
- Fang, J. M. — MB5
 Farr, J. R. — WC4
 Feit, M. D. — WE2
 Fejer, Martin M. — MB4, TuC
 Field, S. J. — WF6
 Findakly, Talal K. — TuG2, WB
 First, P.N. — TuE5
 Fleck, J. A. — WE2
 Forrest, Stephen Ross — MF6, TuA
 Franke, D. — MC4
 Frankena, H. J. — TuD2
 Freund, R. S. — MC6
 Fujiwara, Takumi — WB6
- Gallion, Philippe — MD5
 Garmire, E. M. — WH2
 Gaylord, Thomas K. — MD2, TuE5
 Gerdes, J. — MB15
 Gibbings, C. J. — WC4
 Gibbs, H. M. — MF1
 Gill, D. M. — WB7
 Girtton, D. G. — WB3
 Glasner, Moses — WE1
 Glew, R. W. — TuH4
 Gliński, J. — TuC5
 Glytsis, Elias N. — MD2, TuE5
 Goorjian, Peter M. — TuI3
 Goossen, K. W. — MB22, WH3
 Gopalakrishnan, G.K. — TuG3
 Gopinath, Anand — MB16, TuB
 Gordon, J. P. — TuI1, TuI5
 Grant, M. F. — TuD6
 Grant, R. — WA3
 Grattan, K. T. V. — TuE4
 Greenblatt, A. S. — TuG3
- Hadley, G. Ronald — TuH5, WE3
 Haelterman, M. — MF5
 Hanafusa, Hiroaki — WG1
 Hance, B.K. — TuH2
 Hanna, D. C. — MA2, WF6
 Hansen, P. B. — WC2
 Hasenberg, T. C. — WH2
 Hasnain, G. — MC6
 Hattori, Takeo — WC6
 Hawkins, Raymond J. — MA, MB, MB17,
 MD6, WH1
 Hayes, R. — TuA2
 Heidrich, H. — MB20, MD7
- Heismann, F. — TuG1
 Helfert, S. — MB15
 Helkey, R. J. — WC3
 Henderson, Gregory N. — MD2, TuE5
 Hermansson, Bjorn R. — WE1
 Herrmann, H. — ME3
 Herzog, H.J. — TuA4
 Hill, K. O. — MB1
 Hinton, H. Scott — MA3
 Hoffman, D. — MC4
 Hong, B. J. — TuF3
 Hong, J. — MB14
 Hong, M. — MC6
 Howerton, M. M. — TuG6
 Hsu, T. Y. — WH2
 Hu, Shiqing — MB3
 Huang, T. C. — WH7
 Huang, W.P. — MB12, MB14
 Huber, David R. — WG3
 Hunte, G. — TuC3
 Hwang, D. M. — MC2
- Iga, Kenichi — MC5, WC1, WC6
 Ikegami, T. — MF1
 Inoue, Hiroaki — WH6
 Ippen, Erich P. — MA1
 Ironside, C. N. — WA2, WA3
 Ishikawa, Takuya — WH4
 Islam, Mohammed N. — MF, TuF3, WA1
 Iwamura, H. — MF1
- Jackel, Janet Lehr — MB3
 Jan, W. Y. — MB22, WH3
 Janszky, J. — MB8
 Januar, Indra — WF4
 Janz, S. — TuC5
 Janzen, G. — TuD5
 Jayaraman, V. — WF1
 Johnson, D. C. — MB1
 Johnson, J. J. — ME1
 Jupina, M. H. — WH2
- Kajrys, G. — MB1
 Kao, T. W. — WA6
 Kapon, E. — MC2
 Kappe, F. — MC4
 Kar-Roy, A. — ME2, ME5
 Kasahara, Kenichi — TuA1
 Kasper, E. — TuA4
 Katoh, Hisayuki — WC6
 Kawahara, M. — MB18
 Kawamura, Y. — MF1
 Kayser, O. — TuA3
 Kemmerer, C. T. — TuG4
 Kendall, P.C. — TuE1
 Kennedy, G.T. — WA3
 Kenney, J. T. — WB3
 Khanarian, G. — TuC3
 Khitrova, G. — MF1
 Kibbel, H. — TuA4
 Kiely, P. A. — TuA5
 Kiselev, A. V. — MB19
 Klem, J. F. — TuH5
 Knoche, T. — WB2
 Kobayashi, Kohroh — TuA1
 Koch, T. L. — WF2
 Kodama, Y. — TuF4
 Koehler, S. D. — WH2
 Koren, U. — WC2, WF2, WF4
 Korotky, Steven K. — ME, TuG4
 Kost, A. R. — WH2
 Koyama, F. — MC5
 Kravitz, S. H. — TuH5
- Large, A. C. — WF6
 Lau, Kam-Yin — WC5, WF
 Lau, S.D. — TuE2
 Laughton, F. R. — MF4
 Laybourn, P. J. R. — WB8

- Lee, Yong — MC1
 Leibenguth, R. E. — MC6
 Leminger, Ottokar — TuB3
 Lenstra, Daan — MB13, MD3, TuE
 Levy, M. — WH5
 Li, C. S. — TuB6
 Li, Guifang — MF3
 Li, K. C. — MC4
 Li, K.H. — TuH2
 Liakhou, G. — MB9
 Li kam wa, P. — WA4, WA6
 Lipscomb, G. F. — TuG5, WB3
 Locati, F. S. — WD4
 Lorenzo, Joe — TuD
 Luchnikov, A. V. — MB7
 Lui, Wayne — MD4
 Luther-Davies, Barry — MF2
 Lytel, R. S. — TuG5, WB3
- Malo, B. — MB1
 Mamyshev, Pavel V. — MB6
 Mannaerts, J. P. — MC6
 Mar, A. — WC3
 Marsh, J. H. — MF4, TuH4
 Marx, J. M. — MB2
 Maslov, V. A. — MB19
 Mathur, A. — WF1
 Matsumoto, Masayuki — TuC4
 McCaughan, Leon — WB7
 McDonald, David — WC7
 McElhanon, R.W. — TuG3
 McLeod, Robert R. — MB17
 Menyuk, Curtis R. — TuI4, WE
 Michelotti, F. — MB9
 Mickelson, Alan R. — WB4
 Miller, A. — WA4, WA6
 Miller, B. I. — WC2, WF2, WF4
 Minford, W. J. — TuG4
 Miscalco, William Joseph — WD, WD2, WD3
 Modavis, R. A. — WG4
 Moeller, R. P. — TuG6
 Mollenauer, L. F. — TuI1
 Moretti, A. L. — WA4
 Moriki, Kazunori — WC6
 Morthier, G. — WF3
 Moser, D. T. — TuG4
 Mukaihara, T. — MC5
 Muller, L. — WB2
 Muller-Reich, P. — ME3
 Mustieles, F. J. — TuE3
- Nada, Naoji — TuC2
 Narayanan, A. — TuA2
 Newkirk, M. A. — WF4
 Neyer, A. — WB2
 Ng, Willie Wing — TUA2, WC
 Nicklin, R. — TuH4
 Nishimura, Shinji — WH6
 Noda, Juichi — WG1
 Nolting, H.P. — MB20, TuB2, WE6
 Normandin, R. — TuC5
 Noteborn, H. J. M. F. — MB13
 Noutsios, Peter C. — TuD1
 Nurmikko, A. V. — TuH1
- O'Dowd, Ronan F. — WC7
 Ogawa, M. — WA6
 Oguchi, Taisuke — WG1
 Ohnishi, Yoshihumi — WC6
 Okayama, H. — MB18
 Okhotnikov, O. G. — MB11
 Olsen, C. M. — TuB6
 Osgood, R. M. Jr. — WH5
 Ovadia, Shlomo — WC5
- Park, R. M. — WA6
 Pedersen, B. — WD2, WD3
 Pennings, E. C. M. — MD6, TuH6, WH1
 Perrin, S. D. — WC4
 Petermann, K. — TuA4, TuD4, WE5
- Pilipetskii, A. N. — MB7
 Potasek, M. J. — MB5, MB10
 Pregla, R. — MB15
 Prokhorov, A. M. — MB7
 Prucnal, P. R. — WA1
- Quimby, R. S. — WD3
- Rahman, B. M. A. — TuE4
 Ramaswamy, Ramu V. — WB6
 Ratowsky, R. P. — WE2
 Raybon, G. — WC2, WF2
 Rees, G. J. — TuE1
 Reier, F. — MB20
 Reimann, V. — ME3
 Ricken, R. — ME3
 Roberts, J. S. — MF4
 Robson, P. N. — TuE1
 Romagnoli, M. — WD4
 Ruberto, M. N. — WH5
 Rust, U. — ME4
 Ryuo, T. — ME6
- Sakaguchi, Takahiro — WC6
 Salenink, H. — TuH3
 Sano, Hirohisa — WH6
 Scarmozzino, R. — WH5
 Scaturro, M. G. — TuG2
 Scelsi, G. — WH5
 Scherer, A. — MC2
 Schiavone, L. M. — TuH6
 Schlak, M. — MB20
 Schmidt, F. — WE6
 Schmidtchen, J. — TuD4
 Schreurs, J. W. H. — WG4
 Schuppert, B. — TuA4, TuD4
 Seibert, H. — ME3, TuD5
 Seki, Shunji — MD, MD4
 Seltzer, G. P. — WC4
 Serkin, V. N. — MB11
 Settembre, M. — WD4
 Shcherbakov, E. A. — MB19
 Shelby, Robert M. — TuF1
 Shepherd, D. P. — WF6
 Short, K. T. — WH3
 Sibbett, W. — WA3
 Sibilica, C. — MB8
 Silberberg, Yaron — TuF2, WA
 Simpson, J. R. — TuF3
 Smith, D. A. — ME1, TuD3, TuG
 Smith, N. J. — TuF5
 Smith, R. W. — TuG4
 Snyder, Allan W. — MF2
 Soccolich, C. E. — TuF3, WA1
 Sohler, W. — ME3, TuD5, WF5
 Sonek, G. J. — TuB5
 Song, G. Hugh — TuH6
 Song, H. — MC2
 Sornsin, Elizabeth A. — WB1
 Splett, A. — TuA4, TuD4, WE5
 Srivastava, Ramakant — WB6
 Stair, K. A. — WA4
 Stegeman, G. I. — WA2
 Stillier, M. — WB3
 Strake, E. — ME4
 Suche, H. — WF5
 Svilans, M. — TuC5
 Swenson, V. P. — MB2
 Sztafka, Georg — TuB4
- Tada, Kunio — WB5, WH4
 Tafflove, Allen — TuI3
 Tamada, Hitoshi — TuC1
 Tamburrini, M. — WD4
 Tanaka, Kohsuke — TuC4
 Tang, Z. — MB2
 Tasgal, R. S. — MB10
 Tatham, M. C. — WC4
 Taylor, G. W. — TuA5
 Taylor, H. F. — MB2
 Tekippe, Vincent J. — WG
- Teng, C.C. — TuG2
 Ticknor, A. J. — TuG5, WB3
 Townsend, P. D. — WF6
 Tozowonah, E. — TuH4
 Trillo, S. — MF5
 Trommer, D. — TuA3
 Tropper, A. C. — WF6
 Trudeau, Y. B. — MB1
 Tsai, C. — TuH2
 Tsai, C. S. — MB23, ME2, ME5, ME6
 Tsang, Won-Tien — TuH
- Uhlendorf, D. — WE5
 Umbach, A. — TuA3
 Unterborsch, G. — TuA3
- van Tartwijk, G. H. M. — MD3
 van der Linden, P. — MD3
- Valley, J. F. — TuG5, WB3
 Van Eck, T. E. — TuG5, WB3
 Vawter, G. A. — TuH5
 Verdiell, J.M. — WC2
 Verdiell, J. M. — WF4
 Veselka, J. J. — TuG4
 Villeneuve, A. — WA2
 Vu, T. Q. — MB23
- Wabnitz, S. — MF5, TuF4, WD4
 Wada, Osamu — WH
 Walker, D. B. — TuE5
 Walker, J. A. — WH3
 Walther, M. — MC2
 Wang, C.L. — ME6
 Wang, M. R. — TuB5
 Wasserbauer, J. G. — WC3
 Watanabe, Kenjiro — TuC2
 Wegener, M. — MC4
 Wei, T. — WD2
 Weinert, C. M. — MD7
 Wetzel, R. C. — MC6
 Whalen, M. S. — TuG1
 White, A. E. — V/H3
 White, J. M. — TuH2
 Wickman, R. W. — WA4
 Wigley, P. G. J. — WA2
 Willems, J. — WF3
 Wilson, D. W. — TuE5
 Wu, J. W. — WB3
 Wu, S. — TuD2
 Wu, Zhiqiang — MB16
 Wynn, J. D. — MC6
- Xu, C. L. — MB12
- Yamada, Masahiro — TuC2
 Yamaguchi, Takeharu — WH4
 Yamanaka, Takayuki — MD4
 Yamanishi, Masamichi — MC1
 Yang, C. C. — WA2
 Yang, T. C. — WH7
 Yang, Xiaoping — MF2
 Yap, D. — TuA2, WH2
 Yevick, David — WE1
 Yi, Jong Chang — MC3
 Yip, G. L. — TuD1
 Yokoyama, Kiyoyuki — MD4
 Yoshikuni, Yuzo — MD4
 Young, M. G. — WC2, WF2, WF4
 Yuhara, Toshiya — WB5
- Zang, D. Y. — MF6
 Zengerle, Remigius — TuB3
 Zha, Jun — TuI2
 Zhang, L. — WF6

INTEGRATED PHOTONICS RESEARCH

Approved for public release;
distribution unlimited.

SEP

AIR FORCE OFFICE OF SCIENTIFIC RESEARCH
NOTICE: This report is the property of the
Air Force Office of Scientific Research and
is loaned to your organization; it and its
contents are not to be distributed outside
your organization.

SEP 15 1992

Sponsored by
U.S. Air Force Office of Scientific Research
U.S. Army —Harry Diamond Laboratory
National Science Foundation
U.S. Office of Naval Research
Defense Advanced Research Projects Agency

for
IEEE/Lasers and Electro-Optics Society
Optical Society of America

POSTDEADLINE PAPERS

APRIL 13-16, 1992

NEW ORLEANS, LOUISIANA

INTEGRATED PHOTONICS RESEARCH
April 13-15, 1992
New Orleans, LA

Hotel Inter-Continental
La Salle B Ballroom

4:00pm

PD01 Monolithic wavelength demultiplexer and high density p-i-n array for 1.5 um WDM applications, Julian B. Soole, A. Scherer, Yaron Silberberg, H. P. LeBlanc, N. Andreadakis, C. Caneau, Bellcore, USA..... 1

We report a grating based wavelength demultiplexer monolithically integrated with a high density, 92 element, p-i-n detector array. A novel waveguide/detector array. A novel waveguide/detector coupling geometry is also demonstrated.

4:10pm

PD02 50 GHz velocity-matched, broad wavelength LiNbO3 modulator with multimode active section, David W. Dolfi, T.R. Ranganath, Hewlett-Packard Lab, USA 5

A velocity-matched LiNbO3 modulator is described which which achieves an optical 3dB bandwidth greater than 50 GHz, with excellent loss and drive voltage characteristics from 1.3 to 1.55 um wavelengths.

4:20pm

PD03 Circular grating surface-emitting laser, Chi Wu, M Svilans, T Makino, Jan M. Glinski, C Blaauw, C Maritan, Douglas Gordon Knight, Bell-Northern Res., Canada M. Fallahi, I. Templeton, National Res. Council, Canada Roman Maciejko, S. Iraj Najafi, Ecole Polytechnique, Canada..... 9

We report the first electrically-pumped circular grating surface-emitting DBR laser. The InGaAsP/InP device lases with a 1.3 um wavelength at room temperature under pulsed excitation.

4:30pm

PD04 Broad band array multiplexers made with silica waveguides on silicon, Renen Adar, C. H. Henry, C. Dragone, R. C. Kistler, M. A. Milbrodt, AT&T Bell Labs., USA..... 12

Broad band two channel waveguide array multiplexers are demonstrated. Cross talk and fiber-to-fiber insertion loss are the lowest yet reported for array multiplexers: -35dB and -2dB, respectively

4:40pm

PD05

Spectroscopic studies of Erbium-Titanium codoping of Lithium Niobate waveguides for active device applications, Feng Zhou, Pisu S. Jiang, R. M. DeLaRue, Charles N. Ironside, T. Han, Brian Henderson, Allister I. Ferguson, Univ. of Strathclyde, United Kingdom..... 16

A technique which combines Er doping directly with Ti:LiNbO₃ waveguide fabrication is described and luminescence and absorption techniques are used to characterize the doped waveguides.

4:50pm

PD06

Quantum-confined Stark effect of InGaAsP quantum wells grown on (110)InP substrates, Kunishige Oe, Koichi Wakita, NTT, Japan, R. Bhat, M. A. Koza, Bellcore, USA..... 18

A new phenomenon of the quantum-confined Stark effect has been found in InGaAsP quantum well grown on (110)InP substrates by OMVPE. Enhanced exciton absorption concurrent with the applied voltage is observed for the first time.

5:00pm

PD07

Polarization-independent electro-optic waveguide switch using strained InGaAs/InP quantum wells, Jane Zucker, Kevin Jones, T. H. Chiu, B. Tell, K. Brown-Goebeler, AT&T Bell Labs., USA..... 22

We demonstrate the first polarization-independent quantum well waveguide switch. We achieve low voltage and compactness via excitonic electrorefraction and engineer TM-to-TE efficiency using built-in strain.

5:10pm

PD08

Single-sideband modulator in GaAs integrated optics for microwave frequency operation, M J. Wale, Robert G. Walker, Colin Edge, GEC Marconi Materials Tech., United Kingdom..... 25

We describe the first experimental realization of an integrated optical single sideband modulator operating at microwave frequencies (10-14 GHz).

La Sallie C Ballroom

4:00pm

PD09 Ultrafast all-optical switching in an AlGaAs X-junction, J. Stewart Aitchison, Univ. of Glasgow, United Kingdom, Alain Villeneuve, George I. Stegeman, Univ. of Central Florida, USA..... 29

We report the first experimental observation of ultrafast, all-optical switching in a nonlinear X-junction, fabricated in Al_{0.18}Ga_{0.82}As and operating in the region of half the band gap.

4:10pm

PD10 Acousto-optic tunable filter for time-domain processing of ultra-short optical pulses, Martin Emanuel Fermann, Valeria L. da Silva, D.A. Smith, Yaron Silberberg, Andrew M. Weiner, Bellcore, USA..... 33

The application of acousto-optic tunable filters for shaping of ultra-fast pulses in the time domain is analyzed and demonstrated.

4:20pm

PD11 Polarization mode locking in erbium doped fiber ring lasers, M Romagnoli, A. Tajani, Mario Tamburrini, Stefan Wabnitz, B. Daino, Fondazione Ugo Bordoni, Italy, Flavio Fontana, N. Manfredini, G. Grasso, Societa Cavi Pirelli, Italy, Pierluigi Franco, Michele Midrio, Universita di Padova, Italy 38

We observed self-starting mode-locking of multiple frequency and polarization, and 300 GHz repetition rate femtosecond pulses from active locking of erbium doped fiber ring lasers.

4:30pm

PD12 Finite difference generalized Pade approximant propagation methods, David O. Yevick, Queens University, Canada, Moses Glasner, Penn State Univ. USA, Bjorn R. Hermansson, Telia Res. Sweden 42

We present a simple series of high-order finite difference and finite element propagation procedures based on approximating the exponential of two noncommuting operators as a product of single-operated Pade approximants.

4:40pm

PD13

Theory of square meander-type couplers, Hans-Peter Nolting, Heinrich Hertz Inst., Fed. Rep. Germany..... 46

This theory calculates coupling efficiency, period length, dispersion behavior etc. on the basis of the eigenmodes of the asymmetrical coupler using mode matching at the boundaries.

4:50pm

PD14

Optical nonlinear wakefield vortices: results from full-wave vector maxwell equation simulations in two spatial dimensions and time, Richard W. Ziolkowski, Justin B. Judkins, Univ. of Arizona, USA..... 50

We have discovered optical vortices trailing foci produced during the self-focusing of ultra-short pulses in Kerr media using a multi-dimensional nonlinear finite differences time domain (NL-FDTD) method.

5:00pm

PD15

Truly form birefringent fibres, Danny Wong, Simon B. Poole, Optical Fibre Techn. Ctr., Australia..... 52

In some fibre sensors, temperature drift causes phase noise which degrades the sensor severely. A novel intrinsic technique is presented in which the thermal independency is built into the preform of polarimetric sensors fibres. Experiment shown that this technique offers zero temperature sensitivity over a much wider range of temperature than previously reported techniques.

5:10pm

PD16

Stress relief: proof of the mechanism of photo-induced index change, Danny Wong, Simon B. Poole, Mark Geoffrey Sceats, Optical Fibre Techn. Ctr., Australia..... 56

It is demonstrated, for the first time, that stress-relief is responsible for the photo-induced index changes in optical fibres. This mechanism is a consequence of the breakage of wrong-bonds in the glass network through single- or multi-photo absorption, which allows relaxation of the stresses. The index changes through the stress-optic effect.

Key to authors..... 61

INTEGRATED PHOTONICS RESEARCH
April 13-15, 1992
Hotel Inter-Continental

- PD01 Monolithic wavelength demultiplexer and high density p-i-n array for 1.5 um WDM applications, Julian B. Soole, A. Scherer, Yaron Silberberg, H. P. LeBlanc, N. Andreadakis, C. Caneau, Bellcore, USA..... 1

We report a grating based wavelength demultiplexer monolithically integrated with a high density, 92 element, p-i-n detector array. A novel waveguide/detector array. A novel waveguide/detector coupling geometry is also demonstrated.

- PD02 50 GHz velocity-matched, broad wavelength LiNbO3 modulator with multimode active section, David W. Dolfi, T.R. Ranganath, Hewlett-Packard Lab, USA 5

A velocity-matched LiNbO3 modulator is described which achieves an optical 3dB bandwidth greater than 50 GHz, with excellent loss and drive voltage characteristics from 1.3 to 1.55 um wavelengths.

- PD03 Circular grating surface-emitting laser, Chi Wu, M Svilans, T Makino, Jan M. Glinski, C Blaauw, C Maritan, Douglas Gordon Knight, Bell-Northern Res., Canada M. Fallahi, I. Templeton, National Res. Council, Canada Roman Maciejko, S. Iraj Najafi, Ecole Polytechnique, Canada..... 9

We report the first electrically-pumped circular grating surface-emitting DBR laser. The InGaAsP/InP device lases with a 1.3 um wavelength at room temperature under pulsed excitation.

- PD04 Broad band array multiplexers made with silica waveguides on silicon, Renen Adar, C. H. Henry, C. Dragone, R. C. Kistler, M. A. Milbrodt, AT&T Bell Labs., USA..... 12

Broad band two channel waveguide array multiplexers are demonstrated. Cross talk and fiber-to-fiber insertion loss are the lowest yet reported for array multiplexers: -35dB and -2dB, respectively

- PD05 Spectroscopic studies of Erbium-Titanium codoping of Lithium Niobate waveguides for active device applications, Feng Zhou, Pisu S. Jiang, R. M. DeLaRue, Charles N. Ironside, T. Han, Brian Henderson, Allister I. Ferguson, Univ. of Strathclyde, United Kingdom..... 16

A technique which combines Er doping directly with Ti:LiNbO₃ waveguide fabrication is described and luminescence and absorption techniques are used to characterize the doped waveguides.

- PD06 Quantum-confined Stark effect of InGaAsP quantum wells grown on (110)InP substrates, Kunishige Oe, Koichi Wakita, NTT, Japan, R. Bhat, M. A. Koza, Bellcore, USA..... 18

A new phenomenon of the quantum-confined Stark effect has been found in InGaAsP quantum well grown on (110)InP substrates by OMVPE. Enhanced exciton absorption concurrent with the applied voltage is observed for the first time.

- PD07 Polarization-independent electro-optic waveguide switch using strained InGaAs/InP quantum wells, Jane Zucker, Kevin Jones, T. H. Chiu, B. Tell, K. Brown-Goebeler, AT&T Bell Labs., USA..... 22

We demonstrate the first polarization-independent quantum well waveguide switch. We achieve low voltage and compactness via excitonic electrorefraction and engineer TM-to-TE efficiency using built-in strain.

- PD08 Single-sideband modulator in GaAs integrated optics for microwave frequency operation, M J. Wale, Robert G. Walker, Colin Edge, GEC Marconi Materials Tech., United Kingdom..... 25

We describe the first experimental realization of an integrated optical single sideband modulator operating at microwave frequencies (10-14 GHz).

- PD09 Ultrafast all-optical switching in an AlGaAs X-junction, J. Stewart Aitchison, Univ. of Glasgow, United Kingdom, Alain Villeneuve, George I. Stegeman, Univ. of Central Florida, USA..... 29

We report the first experimental observation of ultrafast, all-optical switching in a nonlinear X-junction, fabricated in Al_{0.18}Ga_{0.82}As and operating in the region of half the band gap.

- PD10 Acousto-optic tunable filter for time-domain processing of ultra-short optical pulses, Martin Emanuel Fermann, Valeria L. da Silva, D.A. Smith, Yaron Silberberg, Andrew M. Weiner, Bellcore, USA..... 33

The application of acousto-optic tunable filters for shaping of ultra-fast pulses in the time domain is analyzed and demonstrated.

- PD11 Polarization mode locking in erbium doped fiber ring lasers, M Romagnoli, A. Tajani, Mario Tamburrini, Stefan Wabnitz, B. Daino, Fondazione Ugo Bordoni, Italy, Flavio Fontana, N. Manfredini, G. Grasso, Societa Cavi Pirelli, Italy, Pierluigi Franco, Michele Midrio, Universita di Padova, Italy 38

We observed self-starting mode-locking of multiple frequency and polarization, and 300 GHz repetition rate femtosecond pulses from active locking of erbium doped fiber ring lasers.

- PD12 Finite difference generalized Pade approximant propagation methods, David O. Yevick, Queens University, Canada, Moses Glasner, Penn State Univ. USA, Bjorn R. Hermansson, Telia Res. Sweden 42

We present a simple series of high-order finite difference and finite element propagation procedures based on approximating the exponential of two noncommuting operators as a product of single-operated Pade approximants.

- PD13 Theory of square meander-type couplers, Hans-Peter Nolting, Heinrich Hertz Inst., Fed. Rep. Germany..... 46

This theory calculates coupling efficiency, period length, dispersion behavior etc. on the basis of the eigenmodes of the asymmetrical coupler using mode matching at the boundaries.

- PD14 Optical nonlinear wakefield vortices: results from full-wave vector maxwell equation simulations in two spatial dimensions and time, Richard W. Ziolkowski, Justin B. Judkins, Univ. of Arizona, USA..... 50

We have discovered optical vortices trailing foci produced during the self-focusing of ultra-short pulses in Kerr media using a multi-dimensional nonlinear finite differences time domain (NL-FDTD) method.

PD15 Truly form birefringent fibres, Danny Wong, Simon B. Poole, Optical Fibre Techn. Ctr., Australia..... 52

In some fibre sensors, temperature drift causes phase noise which degrades the sensor severely. A novel intrinsic technique is presented in which the thermal independency is built into the preform of polarimetric sensors fibres. Experiment shown that this technique offers zero temperature sensitivity over a much wider range of temperature than previously reported techniques.

PD16 Stress relief: proof of the mechanism of photo-induced index change, Danny Wong, Simon B. Poole, Mark Geoffrey Sceats, Optical Fibre Techn. Ctr., Australia..... 56

It is demonstrated, for the first time, that stress-relief is responsible for the photo-induced index changes in optical fibres. This mechanism is a consequence of the breakage of wrong-bonds in the glass network through single- or multi-photo absorption, which allows relaxation of the stresses. The index changes through the stress-optic effect.

Key to authors..... 61

Monolithic Wavelength Demultiplexer and High Density p-i-n Array for 1.5 μ m WDM Applications

J.B.D.Soole, A.Scherer, Y.Silberberg, H.P.LeBlanc,
N.C.Andreadakis, and C.Caneau.

Bellcore, 331 Newman Springs Road, Red Bank, NJ 07701

Abstract

We report a grating based wavelength demultiplexer monolithically integrated with a high density, 92 element, p-i-n detector array. A novel waveguide / detector coupling geometry is also demonstrated.

Summary

Wavelength Division Multiplexing (WDM) is currently being advocated for use in future communication networks, in applications ranging from high speed point-to-point links and wavelength-addressed processors in distributed computing environments, through multi-wavelength all-optical networks, to customer and service segregation in the telephone local loop [1].

In WDM systems, considerable advantage may be gained if the demultiplexing and detection can be achieved by a single monolithic component. In this paper, we report such a device: an InP-based chip that monolithically integrates a grating wavelength demultiplexer and 92 high speed p-i-n photodetectors. It operates in the 1.5 μ m fiber band and separates channels spaced in wavelength by 1nm. A 42 channel, 4nm-spacing, device operating on similar principles was recently reported [2]. The present paper, however, is the first to report integrated WDM detection with the closer channel spacing of 1nm. In addition, a novel waveguide / detector coupling geometry is demonstrated for the first time, and shown to be capable of providing detection with simultaneous high speed and efficiency.

A schematic of the device and its operation is given in figure 1. The integrated grating wavelength demultiplexer is similar to that reported in [3], and is formed in an InP/InGaAsP/InP double heterostructure planar waveguide. A single mode ridge waveguide provides the input to the demultiplexing 'spectrometer' body, a chemically-assisted ion beam etched vertical reflection grating provides the wavelength dispersion and focusing, and output ridge waveguides collect the wavelength demultiplexed light and funnel the separate signals to waveguide p-i-n photodiodes.

The curved diffraction grating was etched through the full waveguide heterostructure using chemically assisted ion beam etching ($<3^\circ$ to vertical), and was coated with (Ti/Au) reflector metal. The grating operated in 16th order, and was blazed for retro-reflective diffraction. We used a InP(0.5 μ m)/InGaAsP($\lambda_g=1.1\mu$ m; 0.6 μ m)/InP planar waveguide for the demultiplexer body and

n-InP(0.1 μ m)/i-InGaAs(0.6 μ m)/p-InGaAsP(λ_g =1.3 μ m, 0.4 μ m)/p-InP structure for the p-i-n's. A photomicrograph of a section of the fabricated p-i-n array and integrated waveguides is shown in Figure 2.

The waveguide detectors employed a novel structure, which a hybrid between the more conventional butt-coupling and vertical coupling approaches [4]. The guide core and the detector structure is grown first, by OMCVD, on a semi-insulating InP. The detector structures is then mesa-etched and the InP waveguide cladding regrown over the body of the demultiplexer and up against the mesa side-walls. After grating etching, fabrication of the p-i-n diodes is completed. The resulting waveguide / detector geometry is shown in figure 3.

The demultiplexing performance of the device is shown in figure 4. Every other channel of a 75 channel span was examined. The peak detection wavelength is plotted against channel number. The channel separation is accurately 1nm. The inset shows the wavelength response of a single detector; bandpasses were typically 6 \AA -8 \AA , FWHM. Some coupling was observed between the output guides, with nearest neighbor crosstalk at -7.8dB, next nearest neighbor crosstalk at \sim -15dB, and coupling to remote guides at the background level of <-30dB.

The 'hybrid' waveguide / detector coupling does not require regrowth of any of the critical waveguiding surfaces and yields a planar, or pseudo-planar, surface that facilitates further degrees of integration. The structure, nevertheless, provides strong coupling between the guided light and the detector, leading to rapid waveguide attenuation. A BPM simulation of attenuation against detector length is given in figure 5, showing the rapid absorption of guided light. The p-i-n diodes fabricated had a length of just 25 μ m, and were found to absorb \sim 90% of the incident guided light.

In a separate experiment, the high speed performance of the waveguide diodes was examined. The bandwidths were found to be \sim 15GHz, in agreement with fitted S-parameters. This is, to our knowledge, the highest speed reported to date for a waveguide integrated photodetector. The bandwidth was limited by poor n-InP contact resistance (C, just \sim 50fF). With reduced series resistance, bandwidths in excess of 30GHz are to be expected.

In summary, we report a high density, 1nm-spacing, wavelength demultiplexing detector array operating in the 1.5 μ m fiber band. A novel waveguide / detector coupling geometry providing efficient high speed detection is also demonstrated.

[1] C. Brackett, *J.Sel Areas in Comm.*, 8, 948, 1990.

[2] C.Cremer et. al., *I.E.E.E. Phot. Tech Lett.*, 4, 108, 1992.

[3] J.B.D. Soole et al., *Appl. Phys. Lett.*, 58, 1949, 1991.

[4] J.B.D.Soole et. al., *O.S.A. Topical Meeting on Optoelectronics*, Monterey, July 1990.

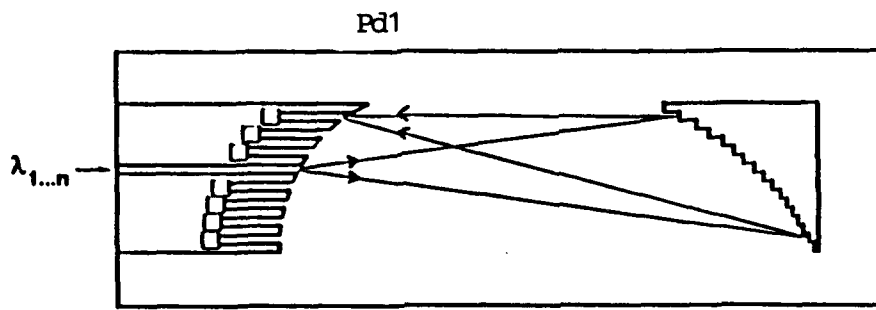


Figure 1. Schematic of the monolithic WDM detector chip.

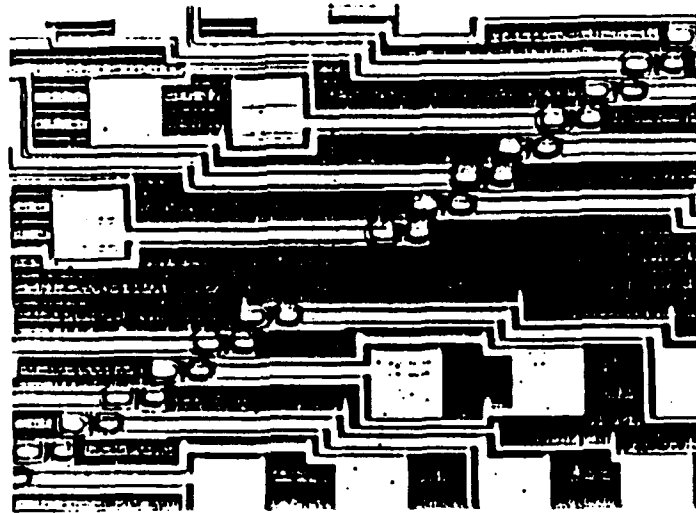


Figure 2. Photomicrograph of a portion of the central section of the fabricated detector array.

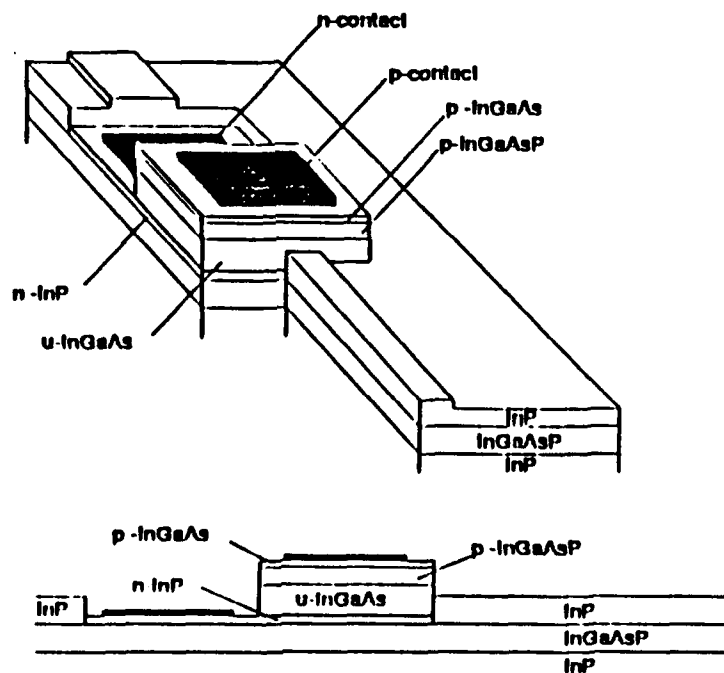


Figure 3. Schematic of the 'hybrid' detector / waveguide geometry.

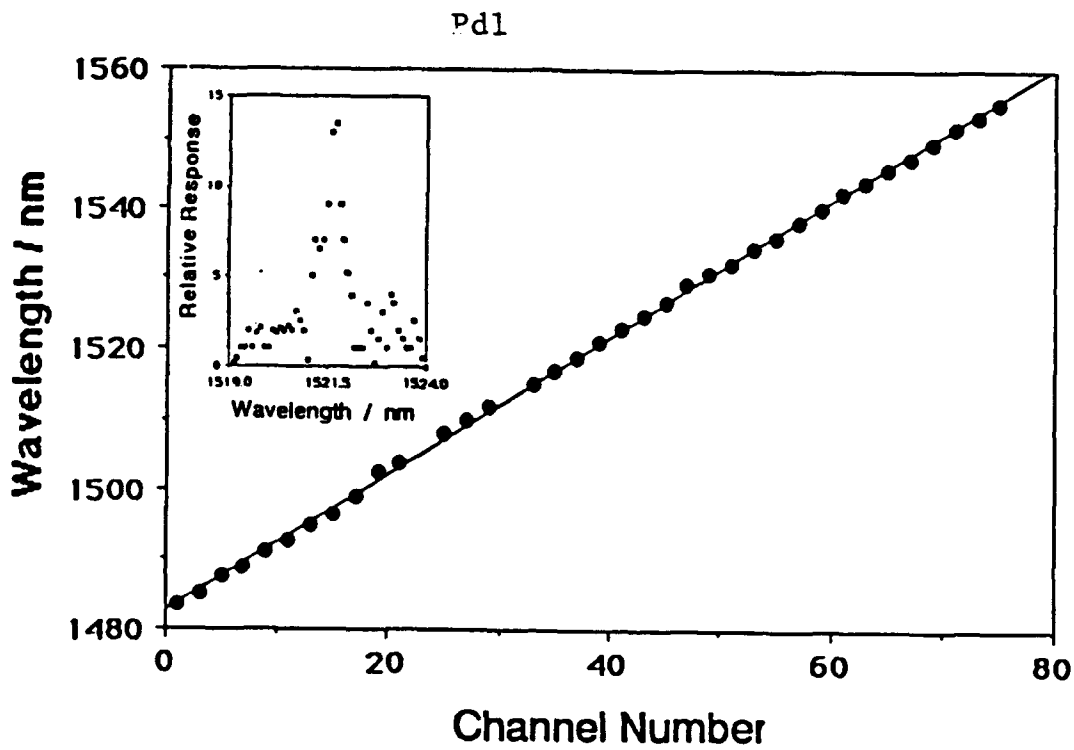
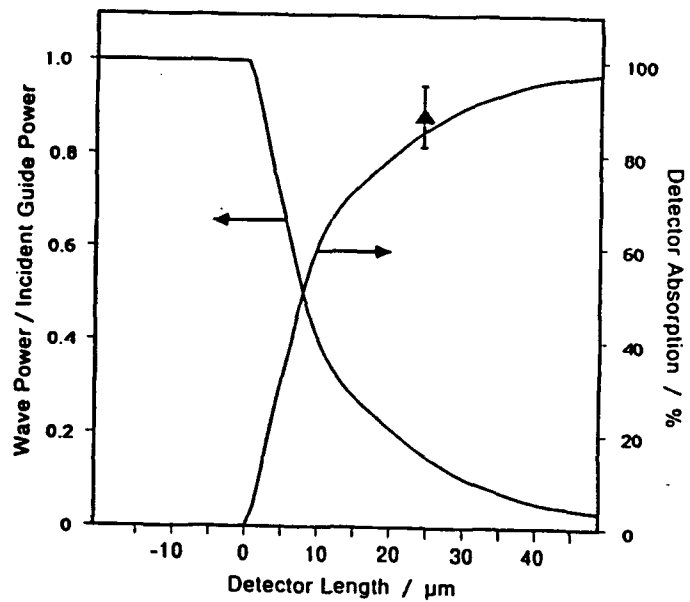


Figure 4. Wavelength demultiplexing performance. Peak wavelength position v. channel number; the inset shows the wavelength selectivity for a single detector.

Figure 5. BPM simulation of the waveguide attenuation under a detector. Also given, the measured absorption of the 25 μ m long fabricated device.



50 GHz Velocity-matched, broad wavelength LiNbO₃ modulator with multimode active section

David W. Dolfi and T.R. Ranganath
 Hewlett-Packard Laboratories
 3500 Deer Creek Road, Palo Alto, CA 94304

Summary: Improved velocity matching in LiNbO₃ modulators has been achieved by several workers [1-4], using a combination of relatively thick ($\geq 1 \mu\text{m}$) SiO₂ buffer layers and thick (typically $\geq 10 \mu\text{m}$) plated electrodes. Utilizing this combination, microwave indices ≤ 2.5 have been achieved. However, increase in electrode thickness lowers device impedance, which raises drive power requirements and causes mismatch to most common 50 Ω sources. This decrease is partially compensated by the thicker buffer layer and by employing large gaps (typically 15 μm) between the hot and ground electrode(s), both of which maintain the impedance at a high value. They also increase the drive voltage, however, resulting in a larger voltage-length product relative to conventional modulators. To achieve closer velocity matching would require additional increases in electrode/buffer thicknesses, resulting in even higher voltages.

Here we describe a device which also utilizes a thick electrode/buffer layer geometry. However, it also introduces two novel features, resulting in a device which achieves almost exact velocity matching to the optical index, maintains high impedance, and has a voltage-length product which is as good or better than previous devices of this type. In addition, it maintains this performance over the whole range of wavelengths from 1.3 to 1.55 μm . This latter property is very important for optical measurement applications such as network analysis and optical sampling.

The microwave structure of the device - a Mach-Zehnder (MZ) modulator - is shown in Fig. 1. The optical waveguides are either centered in the electrode gaps (for x-cut geometry) or moved laterally to lie under the electrode edges (z-cut). Devices of both types have been fabricated. Unlike previous designs, the structure utilizes a narrow ground plane whose width is only slightly larger than either the hot electrode width or gap. Decreasing the ground plane width introduces an extra degree of freedom which allows further decrease of microwave index as well as a slight reduction of the gap, while maintaining the same impedance. Referring to Fig. 1, the parameters are as follows. The hot electrode width $W = 9 \mu\text{m}$, the ground electrode width $W_g = 15 \mu\text{m}$, and the electrode gap $G = 10 \mu\text{m}$. The electrode and buffer layer thickness are $t_e = 10 \mu\text{m}$ and $t_b = 1 \mu\text{m}$, respectively. Calculations predict that this structure has an impedance $Z \simeq 40 \Omega$ and a microwave index $n_m \simeq 2.15$, essentially equal to the optical index at 1.3 μm .

The second novel feature, shown in Fig 2, concerns the optical waveguides themselves. The waveguides in the active section of the device have sufficiently high index difference to be multimode at $1.3 \mu\text{m}$. The resulting higher index improves mode confinement, reducing drive voltage and enabling efficient, low-loss operation over an extended wavelength range. The input and output waveguide sections are reduced in width, and are single-mode over the same wavelength range. The symmetric, adiabatic nature of the Y-junction connecting these two regions insures that no higher order modes are excited in the active section. For the devices fabricated here, the narrow and wide waveguide widths are 4 and $6 \mu\text{m}$, respectively. The titanium (Ti) thickness is 1100 \AA (x-cut) and 1150 \AA (z-cut). Diffusion times are 6 and 8 hours for x and z cut, respectively. The diffusion temperature is $1050 \text{ }^\circ\text{C}$.

M-Z modulators were fabricated in both x and z cut LiNbO_3 as well as straight guides and y-junctions (one-half of an interferometer). It was verified that the $6 \mu\text{m}$ straight guides supported at least two modes at $1.3 \mu\text{m}$ wavelength. When y-junctions were excited at the $4 \mu\text{m}$ end, however, only the well-confined, lowest order mode of the $6 \mu\text{m}$ output guides was observed, independent of input alignment, verifying the principle of operation.

Drive voltages of 1 cm active length modulators were measured at both wavelengths. The results are summarized in Fig. 3. The drive voltage scales roughly as λ and λ^2 for x and z cut devices, respectively. The stronger dependence in the z-cut case is due to the sensitivity of the overlap of the optical mode and fringing microwave field to the size of the mode, and suggests that further reduction in the voltage-length product is possible by using even higher Ti concentrations. Preliminary measurement of on/off ratios at $1.3 \mu\text{m}$ are well in excess of 20 dB for both x and z cut. Fiber-to-fiber insertion loss, based on measurements thus far on 1 cm active length devices, is estimated to be < 3 dB for z-cut and < 4 dB for x-cut, with some measurements as low as 2 dB for z-cut. The difference is mainly due to the more symmetric mode of the z-cut devices, which matches more closely to singlemode fiber.

High frequency measurements have been performed on a few x-cut devices. Fig. 4 shows a device response to 50 GHz measured at $1.3 \mu\text{m}$. The 3 dB electrical bandwidth is $\simeq 40$ GHz. The 3 dB optical bandwidth exceeds 50 GHz, and is estimated > 60 GHz by extrapolation of the data. Fig. 5 shows the response when optical and electrical signal are counter-propagating. This induces a velocity mismatch which generates the sinc-like response shown. The dashed vertical line near 7 GHz represents the theoretically predicted location of the first null for exact velocity matching. The small deviation of the actual null from this line implies that the microwave and optical indices differ by less than 3.5 %.

In summary, a novel Mach-Zehnder modulator in LiNbO_3 is described. It utilizes a novel microwave structure with narrow ground planes to achieve 50 GHz frequency response and almost exact velocity matching. In addition, a novel waveguide concept - the use of multimode guides with only lowest order mode excitation - has been used in the interferometer design to achieve good mode confinement over the entire wavelength range of 1.3 to $1.55 \mu\text{m}$, resulting in low optical insertion loss, no degradation in on/off ratio, and voltage-length products as low as 8.3 volts-cm for z-cut LiNbO_3 .

References:

- [1] M. Seino, et.al., *ECOC '89*, paper ThBB22-5, 1989. see also M. Seino, et. al., *ECOC '90*, postdeadline paper ThG1.4, 1990.
- [2] H. Miyamoto, et. al., *Japanese Jour. Appl. Phys.*, **30**, p. L-383, 1991.
- [3] S.K. Korotky, et. al., *IPR '91*, paper TuG2, 1991.
- [4] H. Ohta, et. al., *OFC '92*, paper ThG3, 1992.

Figure Captions:

Fig. 1 - Cross-section of microwave co-planar structure. In x-cut (z-cut) geometry, waveguides are located between (under) the electrode edges. Parameter values are given in text.

Fig. 2 - Geometry of M-Z interferometer, with view of y-junction. Widths of waveguide(s) are 4 and 6 μm in input/output and active regions, respectively.

Fig. 3 - Voltage-length product of devices for different orientations and wavelengths.

Fig. 4 - Frequency response of 1 cm x-cut device in normal mode of operation, with optical and microwave fields propagating in same direction.

Fig. 5 - Frequency response of device in Fig. 4 with optical and microwave fields propagating in opposite directions. Vertical dashed line represents null frequency for exact velocity matching.

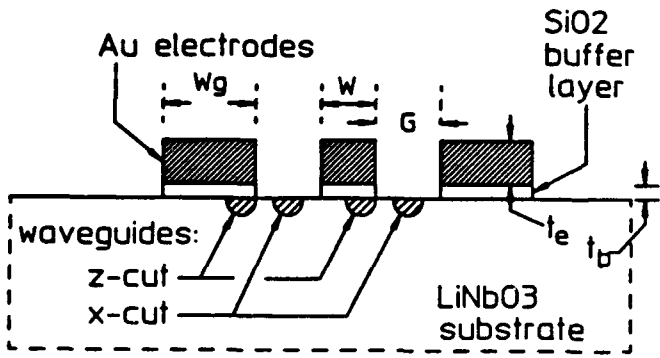


Figure 1

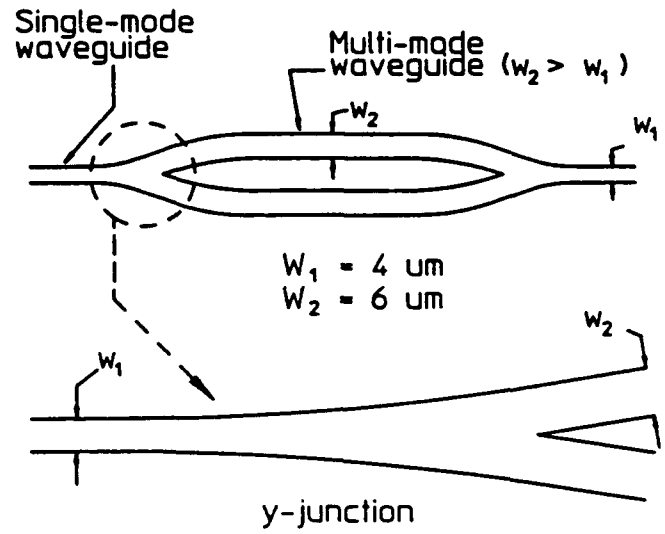


Figure 2

Voltage-length product (volt-cm)

	x-cut	z-cut
1.3 micron	10.4	8.4
1.55 micron	12.8	12.3

Active length: 1 cm

Figure 3

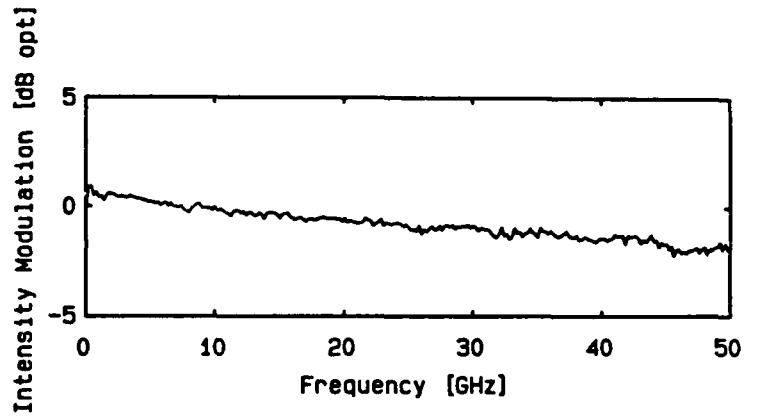


Figure 4

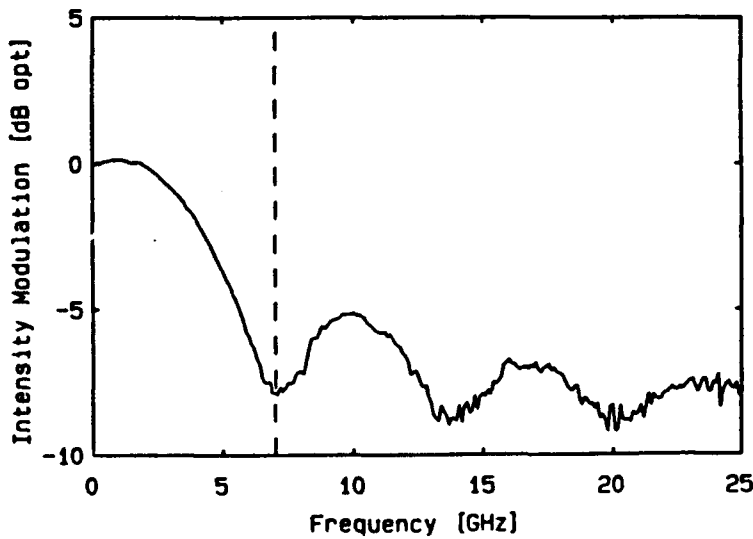


Figure 5

Circular Grating Surface-Emitting Laser

C. Wu, M. Svilans, T. Makino, J. Ginski, C. Blaauw, C. Maritan, D.G. Knight
Solid-State Opto-Electronics Consortium, Bell-Northern Research, Ottawa, Canada

M. Fallahi, I. Templeton
Solid State Opto-Electronics Consortium, National Research Council, Ottawa, Canada

Romain Maciejko, S. Iraj Najafi
Département de Génie Physique, Ecole Polytechnique de Montréal, Montreal, Canada

Although surface-normal emission from a laser using a one-dimensional second-order grating has been published for some time [1], it is only in the last few years that the theory of circular (i.e. two-dimensional) gratings has been considered theoretically [2-4]. Last year lasing in an optically-pumped circular grating structure was observed [5]. Here we report for the first time lasing at room temperature in an electrically-pumped circular grating laser.

The structure of the laser consists of a circular active region with a conventional double-heterostructure(DH) surrounded by a waveguide region. A concentric second-order circular grating patterned on top of it (Fig. 1) serves the dual purpose of a distributed Bragg reflector (DBR) for the in-plane cavity, as well as the coupler for the surface-normal output with a circular symmetry.

Fabrication of the device entailed two epitaxial steps. Metallo-organic vapour phase epitaxy (MOVPE) was first used to grow the GaInAsP/InP DH in the standard way. Circular mesas were then formed with reactive ion etching (RIE) to a depth just past the active layer. Regrowth of the waveguiding region followed, after which contacts were evaporated to the central mesa and the n-type InP substrate. Focused ion beam (FIB) was used to pattern the DBR circular grating in PMMA with a length of 140 μm and period of 0.4 μm . Using this resultant mask the grating pattern was transferred to the guiding layer by CH₄/H₂ RIE to a depth of 0.2 μm . A scanning electron micrograph of a finished device is presented in Fig. 2.

The finished lasers were tested at room temperature directly on the wafer using 100ns pulses with a period of 10 μs . A large-area photodetector was used above the laser to collect the light output. The measured surface-emitted output power was plotted against the injection current (Fig. 3). The threshold current for a 60 μm diameter laser is 140mA, with the output power reaching 4mW at 600mA. The output spectrum (Fig. 4) exhibits relatively thick lines indicative of multi-mode operation, which is expected from theoretical analysis of the structure.

In conclusion, the performance of the first circular grating DBR surface-emitting laser at room temperature indicates that this design has potential for practical applications including integration into arrays. Room temperature CW operation should be achievable by optimizing the present device design.

- [1] Zh. I. Alferov et al., *IEEE J. Quantum Electron.* QE-11 no.7 (1975) pp. 440-451
- [2] M. Toda, *IEEE J. Quantum Electron.* QE-26 no.3 (1990) pp. 473-481
- [3] T. Erdogan and D. G. Hall, *J. Appl. Phys.* 68 no.4 (1990) pp.1435-1444
- [4] C. Wu et al., *J. Lightwave Technol.* 9 no.10 (1991) pp.1264-1277
- [5] C. Wu et al., *Electron. Lett.* 27 no.20 (1991) pp.1819-1820

Pd3

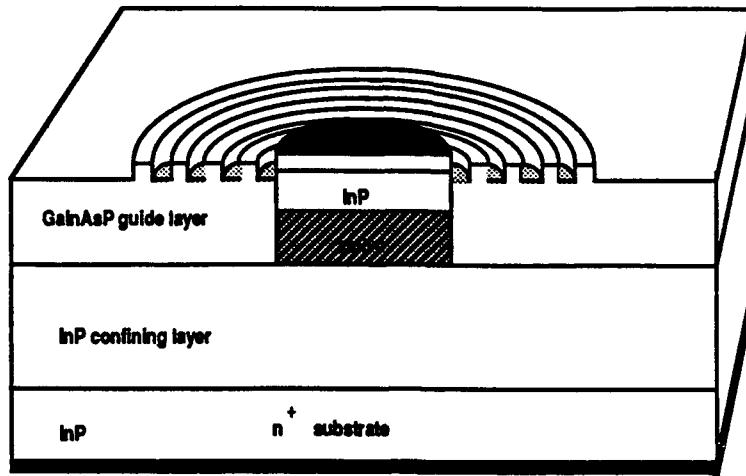


Fig. 1 Circular grating laser structure



Fig. 2 SEM micrograph of finished and wire-bonded circular grating laser

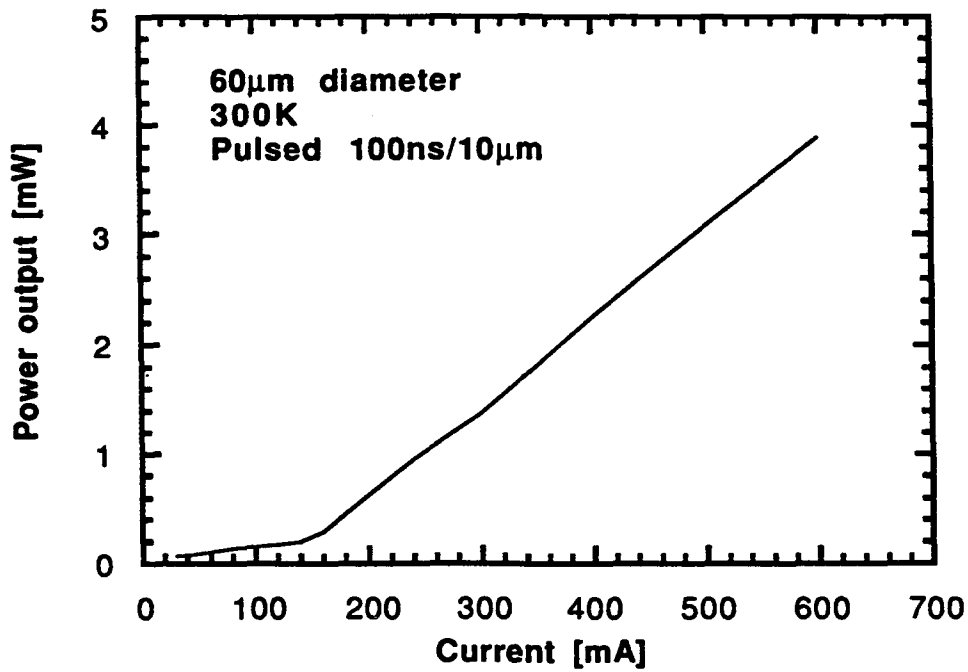


Fig. 3 Optical power output characteristic

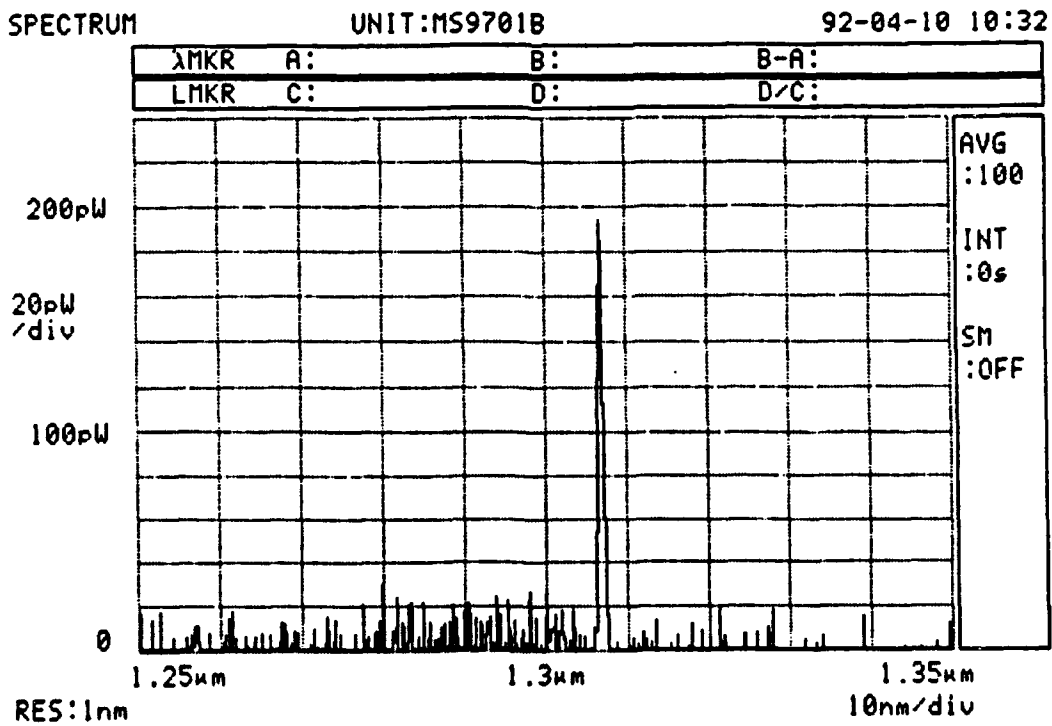


Fig. 4 Room temperature optical spectrum at 400mA(pulsed).

Broad band array multiplexers made with silica waveguides on silicon

R. Adar, C. H. Henry, C. Dragone ^{a)}, R. C. Kistler and M. A. Milbrodt
AT&T Bell Laboratories, Murray Hill, NJ 07974

ABSTRACT

Broad band two channel waveguide array multiplexers are demonstrated. Cross talk and fiber-to-fiber insertion loss are the lowest yet reported for array multiplexers: -35dB and -2dB, respectively.

Narrow and broad band wavelength division multiplexers (WDMs) have many applications in optical communications and recently high order integrated optic multiplexers have been fabricated using waveguide arrays [1-4]. In this paper, we introduce a new design which enables us to make low order array multiplexers. Broad band WDM's with orders 1, 3 and 8 (corresponding to two channel multiplexing of 1.1-1.55 μm , 1.31-1.53 μm and 1.47-1.55 μm) are demonstrated.

The design of an array multiplexer consists of an input and output slab couplers connected with an array of n waveguides [2]. In this paper the input coupler couples the fundamental mode from a single input waveguide into the n array waveguides. The output coupler couples the light back from the array to two output waveguides. The operation of the array multiplexer is based on the requirement that the waveguides connecting the input and output couplers are laid out with equal length differences between neighboring waveguides. This requirement has been obtained earlier in the case of high order array multiplexers with a symmetrical arrangement of the input and output sections of the array [1,3]. To be able to make a low order multiplexer one needs to eliminate the extra path difference associated with the couplers fanout geometry. However, this is impossible to achieve with the symmetrical design. The arrangement we choose to realize such multiplexers is an anti-symmetric arrangement shown schematically in Fig. 1.

In section I of this figure, the straight waveguides forming the input coupler fanout are bent down to normal incidence on line $A-A'$ which is tilted by an angle of $\frac{\pi}{2} - \gamma_0$ relative to the input optical axis. Each waveguide in this section consists of two straight segments connected with a circular arc having radius of curvature equal or larger than 15 mm. The waveguides in section I have equal length differences between

a) Crawford Hill Laboratories, Holmdel, NJ 07733

neighboring waveguides and are arranged in increasing length such that array guide 1 is the shortest guide and array guide 8 is the longest guide. The waveguides are also equally spaced at their intersection on line $A-A'$. The angle γ_0 was optimized to minimize the overall device dimension. We used $\gamma_0 = 30^\circ$ and the array multiplexers total length and height are about 25 mm and 4 mm respectively.

Section III of the array is identical to section I but is turned over in such a way that points A and A' are moved to points B' and B respectively. In this arrangement section III completely compensates for the path difference between waveguides in section I. In the absence of section II all waveguides would have the same length and the array would function as an integrated optical lens.

The waveguides in section II are concentric arcs of small angle Θ_w and radii of curvature equal or greater than the minimum allowed, $R_{\min} = 15\text{mm}$. The path difference between waveguides in this section, which determines their total path length difference s , is related to the angle Θ_w and to the separation, dh , between waveguides along lines $A-A'$ and $B-B'$ by, $s = \Theta_w \cdot dh$. By controlling Θ_w , array multiplexers of any desired order can be obtained using the same design for sections I and III. We selected orders 1, 3 and 8 for broad band two channel multiplexing at 1.0-1.55, 1.31-1.53 and 1.47-1.55 μm respectively.

A theoretical study of the operation of the array multiplexer was made in order to optimize its performance and in particular to decrease the excess coupling loss of the input and output array couplers [5]. Using detailed beam propagation modeling of these couplers [6] the design was optimized to correspond to total theoretical excess loss of about 0.5 dB.

We fabricated the array multiplexers using our phosphorus doped glass waveguides as described earlier [7]. They consist of a silicon substrate with a base layer made of $15\mu\text{m SiO}_2$ grown by high pressure steam oxidation. A core layer made of 8% phosphorus doped glass is deposited using LPCVD and dry etched to pattern the waveguides. Core thicknesses of three and four μm and core widths ranging from 4.5 to 6.5 μm , depending on the particular device, were used. After annealing of the core, a 7 μm of phosphorus and boron doped glass layer was deposited to form the top cladding. This top cladding was found to be especially suitable for filling in the small gaps between waveguides which are present in the array multiplexer design.

Fig. 2 shows calculated and measured power transmission spectra of the two channels of the 1.31-1.53 μm multiplexer which is designed with order $m=3$. The waveguides width in this device is 6.5 μm and the core thickness is 3 μm . This device shows near ideal spectral performance with very high rejection of the unwanted wavelength over a broad range and low peak transmission insertion loss. Using a white light source, we could not measure the low transmission values at the rejected bands, and a combination of AR coated semiconductor lasers covering the range 1.1 to 1.7 μm was used to spectrally characterize this device. The polarization dependence of the transmission characteristics of the device was found to be negligible. Aside from a vertical shift of about 2 dB, due to insertion loss, the transmission characteristics are in excellent agreement with the theoretical prediction. The theoretical curves were based on

detailed beam propagation modeling of the input and output couplers to get the field amplitude and phase relations between the 8 array waveguides.

Fig. 2 shows record cross talk values of about -35 dB over broad ranges for both the 1.31 and the 1.53 μm channels. The maximum transmission of the device is -2.15 dB at 1.31 μm and -1.7 dB at 1.53 μm . The power budget of the device in the 1.55 μm channel is summarized in table I.

To summarize, we have presented a new array multiplexer design which is applicable to both low order and high order array multiplexers. We investigated for the first time broad band array multiplexers with low order arrays. The 1.31-1.53 μm multiplexer had the lowest insertion losses yet reported for array multiplexers: as low as 1.7-2.1 dB, fiber-to-fiber, for the two channels. This array multiplexer had the lowest cross talk reported so far: about -35 dB. The insertion loss associated with coupling to and from the array is only 0.8 dB. This is consistent with a theoretical estimate of 0.5 dB for this loss.

REFERENCES

1. A. R. Vellekoop and M. K. Smit, *J. Lightwave Technol.*, vol. 9, 310-314 (1991).
2. C. Dragone, *Photonics Technol. Letters*, vol. 3, 812-815, (1991).
3. C. Dragone, C. A. Edwards and R. C. Kistler, *Photonics Technol. Letters*, vol. 3, 896-899, (1991).
4. C. Dragone, C. H. Henry, I. P. Kaminow, and R. C. Kistler, *Photonics Technol. Letters*, vol. 1, 241-243, (1989).
5. R. Adar, C. H. Henry, C. Dragone, R. C. Kistler and M. A. Milbrodt, to be published in *J. Lightwave Technol.*
6. C. H. Henry and Y. Shani, *IEEE J. Lightwave Technol.*, vol. 27, 523-530 (1991).
7. R. Adar, Y. Shani, C. H. Henry, R. C. Kistler, G. E. Blonder and N. A. Olsson, *Appl. Phys. Lett.*, vol. 58, 444-445 (1991).

TABLE I

Power Budget for peak transmission of the 1.31-1.53 μm multiplexer at 1.53 μm

1	Butt coupling loss	0.45 dB
2	Propagation loss	0.15 dB
3	Bend and bend to straight losses	0.3 dB
4	Input and output array couplers loss	0.8 dB
	Total fiber-to-fiber insertion loss	1.7 dB

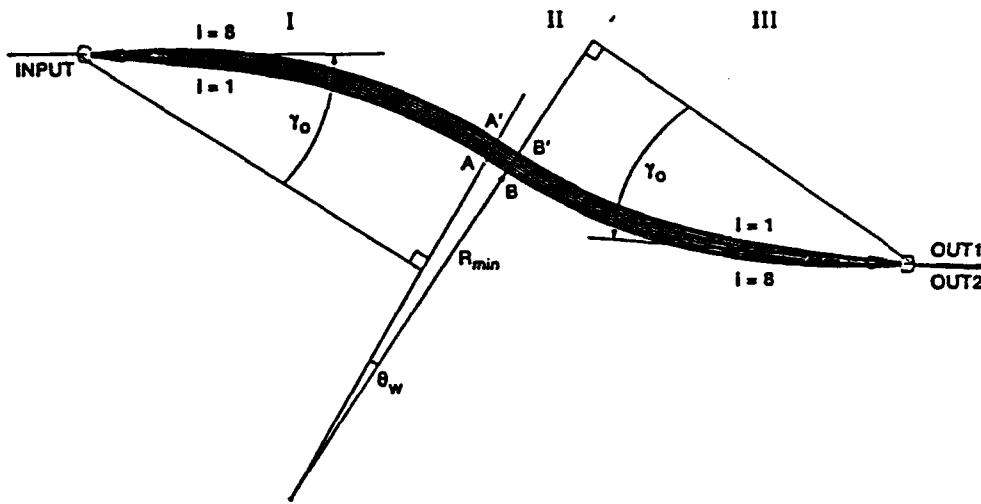


Fig. 1 The design used for the broad band array multiplexers is shown. In the absence of section II ($\Theta_w=0$) all waveguides are of equal length. The path difference between array waveguides is determined by the angle Θ_w so the same design can be used for different array orders.

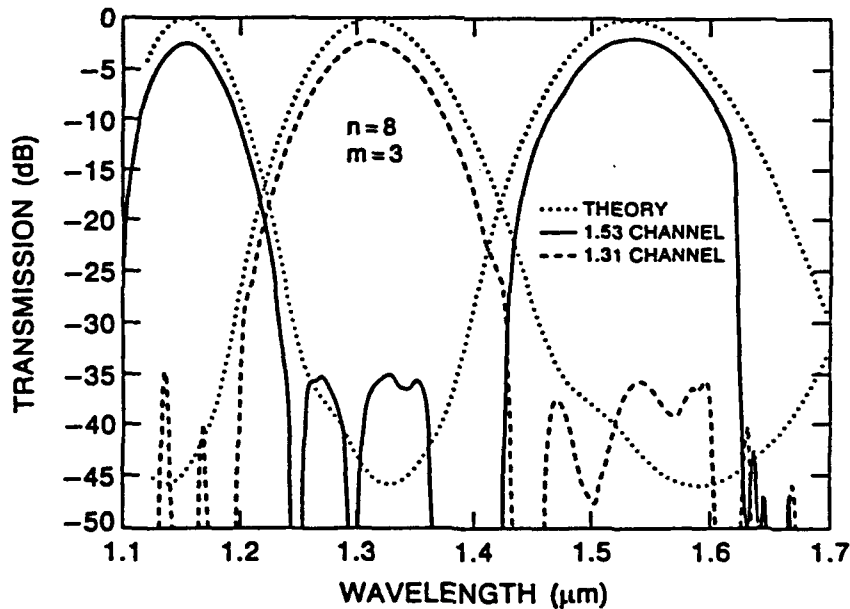


Fig. 2 Theoretical calculated and measured transmission spectra of the 1.31-1.55 μm multiplexer made with order $m=3$. Transmission loss is about 2.0 dB fiber-to-fiber and the cross talk is about -35 dB. The theoretical curves are calculated based on beam propagation analysis of both input and output array couplers.

Spectroscopic studies of Erbium-Titanium codoping of Lithium Niobate waveguides for active device applications

F. Zhou, P. S. Jiang, R. M. DeLaRue and C.N. Ironside, Department of Electronics and Electrical Engineering, University of Glasgow, Glasgow G12 8QQ, U.K. and
T. Han, B. Henderson and A. I. Ferguson, Department of Physics and Applied Physics, University of Strathclyde, Glasgow, U.K.

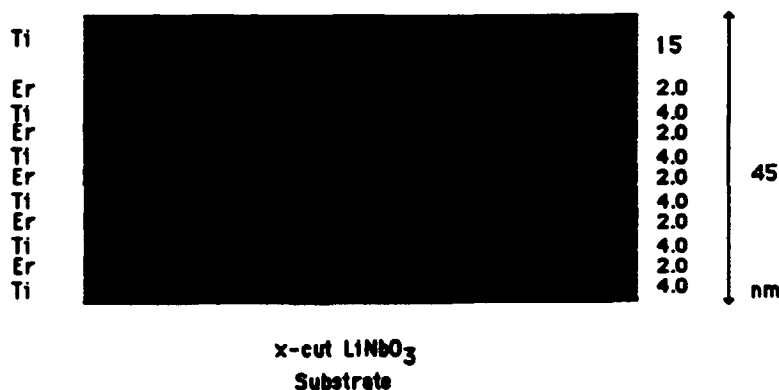
Summary

Erbium doped optical fibres have proved to be very useful optical amplifiers and are currently being installed in optical communications systems. The prospect of extending the concept to integrated optical formats and doping electro-optic materials such as Lithium Niobate with rare earth laser active ions has attracted considerable interest (1), (2). The device objectives are to produce laser media with modulation capabilities. In this paper we discuss a convenient technique which combines fabrication of the waveguide with Er doping.

A waveguide Er laser fabricated in LiNbO₃ has recently been demonstrated (1). The technique used to dope the waveguide with Er was diffusion doping where a thin layer, ~10.7 nm, of Er metal is deposited on the surface of the z-cut LiNbO₃; the coated LiNbO₃ is then placed in a furnace at 1060 C for 80 hours. The Er diffuses into the top 5 μm layer of the material. Subsequently Ti waveguides are fabricated in the doped material by the usual methods. An important point is that inhomogeneous doping of the waveguide is obtained by this method compared to the homogeneous doping that is obtained if the Er is introduced at the crystal growth stage. If we compare the Er laser with the Nd laser an important difference is that the Er laser is a three level laser compared to the Nd laser which is a four level laser. Consequently if an Er doped part of the laser medium is not pumped and thereby is not contributing gain it is contributing loss. Whereas in the Nd laser unpumped parts of the laser medium do not contribute loss. The above difference between the lasers appears to account for the fact that a homogeneously doped Nd waveguide laser in LiNbO₃ has been demonstrated(2) whereas it has not been demonstrated in an Er waveguide laser in LiNbO₃.

In this paper we report a technique for inhomogeneously doping with Er and simultaneously producing a waveguide. The technique is a simple adaptation of the usual method for fabricating Ti:LiNbO₃ waveguides. It relies on codoping the Er with Ti. Figure (1) shows the layer structure that is deposited on the LiNbO₃ substrate before placing in an oven at 1000 C for between 4 and 90 hours in a wet oxygen environment. The results which are presented here are for 4 hour diffusion. The technique used is similar to a method recently reported (3) to increase the Er diffusion by a factor of 15, the main difference in our technique is that we employ a sandwich layer structure for the Er doping layers.

Figure(1) Layer structure for codoping

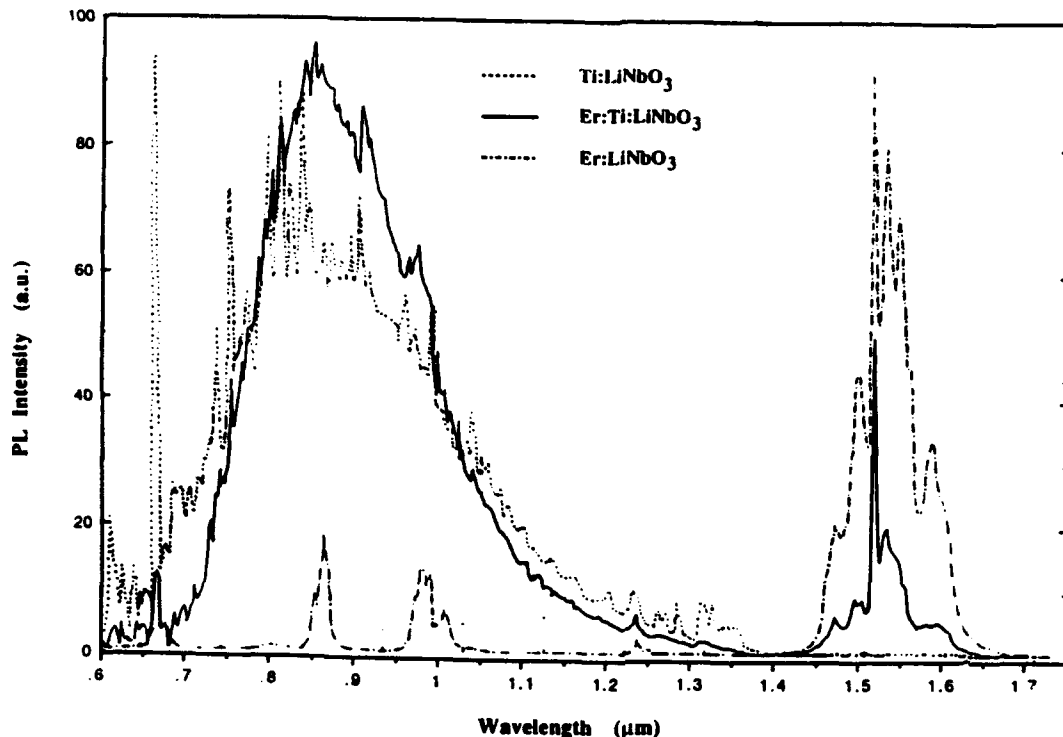


The process produces a single-mode slab waveguide at 633 nm.

Figure (2) below shows the comparison of three photoluminescence spectra from the slab waveguides where some care has been taken to eliminate luminescence from anywhere other than the slab waveguide. The luminescence was excited using the 488 nm line of an Argon ion laser. The luminescence spectra are from Ti:LiNbO₃, Er:Ti:LiNbO₃, and Er:LiNbO₃ which is homogeneously doped at 0.2% mole and has proton exchange waveguide. The broad peak between 0.7 and 1.2 μm is associated with the Ti. The Ti transition is at a similar wavelength to the transition in Ti:sapphire which is the ²E- to ²T₂ transition of the Ti³⁺ ion. This is evidence that at least some of the Ti is not in the fully oxidised state of Ti⁴⁺. The narrow feature at 1.45 and 1.65 μm is associated with the Er³⁺ ⁴I_{13/2} to ⁴I_{15/2} transition. The absorption spectra also show Er doping dependent features however, the features are

somewhat masked by Ti dependent features and as yet we have not been able to obtain an accurate estimate of Er concentration from the absorption spectrum.

Figure (2) Luminescence spectrum of codoped Er-Ti waveguide



Caption: The photoluminescence spectrum of the three LiNbO_3 waveguides excited by the 488 nm line of an Argon ion laser. The spectra from Ti:LiNbO_3 waveguide, Ti:Er:LiNbO_3 waveguide and bulk doped Er:LiNbO_3 proton exchange waveguide are compared. Spectrum resolution is 1 nm. Care was taken to ensure that the spectra between different samples were comparable; we estimate that the relative accuracy is around 20%.

In summary, we have presented a new technique for inhomogeneously doping Er into LiNbO_3 waveguides. The technique is more convenient than the previously reported method of inhomogeneously doping because the doping and waveguide fabrication are combined into one process and furthermore the process is considerably faster than the previous method.

Currently, an investigation of the laser properties of these waveguides is underway.

References

- (1) R. Brinkmann, W. Sohler, H. Suche "Continuous-wave erbium-diffused LiNbO_3 waveguide laser", Electronics Lett 27 415, 1991.
- (2) E. Lallier, J. P. Pocholle, M. Papuchon, M. de Micheli, M. J. Li, Q. He, C. Grezes-Besset and E. Pelletier "Nd:MgO: LiNbO_3 waveguide laser and amplifier" Opt. Lett 15 682 1990.
- (3) D. M. Gill, A. Judy, L. McCaughan, J. C. Wright "Method for the local incorporation of Er into LiNbO_3 guided wave optic devices by Ti co-diffusion" Appl. Phys. Lett 60 1067-1069 1992

Quantum-confined Stark Effect of InGaAsP
Quantum Wells Grown on (110) InP Substrates

K.Oe and K.Wakita
NTT Opto-electronics Laboratories
3-1, Morinosato Wakamiya, Atsugi,
Kanagawa, 243-01, Japan
Tel: (0462)40-2802, Fax: (0462)40-4302

R.Bhat and M.A.Koza
Bellcore, 331 Newman Springs Rd., Red Bank,
NJ 07701-7040, USA

Quantum well structures show interesting optical properties associated with their remarkable exciton absorption resonances. In the quantum-confined Stark effect (QCSE), electric fields applied perpendicular to quantum well (QW) layers can shift the optical absorption edge to lower photon energies with the exciton absorption peaks remaining clearly resolved. This effect has been studied extensively as it is useful in optical modulation and photonic switching applications.

At this time, most QCSE studies concentrate on the (100) orientation or, in a few cases, on (111) strained QWs to obtain a blue shift originating from piezoelectric built-in potentials¹⁾. The (110)-oriented QWs are expected to exhibit peculiar characteristics as the lower symmetry of the quantum-confined direction results in in-plane polarization anisotropy of the optical transitions. Anisotropic properties are reported in GaAs/AlGaAs (110)-oriented QWs²⁾. It is believed that strained QWs on (110) substrates will also generate in-plane piezoelectric fields which will provide bi-refringence for light propagating along the MQW growth axis³⁾.

This paper presents the QCSE of (110)-oriented quaternary InGaAsP QWs. Clear exciton absorption is obtained and a peculiar QCSE phenomenon is observed for the first time in (110)-oriented QWs. The InGaAsP quaternary MQW sample was grown on a (110)-oriented n^+ InP substrate by OMVPE and growth was carried out in a horizontal, low pressure (76 torr) reactor. The (110) substrate was misoriented by 3 degrees towards the nearest (111)B plane to obtain smooth layers. Special care was taken in creating the growth conditions to obtain high-quality MQWs. Details of the growth will be presented elsewhere⁴⁾.

The layer structure is shown in Fig. 1. It has a 3 QW SCH structure with 20 nm thick InGaAsP ($\lambda_g=1.3\ \mu\text{m}$) barrier layers and 6 nm thick $\text{In}_{0.62}\text{Ga}_{0.38}\text{As}_{0.86}\text{P}_{0.14}$ ($\Delta a/a=+0.17\%$, $\lambda_g=1.64\ \mu\text{m}$) well layers. The quaternary well was chosen because, at present, it is difficult to grow an InGaAs QW on a (110) orientation. This wafer was processed into a high-mesa type geometry 70 μm wide and 300 μm long. The stripe direction was aligned parallel to the $\langle\bar{1}10\rangle$ direction to illuminate the $(\bar{1}10)$ cleaved facet as shown in Fig. 2. Photocurrent spectra were taken with a broadband optical source and grating spectrometer. Incident light is polarized parallel to the plane of the layers.

Figure 3 shows the photocurrent spectra at room temperature for various bias voltages. The incident light is coupled to the $(\bar{1}10)$ cleaved facet of the waveguide. The electron-to-heavy hole (e-hh) exciton resonance at 1.573 μm and the electron-to-light hole (e-lh) resonance at 1.550 μm are clearly observed for zero bias spectra. This shows that the QW structures grown on this unusual substrate by OMVPE are uniform. When the applied reverse voltage is increased, the e-hh absorption peak shifts to a longer wavelength, while the e-lh peak stays near the same wavelength. The most interesting aspect is that the e-hh exciton absorption is enhanced along with the applied voltage. This enhanced exciton absorption along with applied voltage has never been reported before for any material system such as GaAs/AlGaAs, InGaAs/InAlAs, InGaAs/InP, or InGaAsP/InGaAsP as far as we know. It is presumed that this peculiar phenomenon might come from the in-plane anisotropic band structure of the (110)-oriented QW. To investigate the in-plane anisotropy, the photocurrent spectra were measured by changing the incident light direction. Figure 4 shows the result for when light is coupled to the (001) etched facet of the waveguide. The e-hh exciton absorption at 1.573 μm is sharper than that in Fig. 3 at zero bias. When reverse bias is applied, the absorption edge shifts to a longer wavelength but absorption is decreased and exciton peaks are not observed at more than 4 V. This behavior is quite different from the QCSE shown in Fig. 3. The cause of the peculiar QCSE for the (110)-oriented QW might be attributed to the in-plane anisotropic band structure of the QW.

In summary, the quantum-confined Stark effect of an InGaAsP quantum well structure grown on a (110) InP substrate by OMVPE has been studied. Clear exciton absorption is observed for the QW. Enhanced exciton absorption concurrent with applied voltage is found when incident light is coupled to the $(\bar{1}10)$ cleaved facet. When the incident light is coupled to the (001) facet, the absorption edge shifts without enhanced exciton absorption. This new QCSE phenomenon might be attributed to the in-plane anisotropic band structure of the

(110)-oriented QW. This effect is not only interesting from a scientific point of view but it is also useful in optical modulation and photonic switching applications.

One of the authors (K.O.) would like to thank T. Ikegami and T.P. Lee for supporting the collaboration.

References

- (1) K.W.Goosen, E.A.Caridi, T.Y.Chang, J.B.Stark, D.A.D.Miller, and R.A.Morgan; Appl. Phys. Lett. 56, 715(1990)
- (2) D.Gershoni, J.S.Weiner, S.N.G.Chu, G.A.Baraff J.M.Vandenberg, L.N.Pfeiffer, K.West, R.A.Logan, and T.Tanbun-Ek; Phys. Rev. Lett. 63, 1631(1990)
- (3) D.L.Smith and C.Mailhot; J. Appl. Phys. 63, 2717(1988)
- (4) R.Bhat, M.A.Koza, D.M.Hwang, M.J.S.P.Brasil, R.E.Nahory, and K.Oe; to be presented at ICMOVPE, Cambridge, MA(1992)

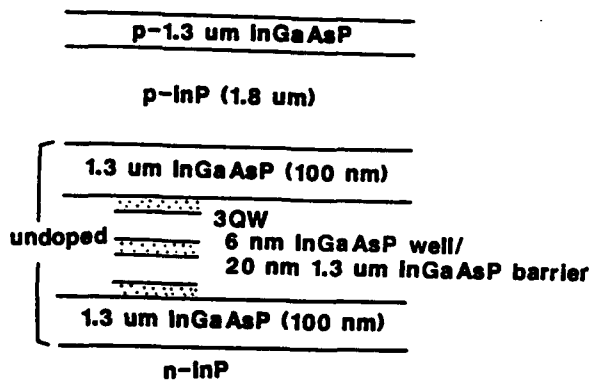


Fig. 1 Sample layer structure

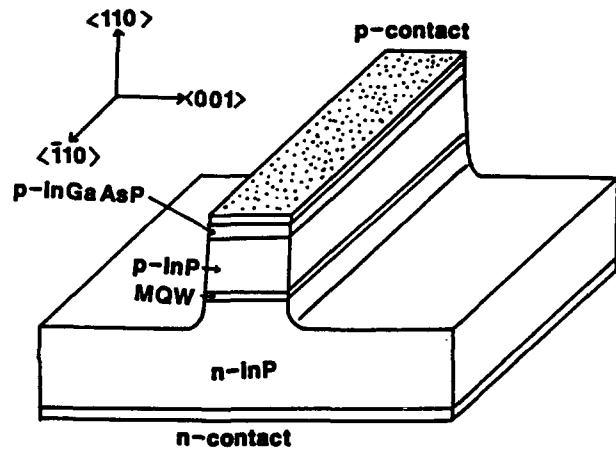


Fig. 2 Schematic view of an InGaAsP MQW p-i-n diode sample

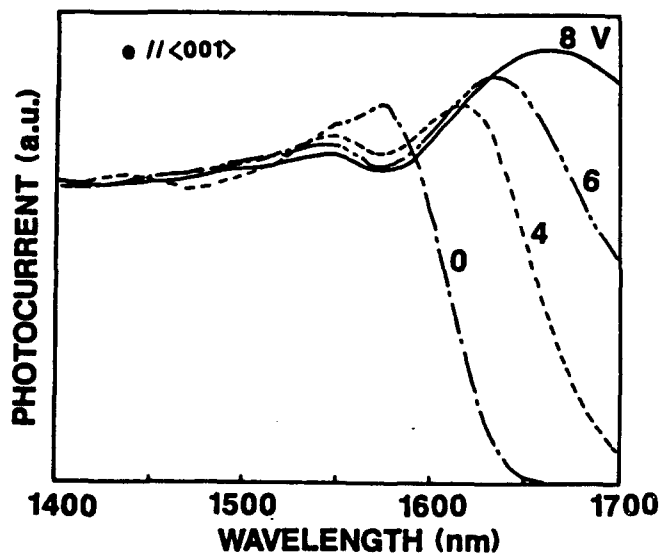


Fig. 3 Photocurrent spectra as a function of applied voltage. Incident light is coupled to $\langle \bar{1}10 \rangle$ facet.

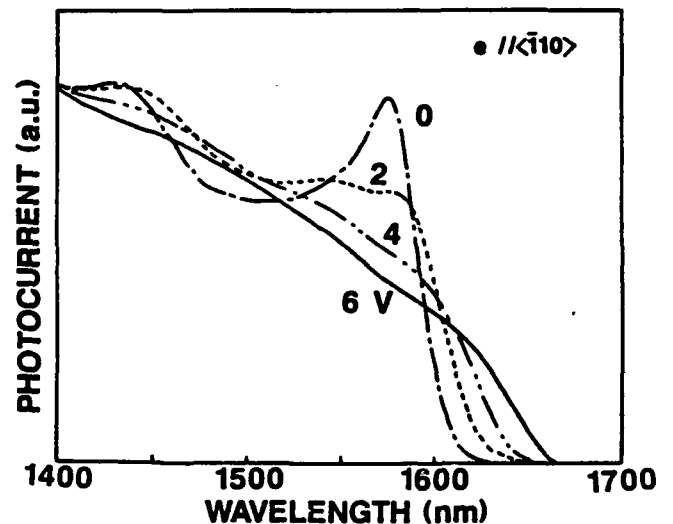


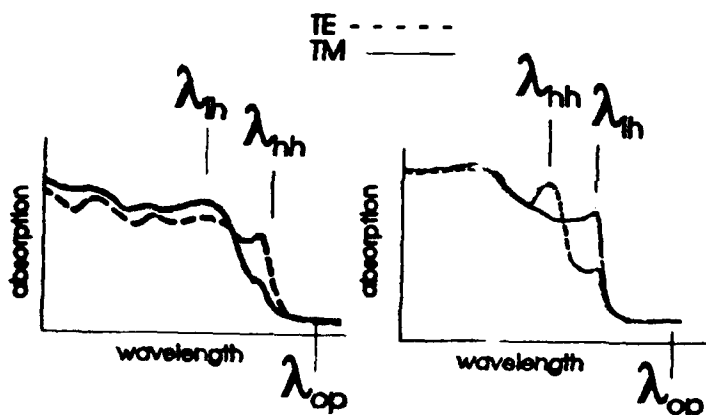
Fig. 4 Photocurrent spectra as a function of applied voltage. Incident light is coupled to $\langle 001 \rangle$ facet

Polarization-Independent Electro-optic Waveguide Switch Using Strained InGaAs/InP Quantum Wells

J. E. Zucker, K. L. Jones, T. H. Chiu, B. Tell, K. Brown-Goebeler
AT&T Bell Laboratories, Holmdel, New Jersey 07733

Most current applications for electro-optic space-division switches call for polarization-independence as a top systems requirement. However, in both LiNbO₃ [1] and bulk semiconductor [2] devices polarization-independent switching has thus far been achieved only at the expense of greatly increased switching voltage. Moreover in these materials there is no means, other than substrate orientation, for adjusting the relative strength of TE and TM electro-optic coefficients. In this paper we demonstrate a novel approach to polarization independence: control of electro-optic coefficients via bandgap engineering. By design of layer thicknesses and composition in a quantum well heterostructure, we show that it is possible to use strain to adjust the ratio of refractive index changes in the TE and TM polarizations such that $(\Delta n_{TE})/(\Delta n_{TM}) \sim 1$. At the same time, we make use of the same enhanced excitonic electro-optic effects found in unstrained quantum wells [3,4] to produce a polarization-independent 2x2 switch with voltage-length product 30 times smaller than in bulk semiconductors and 150 times smaller than in LiNbO₃.

In lattice-matched quantum wells, splitting of the valence-band degeneracy by the superlattice potential gives rise to the absorption spectrum shown in Fig.1a. In TM polarization, the lowest-lying peak (corresponding to the light-hole exciton) is at wavelength λ_{lh} , while in TE polarization the heavy-hole exciton is at a longer wavelength λ_{hh} . Hence when electric field is applied to the structure, the refractive index change at the wavelength of operation λ_{op} will be much greater in the TE than in the TM polarization. However, this anisotropy can be reversed by growing non-lattice-matched quantum wells as shown in Fig.1b, since the effect of tensile strain on the valence band energies opposes that of the superlattice potential. In the case of In_{1-x}Ga_xAs/InP quantum wells, the wells are under tension for $x > 0.47$. Thus by proper choice of well thickness to adjust the superlattice potential and composition x to control the amount of strain, polarization independence at λ_{op} can be obtained.



(a) lattice-matched well (b) well under tension

Fig.1 Absorption spectra in TE and TM polarizations for lattice-matched (a) and tensile-strained (b) quantum wells. The valence-band splitting in lattice-matched wells produces a heavy-hole exciton peak λ_{hh} at wavelength longer than that of the light exciton λ_{lh} . By adjusting the well composition, tensile-strained quantum wells are produced with the reverse order, $\lambda_{hh} < \lambda_{lh}$. Through proper design of layer thickness and strain, the quantum wells in (b) will yield field-induced changes in refractive index $\Delta n_{TE} \sim \Delta n_{TM}$ at the desired wavelength λ_{op} .

Our calculation of λ_{lh} and λ_{hh} as a function of Ga concentration (and hence strain) is shown in Fig. 2 for the case of a 80 Å $\text{In}_{1-x}\text{Ga}_x\text{As}/80$ Å InP quantum well. Here we have taken into account quantum confinement effects as well as the influence of strain on the well bandgap and on the band offset at the lattice-mismatched interface [5]. For $x=0.47$ we have the lattice-matched condition $\lambda_{hh} > \lambda_{lh}$, with the two peaks brought into coincidence at $x \sim 0.55$. Since the oscillator strengths of the two transitions differ, it is necessary to go beyond this crossing point to achieve polarization-independent electrorefraction at a below-gap wavelength. In general, the flexibility of quantum well material growth lends itself to custom applications, and has been exploited in other devices such as polarization-independent intensity modulators using parabolic wells [6] or polarization-independent amplification using strained barriers [7].

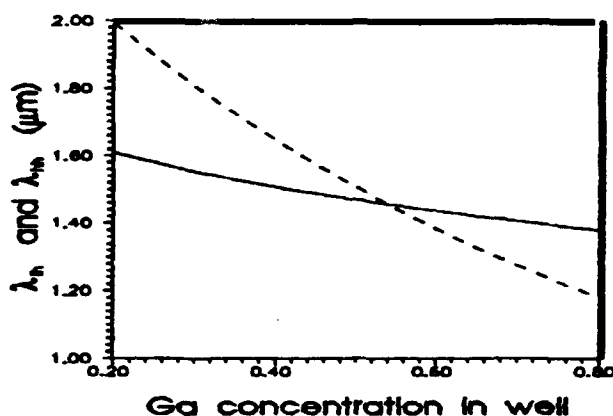


Fig.2 Calculated wavelengths for light-hole (λ_{lh} - solid line) and heavy-hole (λ_{hh} - dashed line) ground-state exciton transitions in 80 Å $\text{In}_{1-x}\text{Ga}_x\text{As}/80$ Å InP quantum well as a function of Ga concentration x .

The strip-loaded waveguide interferometric switch, shown schematically in Fig.3, is formed from a p-i-n structure grown by chemical beam epitaxy containing 10 tensile-strained InGaAs/InP quantum wells as the active core. Normal-incidence photocurrent spectra of this wafer show zero-field absorption edge at 1.45 μm , clear excitonic absorption features, and large red-shifts of exciton peaks with applied field. The 3 dB splitters of length L_{3dB} are 8- μm -wide multimode interference regions [8]. All other sections are straight 2- μm -wide waveguides. Electrical isolation is provided by ion implants so that reverse bias voltage can be independently applied across the quantum wells in each active section of length L_{active} . The substrate is held at ground. A lensed single-mode fiber is used to couple a color-center laser into the cleaved chip, with microscope objective collecting the output.

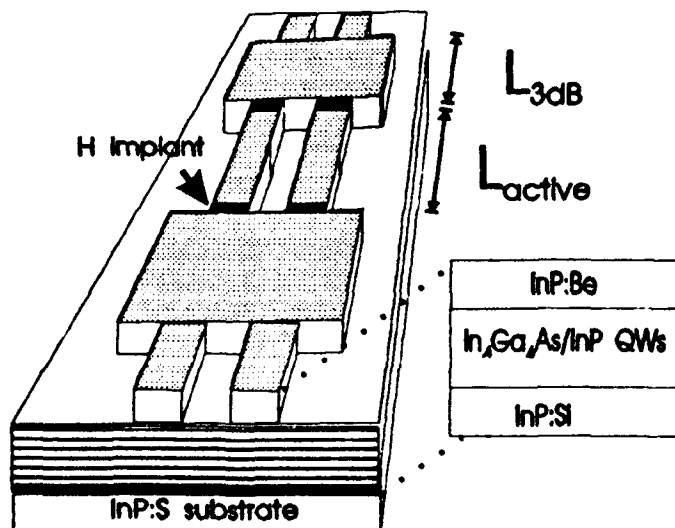


Fig.3 Schematic of waveguide interferometric switch, with strip-loading of quantum well waveguide provided by 0.85 μm InP:Be upper cladding layer. Active undoped core consists of ten tensile-strained 80 Å $\text{In}_x\text{Ga}_y\text{As}/80$ Å InP quantum wells. Center-to-center separation of 2- μm -wide straight ribs is 7 μm . Multi-mode 3 dB coupler regions are 8 μm wide with length $L_{3dB} = 350$ μm . Not shown are the metallized pads contacting the top of each $L_{active} = 675$ μm active section. Total cleaved length of the switch is 1.84 mm.

Fig.4 shows the measured switching characteristics at $1.6 \mu\text{m}$. For this wavelength, far from the quantum well absorption edge, there is no difference in loss between TE and TM polarizations. At zero bias, the switch is in the bar state, with crosstalk $< -17.6 \text{ dB}$ for both TE and TM polarizations. At switching voltage $V_{sw} = -4.5 \text{ V}$, crosstalk in the cross state is -10.1 dB for both polarizations. At bias points other than $V=0$ and $V=V_{sw}$, the difference in power between TE and TM is less than 2 dB , indicating that we are close to balancing the electro-optic effects in the two polarizations. We note here that if the well were unstrained, we would obtain a ratio $\Delta n_{TE}/\Delta n_{TM} \sim 4.4$ [9], which would make polarization-independent switching impossible.

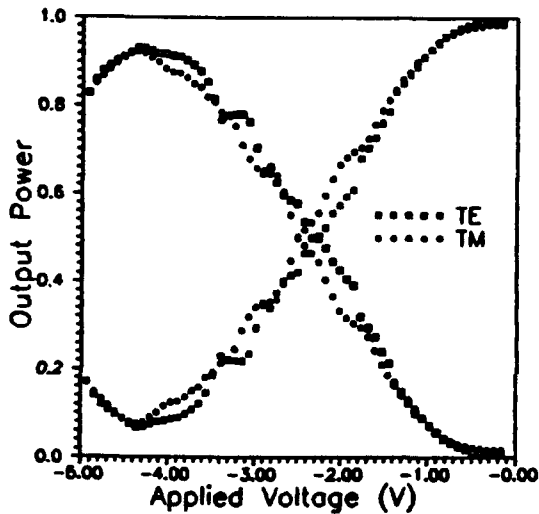


Fig.4 Switching characteristics at $1.6 \mu\text{m}$ measured for TE (dashed line) and TM (solid) polarizations for the device shown in Fig.3. Voltage-length product for the switch is $3.0 \text{ V}\cdot\text{mm}$.

In summary, we have demonstrated the first polarization-independent quantum well electro-optic switch. The 2×2 interferometric crosspoint uses tensile-strained InGaAs/InP quantum wells as a highly efficient electro-optic medium to achieve voltage-length product $V_{sw} \times L_{active} = 3.0 \text{ V}\cdot\text{mm}$, a figure-of-merit comparable to the record voltage-length products produced using unstrained quantum wells [4]. We note that the polarization-independent property is made possible here by engineering of the material rather than the particular device structure. Thus our approach can be used in other switch geometries, such as directional couplers, and for other electrorefractive devices like intensity modulators. The materials and fabrication methods used here are also compatible with those standard in other electronic and photonic InP-based devices. For example, these switches are fully integratable with heterojunction bipolar transistor drivers and laser optical amplifiers. Finally, since the crosspoint is driven under reverse bias and is compact enough to be regarded as a lumped capacitance, we can expect a modulation bandwidth that is RC-limited and hence multi-gigahertz reconfiguration rates for the switch.

REFERENCES

- [1] H. Nishimoto, S. Suzuki, and M. Kondo: "Polarization-independent LiNbO₃ 4×4 matrix switch," *Electron. Lett.* 24, 1122 (1988).
- [2] K. Komatsu, K. Hamamoto, M. Sugimoto, Y. Kohga, and A. Suzuki: "Polarization independent GaAs/AlGaAs electro-optic guided-wave directional coupler switch using (111)-oriented GaAs substrate," *OSA Proceedings on Photonic Switching*, 8, 24 (1991).
- [3] J. E. Zucker, K. L. Jones, M. G. Young, B. I. Miller, U. Koren: "Compact directional coupler switches using quantum well electrorefraction," *Appl. Phys. Lett.* 55, 2280 (1989).
- [4] J. E. Zucker, K. L. Jones, B. I. Miller, M. G. Young, U. Koren, J. D. Evankow, C. A. Burrus: "Zero-loss quantum well waveguide Mach-Zehnder modulator at 1.55 μm," *Appl. Phys. Lett.* 60, 277 (1992).
- [5] J. E. Zucker, C. H. Joyner, A. G. Dentai: "Optical transitions in strained In_{0.53}Ga_{0.47}As/In_{1-x}Ga_xAs Quantum Wells," *Photon. Technol. Lett.*, May, 1992.
- [6] K. Tada, S. Nishimura, T. Ishikawa: "Polarization-independent optical waveguide intensity switch with parabolic quantum well," *Appl. Phys. Lett.* 59, 2778 (1991).
- [7] K. Magari, M. Okamoto, H. Yasaka, K. Sato, Y. Noguchi, O. Mikami: "Polarization insensitive traveling wave type amplifier using strained multiple quantum well structure," *IEEE Photon. Technol. Lett.* 2, 556 (1990).
- [8] L. B. Soldano, F. B. Veerman, M. K. Smit, B. H. Verbeek, A. H. Dubost, E. C. M. Pennings: "High-performance monomode planar couplers using a short multi-mode interference section," *ECOC/IOOC Proceedings*, Paper TuB5-2, pp.225-228(1991).
- [9] J. E. Zucker, T. L. Hendrickson, C. A. Burrus: "Electro-optic phase modulation in GaAs/AlGaAs quantum well waveguides," *Appl. Phys. Lett.* 52, 945 (1988).

Single-Sideband Modulator In GaAs Integrated Optics for Microwave Frequency Operation

Michael J Wale, Robert G Walker and Colin Edge
GEC-Marconi Materials Technology Ltd
Caswell, Towcester, Northants, NN12 8EQ
U.K.

Abstract

We describe the first experimental realization of an integrated optical single sideband modulator operating at microwave frequencies (10-14 GHz).

Introduction

A single sideband optical modulator has been keenly sought by system designers in view of its importance in developing optical analogues of conventional microwave signal processing schemes. To date, however, SSB modulators have only been realized for operation at low frequencies (~1 GHz). Furthermore these designs have required high drive powers [1] or have been dependent upon critical phase shift adjustments in order to achieve acceptable carrier and image sideband rejection ratios [2].

The GaAs device described in this paper has intrinsically high image sideband suppression and has a bandpass response which can be designed for a wide range of centre frequencies, in our case to cover the 10-14 GHz band. High carrier and image sideband rejection ratios have been achieved. The device has been built into a fibre coupled module with a fibre-to-fibre insertion loss of 8.5 dB.

Device Design

The SSB modulator is based on the concept described theoretically by Désormière et al [3] and shown schematically in figure 1. The key element in the design is a Y-fed electro-optic directional coupler, whose electrode structure carries a travelling microwave signal. Since the coupler is excited symmetrically by the Y-branch, in the absence of a modulating RF wave the optical distribution at the output of the coupler is also symmetric. If the two opposite halves of this distribution are sampled in output waveguides and then summed out of phase in the Mach-Zehnder interferometer section, the optical output of the device will accordingly be zero. This provides the carrier suppression feature of the device.

When a modulating signal is applied to the electrodes, mode-coupling can take place between the symmetric and antisymmetric modes. Since the output interferometer is set to add opposite sides of the incoming light distribution in anti-phase, the *antisymmetric* components add to form a signal in the output waveguide. The magnitude of this signal will depend upon the drive voltage, geometrical factors and the electro-optic coefficient of the waveguide medium.

The propagation constants of the symmetric and the antisymmetric modes are quite widely spaced and hence with a static applied voltage the coherent interaction length for the mode coupling interaction is very short (much less than the device length) and the modulation efficiency is correspondingly very low. By choosing a geometry in which the microwave signal travels unidirectionally along the device in the opposite direction to the optical wave, however, we can arrange a phase matching condition to be achieved for a specific radio frequency Ω , according to the equation

$$\beta_s(\omega) - \beta_a(\omega + \Omega) = B(\Omega), \quad (1)$$

where β_s and β_a are the propagation constants of the symmetric and antisymmetric modes, B is the propagation constant of the microwave field and ω , Ω are respectively the optical and microwave frequencies. When this phase matching condition is satisfied, the coherent interaction length for the upward frequency-shifted component becomes infinite and the effective modulation efficiency for this sideband is greatly enhanced since its amplitude will now increase monotonically along the device. Correspondingly, the image sideband is moved even further out of phase-match, thereby reducing the amplitude of this frequency component observed at the output. Single sideband operation is therefore an intrinsic characteristic of the device and a high rejection ratio for the image sideband (and indeed all other sidebands) is not dependent upon any critical phase shift adjustments. The analysis presented in [3] shows that the image rejection should be at least -30 dB even when the coupling length departs from the ideal by as much as 30%.

In terms of device parameters, the phase matching condition of equation (1) corresponds to the relationship

$$L_b = \frac{2\pi c}{\Omega(N+n)}$$

where L_b is the beat length between the antisymmetric and symmetric modes, c/N is the microwave phase velocity and c/n is the optical phase velocity. It is readily shown that L_b is equal to twice the natural coupling length of the directional coupler. The central operating frequency of the device depends upon the relative phase velocities of the optical and microwave signals in the device, i.e. on directional coupler and transmission line parameters. These may be chosen to suit a wide range of microwave frequencies: in this work, we selected a centre frequency in the 12 GHz region.

Our implementation of the SSB modulator concept was realised in GaAs/AlGaAs integrated optics with Schottky contacts, following the same principles as have been reported previously for wideband amplitude modulators [4]. In the latter case the objective was to obtain a precise velocity match in a codirectional configuration; here, on the other hand, the objective was to obtain a precise mismatch in counter-propagation. The required phase match condition is adjusted during the design phase by selection of the capacitance per unit length, which is determined by the epitaxial layer structure, etch depth and waveguide separation in the directional coupler region. The wavelength of operation is 1.3 μm and the device is designed to operate with TE-polarized light.

The modulator chip is 19 mm in length, of which 10 mm is the active Y-fed directional coupler carrying the microwave modulation signal. These parameters lead to a full conversion voltage in the SSB modulator of 9V and a V_{π} in the static interferometer of 25V.

Since the waveguide mode size in this device is somewhat smaller than conventional optical fibres, we employ an etched fibre lens [5] to effect a mode size transformation for improved optical coupling. Polarization maintaining fibres were used (York VSOP type HB1250). The overall module size is 70x25x10 mm. Microwave interfaces at both ends of the travelling wave device are via Wiltron 'K' connectors: the connector adjacent to the optical input is used to feed a 50 Ω coaxial termination. The fibre-fibre loss achieved in the assembly was 8.5 dB, of which 3.5dB is attributable to the chip and 2.5 dB to each interface.

Experimental Results

Initial frequency response measurements were made by the swept frequency method, in which the modulator is biased at minimum transmission and the change in mean light output is observed as a microwave signal is applied. This measurement does not discriminate between the upper and lower sidebands but is very straightforward and does not involve any high frequency optical detection equipment; its accuracy as a measure of the single sideband response has been verified using the Fabry-Perot analyser as discussed later. A typical frequency response obtained using this technique is shown in figure 2. The phase matching closely matches the design objectives and achieves a ± 2 GHz total response width at -3 dB, centred on 11.5 GHz.

An initial check of carrier rejection can be made at low frequency as this is primarily determined by the interferometer balance. It was found that a null to -30 dB (optical power) was readily obtained by adjustment of the interferometer bias voltage. This bias level was then employed in the subsequent RF measurements.

RF performance was assessed using a scanning Fabry-Perot interferometer, thereby displaying the optical carrier, selected sideband and image sidebands directly. This assessment confirmed the expected modulation sensitivity (corresponding to 9V for full conversion) and the image sideband was fully suppressed with respect to the experimental noise level (around -15 dB electrical). It is emphasized that this is an instrument-limited upper limit: theoretical considerations indicate that the image sideband level should be much lower. Experimental work is in progress to obtain a more detailed assessment.

As mentioned earlier, the device operates on TE-polarized light. The TM-polarized mode is not modulated to any appreciable extent: in our measurements the TM-response is at least 30 dB down at microwave frequencies. The overall transmission of the device for the TM-mode is however comparable with the TE-mode.

Conclusions

We have described the first experimental single sideband optical modulator for operation at microwave frequencies. This GaAs device has a response centred at 11.5 GHz with 4 GHz bandwidth (-3dB), carrier rejection >30 dB and inherently high image sideband rejection. A fibre-fibre insertion loss of 8.5 dB was achieved. The availability of a convenient SSB modulator at microwave frequencies is expected to open up new possibilities for microwave signal processing systems.

Acknowledgments

The authors thank R I Taylor for theoretical analysis, J Hendy for device fabrication and M Owen for module construction. This work was carried out with the support of European Space Agency under ESTEC contract no. 8354, "Advanced Optical Techniques for Telecommunications Payloads".

References

- [1] Heismann, F. and Ulrich, R., "Integrated optical frequency translator with stripe waveguide", *Appl. Phys. Lett.*, **45**, pp. 490-492 (1984).
- [2] Izutsu, M., Shikama, S. and Sueta, T., "Integrated optical SSB modulator/frequency shifter", *IEEE J. Quantum Electron.*, **QE-17**, pp. 2225-2227 (1981).
- [3] Désormière, B., Macfeld, C. and Desbois, J., "An integrated optic frequency translator for microwave lightwave systems", *J. Lightwave Technol.*, **8**, pp. 506-513 (1990).

- [4] Walker, R.G., "High speed III-V semiconductor intensity modulators", IEEE J. Quantum Electronics, 27(3), March 1991, pp. 654-667.
- [5] Farries, M.C. and Stewart, W.J., "Fibre Fresnel phaseplates with efficient coupling to semiconductor lasers and low reflective feedback", European Conf. Optical Communication, Amsterdam, 1990, pp. 291-294.

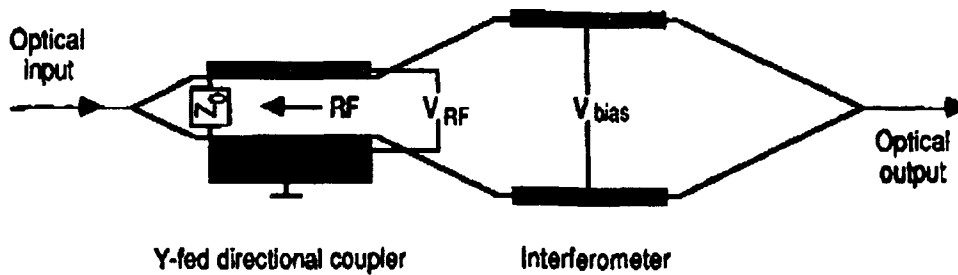


Figure 1. SSB MODULATOR DESIGN: SCHEMATIC REPRESENTATION

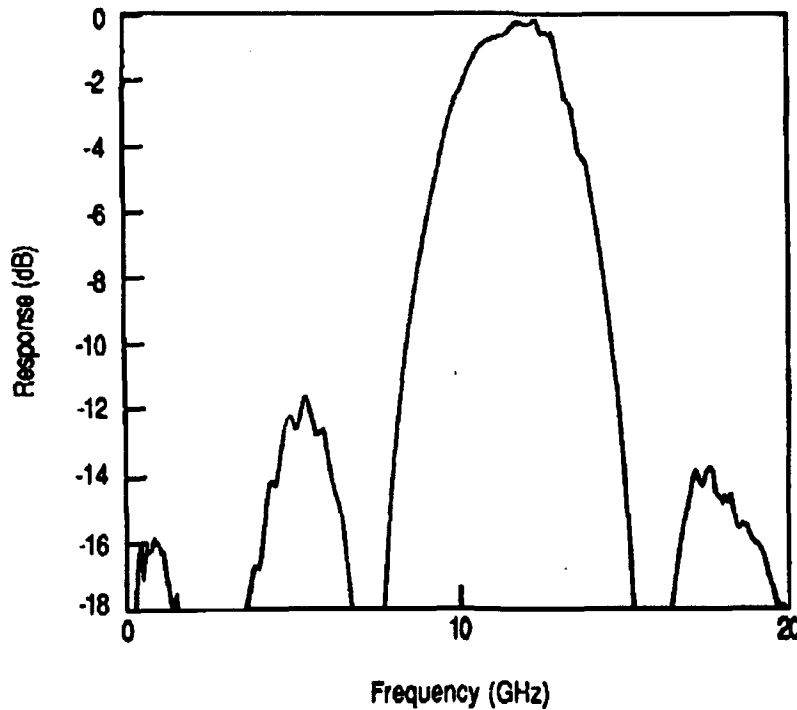


Figure 2. FREQUENCY RESPONSE OF SSB MODULATOR DEVICE

Ultrafast All-Optical Switching in an AlGaAs X-Junction

J.S. Aitchison,
Department of Electronics and Electrical Engineering,
University of Glasgow.
Glasgow. G12 8QQ

A. Villeneuve and G.I. Stegeman,
CREOL,
University of Central Florida,
Orlando,
Florida.

Introduction:

Several recent experiments have verified the existence of relatively large refractive nonlinearities in the region of half the band gap of AlGaAs and GaAs/AlGaAs quantum well structures¹⁻³. Working in this wavelength region has several advantages; it minimizes the effects of two-photon absorption (TPA), which has limited the usefulness of previous devices, it gives rise to devices with very low linear loss and hence high throughput, finally, it also allows the material to be chosen so that the operating wavelength is in the low-loss, 1.55 μm , telecommunications window.

We have previously reported ultrafast all-optical switching in $\text{Al}_{0.18}\text{Ga}_{0.82}\text{As}$ directional couplers^{2,3}. These devices use the nonlinear refractive index change to break the coupling between two modes and hence change the relative output states of the device. The nonlinear switching characteristics of the directional coupler are a relatively broad function of input power and may not be the optimum for a practical device. Recent theoretical investigations have predicted all-optical switching in nonlinear X-junctions as a consequence of symmetry breaking^{4,5}. The switching characteristics of such devices show the potentially useful feature of a digital-like response. In this paper we report the first experimental observation of ultrafast, all-optical switching in nonlinear X-junctions.

Device Design:

X-switches were fabricated from an MBE grown, AlGaAs wafer containing 18% Al in the high index region, sufficient to eliminate TPA in the 1.55 μm spectral region. The wafer used was composed of the following layers: a 4 μm thick isolation layer, containing 24% Al, a 1.5 μm thick guiding layer, with 18% Al and a 1.5 μm thick cladding containing 24% Al. The relatively thick isolation layer minimized losses into the high index n-type GaAs substrate. Two-dimensional, strip loaded waveguides were fabricated by a combination of photolithography and dry-etching to a depth of 1.25 μm using SiCl_4 .

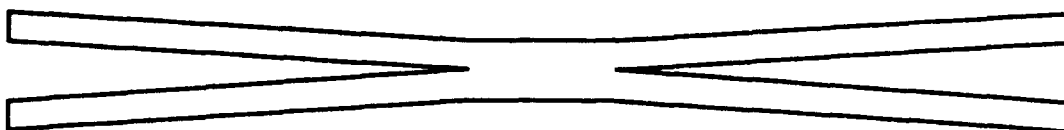


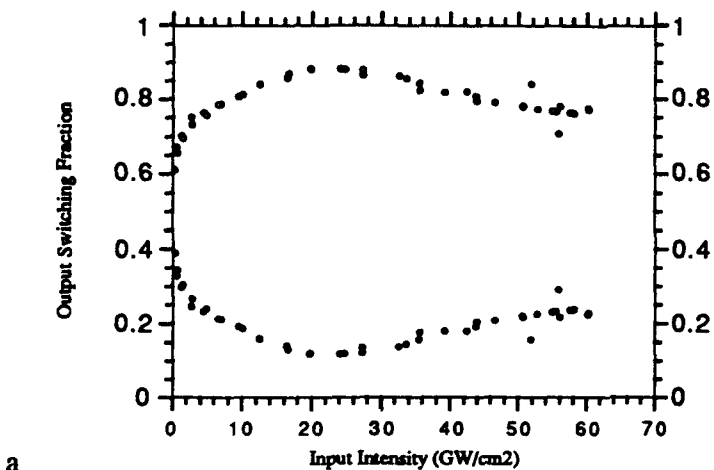
Fig.1 Schematic representation of the symmetric X-switch.

Figure 1 shows a schematic diagram of the X-switch, the mask used to produce the devices was reverse written using a focused electron beam. The input and output waveguides were all $4\ \mu\text{m}$ wide and supported only a single mode. The taper occurred over a propagation length of 4mm , the angle between the input and output guides was 0.1° and 0.2° , resulting in waveguide separations of $7\ \mu\text{m}$ and $14\ \mu\text{m}$ for the devices tested. The center section was $500\ \mu\text{m}$ long, $8\ \mu\text{m}$ wide and supported both the zero and first order modes.

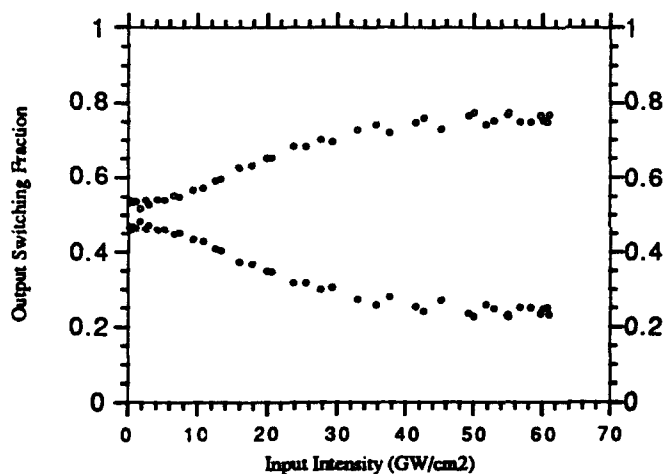
The operation of the nonlinear X-switch can be understood as follows: light is coupled into one of the guides on the left of fig 1. The adiabatic change in separation of the two inputs leads to coupling between the two guides as the light propagates into the central region. The coupling depends on the input power level, hence the relative amount of the zero and first order modes excited in the central $8\ \mu\text{m}$ wide region will depend on the input power. One propagating out of the junction to the right the power will switch between the guides, depending upon the amount of the first order mode excited: a purely symmetric mode in the central region will result in a 50/50 split at the output. However, adding a small amount of the first order mode will cause the output to appear, almost completely at one or other of the two outputs.

Experimental:

The devices were tested by end-fire coupling the output from a additive-pulse mode-locked color center laser into one of the input arms. The laser operated at $1.55\ \mu\text{m}$ and produced $400\ \text{fs}$ pulses. The two outputs were collected with a $60\times$ objective and spatially separated onto two Ge photo detectors. The input power was controlled with a half wave plate/polarizer combination. The waveplate was controlled by the same computer which monitored the input and the two output signals.



a



b

Fig 2. Experimentally measured transmission of a) a 0.1° and b) a 0.2° symmetric X-switch as a function of input intensity.

Figure 2 shows the transmission data taken for 0.1° and 0.2° symmetric X-switches. From the figures it is clear that the power is redistributing between the outputs. Theoretical modeling of the transmission characteristics predict very sharp switching features. The nonresonant nonlinearity responsible for the refractive index change has a response time much faster than the 400fs input pulse, therefore the data in figure 2 represents the time averaged output. In order to simulate the effects of the time average we used the transmission data in fig 2 of ref 5, and performed a time average with a sech^2 temporal pulse. The results of this simulation show good agreement with the experimental results of fig2. We will present results on both symmetric and asymmetric X-switch structures and compare these results to those expected.

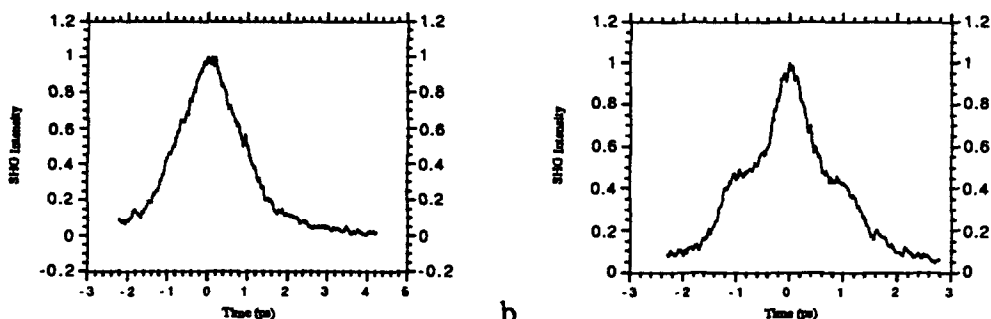


Fig 3. a) Autocorrelation of the low output for an input of 70 mW and b) autocorrelation of the same output at 120 mW input power.

Autocorrelation measurements were performed on the pulses emerging from the two output channels. The output from the low intensity channel, taken at two different power levels is shown in fig.3. The output taken at 70mW shows a distinctly triangular shape, fig 3a, indicating that the actual pulse had a flat top profile. At High input power levels this autocorrelation evolves into the triple peaked distribution shown in figure 3b. Such an autocorrelation would be consistent with a temporal pulse which consisted of a high intensity center and flat wings. This type of profile would be consistent with the digital response predicted by theory. The pulse break-up also indicates that the response time of the device is much shorter than the 400 fs width of the input pulse.

Conclusion:

We have observed ultrafast all-optical switching in a nonlinear X-switch fabricated in AlGaAs. The device was tested at 1.55 μm , close to half the band gap, where the effects of TPA were minimized. The experimentally measured switching characteristics were consistent with those predicted by theory, once the appropriate time averaging had been performed. Autocorrelation measurements confirm that the response time is ultrafast and suggest that switching is digital-like.

Acknowledgments:

The work was supported by the SERC in the UK and by NSF under grant EET-88-14663 in the USA. JSA would like to thank the Carnegie Trust and AV the FCAR for financial assistance.

References.

1. M.N. Islam, C.E. Socolich, R.E. Slusher, A.F.J. Levi, W.S. Hobson and M.G. Young, *J. Appl. Phys.* 71, p.1927, (1992)
2. J.S. Aitchison, A.H. Kean, C.N. Ironside, A. Villeneuve and G.I. Stegeman, *Electrn. Lett.*, 27, p.1709, (1991)
3. A. Villeneuve, J.S. Aitchison, P.G.J. Wigley, C.N. Ironside and G.I. Stegeman, "Ultrafast All-Optical Switching in Semiconductor Nonlinear Directional Couplers at Half the Band Gap", to appear in *Appl. Phys. Lett.* (1992)
4. Y. Silberberg and B.G. Sfez. *Opt. Lett.*, 13, p.1132, (1988)
5. J.P. Sabini, N. Finlayson and G.I. Stegeman. *Appl. Phys. Lett.* 55, p.1176, (1989)

Acousto-Optic Tunable Filter for Time-Domain Processing of Ultra-Short Optical Pulses

M.E. Fermann, V. da Silva, D.A. Smith,
Y. Silberberg and A.M. Weiner

Bell Communications Research
331 Newman Springs Rd.
Red Bank, N.J. 07701

Abstract

The application of acousto-optic tunable filters for shaping of ultra-fast pulses in the time domain is analyzed and demonstrated.

With the rapid advance of acousto-optic tunable filter (AOTF) technology^[1], the opportunity for sophisticated signal processing capabilities arises. AOTFs offer unique processing functions, since they may be designed for operation at 1.55 μm and allow the simultaneous handling of up to 100 frequency channels with a high spectral resolution and with processing times of a few μsec , i.e. some three orders of magnitude faster than possible with any other technology^[1]. Previous applications of the multi-channel capability of the AOTF have concentrated on narrow-bandwidth optical signals like in gain equalization of erbium doped fiber amplifiers. Here we show that AOTFs can also be used for the manipulation of ultra-short optical pulses by correlated amplitude and phase filtering of the multiple optical frequency components composing the ultrashort pulse. To our knowledge this is the first demonstration of the AOTF for ultra-fast time-domain signal processing. Thus, the AOTF may serve as an integrated device for shaping and processing of ultra-short pulses. Similar functions were previously demonstrated using either bulk-optic pulse encoders^[2] or photon echoes in Er fibers cooled to liquid helium temperatures^[3].

In order to employ a single-stage AOTF for signal processing, we use a polarized signal and ensure that the input and output polarization axes are parallel, i.e. the AOTF is operated as a notch filter rather than a band-pass filter. This avoids the frequency shift associated with TE to TM mode conversion, which would lead to time-varying phase-shifts and interference patterns in the time domain. Further, to avoid time dependent coherent grating cross talk^[4], the gratings have to be "weak", i.e. shorter than (or equal to) one coupling length and their resonance wavelengths have to be well separated, i.e. by about twice the grating bandwidth. When N acoustic gratings are present in the AOTF, the overall transfer function of the device may then be written as

$$T(\omega) = 1 - \sum_j A_j(\kappa_j, \omega - \alpha \Omega_j)$$

where $A_j = 1 - T_j(\kappa_j, \omega - \alpha \Omega_j)$ is the light rejected by each individual grating. A_j has both amplitude and phase components and depends on the mode-coupling parameter κ_j , the optical frequency ω and the

acoustic drive frequency Ω_j . α is a factor that scales the acoustic drive frequency to the optical resonance frequency. In our filter we have $\alpha \approx 1.1 \cdot 10^6$. It is then easy to show that the output waveform for a δ -function input pulse (i.e. a pulse with a spectral bandwidth much larger than the grating bandwidth) is given by

$$E_{out}(t) = \delta(t) - F(A(\omega')) \sum e^{i\alpha\Omega_j t}$$

where F denotes a Fourier transform. For simplicity we have assumed here that all gratings have the same coupling strength κ . From this we can see that different pulse forms may be generated by selecting a range of resonance frequencies ω_i . The temporal width of $F(A(\omega'))$ is proportional to the inverse of the filter bandwidth in the frequency domain. From this we may infer that the output waveform occupies a time window corresponding to the group-velocity walk-off between the two polarization axes of the AOTF. For a 10 cm long filter and a typical refractive-index difference between the two polarization axes of 0.07, we thus obtain a time window of 23.4 psec and hence the AOTF is particularly suitable for the processing of ultra-fast waveforms on time scales of femtoseconds up to a few tens of psec.

For an initial demonstration of the ideas developed above we performed a range of experiments, where the AOTF was driven with two well-separated acoustic frequencies near 175 MHz with an acoustic power of 10 mW each. This gives rise to two notches in the filter transmission near 1.53 μm , where the notch separation $\delta\lambda$ was varied between 3 and 10 nm. A train of 500 fsec pulses (derived from an APM-modelocked colour center laser) at 1.53 μm was then coupled into the filter and the output waveform studied in the time domain by cross-correlating it with a reference pulse of 100 fsec width. In this the 500 fsec pulses were obtained by broadening via gain narrowing in an erbium amplifier, as shown schematically in Fig. 1.

The spectrum of the pulse train transmitted by the AOTF is given in Fig. 2, where the two generated notches (separated by $\delta\lambda=4$ nm) are clearly visible. Fig. 3 shows the output pulse shapes with a) no RF applied, b) light launched along the slow and c) light launched along the fast axes. The diffracted signal is either observed before or after the undiffracted pulse part. This is again a manifestation of the fact that the diffracted signal has to have a group-velocity between the two boundaries given by the group-velocity along the two polarization axes of the AOTF. The observable beats in the time domain result from interference of the two selected notches, where the beat period may be derived from eq. (2) as $\delta t = \lambda^2 / 2c\delta\lambda$ in excellent agreement with experiment.

Note that the experiments are an initial demonstration of the proposed operation principle. To show the potential for more

complex processing functions we have developed a detailed numerical model of the AOTF including grating interactions and have solved for the diffracted waveform generated with a single read pulse. Fig. 4 shows the generation of a double pulse with a 10 cm long filter, a 100 fsec input pulse and 29 acoustic channels. The residual signal background signal arises from grating interactions and could be minimized by minimizing channel overlap. Indeed we have found that grating cross talk poses a severe limitation for the generation of longer bit patterns. Therefore we are currently investigating in as far the phase contributions to the gratings may be decoupled from the amplitude part for more efficient pulse-shaping.

Finally we would like to point out that the processing capabilities described here are very closely related to functions performable with photon echoes. The common denominator is that both interactions are resonant and result from diffraction of optical pulses from correlated amplitude and phase gratings in the frequency domain, i.e. gratings which do not allow independent control of phase and amplitude. The advantage here is that the grating writing and reading process may be separated and that the writing process may be performed electronically by generating arbitrary gratings with acoustic waves and the device may be operated at room temperature. The disadvantage is that the spectral resolution at present is at least some two orders of magnitude lower than possible with Er-fibers and other solid-state gain media.

In conclusion we have proposed time-domain manipulation of ultra-short pulses by multi-channel operation of acousto-optic tunable filters and demonstrated the operation principle experimentally.

Acknowledgements

M.E. Fermann gratefully acknowledges financial support from the Alexander von Humboldt Stiftung.

References

1. D.A. Smith, J.J. Johnson, J.E. Baran and K.W. Cheung, Proc. IEEE Ultrasonics Symposium, Orlando, 1991
2. A.M. Weiner, J.P. Heritage and J.A. Salehi, Opt. Lett., 13, 300 (1988)
3. V.L. Da Silva, Y. Silberberg, J.P. Heritage, E.W. Chase, M.A. Saifi and M.J. Andrejco, Opt. Lett., 16, 1340 (1991)
4. D.A. Smith and J.J. Johnson, IEEE Photonics Lett. 3, 923 (1991)

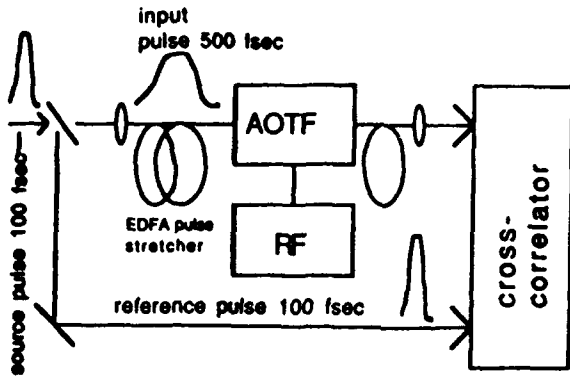


Fig. 1) Experimental set-up. The 100 fsec source pulses are broadened to 500 fsec in the erbium amplifier.

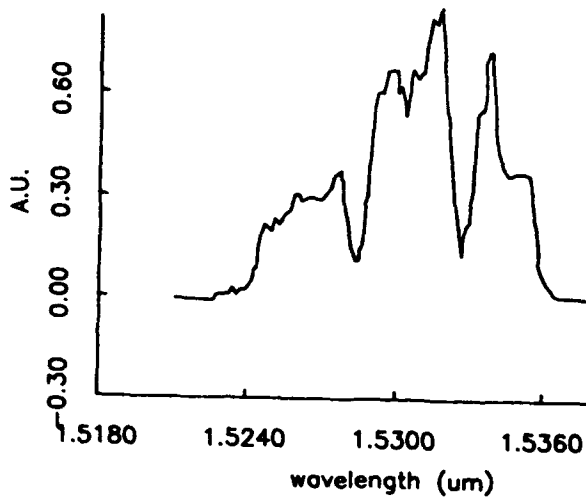


Fig. 2) Transmission spectrum of pulses diffracted by the AOTF.

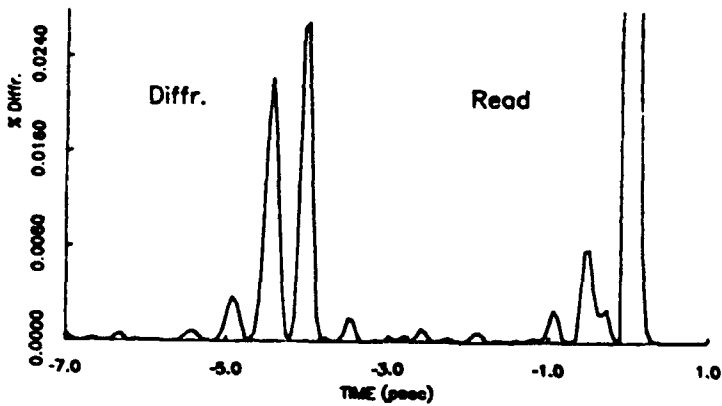


Fig. 4) Calculated two-bit pulse pattern generated with 29 acoustic gratings.

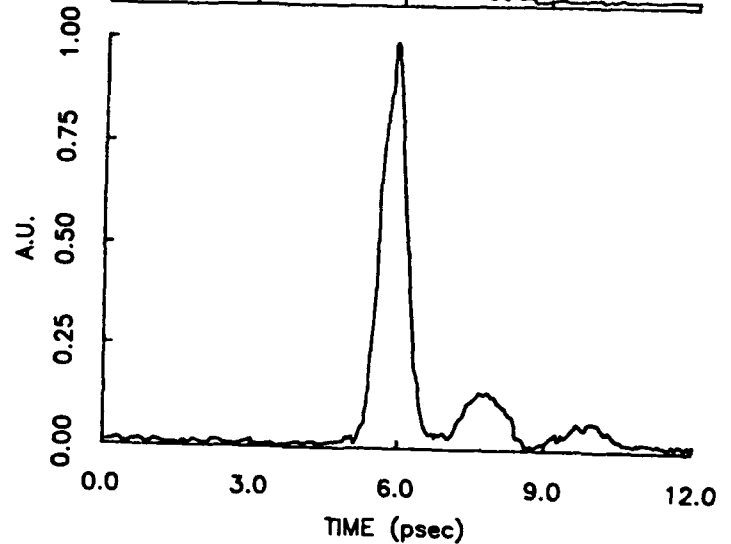
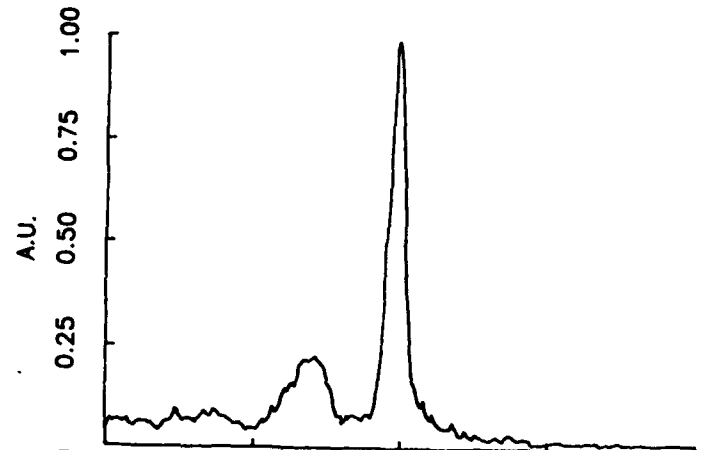
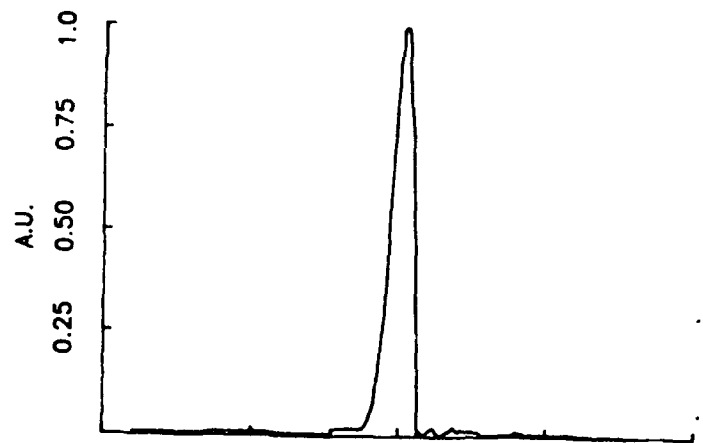


Fig. 3) top to bottom:
a) Unperturbed transmitted read pulse, b) diffracted pulse launched along slow axis
c) diffracted pulse launched along fast axis.

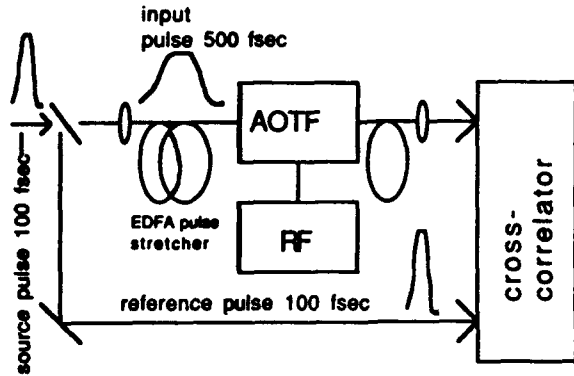


Fig. 1) Experimental set-up. The 100 fsec source pulses are broadened to 500 fsec in the erbium amplifier.

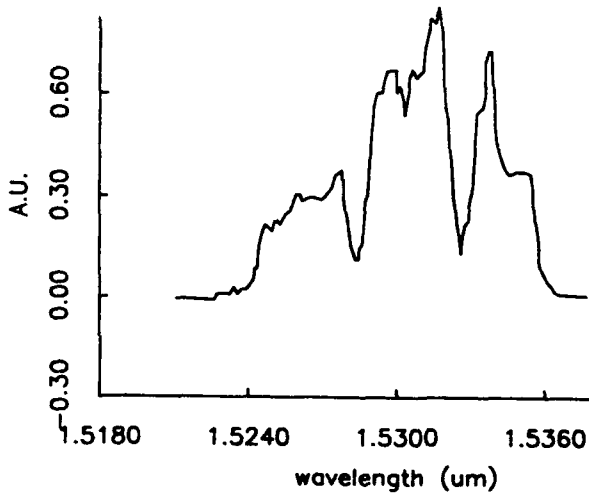


Fig. 2) Transmission spectrum of pulses diffracted by the AOTF.

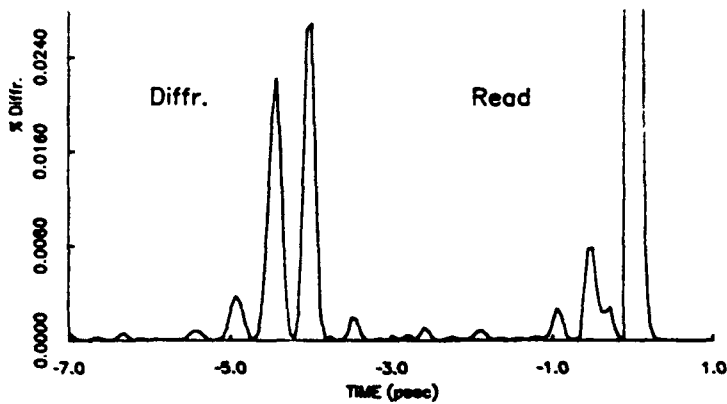


Fig. 4) Calculated two-bit pulse pattern generated with 29 acoustic gratings.

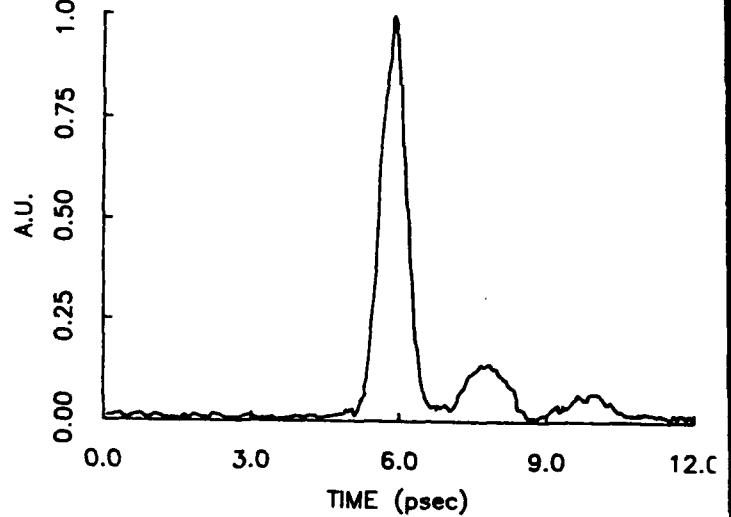
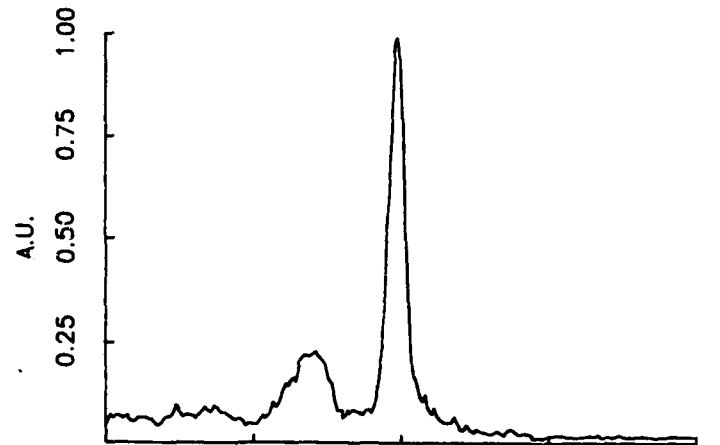
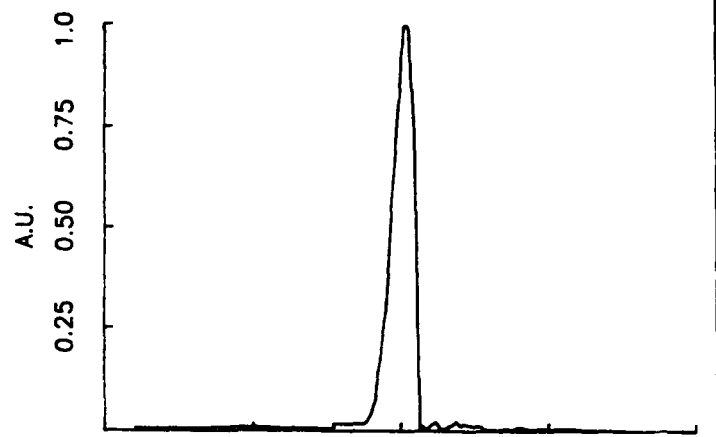


Fig. 3) top to bottom:
a) Unperturbed transmitted read pulse, b) diffracted pulse launched along slow axis
c) diffracted pulse launched along fast axis.

Polarization Mode Locking in Erbium Doped Fiber Ring Lasers

M. Romagnoli, A. Tajani, M. Tamburrini, S. Wabnitz, B. Daino
Fondazione Ugo Bordoni, Via B. Castiglione 59, 00142 Roma, Italy

F. Fontana, N. Manfredini, G. Grasso
Società Cavi Pirelli, Viale Sarca 2, 20126 Milano, Italy

P. Franco, M. Midrio
*Dipartimento di Elettronica ed Informatica, Università di Padova, Via Gradenigo 6/A, 35131,
Padova, Italy*

Introduction: Mode-locking (ML) with erbium doped fiber lasers permits to combine the wide spectral bandwidth of the gain medium with the anomalous group velocity dispersion of the fiber. As a result, soliton pulse shaping plays a key role in the ML dynamics [1-2]. By combining ultrashort soliton amplification and soliton switching [3], it has been demonstrated that ML erbium doped fiber lasers may operate in the femtosecond regime [4]. These ML sources are intrinsically self-starting and unstable [5], and the origin of the observed complex temporal behavior has been recently ascribed to soliton resonances with the laser cavity length [6].

In this work we present results of experimental studies of the role of polarization rotation as a switching mechanism [7] in both active and passive ML in erbium doped fiber ring lasers. In the active case, by controlling the state of polarization we observed the generation of ML 100 femtosecond pulse trains, with repetition rates as high as 300 GHz. In the passive case, ML is self-starting and we observed the generation of multiple pulses with different wavelengths and polarization states [8]. Here the control of the state of polarization permits the selection of the output wavelengths.

Experiment: The experimental configurations for active and passive ML in erbium doped fiber ring lasers are shown in fig.(1). In both cases, gain is provided by a 10 m long erbium doped fiber (aluminium codoped), with the numerical aperture $NA = 0.2$, and the absorption of 5.5 dB/m at the wavelength $\lambda = 1532$ nm. Whereas the cutoff wavelength is 900 nm, which permits single mode propagation of the 980 nm pump from a dichroic coupler. The maximum power from the semiconductor pump laser was equal to 39 mW. Unidirectional operation was ensured by means of a polarization insensitive optical isolator. Active ML was initiated by $LiNbO_3$ phase modulator, and the state of polarization after the isolator was manipulated by means of an all-fiber polarization controller. In the passive case, a bulk polarizing beam splitter was employed in order to reject one

polarization component (vertical) from the cavity. Whereas in the active case polarization discrimination was achieved through a directional coupler. In the passive configuration, we also monitored the polarization state inside the cavity (horizontal) by means of a beam sampler. In either case, the average output power from the lasers ranged from 0.2 to 2 mW. The output light was detected with fast photodiodes and sampling oscilloscopes, which in some cases permitted to directly measure the repetition rate of the circulating trains. In the femtosecond ML regime, we have performed autocorrelations of the output pulse trains after an erbium doped fiber amplifying stage (with a linear gain of 20 dB).

Results: In the active case, as the modulator was turned on the cw laser oscillation broke up into a regular train of ML pulses. The repetition rate of the train was equal to the fundamental frequency of the cavity (7.5 MHz), irrespectively to some extent of the modulation frequency. The time duration of the ML train in the envelope was 5 ns. Figure (2) shows the autocorrelation of the ML pulses, which reveals the 100 fs full width of the pulses (possibly time compressed along the amplifier). The inset in figure (1) shows that the repetition rate of the ML train was as high as 300 GHz. The control of the state of polarization in the ring was critical for obtaining ultrashort pulse ML. Nevertheless, once it was achieved the ML was relatively stable.

In the passive case, self-starting ML was observed to prevail over cw oscillation. The temporal characteristics of the generated pulses consisted of a superposition pulses circulating at the fundamental cavity frequency and at higher harmonics. Therefore we have characterized the laser output in the spectral domain. We found that the laser tends to mode lock pulses with different wavelengths and polarizations. Figure (3) shows a case of single-frequency emission, which is accompanied by several satellite sidebands. From the main spectrum of fig.(3) we infer a ML pulse width of the order of 30 ps, which would rule out the soliton resonances with the loop length [6] as a possible mechanism for sideband generation. Moreover, here the sidebands are equally spaced whereas soliton resonance leads to wavelength separations that are proportional to the square root of the sideband order [6].

Figure (4) shows dual-frequency ML in the passive ring laser. Here we have removed the polarizer since only the beam splitter introduces polarization sensitive losses in the cavity. The polarization decomposition that is shown in fig.(4) follows the directions which are either parallel or orthogonal to the entry plane of incidence of the splitter. As it can be seen, the polarization state of the two peaks is different. Moreover, the sidebands only appear in one polarization. The observed anisotropy disappears reducing the pump power.

ML was not only limited to pulses with two different frequencies. By simply rotating the polarization controller, it was possible to introduce several polarized optical paths in the cavity which leads to multiple frequency ML (see fig.(5)) [8].

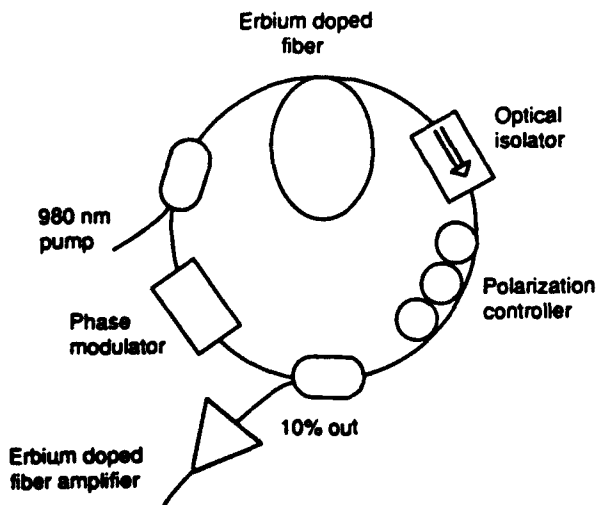
Conclusions: We have studied polarization induced passive and active ML in a simple erbium doped fiber ring laser configuration. In the active case, we have demonstrated the generation of ultrahigh repetition rate femtosecond pulse trains. In the case of self-starting passive ML, we have revealed the generation of polarized sidebands and multiple frequency ML.

Acknowledgements: This work was carried out in the framework of the agreement between Fondazione Ugo Bordoni and the Italian P.T. Administration.

References

- [1] J. D. Kafka, T. Baer, and D. W. Hall, *Opt. Lett.* **14**, 1269 (1989).
- [2] K. Smith, J. R. Armitage, R. Wyatt, and N. J. Doran, *Electron. Lett.* **26**, 1149 (1990).
- [3] A. G. Bulushev, E. M. Dianov, and O. G. Okhotnikov, *Opt. Lett.* **15**, 968 (1990).
- [4] I. N. Duling, *Electron. Lett.* **27**, 544 (1991).
- [5] R. P. Davey, N. Langford, and A. I. Ferguson, *Electron. Lett.* **27**, 1257 (1991); D. J. Richardson, R. I. Laming, D. N. Payne, V. J. Matsas, and M. W. Phillips, *Electron. Lett.* **27**, 1451 (1991).
- [6] N. Pandit, D. U. Noske, S. M. J. Kelly, and J. R. Taylor, *Electron. Letters* **28**, 455 (1992).
- [7] M. Hofer, M. E. Fernmann, F. Haberl, M. H. Ober, and A. J. Schmidt, *Opt. Lett.* **16**, 502 (1991).
- [8] J. B. Schlager, S. Kawanishi, M. Saruwatari, *Electron. Lett.* **27**, 2073 (1991).

Active configuration



Self-starting configuration

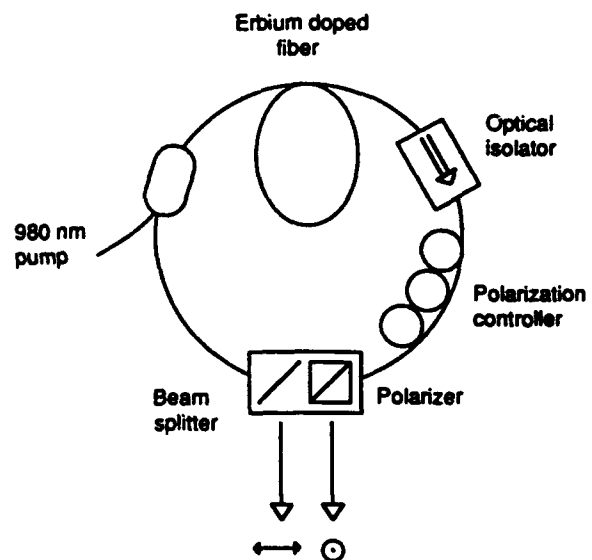


Figure 1: Schematic of active and passive polarization mode-locking with erbium doped fiber ring lasers.

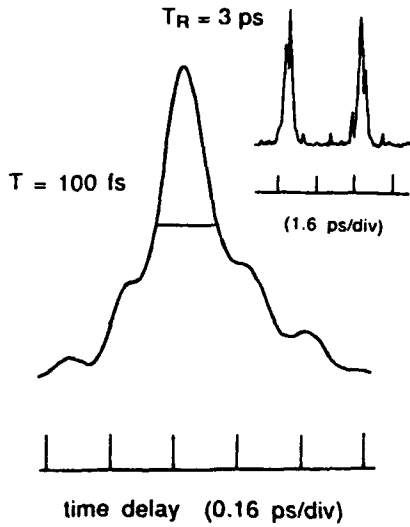


Figure 2: Autocorrelation of 100 fs output pulse from actively mode locked erbium fiber ring laser. The inset shows the autocorrelation of the pulse train with 3 ps repetition rate.

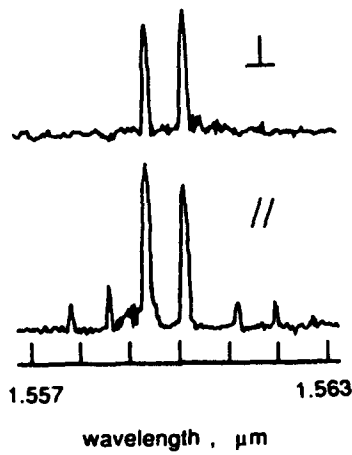


Figure 4: Polarization decomposition of dual frequency passive mode locking at high pump powers.

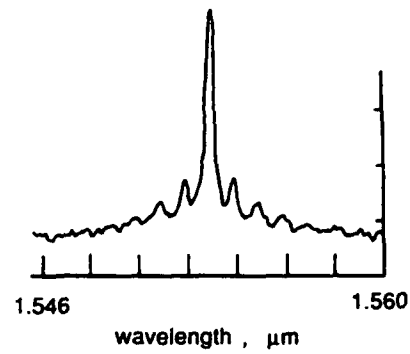


Figure 3: Multiple sideband generation from self-starting passive mode locked laser.

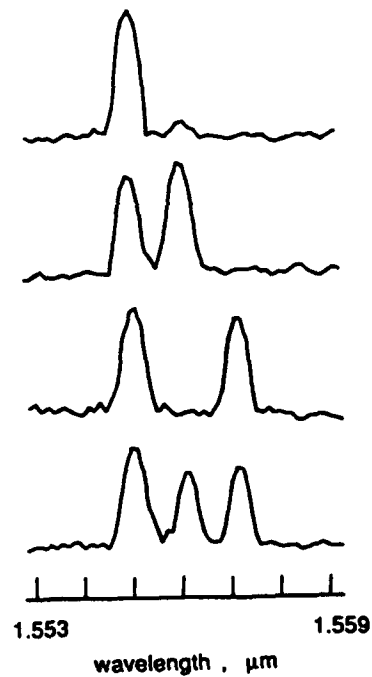


Figure 5: Birefringence-controlled triple frequency passive mode locking.

Finite Difference Generalized Padé Approximant Propagation Methods

David Yeavick, Department of Electrical Engineering, Queen's University Kingston, Ontario K7L 3N6, Canada, Moses Glasner, Department of Mathematics, Penn State University, 221 McAllister Building, University Park, PA 16802, Björn Hermansson, Telia Research, Sfo, S-136 80 Haninge, Sweden

Abstract: We present a simple series of high-order finite difference and finite element propagation procedures based on approximating the exponential of two noncommuting operators as a product of single-operator Padé approximants.

We have previously generated a class of precise split-step fast Fourier transform propagation techniques from an expansion of e^{A+B} , where A and B are noncommuting operators, into an alternating product of exponentials of the individual component operators.[1,2] We here extend this formalism to split-operator finite difference and finite element alternating direction implicit procedures[3] by defining the generalized Padé approximant of e^{A+B} as a product of Padé approximants of each individual operator. We demonstrate the central fact that that high-order propagation methods often require only (1,1) component approximants. Our results, which are found numerically to apply in fourth and sixth order even to longitudinally varying refractive index distributions, are verified by analyzing light propagation through an integrated optic microlens.

We consider the Fresnel equation

$$\frac{\partial E}{\partial z} = (D + N(x, y, z))E \quad (1)$$

for the envelope, E , of a single polarization component of a monochromatic electric field with vacuum wavevector k_0 in a medium characterized by a reference refractive index n_0 . In Eq.(1)

$$D = D_x + D_y \quad (2)$$

with ($\alpha \in \{x, y\}$)

$$D_\alpha = -\frac{i}{2k_0 n_0} \frac{\partial^2}{\partial \alpha^2} \quad (3)$$

and

$$N(x, y, z) = -\frac{ik_0 n_0}{2} \left(\frac{n^2(x, y, z)}{n_0^2} - 1 \right). \quad (4)$$

Specializing for simplicity to z -independent operators $A = D$ and $B = N(x, y)$, standard split-step fast Fourier transform or split-operator finite difference and finite-element methods are based on the relation

$$e^{z(A+B)} = e^{z\frac{A}{2}} e^{zB} e^{z\frac{A}{2}} + O(A, B, 3) \equiv \Lambda_2(z) + O(A, B, 3). \quad (5)$$

where $O(\mathcal{O}_1, \mathcal{O}_2, \dots, K+1)$ represents a generic homogeneous function with the property that $O(\alpha \mathcal{O}_1, \alpha \mathcal{O}_2, \dots, K+1) = O(\alpha^{K+1})$. To increase the accuracy of Eq.(5) while remaining within the framework of existing theoretical and numerical techniques, we have previously determined for $K = 4$, $K = 6$ and $K = 8$ the constants m , a_i^K and b_i^K in the formula

$$e^{z(A+B)} = \prod_{i=1}^m e^{z b_i^K B} e^{z a_i^K A} + O(A, B, K+1). \quad (6)$$

Here $\prod_{i=1}^m \mathcal{A}(i) \equiv \mathcal{A}(m)\mathcal{A}(m-1)\dots\mathcal{A}(1)$, K is a fixed positive integer, m is an unknown positive integer and $a_i^K, b_i^K, i = 1, 2, \dots, m$, are unknown real numbers. For a symmetric procedure $a_{m-i+1}^K = a_i^K, b_{m-i}^K = b_i^K$ and $b_m^K = 0$ with $i = 1, 2, \dots, m-1$. While Eq.(6) translates directly into a split-operator fast Fourier transform method, we here examine its finite difference or finite element implementations.

We have previously derived recursion relations which allow higher-order solutions of Eq.(6) to be constructed from lower-order methods.[1] While our $K \rightarrow K+2$ and $K \rightarrow K+4$ recursions were found to be valid even for longitudinally varying A and B ,[2] we examine below only the z -independent $K \rightarrow K+4$ case.

To generate a K th order finite-difference or a finite-element procedure, we replace the exponential operators in Eq.(6) by Padé approximants. In particular, for any operator $e^{za_i^K \mathcal{O}}$, we may substitute

$$\begin{aligned} \left(\frac{1 + za_i^K \mathcal{O}/2}{1 - za_i^K \mathcal{O}/2} \right) &= e^{\log \left(\frac{1 + za_i^K \mathcal{O}/2}{1 - za_i^K \mathcal{O}/2} \right)} \\ &= e^{za_i^K \mathcal{O} + \frac{z^3 (a_i^K)^3}{12} \mathcal{O}^3 + \frac{z^5 (a_i^K)^5}{80} \mathcal{O}^5 + O(\mathcal{O}, 7)}. \end{aligned} \quad (7)$$

In three-dimensional problems, since $\frac{\partial^2}{\partial x^2}$ and $\frac{\partial^2}{\partial y^2}$ commute, a (1,1) approximant for $e^{za_i^K D}$ is

$$e^{za_i^K D} = e^{za_i^K D_x} e^{za_i^K D_y} = \left(\frac{1 + za_i^K D_x/2}{1 - za_i^K D_x/2} \right) \left(\frac{1 + za_i^K D_y/2}{1 - za_i^K D_y/2} \right) + O(D, 3). \quad (8)$$

The required order of these Padé approximants is less than that of the overall method. To illustrate, we demonstrate that for the sixth order solution, (1,1) Padé approximants are sufficient. We in fact achieve a sixth order method by repeatedly multiply the 3-operator second-order products

$$\tilde{\Lambda}_2(z) = \left(\frac{1 + zA/4}{1 - zA/4} \right) \left(\frac{1 + zB/2}{1 - zB/2} \right) \left(\frac{1 + zA/4}{1 - zA/4} \right). \quad (9)$$

We now consider a symmetric K th order solution $\tilde{\Lambda}_K(x)$ of Eq.(6) composed of generalized Padé approximants. Since Eq.(7) only contains odd powers of \mathcal{O} , we find

$$\tilde{\Lambda}_K(z) = e^{z(A+B) + z^{K+1} \tilde{C}^{K+1} + z^{K+3} \tilde{C}^{K+3}} + O(A, B, K+4) \quad (10)$$

where the \tilde{C}^k are homogeneous polynomials of degree k in A and B . The $\tilde{C}^k = 0$ vanish for even k for symmetric $\tilde{\Lambda}_K$. [4,5].

A $K \rightarrow K+4$ recursion relation is generated by finding $\{u, v, x, y\}$ such that [6]

$$\begin{aligned} \tilde{\Lambda}_K(u) \tilde{\Lambda}_K(v) \tilde{\Lambda}_K(x) \tilde{\Lambda}_K(y) \tilde{\Lambda}_K(x) \tilde{\Lambda}_K(v) \tilde{\Lambda}_K(u) &= e^{\tilde{W}(u, \tilde{W}(v, \tilde{W}(x, \tilde{\Lambda}_K(y))))} + O(A, B, K+4) \\ &= e^{A+B} + O(A, B, K+4). \end{aligned} \quad (11)$$

This is done by considering the general expression

$$\tilde{\Lambda}_0 = e^{\alpha(A+B) + \beta \tilde{C}^{K+1} + \beta_1 \tilde{C}_1^{K+1} + \beta_2 \tilde{C}_2^{K+1} + \gamma \tilde{C}^{K+3}} \quad (12)$$

in which $\tilde{C}_i^{K+1} = [A+B, \tilde{C}_{i-1}^{K+1}]$ and $\tilde{C}_0^{K+1} = \tilde{C}^{K+1}$. We then search for the transformation of the variables $\alpha, \beta, \beta_1, \beta_2$ and γ associated with the product

$$\tilde{\Lambda}_K(x)\tilde{\Lambda}_0\tilde{\Lambda}_K(x) = e^{\tilde{W}(x,\tilde{\Lambda}_0)} + O(K+4). \quad (13)$$

Since β_1 remains zero in \tilde{W} by symmetry, the condition that the coefficients of $A+B, \tilde{C}^{K+1}, \tilde{C}_2^{K+1}$ and \tilde{C}^{K+3} in $\tilde{W}(u, \tilde{W}(v, \tilde{W}(x, \tilde{\Lambda}_K(y))))$ be 1, 0, 0, and 0 respectively yields the same algebraic equations and sixth order defining constants a_i^K and b_i^K as those presented in Eqs.(A14)-(A17) and Table 1 of [6] - except that $x^K + y^K$ in (A16) is incorrect and should be $x^K - y^K$. The symmetry of the resulting $(K+3)$ rd order solution of Eq.(6) then automatically insures $(K+4)$ th order accuracy as we have verified by multiplication of the Padé approximants.[6,5] Note that the generalized Padé approximant procedure contains 21 operators in place of the 15 operator fast Fourier transform method since adjacent Padé approximants of a single operator cannot be combined.

To illustrate that our sixth-order generalized Padé approximant method is even valid for a z -dependent profile, we calculate in quadruple precision the width of a $\lambda = 1\mu\text{m}$ light beam focused by a one-dimensional graded index microlens with a normalized refractive index distribution given by

$$n(x, z) = \frac{n_0}{1 + \frac{x^2 + z^2}{h^2}} \quad (14)$$

for $n_0 = 1$ and $h = 1000\mu\text{m}$. The input excitation is $E(x, 0) = e^{-\frac{x^2}{(400)^2}}$ and the split-operator implicit finite difference method[7] is applied according to Eq.(6) on a $N_x = 512$ point grid with transverse dimension $L_x = 400\mu\text{m}$. In Fig.(1), we display the magnitude of the absolute error after a propagation distance of $z = 15\mu\text{m}$ as a function of the number of propagation steps of the approximate beam width defined as

$$W(z) = 4 \left(\frac{\int_{-L_x}^{L_x} x^2 |E(x, z)|^2 dx}{\int_{-L_x}^{L_x} |E(x, z)|^2 dx} \right)^{\frac{1}{2}}. \quad (15)$$

The solid, dashed, dashed dotted and dotted lines correspond to the 21 operator sixth-order generalized Padé method in which (1,1) Padé approximants are employed for all operators, the standard second-order propagation procedure, Eq.(5), a modified 21 operator sixth-order generalized Padé method in which (1,1) Padé approximants are substituted only for the propagation operators $e^{za_i^K D}$ and the 15 operator sixth-order generalized fast Fourier transform procedure, respectively. As a consequence of the different representations of the transverse derivative operator, the asymptotic value of the beam width for $\Delta z \rightarrow 0$ is set to 703.570672400471195195629579870569 for the fast Fourier transform and 703.568017913172361935414538571079 for the finite difference calculations. The inaccuracy of the finite difference results can however be partly circumvented by employing a more accurate representation of the second derivative operator, c.f. Eq.(3) of [3]. For our input values the finite difference method, despite the somewhat larger number of operators, is as rapid as the fast Fourier transform procedure.[7]

In conclusion we have verified that high-order split-operator alternating direction implicit electric field propagation techniques can be obtained from multiplication of a relatively small number of (1,1) Padé approximants. The generalized Padé approximant procedures are similar in structure to and provide nearly the same convergence properties and computational efficiency as generalized fast Fourier transform algorithms.

Support for this work was provided by Bell Northern Research, Corning Glass, the Ontario Centre for Materials Research, the Ontario Laser and Lightwave Research Center, Swedish Telecom and the National Sciences and Research Council of Canada.

- [1] M. Glasner, D. Yevick, and B. Hermansson, "Computer generated generalized propagation techniques," *Appl. Math. Lett.*, vol. 4, pp. 85-90, 1991.
- [2] M. Glasner, D. Yevick, and B. Hermansson, "Generalized propagation techniques for longitudinally varying refractive index distributions," To be published in *Math. and Comp. Modelling*.
- [3] B. Hermansson, D. Yevick, W. Bardyszewski, and M. Glasner, "The unitarity of split-operator finite difference and finite-element methods: Application to longitudinally varying semiconductor rib waveguides," *IEEE J. Lightwave Technology*, vol. 7, pp. 1866-1874, 1990.
- [4] M. Glasner, D. Yevick, and B. Hermansson, "Sixth order generalized propagation techniques," *Electron. Lett.*, vol. 27, pp. 475-478, 1991.
- [5] M. Glasner, D. Yevick, and B. Hermansson, "High order generalized propagation techniques," *J. Opt. Soc. B*, vol. 8, pp. 413-415, 1991.
- [6] M. Glasner, D. Yevick, and B. Hermansson, "Generalized propagation formulas of arbitrarily high order," *J. Chem. Phys.*, vol. 95, pp. 8266-8272, 1991.
- [7] D. Yevick and B. Hermansson, "Efficient beam propagation techniques," *IEEE J. Quant. Electron.*, vol. 26, pp. 109-112, 1990.

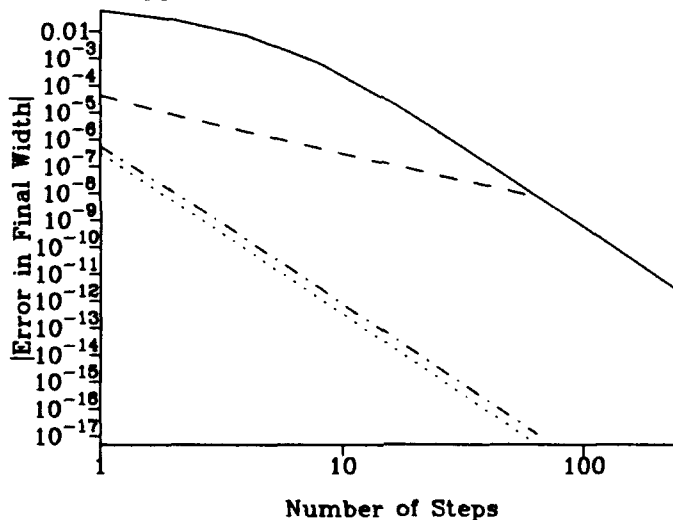


Figure 1: The magnitude of the absolute error in the beam width at $z = 15\mu\text{m}$ referred to $\Delta z \rightarrow 0$ values as calculated with the sixth-order generalized finite difference procedure (solid line), the standard second-order fast Fourier transform method (dashed line), the sixth-order modified generalized finite difference procedure (dashed dotted line) and the sixth-order generalized fast Fourier transform procedure (dotted line).

Theory of Square Meander-type Couplers

H.- P. Nolting

Heinrich-Hertz Institut für Nachrichtentechnik Berlin GmbH,
Einsteinufer 37, 1000 Berlin-10, Germany, ++ 30 31002 427

Introduction

Experimental results on the square meander or grating-assisted codirectional coupler have been published recently. The device was employed as a passive wavelength sensitive multiplexer / demultiplexer and as part of a tunable laser [1,2]. Theoretical analyses were based on a coupled mode method [1,3], but no method to calculate the coupling efficiency from a first principles approach, including the case of strong coupling, has been published so far to the best of our knowledge. As will be shown in this paper, a standard coupled mode approach which is based on the eigenmode of the *isolated* waveguides, cannot be used for this device. Instead we will describe a method to calculate the period length and the coupling length as a function of the waveguide and grating architecture by using mode matching theory at the boundaries of the grating and mode propagation in the constant waveguide sections in between. This way the exact grating and waveguide architecture is taken into account. This approach is straight forward and leads to a deeper understanding of the physical behaviour of the device. A few examples shall demonstrate the usefulness of this calculation method for the design of square meander type couplers.

For simplicity we neglect the feeding branches in a first approach, but they can be added in an easy way at a later stage. In an asymmetric coupler most of the energy of the two fundamental modes (even or odd mode, E_c

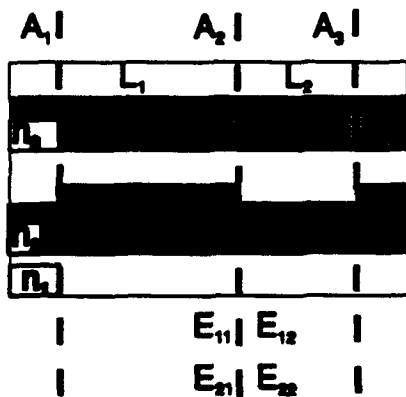


Fig. 1 : Architecture of one period of the square meander

and E_o) is concentrated into one of the two waveguides. So energy exchange of waves from one waveguide to the other can be described as coupling from one fundamental mode to the other. For an undisturbed coupler the eigenmodes are orthogonal, which means they propagate independently along the device. It will be shown, that any discontinuity in the waveguide results in a coupling between both fundamental waves. So total energy transfer can be accomplished by introducing a properly designed periodic perturbation to the coupler, whose period length compensates the phase mismatch of both modes. The simplest way to realize the perturbation is to vary the waveguide cross section, as is shown for one "unit" period in a 1D cross section in figure 1. This way we get a so called meander or grating structure, superposed to the asymmetrical coupler. In the following we will develop the optimal length L_1 and L_2 of both sections for the shortest possible device length L_c if coupler and grating structure are given. Due to the fact, that this is a wavelength dependent resonance condition, we can also calculate the dispersion behaviour of the device. The fundamental ideas, which are used here for the meander coupler, can be used also for other periodic devices with two interacting fundamental modes such as a TE/TM mode converter [4] or a grating-assisted contradirectional asymmetrical coupler [3].

Theory

Figure 1 shows one period of an asymmetric square meander coupler. A is the period length of the waveguide structure with the individual lengths L_1 and L_2 . We have butt coupling between consecutive sections at the boundaries A_1 , A_2 , A_3 and so on. So in a first approximation we can represent the guiding modes of the structure as a sum of both eigenmodes in each section, neglecting the radiation modes and reflections at the boundaries. The justification of this approach has been proved by using the more general Bidirectional Eigenmode Propagation (BEP) Method [5]. It is important to note, that nearly all energy is exchanged between the fundamental guided modes, and none is transferred to the radiation modes. This is in contrast to an isolated waveguide with the same grating which naturally generates radiation modes. So in each section j with $j=1$ and 2 we have the two modes E_{jj} with the amplitude coefficients q_{jj} and the effective refractive index

of the waveguides n_{ij} . The index $i=1$ refers to the even and $i=2$ to the odd mode. At the boundaries both fields have to be equal (Maxwell's boundary conditions) leading to the equation:

$$n_{11}q_{11}E_{11} + n_{21}q_{21}E_{21} + \dots = n_{12}q_{12}E_{12} + n_{22}q_{22}E_{22} + \dots \quad (1)$$

and by mode matching we can calculate the fields at the boundaries A_i using the relations:

$$\bar{q}_2 = \begin{pmatrix} n_{12}q_{12} \\ n_{22}q_{22} \end{pmatrix} = \begin{pmatrix} a_{11} & a_{12} \\ a_{21} & a_{22} \end{pmatrix} \begin{pmatrix} n_{11}q_{11} \\ n_{21}q_{21} \end{pmatrix} = \bar{A}_{21}\bar{q}_1 \quad \bar{q}_1 = \bar{A}_{21}^{-1}\bar{q}_2 = \bar{A}_{12}\bar{q}_2 \quad (2)$$

with

$$a_{\mu} = \int_{-\infty}^{\infty} E_{k1}E_{l2}dx \quad \int_{-\infty}^{\infty} E_{k1}E_{l1}dx = \delta_{kl} \quad (3)$$

The expansion coefficients a_{ij} are the overlap integrals between the even and odd eigenfunctions in both sections, respectively. On the constant waveguide sections we have an independent transmission of both modes with the related phase constants β_{ij} . This is described in the well known transfer matrix :

$$\bar{q}_j = \begin{pmatrix} n_{1j}q_{1j} \\ n_{2j}q_{2j} \end{pmatrix} = \begin{pmatrix} \exp(j\beta_{1j}z) & 0 \\ 0 & \exp(j\beta_{2j}z) \end{pmatrix} \begin{pmatrix} n_{1j}q_{1j} \\ n_{2j}q_{2j} \end{pmatrix} = \bar{T}_j\bar{q}_j \quad (4)$$

By combining mode matching and mode transfer for both sections we have calculated the matrix corresponding to one period, the "unit" period. If we choose the length of each section in such a way that the phase difference between both eigenmodes is $\pi/2$, we have the optimum transfer from one eigenmode to the other. The resonance condition (commonly called phase matching) and the reduced transfer matrix is given by:

$$L_j = \frac{\pi}{\beta_{1j} - \beta_{2j}} \quad \Lambda_u = L_1 + L_2 \quad \bar{T}_j = \begin{pmatrix} 1 & 0 \\ 0 & -1 \end{pmatrix} \quad (5)$$

The resulting unit transfer matrix T_u , is then given by:

$$\bar{T}_u = \bar{T}_2\bar{A}_{21}\bar{T}_1\bar{A}_{12} = \begin{pmatrix} a_{11}^2 - a_{21}^2 & a_{11}a_{12} - a_{22}a_{21} \\ -(a_{11}a_{12} - a_{22}a_{21}) & a_{22}^2 - a_{12}^2 \end{pmatrix} \quad (6)$$

Let us assume we start with all energy in only one mode, for instance $q_1=1$, $q_2=0$. Then multiplication with matrix T_u results in a new set of q values in the order of $q_1=1-\epsilon$ and $q_2=\epsilon$, with $\epsilon \ll 1$, while the energy stored in both modes is nearly conserved. So the action of matrix T_u on the eigenmodes E_e and E_o can be interpreted as a rotation with the angle α in the orthogonal vectorsystem. This rotation angle α is calculated by equation (8) and illustrated in figure 2:

$$\alpha = \tan^{-1} \left(\frac{a_{22}a_{21} - a_{11}a_{12}}{a_{11}^2 - a_{21}^2} \right) = \tan^{-1} (|a_{12}| + |a_{21}|) \quad (7)$$

The matrix T_u is related to a rotation matrix (which is similar to coupled mode theory). As we have to repeat this period n times to get an angle of $\pi/2$, a total device length $L_c = n \Lambda$ is required for full power transfer. In many cases it is usefull to employ gratings with equal lengths of each section. So we have additionally calculated the period length Λ_e , where phase matching is accomplished only every period. This period length is slightly longer than the basic period length Λ :

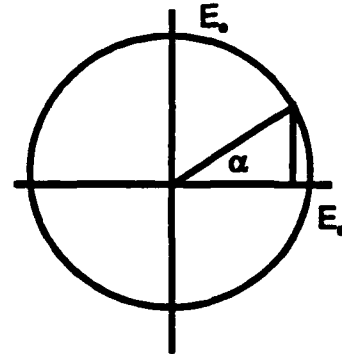


Fig. 2 : Vector representation of eigenmode behaviour after one period

$$n = \frac{\pi}{\alpha} \quad L_c = n\Lambda = n(L_1 + L_2) \quad \frac{1}{\Lambda_c} = \frac{1}{2} \left(\frac{1}{2L_1} + \frac{1}{2L_2} \right) \quad (8)$$

Using wavelength sensitive transfer matrix (4) with fixed device and period lengths allows to calculate the dispersion characteristic of the device. The sum of the square of the amplitude coefficients, which is proportional to the pointing vector, gives a rough estimate of the loss of the device.

Applications

In the following we will calculate for a 1D refractive index profile (similar to profile given in fig.5, but with $w_1=0.4\mu\text{m}$; $c=0.5\mu\text{m}$) the characteristics of different square meander structures shown in figure 3 to demonstrate the influence of the position of the grating on the coupling efficiency. In these examples the main waveguides and the centre-centre distance remain unchanged and the grating is designed to let the body of the waveguide (Δn times Δt) constant.

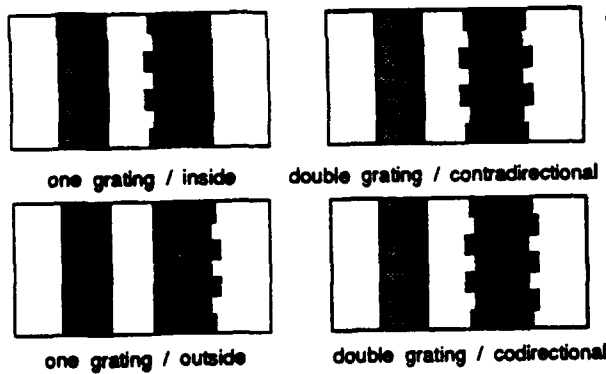


Fig. 3 : Examples of meander couplers with the same waveguide composition and gratings at different positions.

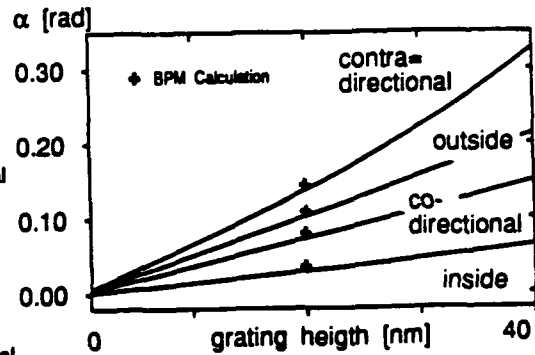


Fig. 4 : Coupling efficiency for different grating positions

It is well known that high coupling efficiency can be obtained by placing the grating in the high contrast waveguide. We have verified this behavior in our example and found one order of magnitude larger efficiency in this case. The results shown in figure 4 (grating in the high contrast waveguide) demonstrate a strong influence of the grating position on the coupler efficiency, which is measured by the rotation angle α of the device for one unit period. In the case of single grating "inside" and "outside" of the coupler, the outside position is much stronger, in contrast to results obtained by using common coupled mode arguments. There the field distributions of isolated waveguides are used, leading to higher coupling efficiency for inside position (both field strengths are much higher there than outside!). In the case of co- and contradirectional gratings we investigated the superposition of two gratings. First results induce the expectation of a sum and difference behaviour for the rotation angle compared to the single grating cases.

For all structures (but keeping the grating depth constant) we have compared the results with a BPM (FD/FE algorithm) and a BEP simulations to verify the theoretical equations) results are marked in figure 4 by a cross). The calculated BPM values for the coupling length are about 10% higher, but the same is true for the beat length of the asymmetric coupler without any grating. So we are led to the conclusion that the precision of the new method is higher than that of BPM which requires a discretization.

To demonstrate the usefulness of this approach we have designed a pair of meanders with high and zero

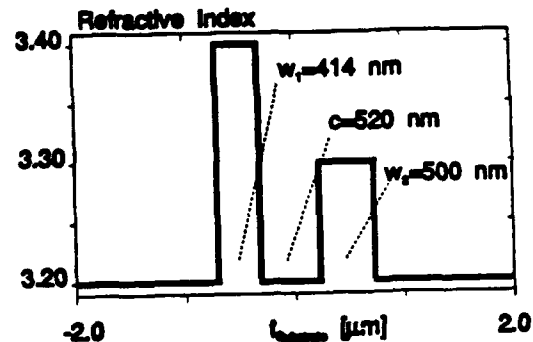


Fig. 5 : Main waveguide architecture:
 $n_1=3.4$ $n_2=3.3$ $n_3=3.2$
 $w_1=414\text{nm}$ $c=520\text{nm}$ $w_2=500\text{nm}$

coupling efficiency by placing a grating with a reasonable modulation depth at two properly chosen positions. As is demonstrated in the next figure, in case of "outside" position we have good efficiency, but for "inside" position coupling efficiency is drastically reduced to nearly zero. This behaviour also has been verified by a BPM calculation. The designed waveguide structure for TE modes at a wavelength of $1.3 \mu\text{m}$ is shown in figure 5 and the calculated rotation angles are shown in fig.6 .

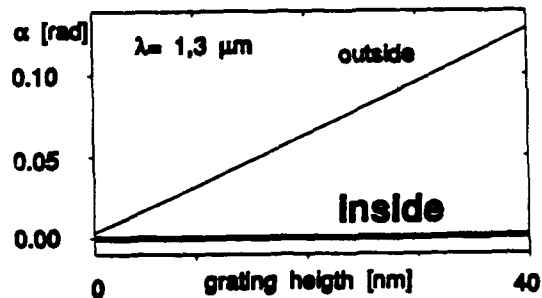


Fig. 6 : Rotation angle of meander coupler for in- and outside position, demonstrating high and zero efficiency

Discussion

The basic principle is to describe a periodically disturbed device as a product of matrices covering one unit period. Each unit period is calculated by two "rotation matrices" of the eigenfunction system of the waveguide and two transfer matrices. The "rotation matrices" are constructed from the four overlap integrals between both eigenvectors on both sides of the boundary. This can be done for 1D and 2D cross sections, depending on the actual device. To calculate the field distribution we need the eigenvalues of the eigenfunctions in both sections, which are also used for the transfer matrices. The resonance conditions are easily calculated, as shown before. So an optimum design (period length Λ , coupling length L_c) is easily obtained. Using the complete matrices and varying the wavelength gives the spectral behaviour of the device. This method is very fast, simple and gives a good insight in the physical behaviour of periodic devices in general, including also a passive TE/TM converter or a contradirectional coupler with grating.

Conclusion

We have demonstrated a simple and fast calculation scheme to simulate periodic devices such as the square meander coupler. The main energy exchange mechanism of the periodic disturbed (e. g. grating) asymmetrical coupler is demonstrated to be coupling between the two fundamental eigenmodes, which can be described as a rotation between the two eigenmodes of the undisturbed waveguide. Total energy exchange between the two eigenmodes can be accomplished, if phase matching is fulfilled in a periodic manner. Some examples are given to show the usefulness of the method.

Acknowledgement

The author is indebted to G. Sztefka for providing the BEP computer program and to M. Grawert for helping to implement algorithms. The author further acknowledges helpful discussions with C. M. Weinert and H. Venghaus.

Literature

- [1] C. M. Weinert, "Three-dimensional coupled mode method for simulation of coupler and filter structures", Integrated Photonics Research 1991, Monterey, paper ThG1.
- [2] R. C. Alferness et. al., "Widely tunable InGaAsP/InP Laser based on a vertical coupler intracavity filter", Conference on Optical Fiber Communication, Feb. 2-7, 1992, San Jose, Postdeadline Paper PD2.
- [3] R. März, H.-P. Nolting, "Spectral properties of asymmetrical optical directional couplers with periodic structures", Optical and Quantum Electronics 19 (1987), p.273-287.
- [4] C. M. Weinert, H. Heidrich, "Vectorial simulation of passive mode converter devices on InP", Integrated Photonics Research 1992, New Orleans, paper MD7.
- [5] G. Sztefka, "Bidirectional propagation algorithm for large refractive index steps and systems of waveguides based on the mode-matching method", Integrated Photonics Research 1992, New Orleans, paper TuB4.

Optical Nonlinear Wakefield Vortices: Results from Full-Wave Vector Maxwell Equation Simulations in Two Spatial Dimensions and Time

Richard W. Ziolkowski and Justin B. Judkins

Department of Electrical and Computer Engineering, The University of Arizona
Tucson, AZ 85721 (602) 621-6173

In this paper we report the first multi-dimensional, full-wave, vector Maxwell's equation solutions to problems describing the interaction of ultra-short, pulsed beams with a nonlinear Kerr material having a finite response time. These solutions have been obtained [†] with a nonlinear finite difference time domain (NL-FDTD) method which combines a nonlinear generalization of a standard, FDTD, full-wave, vector, linear Maxwell's equation solver with a currently used phenomenological time relaxation (Debye) model of a nonlinear Kerr material. In contrast to a number of recently reported numerical solutions of the full-wave, vector, *time-independent* Maxwell's equations and of vector paraxial equations, the FDTD approach is a *time-dependent* analysis which accounts for the complete time evolution of the system with no envelope approximations. Nonlinear self-focusing numerical solutions in two space dimensions and time obtained with this NL-FDTD method as well as related NL-FDTD results for normal and oblique incidence nonlinear interface problems will be presented. Although these basic geometries are straightforward, the NL-FDTD approach can readily handle very complex, realistic structures. These example *TE* and *TM* nonlinear optics problems will highlight the differences between the scalar and the vector approaches and the effects of the finite response time of the medium. The NL-FDTD method is beginning to resolve several very basic physics and engineering issues concerning the behavior of the full electromagnetic field during its interaction with a self-focusing medium. In particular, using the NL-FDTD approach we have (to the best of our knowledge) (1) shown the first back reflections from the nonlinear focus; (2) discovered optical vortices are formed in the trailing wakefield behind the nonlinear focus; (3) identified that the longitudinal field component plays a significant role in limiting the self-focusing process; and (4) performed the first complete full wave, vector treatment of *both* the *TM* and *TE* nonlinear interface problems.

The NL-FDTD method solves numerically Maxwell's equations

$$\partial_t [\mu_0 \vec{H}] = -\nabla \times \vec{E} \quad (1)$$

$$\partial_t [\epsilon_L \vec{E}] = \nabla \times \vec{H} - \partial_t \vec{P}^{NL}, \quad (2)$$

where the nonlinear polarization term $\vec{P}^{NL} = \chi^{NL}(\vec{r}, t, |\vec{E}|^2) \vec{E}$ is specified by solving simultaneously a Debye model for the third order, nonlinear susceptibility χ^{NL} of the Kerr medium:

$$\partial_t \chi^{NL} + \frac{1}{\tau} \chi^{NL} = \frac{1}{\tau} \epsilon_2 |\vec{E}|^2. \quad (3)$$

This approach models the medium as having a finite response time τ . If T represents the pulse width, then by setting $T \geq \tau$, one obtains an instantaneous response model: $\chi^{NL} \approx \epsilon_2 \tau |\vec{E}|^2$, i.e., the medium follows the pulse. On the other hand, if $T \ll \tau$, then the finite response time effects are maximal and the medium's response significantly lags the pulse. The NL-FDTD approach can treat both extremes. Moreover, the divergence equation associated with this system includes the nonlinear source term: $\nabla \cdot [\epsilon_L \vec{E}] = -\nabla \cdot \vec{P}^{NL}$. In two space dimensions and time with coordinates the (x, z, t) and with the choice of a *TM_z* polarized wave, the NL-FDTD method solves for the complete time history of each of the components (E_x, E_z, H_y) . The equations for a *TE_z* polarized wave can be obtained by reciprocity: $\vec{E} \rightarrow \vec{H}$ and $\vec{H} \rightarrow -\vec{E}$, and they lead to the NL-FDTD solution of the components (E_y, H_x, H_z) . The nonlinear source term strongly couples the transverse and longitudinal electric field components in the *TM* case; the corresponding magnetic field components in the *TE* case are driven by the transverse electric field component which exhibits the nonlinear growth. Additionally, when the linear-nonlinear interface problem is treated, Maxwell's equations naturally

[†] R. W. Ziolkowski and J. Judkins, "Full-wave vector Maxwell equation modeling of the self-focusing of ultrashort optical pulses in a nonlinear Kerr medium exhibiting a finite response time", submitted to JOSA B, March 1992.

provide the boundary conditions appropriate for this lossy dielectric interface. Thus, the linear-nonlinear interface problem can be handled without imposing any additional constraints on the fields. Note that we have taken $\epsilon_L = \epsilon_0$. We can incorporate linear dispersion in the FDTD approach at a later date with a number of techniques. Because of the versatility of the FDTD approach, we will be able to "turn-on" the dispersion effects to analyze their impact on the nonlinear self-focusing and interface reflection-transmission processes. The NL-FDTD results to be reported were obtained by carefully designing and testing the numerical grid, material parameters, and the algorithm to insure stability, accuracy, and efficiency. *

With the NL-FDTD method we have demonstrated that the growth of the longitudinal electric field component causes a transverse power flow and reflections from the self-focusing region. The first-ever illustration of this behavior is shown in Fig. 1 where the Poynting's vector $\vec{S} = E_x H_y \hat{a}_z - E_z H_x \hat{a}_y$ in the instantaneous response case $T = 20 \tau$ is plotted in the wakefield of the focal region shown in Fig. 2 where the field structure at the self-focus is represented by a contour plot of the total electric field intensity $I = |E_x|^2 + |E_z|^2$. For visual purposes, the lengths of vectors with negative longitudinal components have been increased 20x, and all vectors shorter than 10% of the maximum length have been removed. In Fig. 2 one can see that the high intensity regions continuously radiate a significant amount of light away from them at large angles as they propagate. The front (large z) portion corresponds to the linear diffraction region; the rear (smaller z) portion incorporates the nonlinear effects. In Fig. 1 one can see the power flow in the frontal lobe exhibits the expected linear behavior; the negative power flow occurs behind the region of the maximum field intensity. The transverse power flow feeds the next self-focusing region. Fig. 2 recovers the well-known horn pattern, but it also shows that the actual field structure is more complicated than this simple scalar equation picture. Two field lobes are formed in the focal region due to the growth of not only the transverse field components E_x and H_y , but also the longitudinal component E_z . Self-focusing is restrained by these non-longitudinal power flow mechanisms since they channel power away from the focus. The transverse and reflected power flow gets recycled back into the next focus by the nonlinear waveguiding channel. This recycling process forms an optical vortex in the wakefield of each foci. Augmented paraxial scalar models also predict that the beam does not experience any catastrophic focusing, i.e., does not focus to a point. However, in contrast to the NL-FDTD approach, they depend upon nonphysical loss mechanisms that limit the self-focusing. In particular, they do not model the important energy transfer mechanisms between the transverse and longitudinal field components which occurs during self-focusing.

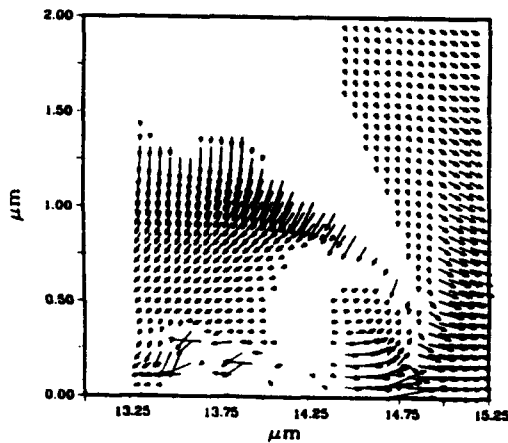


Fig. 1. The Poynting's vector field in the wakefield of the self-focus reveals both transverse and reflected power flows which form an optical nonlinear vortex.

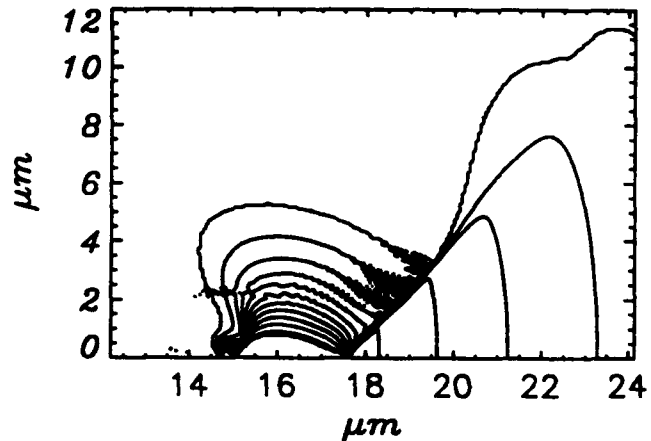


Fig. 2. The total electric field intensity $|E_x|^2 + |E_z|^2$ contour plot at the self-focus shows the classic horn shape as well as the breakup of the pulse into distinct linear and nonlinear lobes.

* We used a square grid with $\Delta z = 0.020 \mu\text{m}$ and $\Delta t = 0.018 \text{ fs}$ resolution. The nonlinear medium parameters were set to the value $n_2 = \epsilon_2 / (2n_0) = 1.0 \times 10^{-18} \text{ (m}^2/\text{V}^2\text{)}$, where $n_0 = 1.0$, and we set the input electric field amplitude to $E_0 = 18.25 \times 10^6 \text{ (V/m)} = 5.5 E_{crit}$. The initial pulse was a Gaussian tapered, raised cosine pulse. The initial transverse waist was taken to be $w_0 = 10.0 \mu\text{m}$. The total pulse width was $T = 20.0 \text{ fs}$ and contained wavelengths from $1.0 \mu\text{m}$ to $10.0 \mu\text{m}$. These discretizations thus provided an average spatial resolution of $\Delta z = \lambda/250$. Several medium response times τ were investigated from $\tau = 5.0 T$ to $\tau = 0.05 T$.

Truly Form Birefringent Fibres

Danny Wong and Simon Poole

Optical Fibre Technology Centre
Sydney University
Australia 2006

Abstract

In some fibre sensors, temperature drift causes phase noise which degrades the sensor severely. A novel intrinsic technique is presented in which the thermal independency is built into the preform of polarimetric sensor fibres. Experiment shown that this technique offers zero temperature sensitivity over a much wider range of temperature than previously reported techniques.

I. INTRODUCTION

Temperature dependence of stress birefringence in fibres is a severe problem in fibre sensors which rely upon changes in the birefringence for the measurement of external parameters [1],[2]. In overcoming the temperature sensitivity, Kikuchi *et al.* [1] employed the jacketing technique while Dakin *et al.* [2] and Lefevre *et al.* [3] utilised differential configuration for their fibre sensor. The former has limited temperature range of operation while the latter require splicing of the two identical lengths of fibre with identical temperature distribution. The present technique is intrinsic because the phase difference between the polarisation modes is made independent of the temperature distribution along the preform and hence the corresponding fibre. It has a much wider temperature range of operation than [1] and has no requirement as those imposed by [2] and [3]. The purpose of this letter is to report this novel technique together with preliminary experimental results.

II. FIBRE DESIGN

Consider the case of an elliptical-core fibre having a germanium doped core and a silica cladding. Since the cladding has a higher fictive temperature than that of the core, on cooling down during fibre drawing, the core is in tension due to its volume contraction with no free boundary. As far as the core is concerned, due to its geometry, the tensile stress along the major axis is larger than that along the minor axis. The elliptical core fibre thus exhibits both stress and form birefringence.

Stress birefringence in the elliptical-core fibre can be eliminated if the tensile stresses along the major and minor axes are made equal for the temperature range of interest. This can be achieved by either, or both, of the following methods : (a) introduction of holes on both sides of the core along the major axis to release the tensile stress in the core along this axis to a level equal to that along the minor axis; (b) introduction of stress side-lobes on both sides of the core along the minor axis to enhance the tensile stress in the core along this axis to a level equal to that along the major axis.

It should be noted that the second method can produce a very wide operating temperature range by fabricating the core and the stress side-lobes from identical materials regardless of its thermal properties. Since the temperature sensitivity is nulled by equalising the differential stresses in the elliptical-core by the bowtie stress field, this structure is well suited to post-tuning the temperature sensitivity by preform etching if any material and geometrical variation occur in the preform during the manufacturing process. This is due to the penetration of the bowtie stress field into the core which is a function of the outer cladding thickness. Figure 1 shows the cross-section of an elliptical-core fibre with temperature compensating stress regions. In this fibre, the bowtie regions were doped to over compensate the sensitivity to demonstrate the effect of post-tuning.

III. EXPERIMENTAL RESULTS

Figure 2 shows the experimental setup used for measuring the temperature dependence of phase sensitivity. A Helium-Neon laser is launched into the fibre through a polariser and a quarter-wave plate to excite both polarisation modes. A section of the fibre is heated and the output state of polarisation is monitored by an analyser and a detector. A computer is used to record both the optical power at the detector and the temperature of the fibre.

Figure 3 shows the measured phase sensitivity of the present fibre, before and after post-tuning, the YORK HB600 bowtie fibre and the OFTC AD023 elliptical-core fibre. The measured beat lengths of the present fibre, before and after post-tuning, the York HB600 and OFTC AD023 fibres at 647 nm, at room temperature, are 4.0, 2.5, 1.0 and 7.5 mm, respectively.

VI. CONCLUSION

A novel method of eliminating the temperature dependence of phase sensitivity in polarimetric fibre sensors is presented. A birefringent fibre of beatlength 2.5 mm with a measured temperature sensitivity of 2.5×10^{-3} rad/°C-m in polarimetric configuration has been produced. This fibre should find applications in the area of polarimetric fibre sensors.

VII. ACKNOWLEDGMENT

This work was funded by the Department of Industry, Technology and Commerce of the Australian Government through Generic Industrial Research and Development Grant number 17011. Sponsorship of the OFTC by OTC limited is acknowledged.

VIII. REFERENCES

- [1] Y. Kikuchi, R. Yamauchi, M. Akiyama, O. Fukuda and K. Inada, "Polarimetric strain and pressure sensors using temperature-independent polarisation maintaining optical fibre," *Proc. 2nd Int. Conf. OFS.*, pp.395-398, 1984.
- [2] J.P. Dakin and C.A. Wade, "Compensated polarimetric sensor using polarisation-maintaining fibre in a differential configuration," *Electron. Lett.*, vol.20, no.1, pp.51-53, 1984.
- [3] H. Lefevre, D. Rojas and M. Turpins, "Optical fiber hydrophone and antenna associating a series of hydrophones," *US Patent* 4882716, 1989.

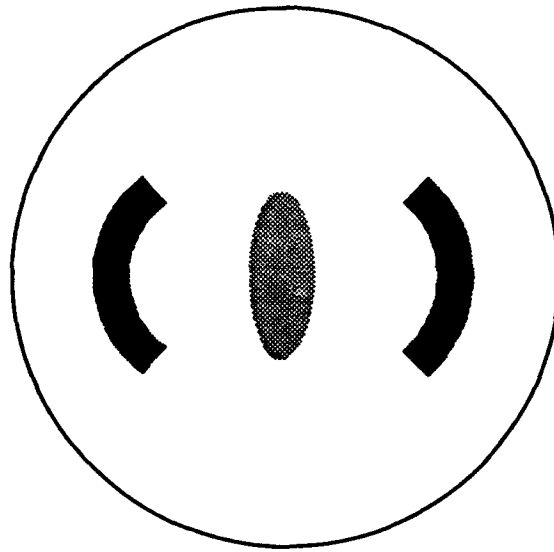


Figure 1 Cross-section of temperature insensitive polarimetric sensor fibre

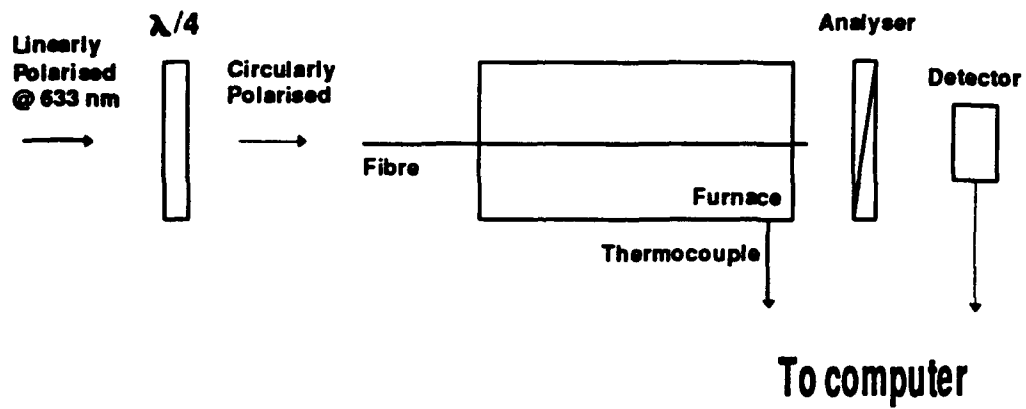


Figure 2 Experimental setup for measuring temperature sensitivity

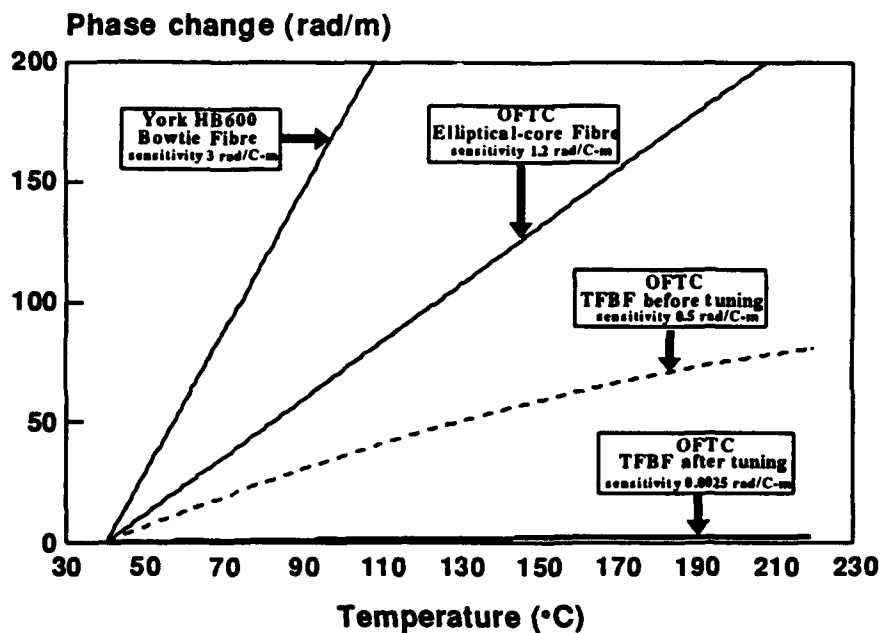


Figure 3 Measured phase sensitivity for the present fibre, before and after post-tuning, the York HB600 bowtie and OFTC AD023 elliptical-core fibres

Stress relief : proof of the mechanism of photo-induced index change

D. Wong, S.B.Poole and M.G.Sceats

Optical Fibre Technology Centre
University of Sydney
Sydney
Australia 2006

Abstract

It is demonstrated, for the first time, that stress-relief is responsible for the photo-induced index changes in optical fibres. This mechanism is a consequence of the breakage of wrong-bonds in the glass network through single- or multi-photo absorption, which allows relaxation of the stresses. The index changes through the stress-optic effect.

Introduction

One of the most exciting areas for current research in optical fibres is associated with the formation of periodic structures in the fibre core¹⁻³. These gratings have, to date, believed to be related in some way to the presence of germania-related colour centres^{4,5}, which are implicated in the phenomenon of second harmonic generation in fibres⁶ and non-linear power transmission⁷. The mechanism by which these colour centres produce an index change in the glass has, to date, also been unclear, with the various models in the literature being well summarised in the paper by Russell *et al*.⁸

The generally accepted model to date has been that of Russell⁸ in which the creation of GeE' centres from an oxygen deficient Ge-Si or Ge-Ge "wrong-bond" liberates electrons which are trapped at Ge(1) and Ge(2) acceptor sites. The index change was thought to arise from the optical properties of these colour centres, through the Kramers-Kronig relationship between absorption and refraction. However, this model has a number of shortcomings, most noticeably that the estimate of the magnitude of the refractive index change achievable through this process⁸ is two orders of magnitude less than observed experimentally⁹.

In recent work, we developed the hypothesis that the index change arises from a relaxation of the thermoelastic stresses in the core of the fibre¹⁰. The cores of germanosilicate fibres are under tension due to the difference in coefficients of thermal expansion between the core and cladding, with the stresses developed as the fibre is cooled during drawing. It is well known from the time of Brewster that tension reduces the refractive index - through the stress-optic effect - so that stress relief is expected to increase the refractive index, as is observed experimentally. For photo-refractive change, it is the intense uv-irradiation which breaks bonds in the glass network, hence promoting relaxation of the stresses.

In this paper, we report the results of an experiment designed to test our hypothesis. The hallmark of thermoelastic stress is its linear temperature dependence which is readily and quantitatively evaluated from a knowledge of the composition and structure of the optical fibre core. Stress relaxation by uv-processing should change the magnitude of this temperature dependence in a predictable manner. Small changes in refractive index are best measured using interferometry, and polarimetry has the advantage of eliminating problems associated with two-arm interferometer. Thus we use an elliptical core fibre in which the stress anisotropy induces a stress birefringence, and measure the temperature dependence of this birefringence by polarimetry before and after uv-irradiation. The geometric birefringence of the elliptical core fibre also gives rise to a birefringence which is opposite in sign and essentially temperature independent. A fibre design in which these terms are the same order of magnitude provides a convenient calibration. We demonstrate below that the temperature dependence of the fibre birefringence before and after uv-processing proves that stress relaxation accompanies uv-processing.

Experiment

Consider an elliptical core fibre, with the z-axis along the core. The stress contribution to the refractive indices n_x , n_y at any point in the fibre is related to the principal stresses σ_x , σ_y , σ_z at that point by

$$\begin{aligned} n_x &= n + C_1 \sigma_x + C_2 (\sigma_y + \sigma_z) \\ n_y &= n + C_1 \sigma_y + C_2 (\sigma_x + \sigma_z) \end{aligned}$$

At 633nm, the direct, C_1 , and transverse, C_2 , stress optical coefficients have the values $-7.7 \times 10^{-13} \text{ m}^2 \text{ N}^{-1}$ and $-4.1 \times 10^{-12} \text{ m}^2 \text{ N}^{-1}$, respectively. Table 1 shows the thermoelastic parameters, the calculated and measured phase sensitivities before UV irradiation. It can be seen that the theoretical sensitivity agrees well with the measured values. A reduction in the residual tensile stresses, in particular the differential stress in the core, will result in a corresponding reduction in phase sensitivity due to a reduction in stress birefringence. Stress relief can be achieved by, for example, UV irradiation.

Figure 1 shows the experimental setup used to determine the influence of uv-irradiation on the birefringence. A polarised 633nm He-Ne laser was launched into the birefringent fibre through a quarter-wave plate, to equally excite both polarisation modes in the fibre. A section of the fibre was placed in a 5 cm long furnace. At the fibre output, a polarising beam splitter, was used to decompose the output state of polarisation into two orthogonal components. The intensities of these two orthogonal components, I_1 and I_2 , were sensed by the two calibrated detectors, D_1 and D_2 , respectively. A computer with an analogue-to-digital converter card was used to sample and store the intensities on the detectors as well as the temperature of the furnace. The furnace temperature was kept below 90°C to avoid thermal annealing of the fibre which takes place around 200°C for the fibre used. Approx 2.5cm of the fibre was illuminated by an unpolarised pulsed excimer laser operating at 248nm, with up to 100,000 pulses at energy densities of up to 67 mJ cm^{-2} . All the illumination was carried out at room temperature.

A significant change of birefringence and transmission was observed during the irradiation. However, this could arise from a multitude of mechanisms. However, most of these mechanisms other than stress-relief would not give rise to a large reversible change in the temperature dependence of the birefringence. Figures 2a and 2b show the phase shift evaluated from the normalised intensity, $I_1/(I_1+I_2)$, plotted against temperature for different degrees of exposure to the UV laser light with pulse energy density 33.5 mJ cm^{-2} and 67 mJ cm^{-2} , respectively. In both cases, it can be seen that the temperature sensitivity falls, as expected for the stress-relief model. Since only 50% of fibre in the furnace is illuminated by the excimer laser, we would not expect to achieve total temperature insensitivity, but at most a 50% reduction (assuming complete stress relief of the illuminated region). Figure 3 shows the plot of the change in phase sensitivity to temperature with uv-exposure obtained from the results shown in Figure 2. As expected, the processing exhibits saturation. It can be seen that a 40% reduction in phase sensitivity was achieved, corresponding to some 80% stress relief in the illuminated region. This is a very large effect, and the unique temperature signature proves that significant stress relaxation accompanies uv-photolytic processing. This is the core of our hypothesis previously presented.

Conclusions

We have demonstrated that stress-relief is responsible for the photo-induced index changes in optical fibres. This mechanism is a direct consequence of the relaxation of the stressed glass network initiated by breakage of 'wrong bond' by the uv-light. This understanding should enable optimisation of fibres for in-line grating based fibre devices. In forthcoming work, we develop a model of the mechanism of such stress relief.

Acknowledgments

The authors would like to thank the Defects Group of the Optical Fibre Technology Centre for useful discussions and Dr Peter Krug for assistance with the Excimer laser. The sponsorship of the OFTC by AOTC Ltd is acknowledged. This work was partially funded under DITAC GIRD program 17011.

References

1. K.O.Hill, Y.Fujii, D.C.Johnson, B.S.Kawasaki, "Photosensitivity in Optical Fibre Waveguides: Application to reflection filter fabrication", *Appl. Phys. Lett.*, **32**, pp. 647-649, 1978.
2. G.Meltz, W.W.Morey, W.H.Glenn, "Formation of Bragg gratings in optical fibres by a transverse holographic method", *Opt. Lett.*, **14**, pp.823-825, 1989.
3. R.Kashyap, J.R.Armitage, R.Wyatt, S.T.Davey, D.L.Williams, "All-fibre narrow-band reflection gratings at 1500nm", *Electron. Lett.*, **26**, pp.730-732, 1990.
4. E.J.Friebele, "Defect centers in a germanium-doped silica-core optical fiber", *J. Appl. Phys.*, **45**, pp.3424-3428, 1974.
5. P.St.J.Russell, L.J.Poyntz-Wright, D.P.Hand, "Frequency Doubling, Absorption and Grating Formation in Glass Fibres: Effective Defects or Defective Effects?", *Proc SPIE Conf on Fiber Laser Sources and Amplifiers II*, Boston, SPIE Vol 1373, pp126-137, 1990.
6. U.Osterburg, W.Margulis, "Dye Laser Pumped by Nd:YAG Laser Pulses Frequency Doubled in a Glass Optical Fiber", *Opt. Lett.*, **11**, pp.516-518, 1986.
7. R.G.W.Brown, D.A.Jackson, J.D.C.Jones, R.K.Y.Chan, "High power fibre optic laser anemometry", *Proc ICO-13*, Japan, 1984.
8. D.L.Williams, S.T.Davey, R.Kashyap, J.R.Armitage, B.J.Ainslie, "Direct Observation of UV Induced Bleaching of 240nm Absorption Band in Photosensitive Germanosilicate Glass Fibres", *Electron. Lett.*, **28**, pp.369-371, 1992.
9. G.Meltz, W.M.Morey "Narrow Linewidth Fibre Devices", *OFC'92*, Technical Digest, pp.95, 1992.
10. M.G.Sceats, S.B.Poole, "Stress-Relief - The Mechanism of Photorefractive Index Control in Fibre Cores", *Proc. 16th Australian Conference on Optical Fibre Technology*, pp.302-305, 1991.

Parameters		Core	Cladding
Youngs Modulus	(GPa)	72.45	72.45
Poisson's ratio		0.171	0.171
Expansion coefficient	($\times 10^{-6} \text{ } ^\circ\text{C}^{-1}$)	1.673	5.0
Fictive temperature	($^\circ\text{C}$)	1519	1590
Stress-free index	@ 633nm	1.47338	1.45875
Semi-major axis of core	(micron)	1.87	
Semi-minor axis of core	(micron)	0.35	
Calculated phase sensitivity	($\text{rad}/^\circ\text{C}\cdot\text{m}$)	0.32	
Measured phase sensitivity	($\text{rad}/^\circ\text{C}\cdot\text{m}$)	0.40	

Table 1 Thermoelastic parameters, predicted and measured phase sensitivity of the elliptical-core fibre used.

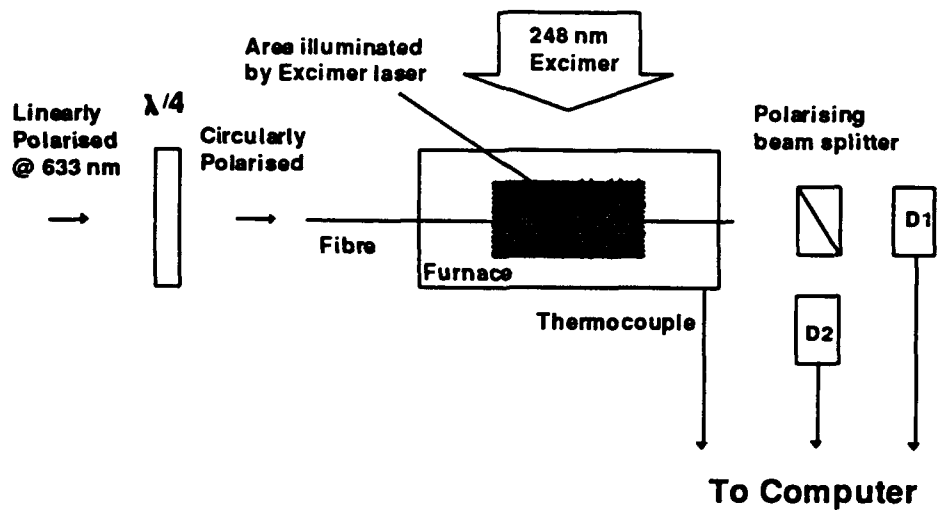


Figure 1 The experimental apparatus used to measure the in-situ birefringence of a fibre during uv-processing.

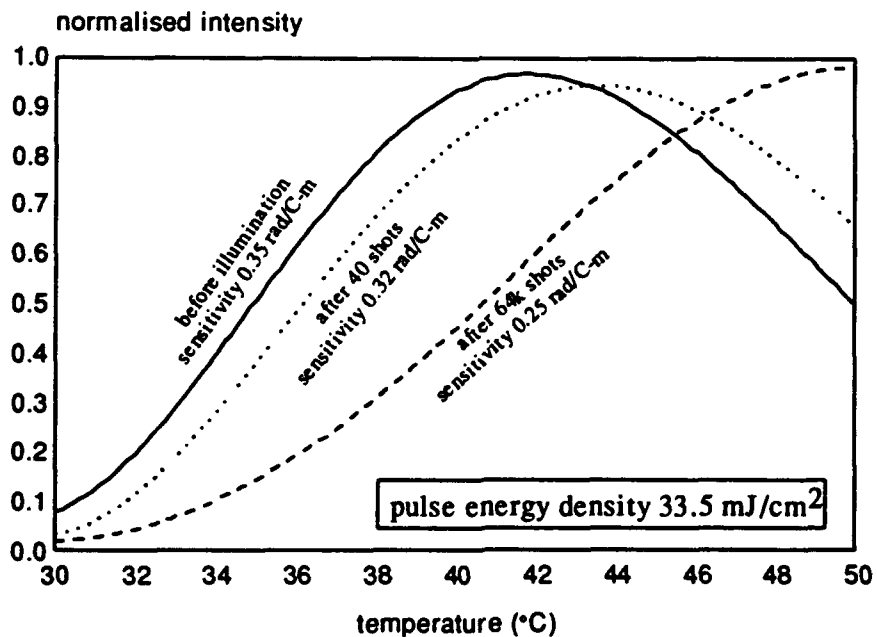


Figure 2a The temperature dependence of the polarimetric phase shift before and after UV processing by an excimer laser at 240nm with pulse energy density 33.5mJ cm⁻².

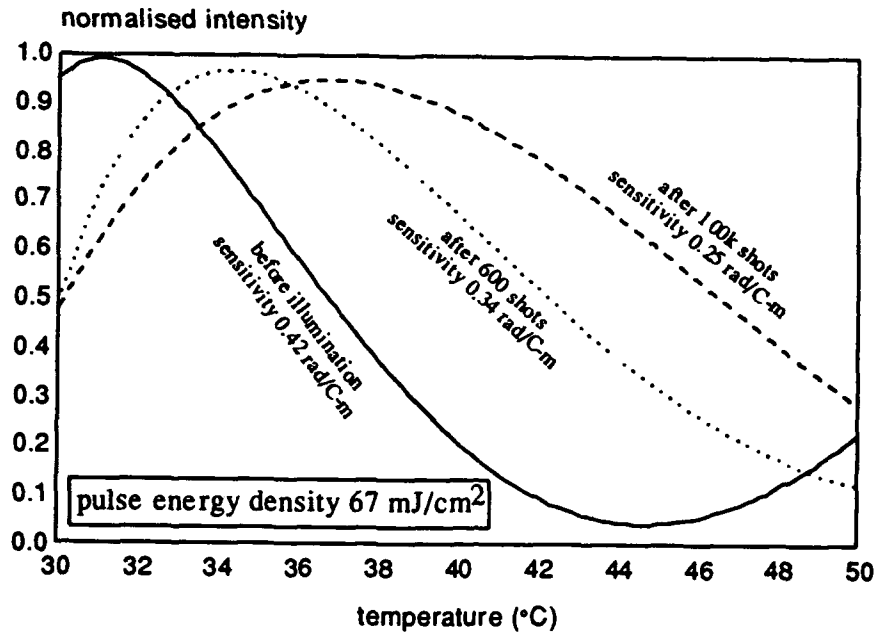


Figure 2b The temperature dependence of the polarimetric phase shift before and after UV processing by an excimer laser at 240nm with pulse energy density 67mJ cm⁻².

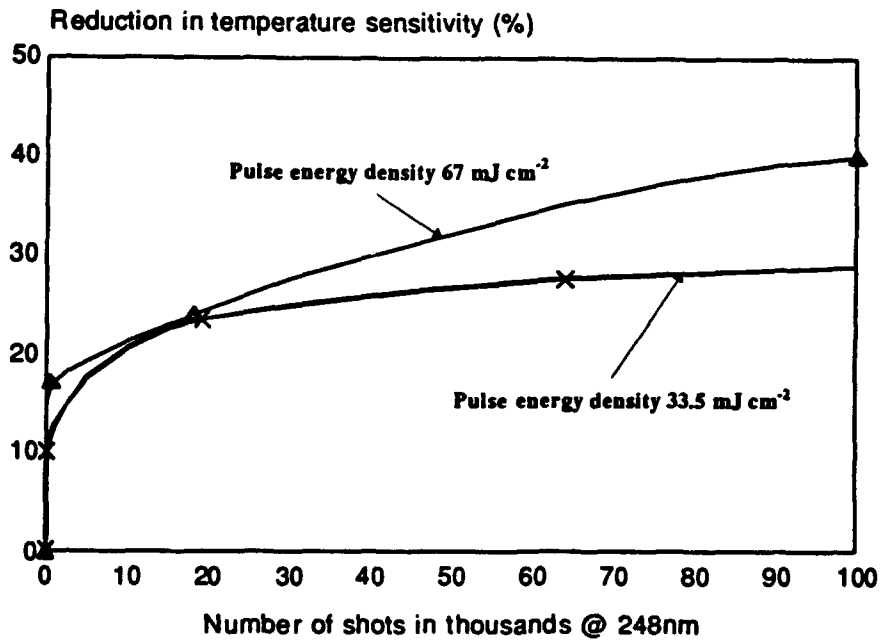


Figure 3 The temperature sensitivity of the polarimetric phase shift of an elliptical core fibre is plotted against exposure (number of pulses) to an excimer laser at 240nm.

Adar, Renen - PD04
Aitchison, J. Stewart - PD09
Andreadakis, N. - PD01

Bhat, R. - PD06
Blaauw, C - PD03
Brown-Goebeler, K. - PD07

Caneau, C. - PD01
Chiu, T. - PD07

Da Silva, Valeria - PD24
Daino, B - PD11
DeLaRue, R. - PD05
Dolfi, David - PD02
Dragone, C. - PD04

Edge, Colin - PD08

Fallahi, M - PD03
Ferguson, Allister - PD05
Fermann, Martin Emanue - PD24
Fontana, Flavio - PD11
Franco, Pierluigi - PD11

Glasner, Moses - PD12
Glinski, Jan - PD03

Grasso, G. - PD11

Han, T. - PD05

Henderson, Brian - PD05

Henry, C. - PD04

Hermansson, Bjorn - PD12

Ironside, Charles - PD05

Jiang, Pisu - PD05

Jones, Kevin - PD07

Judkins, Justin - PD14

Kistler, R. - PD04

Knight, Douglas Gordo - PD03

Koza, M. - PD06

LeBlanc, H. - PD01

Maciejko, Roman - PD03

Makino, T - PD03

Manfredini, N - PD11

Maritan, C - PD03

Midrio, Michele - PD11

Milbrodt, M. - PD04

Najafi, S. Iraj - PD03

Nolting, Hans-Peter - PD13

Oe, Kunishige - PD06

Poole, Simon - PD16

Ranganath, T. R. - PD02

Romagnoli, M - PD11

Sceats, Mark Geoffrey - PD16

Scherer, A. - PD01

Silberberg, Yaron - PD24

Smith, D.A. - PD24

Soole, Julian - PD01

Stegeman, George - PD09

Svilans, M - PD03

Tajani, A. - PD11

Tamburrini, Mario - PD11

Tell, B. - PD07

Templeton, I - PD03

Villeneuve, Alain - PD09

Wabnitz, Stefan - PD11

Wakita, Koichi - PD06

Wale, M - PD08

Walker, Robert - PD08

Weiner, Andrew - PD24

Wong, Danny - PD16

Wu, Chi - PD03

Yevick, David - PD12

Zhou, Feng - PD05

Ziolkowski, Richard - PD14

Zucker, Jane - PD07

TECHNICAL PROGRAM COMMITTEE

William Burns, *Conference Chair, Naval Research Laboratories*
Larry Coldren, *Program Chair, University of California, Santa Barbara*
Ray Hawkins, *Program Chair, Lawrence Livermore National Laboratory*

A. SUBCOMMITTEE ON PHOTONIC DEVICES AND CIRCUITS

Stephen Forrest, *Subcommittee Chair, University of Southern California*
Piers Dawe, *BNR Europe Harlow*
Tatsuo Izawa, *NTT*
Steve Korotky, *AT&T Bell Laboratories*
Kam Lau, *UC Berkeley*
Joe Lorenzo, *Rome Air Development Center*
Willie Ng, *Hughes Research Laboratories*
David Smith, *Bellcore*
Osamu Wada, *Fujitsu*

B. SUBCOMMITTEE ON NONLINEAR GUIDED-WAVE PHENOMENA

Yaron Silberberg, *Subcommittee Chair, Bellcore*
M. Cada, *Technical University of Nova Scotia*
M. Fejer, *Stanford University*
S. Friberg, *NTT Basic Research Labs*
H. Gibbs, *University of Arizona*
C. Ironside, *University of Glasgow*
M. Islam, *AT&T Bell Laboratories*
G. Khanarian, *Hoechst Celanese*
A. Snyder, *Australian National University*
D. Weinberger, *University of Michigan*

C. SUBCOMMITTEE ON MODELING, NUMERICAL SIMULATION, AND THEORY

Curtis R. Menyuk, *Subcommittee Chair, University of Maryland Baltimore County*
Govind Agrawal, *University of Rochester*
Keith Blow, *British Telecom Research Laboratories*
Anand Gopinath, *University of Minnesota*
Paul Lagasse, *Rijks Universitet Gent*
Daan Lenstra, *Technische Universiteit Eindhoven*
H. P. Nolting, *Heinrich Hertz Institute fuer Nachrichten*
Shunji Seki, *NTT Opto-Electronics Laboratory*
Akira Shimizu, *Sakaki Quantum Wave Project*
Herbert Winful, *University of Michigan*

D. SUBCOMMITTEE ON PHYSICS, MATERIALS, TECHNOLOGY AND CHARACTERIZATION

Joe C. Campbell, *Subcommittee Chair, University of Texas-Austin*
Harold Craighead, *Cornell University*
P. D. Dapkus, *USC*
T. Findakly, *Hoechst Celanese Corporation*
T. Koch, *AT&T Bell Laboratories*
Alan Mickelson, *University of Colorado*
K. Oe, *NTT*
W. T. Tsang, *AT&T Bell Laboratories*

E. SUBCOMMITTEE ON ACTIVE AND PASSIVE FIBER COMPONENTS

Roger Stolen, *Subcommittee Chair, AT&T Bell Laboratories*
E. Desurvire, *Columbia University*
M. J. S. Dignonet, *Stanford University*
W. L. Emkey, *AT&T Bell Laboratories*
W. J. Miniscalco, *GTE*
D. A. Nolan, *Corning*
K. Okamoto, *NTT Optoelectronics Laboratories*
S. Poole, *University of Sydney*
W. J. Stewart, *Plessey*
W. J. Tekippe, *Gould*

INTEGRATED PHOTONICS RESEARCH 1992 ADVISORY BOARD

W. J. Tomlinson, *Chair, Bellcore*
W. K. Burns, *U.S. Naval Research Laboratory*
W. S. C. Chang, *University of California, San Diego*
L. A. Coldren, *University of California, Santa Barbara*
F. J. Leonberger, *United Technologies Research Center*
G. I. Stegeman, *University of Central Florida*
R. H. Stolen, *AT&T Bell Laboratories*